Aston University

Some pages of this thesis may have been removed for copyright restrictions.

If you have discovered material in AURA which is unlawful e.g. breaches copyright, (either yours or that of a third party) or any other law, including but not limited to those relating to patent, trademark, confidentiality, data protection, obscenity, defamation, libel, then please read our Takedown Policy and contact the service immediately

STRUCTURE AND FUNCTION IN PRIMARY OPEN ANGLE GLAUCOMA

SHIRLEY ANN HANCOCK

Doctor of Philosophy

ASTON UNIVERSITY

September 2000

This copy of the thesis has been supplied on condition that anyone who consults it is understood to recognise that its copyright rests with its author and that no quotation from the thesis and no information derived from it may be published without proper acknowledgement.

Aston University

Structure and Function in Primary Open Angle Glaucoma

Shirley Ann Hancock

Doctor of Philosophy

2000

The study utilised a Normal group, an Ocular Hypertensive (OHT) group and a Primary Open Angle Glaucoma (POAG) group to investigate two aspects. Firstly, the within- and between-visit variability for stereometric measurements of the optic nerve head (ONH) using the Heidelberg Retina Tomograph (HRT); retinal nerve fibre layer (RNFL) thickness using the HRT and using optical coherence tomography with the Optical Coherence Tomography Scanner (OCT); the visual field using white-on-white (W-W), short-wavelength (SWAP) and Frequency Doubling perimetry (FDT); and retinal haemodynamics using the Heidelberg Retinal Flowmeter (HRF). Secondly, the association demonstrated between some of the derived variables.

The within- and between-visit variability for stereometric measurements of the entire ONH and the between-visit variability for sectoral measurements were similar for Normals and OHTs but greater for POAGs.

The within-visit variability of the visual field pointwise parameters for SWAP were greater than for W-W and FDT particularly with increase in eccentricity and for the OHT group. The between-visit variability increased with increase in defect depth for the POAG group, across all types of perimetry. The MS was greater, the MD and PSD smaller and the examination duration shorter in FDT compared to W-W and SWAP across all groups.

The within-visit variability was less than the between-visit variability for the OCT circumferential and sector RNFL thickness using the 1.5R, 2.0R and the fixed 1.73mm circular scan radii, across the three groups. The variability increased with decrease in the RNFL thickness, and was least for the 2.0R scan radius.

The within- and between-visit variability in HRF blood volume, flow and velocity was similar for the Normal and the POAG group, but greater for the OHT group.

The Global OCT RNFL thickness correlated ($R^2 \geq 0.25$) with the HRT stereometric parameters of mean RNFL thickness, CA, CDAR, RDAR and CSM across the three scan radii. The relationship between the OCT RNFL thickness and the MD and PSD for W-W and FDT was curvilinear.

Selected structural and functional parameters determined using the HRT, OCT or FDT perimetry provide a clinically acceptable test-retest performance for individuals diagnosed as normal, OHT or POAG.

HRT, FDT, OCT, HRF, Test-Retest

To

My dear Jonathan

ACKNOWLEDGEMENTS

I would like to thank my supervisor, Dr John Wild, for his advice, encouragement and help.

I am also very grateful to: Mr Ian Cunliffe, for his help with the recruitment and assessment of ocular hypertensive and glaucoma patients, and normal volunteers; the staff of the Ophthalmology Department at Birmingham Heartlands Hospital, for access to the facilities and photographic expertise. I am also grateful to Mr David Shaw for his statistical advice and all of the subjects and patients who volunteered to take part in the clinical studies.

Finally, I would like to thank my dear and loving parents, Bill and Bett, and especially my darling husband, Jonathan for their support particularly during my studies at Aston University.

LIST OF CONTENTS

LIST OF TABLES

LIST OF FIGURES

CHAPTER 1. STRUCTURAL AND FUNCTIONAL ASPECTS OF PRIMARY OPEN ANGLE GLAUCOMA.

1.1 Introduction.

Glaucoma is a major cause of blindness in the western world (Ghafour et al. 1983) and is considered to be a progressive optic neuropathy whose pathogenesis, though unclear, is multifactorial (Anderson 1989; Drance 1992; Drance 1997). Evidence suggests that there is both a mechanical and a vascular origin to the pathogenesis of glaucoma (Sommer 1991; Van Buskirk and Cioffi 1992; Sonnsjo and Krakau 1993; Fechtner and Weinreb 1994).

1.2 Epidemiology.

It is generally accepted that the risk factors for glaucomatous optic neuropathy include raised intraocular pressure (IOP) (Sommer 1991), myopia (Perkins and Phelps 1982), age (Tuck and Crick 1998), Afro-Caribbean race (Tielsch et al. 1991b), family history of glaucoma (Tielsch et al. 1994), diabetes (Becker 1971), systemic hypertension (Wilson et al. 1987) and vascular dysregulation (Flammer et al. 1999). Clinical observation and extensive evidence supports the concept of single and/or multiple aetiologies to account for the continuum of normal tension glaucoma, ocular hypertension and high tension glaucoma, namely, sustained or transient periods of abnormally high IOP, mechanical weakness of the connective tissue within the optic nerve head with between-individual vulnerability of the actual neural tissue and ischaemic neuropathy (Minckler and Spaeth 1981; Leske 1983; Radius 1987; Wilson 1990; Fechtner and Weinreb 1994).

The prevalence of POAG in Caucasians over the age of 40, has been estimated from a number of studies to be approximately 0.5-2% (Hollows and Graham 1966; Bengtsson 1981; Tielsch et al. 1991a; Tielsch et al. 1991b; Klein et al. 1992; Coffey et al. 1993; Tuck and Crick 1998). Age (Tuck and Crick 1998) and race (Wilensky et al. 1978; Tielsch et al. 1991b) appear to have a profound effect on the prevalence. Virtually no cases of primary open angle glaucoma occur before the age of 40, the prevalence rises to 1.3% at 55-74 years and approximately 4% over the age of 80 years (Leske 1983; Tuck and Crick 1998). The difference in prevalence with increasing age is exacerbated by ethnicity, with African-Caribbeans having at least two and a half times the prevalence found for Caucasians (Wilensky et al. 1978). With age-adjusted prevalence rates African-Caribbeans exhibit four to five times greater risk than Caucasians (Tielsch et al. 1991b) The influence of gender is equivocal (Armaly 1965; Wilson 1990); however, incidence rates are higher in women (Wilson 1990). Variations in published estimates arise from differing definitions of the condition, different sampled populations and differing methods of sampling (Leske 1983). The prevalence of ocular hypertension (OHT) defined as an IOP value of $\geq$ 21mmHg in a person with normal optic disc appearance, normal anterior eye segment and a normal visual field, is considerably greater than for primary open angle

glaucoma, and has been estimated to be as high as 8.6% (Hollows and Graham 1966). Community-based studies may overestimate the risk associated with a family history of glaucoma as a result of health care promotion campaigns (Tielsch et al. 1994). Hospital-based studies may overestimate the association with myopia (Perkins and Phelps 1982) and diabetes (Becker 1971) through selection bias, since these conditions may be referred more often following more frequent community review procedures (Fraser et al. 1999).

The incidence, derived from a number of prevalence curves (Tuck and Crick 1998), of primary open angle glaucoma per year has been estimated at 0.02% per year for 40 year olds increasing to about 0.17% per year for 70 year olds, but the insidious onset makes the early recognition of POAG difficult.

The diagnosis of glaucoma is usually based upon a consideration of the level of IOP, appearance of the optic nerve head (ONH), and of the visual field and upon the presence of risk factors. Glaucomatous damage has been experimentally produced by acutely (Quigley and Anderson 1976) and chronically (Gaasterland et al. 1978; Quigley and Addicks 1980), raising the IOP in animals. The induced damage suggests a mechanical element in the pathogenesis of glaucoma. Indeed, in human, a unilateral elevation of the intraocular pressure is associated with unilateral optic disc cupping and visual field abnormalities (Caprioli et al. 1987a; Crichton et al. 1989). However, surgically lowered IOP in monkey and human does not unequivocally prevent or reduce glaucomatous damage. In human, some individuals show glaucomatous damage in the absence of elevated IOP (Levene 1980) and some do not appear to develop damage even in the presence of IOP values generally considered to lie above the statistically normal range (Quigley et al. 1994). The fact that IOP, alone, also does not reliably predict glaucomatous progression, may, in part, be attributable to the definition of a normal range. Armaly (1965), described a Gaussian distribution for IOP under the age of 40 years, and a positively skewed distribution across the entire range. For those under 40 years, the mean IOP (15mm Hg) plus 2 standard deviations (6mmHg) provided an upper 95% confidence limit of 21mmHg. The clinical significance of a single, value of IOP is influenced the vascular perfusion of the ONH (Hayreh 1997b) and the state of the neural and supportive tissue at the lamina cribrosa (Hernandez et al. 1990), and subject to the diurnal variation in IOP (Wilensky 1991).

1.3 Site of glaucomatous damage.

It is recognised that the site of damage in glaucomatous optic neuropathy is at the level of the lamina cribrosa (Anderson and Hendrickson 1974; Quigley et al. 1981; Quigley et al. 1983). Interference of axoplasmic flow caused by pressure-induced compression and misalignment of pores in the lamina has been demonstrated in monkey (Quigley and Addicks 1980). The axonal transport abnormality is limited to the level of the lamina cribrosa, and correlates with elevated IOP (Anderson and Hendrickson 1974). Neurotrophin deprivation caused by axonal transport blockade from periods of elevated IOP, and glutamate toxicity associated with ischaemia, are

two of the stimuli believed to trigger cell atrophy through apoptosis. (Osborne et al. 1999). Histological observations of the retinal ganglion cells, using light and electron microscopy indicate that ganglion cell atrophy is by apoptosis (Quigley et al. 1995). Chromatin accumulates in the nuclear envelope of the cell and eventually fills the nucleus. The cell then breaks into fragments and is rapidly phagocytosed by adjacent cells without the inflammatory response found with necrosis (Nickells 1996). However, the strong evidence for the rapid apoptosis occurring in experimental glaucoma has not been replicated in human as the disease process is much slower and fewer apoptotic cells are available for identification in autopsied eyes. Atrophy of axons within the neural rim causes the rim tissue to become progressively thinned. The rim collapses outwards, with an associated diffuse or focal enlargement (Airaksinen and Drance 1984) and an excavation of the cup (Emery et al. 1978). Progressive atrophy of the nerve tissue leads to both diffuse and focal thinning of the retinal nerve fibre layer, across the retina (Airaksinen and Alanko 1983).

1.4 Imaging in Glaucoma.

Examination of the ONH and evaluation of the retinal nerve fibre layer (RNFL) are the most reliable clinical methods for detecting glaucomatous optic neuropathy. Evaluation of the disc is considered to be more sensitive in detecting the earliest signs of glaucoma than perimetry (Zeyen and Caprioli 1993; Jonas and Grundler 1997) and clinically detectable changes in the RNFL have been found to precede the onset of visual field loss in glaucoma (Sommer et al. 1977; Quigley et al. 1980).

Various techniques have been employed to quantitatively document the topography of the ONH. Topographical analysis relies on accurate and reliable identification of the optic disc and cup margins, both of which can be obscured by overlying blood vessels or oblique insertion of the optic nerve in the scleral canal (Rohrschneider et al. 1994; Burk et al. 2000). Direct and indirect ophthalmoscopic examination of the ONH topography for cup-disc ratio (CDR) estimation is quite variable even between glaucoma experts (Lichter 1976). The diagnostic precision of the vertical CDR in predicting the integrity of the visual field is limited (Damms and Dannheim 1993; O'Connor et al. 1993). The diameter of the optic disc and of the optic cup covary, such that the CDR is dependent on the optic disc size (Bengtsson 1976). The predictive power limit of the CDR is partially attributable to the large normal between-subject variability of the optic disc size and ONH configuration.

Stereo-photography of the ONH permits quantitative measurements of the optic disc, cup and neuroretinal rim. Stereo-photographs can be achieved from either simultaneous or sequential acquisition of images, provided care is taken to ensure that the film plane of the fundus camera is kept parallel to the fundus image (Hitchings et al. 1993). Manual (Damms and Dannheim 1993) and computer-assisted planimetry (Odberg and Riise 1985; Jonas et al. 1988a; O'Connor et al. 1993) of stereophotographs permits the measurement of the cup and disc diameter, CDR,

neuroretinal rim width, and cup, disc and neuroretinal rim areas. Within- and between-observer reliability of the estimation of the CDR improve with stereoscopic viewing (Tielsch et al. 1988), although a lack of between-observer agreement as to the contour of the ONH influences the reliability of between-observer assessments (Varma et al. 1992). Computerised-assisted planimetry reduces the time necessary for analysis (Mikelberg et al. 1986a) and improves within- and between-observer reproducibility (Caprioli et al. 1986). Stereophotogrammetry uses simultaneously acquired stereophotographs to provide measures of three-dimensional (volumetric) optic disc parameters (Takamoto and Schwartz 1993). Measurements of photographic images are generally corrected using Littmann's method (1992) to account for variations in ocular magnification introduced by refractive error, axial length and corneal power. The correction permits comparison between individuals; however, the use of a single magnification correction value is not appropriate for all fundus imaging systems (Rudnicka et al. 1998).

The development of confocal laser scanning tomography has provided access to high quality three-dimensional imaging and quantitative analysis of the ONH (Webb et al. 1987). The technique is accurate (Janknecht and Funk 1994) and highly reproducible (Cioffi et al. 1993; Lusky et al. 1993; Mikelberg 1993; Rohrschneider et al. 1994) for topographical measurements of the ONH. Much of the early reproducibility and validation evidence was obtained with the Laser Tomographic Scanner (LTS) (Heidelberg Instruments, GmbH, Heidelberg, Germany) (Kruse et al. 1989; Dreher et al. 1991; Dreher and Weinreb 1991), whilst later studies are based upon the Heidelberg Retina Tomograph (HRT), (Heidelberg Instruments) (Mikelberg 1993; Weinreb et al. 1993; Chauhan and LeBlanc 1994; Brigatti et al. 1995; Chauhan and Macdonald 1995; Janknecht and Funk 1995). Initially, it was claimed that pupillary dilation was unnecesary to achieve highly reproducible topographic data provided the pupil diameter was greater than 1.5mm (Lusky et al. 1993). However, errors can arise from misalignment of the scanner when imaging through very small or very large pupils (Tomita and Honbe 1994; Zangwill et al. 1997). It has subsequently been shown that image quality can be marginally improved with pupillary dilation, particularly where the images are degraded by the presence of cataracts.

With the HRT, a diode laser beam (670nm) is directed onto the retina via a confocal optical system. The scanning beam is deflected horizontally and vertically across the x-y plane to create a two-dimensional optical image conjugate with the focal plane of the instrument. A further 31 consecutive scans are performed at a series of progressively deeper focal planes along the z-axis within a scanning depth range of 0.5 to 4.0mm. From the series of optical sections created, height positions of maximum reflectivity are calculated for each of 256 x 256 pixels contained within the image to create both a reflectivity and a topography image. Images can be viewed and analysed separately, or alternatively, combined or contrasted with one or more further acquired images. An area of interest can be subsequently defined by the operator and various stereometric measurements can be generated to describe topographical features within the image.

Single stereometric parameters of the ONH, determined by the HRT permit differentiation between glaucomatous and normal eyes (Uchida et al. 1996; Iester et al. 1997b). Improved discrimination can be achieved by either using a combination of parameters (Mikelberg 1995; Bathija et al. 1998; Mardin et al. 1999); selecting parameters which are independent of the reference plane (Uchida et al. 1996; Iester et al. 1997b); using sector analysis particularly where localised damage is suspected (Iester et al. 1997c; Emdadi et al. 1998; Iester et al. 1998); or stratifying the results according to optic disc size (Iester et al. 1997a; Iester and Mikelberg 1997; Bathija et al. 1998; Mardin and Horn 1998; Wollstein et al. 1998). Despite the wide between-individual variation in the appearance of the normal and of the glaucomatous ONH a limited association is present between many of the optic disc parameters derived by the HRT and the functional parameters obtained with automated static perimetry (Brigatti and Caprioli 1995; Yamagishi et al. 1997; Emdadi et al. 1998; Iester et al. 1999a).

Evidence suggests that changes in retinal nerve fibre layer (RNFL) and retinal thickness may precede ONH changes, including cupping (Quigley et al. 1980). Reports have claimed that between 20% and 40% of optic nerve axons may be lost prior to visual field damage determined by kinetic perimetry (Quigley et al. 1982a). Vogt (1917) introduced the concept of red-free illumination for ophthalmoscopic evaluation of the RNFL, and his method was later adapted by Hoyt (1972) for observing nerve fibre defects associated with optic nerve disease. Hoyt and colleagues (1972) originally demonstrated RNFL defects in glaucoma, and subsequent reports have suggested that RNFL evaluation can provide evidence of glaucomatous damage prior to clinically detectable nerve head changes. (Sommer et al. 1977; Airaksinen and Alanko 1983). High resolution red-free images of the parapapillary retina and arcades now provides qualitative information about the integrity of the RNFL (Sommer et al. 1983; Airaksinen and Nieminen 1985; Peli et al. 1987; Jonas and Schiro 1994). However, a large between-individual normal variability in ganglion cell and optic nerve fibre count results in between-individual variations in the normal RNFL thickness (Mikelberg et al. 1989). The distribution and course of the axonal bundles towards the ONH is also known to vary (Radius 1979). Glaucomatous damage tends to cause loss of axons mainly at the superior and inferior neuroretinal rim with the subsequent reduction in nerve fibre layer thickness. Focal wedge-shaped defects in the RNFL are more readily discerned than diffuse loss particularly in the superior and inferior parapapillary regions (Jonas and Schiro 1994).

Several other non-invasive techniques are used to quantitatively evaluate the RNFL thickness, including photogrammetry (Takamoto and Schwartz 1989), scanning laser ophthalmoscopy (Burk et al. 1998; Caprioli et al. 1998; King et al. 2000), scanning laser polarimetry (Weinreb et al. 1995b; Tjon-Fo-Sang et al. 1996; Morgan et al. 1998) and optical coherence tomography (Schuman et al. 1995b; Pieroth et al. 1999). Measurements of the RNFL have been compared between techniques (Weinreb et al. 1995b; Caprioli et al. 1996; Mistlberger et al. 1999) with various ONH parameters (Tsai et al. 1995b; Weinreb et al. 1995a; Iester et al. 1998) and with

perimetric findings (Caprioli et al. 1998; Pieroth et al. 1999; Shirakashi et al. 1999). The attenuated RNFL thickness in primary open angle glaucoma is consistent with the loss of neuroretinal rim and the enlargement of the optic cup and with visual field loss.

1.5 Perimetry in Glaucoma.

Considerable loss of retinal nerve fibre tissue occurs prior to functional impairment being detected with conventional automatic static threshold perimetry using a white stimulus on a white background (W-W) (Quigley et al. 1989). A 'lead' time of up to 5 years has been reported in some cases whereby RNFL damage occurs prior to field loss (Airaksinen and Heijl 1983; Sommer et al. 1991). The ensuing disruption of ganglion cell function can be assessed by suitable psychophysical testing strategies (Stewart and Chauhan 1995).

The ganglion cell population is not homogenous (Dacey 1994) being comprised of broadly two groups, those that project to the magnocellular layers (M-cells) in the lateral geniculate nucleus (LGN) and those destined for the parvocellular layers (P-cells). Animal studies have provided evidence for the different anatomical and physiological properties of the ganglion cells. The M, or parasol cells, are widely distributed have relatively large cell bodies, axonal diameters, and receptive fields (Silveira and Perry 1991; Lee 1996). The response of the M cells to high temporal and to low spatial frequencies is larger than that of the P-cells and the M cells are thought to be involved in motion and high-frequency flicker perception (Lennie 1980). The P, or midget cells tend to be concentrated within the foveal region, and decline rapidly with increase in eccentricity (Dacey 1993b). The P cells have small cell bodies, axonal diameters and receptive fields and account for about 80-90% of the total retinal ganglion cell population (Lee 1996). The P-cells exhibit red-green on- or off-centre colour-opponency; their response differs with stimulus wavelength and they are considered to be responsible for chromatic information processing. They are more responsive to high spatial and low temporal frequency stimuli (Shapley 1993).

Midget cells, however, are not the only ganglion cells that project to the parvocellular layers. A group of ganglion cells, the small bi-stratified ganglion cells, have larger cell bodies and receptive fields than the midget cells and are more sparsely distributed across the retina (Rodieck 1991). The small bi-stratified cells receives input from the short-wavelength sensitive (SWS) cones, opposed by the combined input from the medium wavelength sensitive (MWS) cones and long wavelength sensitive (LWS) cones and convey the SWS cone excitatory signals to the parvocellular layers of the LGN (Dacey 1993a).

Histological studies also suggest that some ganglion cell types may be more susceptible to glaucomatous damage than others (Quigley and Sanchez 1987). Optic nerve axon counts in monkey and human glaucoma show a greater loss of the larger than average diameter axons compared to those in the normal optic nerve (Quigley and Sanchez 1987; Quigley et al. 1988;

Mikelberg et al. 1989). Similarly, a scarcity of large diameter cells has been observed in prepared sections of retinal tissue from glaucomatous eyes (Quigley et al. 1989; Glovinsky et al. 1991) which suggests that the large cells are more susceptible to glaucomatous damage (Quigley 1986; Quigley and Sanchez 1987). Since cell size correlates with cell type, it is argued that the M-cells are likely to be more at risk of damage (Glovinsky et al. 1991). The use of psychophysical tests, sensitive to and specific for M-cell properties, might provide a means to detect early glaucomatous damage.

Despite strong evidence for selective functional damage to the M pathway (Silverman et al. 1990; Anderson and O'Brien 1997), some doubts exist as to the interpretation of the histological findings (Morgan 1994). In reviewing the literature, Morgan concluded that the selective cell death could be attributed to cell shrinkage and errors in the cell labelling technique. Curcio (1990), remarked that the use of small sample sizes and the large normal between-individual variability in cell size, frequency and population within a given location together with the changes in cell size due glaucomatous damage and variations in tissue preparation could all confound the results.

The parvocellular and the magnocellular pathways both sustain damage in glaucoma (Vogt et al. 1998; Weber et al. 1998). However significantly greater damage occurs in the magnocellular pathway compared to the parvocellular pathway in ocular hypertension (Vogt et al. 1998). Abnormal results for temporal modulation perimetry and short-wavelength automated perimetry (SWAP) have also been shown prior to white-on-white (W-W) perimetric deficits which also suggests that ganglion cell loss may not be pathway specific (Casson et al. 1993).

Selective and non-selective losses of ganglion cell types may be occurring at different locations within the visual field and at different times of the disease course dependent on the pathogenesis and stage of glaucoma damage. Indeed, it is known that the dendritic arbors of the ganglion cells in the monkey glaucoma model are reduced prior to either reduction of the soma size or attenuation of the axon thickness (Weber et al. 1998). Functional loss should theoretically be detected at an earlier stage compared to conventional W-W perimetry if selective test stimuli either stimulate a sparsely represented subgroup of ganglion cells (the reduced redundancy hypothesis) or stimulate ganglion cells that are preferentially vulnerable to early glaucomatous damage (the selective loss hypothesis) (Johnson 1994). It can be argued that functional evaluation using a variety of selective tests that provide complimentary evidence of early change may prove most effective.

A test considered capable of evaluating the integrity of the magnocellular pathway is Frequency Doubling Technology (FDT) Perimetry (Johnson and Samuels 1997; Quigley 1998). The stimuli consist of a low spatial frequency (0.25 or 0.5cycles per degree) sinusoidal, black and white, grating which undergoes high temporal frequency counterphase flicker (25Hz). The perceived stimulus, for most individuals, is of a flickering, vertically striped, black and white target whose

spatial frequency appears to have twice the fundamental spatial frequency. The stimulus is reportedly less susceptible to blur and to the influence of media opacities (Sponsel et al. 1998). Variability does not increase with eccentricity out to 20° but as would be expected increases with increase defect depth (Chauhan and Johnson 1999). The use of suprathreshold FDT perimetry has been advocated for the screening of glaucoma (Quigley 1998). Threshold FDT perimetry, yields similar results to conventional automated threshold static perimetry both in normal volunteers (Adams et al. 1999), and glaucoma patients (Johnson and Samuels 1997; Chauhan and Johnson 1999; Johnson et al. 1999).

Acquired colour vision defects have been demonstrated in optic nerve and retinal disease, including, primary open-angle glaucoma (Hart 1987). The form of dyschromatopsia described in primary open-angle glaucoma indicates that the short-wavelength sensitive (SWS) pathway is vulnerable. With careful selection of chromatic and luminance properties for the background illumination and the stimulus, it is possible to isolate a subset of the ganglion cells that are specifically sensitive to short-wavelength stimuli (Demirel and Johnson 2000). Commercially available short-wavelength automated perimetry (SWAP) utilises a yellow filtered background with a luminance of $100cdm^{-2}$ to saturate the long- and medium-wavelength system, and suppress rod photoreceptor activity, whilst a narrow-band blue 440nm filter, Goldmann size-V target stimulates the short-wavelength pathway. The coexistence of age-related cataract and glaucoma is common in the elderly population. The presence of media opacities in SWAP can mimic the pattern of diffuse glaucomatous loss (Moss et al. 1995), whilst macular pigment absorption causes a depression in the foveal peak (Wild and Hudson 1995). Studies using SWAP generally compensate for the effect of ocular media absorption on the short-wavelength stimulus by comparing the results from the abnormal eye with those from the age-matched normal eye (Sample et al. 1994; Sample et al. 1997a), however, attempts to determine and correct for ocular media (Sample and Weinreb 1990; Johnson et al. 1993b; Johnson et al. 1993a; Sample et al. 1993; Johnson et al. 1995) and macular pigment absorption (Wild and Hudson 1995) on an individual basis are not clinically viable. The stimulus parameters used in the commercially available SWAP produces a greater within- and between-individual variability (Wild and Moss 1996) than that present with a broadband blue stimulus filter and a higher background luminance (Hudson et al. 1993).

Deficits have been reported for SWAP at locations that subsequently develop W-W defects both in ocular hypertension and in glaucoma suspects (Johnson et al. 1993a; Sample et al. 1993). SWAP has also been shown to identify progressive visual field loss, both in the extent and in the depth of defect, in glaucoma earlier than for W-W perimetry (Sample and Weinreb 1992; Johnson et al. 1993b). SWAP defects in ocular hypertension are associated with age and vertical cup-to-disc ratio, but surprisingly not the level of IOP or a family history of glaucoma (Johnson et al. 1995). SWAP defects, also correlate with RNFL defects determined by red-free photography (Polo et al. 1998). However, the normal within- and between-individual short-term and long-term variability is greater for SWAP than for W-W perimetry (Wild and Moss 1996).

Both the fatigue and the learning effects appear to contribute to wider confidence limits for normality with SWAP and further reduce the clinical benefits of this test (Cubbidge 1997; Pacey 1998).

1.6 Ocular Blood Flow in Glaucoma.

The hypothesis for a vascular involvement in the pathogenesis of glaucoma has wide support (Minckler and Spaeth 1981; Sonnsjo and Krakau 1993; Hayreh 1995; Flammer and Orgül 1998). Opinions differ as to the primary or secondary nature of this involvement. Glaucomatous optic neuropathy is frequently associated with diabetes (Leske 1983), systemic hypertension (Leske 1983) and vasospastic disorders (Broadway and Drance 1998), including migraine (Phelps and Corbett 1985) which suggests an impaired autoregulatory system (Wilson et al. 1987). Optic disc haemorrhages have also been associated with the presence of glaucoma and are considered to be a sign of ischaemia from micro-infarction within the ONH. The location of haemorrhage provides an indication of the site for future development of RNFL abnormalities (Airaksinen et al. 1981). Since damage is considered to occur initially at the level of the lamina cribrosa, evaluating the state of the ocular circulation in this region is of great importance (Williamson 1994). However, despite attempts to obtain direct information in human about the complex vascular bed in the lamina region, there is no single method that can yet provide reliable clinical information about ONH blood flow (Hayreh 1997a; Harris et al. 1998b). This presents an obstacle to acquisition of direct evidence for a vascular theory. Investigations have been largely confined to the larger retrobulbar vessels using colour Doppler imaging (Williamson and Harris 1996) or the central retinal artery and choroid using semi-invasive fundus fluorescein angiography or indocyanine green angiography (Hayreh 1997a). It has been suggested that the haemodynamic parameter of pulsatile ocular blood flow (POBF) may be useful in the assessment of glaucoma. POBF theoretically reflects the pulsatile component of arterial inflow of blood to the intraocular structures, and is derived mathematically from recordings of ocular pulse pressure changes (Silver and Farrell 1994; Yang et al. 1997). The introduction of laser Doppler flowmetry (LDF) (Riva et al. 1981; Joos et al. 1997) and confocal scanning laser Doppler flowmetry (SLDF) (Michelson and Schmauss 1995), has allowed measurement of the blood flow on the surface of the optic disc and through the capillaries in the retina. Knowledge of vessel calibre is necessary to calculate absolute values for blood flow, however there is evidence that despite several limitations of these techniques, glaucoma is associated with reduced ocular blood flow (Michelson et al. 1996a; Nicolela et al. 1996a; Nicolela et al. 1996b; Fontana et al. 1998; Grunwald et al. 1998; Kerr et al. 1998).

1.7 Progression of Glaucomatous Damage.

Morphological evidence suggests that chronically elevated IOP that interferes with the axoplasmic flow at the lamina cribrosa (Anderson and Hendrickson 1974) leads to a reduced dendritic field of the ganglion cells (Weber et al. 1998). Clinically the anatomical change to the dendritic field may contribute to the functional evidence of damage demonstrated by reduced

pattern electroretinogram response (Ruben et al. 1994), motion detection impairment (Ruben et al. 1994) and increased short-term fluctuation in perimetry (Flammer et al. 1984b). Subsequently the ganglion cell soma shrinks with reduction in axonal diameter (Weber et al. 1998).

The rate of progressive damage is thought to depend upon the threshold level of insult and the temporal relationship between ganglion cell degeneration and initiation of an apoptotic signal (Weber et al. 1998). Ganglion cell death tends to be slow and variable in glaucoma, occurring over several months and years (Osborne et al. 1999).

Axon degeneration is associated with progressive thinning of the neuroretinal rim, which often sequentially involves the inferotemporal, superotemporal, temporal horizontal, inferionasal and superonasal regions of the rim (Pederson and Anderson 1980; Jonas et al. 1993; Tuulonen 1993). The normal annual loss of neuroretinal rim is 0.23% of the initial area, in almost half of a glaucoma group studied a linear pattern of rim loss occurred, whilst in the remainder the loss was either episodic or curvilinear (Airaksinen et al. 1992). Localised visual field defects associated with glaucoma include arcuate and paracentral defects, whilst diffuse loss is characterised by a generalised reduction in differential light sensitivity (Caprioli et al. 1987b). Visual field studies have shown that the greater the visual field loss is, the greater the rate of progression (Mikelberg et al. 1986b). It is generally accepted that a combination of diffuse and focal changes eventually develop in glaucoma, particularly in the advanced stages, and the pattern can be related to the level of the IOP (Chauhan et al. 1989). There is also evidence that a purely localised (Caprioli et al. 1987b) or a purely diffuse visual field defect can be the earliest sign of glaucomatous damage (Drance 1991), although there is some contention whether exclusive (Åsman and Heijl 1994) diffuse loss can occur in the absence of miosis, or lens opacities.

Cases of primary open angle glaucoma attributable to ischaemia, whether acute or chronic can produce a diverse pattern of damage dependent upon the specific blood vessels involved the tissue perfused by those vessels and the severity of the condition (Hayreh 1995). Glaucomatous damage caused by more than one pathogenetic mechanism can continue to progress despite well-controlled levels of IOP (Drance et al. 1987).

1.8 Reversal of Glaucomatous Damage.

The optimal structural and functional parameters, capable of distinguishing glaucomatous eyes from normal eyes, especially those in the early stages of glaucoma are still unclear. Newly introduced diagnostic techniques require supportive evidence of adequate levels of reproducibility, accuracy and validation against existing procedures. Early intervention in the course of the disease may prevent optic nerve atrophy and preserve axonal integrity (Jay and Murdoch 1993). Once the axons are lost, the glaucomatous damage to the ONH and visual field

is irreversible. However, reversible changes in the RNFL height (Sogano et al. 1993), cup volume, neural rim (Irak et al. 1996) and visual field (Spaeth 1994) have been demonstrated in adults following marked reduction in IOP by medical or surgical intervention. The improvement in the parameters is not attributable to post-operative optic disc oedema (Greenidge et al. 1985) or transient changes in the reference plane associated with hypotony maculopathy (Topouzis et al. 1999). However, any apparent recovery of visual function may be due to the fluctuation in threshold estimation (Hutchings et al. 1993; Spaeth 1994). It has been suggested that a transitional period occurs where reversible changes can take place in both structure and function (Greenidge et al. 1985).

Improving ocular blood flow in human is considered to be beneficial (Harris et al. 1997), although there is a paucity of evidence as to the effect of treatment to improve the blood flow in glaucoma (Evans et al. 1998). The characteristics of the within- and between-individual variations in normal and glaucomatous blood flow measured by current techniques are currently being documented and the full significance of these variations has yet to be appreciated. Those considered at risk, but who show no evidence of functional or structural damage are generally not offered preventative drug therapy, The use of preventative therapy relies upon sufficiently sensitive methods of assessment. Once the initial damage has been identified treatment can be instigated depending on the side effects, cost and the likely compliance of each individual. However, the benefits of early treatment are still under debate. Identification of the onset, progression and ideally, reversal of glaucoma, through the recognition of both structural and functional abnormality, is obviously a potentially useful objective, and continues to be explored by newly introduced technology. Techniques and instrumentation that offer improved detection of glaucomatous progression and contribute to decisions regarding the ongoing management in glaucoma are considered to be highly desirable, and it is this line of approach that has been investigated in this study.

CHAPTER 2. RESEARCH OUTLINE.

2.1 Aims of the Study.

The overall aim of the thesis was to investigate, by means of a cross-sectional study, the structural and functional relationship in normals, in ocular hypertension and in primary open-angle glaucoma, and to relate the parameters to selected haemodynamic features.

The specific aims were:

- To determine the within- and the between-visit variability, as a function of the number of repeated images, for stereometric parameters of the ONH as derived by the Heidelberg Retina Tomograph (HRT, software version 2.01), for global analysis, correcting for age and disc area across the three diagnostic groups.
- To determine the corresponding between-visit variability for the HRT sector analysis, correcting for age and disc area across the three diagnostic groups.
- To determine the within- and between-visit variability for pointwise and global measures of sensitivity for a frequency doubling stimulus using Frequency Doubling Technology (FDT) across three diagnostic groups.
- To compare the within- and between-visit variability of FDT perimetry with that of conventional W-W perimetry and SWAP thereby evaluating non-selective perimetry (W-W) with that apparently reflecting magnocellular pathway function (FDT) and that apparently reflecting either small bi-stratified ganglion cell function and/or parvocellular pathway function (SWAP).
- To determine the within- and the between-visit variability for optical coherence tomography of the retinal nerve fibre layer thickness as determined by the Humphrey Systems Optical Coherence Tomography Scanner (OCT, software version A4.1), for both global and sector analysis, as a function of the type and number of circular scans.
- To determine the relationship between the RNFL thickness, derived by global and sector evaluation, and age, diagnosis and the functional and structural integrity of the eye thereby providing information on the validity of the technique of optical coherence tomography.
- To determine the within-individual, within-visit, and between-visit variation in parapapillary retinal and neural rim capillary blood flow, volume and velocity across the three diagnostic groups using the Heidelberg Retina Flowmeter (HRF).
- To determine the relationship between the retinal haemodynamics, as derived by the HRF, and the functional integrity derived by the various visual field techniques; the structural integrity of the ONH and RNFL thickness, derived by the HRT; and the RNFL integrity derived by the OCT.

2.2 Rationale.

The identification of the smallest possible measurable change in structure or function is highly desirable as it would provide the earliest opportunity for detecting the presence, and/or progression, of glaucoma, and for instigating the appropriate therapy to reduce the risk of further damage (David et al. 1977; Leske 1983). The most efficient method of detection for primary open-angle glaucoma may depend upon the characteristics and stage of the damage (Read and Spaeth 1974; Pederson and Anderson 1980; Hart and Becker 1982; Airaksinen et al. 1992; Zeyen and Caprioli 1993; Caprioli et al. 1996). Although progressive damage can generally be recognised by retrospective analysis of data over many visits, the identification of change from one visit to another is dependent upon the acquisition of sensitive and reproducible measurements within- and between-visits.

The identification of early structural damage to the ONH is also confounded by the inherent normal variation of the optic disc size and shape (Jonas et al. 1988a), the number and size of the optic nerve fibres (Mikelberg et al. 1989; Jonas et al. 1992c) and the related neuroretinal rim area (Jonas et al. 1988a) and RNFL thickness (Jonas and Dichtl 1996; Varma et al. 1996; Dichtl et al. 1999). In addition, age-related changes occur to the optic nerve and in the RNFL thickness (Balazsi et al. 1984; Mikelberg et al. 1991; Jonas et al. 1992c; Varma et al. 1996).

Functional assessment, using psychophysical tests, is limited, both for normal subjects and patients with either ocular hypertension or glaucoma, by several factors including the short and long-term fluctuation in the threshold estimate (Zulauf and Caprioli 1991; Hutchings et al. 1993), the fatigue effect (Johnson et al. 1988b; Hudson et al. 1994) and the learning effect (Wild et al. 1989; Heijl and Bengtsson 1996).

The measurement of ocular blood flow can also provide an insight into the development and progression of glaucomatous damage, as there is evidence for vascular dysfunction in glaucoma. The considerable normal between-individual variation in the ocular vasculature and the dynamic nature of blood flow control presents a complex background which is further confounded by the glaucomatous damage.

The inter-relationship between the structural, functional and physiological parameters in glaucoma is not fully understood. The thesis was concerned with the determination of the within-and between-visit variability of various measures which provide evidence of glaucomatous damage, and also with the relationship between each of the various parameters.

2.2.1 Determination of the within- and between-visit variability as a function of the number of repeated images, for stereometric parameters of the ONH as derived by the Heidelberg Retina Tomograph (HRT, software version 2.01), for global analysis, correcting for age and disc area across the three diagnostic groups.

The Heidelberg Retina Tomograph is a confocal scanning laser microscope which has been widely used in research for imaging the ONH (Brigatti and Caprioli 1995; Mikelberg 1995; Uchida et al. 1996; Zangwill et al. 1996; Hatch et al. 1997; Iester et al. 1997b; Broadway et al. 1998; Mardin et al. 1999) and the peripapillary region (Tsai et al. 1995b; Weinreb et al. 1995a; Iester et al. 1998). Less attention has been paid to those parameters that represent the RNFL integrity (Burk et al. 1998). The mean Retinal Nerve Fibre Layer Thickness (RNFLT), the Retinal Nerve Fibre Layer cross-sectional area and the Height Variation in Contour (HVC) measurements are pre-defined parameters that are provided with the standard report of the HRT. These stereometric parameters provide relative measurements, which rely, as do the majority of the stereometric parameters, on the establishment of a contour line-based reference plane within the software. This artificial reference plane does not purport to correspond to an anatomical retinal structure and is determined with respect to a very small sample of height measurements at the border of the optic disc as defined by the operator. The within- and between-visit variability both of the global and sector RNFL related topographical measurements and the relationship of these measurements to the thickness measurement derived by optical coherence tomography, which does not rely upon a reference plane, is not fully documented.

The study was designed to determine the variability both of the global and sector regional stereometric parameters, with particular reference to those measures that reflect the RNFL status, derived by the HRT software version 2.01 using the conventionally drawn contour line at the ONH. Since the number of retinal nerve fibres decreases with increase in age and the number of nerve fibres is related to the disc area, each HRT parameter was corrected for both age and disc area, where appropriate.

2.2.2 Determination of the within- and between-visit variability for pointwise and global measures of sensitivity for a frequency doubling stimulus using Frequency Doubling Technology (FDT) across three diagnostic groups.

FDT perimetry uses stimulus characteristics chosen to exploit the response properties of the m_γ cells, a subset of the magnocellular ganglion cell population, which account for between 5% and 20% of the M cells and may be particularly vulnerable to glaucomatous damage. FDT perimetry has been advocated for use in the screening of glaucoma (Johnson and Samuels 1997).

Ideally, the variability associated with a threshold estimate should be unaffected by the defect depth and should be similar across the visual field. Such an outcome is not achieved with conventional W-W perimetry or with short-wavelength automated perimetry (SWAP) and the variability increases with defect depth and with eccentricity (Heijl et al. 1989a). Test-retest characteristics for FDT perimetry are less variable than for conventional W-W perimetry (Chauhan and Johnson 1999) and are seemingly unaffected by eccentricity. However, the characteristics of FDT compared to those for SWAP have not been reported.

The study was designed to determine the within- and between-visit variability for pointwise and global measures of sensitivity using FDT perimetry. The subjects were naïve to FDT perimetry.

2.2.3 To compare the within- and between-visit variability of FDT perimetry with that of conventional W-W perimetry and SWAP thereby evaluating non-selective perimetry (W-W) with that apparently reflecting magnocellular pathway function (FDT) and that apparently reflecting either small bi-stratified ganglion cell function and/or parvocellular pathway function (SWAP).

The extent and depth of glaucomatous visual field loss is similar between FDT and W-W perimetry (Johnson and Samuels 1997). Short-wavelength automated perimetry can exhibit visual field loss prior to W-W perimetry (Johnson et al. 1993a; Sample et al. 1993); however there has been no published work on the relationship between FDT perimetry and SWAP.

The study was designed to determine the extent of any differences in the estimation of sensitivity between the FDT, SWAP and W-W perimetry.

2.2.4 Determination of the within- and between-visit variability for optical coherence tomography of the retinal nerve fibre layer thickness as determined by the Humphrey Systems Optical Coherence Tomography Scanner (OCT, software version A4.1), for both global and sector analysis, as a function of the type and number of circular scans.

Optical Coherence Tomography, is a technique that has shown promise for quantitative and qualitative evaluation of the retina and ONH (Schuman et al. 1995a; Schuman et al. 1995b). The technique is based upon the principle of optical echo-delay and interferometry, and uses a low coherent diode laser (830-850nm) (Swanson et al. 1993; Hee et al. 1995b). Clinical studies have demonstrated the potential of optical coherence tomography both in the diagnosis and in the monitoring of conditions capable of increasing or decreasing tissue substance, such as macula oedema and glaucomatous retinal nerve fibre atrophy (Hee et al. 1995c; Schuman et al. 1996; Baumann et al. 1998).

Measurements of the overall RNFL thickness derived by a prototype OCT scanner using repeated parapapillary circular scans exhibit a within- and between-subject standard deviation of approximately 10-20μm (Schuman et al. 1996). Variability, as determined by intraclass correlation coefficent for a given eye, was reportedly better within a single visit than between visits. (Schuman et al. 1996). The variability of RNFL thickness as a function of the number of successive scans has not been documented.

Structural analysis appears to offer a better prospect than functional analysis for identifying abnormality in the early stages of glaucoma. The ability to detect damage is related to the size of the optic disc, with detection being easier for larger discs (Iester and Mikelberg 1997; Bathija et al. 1998). Studies utilising the OCT have employed fixed radii scans, irrespective of disc size, and have not taken into account the variation in nerve fibre distribution associated with different

disc sizes. It would therefore seem appropriate, whilst investigating the parapapillary RNFL thickness, to consider the influences of optic disc size and age-related change.

The study was designed to determine the within-and between-visit variability in the commercial OCT derived RNFL thickness, as a function of the number of successive scans, between two circular scans whose radii were related to disc size and also for a single fixed radius scan. Each scan had a sampling density of 100 'A'-scans per solid angle and was centred upon the ONH. The results were analysed on a global and a sectoral basis.

2.2.5 Determine the relationship between the RNFL thickness, derived by global and sector evaluation, and age, diagnosis and the functional and structural integrity of the eye thereby providing information on the validity of the technique of optical coherence tomography.

The ability to identify progression in glaucoma using either structural or functional parameters is considered to be dependent upon the stage of the glaucoma (Zeyen and Caprioli 1993). In the early stages, the RNFL thickness and ONH appearance demonstrate glaucomatous damage prior to conventional W-W perimetry. (Drance 1989; Tuulonen and Airaksinen 1991). In the later stages, visual field loss provides evidence of progression that is not detectable by structural evaluation (Weber et al. 1989; Zalta 1991).

A moderate correlation exists between the global mean RNFL thickness, as determined by HRT, and the W-W visual field indices MD, PSD and CPSD (Iester et al. 1998). Surprisingly, the HRT peripapillary retinal height (Tsai et al. 1995b) and mean RNFL thickness (Teesalu et al. 1998) parameters show a better correlation with W-W perimetry than with SWAP both for global and regional MD. The RNFL thickness derived by OCT is moderately correlated with the HRT parameters, rim area, cup-disc ratio, cup shape measure, mean RNFL thickness and RNFL cross-sectional area (Mistlberger et al. 1999), and with W-W perimetry (Schuman et al. 1995b; Mistlberger et al. 1999). No studies have investigated the relationship between RNFL thickness derived by OCT and either SWAP or FDT.

The study was designed to determine the relationship between the outcomes of FDT perimetry, W-W perimetry and SWAP and the peripapillary RNFL thickness and ONH topography determined using the HRT and the RNFL thickness derived by OCT.

2.2.6 Determination of the within-individual, within-visit, and between-visit variation in parapapillary retinal and neural rim capillary blood flow, volume and velocity across the three diagnostic groups using the Heidelberg Retina Flowmeter (HRF).

Confocal scanning retinal laser doppler flowmetry using the HRF offers non-invasive quantitative and qualitative blood flow measurements for the retina and ONH (Michelson et al. 1996a; Nicolela et al. 1996b). Reports have shown the within-visit variability for haemodynamic parameters to be dependent upon the region analysed and its proximity to major blood vessels (Michelson and Schmauss 1995; Nicolela et al. 1997). Within-visit variability, represented by the

Coefficient of Variation of repeated measures, for retinal blood velocity, volume and flow over successive scans averaged less than 10% (Michelson and Schmauss 1995; Kagemann et al. 1998). Between-visit variability with the default sampling areas is reportedly larger than the within-visit variability (Nicolela et al. 1997; Kagemann et al. 1998).

The study was designed to determine the regional within- and between-visit variability of parapapillary retinal blood flow.

2.2.7 Determination of the relationship between the regional retinal haemodynamics, as derived by the HRF, and the functional integrity derived by the various visual field techniques, the structural integrity of the ONH and RNFL thickness, derived by the HRT, and the RNFL integrity derived by the OCT.

Few studies have commented upon the association of retinal haemodynamics with either the appearance of the ONH, the RNFL thickness or the visual field loss in glaucoma. However, Michelson et al (1998a) found no relationship between juxtapapillary or neuroretinal rim area blood flow reduction and the visual field index MD.

RNFL thinning in glaucoma is likely to be associated with an altered range of ocular blood flow measurements. However, there are no reports on the quantitative relationship between parapapillary RNFL thickness and haemodynamic parameters.

The study was designed to determine the relationship between temporal and nasal parapapillary retinal blood flow and visual field loss as determined by W-W perimetry, FDT perimetry and SWAP, and RNFL thickness derived by the HRT and OCT respectively.

2.3 Logistics.

The data collection for the study was undertaken mainly within the Department of Ophthalmology at Birmingham Heartlands Hospital, with ethical approval being provided by the Birmingham Heartlands Research and Ethics Committee. The research followed the tenets of the Helsinki Declaration.

Ocular hypertensive and glaucoma patients who conformed to the inclusion criteria from their existing clinical records were provided with a general outline of the proposed study. Those individuals who showed interest and who were prepared to attend for several appointments were assessed by Mr Ian A Cunliffe, Consultant Ophthalmologist in the Department, for confirmation of their eligibility for inclusion in the study. Normal volunteers were recruited from the students and staff at Aston University, and from local senior citizen organisations. Informed written consent was obtained from the normal volunteers and from the patients, following the provision of a full explanation, both verbally and in writing, of the nature of the study.

Glaucoma patients were required to attend for four visits following recruitment; each visit lasted on average one hour. The normal volunteers attended for an extra pre-study session in order to verify current refractive information, ocular status and to undertake an introductory visual field examination.

Some difficulties in recruiting the sample were encountered, as the inclusion criteria were quite restrictive. The presence of moderate/dense cataracts, common in older individuals who are considered more likely to develop primary open-angle glaucoma, can degrade the results from ocular imaging. Pseudophakics were excluded, as differing intraocular lens implants would have affected the calculation of magnification based upon Gullstrand's schematic eye. A dilated pupil was a prerequisite for the imaging appointments. However, pupil dilation can cause temporary blurred vision and depth perception disturbances and as a result was not always convenient for those subjects wishing to drive to, and from, the imaging appointments.

Data analysis and conversions between several software revisions for the FDT instrument involved collaboration with technical advisors based in San Diego, California, U.S.A. Amendments to data and replies to queries relating to the FDT were significantly delayed on a number of occasions. In addition, the imaging instruments were unavailable for use at various times throughout the study as a result of software and hardware malfunctions and, on one occasion, computer theft.

Despite some minor delays in the acquisition and analysis of data, the patience and co-operation shown by the volunteers and professional colleagues ensured that a wealth of valuable information was collected and could be presented in the thesis. A period of 24 months was required to achieve the sample size described in the thesis. In total, 90 volunteers provided 540 visual fields, 3780 OCT images, 1260 HRT images and 2160 HRF images for the study.

Progress in the study was impeded by two exceptional circumstances concerning the equipment used for data collection. The computer used to operate the Optical Coherence Tomograph (OCT) scanner was stolen from Birmingham Heartlands Hospital in November 1997 and was replaced after a 6-week delay. An undergraduate student acting as a volunteer subject for a pilot study involving the Heidelberg Retinal Flowmeter (HRF) reported a sustained reduction in visual acuity in the studied eye following use of the instrument. The HRF was being used by a research student in a different study unconnected with this thesis. It was not clear at the time whether the reduction in acuity could be attributed to the instrument. Accordingly, all data collection with the instrument was halted in early May 1999 and the instrument was returned to Heidelberg Instruments in Germany for inspection. Despite safety clearance from Heidelberg and the reinstallation of the HRF in the Department of Ophthalmology, Birmingham Heartlands Hospital, at the end of July 1999, a decision was taken to cease using the HRF instrument on the grounds of safety.

CHAPTER 3. METHODOLOGY.

3.1 Sample.

The sample for the thesis comprised one designated eye from each individual drawn from three groups: a Normal group of 26 normal individuals, a group of 27 patients with ocular hypertension (OHT), and a group of 24 patients with POAG. The group with OHT contained 9 patients with high-risk ocular hypertension (OHT(H)). The mean age of the Normal group was 56.0 (SD 17.9) years, of the OHT group 65.2 (SD 10.4) years, and of the POAG group 67.5 (SD 10.4) years. The age distribution of the Normal group deliberately embraced all age ranges in order to facilitate the documentation of each given normal variable as a function of age.

3.2 Inclusion criteria.

The three groups conformed to standard inclusion criteria that consisted of a visual acuity of better than, or equal to, 6/9; a refractive error not greater than 6.0 dioptres mean sphere and not greater than 2.5 dioptres cylinder and no history of amblyopia. Lenticular changes, graded by LOCS III (Chylack et al. 1993), were not worse than NC(3.0), NO(3.0), C(1.0) or P(1.0). All subjects had a negative history of diabetes mellitus, of systemic medication known to influence the visual field and, with the exception of those specifically recruited as having POAG, a negative history of ocular disorder. All individuals had undergone at least one automated static threshold visual field examination using W-W perimetry prior to inclusion in the study. One individual with ocular hypertension had early nuclear lens changes with a visual acuity of 6/18. Four individuals with glaucoma and early nuclear lens changes had visual acuities of 6/12 to 6/18. Two individuals with extremely advanced and end-stage POAG with visual acuities of 6/5 and 6/24 respectively (but with good fixation) were deliberately included within the sample to ensure the complete range of glaucomatous damage.

The diagnosis of POAG or OHT in the designated eye was based upon the appearance of the ONH, assessed with non-simultaneous stereo photography, and upon the presence of visual field loss characteristic of glaucoma. The assessment of the ONH was made by a consultant ophthalmologist experienced in glaucoma (IAC) and was based upon the documentation of features characteristic of glaucomatous optic neuropathy (including an increase in cup size, increase in cup-disc ratio, disc asymmetry, changes in the lamina cribrosa, loss of the neuroretinal rim, pallor, evidence of peripapillary atrophy, vessel changes of disc margin haemorrhage) (Airaksinen et al. 1996). The visual field had been determined prior to entry into the study by static automated threshold W-W perimetry using the Full Threshold algorithm and Programs 30-2 or 24-2 of the Humphrey Field Analyzer. The assessment of the visual field was made by an individual experienced in the interpretation of automated perimetry (JMW). Each assessor was masked as to the outcome of the other assessment. The visual field loss was classified after Hodapp, Parrish and Anderson (1993). 13 of the 24 POAG patients exhibited early loss, 4 moderate loss and 7 severe loss. Seventeen patients had presented initially with

an IOP greater than or equal to 21mmHg, whilst seven patients had presented initially with an IOP less than 21mmHg and could be subclassified as having Normal Tension Glaucoma.

The patients with ocular hypertension had initially presented with either an intraocular pressure (IOP) greater than 24mmHg, or an IOP greater than 22mmHg and a vertical cup-to-disc (C/D) ratio greater than 0.5, or an IOP greater than 22mmHg, a C/D less than 0.5 and a family history of glaucoma. In nine eyes of patients with OHT, an abnormal ONH, characteristic of glaucoma existed in the presence of an apparently normal visual field. These 9 cases were deemed to have high-risk ocular hypertension.

All individuals using topical anti-glaucoma medication remained on the same therapeutic regime during the period of data collection. The 24 patients with POAG all manifested well-controlled intraocular pressures (mean at the time of data collection 19.0mmHg; SD 3.3) and stable visual fields. Three patients were using no topical agent, sixteen patients were controlled on a single topical agent, either a selective or non-selective β blocker, a topical carbonic anhydrase inhibitor or a prostaglandin analogue. Four patients required more than one topical agent for intraocular pressure control. One patient had undergone previous trabeculectomy at least 12 months prior to inclusion in the study and required no further medical treatment for intraocular pressure control. Of the 27 patients with OHT, 16 were using topical anti-glaucoma medication; and of these, 14 were on a single topical agent and two required more than one topical agent for intraocular pressure control.

One eye from each individual was selected for the study. For the normal group, the designated eye was chosen at random. In the case of the individuals with OHT, the eye at greatest risk was selected. In the case of the patients with POAG, the eye with the most damage was chosen.

3.3 Informed consent.

The study had approval from the Research and Ethics Committee of Birmingham Heartlands and Solihull NHS Trust (Teaching). The limit for safe ocular exposure to the light from the near infra-red superluminescent diode (wavelength 850nm) used in OCT, the infrared diode laser (wavelength 780nm) used in the HRF and the visible red diode laser (wavelength 670nm) used in the HRT is based on and documented by the American National Standards Institute (ANSI 1993). Use of the OCT, HRT and HRF imposed no known risk to those who took part in the study.

All individuals were provided with a full verbal and written explanation of the procedures and informed consent was obtained using a consent form approved by Research and Ethics Committee of Birmingham Heartlands and Solihull NHS Trust (Teaching) according to the tenets of the Declaration of Helsinki.

3.4 Recruitment and sequence of visits.

The normal subjects were recruited from students and staff at Aston University, and also from local senior citizen groups. The individuals with OHT or POAG were recruited from patients attending the out patient clinics of the Department of Ophthalmology at Birmingham Heartlands Hospital. Individuals considered to be within the inclusion criteria according to their existing clinical records were provided with a general outline of the proposed study. Those individuals who showed an interest in participating in the study were assessed by a consultant ophthalmologist experienced in glaucoma (IAC) for confirmation of their eligibility for inclusion in the study. Similarly, the normal individuals all received an ophthalmological examination to confirm eligibility for inclusion in the study.

All participants were required to attend Birmingham Heartlands Hospital for four visits of alternate visual field and imaging sessions. Each visit lasted, on average, ninety minutes.

At the first visit, all individuals underwent W-W, SWAP, and FDT perimetry. W-W perimetry and SWAP were performed on the designated eye of each patient using the Humphrey Field Analyzer (HFA) 750 Program 24-2 and the Full threshold algorithm (software revisions A7 x 08 and A9 x 18). The default stimulus and background conditions were employed for both W-W perimetry and SWAP; specifically a white, Goldmann size III stimulus presented against a $10cdm^{-2}$ white background with a stimulus duration 200ms, and a blue, Goldmann size V stimulus of duration 200ms presented against a $100cdm^{-2}$ yellow background. FDT perimetry was undertaken with the Humphrey FDT Instrument using Program C-20 and the Full Threshold algorithm (software revisions 7.11, 1.2 or 2.6). The default stimulus employed for FDT perimetry comprised a low spatial frequency (0.5 cycles per degree) sinusoidal, black and white, grating which undergoes high temporal frequency counterphase flicker at 25Hz. The maximum stimulus presentation duration is 720ms. For an initial 160ms period the stimulus contrast is increased gradually from zero to the required level chosen for that presentation. If the response button is not pressed, the contrast is maintained at this level for up to 400ms, and then gradually faded out over a further 160ms. Thus avoiding erroneous responses caused by sudden contrast changes. A random interval of up to 500ms is allowed between stimulus presentations. If the response button is not pressed within 100ms of the stimulus initiation and for 1 second after it has been withdrawn, the presentation is recorded as 'not seen'.

All patients had experience of W-W perimetry but were naïve to SWAP and to FDT perimetry. The three visual field examinations were each separated by an interval of 10 minutes. The visual field protocol was repeated after an interval of approximately 14 days, i.e. at Visit 3. The order of perimetry (selected from the protocols A to F) for the within- and between-visits was randomised between patients but held constant within each patient for each visit.

Refractive correction appropriate for the viewing distance of the perimeter bowl was used for each subject for W-W perimetry and SWAP, as recommended in the instruction manual for the

instrument. In FDT perimetry, for refractive errors of less than 7 dioptres, the instruction manual deems that no corrective lens is necessary, and therefore no refractive correction was employed in the study.

At the second visit, all subjects and patients underwent imaging using the Humphrey Systems Optical Coherence Tomography (OCT) scanner, the Heidelberg Retina Tomograph (HRT) and the Heidelberg Retina Flowmeter (HRF). For each individual, the appropriate information selected from; age, ocular axial length (obtained using A-scan), corneal curvature measurements (K readings) and best sphere refractive correction were input onto the respective instruments database, prior to scanning. This latter data had been obtained prior to commencement of the session.

For the image acquisitions, the eye previously selected for the perimetric investigations was dilated with 1% Tropicamide at least thirty minutes prior to the scanning. Examinations with each instrument comprised the acquisition of a series of repeat scanned images. A more detailed description of the imaging protocols is given in Chapters 4, 6 and 7.

	Visit 1			Visit 3		
	First Test	Second Test	Third Test	First Test	Second Test	Third Test
Protocol A	W-W	SWAP	FDP	W-W	SWAP	FDP
Protocol B	FDP	W-W	SWAP	FDP	W-W	SWAP
Protocol C	SWAP	FDP	W-W	SWAP	FDP	W-W
Protocol D	FDP	SWAP	W-W	FDP	SWAP	W-W
Protocol E	W-W	FDP	SWAP	W-W	FDP	SWAP
Protocol F	SWAP	W-W	FDP	SWAP	W-W	FDP
	Visit 2			Visit 4		
	First Test	Second Test	Third Test	First Test	Second Test	Third Test
Protocol 1	HRT	HRF	OCT	HRT	HRF	OCT
Protocol 2	HRF	HRT	OCT	HRF	HRT	OCT
Protocol 3	OCT	HRT	HRF	OCT	HRT	HRF
Protocol 4	OCT	HRF	HRT	OCT	HRF	HRT
Protocol 5	HRT	OCT	HRF	HRT	OCT	HRF
Protocol 6	HRF	OCT	HRT	HRF	OCT	HRT

Table 3.1. A summary table of the examination protocols assigned to each individual. W-W is the HFA white-on-white perimetry; SWAP is the HFA short-wavelength automated perimetry; FDP is the frequency doubling technology perimetry; OCT is optical coherence tomography; HRT is Heidelberg retinal tomography; and HRF is Heidelberg retinal flowmetry.

The imaging sessions performed on the different instruments were each separated by an interval of 10 minutes. The protocol was repeated after an interval of approximately 14 days, i.e. at Visit 4. The order of imaging (selected from the protocols 1 to 6) for the within- and between-visits was randomised between patients but held constant within each patient for each visit.

3.5 Analysis.

For all data, the results for the left eye were converted into right eye format. All visual fields included in the analysis met the inclusion criteria for reliability, specifically less than 33% fixation losses (Johnson and Nelson-Quigg 1993) and less than 33% false negative and false positive catch trials (Sanabria et al. 1991).

One individual with ocular hypertension was excluded from the visual field test-retest study as the reliability indices fell outside the established inclusion criteria. One individual with glaucoma whose dilated pupil size remained less than 3.5mm was excluded from the OCT study. The reduced aperture prevented adequate visualisation of the scan location, and would prevent subsequent accurate re-alignment, which relies upon a sufficiently good view of the fundus on a real-time video screen. Sixteen normal individuals and one individual with POAG were excluded from the blood flow study as the HRF instrument was unavailable during the period of their imaging sessions, and no data could be collected. One individual with POAG was excluded entirely from the blood flow study, as no acceptable quality HRF images were obtainable. Eight individuals with ocular hypertension and seven individuals with POAG failed on at least one occasion to provide an acceptable quality of HRF image for a particular sequence of images, a particular region, or a particular repeated session.

The specific details concerning the analysis of each data set is described in the given chapter.

CHAPTER 4. HEIDELBERG RETINA TOMOGRAPHY IN THE STRUCTURAL ASSESSMENT OF THE OPTIC NERVE HEAD.

4.1 Morphology of the ONH in the normal and glaucomatous eye.

The optic nerve head (ONH) is a three-dimensional structure that includes the transitional region where the retinal tissue becomes the optic nerve, passing through the scleral canal before it exits the orbit. The ONH is commonly divided into three regions, defined according to the position relative to the lamina cribrosa, as the pre-lamina, lamina and post-lamina regions. The ONH horizontal boundary is provided by the scleral canal, and the border tissue of Jacoby, whilst the upper boundary is the rear face of the vitreous gel, and the central meniscus of Kuhn (Hogan et al. 1971).

Morphological changes to the ONH in glaucoma, reported by Quigley et al (1983) involved the compression of the lamina cribrosa sheets, with posterior bowing and outward rotation of the peripheral lamina, particularly at the superior and inferior poles as the disease progresses. Mechanical distortion of the lamina plates damages the axons passing through channels within the pores that riddle the lamina. Axonal compression blocks the orthograde and retrograde axonal transport of materials between the ganglion cell and the Lateral Geniculate Nucleus (LGN) which impairs the visual pathway function (Gaasterland et al. 1978; Quigley and Addicks 1980). Distension of the pores (Miller and Caprioli 1992) with loss of supportive tissue puts further stress on the axons. There can be considerable between-individual response to mechanical forces at the ONH, particularly in the presence of inherent or age-related defects within the connective tissue of the sclera or the extracellular matrix of the optic nerve head (Hernandez et al. 1989; Hernandez et al. 1990). Despite the extensive axonal damage and loss in advanced glaucoma, astrocytes are preserved in the anterior ONH suggesting greater resistance of the astrocytes to damage and no evidence for their selective loss (Quigley 1979).

Careful observation of progressive changes to the configuration of the ONH and its immediate surrounding tissue provides an insight into the development of both glaucomatous and non-glaucomatous optic neuropathies. Progressive enlargement and excavation of the optic cup associated with thinning of the neural rim through nerve fibre loss provides a reliable indicator of glaucomatous damage (Tuulonen and Airaksinen 1991). However, a wide between-individual variation in the normal appearance of the ONH structures is present (Jonas et al. 1988a). A lack of agreement between experienced clinicians (Lichter 1976; Varma et al. 1992) in discriminating normal from abnormal is also present.

4.1.1 Optic disc dimensions in the normal and glaucomatous eye.

Histologically, the boundary of the optic disc is provided by the termination of Bruchs' membrane, the retinal tissue and a scleral rim, separated from the nerve fibre fascicles by a layer of astrocytes. The mean optic nerve scleral canal area, determined from unfixed donor

eyes, is 2.59 ± 0.72mm^2, ranging from 0.68 to 4.42mm^2 (Jonas et al. 1988b). The optic disc is the ophthalmoscopically visible intraocular portion of the optic nerve. The optic disc is surrounded by the peripapillary scleral ring of Elschnig, and comprises the neuroretinal rim and the optic cup (Jonas et al. 1988a). The, in vivo, mean optic disc area determined is 2.69 ± 0.70mm^2, ranging from 0.86 to 5.56mm^2 (Jonas et al. 1989c) in normal eyes, comparing favourably with the post-mortem specimens. The optic disc is slightly vertically oval (Jonas et al. 1988a). The mean horizontal disc diameter is 1.76 ± 0.29mm ranging from 0.91 to 2.6mm, with the vertical disc diameter about 9% larger than the horizontal diameter (Jonas et al. 1988a). Image analysers have provided further evidence both for a large between-individual (Iester et al. 1997a; Saruhan et al. 1998; Wollstein et al. 1998) and a between-instrument variation (Caprioli and Miller 1987; Lim et al. 1996; Vihanninjoki et al. 1997) in the optic disc size.

The mean disc area has been quoted in several studies using the HRT, with values ranging from 1.806 ± 0.35 mm^2 to 2.60 ± 0.82 mm^2 in normal eyes, 1.72 ± 0.07 mm^2 to 2.35 ± 0.57 mm^2 in patients with ocular hypertension and 1.89 ± 0.34 mm^2 to 2.60 ± 0.70 mm^2 in patients with glaucoma (Zangwill et al. 1996; Iester et al. 1997a; Iester and Mikelberg 1997; Bathija et al. 1998; Mardin and Horn 1998; Saruhan et al. 1998; Wollstein et al. 1998)

The mean optic disc area with HRT (1.97 ± 0.57 mm^2) was found to be approximately 0.13 mm^2 smaller compared with manual planimetric techniques (Vihanninjoki et al. 1997). Varma and associates (1994) using the Topcon Imagenet system found the mean disc area in whites ranged from 1.15 to 4.94 mm^2, with a mean of 2.63 ± 0.46 mm^2, whilst the mean disc area with the Rodenstock Analyser was 1.70 ± 0.37mm^2 (Caprioli and Miller 1987). However, measurements of disc parameters are not directly comparable between the various digital analysers due to their different optical arrangements and methodologies (Littmann and Williams 1992; Rudnicka et al. 1998).

There is evidence for a racial variation in the disc size with a significantly larger disc area in blacks compared to whites (Tsai et al. 1995a). Gender-related differences on the optic disc size, in the literature, vary. The disc area is generally similar between sexes (Jonas et al. 1988a; Tsai et al. 1992) with a slight tendency to be larger in men than women (Quigley et al. 1990; Varma et al. 1994; Ramrattan et al. 1999). The number of optic nerve fibres is directly related to the area of the disc (Quigley et al. 1991; Jonas et al. 1992c). However, despite the decline in optic nerve fibres with age (Mikelberg et al. 1989), studies have failed to show an association between the disc area and age (Jonas et al. 1988a; Ramrattan et al. 1999). For low to moderate refractive errors there appears to be no relationship with disc area (Varma et al. 1994). In the highly myopic eye the disc size is positively correlated with the refractive error (Jonas et al. 1988e). For eyes with more than 5 dioptres of hyperopia, the optic disc is significantly smaller than the emmetropic eye (Varma et al. 1993).

Jonas and co-workers (1991b) consider that the susceptibility of nerve fibre loss with glaucoma is independent of the optic disc size in Caucasians, and this is supported by Quigley and colleagues (1999). Glaucomatous disc size (Jonas et al. 1988c) and shape (Jonas and Papastathopoulos 1996) are similar to normal eyes suggesting that the optic disc area does not increase in adult glaucoma. However, evidence that African-Americans, with a higher risk of developing glaucoma, tend to have an increased prevalence of larger disc sizes compared to the Caucasian population, has led to the hypothesis that the larger optic disc sizes are more highly susceptible to glaucomatous damage (Chi et al. 1989; Tsai et al. 1995a). The increased prevalence of glaucoma associated with a large disc in high myopia has supported this argument (Jonas and Dichtl 1997). Burk and colleagues (1992) have suggested that large discs can be susceptible to enlargement of the cup, and associated visual field loss, at statistically normal IOP. However, it is not conclusive that larger discs are more susceptible to glaucomatous damage, since crowding of the nerve fibres in the confined area of a small disc could pose a risk of mechanical damage to the nerve fibres (Quigley et al. 1991; Jonas et al. 1992c). The higher pore to lamina area in smaller optic discs compared to large discs could predispose the eye to glaucomatous damage (Quigley and Addicks 1981).

4.1.2 Optic cup in the normal and glaucomatous eye.

The central excavation within the optic disc boundary, not occupied by nerve fibres is the optic cup, and if present, the contour of the cup is more readily observed by stereoscopic viewing. Several layers of perforated sheets of collagen and elastin fibres form the floor of the cup, the lamina cribrosa (LC). The numerous pores within the lamina tend to be small and round in the normal eye becoming progressively more oval and slit-shaped as glaucomatous damage occurs (Miller and Quigley 1988). The normal cup, in general is horizontally oval, lying within a vertically oval disc (Jonas et al. 1988a). The cup size, is correlated with the size of the disc in normal individuals (Bengtsson 1976). There is no significant relationship between cup size and age, gender or refraction (excluding high myopes) (Varma et al. 1994). A cup is not generally apparent in optic discs with an area of less than 1.6mm^2 (Varma et al. 1993). A large cup in a large disc is commonly a physiological finding but tends to carry a naturally higher suspicion of abnormality. However, any size of cup, however small, in a small disc, typically regarded with a lower degree of suspicion, can be of greater significance (Jonas et al. 1990a).

In glaucoma, the layers of the LC are compressed and progressively bowed backwards in a 'saddle-type' configuration with advancing glaucoma (Quigley et al. 1983). Enlargement of the cup area over time, is a characteristic sign of developing glaucomatous optic neuropathy. The initial optic cup enlargement in early glaucoma is frequently confined to the inferior temporal and upper disc margins (Jonas et al. 1988c) causing the cup to become vertically oval in shape.

4.1.3 Neuroretinal rim in the normal and the glaucomatous eye.

The neuroretinal rim (NRR) region is formed by the ganglion cell axons that extend over, and turn sharply into, the scleral canal (Hogan et al. 1971). The NRR is surrounded on its outer circumference by the peripapillary scleral ring, and on its inner, by the optic cup, at the centre of the disc. The NRR area in the normal eye varies greatly between individuals and can be related to the variability in diameter (Sanchez et al. 1986) and to the numbers of nerve fibres present (Quigley et al. 1991). The NRR area is correlated with the size of the optic disc, being larger in large discs, and smaller for small disc areas (Britton et al. 1987; Varma et al. 1994). The optic disc size should therefore be considered in rim area evaluation (Caprioli and Miller 1987). The NRR is generally broadest at the inferior pole and progressively narrows at the superior, nasal and finally temporal rim region (Jonas et al. 1988a). The regional variation in the breadth of the NRR rim coincides with the regional variation in the calibre of the major retinal vessels (Jonas and Naumann 1989b), the lamina pore size (Quigley and Addicks 1981) and the RNFL visibility (Jonas and Schiro 1993). There is no significant relationship between NRR area and age, gender or refraction (excluding high myopes) (Jonas et al. 1988a).

The NRR area has shown good correlation with tests of visual function (Airaksinen et al. 1985b), and with estimates of the RNFL thickness (Jonas et al. 1989b). The axons are retinotopically arranged within the rim. Axons from the retina, above and below the temporal raphe converge on the superior and inferior rim respectively; the maculopapillae fibres form the temporal rim and the nasal fibres, the nasal rim. Those axons originating from ganglion cells in the peripheral retina occupy the outer rim margins whilst those axons arising close to the disc occupy a more central position (Minckler 1980).

Optic nerve damage is generally accompanied by pallor of the NRR, but the degree of pallor is more specific to non-glaucomatous optic neuropathy than glaucoma (Tuulonen et al. 1992). Quigley and colleagues (1977; 1982b) postulated that the pink colour of the rim tissue is primarily determined by the thickness of the nerve fibre bundles and their orientation within the glial channels, with a minor role provided by the capillaries. Glaucomatous damage leads ultimately to loss of axons and, in turn, to thinning of the NRR, whilst the capillary density remains the same as normal eyes. The number of remaining nerve fibres may be estimated by measuring the NRR area (Quigley et al. 1991). The NRR area reduces progressively with glaucoma damage with early changes tending to occur in the inferotemporal region followed by the superio-temporal, temporal, inferio-nasal and superio-nasal regions. In advanced glaucoma, residual rim can remain in the nasal border (Jonas et al. 1993). Overall thinning of the NRR, associated with concentric enlargement of the optic cup in diffuse damage is reportedly more common with high-tension glaucoma (Shiose et al. 1987). The NRR damage in low-tension glaucoma is reportedly more likely to be of a localised nature, particularly occurring in the inferior and inferio-temporal region (Caprioli and Spaeth 1985) and following an episodic course (Airaksinen et al. 1992).

4.1.4 Cup-to-Disc ratio (CDR) in the normal and the glaucomatous eye.

Large optic discs tend to have large physiological optic cups, and therefore high CDRs; whilst small cups are more common in small discs, giving small CDRs (Bengtsson 1976). Not surprisingly, therefore, as found with the optic disc sizes, there is a high between-individual variation in the CDR in the normal population with mean of 0.39 ± 0.28 horizontally and a mean of 0.34 ± 0.25 vertically (Jonas et al. 1988a). In addition, determination of the CDR with an ophthalmoscope has shown large between-observer variation (Lichter 1976).

Glaucomatous optic neuropathy can be associated with a disproportionately low CDR in a small ONH (Jonas et al. 1990a). A large CDR in a small disc has a far greater likelihood of being glaucomatous than the same ratio described in a large disc, since a small change in the CDR of a small disc corresponds to a far greater proportional loss of neural rim tissue. An estimate of the disc size should accompany any quoted CDR. Despite the high between-individual variation for the CDR in the normal population, and the low sensitivity and specificity of the CDR alone for glaucoma screening (Harper and Reeves 1999), the value is still routinely quoted following a fundus examination. However, a change in the CDR, particularly the vertical one still provides an early warning of glaucomatous damage (Jonas et al. 1988c).

4.1.5 Peripapillary scleral rim in the normal and the glaucomatous eye.

The intrapapillary region of the ONH is separated from the parapapillary region of the retina by the peripapillary scleral tissue of Elschnig (1900). The scleral tissue extends anteriorly to form a lip which separates the choroid from the ONH (Fantes and Anderson 1989). The scleral rim tends to be broadest in the temporal horizontal sector (Varma et al. 1993). The visibility of the scleral rim is related to the thickness of the overlying nerve fibres and the rim tends to be obscured where the NFL is thickest (Nevarez et al. 1988). In axonal atrophy, the scleral rim, visible at the borders of most optic discs as a complete or incomplete ring, becomes more apparent, however, the rim does not enlarge (Nevarez et al. 1988).

4.1.6 Parapapillary region in the normal and the glaucomatous eye.

The retinal area immediately adjacent to, and surrounding, the optic disc border, beyond the peripapillary scleral ring is termed the parapapillary region. Variations in the appearance of the parapapillary region often arise from misalignment of the edges of the neural retina, retinal pigment epithelium, choroid and the sclera at the optic disc margins (Fantes and Anderson 1989). Congenital parapapillary chorioretinal atrophy has been subdivided into the α and β zone dependent upon the differing degrees of atrophy that may be observed (Jonas et al. 1989a). Histologically, the β zone represents a complete absence of the retinal pigment epithelium and an incomplete loss of the adjacent photoreceptors. The β zone is recognised clinically by areas of exposed white scleral tissue, with visible large choroidal vessels, immediately beside the outer edge of Elschnigs' scleral ring (Elschnig 1900). Outside the hypopigmented β zone, the α

zone is seen as a region of irregular hyper- and hypo-pigmentation of the retinal pigment epithelium and partial atrophy of the nerve tissue (Jonas et al. 1989a). The β zone is less common than the α zone in normal individuals. Care has to be exercised to differentiate these zones from the myopic scleral crescent often associated with high myopes with/without glaucoma (Jonas et al. 1988e).

Functionally, it has been hypothesised that the β zone is associated with an absolute scotoma and that the α zone is associated with a relative scotoma. Indeed, agreement between the optic disc size and surrounding area of chorioretinal atrophy with the blind spot is evident in perimetry (Jonas et al. 1991a).

Parapapillary atrophy can be congenital (Jonas et al. 1989a) or acquired through high myopia (Jonas et al. 1988e) The position of the β zone has been positively correlated with the presence of disc haemorrhages in normal eyes (Sugiyama et al. 1999) and with focal NRR loss in glaucoma (Jonas and Naumann 1989a). Extension of the β zone is accompanied in ocular hypertension (Tezel et al. 1997) and in glaucoma (Jonas et al. 1992b) by the development and progression of visual field defects. The size and frequency of the occurrence of the zones does not differ significantly between low- or high-tension glaucoma, but the zones are less common in primary angle-closure glaucoma (Jonas and Xu 1993; Uchida et al. 1999). A vascular deficiency or ischaemia in the parapapillary choroidal vasculature could account for the atrophy (Kubota et al. 1993). Fantes and Anderson (1989) and Tezel et al (1996) hypothesised that a compromised blood-retinal barrier at the choroid/optic nerve border could contribute to glaucomatous damage at the ONH. Computerised optic disc analysis using the HRT demonstrated that the larger the β zone area, the worse the mean deviation (MD) and corrected pattern standard deviation (CPSD) in W-W perimetry and the CPSD in SWAP (Kono et al. 1999). In addition, β zone parapapillary atrophy is spatially related to NRR thinning (Emdadi et al. 1999).

4.1.7 Optic Disc Haemorrhage.

Disc haemorrhages occur most frequently at the infero-temporal or supero-temporal disc margin, and are generally flame-shaped (Jonas and Xu 1994). Rarely occurring in normal eyes, a disc haemorrhage strongly suggests a mechanical or vascular abnormality and is considered an important risk factor in glaucoma (Drance et al. 1981). There is evidence that disc haemorrhages precede RNFL defects and visual field abnormalities, and can be the first detectable sign of glaucomatous damage (Airaksinen et al. 1981). Disc haemorrhages appear to predict the location of future damage (Bengtsson et al. 1981) and are associated with NRR notches, RNFL defects and visual field loss (Airaksinen and Heijl 1983). Disc haemorrhages are not correlated with the rate of glaucomatous damage (Tuulonen et al. 1997). Distortion of the lamina plates with stretching and rupture of capillaries in the ONH arising from an elevated IOP may be the cause disc haemorrhages (Quigley et al. 1981) although the haemorrhage can

appear prior to detectable morphological change. Disc haemorrhages are associated with branch vein occlusions and with diabetes but not anterior ischaemic optic neuropathies. These findings have led to the hypothesis that impairment of the venous circulation is a causative factor (Bengtsson et al. 1981). Despite a high specificity, the low prevalence of disc haemorrhage results in a low sensitivity (Jonas and Xu 1994).

Current widely practised methods for evaluation of the ONH, that include the ophthalmoscopic assessment, may not be sufficiently sensitive to identify the earliest signs of glaucoma. Digitised image analysers have been developed that allow greater image resolution and reproducible quantitative documentation of the ONH. Scanning laser ophthalmoscopes, which incorporate confocal optics, such as the HRT, are being employed in glaucoma detection and monitoring.

4.2 The Heidelberg Retinal Tomograph (HRT).

4.2.1 Scanning Laser Ophthalmoscopy (SLO).

SLO is a relatively new technique for three-dimensional imaging and assessment of ONH topography (Mainster 1982; Webb et al. 1987; Sharp and Manivannan 1997). The term SLO refers to the use of a generic form of ophthalmic instruments, with a common mode of illumination. A small beam of light is rapidly scanned, pixel-by-pixel, line by line, across the surface of interest, in a similar manner to that used by television monitors. Since the entire image is never illuminated at any single moment and the source beam is small, a natural pupil can be used. The imaging process is generally well accepted by the subject. The image generated, like the laser light source, is monochromatic. The various shades of grey that represent the image reflectance intensity can be colour-coded for ease of image recognition. The introduction of a pinhole in front of the illuminating beam and photodetector, conjugate with the focal plane, permit a greater level of contrast by reducing the influence of random scattered light and suppressing out-of focus reflections. The resultant confocal optical system is employed in the HRT and the LTS (Laser Tomographic Scanner).

The HRT is a commercially available confocal scanning laser instrument that permits both qualitative and quantitative measurements of retinal structures in vivo. The HRT is widely employed in morphometric analysis of the ONH, particularly in the diagnosis and monitoring of glaucoma.

4.2.2 Optical principles of the HRT.

The optical principles of confocal imaging and image analysis have been previously documented (Webb et al. 1987; Nasemann and Burk 1990; Chauhan 1996). In brief, using the HRT, a two-dimensional area of the fundus is illuminated by a helium-neon diode laser light (670nm) focused to a single location on the retina via the confocal system and rapidly scanned. The laser beam is first deflected horizontally, along an x-axis, then shifted vertically by one unit

on the y-axis. Reflected light from each retinal location is measured by a light-sensitive detector as the laser beam sweeps across the surface (Figure 4.1a). The size of the raster scan pattern on the retina can be set to 10° x 10°, 15° x 15° or 20° x 20° depending upon the field of view and lateral resolution desired.

A series of two-dimensional optical sections are then rapidly scanned for thirty-two equidistant positions by moving the focal plane posteriorly along the optical axis. The process takes 1.6 seconds (Figure 4.1b). The confocal optical system, in which the entrance and exit pupil coincide, ensures that light is collected from each focal plane and out-of-focus images are suppressed. The depth of the scanned sections can be chosen from a range of 0.5 to 4.0mm in 0.5mm steps to permit a longitudinal resolution of 16-130 μm between each image plane. To quantify the ONH, the focal plane of the first image section within the series is chosen to be above the NRR surface whilst the last focal plane lies below the presumed level of the optic cup base. The reflectance at each of the resultant 2,097,152 three-dimensionally defined pixels (256 x 256 x 32 voxels) is digitized and a three-dimensional image is then generated (Burk et al. 1990). In confocal SLO, each retinal location is illuminated one at a time. The central 0.09mm of the pupil is used for the laser beam entrance and the remainder of the pupil area is used for collection of the reflected light. Less than 0.001% of the light needed for conventional indirect ophthalmoscopy is required for the HRT thereby avoiding the need for a dilated pupil (Mainster 1982). However, a pupil size of at least 2.5mm diameter is highly desirable (Burk and Rohrschneider 1993). Hazy ocular media can reduce the image quality but to a lesser extent than with a conventional fundus camera due to the efficient light collection (Zangwill et al. 1997).

Figure 4.1a. Schematic Diagram of the HRT Confocal Optical System (from Varma et al. 1993).

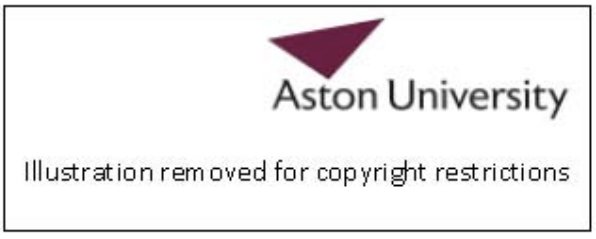

Figure 4.1b Schematic illustration of the series of tomographic image sections. (from Burk et al. 1992).

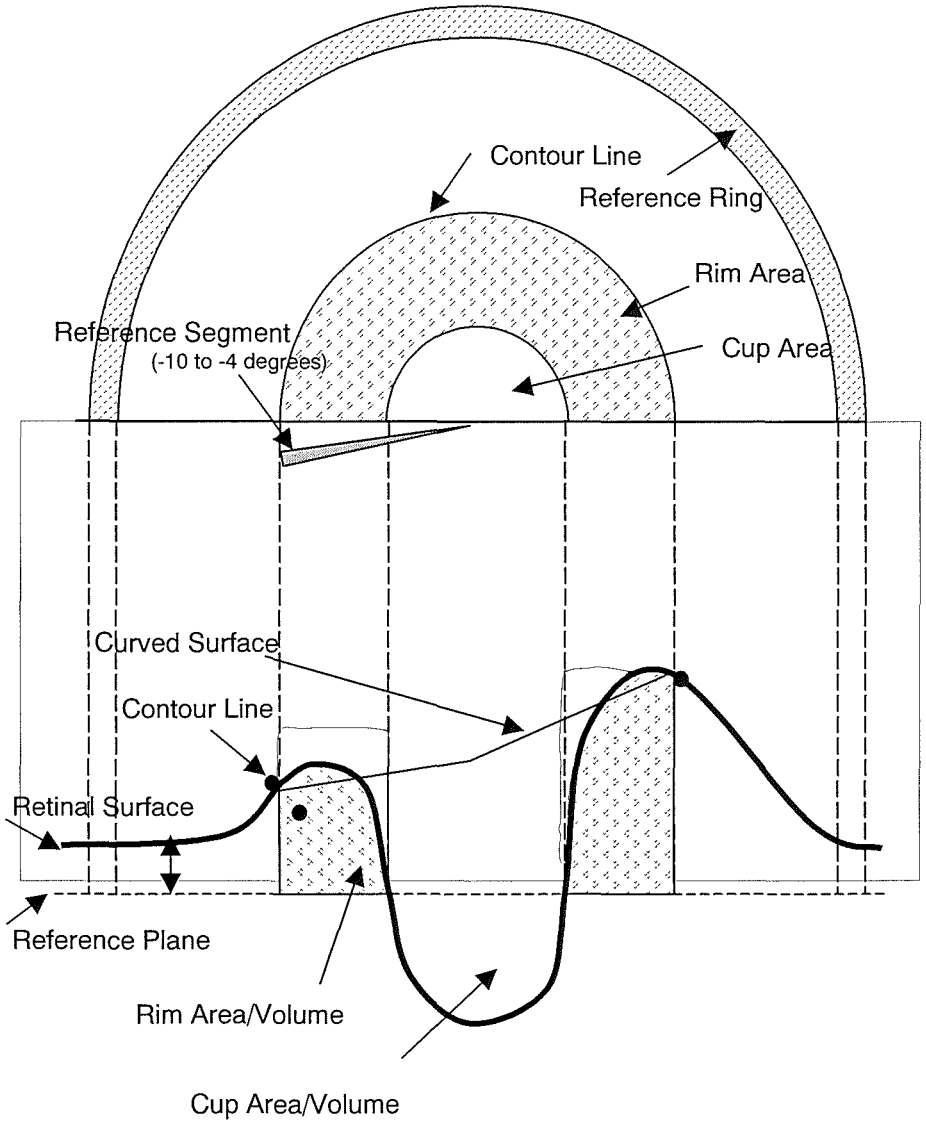

Figure 4.3 Schematic diagram showing the reference regions used to derive the HRT stereometric parameters (after Zangwill et al. 1996).

4.2.3 Inspection of an acquired image series.

The HRT software monitors the quality of the image series during the examination. Recommendations for the focal plane position, the scan depth or the sensitivity of the detector are displayed on the monitor. Once the settings for the acquisition parameters are considered optimal, the image is inspected for the presence of large eye movements. The series of 32 images can be sequentially displayed to aid the quality control. Excessive eye movements which shift the image by more than 25% of the image size cannot be corrected in subsequent processing and degrade the quality of the three-dimensionally generated image. Such images are discarded and further images obtained.

4.2.4 Determination of a Topography Image.

Following the acquisition of an image series, the HRT software generates a reflectivity and topography image. The sequential images are aligned to correct for small eye movements during image acquisition prior to the determination of a topographic and reflectivity image. In the latest software version 2.01, the accuracy of alignment has been improved from one pixel to approximately 0.1 pixel with, reportedly, a better quality image (Manual-HRT 1997). For each aligned pixel, the sum of the reflectivity measurements along the z-axis is used for the generation of the reflectivity image. The location of maximum reflectivity along the z-axis is assumed to indicate the vitreous/internal limiting membrane interface (Chauhan 1996), and the topography image displays the relative height of each location. The values are colour-coded for better contrast and ease of interpretation so the resultant reflectance image is suitable for comparison with a conventional colour photograph.

4.2.5 Determination of a Mean Topography Image.

Two or more topography images, for the same eye with the same field of view, can be selected for determining a Mean Topography Image (MTI). The reflectance values from each image are averaged to create the MTI. The image can permit increased accuracy of height measurement determination and allows an individual reproducibility value to be calculated (Orgül et al. 1997). The images are initially aligned and normalised prior to generating the MTI, the mean reflectance image and a standard deviation image. The normalisation process corrects for horizontal and vertical shifts, height offset, rotation and tilt between images, with additional perspective and magnification corrections (Manual-HRT 1997). In addition, the mean standard deviation of the reflectance values and the mean size of the 95% confidence interval averaged over the entire pixel array are presented.

4.2.6 Displaying the Topography and Mean Topography Images.

Alternate image presentations are available. The topography image can be displayed as a topography map with a superimposed 16 x 16 grid of numerical values that indicate the mean height of the 16 x 16 pixels enclosed within each grid square. The MTI can also present the

standard deviation of the mean heights at each pixel. Each square of the grid can be separately selected to display the values of each pixel. Further displays include a pseudo three-dimensional graph of the surface contours and a red-green stereo pair of images.

4.2.7 Interactive analysis of the Topograhy Image.

One-dimensional cross-sectional analysis of the topography image can be evaluated. The software permits inspection of the height variation along the retinal surface to be graphically superimposed on the topography image. Additionally, the measured reflected light intensity along the optical axis, in an aligned image series, can be inspected.

4.2.8 Stereometric Analysis.

In order to determine a series of stereometric parameters that can describe the three-dimensional shape of the ONH, the upper, lower and outer boundaries to the area of interest need to be defined. The spatial location for each point is defined according to a co-ordinate system.

4.2.9 The Default Co-Ordinate System.

In order to provide spatial measurements, a three-dimensional co-ordinate system employing three perpendicular axes denoted, X, Y and Z is used. The (x, y) planes are parallel to the focal plane of the camera, the plane of the computer monitor display and the two-dimensional topographic, or reflectivity images (these latter two, prior to alignment). Follow-up analysis through mean topography images and difference images require normalisation, which accounts for the rotation (about the Z-axis), the tilt (about the X and Y-axes) and a three-dimensional, shift. The calculation of the elevation at a given location is determined by the reflecting surface where the intensity of the reflected light reaches a maximum. The topographic image height measurements are determined relative to the focal point of the individual eye. Using knowledge of the laser beam deflection and the focal planes, with assumed optics of Gullstrand's schematic eye, measurements can be acquired calibrated in mms.

Four individual co-ordinate systems are available. They include the absolute system, in which the z axis runs parallel with the optical axis of the scanner and the eye. The origin of the z-axis lies at the focal plane of the eye; the relative system, in which the z-axis runs parallel with the optical axis of the scanner and the eye, where the origin of the z-axis is determined by the mean height of the peripapillary surface; the absolute and tilted system, in which the (x,y) plane runs parallel to the retinal surface, and the origin of the z-axis lies at the focal plane of the eye; and finally the 'Relative and Tilted' system in which the (x,y) plane runs parallel to the retinal surface and the origin of the z-axis is determined by the mean height of the peripapillary surface.

A default relative, tilted, co-ordinate system is generally employed in the HRT. The origin of the z (height) axis, in this co-ordinate system coincides with the mean height of the peripapillary retinal surface enclosed by a reference ring defined by the HRT software. The 'x-y' plane runs parallel to the tilted plane of the retinal surface. The z-axis is perpendicular to the retinal surface and parallel to the optical axis of the eye under examination.

4.2.10 Defining the Corrected Contour Line.

Prior to determining any stereometric measurements, a contour line is interactively defined either freehand-drawn or as a computer-generated circle. The contour line from either technique can be resized. Once stored within the HRT database, the contour line is superimposed on the topography and reflectance image. For stereometric evaluation of the ONH, the contour line is usually drawn around the inner border of the scleral ring that forms the optic disc margin. The contour line height is then corrected for artefacts such as blood vessels crossing the border of the line to provide a 'corrected contour line' (Figure 4.2). The height variation along the contour line is displayed graphically. Stereometric parameters can be computed for the region within the contour line or as user-defined segments of the ONH.

4.2.11 Defining the Standard Reference Plane.

A reference plane is used to determine which features within the contour line describe the ONH cup and which describe the NRR. The standard reference plane, employed in HRT software versions 1.11 and subsequent upgrades, is located 50μm posterior to the mean height of the contour line taken from the temporal region, 350° to 356° (Figure 4.2). The definition is based upon a section of the contour line that is thought to change least with glaucoma progression (Burk et al. 1995; Burk et al. 2000). The plane can be operator-defined if desired; however some stereometric parameters, including the mean RNFL thickness (RNFLT) are not automatically calculated for non-standard reference plane settings. The mean height of the reference plane by default is given relative to the mean height of the peripapillary retinal surface lying within a reference ring 2.7mm in diameter and 0.08mm in width for an image size of 10° (Manual-HRT 1997). The mean contour line height in the chosen temporal segment varies between images for a given eye and consequently the z-coordinate for the reference height also varies. However, averaging the measurements for several repeated images can optimise the estimate of a given parameter (Weinreb et al. 1993).

Most HRT stereometric parameters, including the rim area (RA), rim volume (RV), cup area (CA), cup volume (CV), cup/disc area ratio (CDAR), mean RNFL thickness (RNFLT) and the RNFL cross-sectional area, are dependent upon the height position of a defined reference plane. In the earlier software version (version 1.10), a plane 320μm below the mean retinal height of a 'peripheral' reference ring was chosen. This gave rise to a reference plane independent of the observer defined optic disc margin. The definition of the reference plane has been superseded in versions 1.11 and 2.01, and is now derived from a small sample of height

measurements in the contour line. The current reference plane can be very sensitive to small errors in contour line alignment between images, particularly if the region's surface contour is grossly uneven. This can cause a variation in those parameters that are dependent upon the reference plane height (Burk et al. 2000).

Selecting parameters that are known to be independent of a reference plane (Brigatti and Caprioli 1995) can overcome some of the variation associated with reference plane definition. The cup shape measure (CSM), and third moment in contour (TMC) are two of the parameters independent of the reference plane, the other parameters being, the height variation in contour (HVC), the mean cup depth and the maximum cup depth. The CSM is an index of the distribution of cup depth values, with negative values assigned to those shallow cups having gently sloping borders, and positive values for steeply sloping walled cups.

4.2.12 Defining the Curved Surface.

The Curved Surface (CS) provides the upper limit towards the vitreous, of an area defined by the contour line. The CS is bounded by the corrected contour line (Figure 4.2). The CS boundary height is the same as the corrected contour line and its centre height is equal to the mean height of the corrected contour line (Manual-HRT 1997).

4.2.13 Baseline and Follow-up Examinations.

A baseline examination is created when a contour line is defined on the topography, the reflectance, or the mean topography image. The HRT system software allows the contour line to be exported from one image of a series and subsequently imported onto another image for the same eye, either acquired at the same session or at follow-up visits (Manual-HRT 1997). In so doing, the follow-up image is automatically normalised for tilt, rotation and magnification to the topography of the baseline examination. This feature is particularly used for longitudinal studies of topographical change.

Detailed descriptions of the various Parameter Definitions are provided in the Appendix A.I.

4.2.14 Accuracy and Reproducibility.

Accurate (Janknecht and Funk 1995) and highly reproducible (Dreher et al. 1991; Lusky et al. 1993; Mikelberg 1993; Rohrschneider et al. 1994) topographical measurements have been obtained using a SLO.

The magnitude of the reproducibility varies between instruments, software versions, study designs, and statistical analyses employed. Dreher et al (1991) found sources of variability, using the LTS, that included blood vessels, surface contours, reference plane definition and the number of repeated measures. Variability of topographic measurements between normal

subjects and those with glaucoma, or as a function of age, were minimal. Lusky and associates (1993) confirmed these observations using the HRT. To minimise variability, Dreher et al (1991) suggested the exclusion of areas around blood vessels within the optic nerve head, reduced scan acquisition time, and averaged height values for pixel groups offset by loss of lateral resolution. Chauhan and McCormick (1995) advocated the introduction of pulsed-synchronised images to overcome the varying and unpredictable influences of the cardiac cycle.

Other potential sources of variability include the scan separation times (Chauhan and LeBlanc 1994), the regional variation (Brigatti et al. 1995) the scanner alignment, patient fixation and alignment algorithms (Orgül et al. 1996), and the between-observer placement of contour line (Hatch et al. 1999), Short- and long-term variability of HRT measurements have been shown to be similar (Chauhan and LeBlanc 1994).

The majority of studies have incorporated the recommendations for clinical efficiency proposed by Weinreb et al (1993), namely obtaining three successive images and using the mean topography of the three images. Increased variability from poor quality images has been attributed to media opacities, compounded by increasing age (Chauhan and LeBlanc 1994) and to small pupils (Zangwill et al. 1997). Lusky et al (1993) considered the small entrance and exit pupil of the optical system would minimise the influence of pupil size. Zangwill et al (1997) found the image quality to be significantly improved and the variability to be reduced with pupil dilation of greater than 3mm especially in those patients with media opacities. Tomita et al (1994) found the variability in a young, 'normal' sample to increase with pupils constricted by pilocarpine. However, Orgül, (1997) in cautioning the use of dilated pupils, due to the increased risk of misalignment through a wide aperture, advocated the acquisition of at least three images to minimise any random error influences.

Garway-Heath and co-workers (1999) evaluated the within- and between-observer variability and found the coefficient of variation for the within-observer (2.4%) to be slightly lower than for the between-observer (4.4%), yet both were similar to planimetry. RV was particularly sensitive to reference height and showed markedly greater variation than CA, DA or RA, and CSM. The variation can be reduced using an imported disc margin definition for subsequent images (Orgül et al. 1997).

4.2.15 Validity.

High reproducibility does not ensure that the measurements described accurately represent the structure being measured. In order to assess the validity of the HRT, one approach is to assess measurements taken from a model eye. Results have suggested reasonable accuracy for three-dimensional parameters (Dreher and Weinreb 1991; Janknecht and Funk 1994). Accuracy and reproducibility for both excavation and elevation are found to be very good (Janknecht and Funk 1994).

More recently, three-dimensional optic disc measurements obtained with the Glaucoma-Scope (Ophthalmic Imaging Systems, Sacramento, CA), an entirely different system using raster tomography, has provided absolute measurements and an ability to distinguish between normal and glaucomatous eyes similar to that of the HRT (Gundersen et al. 1998; Gundersen et al. 2000). The findings suggest that the information from each system is valid.

4.2.16 The Discriminant Analysis Function.

The sensitivity and specificity of the HRT has shown promise for detecting early glaucomatous visual field loss (Mikelberg 1995; Uchida et al. 1996; Hatch et al. 1997), despite the large between-individual variation in optic disc parameters and the wide diversity of glaucomatous morphometric changes. The choice of parameter or parameters considered to be the most sensitive and specific for glaucomatous damage, however, may depend upon the cross-sectional or longitudinal nature of the study.

It has previously been recognised that the NRR area (Airaksinen et al. 1992), RNFL integrity (Sommer et al. 1977) and optic cup/disc configuration (Jonas and Papastathopoulos 1996) provide suitable parameters for discriminating between glaucomatous and normal individuals. The corresponding parameters defined by the HRT software, volume above reference (VAR), mean height in contour (MHC), and the CSM are also able to identify those individuals with ocular hypertension from those individuals with ONH damage (Hatch et al. 1997). Other cross-sectional studies have confirmed that the CSM is of particular value in demonstrating differences between normal, glaucomatous and ocular hypertensive eyes (Burk and Rohrschneider 1992; Brigatti and Caprioli 1995; Mikelberg 1995). However, Mardin et al (1998) in discriminating between normals and POAGs, found the sensitivity and specificity of the HRT parameters to vary with the optic disc size. They recommended stratifying or applying a corrective factor for optic disc size.

In view of the large between-individual variability in ONH topography a multi-parameter evaluation is likely to be more capable of identifying glaucomatous structural damage than a single parameter (Drance et al. 1978; Drance et al. 1981; Caprioli 1992; O'Connor et al. 1993).

The multivariate statistical technique of discriminant analysis can consider all relevant ONH topography measurement variables simultaneously as opposed to their individual contributions (Mikelberg 1995; Bathija et al. 1998). The ability of each variable to separate a glaucomatous population from a non-glaucomatous population is calculated separately, and the variables are ranked in descending order according to their significance in the differentiation process (Drance et al. 1978; Susanna and Drance 1978; Drance et al. 1981). Each variable is then weighted. The coefficients applied as weighting to each variable ensure that maximal separation is achieved between the two populations. A constant is finally added to the selection of the weighted variables to produce a discriminant analysis function. The value of the constant is chosen in order that the probabilities of misclassification as normal or glaucomatous is equal,

but the value can be changed depending upon the importance of making an error of misclassification in either direction.

Several studies have proposed the use of multivariant discriminant analysis functions, although, the characteristics of the study population are likely to influence the discriminating power of each formula derived from the function (Mikelberg 1995; Iester and Mikelberg 1997; Bathija et al. 1998; Iester et al. 1999a; Mardin et al. 1999). Nevertheless, the different derived formulae have all tended to show a similar ability to discriminate the normal from the glaucomatous individual (Iester et al. 2000a).

4.2.17 Use of Linear Regression for Discriminant Analysis.

Garway-Heath and Hitchings (1998) and Wollstein et al (1998) recommend that optic disc size should be considered when defining the normal range for the ONH. They each employed linear regression statistical techniques to account for the relationship between DA and RA and were able to then differentiate normal from glaucomatous eyes. Further improvement in the identification of focal ONH damage was achieved by applying the technique to the six HRT pre-defined segments. Similar findings were reported for the relationship between DA and CDAR (Garway-Heath et al. 1998; Wollstein et al. 1998).

4.2.18 Ranked-Segment Distribution (RSD) curve.

Asawaphureekorn (1996), proposed the use of a method developed originally by Bebie et al (1989) for differentiating between diffuse and localised visual field defects, and developed the Ranked-Segment Distribution (RSD) curve, as an aid to parameter interpretation and glaucoma detection. The analysis ranks the sector measurements of selected parameters, and compares the results with significance limits derived from a group of normal individuals. Bartz-Schmidt (1996) compiled a normative cumulative frequency distribution curve of 100 volunteers, for the normalised rim/disc area, rim/disc area ratio, rim volume and retinal nerve fibre layer cross-sectional area, corrected for disc size. These RSD curves illustrate the 5^{th} and 95^{th} percentiles, the range between which 90% of all normal ONHs lie. The normalised curves allow a comparison to be made with an examined ONH, independent of the disc area.

However, as with visual field analysis using the Bebie curves (Åsman and Olsson 1995), spatial information is lost during the ranking procedure. Low sector values tend to occur at the temporal disc regions in normal eyes, but the glaucomatous damage is more typical at the vertical pole regions of the ONH. By using a ranked analysis the location of the sector with low values is unknown, and evidence suggests that the analysis is not optimised to distinguish diffuse and localised ONH damage and sensitivity can be compromised (Gundersen and Åsman 2000).

In addition, long-term fluctuations can occur in the normalised rim/disc area ratio due to the variation in scaling between independent images, with or without changes in the refractive error.

In order to minimise the variations, which is of particularly relevance in longitudinal studies, transference of the contour line to follow-up examinations has been advocated (Jonescu-Cuypers et al. 1998).

4.3 Aims.

The aim was two-fold. Firstly, to determine the within- and the between-visit variability, as a function of the number of repeated images, for stereometric parameters of the ONH as derived by the HRT (software version 2.01), for the global analysis, correcting for age and disc area across the three diagnostic groups. Secondly, to determine the corresponding between-visit variability for the HRT sector analysis, correcting for age and disc area across the three diagnostic groups.

4.4 Sample.

The sample comprised 24 healthy, normal volunteers, 18 patients with ocular hypertension (OHT), 9 patients with high-risk ocular hypertension (OHT(H)) and 24 patients with stable primary open-angle glaucoma (POAG). The mean age of the Normal group was 57.3 (SD 17.6) years, and of the OHT group 64.9 (SD 12.3) years, and of the OHT(H) group 65.7 (SD 5.4) years and of the POAG group 67.2 (SD 10.4) years. One POAG individual was excluded from the study due to poor quality HRT images and the relevant individual data is not included in the demographic data.

4.5 Methods.

The chosen eye of each subject was dilated with Tropicamide 1%, 20-30 minutes prior to acquisition of the series of scans, in order to optimise the signal-to-noise ratio (Manual-HRT 1997). The attention of the non-tested eye, throughout scan acquisitions, was directed towards a fixation target placed at eye level on a wall, 2m distance directly in front of the subject.

The initial focal plane was set to the spherical equivalent of the refractive error, the scan depth to 2.5mm, the size of the field to be scanned to 10 degrees and the laser intensity set to maximum (Manual-HRT 1997). The camera objective lens was positioned approximately 15mm from the corneal surface, and adjusted to direct the laser beam through the pupil (Manual-HRT 1997). Fine adjustment was undertaken both of the vertical and horizontal position of the camera to ensure that the optic nerve head image was centred on the real-time monitor and of the focal plane position to achieve optimal retinal and ONH image illumination.

Throughout the 1.6 second period for scan acquisition, the subject was asked to refrain from blinking and between each successive scan the subject was encouraged to remain with their head and chin firmly against the respective head and chin rests. After the image acquisition, both the quality control message display and the image series were examined for unacceptable

image quality and eye movements. A subjective scale of 1 to 10 was used to grade both the image quality and fixation stability. Those images with a combined score totalling less than 15 were immediately discarded (Hosking and Flanagan 1996).

The software subsequently corrected each accepted scan series for small eye movements by aligning consecutive two-dimensional image sections in each series to create a reflectance and topography image. Additionally, using the HRT software version 2.01, the MTI of seven scans for each individual was calculated. The disc margin, as defined by the inner border of Elschnig's scleral ring, was interactively outlined on the MTI whilst the image was being viewed on the computer monitor.

The contour line was transferred onto each of the seven independent original topography images, using the HRT software to align the imported contour line with each imaged disc margin. Alignment failed for a single image of two subjects, and in those circumstances the contour line was redrawn on the two individual images. The transfer of the contour line from the mean topographic image to each of the separate scanned images allows the HRT software to perform image-to-image scaling. The automatic transfer minimises errors attributable to fluctuations in the size of the image pixels between images (Jonescu-Cuypers et al. 1998).

The stereometric parameters were corrected for corneal curvature and refraction. Central curvature was measured using a keratometer (Magnon: model OM 450), and ametropia determined from retinoscopy and confirmatory refractive findings. The information was input into the HRT database prior to scan acquisition.

The global parametric data was generated through the default HRT software for the seven topography images for each individual and the data transferred to an MS Excel spreadsheet for further statistical analysis.

To generate the sector analysis data, only the MTI at each visit was used. Once the contour line had been defined, the operator defined the angular extent and region for each sector. The temporal sector extended from 315° to 45°, where 360° and 0° refer to the temporal horizontal position. The superior sector extended from 45° to 135°, the nasal sector extended from 135° to 225°, and the inferior sector extended from 225° to 315°. For each sector, the HRT software calculated the stereometric parameters, and the unformatted data was transferred into an MS Excel spreadsheet. A macro program converted the data into a useable form and the data collated for the entire sample, for further descriptive and statistical analysis.

4.6 Analysis

4.6.1 Global Analysis.

The within-visit, between-individual variation was expressed in terms of the Coefficient of Variation (%), the SD as a function of the mean and as a distribution of the within-individual SDs for each Global parameter.

The within-group between-visit limits of agreement were determined using the method described by Bland and Altman (1986) for each of the HRT parameters, for each of the diagnostic groups.

The data for each of the selected HRT stereometric parameters were then analysed using repeated measures Analyses of Variance (ANOVA) with age, disc area and diagnosis as between-subjects main effects and age x diagnosis and disc area x diagnosis as between-subjects interactions. The measure of disc area was obtained from the mean topography image acquired at Visit One.

The results from the ANOVA evaluated the within- and the between-visit variability of the global HRT stereometric parameters for the ONH as a function of age, diagnosis and the number of repeated images acquired. The results also permitted an assessment of the capability of the HRT to discriminate the effects of age and diagnostic group on the selected measures of ONH topography.

4.6.2 Sector Analysis.

A similar repeated measures Analyses of Variance (ANOVA) with age, disc area and diagnosis as between-subjects main effects and age x diagnosis and disc area x diagnosis as between-subjects interactions for each of the four sectors. Visit and number of scans were considered as within-subjects factors.

The ANOVA evaluated the between-visit variability of the sector HRT parameters for the ONH as a function of age and diagnosis. The ability of the HRT to discriminate the effects of age and diagnostic group on the measures derived for sector ONH topography was considered in a similar manner to that for the Global evaluation.

4.7 Results.

The Group mean (±SD) standard deviation of the height measurements at a pixel within the MTIs, for Visit One and Visit Two were for the Normal group, 17.03 ± 5.52μm and 16.73 ± 5.23μm; for the OHT group, 27.41 ± 13.54μm and 27.18 ± 15.40μm; and for the POAG group, 23.28 ± 13.23μm and 25.28 ± 16.52μm, respectively.

4.7.1 Within-visit variability of the Global HRT derived stereometric parameters.

The Coefficient of Variation (CoV) for each of the normal individuals, each of the patients with ocular hypertension and each of the patients with POAG at Visit One and at Visit Two are given in Table 4.1. The within-visit variation as defined by one standard deviation is shown as a function of each respective Global mean stereometric parameter in Figure 4.3 and 4.4. The within-visit variation for DA is not shown graphically since the SD was almost invariably zero by using an imported contour line, across the diagnostic groups. The cumulative frequency distribution of the within-visit variation for Visit One, for each of the stereometric parameters across the diagnostic groups is presented in Figures 4.5 and 4.6. The distribution for DA has again been omitted.

The CoV was consistently lowest for the DA. This would be expected from the use of an imported contour line. The RA, and RDAR also had low CoVs. The CSM, mean RNFLT and RNFLT cross-sectional area had the largest CoV's. The CoV's were similar for each visit and were generally greatest for the POAG group across each of the parameters. The SD was greatest for the RNFL cross-sectional area for each of the diagnostic groups and was greater for the OHT and POAG groups than for the Normal group. The SD was least for the Normal group across each of the stereometric parameters.

The cumulative frequency distributions show that the variability with seven images for each parameter, as defined by one SD, was generally less than 0.1 (units), with the notable exception of the RNFL cross-sectional area, across the three diagnostic groups.

	Disc Area (DA)			
	VISIT ONE		VISIT TWO	
	MEAN CoV (%)	SD	MEAN CoV (%)	SD
NORMAL	0.22	1.03	0.01	0.02
OHT	0.21	1.07	0.01	0.02
POAG	0.01	0.01	0.01	0.01

	Cup Area (CA)			
	VISIT ONE		VISIT TWO	
	MEAN CoV (%)	SD	MEAN CoV (%)	SD
NORMAL	0.00	0.00	0.01	0.02
OHT	14.63	16.53	21.75	41.81
POAG	6.30	4.91	6.47	10.13

	Cup/Disc Area Ratio (CDAR)			
	VISIT ONE		VISIT TWO	
	MEAN CoV (%)	SD	MEAN CoV (%)	SD
NORMAL	0.00	0.00	0.00	0.00
OHT	14.06	16.84	21.83	42.05
POAG	6.25	4.82	6.46	10.12

	Rim Area (RA)			
	VISIT ONE		VISIT TWO	
	MEAN CoV (%)	SD	MEAN CoV (%)	SD
NORMAL	2.11	1.20	3.82	6.65
OHT	4.61	4.39	3.78	3.00
POAG	7.94	5.77	6.66	5.43

	Rim/Disc Area Ratio (RDAR)			
	VISIT ONE		VISIT TWO	
	MEAN CoV (%)	SD	MEAN CoV (%)	SD
NORMAL	2.25	1.47	3.82	6.65
OHT	4.82	4.45	3.77	3.00
POAG	7.79	5.68	6.66	5.43

	Height Variation in Contour (HVC)			
	VISIT ONE		VISIT TWO	
	MEAN CoV (%)	SD	MEAN CoV (%)	SD
NORMAL	8.28	6.28	8.62	5.42
OHT	12.69	9.27	9.64	6.26
POAG	14.14	7.37	13.41	6.71

	Cup Volume (CV)			
	VISIT ONE		VISIT TWO	
	MEAN CoV (%)	SD	MEAN CoV (%)	SD
NORMAL	0.00	0.00	0.00	0.00
OHT	0.00	0.00	38.69	71.29
POAG	13.67	12.31	13.45	14.28

	Rim Volume (RV)			
	VISIT ONE		VISIT TWO	
	MEAN CoV (%)	SD	MEAN CoV (%)	SD
NORMAL	7.93	6.27	10.67	11.19
OHT	12.94	6.25	10.66	5.72
POAG	16.16	8.54	15.51	8.83

	Cup Shape Measure (CSM)			
	VISIT ONE		VISIT TWO	
	MEAN CoV (%)	SD	MEAN CoV (%)	SD
NORMAL	-12.96	11.71	-13.27	8.97
OHT	-21.43	14.32	-20.94	12.03
POAG	-28.14	51.26	-62.33	143.81

	Mean RNFL Thickness (RNFLT)			
	VISIT ONE		VISIT TWO	
	MEAN CoV (%)	SD	MEAN CoV (%)	SD
NORMAL	8.26	5.86	12.83	17.57
OHT	12.21	5.62	10.55	5.91
POAG	23.69	30.42	19.43	16.01

	Mean RNFL Cross-sectional Area			
	VISIT ONE		VISIT TWO	
	MEAN CoV (%)	SD	MEAN CoV (%)	SD
NORMAL	8.14	5.59	12.83	17.56
OHT	12.06	5.71	10.54	5.91
POAG	23.71	30.46	19.47	16.05

Table 4.1. The Coefficients of Variation (%) and one SD for the Global HRT stereometric parameters DA, CA, CDAR, RA, RDAR, HVC, CV, RV, CSM, mean RNFLT and RNFL cross-sectional area, for the Normal, OHT, and POAG groups, for each of the two visits.

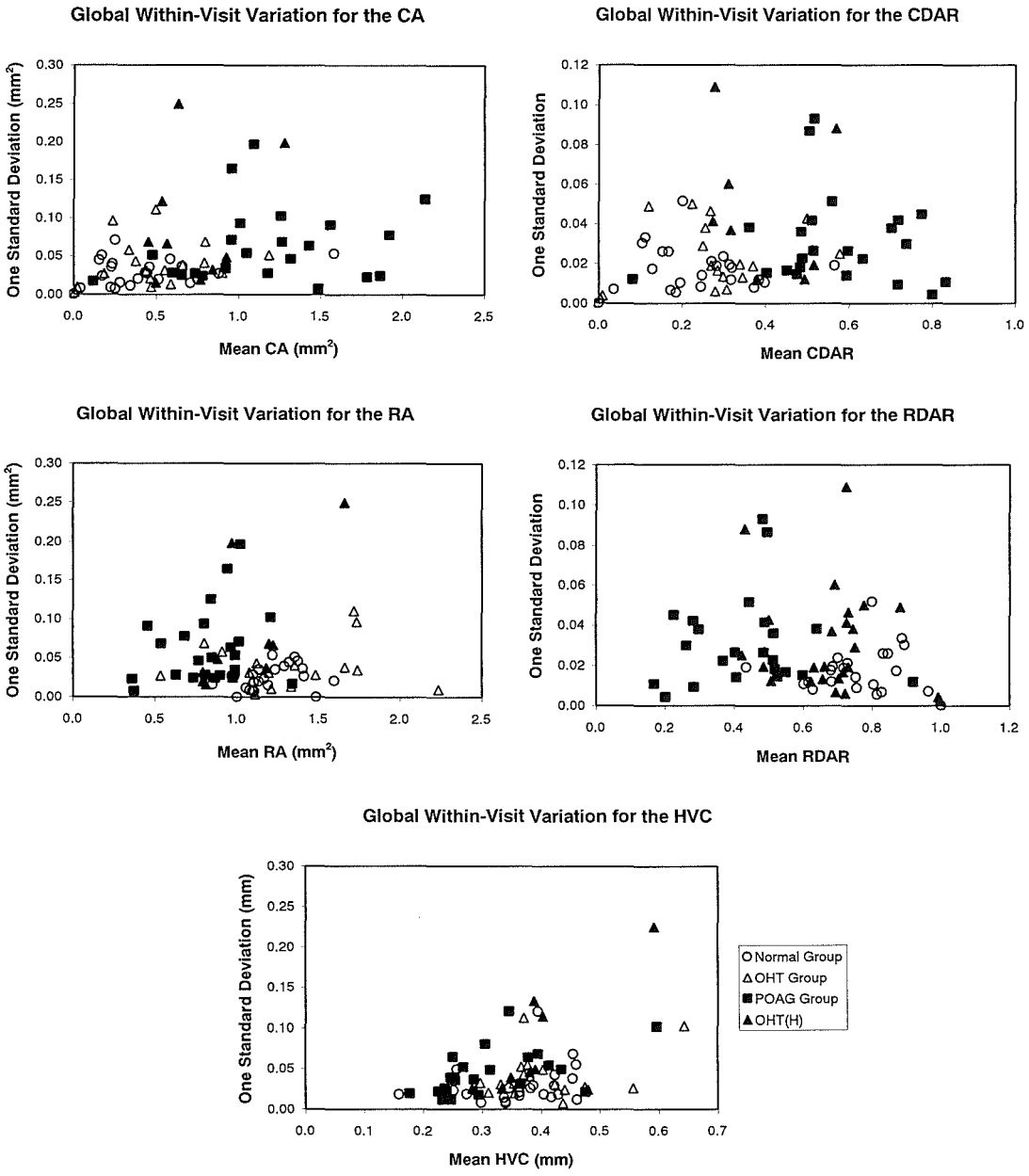

Figure 4.3. The within-visit variation at Visit One as defined by one SD for the HRT stereometric parameters as a function of the respective CA, CDAR, RA, RDAR, and HVC, across the diagnostic groups. Note the different scaling with the ordinate and abscissa axes used for each parameter.

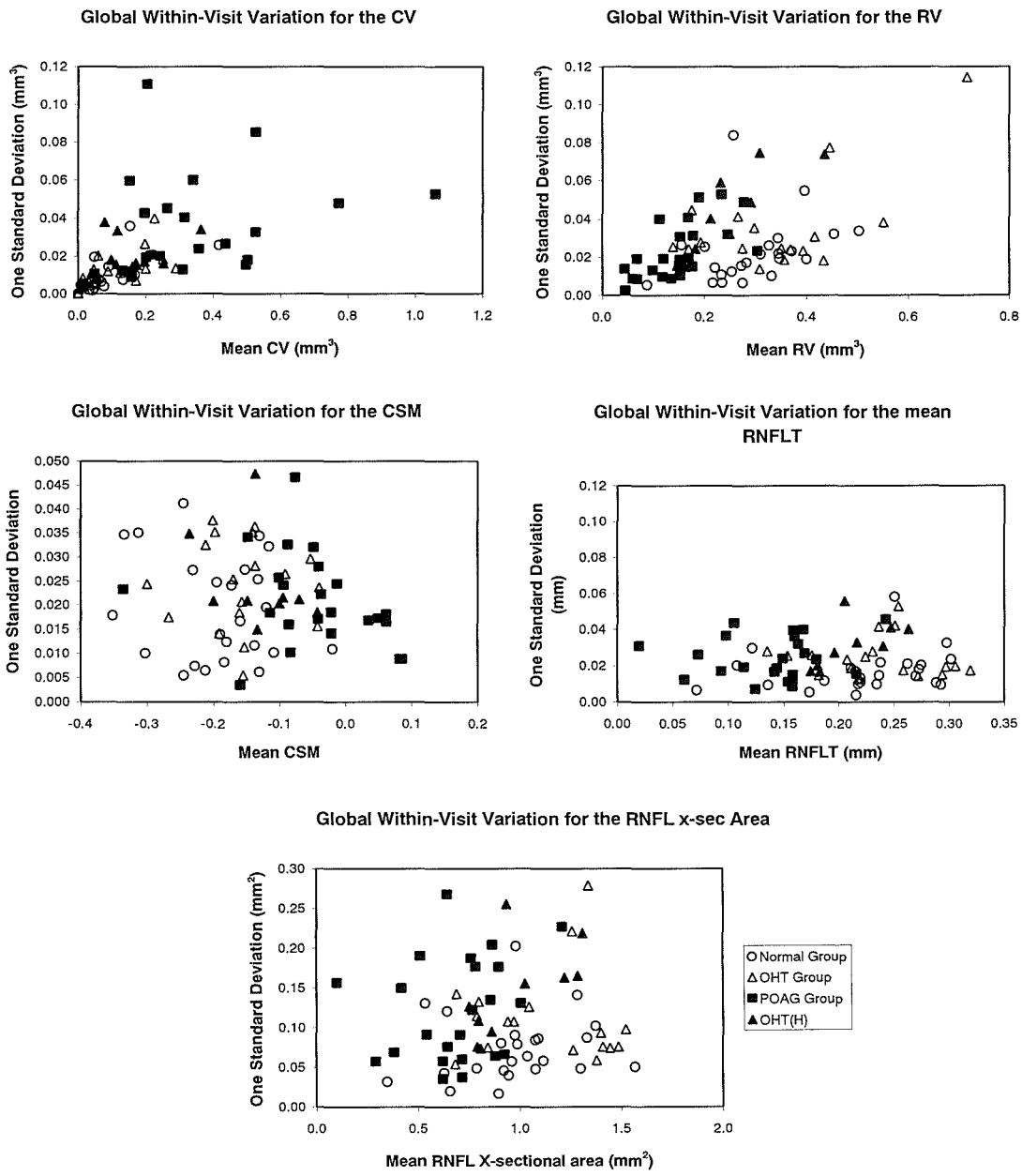

Figure 4.4. The within-visit variation at Visit One as defined by one SD for the HRT stereometric parameters as a function of the respective CV, RV, CSM, mean RNFLT and RNFL cross-sectional area across the diagnostic groups. Note the different scaling with the ordinate and abscissa axes used for each parameter.

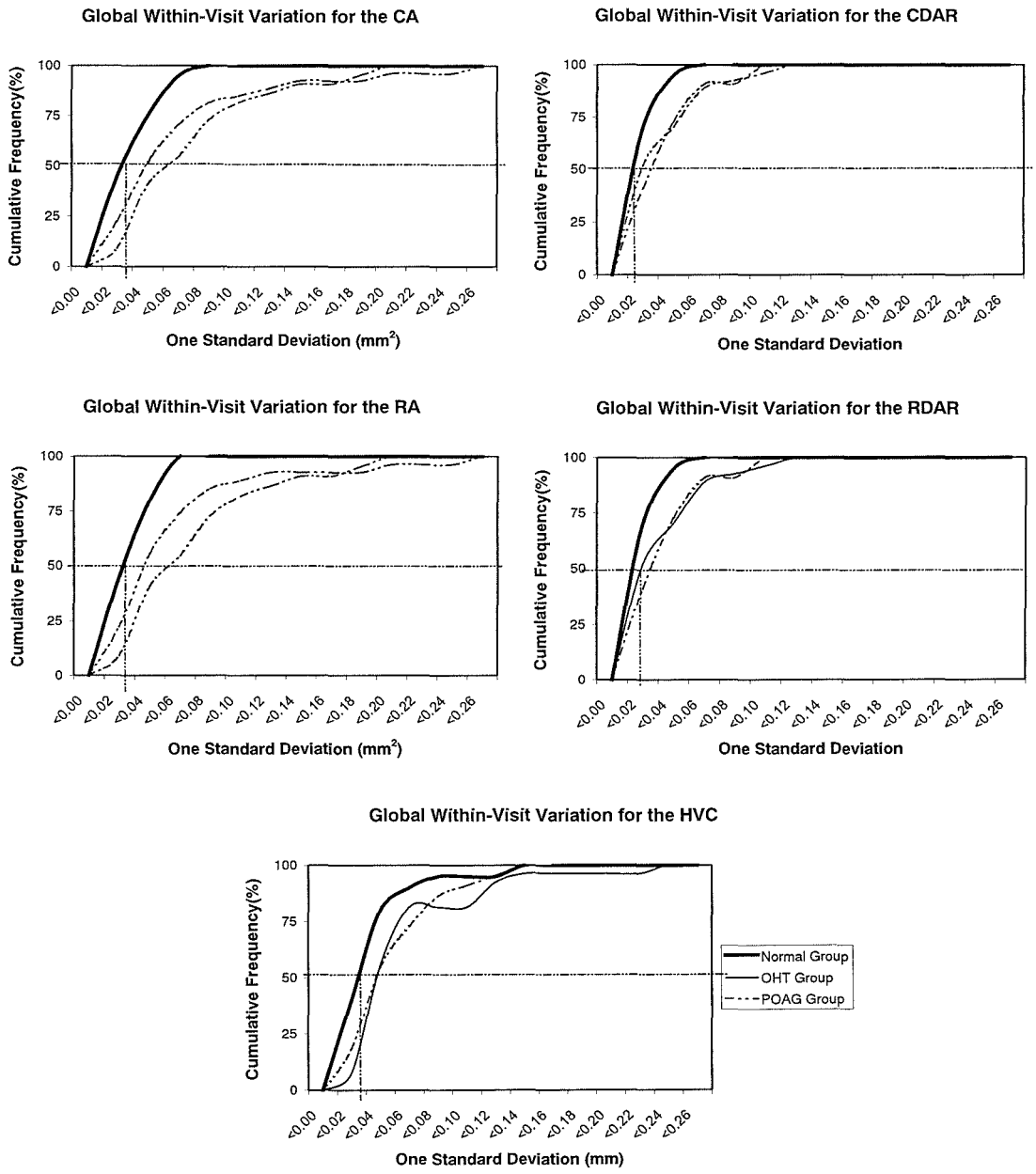

Figure 4.5. The cumulative frequency (%) distribution of the within-visit variation at Visit One for the HRT stereometric parameters CA, CDAR, RA, RDAR, and HVC for the Normal, OHT and POAG group.

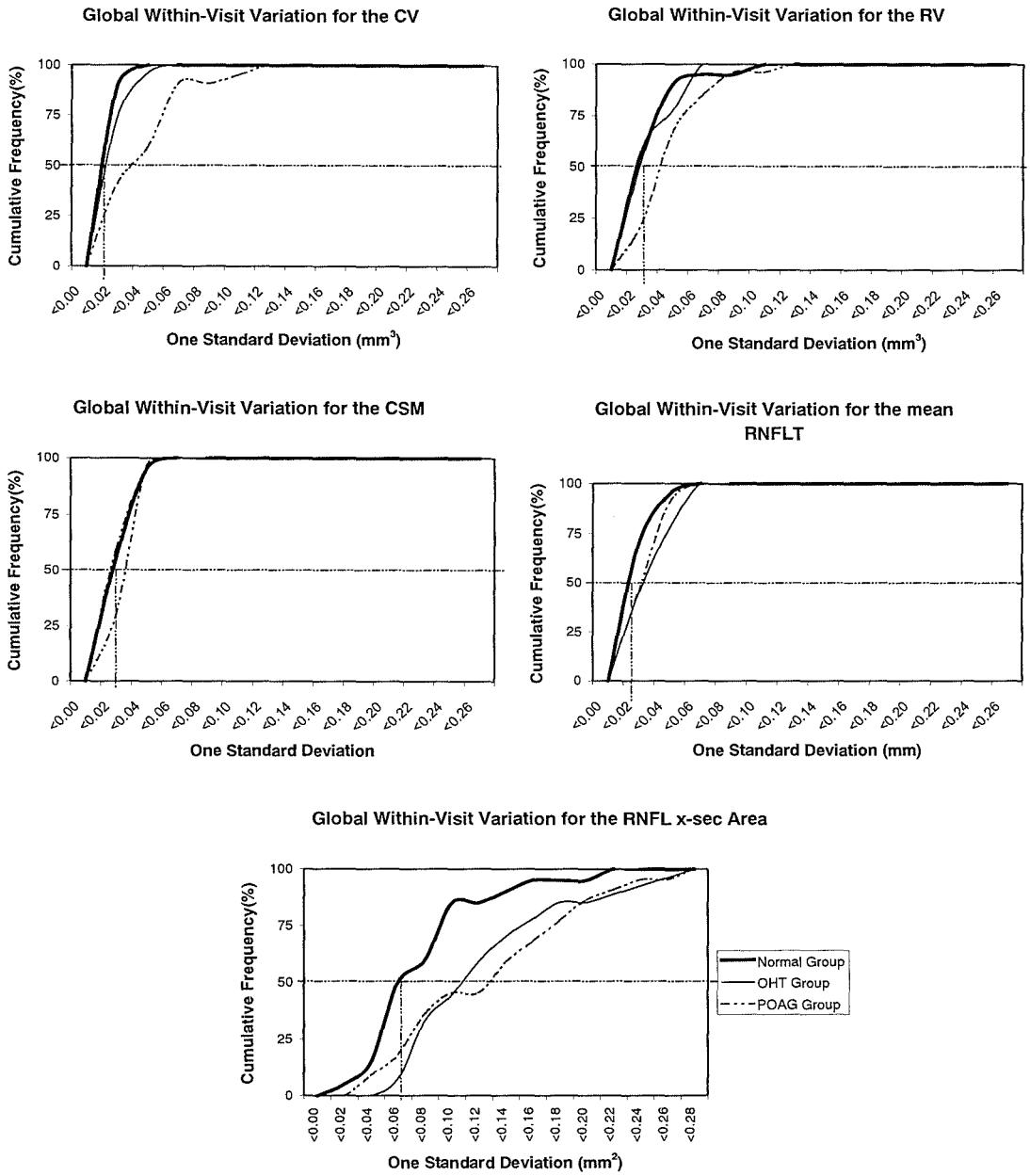

Figure 4.6. The cumulative frequency (%) distribution of the within-visit variation at Visit One for the HRT stereometric parameters CV, RV, CSM, mean RNFLT, and RNFL cross-sectional area for the Normal, OHT and POAG group.

4.7.2 Between-visit variability of the Global HRT derived stereometric parameters.

The Group Mean and one SD for each of the Global stereometric parameters at Visit One and at Visit Two as function of diagnosis is given in Table 4.2. The ANOVA summary table is given in Table 4.3.

4.7.2.1 Disc area (DA).

The Group Mean DA did not vary between the first and second visits ($p=0.509$), nor with the number of scans ($p=0.624$). The limits of agreement for the DA between the first and second visits are given in Table 4.4 and Figure 4.7.

4.7.2.2 Cup area (CA).

The Group Mean CA did not vary between the first and second visits ($p=0.676$) nor with the number of scans ($p=0.951$). The limits of agreement for the CA between the first and second visits are given in Table 4.4 and Figure 4.8. The CA increased with increase in the disc area ($R^2=0.56$; $p<0.001$). The increase in CA with increase in disc area was dependent upon diagnosis ($p<0.001$).

4.7.2.3 Cup-disc area ratio (CDAR).

The Group Mean CDAR did not vary between the first and second visits ($p=0.962$) nor with the number of scans ($p=0.928$). The limits of agreement for the CDAR between the first and second visits are given in Table 4.4 and in Figure 4.9. The CDAR increased with increase in the disc area ($R^2=0.30$; $p<0.001$). The increase in CDAR with increase in disc area was independent of diagnosis ($p=0.082$).

4.7.2.4 Rim area (RA).

The Group Mean RA did not vary between the first and second visits ($p=0.637$) nor with the number of scans ($p=0.957$). The limits of agreement for the RA between the first and second visits are given in Table 4.4. The difference in the RA between the two visits is shown in Figure 4.10. The RA generally increased with increase in the disc area ($R^2=0.05$; $p<0.001$). However, the increase in RA with increase in disc area was dependent upon diagnosis ($p<0.001$), and was minimal, or decreased in the POAG group.

4.7.2.5 Rim-disc area ratio (RDAR).

The Group Mean RDAR did not vary between the first and second visits ($p=0.742$) nor with the number of scans ($p=0.501$). The limits of agreement for the RDAR between the first and second visits are given in Table 4.4 and in Figure 4.11.

4.7.2.6 Height variation in contour (HVC).

The Group Mean HVC did not vary between the first and second visits (p=0.949). The limits of agreement for the HVC between the first and second visits are given in Table 4.4 and in Figure 4.12. The HVC was independent of the disc area (p=0.750) and of the number of scans (p=0.227).

4.7.2.7 Cup Volume (CV).

The Group Mean CV did not vary between the first and second visits (p=0.326) nor with the number of scans (p=0.875). The limits of agreement for the CV between the first and second visits are given in Table 4.4 and in Figure 4.13. The CV increased with increase in the disc area (R^2=0.36; p<0.001). The increase in CV with increase in disc area varied between the groups and was greatest for the POAG group (p<0.001).

4.7.2.8 Rim Volume (RV).

The Group Mean RV did not vary between the first and second visits (p=0.768). The limits of agreement for the RV between the first and second visits are given in Table 4.4 and in Figure 4.14. The RV was independent of the disc area (p=0.071) and of the number of scans (p=0.573).

4.7.2.9 Cup Shape Measure (CSM).

The Group Mean CSM did not vary between the first and second visits (p=0.464). The limits of agreement for the CSM between the first and second visits are given in Table 4.4 and in Figure 4.15. The CSM increased with increase in the disc area (R^2=0.32; p<0.001). The increase in CSM with increase in disc area was independent of diagnosis (p=0.295) and of the number of scans (p=0.664).

4.7.2.10 Mean Retinal Nerve Fibre Layer Thickness (RNFLT).

The Group Mean mean RNFLT did not vary between the first and second visits (p=0.172). The limits of agreement for the mean RNFLT between the first and second visits are given in Table 4.4 and in Figure 4.16. The mean RNFLT was independent of the disc area (p=0.191) and did not vary with the number of scans (p=0.860).

4.7.2.11 RNFLT Cross-sectional Area.

The Group Mean RNFLT cross-sectional area did not vary between the first and second visits (p=0.466), and was independent of the number of scans (p=0.900). The limits of agreement for the RNFLT cross-sectional area between the first and second visits are given in Table 4.4 and in Figure 4.17. The RNFLT cross-sectional area increased with increase in the disc area (R^2=0.01; p=0.011). The increase in RNFLT cross-sectional area with increase in disc area was independent of diagnosis (p=0.118).

	NORMAL		OHT		POAG	
	VISIT 1	VISIT 2	VISIT 1	VISIT 2	VISIT 1	VISIT 2
Disc Area (mm^2)	1.60 (0.41)	1.54 (0.41)	1.80 (0.44)	1.80 (0.44)	1.98 (0.42)	2.02 (0.40)
Cup Area (mm^2)	0.38 (0.35)	0.39 (0.36)	0.59 (0.31)	0.68 (0.30)	1.18 (0.49)	1.17 (0.48)
Cup-Disc Ratio	0.22 (0.14)	0.23 (0.14)	0.32 (0.14)	0.31 (0.14)	0.57 (0.17)	0.56 (0.17)
Rim Area (mm^2)	1.16 (0.16)	1.15 (0.16)	1.21 (0.39)	1.22 (0.38)	0.84 (0.25)	0.85 (0.26)
Rim-Disc Area Ratio	0.78 (0.14)	0.77 (0.14)	0.68 (0.14)	0.69 (0.14)	0.43 (0.17)	0.44 (0.17)
Height Variation in Contour (mm)	0.37 (0.08)	0.38 (0.07)	0.40 (0.09)	0.40 (0.09)	0.31 (0.10)	0.32 (0.10)
Cup Volume (mm^3)	0.07 (0.09)	0.07 (0.10)	0.14 (0.09)	0.14 (0.09)	0.34 (0.24)	0.34 (0.23)
Rim Volume (mm^3)	0.29 (0.08)	0.29 (0.09)	0.31 (0.14)	0.31 (0.14)	0.15 (0.07)	0.15 (0.07)
Cup Shape Measure	-0.19 (0.09)	-0.19 (0.08)	-0.15 (0.07)	-0.14 (0.07)	-0.05 (0.10)	-0.05 (0.11)
Mean RNFL Thickness (mm)	0.23 (0.05)	0.23 (0.06)	0.23 (0.05)	0.24 (0.05)	0.14 (0.05)	0.13 (0.04)
RNFL X-Sectional Area (mm^2)	0.98 (0.20)	0.98 (0.26)	1.08 (0.28)	1.11 (0.31)	0.69 (0.25)	0.68 (0.22)

Table 4.2. The Group Mean and SD of the Global HRT stereometric parameters, at Visit One and Visit Two, based upon the mean of seven images for each individual, for the Normal, the OHT and the POAG group. For the Normal group, [n = 24 on first visit and n = 21 on second visit as the HRT was unavailable for the repeat visit on 3 individuals].

Global

	HRT Stereometric Parameters										
FACTOR	**DA**	**CA**	**CDAR**	**RA**	**RDAR**	**HVC**	**CV**	**RV**	**CSM**	**mean RNFLT**	**RNFLT x-Area**
Age	NS	NS	NS	NS	NS	NS	NS	NS	NS	NS	NS
Diagnosis	p=0.004	p<0.001	p<0.001	p<0.001	p<0.001	p=0.004	p<0.001	p<0.001	p=0.001	p<0.001	p<0.001
Disc Area	*	p<0.001	p<0.001	p<0.001	*	NS	p<0.001	p=0.071	p<0.001	NS	p=0.011
Visit	NS	NS	NS	NS	NS	NS	NS	NS	NS	NS	NS
Age x Diagnosis	p=0.047	NS	NS	NS	NS	NS	NS	NS	NS	NS	NS
Age x Disc Area	*	NS	NS	NS	*	NS	p=0.009	NS	NS	NS	NS
Diagnosis x Disc Area	*	p<0.001	NS	p<0.001	*	NS	p<0.001	p=0.004	NS	NS	NS
Visit x Age	NS	NS	NS	NS	NS	NS	NS	NS	NS	NS	NS
Visit x Diagnosis	NS	NS	NS	NS	NS	NS	NS	NS	NS	NS	NS
Visit x Disc Area	*	NS	NS	NS	*	NS	NS	NS	NS	NS	NS
Number of Scans	NS	NS	NS	NS	NS	NS	NS	NS	NS	NS	NS
Number of Scans x Age	NS	NS	NS	NS	NS	NS	NS	NS	NS	NS	NS
Number of Scans x Diagnosis	NS	NS	NS	NS	NS	NS	p=0.039	p=0.022	NS	NS	p=0.034
Number of Scans x Disc Area	*	NS	NS	NS	*	NS	NS	NS	NS	NS	NS
Visit x Number of Scans	NS	NS	NS	NS	NS	NS	NS	NS	NS	NS	NS
Visit x Number of Scans x Age	NS	NS	NS	NS	NS	NS	p=0.022	NS	NS	NS	NS
Visit x Number of Scans x Diagnosis	NS	NS	NS	NS	NS	NS	NS	NS	NS	NS	NS
Visit x Number of Scans x Disc Area	*	NS	NS	NS	*	NS	NS	NS	NS	NS	NS
Visit x Disc Area x Diagnosis	*	NS	NS	NS	*	NS	NS	NS	NS	NS	NS
Visit x Age x Diagnosis	NS	NS	NS	NS	NS	NS	NS	NS	NS	NS	NS
Number of Scans x Disc Area x Diagnosis	*	NS	NS	NS	*	NS	p=0.001	p=0.003	NS	NS	p=0.006
Number of Scans x Age x Diagnosis	NS	p=0.041	NS	p=0.042	NS	NS	p=0.005	NS	NS	NS	NS
Visit x Number of Scans x Disc Area x Diagnosis	*	NS	NS	NS	*	NS	NS	NS	NS	NS	NS
Visit x Number of Scans x Age x Diagnosis	NS	NS	NS	NS	NS	NS	NS	NS	NS	NS	NS
Visit x Age x Disc Area	*	NS	NS	NS	*	NS	NS	NS	NS	NS	NS
Number of Scans x Age x Disc Area	*	NS	NS	NS	*	NS	NS	NS	NS	NS	NS
Visit x Number of Scans x Age x Disc Area	*	NS	NS	NS	*	NS	p=0.047	NS	NS	NS	NS

Table 4.3. Summary of the ANOVA for the Global HRT derived stereometric parameters. (NS = Non-significant; * = Not applicable).

Disc Area

	Group Mean Difference (mm^2)	SD	95% Limits of Agreement UPPER	LOWER
NORMAL	0.00	0.01	0.02	-0.02
OHT	0.00	0.01	0.02	-0.02
POAG	0.00	0.01	0.01	-0.01

Cup Area

	Group Mean Difference (mm^2)	SD	95% Limits of Agreement UPPER	LOWER
NORMAL	0.02	0.06	0.13	-0.10
OHT	-0.01	0.07	0.12	-0.15
POAG	-0.01	0.10	0.18	-0.20

Cup/Disc Area Ratio

	Group Mean Difference	SD	95% Limits of Agreement UPPER	LOWER
NORMAL	0.01	0.04	0.08	-0.06
OHT	-0.01	0.04	0.07	-0.08
POAG	0.00	0.05	0.09	-0.10

Rim Area

	Group Mean Difference (mm^2)	SD	95% Limits of Agreement UPPER	LOWER
NORMAL	-0.01	0.06	0.10	-0.12
OHT	0.01	0.07	0.15	-0.12
POAG	0.01	0.10	0.20	-0.19

Rim/Disc Area Ratio

	Group Mean Difference	SD	95% Limits of Agreement UPPER	LOWER
NORMAL	-0.01	0.04	0.06	-0.08
OHT	0.01	0.04	0.08	0.07
POAG	0.00	0.05	0.10	-0.90

Height Variation in Contour

	Group Mean Difference	SD	95% Limits of Agreement UPPER	LOWER
NORMAL	0.00	0.03	0.06	-0.06
OHT	0.00	0.05	0.10	-0.09
POAG	0.00	0.06	0.13	-0.13

Cup Volume

	Group Mean Difference (mm^3)	SD	95% Limits of Agreement UPPER	LOWER
NORMAL	0.00	0.01	0.03	-0.02
OHT	0.00	0.03	0.05	-0.05
POAG	0.00	0.04	0.08	-0.08

Rim Volume

	Group Mean Difference (mm^3)	SD	95% Limits of Agreement UPPER	LOWER
NORMAL	0.00	0.03	0.07	-0.07
OHT	0.01	0.04	0.09	-0.07
POAG	0.00	0.03	0.06	-0.06

Cup Shape Measure

	Group Mean Difference	SD	95% Limits of Agreement UPPER	LOWER
NORMAL	0.00	0.02	0.04	-0.04
OHT	0.00	0.02	0.05	-0.04
POAG	-0.01	0.03	0.06	-0.07

Mean RNFL Thickness

	Group Mean Difference (mm)	SD	95% Limits of Agreement UPPER	LOWER
NORMAL	0.00	0.03	0.06	-0.06
OHT	0.01	0.03	0.08	-0.06
POAG	0.00	0.03	0.05	-0.06

Mean RNFL Cross-sectional Area

	Group Mean Difference (mm^2)	SD	95% Limits of Agreement UPPER	LOWER
NORMAL	0.00	0.12	0.23	-0.24
OHT	0.04	0.15	0.33	-0.26
POAG	-0.02	0.15	0.27	-0.30

Table 4.4. The Group Mean difference and SD of the Global HRT stereometric parameters DA, CA, CDAR, RA, RDAR, HVC, CV, RV, CSM, Mean RNFLT and RNFL cross-sectional are between the two visits, for the Normal, OHT, and POAG groups. The upper and lower limits of agreement are provided.

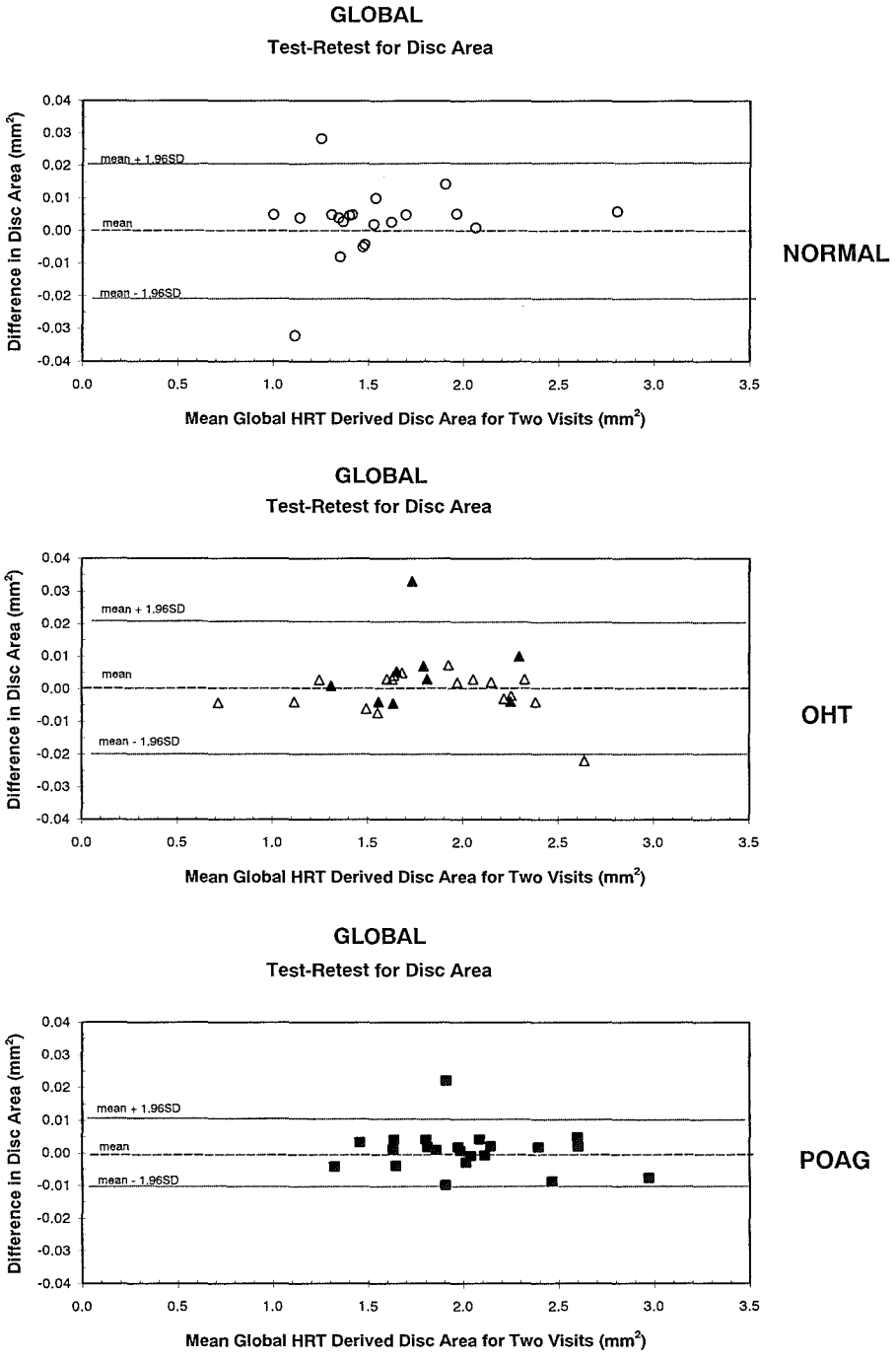

Figure 4.7. The difference in mean Global DA as a function of the mean Global DA for the two visits, for the Normal group (top), for the OHT group (open triangles) and OHT(H) group (closed triangles) (middle) and for the POAG group (bottom). The mean and the 95% confidence limits are shown.

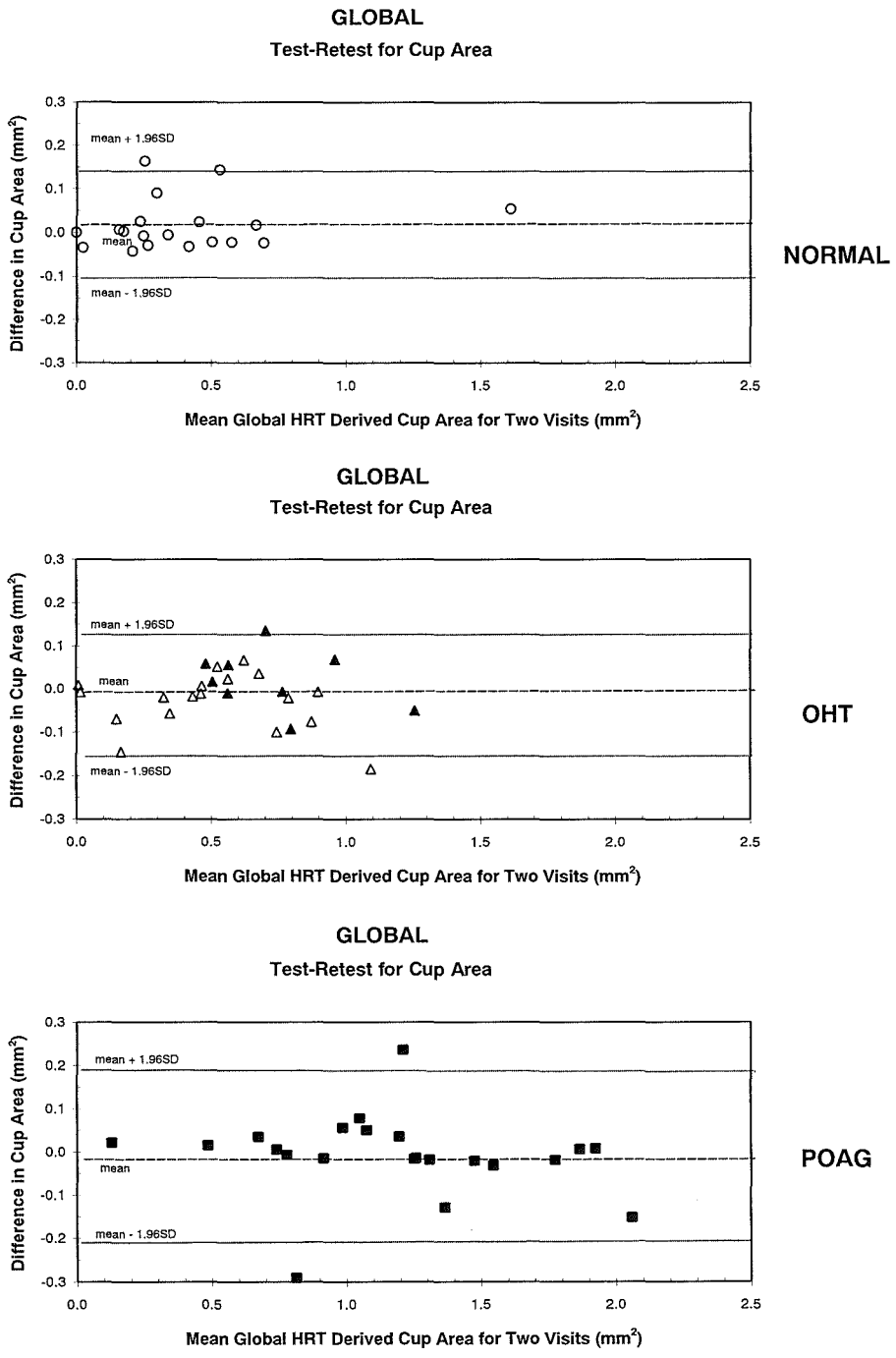

Figure 4.8. The difference in mean Global CA as a function of the mean Global CA for the two visits, for the Normal group (top), for the OHT group (open triangles) and OHT(H) group (closed triangles) (middle) and for the POAG group (bottom). The mean and the 95% confidence limits are shown.

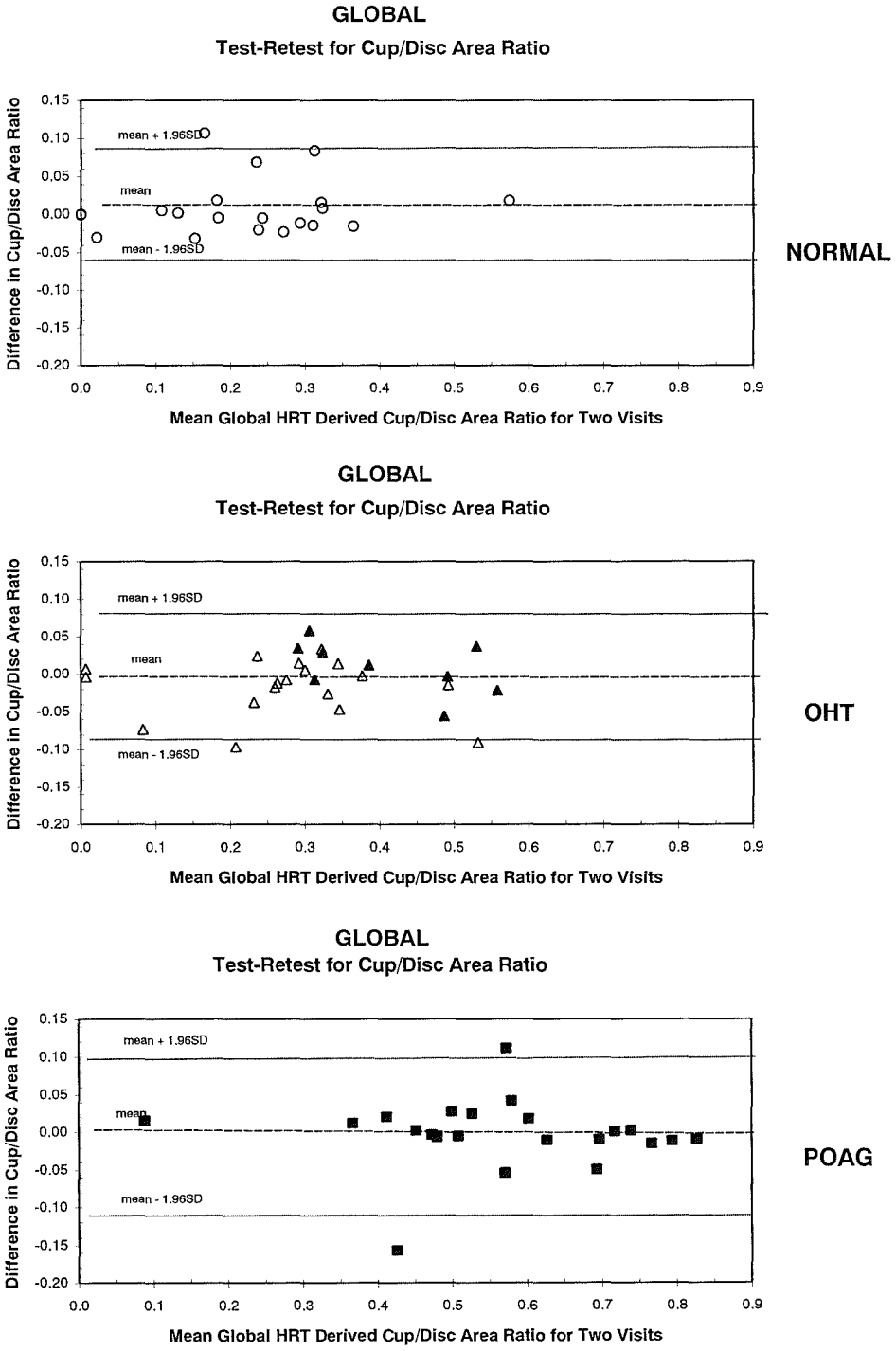

Figure 4.9. The difference in mean Global CDAR as a function of the mean Global CDAR for the two visits, for the Normal group (top), for the OHT group (open triangles) and OHT(H) group (closed triangles) (middle) and for the POAG group (bottom). The mean and the 95% confidence limits are shown.

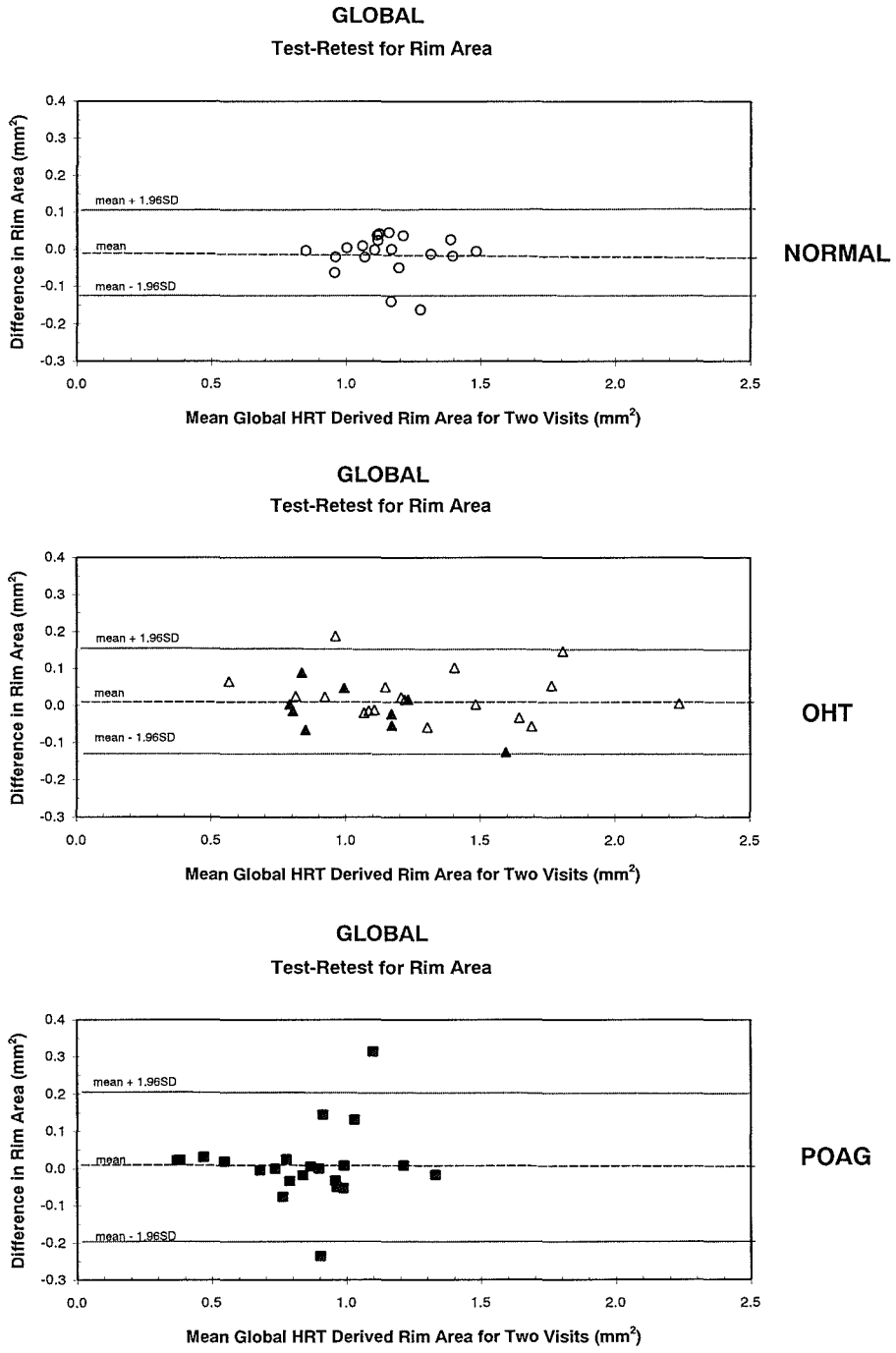

Figure 4.10. The difference in mean Global RA as a function of the mean Global RA for the two visits, for the Normal group (top), for the OHT group (open triangles) and OHT(H) group (closed triangles) (middle) and for the POAG group (bottom). The mean and the 95% confidence limits are shown.

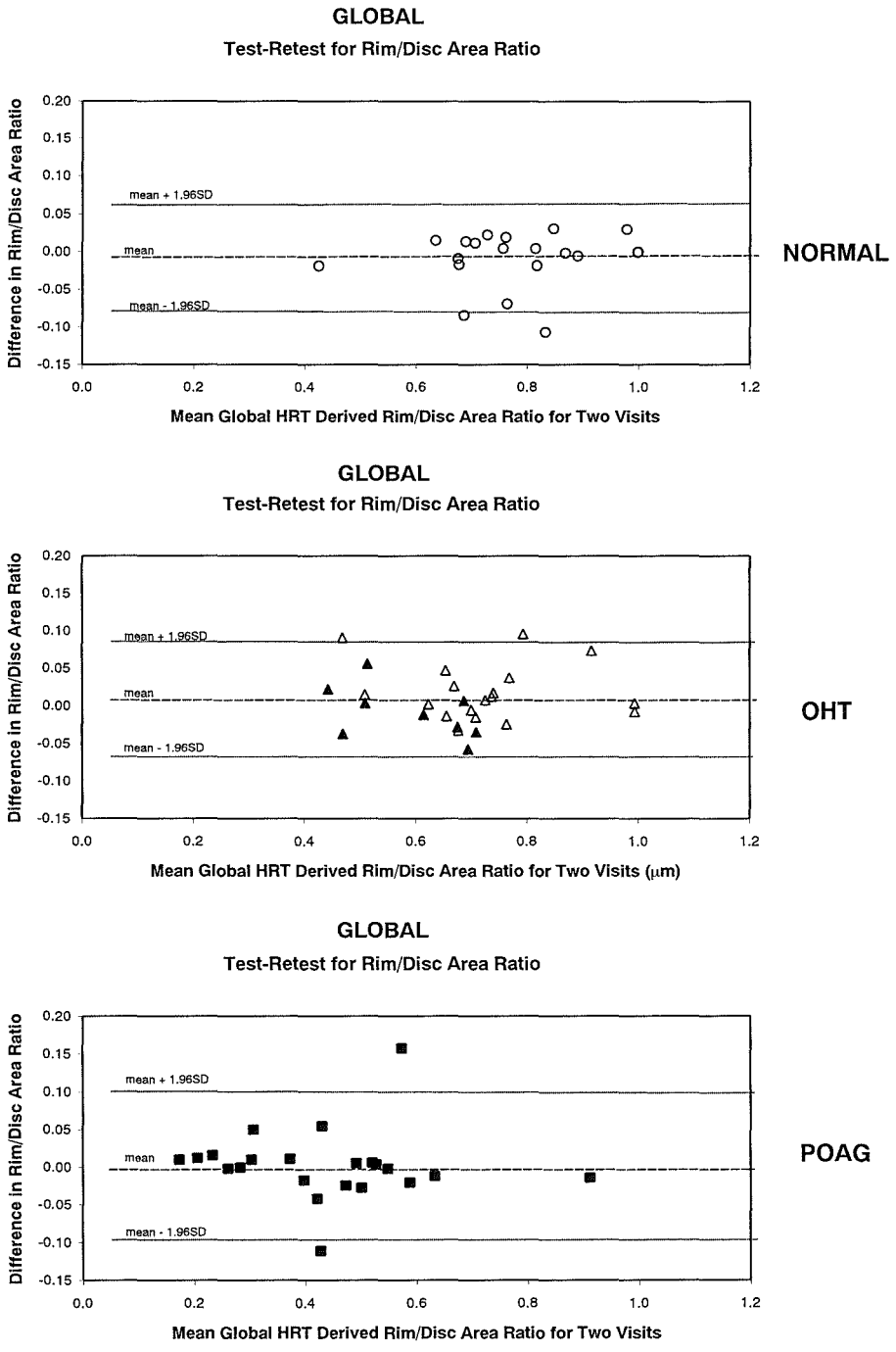

Figure 4.11. The difference in mean Global RDAR as a function of the mean Global RDAR for the two visits, for the Normal group (top), for the OHT group (open triangles) and OHT(H) group (closed triangles) (middle) and for the POAG group (bottom). The mean and the 95% confidence limits are shown.

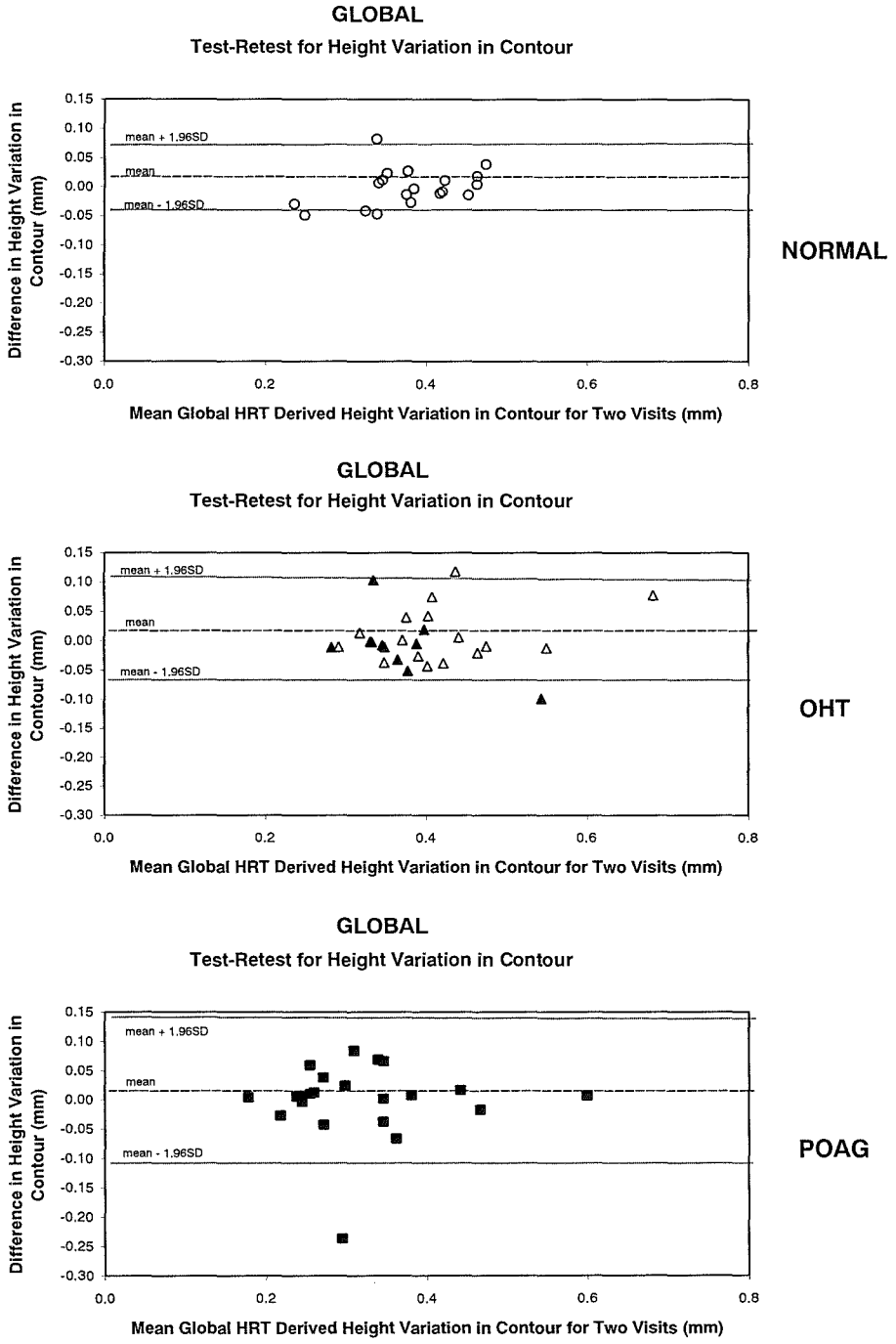

Figure 4.12. The difference in mean Global HVC as a function of the mean Global HVC for the two visits, for the Normal group (top), for the OHT group (open triangles) and OHT(H) group (closed triangles) (middle) and for the POAG group (bottom). The mean and the 95% confidence limits are shown.

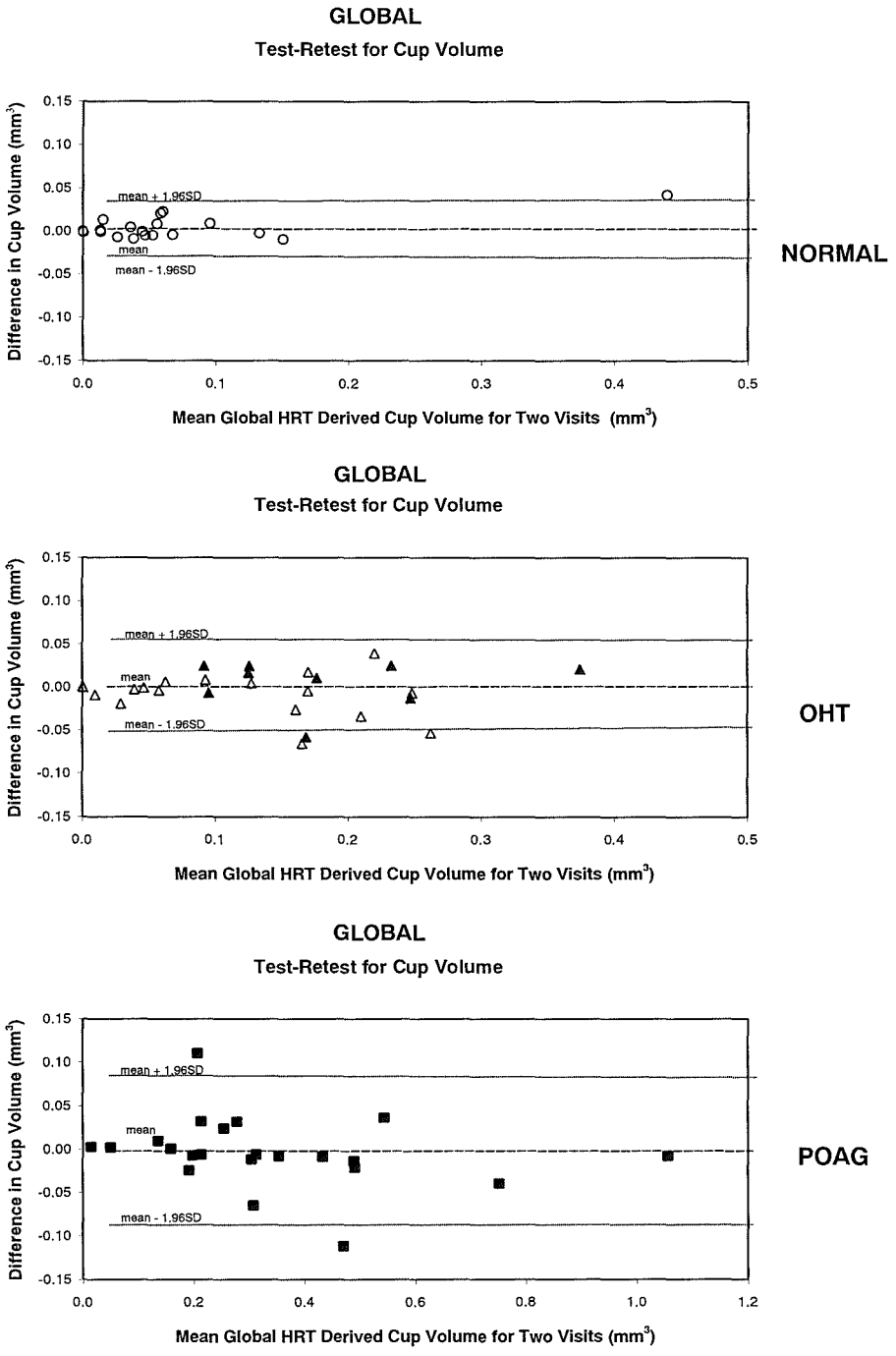

Figure 4.13. The difference in mean Global CV as a function of the mean Global CV for the two visits, for the Normal group (top), for the OHT group (open triangles) and OHT(H) group (closed triangles) (middle) and for the POAG group (bottom). The mean and the 95% confidence limits are shown.

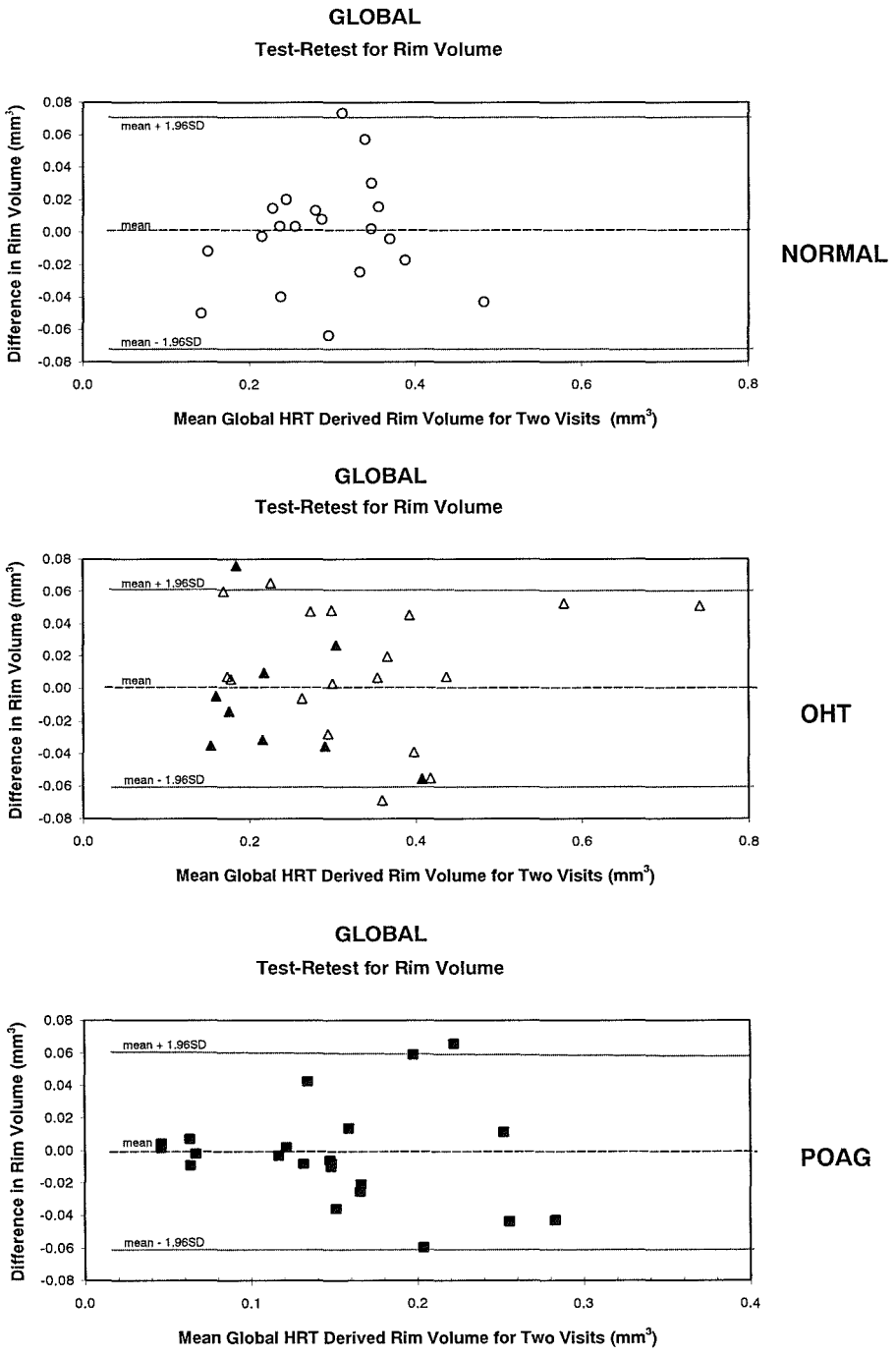

Figure 4.14. The difference in mean Global RV as a function of the mean Global RV for the two visits, for the Normal group (top), for the OHT group (open triangles) and OHT(H) group (closed triangles) (middle) and for the POAG group (bottom). The mean and the 95% confidence limits are shown.

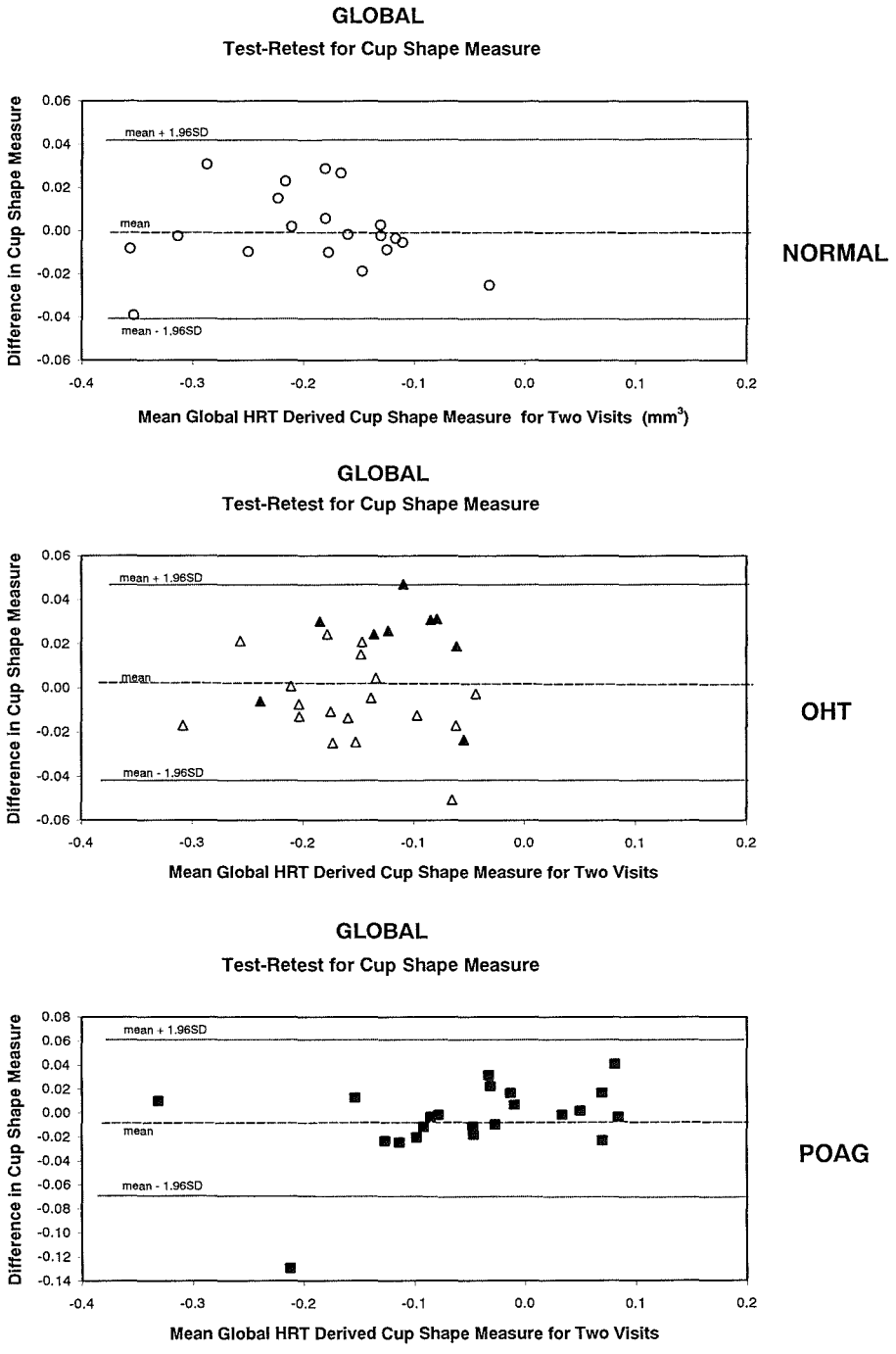

Figure 4.15. The difference in mean Global CSM as a function of the mean Global CSM for the two visits, for the Normal group (top), for the OHT group (open triangles) and OHT(H) group (closed triangles) (middle) and for the POAG group (bottom). The mean and the 95% confidence limits are shown.

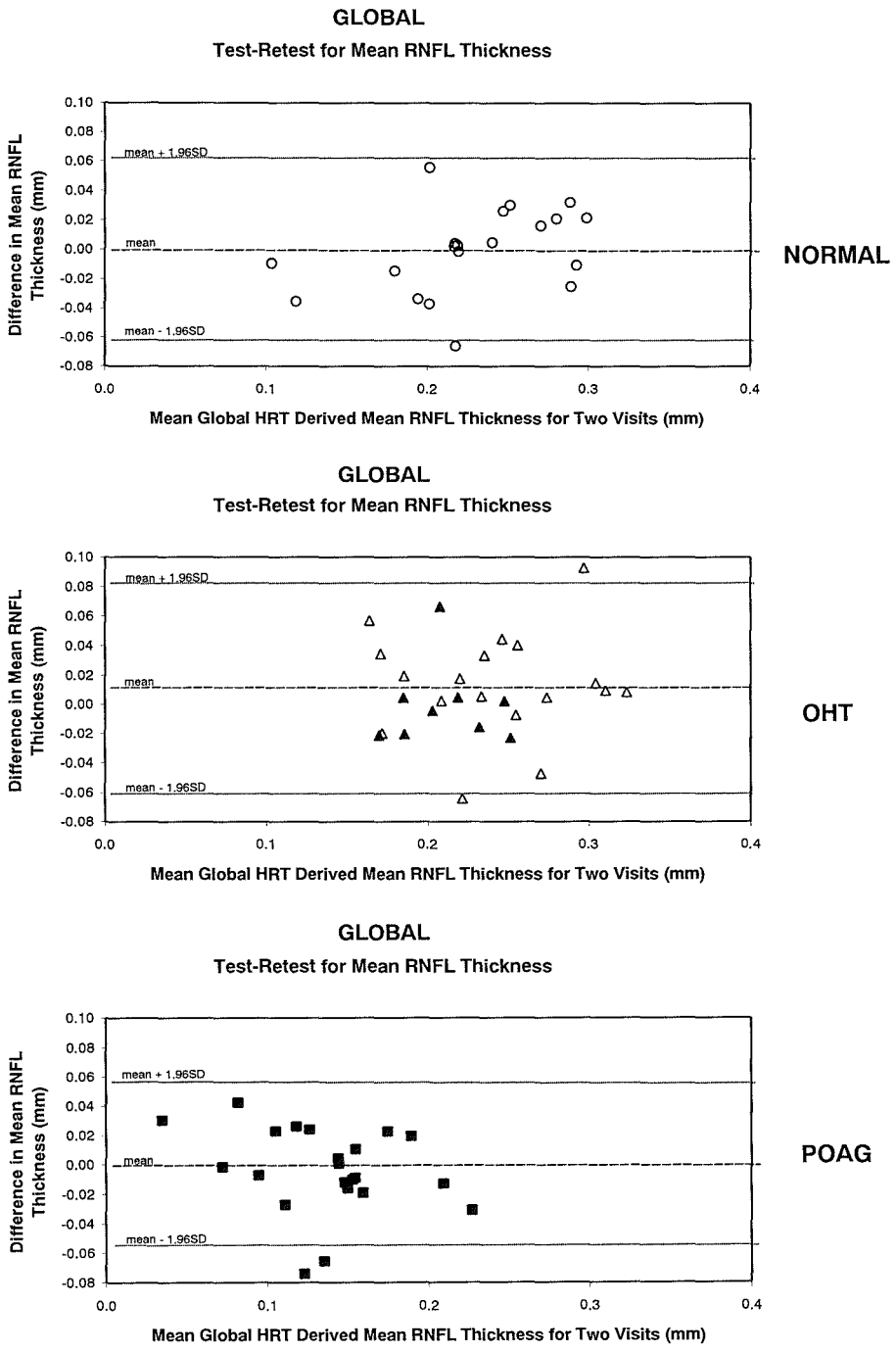

Figure 4.16. The difference in mean Global Mean RNFLT as a function of the mean Global Mean RNFLT for the two visits, for the Normal group (top), for the OHT group (open triangles) and OHT(H) group (closed triangles) (middle) and for the POAG group (bottom). The mean and the 95% confidence limits are shown.

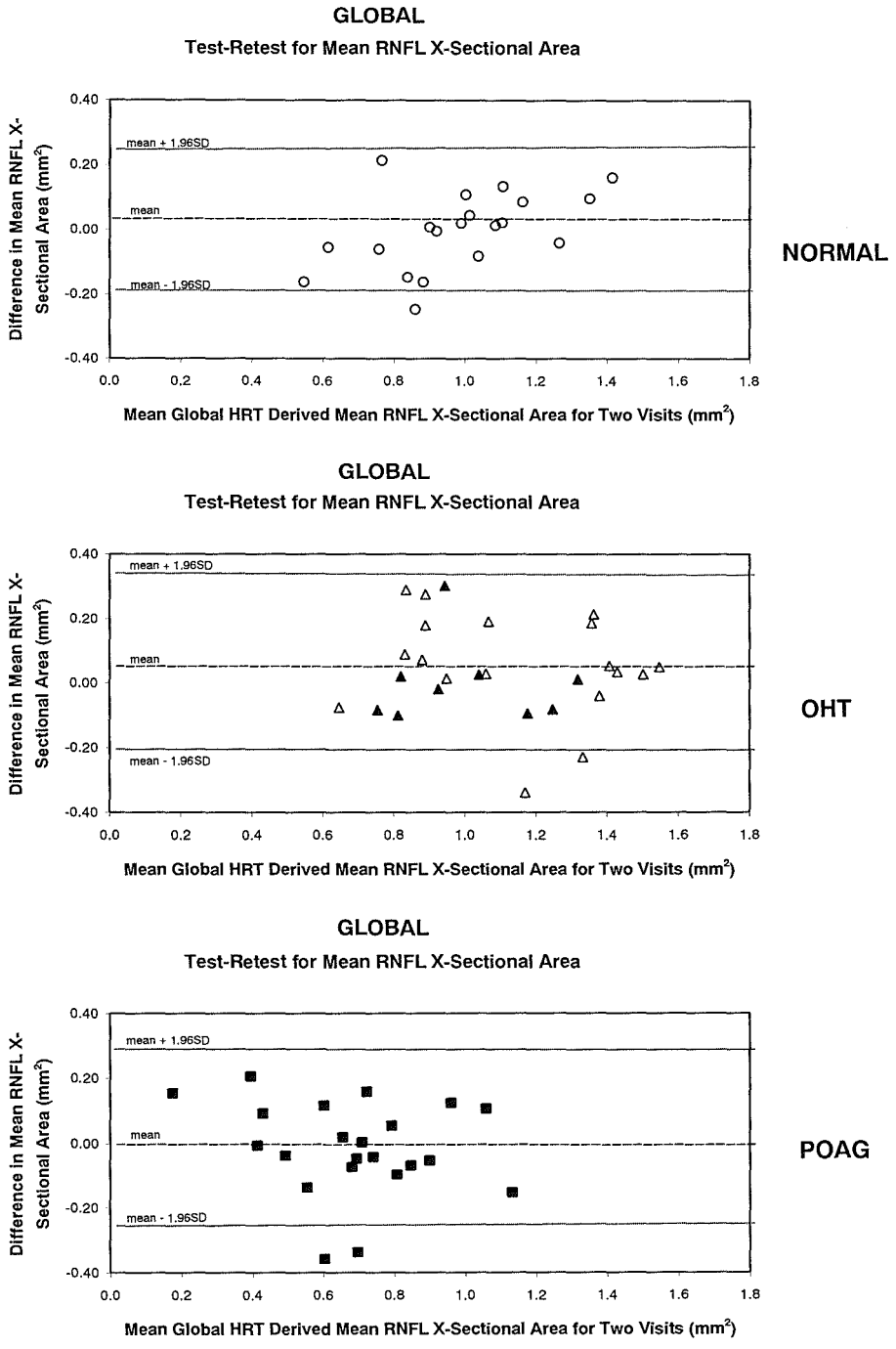

Figure 4.17. The difference in mean Global RNFL cross-sectional area as a function of the mean Global RNFLT cross-sectional area for the two visits, for the Normal group (top), for the OHT group (open triangles) and OHT(H) group (closed triangles) (middle) and for the POAG group (bottom). The mean and the 95% confidence limits are shown.

4.7.3 Relationship between Global HRT derived stereometric parameters and age, and diagnostic group (i.e. Validity).

4.7.3.1 Disc area (DA).

The DA was independent of age (p=0.828). The DA varied across the three diagnostic groups (p=0.004) and was largest for the POAG group.

4.7.3.2 Cup area (CA).

The CA was independent of age (p=0.632). The CA varied across the three diagnostic groups (p<0.001) and was largest for the POAG group.

4.7.3.3 Cup-disc area ratio (CDAR).

The CDAR was independent of age (p=0.784). The CDAR varied across the three diagnostic groups (p<0.001) and was largest for the POAG group.

4.7.3.4 Rim area (RA).

The RA was independent of age (p=0.696). The RA varied across the three diagnostic groups (p<0.001) and was smallest for the POAG group.

4.7.3.5 Rim-disc area ratio (RDAR).

The RDAR was independent of age (p=0.734). The RDAR varied across the three diagnostic groups (p<0.001) and was smallest for the POAG group.

4.7.3.6 Height variation in contour (HVC).

The HVC was independent of age (p=0.466). The HVC varied across the three diagnostic groups (p=0.004) and was smallest for the POAG group.

4.7.3.7 Cup Volume (CV).

The CV was independent of age (p=0.246). The CV varied across the three diagnostic groups (p<0.001) and was largest for the POAG group.

4.7.3.8 Rim Volume (RV).

The RV was independent of age (p=0.776). The RV varied across the three diagnostic groups (p<0.001) and was smallest for the POAG group.

4.7.3.9 Cup Shape Measure (CSM).

The CSM was independent of age (p=0.125). The CSM varied across the three diagnostic groups (p=0.001) and was least negative for the POAG group.

4.7.3.10 Mean Retinal Nerve Fibre Layer Thickness (RNFLT).

The mean RNFLT was independent of age (p=0.172). The mean RNFLT varied across the three diagnostic groups (p<0.001) and was thinnest for the POAG group.

4.7.3.11 RNFL Cross-sectional Area.

The RNFL cross-sectional area was independent of age (p=0.152). The RNFL cross-sectional area varied across the three diagnostic groups (p<0.001) and was least for the POAG group.

4.7.4 Between-visit variability of the Sector HRT derived stereometric parameters.

The Group mean and one SD for each of the four sectors stereometric parameters at Visit One and at Visit Two as function of diagnosis is given in Table 4.5. The ANOVA summary tables for each of the four sectors is given in Tables 4.6, 4.7, 4.8, and 4.9. The limits of agreement between the first and second visits, for each of the stereometric parameters, are given in Tables 4.10, 4.11, 4.12 and 4.13.

4.7.4.1 Disc area (DA).

The sector DA's did not vary between the first and second visits (Superior, p=0.882; Inferior, p=0.588; Temporal, p=0.540; Nasal, p=0.956). The difference in the Superior sector DA between the two visits is presented as a function of the mean sector DA for the two visits in Figure 4.18.

4.7.4.2 Cup area (CA).

The sector CA's did not vary between the first and second visits (Superior, p=0.206; Inferior, p=0.233; Temporal, p=0.271; Nasal, p=0.158). The difference in the Superior sector CA between the two visits is presented as a function of the two visits in Figure 4.19. The CA increased with increase in the DA (Superior, p<0.001; Inferior, p<0.001; Temporal, p<0.001; Nasal, p<0.001). The increase in CA with increase in DA was dependent upon diagnosis (Superior, p=0.001; Inferior, p=0.016; Temporal, p=0.292; Nasal, p=0.002), and was greatest for the POAG group.

4.7.4.3 Cup-disc area ratio (CDAR).

The sector CDAR's did not vary between the first and second visits (Superior, p=0.243; Inferior, p=0.450; Temporal, p=0.486; Nasal, p=0.611). The difference in the Superior sector CDAR between the two visits is presented graphically in Figure 4.20. The CDAR increased with increase in the disc area (Superior, p<0.001; Inferior, p=0.002; Temporal, p=0.02; Nasal, p<0.001). The increase in CDAR with increase in DA was generally independent of diagnosis (Superior, p=0.182; Inferior, p=0.181; Temporal, p=0.752; Nasal, p=0.046).

4.7.4.4 Rim area (RA).

The sector RA's did not vary between the first and second visits (Superior, p=0.201; Inferior, p=0.790; Temporal, p=0.282; Nasal, p=0.601). The difference in the Superior sector RA between the two visits is shown in Figure 4.21. The RA increased with increase in the DA (Superior, p<0.001; Inferior, p<0.001; Temporal, p=0.046; Nasal, p<0.001). The increase in RA with increase in DA was dependent upon diagnosis (Superior, p=0.006; Inferior, p=0.038; Nasal, p=0.002), except for the Temporal sector (p=0.152), and was minimal for the POAG group.

4.7.4.5 Rim-disc area ratio (RDAR).

The sector RDAR's did not vary between the first and second visits (Superior, p=0.088; Inferior, p=0.038; Temporal, p=0.152; Nasal, p=0.02). The difference in the Superior sector RDAR between the two visits is given in Figure 4.22.

4.7.4.6 Height variation in contour (HVC).

The sector HVC's did not vary between the first and second visits (Superior, p=0.527; Inferior, p=0.640; Temporal, p=0.981; Nasal, p=0.760). The difference in the Superior sector HVC between the first and second visit is shown graphically in Figure 4.23. The HVC was generally independent of the disc area (Superior, p=0.316; Inferior, p=0.443; Temporal, p=0.200; Nasal, p=0.042).

4.7.4.7 Cup Volume (CV).

The sector CV's did not vary between the first and second visits (Superior, p=0.147; Inferior, p=0.442; Temporal, p=0.195; Nasal, p=0.140). The difference in the Superior sector CV between the first and second visit is presented in Figure 4.24. The CV increased with increase in the DA (Superior, p<0.001; Inferior, p<0.001; Temporal, p<0.001; Nasal, p<0.001). The increase in CV with increase in DA was dependent upon diagnosis (Superior, p<0.001; Inferior, p=0.002; Temporal, p=0.007; Nasal, p<0.001), and was greatest for the POAG group.

4.7.4.8 Rim Volume (RV).

The sector RV's did not vary between the first and second visits (p=0.448; Inferior, p=0.846; Temporal, p=0.612; Nasal, p=0.758). The difference in the Superior sector RV between the first and second visit is given in Figure 4.25. The RV was generally independent of the disc area (Superior, p=0.131; Inferior, p=0.065; Temporal, p=0.455; Nasal, p=0.046).

4.7.4.9 Cup Shape Measure (CSM).

The sector CSM's did not vary between the first and second visits (Superior, p=0.727; Inferior p=0.945; Temporal, p=0.946; Nasal, p=0.167). The limits of agreement for the Superior sector CSM between the first and second visits are given in Figure 4.26. The CSM increased with increase in the DA (Superior, p<0.001; Inferior, p=0.004; Temporal, p=0.010; Nasal, p<0.001).

The increase in CSM with increase in DA was independent of diagnosis (Superior, p=0.304; Inferior, p=0.361; Temporal, p=0.454; Nasal, p=0.614).

4.7.4.10 Mean Retinal Nerve Fibre Layer Thickness (RNFLT).

The sector mean RNFLT's did not vary between the first and second visits (Superior, p=0.492; Inferior, p=0.949; Temporal, p=0.477; Nasal, p=0.610). The difference in the Superior sector mean RNFLT between the first and second visit is shown graphically in Figure 4.27. The mean RNFLT was independent of the disc area (Superior, p=0.168; Inferior, p=0.754; Temporal, p=0.021; Nasal, p=0.433), except for the Temporal sector.

4.7.4.11 RNFLT Cross-sectional Area.

The sector RNFLT cross-sectional area did not vary between the first and second visits (Superior, p=0.560; Inferior, p=0.864; Temporal, p=0.399; Nasal, p=0.589). The difference in the Superior sector RNFLT cross-sectional area between the first and second visit is shown in Figure 4.28. The RNFLT cross-sectional area increased with increase in the DA (Superior, p=0.033; Inferior, p=0.003; Temporal, p=0.021), except for the Nasal sector (p=0.043), in which it decreased. The increase in RNFLT cross-sectional area with increase in DA was independent of diagnosis (Superior, p=0.253 Inferior, p=0.295; Temporal, p=0.643; Nasal, p=0.564).

SUPERIOR SECTOR	NORMAL		OHT		POAG	
	VISIT 1	VISIT 2	VISIT 1	VISIT 2	VISIT 1	VISIT 2
Disc Area (mm^2)	0.41 (0.10)	0.40 (0.09)	0.48 (0.13)	0.48 (0.12)	0.53 (0.11)	0.53 (0.11)
Cup Area (mm^2)	0.09 (0.09)	0.07 (0.09)	0.15 (0.08)	0.14 (0.08)	0.32 (0.15)	0.33 (0.14)
Cup-Disc Ratio	0.19 (0.16)	0.16 (0.14)	0.30 (0.16)	0.29 (0.15)	0.58 (0.21)	0.59 (0.20)
Rim Area (mm^2)	0.32 (0.06)	0.32 (0.05)	0.33 (0.11)	0.34 (0.11)	0.21 (0.07)	0.21 (0.08)
Rim-Disc Area Ratio	0.81 (0.16)	0.84 (0.14)	0.70 (0.16)	0.71 (0.15)	0.42 (0.21)	0.41 (0.20)
Height Variation in Contour (mm)	0.19 (0.06)	0.19 (0.06)	0.21 (0.06)	0.21 (0.07)	0.19 (0.09)	0.18 (0.09)
Cup Volume (mm^3)	0.02 (0.03)	0.01 (0.03)	0.04 (0.03)	0.04 (0.03)	0.10 (0.08)	0.10 (0.07)
Rim Volume (mm^3)	0.08 (0.03)	0.08 (0.02)	0.09 (0.04)	0.09 (0.04)	0.04 (0.02)	0.04 (0.02)
Cup Shape Measure	-0.18 (0.10)	-0.18 (0.09)	-0.11 (0.10)	-0.11 (0.11)	-0.00 (0.13)	0.02 (0.11)
Mean RNFL Thickness (mm)	0.27 (0.08)	0.28 (0.07)	0.29 (0.06)	0.29 (0.06)	0.16 (0.06)	0.16 (0.09)
RNFL X-Sectional Area (mm^2)	0.30 (0.10)	0.31 (0.08)	0.35 (0.09)	0.35 (0.09)	0.21 (0.08)	0.21 (0.11)

INFERIOR SECTOR	NORMAL		OHT		POAG	
	VISIT 1	VISIT 2	VISIT 1	VISIT 2	VISIT 1	VISIT 2
Disc Area (mm^2)	0.41 (0.10)	0.40 (0.10)	0.48 (0.12)	0.48 (0.12)	0.53 (0.12)	0.54 (0.11)
Cup Area (mm^2)	0.10 (0.09)	0.09 (0.09)	0.16 (0.09)	0.15 (0.09)	0.30 (0.12)	0.31 (0.12)
Cup-Disc Ratio	0.23 (0.15)	0.19 (0.16)	0.33 (0.17)	0.32 (0.17)	0.56 (0.16)	0.56 (0.16)
Rim Area (mm^2)	0.31 (0.06)	0.31 (0.05)	0.32 (0.12)	0.33 (0.12)	0.22 (0.08)	0.23 (0.09)
Rim-Disc Area Ratio	0.77 (0.15)	0.81 (0.16)	0.67 (0.17)	0.68 (0.17)	0.44 (0.16)	0.44 (0.16)
Height Variation in Contour (mm)	0.25 (0.10)	0.28 (0.09)	0.30 (0.09)	0.30 (0.11)	0.21 (0.10)	0.20 (0.08)
Cup Volume (mm^3)	0.01 (0.02)	0.01 (0.02)	0.03 (0.02)	0.03 (0.03)	0.09 (0.06)	0.09 (0.06)
Rim Volume (mm^3)	0.08 (0.03)	0.08 (0.03)	0.09 (0.06)	0.09 (0.06)	0.04 (0.02)	0.04 (0.02)
Cup Shape Measure	-0.13 (0.12)	-0.13 (0.12)	-0.09 (0.10)	-0.08 (0.10)	0.03 (0.15)	0.03 (0.16)
Mean RNFL Thickness (mm)	0.26 (0.08)	0.27 (0.07)	0.28 (0.09)	0.30 (0.09)	0.17 (0.08)	0.16 (0.08)
RNFL X-Sectional Area (mm^2)	0.29 (0.09)	0.30 (0.08)	0.34 (0.13)	0.36 (0.12)	0.22 (0.11)	0.21 (0.11)

TEMPORAL SECTOR	NORMAL		OHT		POAG	
	VISIT 1	VISIT 2	VISIT 1	VISIT 2	VISIT 1	VISIT 2
Disc Area (mm^2)	0.40 (0.11)	0.39 (0.11)	0.43 (0.11)	0.43 (0.11)	0.47 (0.10)	0.48 (0.09)
Cup Area (mm^2)	0.20 (0.11)	0.18 (0.11)	0.25 (0.12)	0.23 (0.13)	0.37 (0.13)	0.37 (0.12)
Cup-Disc Ratio	0.47 (0.20)	0.44 (0.22)	0.58 (0.22)	0.54 (0.24)	0.76 (0.18)	0.75 (0.18)
Rim Area (mm^2)	0.20 (0.07)	0.21 (0.07)	0.18 (0.11)	0.19 (0.11)	0.11 (0.06)	0.11 (0.07)
Rim-Disc Area Ratio	0.53 (0.20)	0.56 (0.22)	0.42 (0.22)	0.46 (0.24)	0.24 (0.18)	0.25 (0.18)
Height Variation in Contour (mm)	0.14 (0.07)	0.15 (0.06)	0.13 (0.05)	0.13 (0.04)	0.10 (0.04)	0.11 (0.05)
Cup Volume (mm^3)	0.03 (0.03)	0.03 (0.03)	0.05 (0.04)	0.05 (0.04)	0.09 (0.07)	0.09 (0.06)
Rim Volume (mm^3)	0.02 (0.02)	0.02 (0.02)	0.02 (0.01)	0.02 (0.01)	0.01 (0.01)	0.01 (0.01)
Cup Shape Measure	-0.10 (0.08)	-0.10 (0.06)	-0.06 (0.09)	-0.07 (0.08)	0.01 (0.10)	0.02 (0.11)
Mean RNFL Thickness (mm)	0.08 (0.02)	0.08 (0.02)	0.08 (0.02)	0.08 (0.02)	0.06 (0.02)	0.07 (0.02)
RNFL X-Sectional Area (mm^2)	0.09 (0.03)	0.09 (0.02)	0.09 (0.02)	0.09 (0.02)	0.08 (0.02)	0.08 (0.02)

NASAL SECTOR	NORMAL		OHT		POAG	
	VISIT 1	VISIT 2	VISIT 1	VISIT 2	VISIT 1	VISIT 2
Disc Area (mm^2)	0.40 (0.11)	0.38 (0.11)	0.44 (0.11)	0.44 (0.11)	0.49 (0.12)	0.49 (0.09)
Cup Area (mm^2)	0.05 (0.09)	0.04 (0.09)	0.06 (0.06)	0.06 (0.06)	0.20 (0.16)	0.20 (0.14)
Cup-Disc Ratio	0.09 (0.14)	0.07 (0.13)	0.14 (0.12)	0.14 (0.12)	0.37 (0.25)	0.38 (0.24)
Rim Area (mm^2)	0.35 (0.07)	0.34 (0.06)	0.38 (0.10)	0.38 (0.10)	0.29 (0.10)	0.29 (0.10)
Rim-Disc Area Ratio	0.91 (0.14)	0.93 (0.13)	0.86 (0.12)	0.86 (0.12)	0.63 (0.25)	0.62 (0.24)
Height Variation in Contour (mm)	0.12 (0.07)	0.11 (0.06)	0.15 (0.06)	0.14 (0.06)	0.13 (0.06)	0.12 (0.06)
Cup Volume (mm^3)	0.01 (0.02)	0.01 (0.03)	0.01 (0.02)	0.01 (0.02)	0.05 (0.05)	0.05 (0.05)
Rim Volume (mm^3)	0.11 (0.05)	0.11 (0.04)	0.11 (0.05)	0.11 (0.05)	0.06 (0.03)	0.06 (0.03)
Cup Shape Measure	-0.20 (0.12)	-0.21 (0.15)	-0.22 (0.16)	-0.22 (0.16)	-0.14 (0.14)	-0.13 (0.15)
Mean RNFL Thickness (mm)	0.26 (0.10)	0.29 (0.09)	0.27 (0.09)	0.28 (0.11)	0.17 (0.08)	0.17 (0.08)
RNFL X-Sectional Area (mm^2)	0.29 (0.12)	0.31 (0.10)	0.31 (0.11)	0.33 (0.12)	0.21 (0.10)	0.21 (0.10)

Table 4.5. The Group Mean and SD of the stereometric parameters for each one of the four sectors, at Visit One and Visit Two, based upon the MTI created from seven acquired images for each individual, for the Normal , the OHT and the POAG group. For the Normal group, [n = 24 on the first visit and n = 21 on the second visit as the HRT was unavailable for the repeat visit on 3 individuals].

Superior Sector

	HRT Stereometric Parameters										
FACTOR	**DA**	**CA**	**CDAR**	**RA**	**RDAR**	**HVC**	**CV**	**RV**	**CSM**	**mean RNFLT**	**RNFLT x-Area**
Age	NS	NS	NS	NS	NS	NS	NS	NS	NS	p=0.018	p=0.027
Diagnosis	p=0.001	p<0.001	p<0.001	p<0.001	p<0.001	NS	p<0.001	p<0.001	p<0.001	p<0.001	p<0.001
Disc Area	*	p<0.001	p<0.001	p<0.001	*	NS	p<0.001	NS	p<0.001	NS	p=0.033
Visit	NS	NS	NS	NS	NS	NS	NS	NS	NS	NS	NS
Age x Diagnosis	p=0.023	NS	NS	NS	p=0.036	NS	NS	NS	NS	NS	NS
Age x Disc Area	*	NS	NS	NS	*	NS	p=0.003	NS	NS	NS	NS
Diagnosis x Disc Area	*	p=0.001	NS	p=0.006	*	NS	p<0.001	p=0.018	NS	NS	NS
Visit x Age	NS	NS	p=0.012	NS	NS	NS	NS	p=0.016	NS	NS	NS
Visit x Diagnosis	NS	NS	p=0.037	p=0.039	NS	NS	NS	p=0.023	NS	NS	NS
Visit x Disc Area	NS	NS	p=0.034	NS	NS	NS	NS	p=0.015	NS	NS	NS
Visit x Age x Diagnosis	NS	NS	NS	NS	NS	NS	NS	NS	NS	NS	NS
Visit x Age x Disc Area	*	NS	p=0.031	NS	*	NS	NS	p=0.018	NS	NS	NS
Visit x Diagnosis x Disc Area	*	NS	NS	NS	*	NS	NS	NS	NS	NS	NS

Table 4.6. Summary of the ANOVA for the Superior Sector stereometric parameters. (NS = Non-significant; * = Not applicable).

Inferior Sector

	HRT Stereometric Parameters										
FACTOR	**DA**	**CA**	**CDAR**	**RA**	**RDAR**	**HVC**	**CV**	**RV**	**CSM**	**mean RNFLT**	**RNFLT x-Area**
Age	NS	NS	NS	NS	NS	NS	NS	NS	NS	NS	NS
Diagnosis	p<0.001	p<0.001	p<0.001	p<0.001	p<0.001	p=0.002	p<0.001	p<0.001	p=0.015	p<0.001	p<0.001
Disc Area	*	p<0.001	p=0.002	p<0.001	*	NS	p<0.001	NS	p=0.004	NS	p=0.003
Visit	NS	NS	NS	NS	NS	NS	NS	NS	NS	NS	NS
Age x Diagnosis	p=0.021	NS	NS	NS	NS	NS	NS	NS	NS	NS	NS
Age x Disc Area	*	NS	NS	NS	*	NS	NS	NS	NS	NS	NS
Diagnosis x Disc Area	*	p=0.016	NS	p=0.038	*	NS	p=0.002	NS	NS	NS	NS
Visit x Age	NS	NS	NS	NS	NS	NS	NS	NS	NS	NS	NS
Visit x Diagnosis	NS	NS	NS	NS	NS	NS	NS	NS	NS	NS	NS
Visit x Disc Area	NS	NS	NS	NS	NS	p=0.045	NS	NS	NS	NS	NS
Visit x Age x Diagnosis	NS	NS	NS	NS	NS	NS	NS	NS	NS	NS	NS
Visit x Age x Disc Area	*	NS	NS	NS	*	NS	NS	NS	NS	NS	NS
Visit x Diagnosis x Disc Area	*	NS	NS	NS	*	p=0.019	p=0.011	NS	NS	NS	NS

Table 4.7. Summary of the ANOVA for the Inferior Sector stereometric parameters. (NS = Non-significant; * = Not applicable).

Temporal Sector

	HRT Stereometric Parameters										
FACTOR	**DA**	**CA**	**CDAR**	**RA**	**RDAR**	**HVC**	**CV**	**RV**	**CSM**	**mean RNFLT**	**RNFLT x-Area**
Age	NS	NS	NS	NS	NS	NS	NS	NS	NS	NS	NS
Diagnosis	p=0.025	p=0.003	p=0.004	p<0.001	p<0.001	NS	p=0.005	p=0.005	p=0.012	p=0.026	p=0.029
Disc Area	*	p<0.001	p=0.020	p=0.046	*	NS	p<0.001	NS	p=0.010	p=0.021	p=0.021
Visit	NS	NS	NS	NS	NS	NS	NS	NS	NS	NS	NS
Age x Diagnosis	NS	NS	NS	NS	NS	NS	NS	NS	NS	NS	NS
Age x Disc Area	*	NS	NS	NS	*	NS	p=0.011	NS	NS	NS	NS
Diagnosis x Disc Area	*	NS	NS	NS	*	NS	p=0.007	NS	NS	NS	NS
Visit x Age	NS	NS	p=0.032	NS	p=0.016	NS	p=0.016	NS	NS	NS	NS
Visit x Diagnosis	NS	NS	NS	NS	NS	NS	p=0.016	NS	NS	NS	NS
Visit x Disc Area	NS	NS	NS	NS	NS	NS	p=0.039	NS	NS	NS	NS
Visit x Age x Diagnosis	p=0.044	NS	NS	NS	NS	NS	NS	NS	NS	NS	NS
Visit x Age x Disc Area	*	NS	NS	NS	*	NS	p=0.043	NS	NS	NS	NS
Visit x Diagnosis x Disc Area	*	NS	NS	NS	*	NS	NS	NS	NS	NS	NS

Table 4.8. Summary of the ANOVA for the Temporal Sector stereometric parameters. (NS = Non-significant; * = Not applicable).

Nasal Sector

	HRT Stereometric Parameters										
FACTOR	**DA**	**CA**	**CDAR**	**RA**	**RDAR**	**HVC**	**CV**	**RV**	**CSM**	**mean RNFLT**	**RNFLT x-Area**
Age	NS	NS	NS	NS	NS	p=0.009	NS	NS	NS	NS	NS
Diagnosis	p=0.012	p<0.001	p<0.001	p<0.001	p<0.001	NS	p=0.002	p<0.001	NS	p<0.001	p<0.001
Disc Area	*	p<0.001	p<0.001	p<0.001	*	p=0.042	p<0.001	p=0.046	p<0.001	NS	p=0.043
Visit	NS	NS	NS	NS	NS	NS	NS	NS	NS	NS	NS
Age x Diagnosis	NS	NS	NS	NS	NS	NS	NS	NS	NS	NS	NS
Age x Disc Area	*	NS	NS	NS	*	NS	p=0.037	NS	NS	NS	NS
Diagnosis x Disc Area	*	p=0.002	p=0.046	p=0.002	*	NS	p<0.001	p=0.050	NS	NS	NS
Visit x Age	NS	NS	NS	NS	NS	NS	NS	NS	p=0.030	NS	NS
Visit x Diagnosis	NS	NS	NS	NS	NS	NS	NS	NS	NS	NS	NS
Visit x Disc Area	NS	NS	NS	NS	NS	NS	NS	NS	p=0.027	NS	NS
Visit x Age x Diagnosis	NS	NS	NS	NS	NS	NS	NS	NS	NS	NS	NS
Visit x Age x Disc Area	*	p=0.046	NS	NS	*	NS	NS	NS	p=0.043	NS	NS
Visit x Diagnosis x Disc Area	*	p=0.039	NS	NS	*	NS	p=0.024	NS	NS	NS	NS

Table 4.9. Summary of the ANOVA for the Nasal Sector stereometric parameters. (NS = Non-significant; * = Not applicable).

Disc Area

	Group Mean Difference (mm^2)		95% Limits of Agreement	
		SD	UPPER	LOWER
NORMAL	0.00	0.01	0.02	-0.02
OHT	0.00	0.02	0.03	-0.03
POAG	0.00	0.01	0.02	-0.02

Cup Area

	Group Mean Difference (mm^2)		95% Limits of Agreement	
		SD	UPPER	LOWER
NORMAL	0.00	0.01	0.02	-0.03
OHT	0.00	0.02	0.04	-0.05
POAG	0.00	0.03	0.06	-0.06

Cup/Disc Area Ratio

	Group Mean Difference		95% Limits of Agreement	
		SD	UPPER	LOWER
NORMAL	-0.01	0.03	0.05	-0.07
OHT	-0.01	0.05	0.08	-0.11
POAG	0.00	0.05	0.10	-0.10

Rim Area

	Group Mean Difference (mm^2)		95% Limits of Agreement	
		SD	UPPER	LOWER
NORMAL	0.00	0.02	0.04	-0.03
OHT	0.01	0.03	0.07	-0.05
POAG	0.00	0.03	0.06	-0.06

Rim/Disc Area Ratio

	Group Mean Difference		95% Limits of Agreement	
		SD	UPPER	LOWER
NORMAL	0.01	0.03	0.07	-0.06
OHT	0.01	0.05	0.11	-0.08
POAG	0.00	0.05	0.10	-0.10

Height Variation in Contour

	Group Mean Difference		95% Limits of Agreement	
		SD	UPPER	LOWER
NORMAL	0.00	0.03	0.05	-0.05
OHT	0.00	0.04	0.07	-0.08
POAG	0.00	0.08	0.15	-0.15

Cup Volume

	Group Mean Difference (mm^3)		95% Limits of Agreement	
		SD	UPPER	LOWER
NORMAL	0.00	0.00	0.01	-0.01
OHT	0.00	0.01	0.02	-0.02
POAG	0.00	0.02	0.03	-0.04

Rim Volume

	Group Mean Difference (mm^3)		95% Limits of Agreement	
		SD	UPPER	LOWER
NORMAL	0.00	0.01	0.02	-0.01
OHT	0.00	0.02	0.04	-0.03
POAG	0.00	0.01	0.02	-0.02

Cup Shape Measure

	Group Mean Difference		95% Limits of Agreement	
		SD	UPPER	LOWER
NORMAL	0.00	0.06	0.12	-0.11
OHT	0.00	0.05	0.10	-0.11
POAG	0.01	0.06	0.12	-0.11

Mean RNFL Thickness

	Group Mean Difference (mm)		95% Limits of Agreement	
		SD	UPPER	LOWER
NORMAL	0.02	0.03	0.08	-0.05
OHT	0.00	0.05	0.09	-0.09
POAG	0.00	0.05	0.10	-0.09

Mean RNFL Cross-sectional Area

	Group Mean Difference (mm^2)		95% Limits of Agreement	
		SD	UPPER	LOWER
NORMAL	0.02	0.04	0.09	-0.05
OHT	0.00	0.05	0.11	-0.11
POAG	0.00	0.06	0.12	-0.12

Table 4.10. The Group Mean difference and SD of the Superior Sector HRT stereometric parameters DA, CA, CDAR, RA, RDAR, HVC, CV, RV, CSM, mean RNFLT, and RNFL cross-sectional area between the two visits, for the Normal, OHT, and POAG groups. The upper and lower limits of agreement are provided.

Disc Area

	Group Mean Difference (mm^2)	SD	95% Limits of Agreement UPPER	LOWER
NORMAL	0.01	0.01	0.03	-0.02
OHT	0.00	0.01	0.03	-0.03
POAG	0.00	0.01	0.01	-0.02

Cup Area

	Group Mean Difference (mm^2)	SD	95% Limits of Agreement UPPER	LOWER
NORMAL	-0.01	0.02	0.03	-0.05
OHT	-0.01	0.03	0.05	-0.06
POAG	0.00	0.02	0.04	-0.04

Cup/Disc Area Ratio

	Group Mean Difference	SD	95% Limits of Agreement UPPER	LOWER
NORMAL	-0.03	0.05	0.07	-0.12
OHT	-0.01	0.06	0.10	-0.13
POAG	0.00	0.04	0.07	-0.07

Rim Area

	Group Mean Difference (mm^2)	SD	95% Limits of Agreement UPPER	LOWER
NORMAL	0.02	0.02	0.06	-0.03
OHT	0.01	0.03	0.07	-0.06
POAG	0.00	0.02	0.04	-0.04

Rim/Disc Area Ratio

	Group Mean Difference	SD	95% Limits of Agreement UPPER	LOWER
NORMAL	0.03	0.05	0.12	-0.07
OHT	0.02	0.06	0.13	-0.10
POAG	0.00	0.04	0.07	-0.07

Height Variation in Contour

	Group Mean Difference	SD	95% Limits of Agreement UPPER	LOWER
NORMAL	0.01	0.03	0.06	-0.05
OHT	0.00	0.05	0.09	-0.09
POAG	-0.01	0.05	0.09	-0.11

Cup Volume

	Group Mean Difference (mm^3)	SD	95% Limits of Agreement UPPER	LOWER
NORMAL	0.00	0.00	0.00	-0.01
OHT	0.00	0.01	0.01	-0.01
POAG	0.00	0.01	0.03	-0.03

Rim Volume

	Group Mean Difference (mm^3)	SD	95% Limits of Agreement UPPER	LOWER
NORMAL	0.01	0.01	0.02	-0.01
OHT	0.00	0.02	0.04	-0.03
POAG	0.00	0.01	0.02	-0.02

Cup Shape Measure

	Group Mean Difference	SD	95% Limits of Agreement UPPER	LOWER
NORMAL	0.01	0.05	0.12	-0.09
OHT	0.01	0.06	0.12	-0.10
POAG	0.01	0.04	0.10	-0.08

Mean RNFL Thickness

	Group Mean Difference (mm)	SD	95% Limits of Agreement UPPER	LOWER
NORMAL	0.01	0.03	0.07	-0.05
OHT	0.02	0.06	0.13	-0.09
POAG	-0.01	0.05	0.09	-0.11

Mean RNFL Cross-sectional Area

	Group Mean Difference (mm^2)	SD	95% Limits of Agreement UPPER	LOWER
NORMAL	0.01	0.03	0.07	-0.05
OHT	0.02	0.07	0.15	-0.11
POAG	-0.01	0.07	0.12	-0.14

Table 4.11. The Group Mean difference and SD of the Inferior Sector HRT stereometric parameters DA, CA, CDAR, RA, RDAR, HVC, CV, RV, CSM, mean RNFLT, and RNFL cross-sectional area between the two visits, for the Normal, OHT, and POAG groups. The upper and lower limits of agreement are provided.

Disc Area

	Group Mean Difference (mm^2)	SD	95% Limits of Agreement UPPER	LOWER
NORMAL	0.00	0.01	0.03	-0.03
OHT	-0.01	0.03	0.06	-0.07
POAG	0.00	0.01	0.02	-0.02

Cup Area

	Group Mean Difference (mm^2)	SD	95% Limits of Agreement UPPER	LOWER
NORMAL	-0.01	0.03	0.05	0.06
OHT	0.00	0.02	0.07	-0.10
POAG	-0.01	0.03	0.05	-0.06

Cup/Disc Area Ratio

	Group Mean Difference	SD	95% Limits of Agreement UPPER	LOWER
NORMAL	-0.03	0.07	0.12	-0.17
OHT	-0.04	0.09	0.13	-0.21
POAG	-0.01	0.06	0.11	-0.13

Rim Area

	Group Mean Difference (mm^2)	SD	95% Limits of Agreement UPPER	LOWER
NORMAL	0.01	0.03	0.06	-0.04
OHT	0.01	0.03	0.07	-0.05
POAG	0.01	0.03	0.07	-0.05

Rim/Disc Area Ratio

	Group Mean Difference	SD	95% Limits of Agreement UPPER	LOWER
NORMAL	0.03	0.07	0.17	-0.12
OHT	0.04	0.09	0.21	-0.13
POAG	0.01	0.06	0.13	-0.10

Height Variation in Contour

	Group Mean Difference	SD	95% Limits of Agreement UPPER	LOWER
NORMAL	0.02	0.03	0.07	-0.04
OHT	0.00	0.04	0..09	-0.07
POAG	0.01	0.04	0.10	-0.07

Cup Volume

	Group Mean Difference (mm^3)	SD	95% Limits of Agreement UPPER	LOWER
NORMAL	0.00	0.00	0.01	-0.01
OHT	0.00	0.02	0.03	-0.03
POAG	0.00	0.02	0.03	-0.03

Rim Volume

	Group Mean Difference (mm^3)	SD	95% Limits of Agreement UPPER	LOWER
NORMAL	0.00	0.01	0.01	-0.01
OHT	0.00	0.01	0.01	-0.01
POAG	0.00	0.00	0.00	0.00

Cup Shape Measure

	Group Mean Difference	SD	95% Limits of Agreement UPPER	LOWER
NORMAL	0.01	0.05	0.11	-0.09
OHT	0.00	0.04	0.07	-0.07
POAG	0.00	0.04	0.08	-0.08

Mean RNFL Thickness

	Group Mean Difference (mm)	SD	95% Limits of Agreement UPPER	LOWER
NORMAL	0.00	0.01	0.03	-0.02
OHT	0.00	0.02	0.04	-0.03
POAG	0.00	0.01	0.03	-0.02

Mean RNFL Cross-sectional Area

	Group Mean Difference (mm^2)	SD	95% Limits of Agreement UPPER	LOWER
NORMAL	0.01	0.01	0.03	-0.02
OHT	0.00	0.02	0.04	-0.04
POAG	0.00	0.02	0.04	-0.03

Table 4.12. The Group Mean difference and SD of the Temporal Sector HRT stereometric parameters DA, CA, CDAR, RA, RDAR, HVC, CV, RV, CSM, mean RNFLT, and RNFL cross-sectional area between the two visits, for the Normal, OHT, and POAG groups. The upper and lower limits of agreement are provided.

Disc Area

	Group Mean Difference (mm^2)		95% Limits of Agreement	
		SD	UPPER	LOWER
NORMAL	0.00	0.01	0.02	-0.03
OHT	0.00	0.01	0.02	-0.03
POAG	-0.01	0.04	0.08	-0.10

Cup Area

	Group Mean Difference (mm^2)		95% Limits of Agreement	
		SD	UPPER	LOWER
NORMAL	-0.01	0.01	0.01	-0.02
OHT	0.00	0.02	0.03	-0.03
POAG	-0.01	0.03	0.06	-0.07

Cup/Disc Area Ratio

	Group Mean Difference		95% Limits of Agreement	
		SD	UPPER	LOWER
NORMAL	-0.02	0.02	0.02	-0.06
OHT	0.00	0.03	0.06	-0.06
POAG	0.00	0.03	0.07	-0.06

Rim Area

	Group Mean Difference (mm^2)		95% Limits of Agreement	
		SD	UPPER	LOWER
NORMAL	0.00	0.01	0.03	-0.02
OHT	0.00	0.01	0.03	-0.03
POAG	0.00	0.02	0.05	-0.05

Rim/Disc Area Ratio

	Group Mean Difference		95% Limits of Agreement	
		SD	UPPER	LOWER
NORMAL	0.02	0.02	0.06	-0.03
OHT	0.00	0.03	0.07	-0.06
POAG	0.00	0.03	0.06	-0.07

Height Variation in Contour

	Group Mean Difference		95% Limits of Agreement	
		SD	UPPER	LOWER
NORMAL	-0.01	0.04	0.06	-0.08
OHT	-0.01	0.03	0.06	-0.07
POAG	-0.01	0.07	0.12	-0.14

Cup Volume

	Group Mean Difference (mm^3)		95% Limits of Agreement	
		SD	UPPER	LOWER
NORMAL	0.00	0.00	0.01	-0.01
OHT	0.00	0.01	0.01	-0.01
POAG	0.00	0.02	0.03	-0.03

Rim Volume

	Group Mean Difference (mm^3)		95% Limits of Agreement	
		SD	UPPER	LOWER
NORMAL	0.01	0.01	0.02	-0.01
OHT	0.00	0.02	0.03	-0.03
POAG	0.00	0.01	0.03	-0.03

Cup Shape Measure

	Group Mean Difference		95% Limits of Agreement	
		SD	UPPER	LOWER
NORMAL	0.00	0.06	0.12	-0.13
OHT	0.00	0.06	0.12	-0.12
POAG	0.00	0.03	0.07	-0.06

Mean RNFL Thickness

	Group Mean Difference (mm)		95% Limits of Agreement	
		SD	UPPER	LOWER
NORMAL	0.02	0.03	0.08	-0.04
OHT	0.02	0.06	0.13	-0.10
POAG	0.00	0.04	0.08	-0.07

Mean RNFL Cross-sectional Area

	Group Mean Difference (mm^2)		95% Limits of Agreement	
		SD	UPPER	LOWER
NORMAL	0.02	0.03	0.08	-0.05
OHT	0.02	0.06	0.14	-0.11
POAG	0.00	0.06	0.11	-0.11

Table 4.13. The Group Mean difference and SD of the Nasal Sector HRT stereometric parameters DA, CA, CDAR, RA, RDAR, HVC, CV, RV, CSM, mean RNFLT, and RNFL cross-sectional area between the two visits, for the Normal, OHT, and POAG groups. The upper and lower limits of agreement are provided.

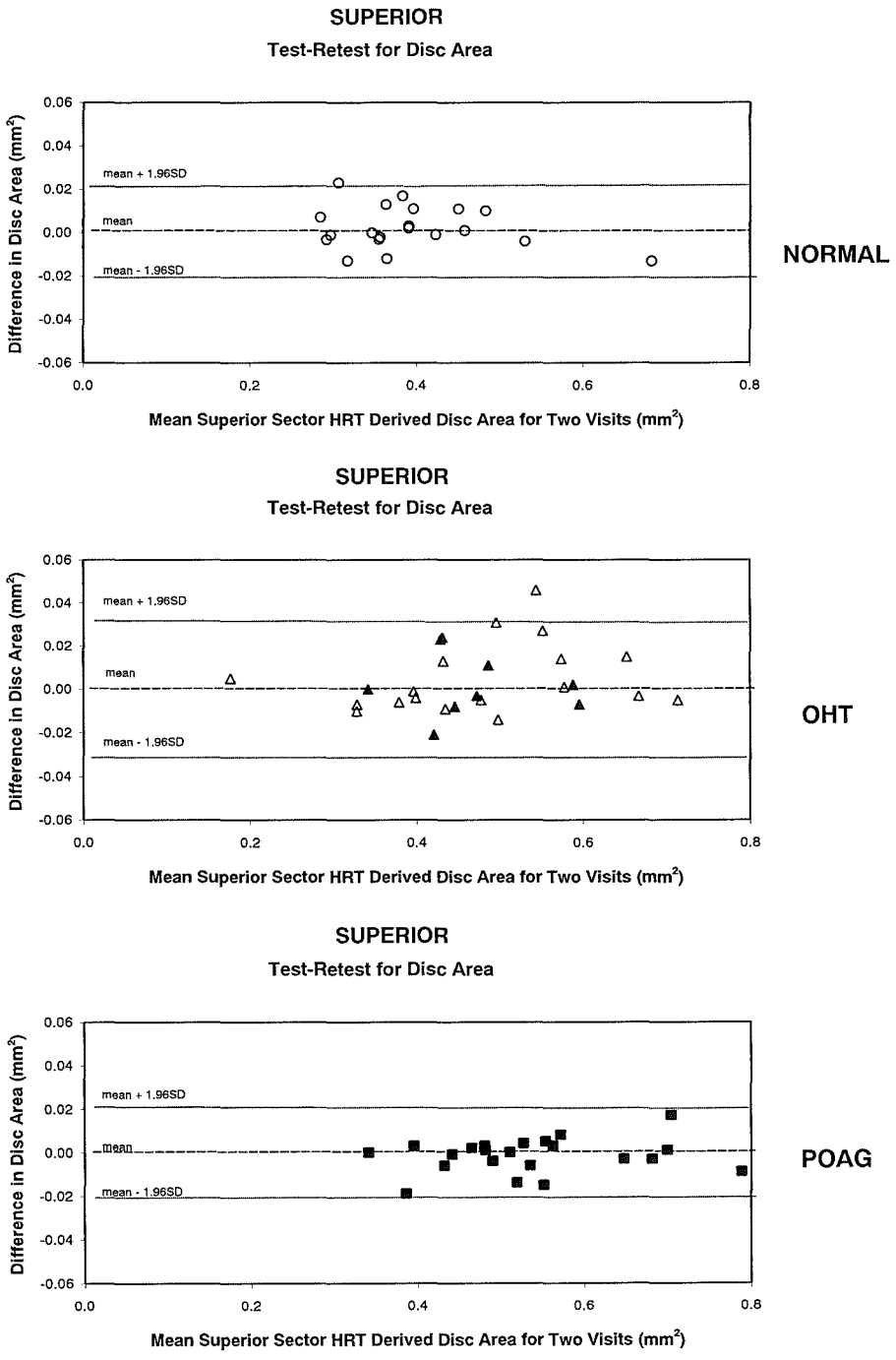

Figure 4.18. The difference in mean Superior Sector DA as a function of the mean Superior Sector DA for the two visits, for the Normal group (top), for the OHT group (open triangles) and OHT(H) group (closed triangles) (middle) and for the POAG group (bottom). The mean and the 95% confidence limits are shown.

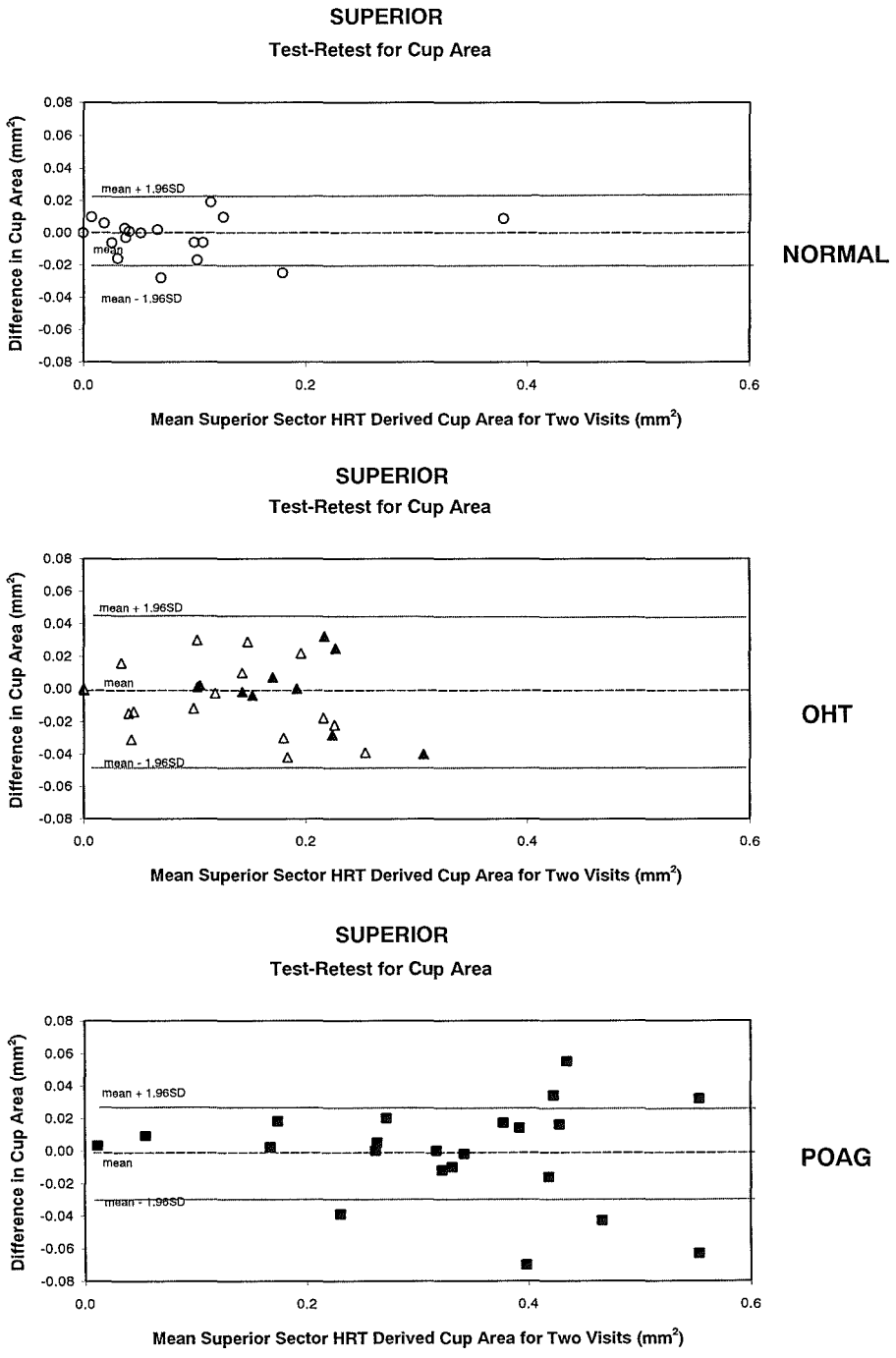

Figure 4.19. The difference in mean Superior Sector CA as a function of the mean Superior Sector CA for the two visits, for the Normal group (top), for the OHT group (open triangles) and OHT(H) group (closed triangles) (middle) and for the POAG group (bottom). The mean and the 95% confidence limits are shown.

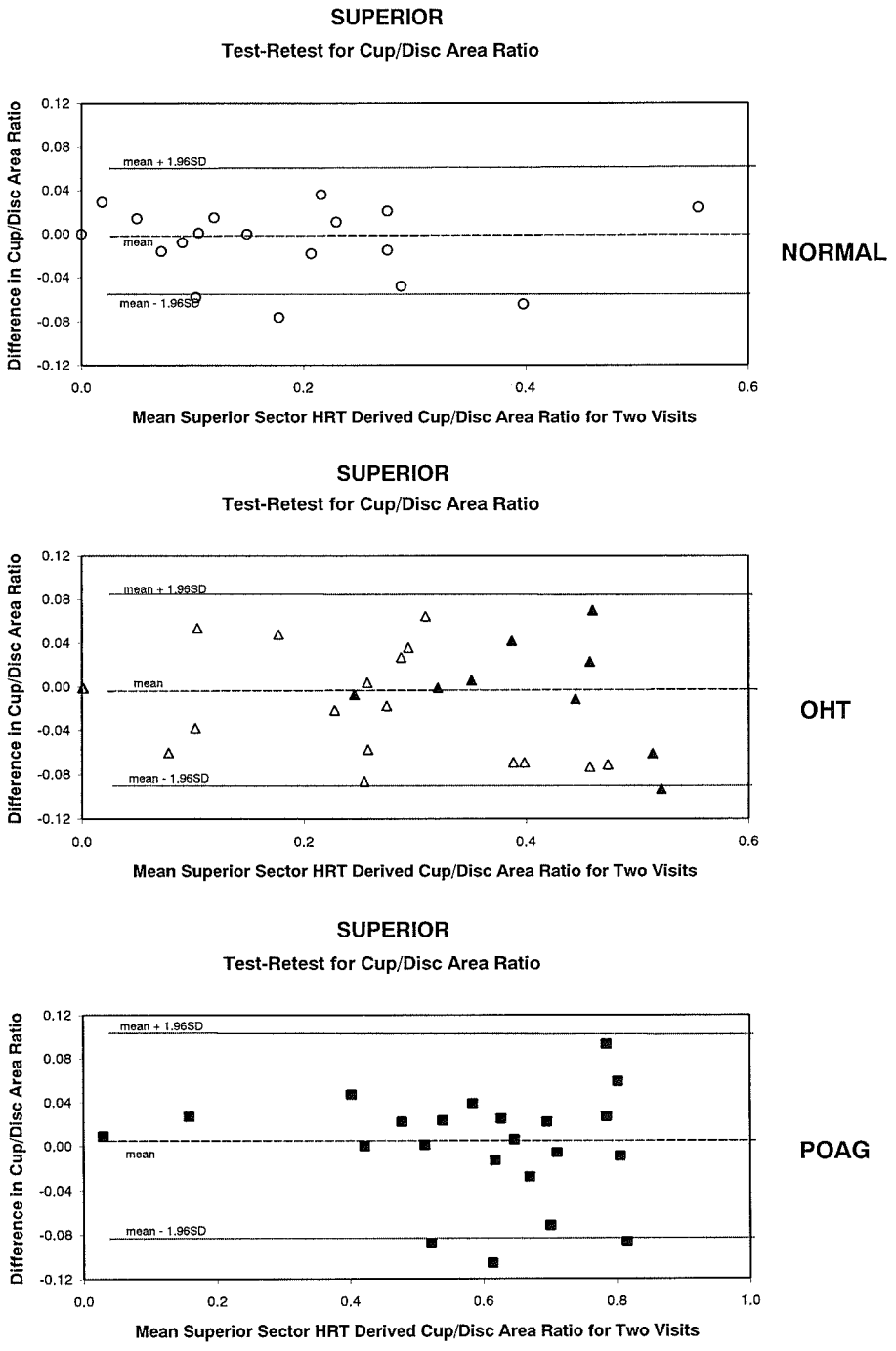

Figure 4.20. The difference in mean Superior Sector CDAR as a function of the mean Superior Sector CDAR for the two visits, for the Normal group (top), for the OHT group (open triangles) and OHT(H) group (closed triangles) (middle) and for the POAG group (bottom). The mean and the 95% confidence limits are shown.

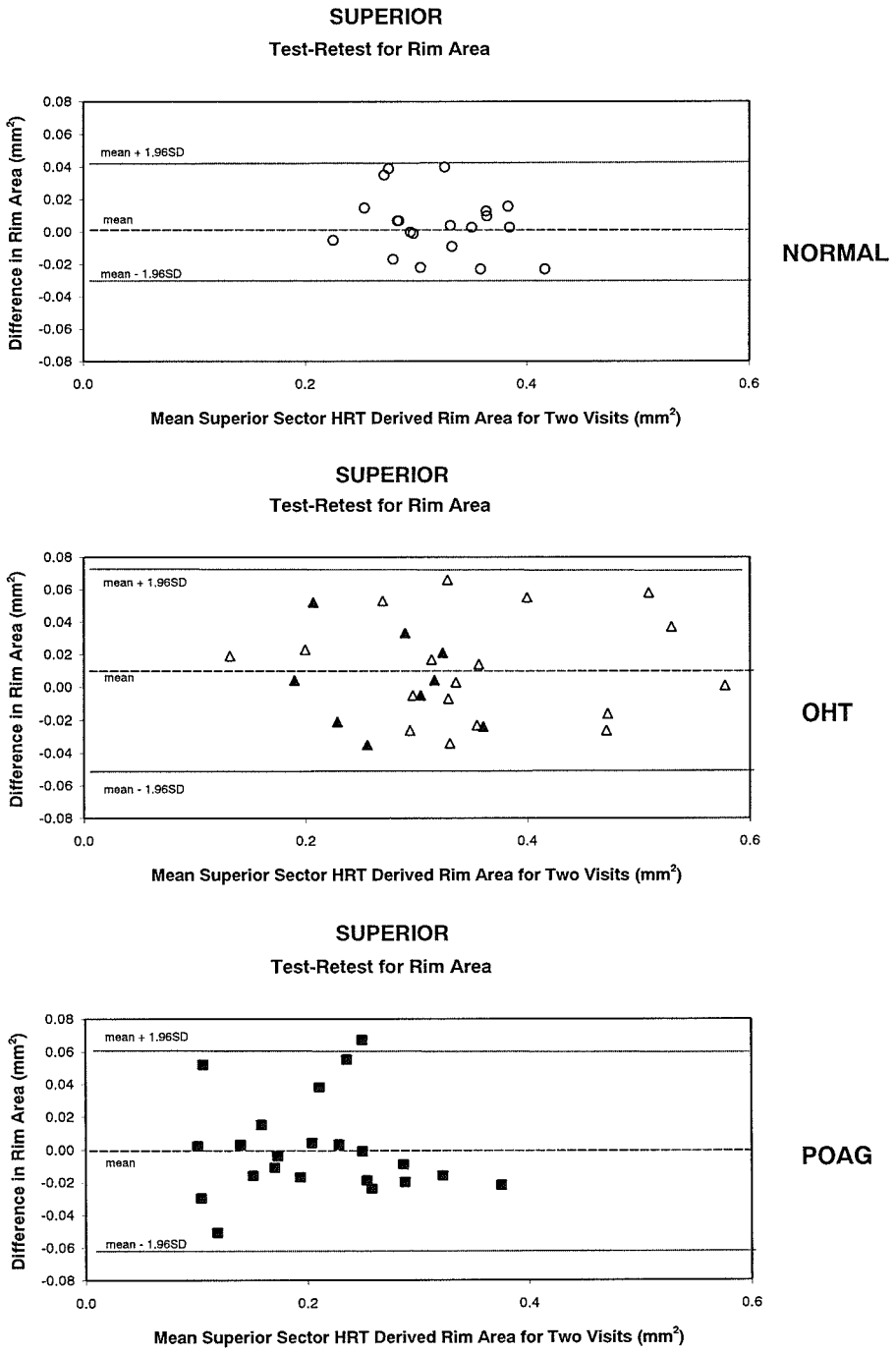

Figure 4.21. The difference in mean Superior Sector RA as a function of the mean Superior Sector RA for the two visits, for the Normal group (top), for the OHT group (open triangles) and OHT(H) group (closed triangles) (middle) and for the POAG group (bottom). The mean and the 95% confidence limits are shown.

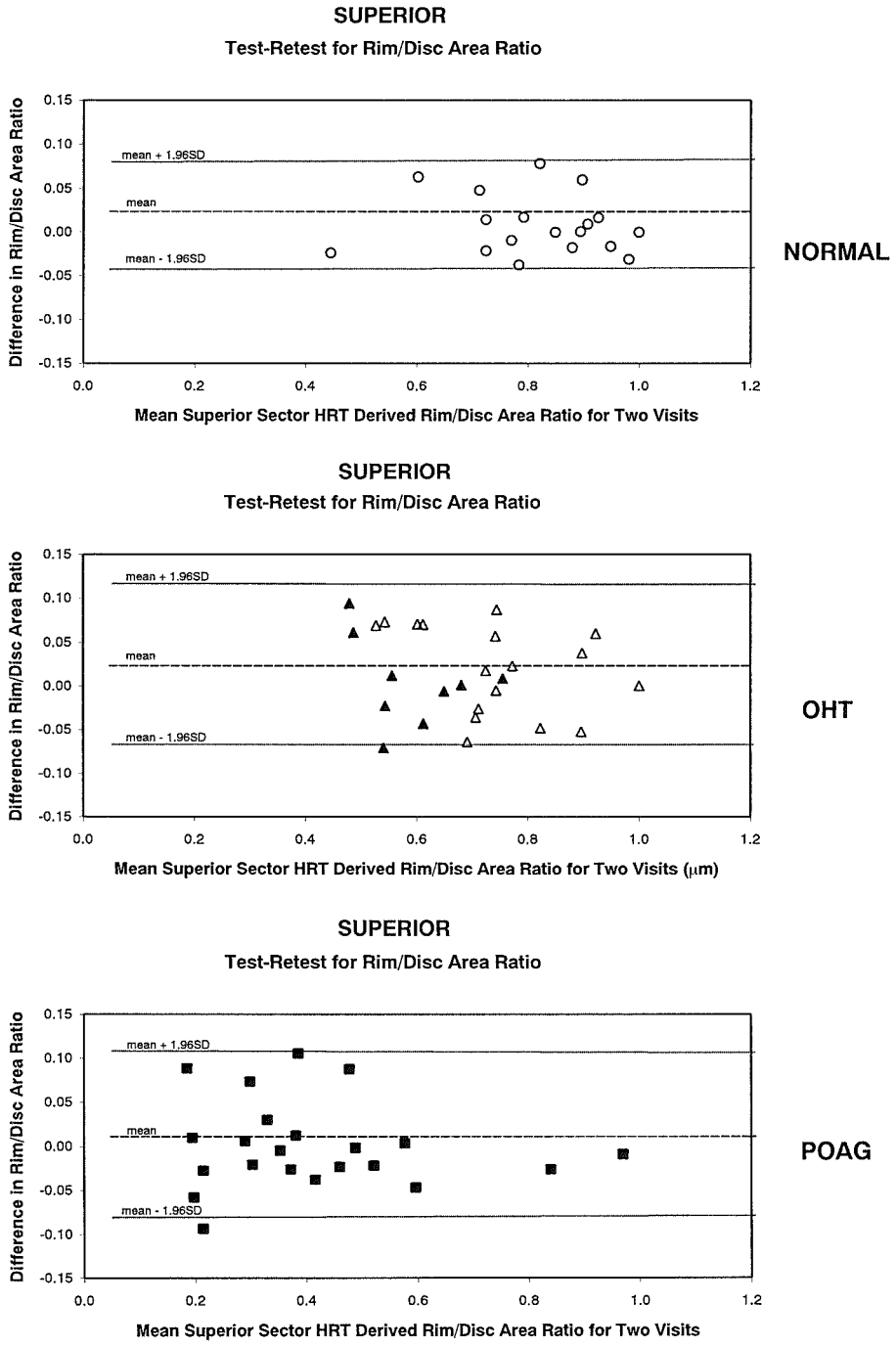

Figure 4.22. The difference in mean Superior Sector RDAR as a function of the mean Superior Sector RDAR for the two visits, for the Normal group (top), for the OHT group (open triangles) and OHT(H) group (closed triangles) (middle) and for the POAG group (bottom). The mean and the 95% confidence limits are shown.

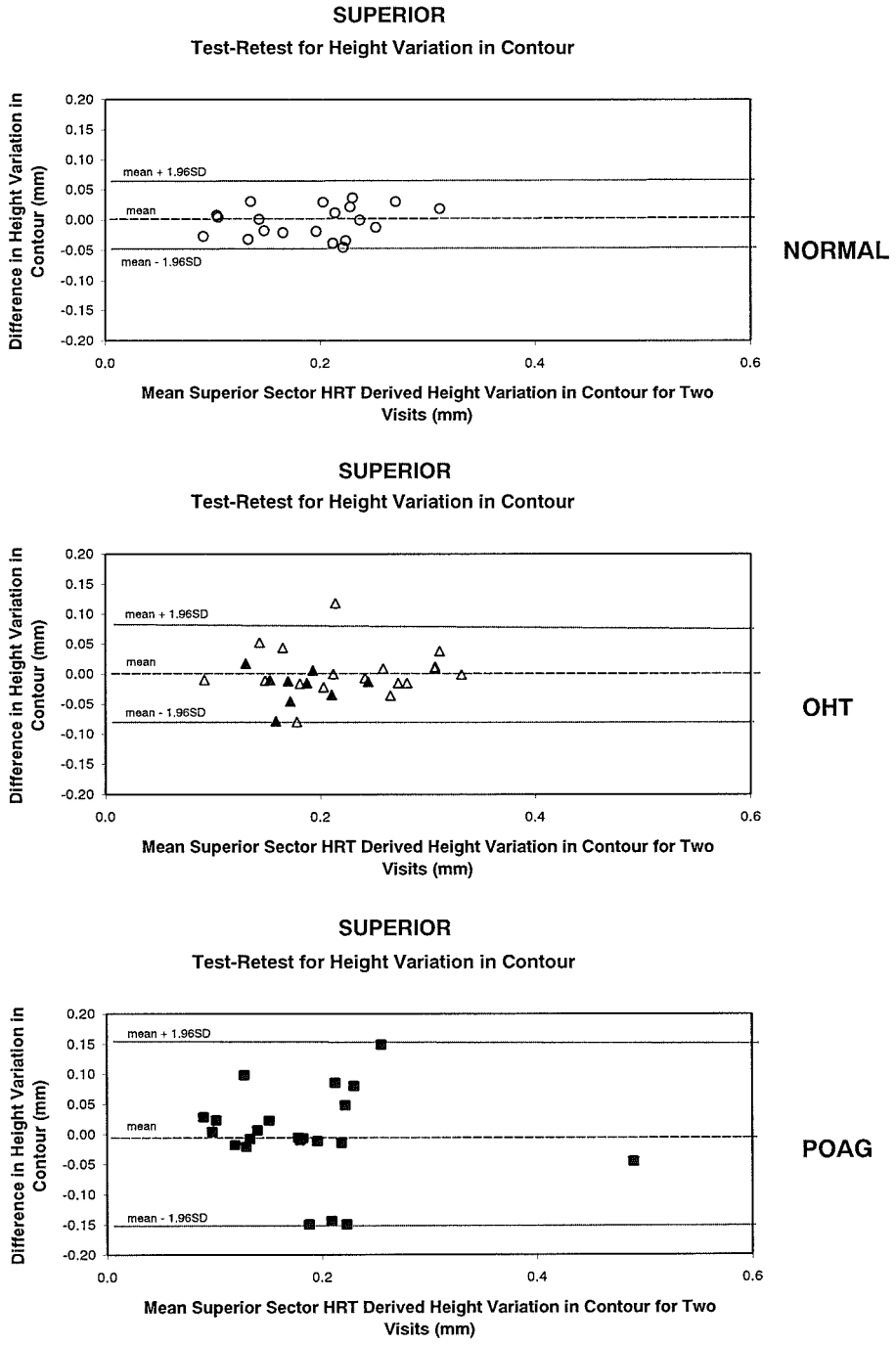

Figure 4.23. The difference in mean Superior Sector HVC as a function of the mean Superior Sector HVC for the two visits, for the Normal group (top), for the OHT group (open triangles) and OHT(H) group (closed triangles) (middle) and for the POAG group (bottom). The mean and the 95% confidence limits are shown.

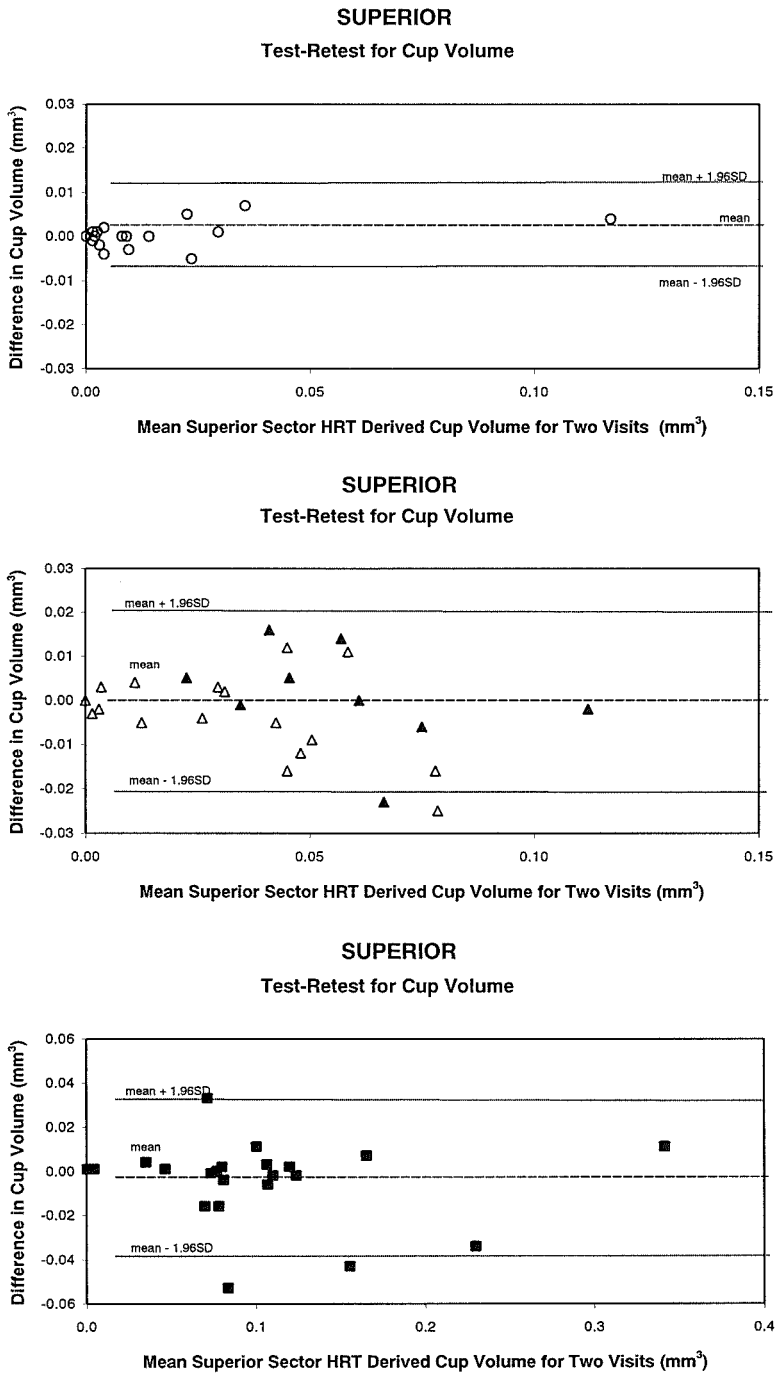

Figure 4.24. The difference in mean Superior Sector CV as a function of the mean Superior Sector CV for the two visits, for the Normal group (top), for the OHT group (open triangles) and OHT(H) group (closed triangles) (middle) and for the POAG group (bottom). The mean and the 95% confidence limits are shown.

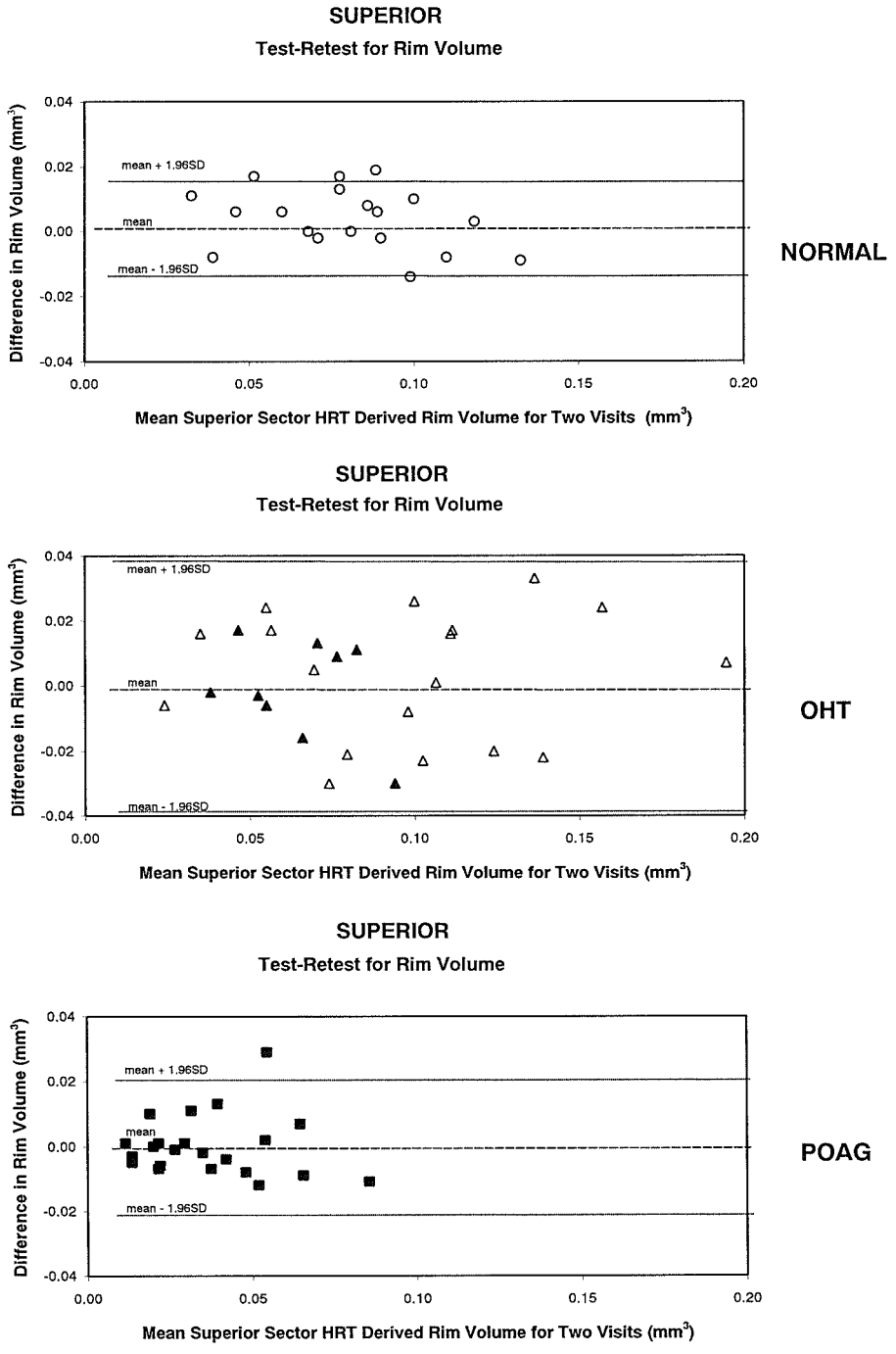

Figure 4.25. The difference in mean Superior Sector RV as a function of the mean Superior Sector RV for the two visits, for the Normal group (top), for the OHT group (open triangles) and OHT(H) group (closed triangles) (middle) and for the POAG group (bottom). The mean and the 95% confidence limits are shown.

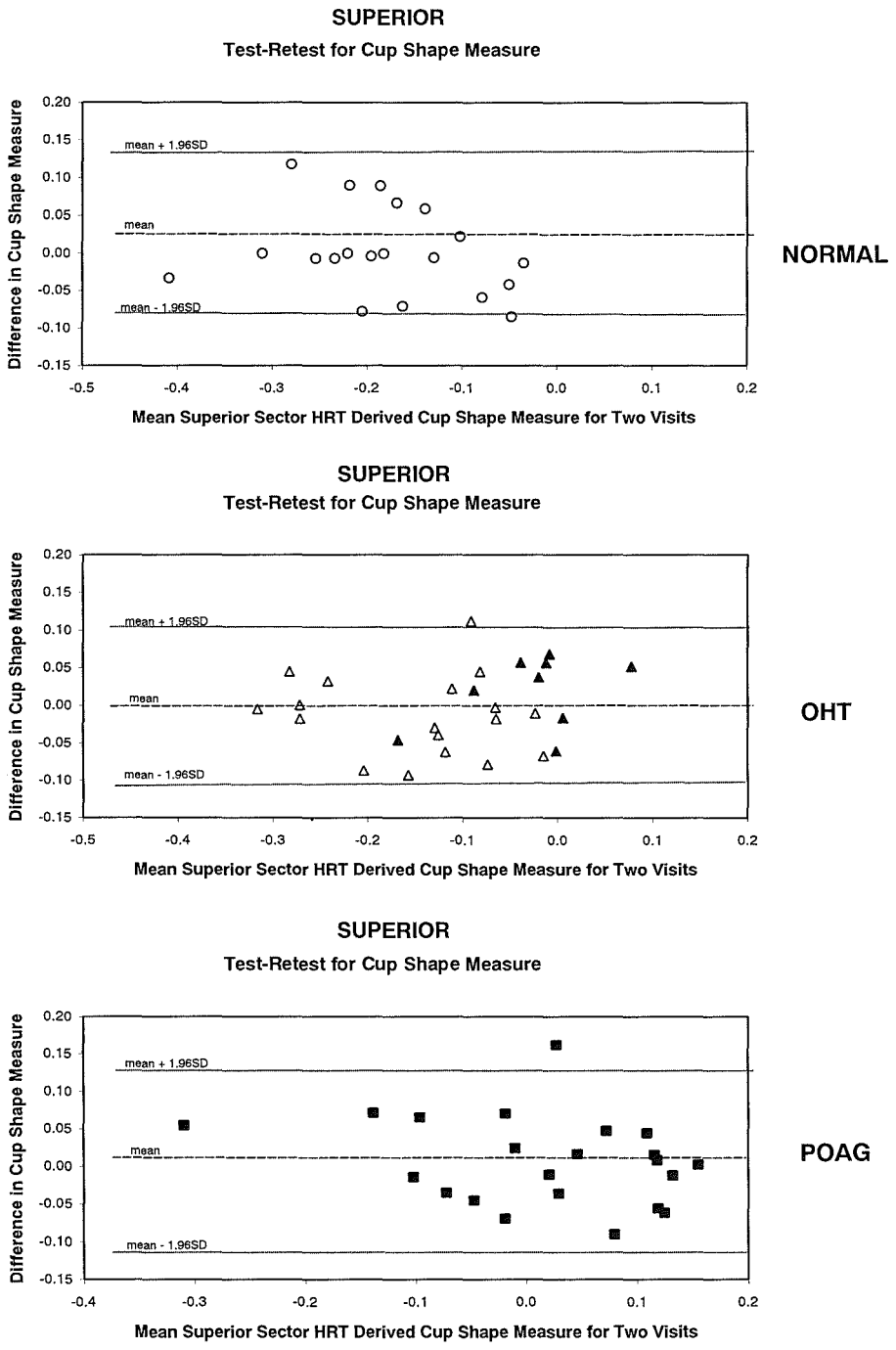

Figure 4.26. The difference in mean Superior Sector CSM as a function of the mean Superior Sector CSM for the two visits, for the Normal group (top), for the OHT group (open triangles) an OHT(H) group (closed triangles) (middle) and for the POAG group (bottom). The mean and the 95% confidence limits are shown.

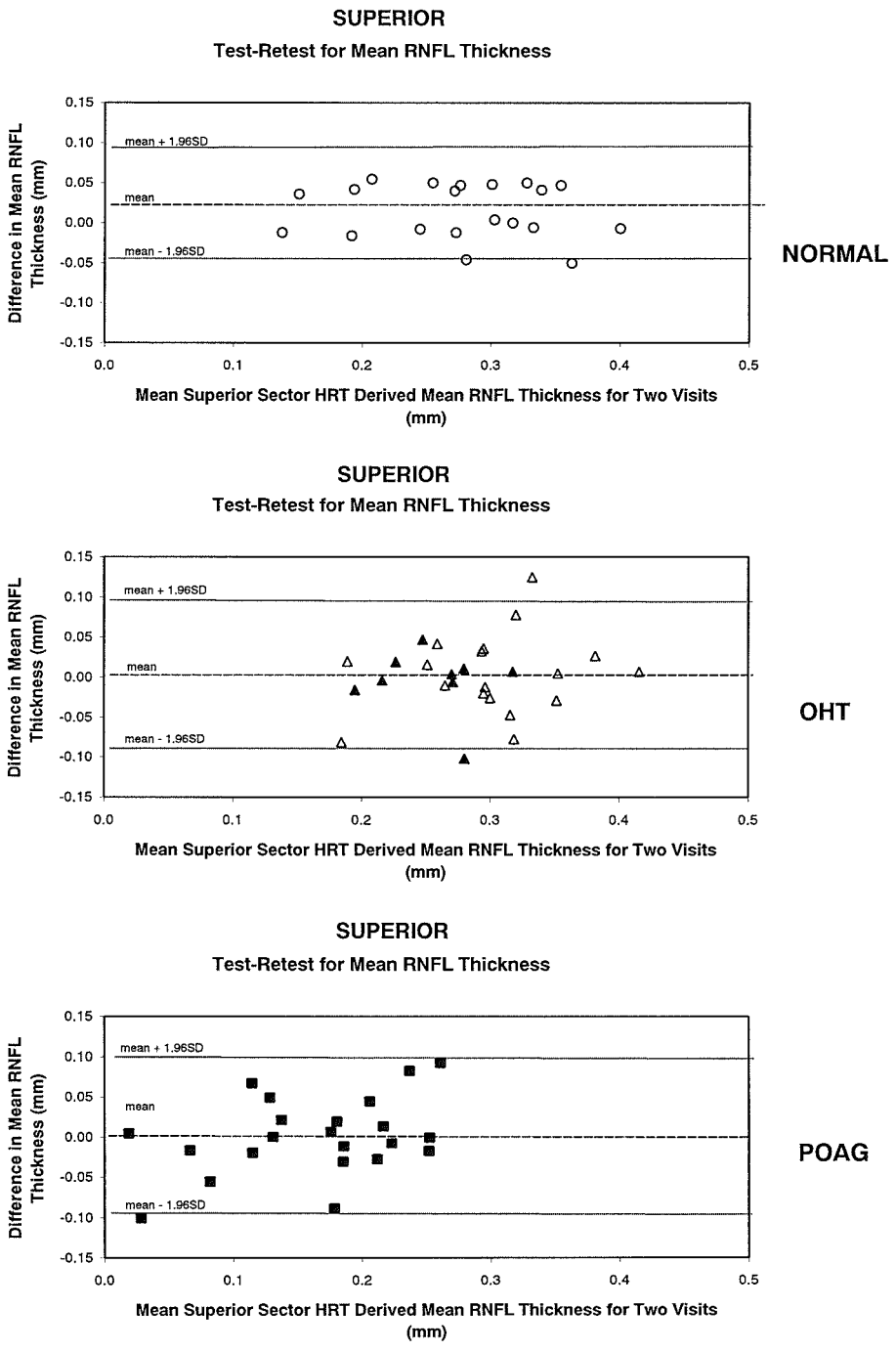

Figure 4.27. The difference in mean Superior Sector Mean RNFLT as a function of the mean Superior Sector RNFLT for the two visits, for the Normal group (top), for the OHT group (open triangles) and OHT(H) group (closed triangles) (middle) and for the POAG group (bottom) The mean and the 95% confidence limits are shown.

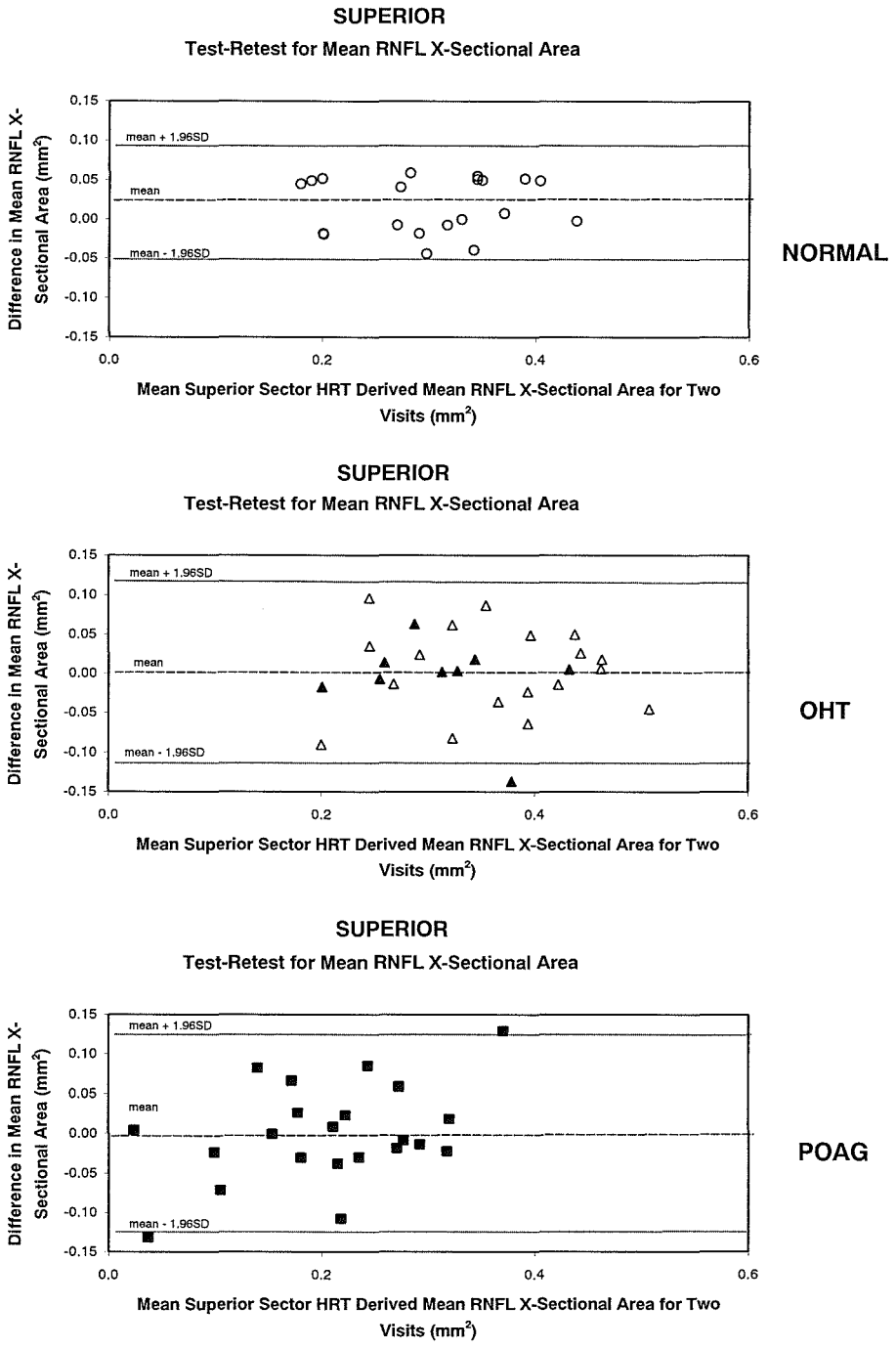

Figure 4.28. The difference in mean Superior Sector RNFL cross-sectional area as a function of the mean Superior Sector RNFL cross-sectional area for the two visits, for the Normal group (top), for the OHT group (open triangles) and OHT(H) group (closed triangles) (middle) and for the POAG group (bottom). The mean and the 95% confidence limits are shown.

4.8 Discussion

In the study the within-and between-visit variability was assessed for a group of normal individuals, a group with ocular hypertension and a group with POAG. The topographic parameters for the ONH were evaluated both globally and for each of four sectors.

The Group mean within-visit, between-image variability in the standard deviation of the pixel height within the images ranged from 16.73 to 27.41μm across the three diagnostic groups. The results compare well to the extensive literature concerned with variability in the topography of HRT images (Lusky et al. 1993; Mikelberg 1993; Rohrschneider et al. 1993; Weinreb et al. 1993; Chauhan and LeBlanc 1994; Chauhan and Macdonald 1995; Chauhan and McCormick 1995; Hosking and Flanagan 1996; Orgül et al. 1996; Orgül et al. 1997).

The Group mean within-visit between-image CoV for various stereometric parameters ranged between 0.00% and 28.14% at Visit One. As expected, the CoV was least for DA and ranged from 0.01% to 0.22% across the three groups. The HRT imported contour line option used for defining the ONH in repeated topographic images allows identical regions to be selected between separate, but related images for the same eye of an individual. The process is recommended for follow-up analysis (Jonescu-Cuypers et al. 1998). In addition, the CoV for RA and the related RDAR was less than 10% across each of the three groups. The CoV's were greatest for the CSM, being larger than 10% at each visit and across the diagnostic groups. The findings are similar to other studies in which the CoV's reportedly ranged from 0.03% to 24.01% (Orgül et al. 1997) and from 4.1% to 30.6% (Mikelberg 1993; Rohrschneider et al. 1993). The mean RNFLT and RNFL cross-sectional area parameters were not available with the software versions of those reproducibility studies, but in this study they ranged from 8.26% to 23.69% and 8.14% to 23.71, respectively.

The CoV's tend to be greater for the POAG group than for the other two groups for each of the parameters, across both visits. An increased variability in a POAG group compared to normals has been found previously (Mikelberg 1993; Brigatti et al. 1995; Chauhan and Macdonald 1995), but not always (Lusky et al. 1993; Rohrschneider et al. 1993; Rohrschneider et al. 1994).

The magnitude of the global measurements did not vary with the number of scans within each visit. However, as fluctuations in the cardiac cycle (Chauhan and McCormick 1995) and misalignment of the head position of the patient (Orgül et al. 1996) can lead to errors in the topographic data, the recommended acquisition of at least three images (Weinreb et al. 1993) still remains appropriate.

The between-visit variability was similar across the diagnostic groups, and was minimal both on a global and a sectoral basis, although generally narrowest for DA. An independent contour line was drawn for each visit, so that the high level of reproducibility is not attributable to the

software but could be due to the consistent approach by the operator in defining the disc margin. The mean RNFL cross-sectional area exhibited the greatest between-visit variability across each of the three groups, but the reason for this is unclear.

Chauhan et al (1995) found the within- and between-visit variability for the HRT, in terms of the height of the pixels for the images, to be similar in normals. The between-visit variation for the stereometric parameters, and across diagnostic groups is seldom mentioned in the literature. However, the similarity in the between-visit variation for the three groups both in their study and in this study, supports the use of the HRT for long-term evaluation of normals, individuals with ocular hypertension and those individuals with POAG.

Each of the stereometric parameters discriminated between the three diagnostic groups. The DA and the HVC exhibited the least difference between the groups, as previously found (Hatch et al. 1997) The CSM has good discriminatory ability to separate groups of normals from those with glaucoma (Uchida et al. 1996; Hatch et al. 1997; Iester et al. 1997b). Evidence for a difference between normals and OHTs is equivocal (Zangwill et al. 1996; Iester et al. 1997a).

There is a large between-individual variation within each diagnostic group of the HRT derived ONH topography, with a marked overlap between the groups, which has been widely reported elsewhere (Mikelberg 1995; Tsai et al. 1995a; Zangwill et al. 1996; Bathija et al. 1998; Burk et al. 1998; Saruhan et al. 1998; Wollstein et al. 1998; Hatch et al. 1999; Iester and Mikelberg 1999; Mardin et al. 1999). Similar results have been found for the ONH as measured by planimetry of stereo disc photos (Jonas et al. 1988c; Jonas et al. 1992a).

The overlap of the measured parameters can be attributed to the heterogeneity of the groups and the subjective outlining of the disc margins. The clinical relevance of the finding is that a single variable may not be capable of discriminating between a POAG individual and a normal individual in the early stages of the disease. Indeed, evidence suggests that discriminant analysis should include at least three variables, particularly, the DA and the CSM (Mikelberg 1995; Bathija et al. 1998; Mardin et al. 1999; Iester et al. 2000a).

The sensitivity and specificity of the HRT for discriminating individuals with early glaucoma from normals (Zangwill et al. 1996; Iester et al. 1997b; Wollstein et al. 1998; Hatch et al. 1999; Iester and Mikelberg 1999; Iester et al. 2000a) or those with ocular hypertension (Zangwill et al. 1996; Mardin et al. 1999) is reasonably good. The discriminatory power is improved by using a combination of at least three stereometric parameters (Mikelberg 1995; Bathija et al. 1998; Wollstein et al. 1998; Mardin et al. 1999; Iester et al. 2000a), and allowing for age (Mikelberg 1995; Iester et al. 1999a; Iester et al. 2000a) and disc area (Iester and Mikelberg 1997; Wollstein et al. 1998; Iester et al. 1999a; Mardin et al. 1999; Iester et al. 2000a) as between-individual confounding factors.

None of the parameters in the study were dependent upon age. A lack of age-related change to the ONH topography has been reported by some (Mardin and Horn 1998; Saruhan et al. 1998) but not all (Garway-Heath et al. 1997; Hatch et al. 1997) investigators.

The mean DA for the Normal group was smaller than that found in most (Zangwill et al. 1996; Iester et al. 1997a; Saruhan et al. 1998; Iester et al. 1999b; Mardin et al. 1999) but not all (Iester et al. 1997a; Bathija et al. 1998) studies. For the OHT group the mean DA was smaller than some studied groups (Hatch et al. 1997; Iester et al. 1997a; Mardin et al. 1999), but similar to others (Zangwill et al. 1996; Iester et al. 1997a). For the POAG group the mean DA was smaller than most studies (Hatch et al. 1997; Iester et al. 1997a; Mardin and Horn 1998; Iester et al. 1999b; Mardin et al. 1999) but similar to others (Zangwill et al. 1996; Iester et al. 1997a; Bathija et al. 1998).

The study found a difference in the DA between the diagnostic groups, however other studies have not found such a variation (Iester et al. 1997a; Iester and Mikelberg 1997; Iester et al. 1997b; Bathija et al. 1998). This could be due to a sampling error, related to the relatively small size of the sample in this particular study, or, in part, due to the criterion used to draw the contour line. In contrast to other reports that employed the HRT (Iester et al. 1997a; Iester et al. 1997b), the data set did not include optic discs with a DA greater than 3.00mm^2. In addition, 50% of the Normal group and 10-20% of the OHT and POAG group had a DA of 1.50mm^2 or less. The distribution of DAs is similar between the OHT and POAG groups, but is skewed towards small DAs, of less than 1.50mm^2 for the Normal group. Eyes with a small DA can be difficult to assess for early glaucomatous damage (Iester and Mikelberg 1997) and loss of neural tissue can remain undetected until a large proportion of the rim volume is reduced.

Different values of sensitivity and specificity arise when patients are stratified according to DA (Iester and Mikelberg 1997). Reported DAs differs between investigating centres, and between imaging systems, due in part to racial difference and selection bias of the patients, between-operator differences and characteristics of the imaging systems. The differences are likely to influence the performance of any discriminant analysis function that is evaluated. Until the procedure for defining the contour line is standardised, direct comparison of diagnostic results between studies should be undertaken with caution (Iester et al. 1999b).

The study found the HVC and mean RNFLT to be independent of DA, as reported by Saruhan and colleagues (1998). The data is consistent with the finding that CV increases with increasing DA (Tsai et al. 1995a). With increase size of the optic disc there was increasing area and volume of the cup, the area of the rim and the excavation of the cup. The RV was not influenced by the disc size. The findings are consistent with the clinical observations that large discs are associated with large cups and NRR areas (Jonas et al. 1989c; Mardin and Horn 1998).

The magnitude of each sector measured parameter varied with the diagnostic group, with the exception of HVC for the superior and inferior sectors and both for HVC and CSM for the nasal sector. The findings suggest that the CSM is least affected by glaucomatous damage in the nasal sector, but the result could be erroneous. Despite the minimal level of variability both within-and between-visits, there are sources of error inherent to confocal scanning laser imaging. The HRT software can correct for artefacts in the contour line position that arise from blood vessels crossing the border, however, the area and volume of major blood vessels which lie within the ONH are included in estimates of the rim area and volume. A consequence of the vessel inclusion is the overestimation of the presumed NRR area and volume (Dichtl et al. 1996; Saruhan et al. 1998), particularly in the nasal region. Nasal displacement of the central retinal vessel trunk within the ONH in glaucoma could contribute to the apparent maintenance of tissue substance in the nasal sector despite neuroretinal rim loss. The HVC provides a measure of the variation in the height of the retinal peripapillary surface with respect to the standard reference plane. A diffuse reduction in the surface height of the ONH margins in glaucoma could be associated with minimal change to the differential height around the disc.

The sector magnitude of each parameter was dependent upon the disc area across each of the four sectors, with the exception of the HVC, RV and RNFLT. The HVC and RV were independent of DA for the superior, inferior and temporal sectors, whilst the mean RNFLT was independent of DA for the superior, inferior and nasal sectors. Whilst the independence of sector HVC and RNFLT from DA is consistent with the findings for global measures, it is unclear, and has not been previously reported why it does not apply for all sectors, and why most sector RVs also exhibit a lack of dependence.

Stability of the reference plane height is a pre-requisite for reproducible topographic analysis both for within-and between-visits. Variations in the contour line definition when drawn separately on sequential images can increase variability in topographic measurements (Orgül et al. 1997). Importing the same contour line onto each image can minimise variations in the reference plane position, within an individual, with improved reproducibility. However, despite the HRT image alignment software correcting for tilt and rotation, that can be attributable to movements of the patients head, and the development of a standard reference plane, it is unclear what effect tilted discs, and irregular retinal and ONH topographies have upon the accuracy of the alignment process (Burk et al. 2000). The marginally greater degree of within-visit variability for the POAG group compared to the Normal and OHT groups could be a consequence of image alignment errors. However, Orgül et al (1997) considered variations incurred during image acquisition were of potentially greater influence on the topometric data than variations attributable to alignment of the contour line.

4.9 Conclusions.

The within-and between-visit variability both for global and sector stereometric data is minimal with the HRT software version 2.01, using the imported contour line from a mean topography image, provided that the published recommended quality control procedures are adhered to during the acquisition of the images.

The magnitude of each of the stereometric parameters evaluated was independent of age, however, they were dependent upon disc area. It is recommended, therefore, that disc area should always be taken into consideration when assessing the variation, between individuals, of parameters that describe the ONH configuration.

CHAPTER 5. FREQUENCY DOUBLING PERIMETRY.

5.1 Introduction.

5.1.1 Organisation of Retinogeniculate Visual Processing.

Light energy entering the eye and reaching the retina is converted into a neural signal by the photoreceptors and can subsequently give rise to a psychophysical response. Sampling of the retinal image information is undertaken by the rod photoreceptors, the short-wavelength sensitive (SWS) cones, the medium-wavelength sensitive (MWS) cones and the long-wavelength sensitive (LWS) cones. Different aspects of the image are filtered and encoded in parallel for axons to carry messages to an assortment of neural centres within the brain for further processing (Boycott and Wassell 1999). The majority of the data is conveyed to the lateral geniculate nucleus (LGN) by at least two parallel pathways, of which the parvocellullar or P-pathway and the magnocellular or M-pathway are the most widely documented (Stone 1983; Kaplan and Shapley 1990; Dacey 1994; Lee 1996). There is strong evidence for a third pathway, known as the konicellular or K-pathway, that is thought to provide a modulatory effect to the magnocellular and parvocellular pathway and may suppress vision during eye movements, although the details of this pathway are not clearly defined or understood (Casagrande 1994).

Anatomical evidence for the pathways is found at the LGN, where retinal ganglion cells synapse in one of 6 clearly defined laminae. Four of the LGN layers, termed the parvocellular or P-layers, contain numerous, relatively small cells whilst the two remaining magnocellular or M-layers, contain relatively large cells. Within the interlaminar regions are the koniocellular or K-layers.

There is psychophysical evidence for the segregation of the parallel pathways based upon the response to shape, colour, motion and depth appreciation (Livingstone and Hubel 1987; Chaturvedi et al. 1993). The M-pathway predominantly conveys information regarding motion and depth discrimination, whilst the P-pathway is predominantly concerned with colour and form.

Eighty percent of all retinogeniculate synapses occur in the parvocellular layers and arise from the midget (or P-cells). A further small percentage of ganglion cells, the small bi-stratified ganglion cells also synapse in the parvocellular layers. The parasol or M-cells, which include a subset of large Mγ-cells comprise a further 10% of the total ganglion cell population (for review, see Lennie 1980), and these synapse in the magnocellular layers. The remaining ganglion cells project to the K-layers or to the superior colliculus (Casagrande 1994).

The parasol retinal ganglion cells tend to have large receptive fields, are particularly sensitive towards low spatial and high temporal frequency stimuli, and exhibit a broadband response to

the chromatic features of stimulus. The midget cells have relatively small receptive fields which are more sensitive to the high spatial and low temporal frequency characteristics of the stimulus, and possess wavelength specific responses, although no evidence has been reported of a SWS-cone input to a midget cell (Dacey 1994).

Conceptual understanding of colour information processing, at the pre-ganglionic retinal level, is based upon a two-stage model that has been developed from the classical trichromatic theories expounded by Helmholtz and Herring. The neural responses from groups of wavelength-sensitive cone photoreceptors in the outer retina are organised by colour-opponency interactions that occur within the inner retina which constitute the origins of the parvocellular pathway (Hurvich and Jameson 1957; Padgham and Saunders 1975). A red-green opponent channel receives an input from the MWS and LWS cones, whilst a blue-yellow opponent channel receives an input from the SWS cones and the combined signal output from LWS and MWS cones. A third oppponent luminance channel, thought to be mediated by the MWS and LWS cones, receives an additional input from the rod photoreceptors (DeValois and DeValois 1993).

5.1.2 Glaucomatous Optic Neuropathy and Visual Processing.

Evidence that selective loss of large ganglion cells (Dandona et al. 1991; Glovinsky et al. 1991; Quigley et al. 1991; Morgan 1994; Weber et al. 1998; Morgan et al. 2000), optic nerve fibres (Quigley and Sanchez 1987; Quigley et al. 1988) and cells in the LGN (Chaturvedi et al. 1993; Weber et al. 2000; Yucel et al. 2000) occurs with glaucoma is equivocal. The apparent selective damage of some ganglion cell types could arise from their sparse distribution and reduced anatomical reserve capacity (Johnson 1994).

Psychophysical evidence for early glaucomatous damage is based upon a variety of techniques that detect loss of function by the ganglion cells; some of which apparently precede morphological abnormality. Apparent deficits in the magnocellular pathway have been shown in tests of resolution acuity (Anderson and O'Brien 1997), temporal modulation (Casson et al. 1993), flicker perception (Lachenmayr et al. 1991), motion perception (Silverman et al. 1990) and frequency doubling perception (Maddess and Henry 1992; Johnson and Samuels 1997). Deficits in the parvocellular pathway have been demonstrated using pattern discrimination perimetry (Stewart and Chauhan 1995) and SWAP (Johnson et al. 1993a; Johnson et al. 1993b; Sample et al. 1993).

Finally, there is evidence for damage in both the parvocellular and magnocellular pathways (Sample et al. 1997a) which can differ in severity between pathways depending upon an individuals susceptibility to damage and upon the stage of the disease.

5.1.3 Characteristics of the Normal Visual Field.

Several psychometric tests employed to quantify glaucomatous damage, including those that are considered to be selective, involve the assessment of the visual function across the field of vision. Each location within the visual field has a corresponding position in the image that falls upon the retina. Traquair (1949) described the distribution of the normal visual response across the visual field as a "hill of vision in a sea of blindness". The greatest sensitivity to a stimulus occurs at the fovea that projects to the point of fixation. Beyond the central 5°, which includes the macula, sensitivity rapidly declines and is greatest nasally. Approximately 15° temporal and 1.5° inferior to the summit of the 'hill' lies a small, extremely deep, vertically-sided 'chasm', corresponding to the projected location of the ONH (Anderson and Patella 1999). At the ONH, there is a total absence of photoreceptors within the scleral canal, giving rise to an absolute scotoma or 'blind spot' in the projected visual field. The term, absolute scotoma refers to an isolated area in the visual field associated with a total absence of response to a visual stimulus, however, in practice the term generally indicates a lack of response to the maximum stimulus brightness available to the perimetric instrument employed. A relative scotoma surrounds the absolute scotoma at the blind spot, the size of which depends upon topography of the ONH and parapapillary retina (Jonas et al. 1991a; Meyer et al. 1997) and upon the size and brightness of the stimulus (Choplin et al. 1990).

The perimetric examination is undertaken to determine, at selected locations within the field of vision, the minimum light energy necessary, to mediate a visual response. The absolute threshold to white light, is the minimum light energy necessary to evoke a sensation of light in a dark-adapted individual. Alternatively, the differential light threshold can be determined which corresponds to the amount of incremental light to be recognised as a noticeable difference with respect to the illuminated surroundings. Sensitivity is defined as the reciprocal of the differential light threshold.

5.1.4 Units of Measurement.

The unit of measure for static perimetry is the decibel (dB). This is a relative unit, for which a value of 0dB corresponds to the maximum stimulus luminance available for the particular perimetric instrument. Each log unit of attenuation of the stimulus corresponds to 10dB, therefore a 2 log unit attenuation is referred to as 20dB. The higher the sensitivity, the more attenuated the stimulus brightness can be, relative to the prevailing background luminance, and the greater the dB value recorded. Sensitivity is defined by the equation:

$$\text{Sensitivity (dB)} = k + 10 \log (L/\Delta L)$$

In the case of the Humphrey Field Analyzer (HFA), the background luminance $L = 10$ cdm^{-2} (31.5 asb), and the maximum stimulus luminance available, $\Delta L = 3183$ cdm^{-2}. The constant k has a value of 25 for the HFA. Other perimeters have different constants.

The differential light sensitivity decreases with age particularly after the age of 55 years (Jaffe et al. 1986; Johnson and Choy 1987). The peak of the hill of vision tends to erode at a lesser rate than the surrounding terrain, and there is a greater age-related decline in the upper field compared to the lower hemifield (Haas et al. 1986).

5.1.5 Characteristics of the Visual Field Loss in Glaucoma.

The shape and location of the field demonstrating impaired function can provide information about the region of the visual pathway that is damaged. The damage is considered to be diffuse if the visual response is decreased across a wide expanse of the visual field, A well-defined deficit that is restricted to a relatively small region is termed a focal abnormality. Typical patterns of field loss found in glaucoma are the paracentral, nasal or arcuate, defects. The defects can involve a single hemifield or both hemifields although there is generally a degree of asymmetry present between eyes or between hemifields within an eye. Progression of the damage causes the defect to become denser and to expand centrally across fixation and peripherally until any remnants of vision are ultimately extinguished.

A diffuse reduction in sensitivity across the whole field is accompanied by the localised paracentral and arcuate defects in glaucoma (Drance 1969; Chauhan et al. 1989; Drance 1989). Evidence of isolated focal damage is widely reported (Caprioli and Spaeth 1984; Heijl 1989b; Samuelson and Spaeth 1993), however some contention arises as to whether purely diffuse damage occurs in glaucoma (Chauhan et al. 1997; Henson et al. 1999).

The rate of visual field loss is quite variable, and appears to depend upon a number of factors including the level of the initial IOP, the level and stability of the treated IOP, and the extent of previous damage (Jay and Murdoch 1993; Quigley et al. 1996).

5.2 Automated Static Perimetry.

The stimuli employed to test the function within the visual field can be stationary or moving. The kinetic method involves the stimulus being introduced at the peripheral extremes of the visual field, and gradually being drawn across the field from a non-seeing to a seeing region. The threshold response is influenced by the degree of spatiotemporal summation (Greve 1973). A large between- and within-individual variation can arise, which is attributed to the variations in the individual reaction time to respond to the stimulus presentation (Lynn 1969; Parrish et al. 1984), or to the speed at which the stimulus is moved.

Static stimuli perimetry is independent of both reaction time and the speed of stimulus presentation. However, large numbers of stimuli presentations are required to estimate the threshold across the visual field. By manual perimetry this process is extremely time-consuming and a source of patient fatigue (Trope and Britton 1987). The introduction of computerised

automated perimetry and new thresholding algorithms reduces the level of fatigue and is accompanied by a reduced variation in the within- and between-test responses (Flanagan et al. 1993b; Bengtsson et al. 1997b; Wild et al. 1999a).

The combined use of a static technique for the central field and a kinetic technique for the peripheral field can offer additional sensitivity for those few glaucomatous individuals that have early deficits in the periphery, prior to central involvement. Attempts to compare the threshold values obtained with kinetic or static techniques should be undertaken with caution however, since the kinetic method has been shown to over-estimate the shape of the static hill of vision by some 4dB (Hudson and Wild 1992). This is referred to as stato-kinetic dissociation.

5.3 Factors influencing Perimeter Design and Quality of Data.

5.3.1 Retinal Adaptation and Background Luminance.

Perimetry can be performed at scotopic, mesopic or photopic levels of adaptation. The luminance of the background determines the level of retinal adaptation, and the presentation of a stimulus should minimally effect this general level of adaptation. The lower the level of retinal adaptation the greater is the dynamic range over which the threshold can be determined (Fankhauser 1979). A large dynamic range is desired when quantifying any depression in the visual field. The minimum light energy to evoke a response is dependent upon the retinal adaptation, and one might assume that the maximum stimulus luminance combined with the minimal background illumination would provide the greatest dynamic range. However, by virtue of the eye's imperfect optical system, very high luminances can introduce unwanted light scatter and thus a reduction in efficacy (Fankhauser and Haeberlin 1980). Similarly, a constant level of retinal adaptation at an extremely low background luminance is difficult to maintain and takes longer to achieve from normal daylight adaptation. Conventional W-W perimetry with the HFA uses a background luminance of 10 cdm^{-2} (31.5asb), to achieve a low photopic level of retinal adaptation (Anderson and Patella 1999).

5.3.2 Refractive Error and Retinal Defocus.

The general outcome from defocus introduced to the retinal image by a refractive error is the reduction of threshold sensitivity that results from an increase in retinal image area for a given amount of light energy, despite the counter-effect provided by spatial summation. Additionally, the contrast between the stimulus and the surrounding background at the blurred edges is depressed compared to that for a focussed image, which becomes particularly significant for a small compared to a large stimulus (Anderson and Patella 1999). A corrective lens is generally recommended to ensure adequate focussing of the test stimuli for the display-to-retina distance employed.

5.3.3 Temporal Summation and Stimulus Duration.

A phenomenon known as temporal summation of the visual response occurs if several stimuli are presented within a critical duration period. The visual system integrates the responses of repeatedly exposed stimuli of short exposure duration, and consecutive stimuli will appear brighter than for an individual stimulus. Similarly, for a stimulus duration less than 100ms, the visibility of the stimulus is proportional to the exposure duration (Anderson and Patella 1999). For a stimulus duration value up to a level of approximately 100ms the summation is almost perfect. For a longer duration, the effect of the stimulus becomes independent of the duration and detection is based solely on the stimulus luminance. However, there should be a sufficient interval between exposure to allow for patient reaction time and response whilst a long exposure can influence the level of retinal adaptation and encourages fixation losses. In the Octopus perimeter a 100ms duration is used, whilst the Dicon perimeter and HFA use a 200ms exposure.

5.3.4 Spatial Summation and Stimulus Size.

For a limited range of stimulus sizes there is an inverse linear relationship between the stimulus size and the threshold. The threshold decreases as the stimulus size is enlarged (Anderson and Patella 1999). This relationship is the result of spatial summation within the visual system and arises from the convergence of the output from the neural elements within the retina. A ganglion cell receptor with a large receptive field requires the energy from several neighbouring rod photoreceptors in order for it to achieve a threshold value at which it generates an output. The degree of spatial summation involved depends upon the eccentricity and adaptation level of the retina. The Goldmann size III stimulus is considered to be the standard choice for automated static perimetry. The size was selected in preference to the size I stimulus routinely used in kinetic perimetry as it is more resistant to the effects of optical defocus and media opacities (Fankhauser 1979; Heijl 1985; Atchison 1987).

5.3.5 Short- and Long-term Fluctuation.

Variability in the measures of visual function arises from the inherent variability of the visual system to respond to a stimulus (Bebie and Fankhauser 1976a). The estimated threshold is generally defined as that value for which the stimulus is recognised on 50% of the occasions on which it is presented to the observer (Weber and Rau 1992). However, repeated testing of the threshold at a location can give rise to variations in the estimate obtained. The standard deviation of the within-test repeated measurements is the short-term fluctuation (SF) (Zulauf and Caprioli 1991). Clinical evidence has shown that the SF tends to be greater at the edges of visual field defects, and in association with fatigue or inattention (Flammer et al. 1984a; Flammer et al. 1984b).

The long-term fluctuation is the between-test variability in threshold determination minus the amount of variation attributable to the short-term fluctuation or to a learning effect. There is both a homogeneous and a heterogeneous component to the long-term fluctuation, in which the variation is generalised and localised, respectively (Hutchings et al. 1993; Stewart and Hunt 1993).

5.3.6 Learning and Fatigue Effects.

Reliable results can often be achieved at the initial examination in most individuals with normal fields provided that adequate instruction is given prior to the test; however patients with glaucomatous field loss generally require repeated examinations in order to provide reliable and stable results (Wild et al. 1989). Learning effects tend to be less for central compared to peripheral regions of the visual field. Less improvement in performance occurs upon repeat testing in those individuals with minimal or with extensive field loss compared to those with moderate loss (Heijl and Bengtsson 1996).

Fatigue effects are associated with increased within-test variability towards the peripheral field. The effects of fatigue are particularly evident in regions of depressed sensitivity in glaucomatous visual fields (Wild et al. 1991). Alternative thresholding strategies, such as FASTPAC and the Swedish Interactive Thresholding Algorithm (SITA) have reduced the number of stimuli presentations, shortening the examination time and reducing the influence of fatigue (Flanagan et al. 1993b; Bengtsson et al. 1998; Bengtsson and Heijl 1999; Wild et al. 1999a; Wild et al. 1999b).

5.3.7 Pupil Size.

Visibility of a stimulus depends upon retinal adaptation and the contrast between the stimulus and the background luminance (Anderson and Patella 1999). The contrast is relatively independent of the size of the pupil since both the light intensity of the background and the stimulus will vary with changes in the pupil size. However, retinal adaptation depends upon the amount of light reaching the retina and is dependent upon the pupil size, particularly under the photopic conditions employed in conventional perimetry. In normal individuals with a pupil size of less than 2mm in diameter, Weber's law no longer applies and indeed, visual function has been shown to worsen (Lindenmuth et al. 1989). However, mydriasis can also be accompanied by reduced performance (Lindenmuth et al. 1990), attributable to the Stiles-Crawford Effect and to spherical and chromatic abberations. Nonetheless, for patients on pilocarpine treatment for glaucoma, dilation of the pupils for the perimetric examination may be necessary to obtain a true estimate of the field integrity (Rebolleda et al. 1992; Webster et al. 1993).

5.4 Examination Strategies.

5.4.1 Suprathreshold Strategies.

Suprathreshold strategies, permit the rapid examination of numerous locations within the visual field. The stimulus luminance of the initial suprathreshold strategies did not increase with increase in eccentricity to compensate for the hill of vision and the magnitude of the suprathreshold level was unrelated to threshold. The current suprathreshold strategies are gradient-adapted (eccentricity-compensated) and the starting level is based either upon the threshold for age or upon the individual threshold.

5.4.2 Thresholding Strategies.

A 'method of limits' strategy was often used in manual perimetry to estimate the threshold level at each stimulus location. The technique was an extremely tedious and time-consuming procedure, particularly if the number of stimulus locations chosen was large. With the advent of computerised automated perimetry, a staircase procedure can be used that is both efficient, and despite the large numbers of presentations necessary, requires less time than with manual testing.

The threshold is taken as the minimum stimulus luminance necessary to identify the stimulus at a given retinal adaptation. The threshold varies from moment to moment, and for a given stimulus brightness there is a range of probabilities, but not certainties, of the light being seen. Hecht et al (1942) attributed the fluctuation in response to the number of quanta, or amounts of light-energy present within a stimulus. The probability of vision being excited increases with the number of quanta and the strength of stimulus. Plotting the probability of seeing a stimulus against the increasing luminance generates a frequency-of-seeing curve, and from this, a threshold can be found at which 50% of the stimuli for a given luminance are seen (Chauhan and Tomkins 1993).

The HFA Full-threshold tests use a standard staircase with initial incremental steps of 4db, which change to 2db increments for the final double reversal crossing of the threshold in either an ascending or a descending direction (Bebie and Fankhauser 1976b). The threshold is deemed to be the last seen stimulus luminance. For central visual field examinations, four primary locations are thresholded twice, using a starting luminance of 25dB. Secondary locations adjacent to the primary locations are then tested using an initial luminance 2dB brighter than an expected value based upon knowledge of the normal topography of the hill of vision and the sensitivity found for the primary locations. Ten pre-selected locations are double determined to provide a measure of the short-term fluctuation within the examination, and any locations whose threshold value differs from the expected value by more than 4dB is also double-determined. Sensitivity with the 4-2dB staircase procedure decreases with increase in examination duration in normals, ocular hypertensives and patients with glaucoma (Wild et al.

1989; Hudson et al. 1994; Heijl and Bengtsson 1996) and is exacerbated by increasing age and visual field defects (Johnson et al. 1988b).

The HFA FASTPAC program uses a constant 3db single-crossing staircase procedure to determine the threshold, with threshold deemed to be the last seen stimulus luminance. The four primary locations are double thresholded in the same manner as in the Full Threshold algorithm. The initial starting luminance used for testing the secondary locations is chosen, however, to be 1dB brighter than the expected value if the value is an even number and 2dB dimmer if the expected value is an odd number. Whilst the examination duration is generally shorter with the FASTPAC algorithm than with the Full Threshold algorithm (Flanagan et al. 1993a; Flanagan et al. 1993b), the MS (Mills et al. 1993) and SF (Flanagan et al. 1993a) are greater, and the MD and PSD smaller (Flanagan et al. 1993b). The differences in the examination duration and in the MD between the FASTPAC and the Full Threshold algorithm decrease with increase in age (Flanagan et al. 1993b). The examination duration and SF increases with increase in defect depth and extent (Flanagan et al. 1993b).

The SITA standard and SITA FAST algorithms recently introduced to the HFA II use a 4-2dB and a 4dB step size respectively. The algorithms compare the responses of a patient with empirically determined models of the normal and glaucomatous visual field. Knowledge of the age-corrected normal values, the interdependency of threshold values at adjacent locations, the slope of the frequency-of seeing curve at each stimulus location, and the between-individual variation in the threshold were considered in the development of the models. Statistical functions within the instruments software evaluate the patient responses with reference to the modelled visual fields to predict the most likely threshold value and provide an indication of the accuracy of this threshold measure. The SITA standard and SITA FAST algorithms exhibit reduced examination durations compared to the equivalent HFA programs using the Full Threshold and FASTPAC algorithms respectively both for normals (Bengtsson et al. 1997b; Bengtsson et al. 1998); and patients with glaucoma (Bengtsson et al. 1997b; Bengtsson and Heijl 1998a; Bengtsson and Heijl 1998b). Examination duration increases with increase in defect depth in glaucoma (Wild et al. 1999b). The global index MS is higher and the TD and PD probability values exhibit greater statistical significance for both SITA algorithms compared to the Full Threshold and FASTPAC algorithms (Wild et al. 1999b). The pointwise between-visit variability is lower in the SITA algorithms than Full Threshold or FASTPAC algorithms (Wild et al. 1999a).

The Octopus perimeters generally employ a dynamic strategy combined with a staged sequence to the examination which can reduce the duration of the test. The step sizes are adapted to the frequency of seeing curve at a location, so that in areas of normal high sensitivity a 2db step size is used, whilst in peripheral or defective locations up to 10dB step sizes are used. The final measured threshold is determined from the mean of the last two stimuli after a reversal in the staircasing. An examination is undertaken in independent stages. A small

selection of key diagnostic locations are evaluated initially. Depending upon the patient responses, the same locations can then be re-thresholded and/or the area tested can be extended in further staged examinations. The procedure allows the test duration and locations of the stimuli presentations to be adapted to suit each individual.

Tendency Orientated Perimetry (TOP) employed as an alternative fast thresholding strategy in Octopus perimeters, uses a bracketing procedure with decreasing step sizes, relative to the age-corrected normal values, to determine the threshold for an initial array of locations (OCTOPUS Tendency Orientated Perimetry (1997) Interzeag AG Switzerland). Subsequent threshold values at other locations are determined and then modified by a linear interpolation process to account for the error in threshold estimation which occurs at adjacent locations due to their interdependency.

5.4.3 Stimulus Locations.

The resolution of the sampled visual field depends on the numbers and the spatial distribution of the tested locations. The visual field loss in glaucoma is most prevalent out to 30° eccentricity (Heijl and Lundqvist 1984), and this has prompted some strategies to concentrate the high density of stimulus locations within the areas of greatest risk (Sujimoto et al. 1998). An alternate approach is to systematically sample with evenly distributed stimulus locations across the visual field.

The optimum approach is an inter-stimulus grid with a 6° separation (Fankhauser and Bebie 1979). Heijl (1993) supported the idea that this spacing was sufficient to detect most glaucomatous field deficits. The grid pattern of presentations for the HFA programs 30-2 and 24-2 of the HFA are offset from the horizontal and vertical midlines by 3° thereby testing regions adjacent to, but not on the midlines. A complementary set of patterns, the 30-1 and 24-1 are arranged so as to test on the midlines. Both sets can be used singly or with its complimentary partner to increase the spatial resolution of the visual field examination.

5.5 Reliability Indicators.

Throughout a visual field test a number of reliability indices, including frequency of fixation losses, false-positive responses, and false-negative responses are generated. The statistical analysis of the visual field data available is based upon a normative database containing results which were not associated with a greater error rate for false-positive and false-negatives responses than 33%, and a fixation loss rate of 20% (Heijl et al. 1987; Katz and Sommer 1988; Anderson and Patella 1999).

5.5.1 Fixation Losses.

Fixation losses (FL) are recorded using the Heijl-Krakau blind spot test. A fixation loss is deemed to have occurred if a response is made to a stimulus that is presented to the area corresponding to the physiological blind spot of the eye under test (Katz and Sommer 1988). A FL error rate greater than 20% suggests that the visual field test results are unreliable, and can increase through poor fixation and also false-positive responses, but also with field loss (Bengtsson and Heijl 2000).

However, the stimuli presentations used for the blind spot test are additional to those presentations used to estimate the thresholds which extends the duration of the test, although the patient responses do not contribute to the measure of retinal sensitivity. Alternate methods of monitoring fixation are employed in the Octopus perimeter systems and in the 700 series of the HFA. II. The Octopus perimeters use four infrared corneal reflex monitors, two at each side of the pupil, to continuously monitor fixation (Manual-OCTOPUS 1990). Significant eye excursions or prolonged eye closure detected by the sensors results in a temporary delay of the stimuli presentations until correct fixation is resumed.

A gaze tracking system is used in the HFA, following a pre-test initialisation procedure, in which the patient is encouraged to maintain steady fixation, without blinking, whilst the instrument software determines the location and distance between the centre of the pupil and the anterior corneal reflex (first Purkinje image). The information is used by the tracking system, which uses light from an infra-red source, as a reference point against which deviations of the eye from steady central fixation are compared. A plot of magnitude of eye movement (during stimulus presentation) against time is displayed on the operator's screen throughout the test and included in the subsequent printouts. Using the gaze monitoring system, fixation is monitored for all the stimuli presentations, instead of only 5% that occurs with the Heijl-Krakau method.

5.5.2 False-Positive and False-Negative Errors.

False-positive (FP) errors occur when a response is made in the absence of a stimulus, either through anticipation, or following an auditory cue that often, but not always, accompanies the visual stimulus. A visual field result associated with a FP rate greater than 33% is considered unreliable, however, all FP responses can potentially affect the overall reliability of the estimated thresholds (Katz and Sommer 1988).

False-negative (FN) errors occur when the response is delayed or not made even though the stimulus is known to have been detected. The common cause for FN errors is inattention and/or fatigue. False-negative error responses can result in a false estimate of the threshold and a negative value for the MD global index (Katz and Sommer 1988).

5.6 Global Indices.

Statistical packages incorporated in the instrument software provide summary statistics of the data. The global indices include the mean sensitivity, the mean deviation which represents the average total difference in dB between the measured values for each location and the age-corrected normal field, and the pattern standard deviation, a weighted standard deviation of the pointwise differences between the measured and normal reference field. The latter function is weighted to allow for the within- and between-individual variation in sensitivity across the visual field.

5.6.1 Mean Sensitivity

The Mean Sensitivity (MS) is calculated for the sum of the measured sensitivities at each of the stimulus locations within the visual field divided by the total number of measured locations. The MS is determined without reference to a set of normal values, however, the MS is influenced by age, and diffuse changes, although less influenced by small areas of localised loss (Flammer 1986). The formula for the calculation of Mean Sensitivity is:

$$\frac{1}{n}\sum_{i=1}^{n} X_i$$

Where n is the number of measured locations and X_i is the threshold estimated value at location i.

5.6.2 Mean Deviation.

The mean deviation is calculated from the average of the weighted values in the Total Deviation plot, excluding the locations immediately above and below the blind spot, and provides a measure of the overall severity of visual field loss (Anderson and Patella 1999). The values are weighted according to the variance of the normal values.
The formula for the calculation of Mean Deviation is:

$$\frac{\frac{1}{n}\sum_{i=1}^{n}\frac{X_i - N_i}{S_{1i}^2}}{\frac{1}{n}\sum_{i=1}^{n}\frac{1}{S_{1i}^2}}$$

where X_i is the estimated threshold; N_i is the normal reference threshold at point i; S^2_{1i} is the variance of normal field measurements at location i; n denotes the number of test points (excluding the blind spot).

5.6.3 Pattern Standard Deviation.

The Pattern Standard Deviation (PSD) for the HFA gives an index of the smoothness of the hill of vision, by providing a measure of the localised variation in the height of the visual field. The PSD value is small for normal and diffusely depressed visual fields, and the value increases when focal loss occurs. The PSD is calculated from the standard deviation of the mean of the values in the Total Deviation plot (Anderson and Patella 1999). Pointwise differences between the measured threshold and the expected normal value at the given location are weighted according to the variance of the normal value at the same location. The formula is:

$$\sqrt{\left\{\frac{1}{n}\sum_{i=1}^{n} S_{1i}^2\right\}\left\{\frac{1}{m-1}\sum_{i=1}^{n}\frac{(X_i - N_i - MD)^2}{S_{1i}^2}\right\}}$$

where Xi is the estimated threshold; N_i is the normal reference threshold at point i; S^2_{1i} is the variance of the normal value at point i; MD is the mean deviation index; and n denotes the number of stimulus locations (excluding the blind spot).

5.6.4 Short-term Fluctuation.

The short-term fluctuation (SF) provides a measure of the within-visit variability. The standard deviation is determined for threshold estimations undertaken twice at ten pre-selected locations and provides the estimate of short-term fluctuation. Each threshold estimate having been weighted according to the normal reference population variance at those locations. The short-term fluctuation for the HFA is calculated from the formula.

$$\sqrt{\left\{\frac{1}{10}\sum_{i=1}^{10} S_{2j}^2\right\}\left\{\frac{1}{10}\sum_{i=1}^{10}\frac{(X_{j1} - X_{j2})^2}{2(S_{2j}^2)}\right\}}$$

where X_{j1} is the first and X_{j2} is the second threshold estimate at a location i; S^2_{2j} denotes the normal within-test variance at the location i.

The normal reliable field is generally accompanied by a SF value of between 1 and 1.25dB. The value tends to increase with visual field defects that encroach upon any of the 10 double-determined threshold locations and with inconsistent patient responses.

5.6.5 Corrected Pattern Standard Deviation.

An 'adjusted' PSD index, termed the Corrected Pattern Standard Deviation (CPSD) which compensates for variability of the responses within a visual field examination assists the interpretation of abnormal visual field plots.
The formula used in the HFA is:

$$(CPSD)^2 = (PSD)^2 - k(SF)^2$$

Where k is a constant greater than 1 dependent upon the spatial distribution of the stimulus locations used in the calculation of the SF. In the HFA Program 24-2 the constant, k, is equal to 1.14 and in the Program 30-2 it is 1.28 (Anderson and Patella 1999).

5.7 Graphical presentation of the Visual Field.

In the numerical data plot, the value of the threshold estimate is given at each stimulus location. Locations that have undergone a repeated threshold determination, including those locations used for the derivation of the short-term fluctuation, exhibit the second estimate in parentheses. In the grey-scale plot, one of eight shades of grey are assigned to the threshold estimates, covering the range of 1 to 40dB, at each location and also to interpolated values for the regions between each discrete test location. Threshold estimates less than or equal to 0dB, or in the range 41 to 50dB are designated as black and white, respectively. The resultant printout provides limited information regarding the degree of abnormality present in the visual field (Heijl 1984).

The Total Deviation (TD) numeric plot provides the numerical difference for each test location between the measured threshold and the normal value for an age-matched individual. Accompanying the numeric plot is a corresponding empirically-derived probability map which represents the given level of statistical significance for each measured deviation. The plots provide an indication of those locations with significantly different threshold values from the expected normal value (Heijl et al. 1987; Heijl 1989a; Heijl et al. 1989b).

The Pattern Deviation (PD) numeric plot and probability map reveals the local regions that have a reduced sensitivity once a generalised depression or elevation of the hill of vision, the "General Height" (GH) has been taken into account (Heijl et al. 1987; Heijl 1989a; Heijl et al. 1989b).

5.7.1 Glaucoma Hemifield Test (GHT).

The glaucoma hemifield comparisons are based upon the assumption that the nerve fibres do not cross the temporal horizontal raphe, and the glaucomatous field losses tends to affect one hemifield more than the other. The tests are often based upon the threshold values but fail to neglect the variability attributed to eccentricity. The GHT is used to detect localised loss and therefore is derived from the pattern deviation map significance points (Åsman and Heijl 1992b; Åsman and Heijl 1992a; Zalta 2000). Sector analysis is used as it has been shown to provide better discriminability than pointwise analysis (Åsman 1992). However, the reliability of the sole use of the test for early glaucoma detection has recently been brought into question. In a large sample of visual field printouts that displayed evidence of glaucomatous defects on the numeric

PD plots approximately 27% were described as "within normal limits" by the GHT analysis (Zalta 2000).

5.7.2 Cumulative defect curve.

The cumulative defect curve or Bebie curve is considered capable of separating early diffuse loss from the normal variation in the visual field (Bebie et al. 1989). The defect depths at each stimulus location are ranked in ascending order of severity and displayed as a function of rank order. The 5^{th} and 95^{th} percentiles for a normal field are included in the graph as a reference for interpretation of the results. A purely diffuse loss will have a similar slope to that of the normal field, but the height of the ranked sensitivity values will be lower. In contrast, a purely focal loss increases the decline of the slope.

However, cumulative defect curve analysis involves a loss of spatial information regarding the visual field defect, and the normal variation in sensitivity with eccentricity can mask the effects of early central visual field defects in glaucoma (Åsman and Olsson 1995).

5.8 Advanced Data Analysis.

5.8.1 Change Analysis.

5.8.1.1 Pointwise topographical and longitudinal modelling.

A pointwise topographical model to describe the pattern of visual field defect progression has been described which utilises a polynomial surface to represent the visual field data at any time period and a longitudinal model based upon multiple linear regression analysis to represent the field over time. The model could also be used to predict the likely course of further visual field deterioration (Wild et al. 1993). The chronological order of the fields was used to indicate the time course of the visual field progression. The model was unable to describe the rate of visual field progression in terms of decibels per year. The model also did not correct for the lack of independence of the individual stimulus locations. The model could describe the sensitivity at any given stimulus location to within an accuracy of 3dB for stable and linearly declining visual fields. The accuracy was poor in cases of episodic progression (Wild et al. 1993) which limited the recognition of this type of event.

5.8.1.2 Change Analysis and Glaucoma Change Probability Analysis.

STATPAC and STATPAC-2 and STATPAC for WINDOWS are statistical packages available on the HFA or for use with a personal computer, for comparing and analysing threshold values with a database of normal age-corrected threshold values.

Several display formats are available in STATPAC (Heijl et al. 1987) including Global indices, Probability maps, Linear Regression charts and Box/whisker plots. The Change Analysis printout provides a summary of a series of visual fields in the form of box plots and graphs. For

each examination, the Total Deviations at each location are calculated and ranked according to their magnitude. A boxplot is generated to include the median deviation as a horizontal line within the box whilst the upper and lower boundaries denote the 85th and 15th percentiles of the distribution of the deviations respectively. Vertical lines extending beyond the box indicate the remaining 15% of the distribution in each direction. The linear regression charts show the magnitude of the global indices over the number of examinations.

STATPAC-2 (Heijl et al. 1990/1991) additionally includes the GHT and a Glaucoma Change Probability (GCP) analysis. For the GCP analysis, at each stimulus location on follow-up fields, the Total Deviation values are compared to a baseline examination or pair of examinations (Bengtsson et al. 1997a). The probability of no change from baseline is determined with reference to a database empirically determined from serial analysis of a group of stable POAG individuals. The GCP analysis using TD values was similar to a clinical evaluation of glaucomatous progression (Morgan et al. 1991).

STATPAC for WINDOWS currently includes a GCP analysis based upon PD values (Bengtsson et al. 1997a).

5.8.1.3 Progressor.

Univariate linear regression of sensitivity at each stimulus location against time to follow-up has become popular (Birch et al. 1995; Fitzke et al. 1996). The technique has been made commercially available as PROGRESSOR (Fitzke and McNaught 1994; Fitzke et al. 1996). The results of the analysis are displayed graphically by colour-coded bar charts spatially arranged according to each stimulus location. The length of each bar is proportional to the defect depth. Two shades of red designate whether the slope of the function is statistically significant different from zero at the $p<0.5$ or $p<0.01$ level respectively. PROGRESSOR is at least as good as (Birch et al. 1995; Fitzke et al. 1996), or better than (Viswanathan et al. 1997), the GCP analysis of the HFA based upon TD in determining stability and progressive loss in glaucoma.

5.8.2 Cluster analysis.

Several different types of cluster analysis have been advocated (Åsman and Heijl 1992c; Åsman et al. 1992) which are based on the assumption that two or more adjacent abnormal locations are less frequently found in a normal field. Chauhan et al (1989) combined information about defect depth and size of adjacent stimulus locations with depressed sensitivities from normal threshold values to derive a cluster index. The principle of cluster analysis in glaucoma was further developed by Åsman and Heijl (Åsman and Heijl 1992c; Åsman et al. 1992). A cluster index was derived from the summed scores assigned to the PD probability values of groups of abnormal stimulus locations that followed the arcuate distribution of the retinal nerve fibre layer, weighted according to location.

5.9 Short-Wavelength Automated Perimetry (SWAP).

5.9.1 Introduction.

Colour vision and colour contrast sensitivity is disturbed particularly along the blue-yellow tritanopic confusion axis in glaucomatous optic neuropathy (Hart and Burde 1985; Sample et al. 1986a; Hart 1987). Heron et al (1988) utilised a two-colour increment threshold technique involving a blue stimulus against a yellow background and demonstrated a general depression of sensitivity and localised defects in some OHT patients when compared to a normal age-matched group. Subsequent studies suggested that blue-on yellow perimetry might be more sensitive to early glaucomatous damage than white-on-white perimetry (Heron et al. 1988; de Jong et al. 1990; Hart et al. 1990; Sample and Weinreb 1990). Conventional W-W perimetry examines the luminance pathway, whilst high luminance colour perimetry can be used to isolate the Short Wavelength Sensitive (SWS) pathway, particularly in the mid-peripheral retina where glaucomatous damage generally occurs first (Sample et al. 1988).

It is believed that the blue-yellow colour opponent channel mediates the SWS pathway. The small bi-stratified ganglion cells are believed to be responsible for the blue-on, yellow-off processing in the primate (Dacey 1993a; Dacey and Lee 1994; Calkins et al. 1998) and in the human (Dacey 1993a) retina. The bi-stratified ganglion cells, which project to the parvocellular layer of the LGN, tend to have relatively large fibre diameters (Calkins et al. 1998) and are relatively sparsely represented (Dacey 1994) throughout the retina. They may therefore be vulnerable to glaucomatous damage whether through selective large fibre loss (Quigley and Sanchez 1987; Quigley et al. 1988; Glovinsky et al. 1991), or from non-selective loss due to their minimal redundancy (Johnson 1994), unlike their smaller, more prolific MWS and LWS counterparts.

By isolating the SWS pathway it is thought that damage to the small bi-stratified ganglion cells can be more readily detected. In order to isolate the SWS pathway a stimulus wavelength less than 475nm (Sample et al. 1986b) is presented on a yellow background which saturates the green or medium-wavelength sensitive (MWS) and the red or long-wavelength sensitive (LWS) pathways. To suppress the activity of the rod photoreceptors a high background luminance of between 120-300 cdm^{-2} is recommended although the increased background illumination potentially reduces the dynamic range in SWAP (Demirel and Johnson 2000).

5.9.2 Clinical Application.

Modifications to automated perimeters have been made to permit blue-on-yellow perimetry. Automated perimeters utilizing a projection system, (including the HFA and the Octopus 101 perimeter) are able to provide a stimulus of specific wavelength and size necessary for SWAP. A Goldmann Size V stimulus increases the isolation and available dynamic range. A narrowband stimulus of 440nm and a background with a broadband of 500-700nm wavelength

and a luminance of 100cdm^{-2} ensures maximal blue isolation (Sample et al. 1996) and an adequate dynamic range. The stimulus locations and test strategies available for SWAP are the same as for W-W perimetry.

An abundance of evidence has shown that SWAP is a sensitive indicator of early functional losses in those glaucoma patients (Sample et al. 1988; Sample and Weinreb 1990; Weinreb and Sample 1991; Sample and Weinreb 1992; Johnson et al. 1995; Sample et al. 1997a) and glaucoma suspects (Johnson et al. 1991; Johnson et al. 1993a; Sample et al. 1993) who are elite perimetric observers. Johnson and colleagues (1995) showed a strong association between early structural and functional losses in glaucoma, as evidenced by optic disc cupping and SWAP respectively. SWAP deficits are present in a small proportion of OHTs with normal W-W visual fields and the prevalence of SWAP abnormalities is increased in high-risk ocular hypertensives. SWAP is capable of predicting the onset and location of visual field damage some 3-5 years in advance of detection by conventional perimetry (Johnson et al. 1993a; Johnson et al. 1993b). The pattern of glaucomatous loss in SWAP is deeper, more extensive and tends to progress to a greater degree than for conventional W-W perimetry (Johnson et al. 1993a; Johnson et al. 1993b).

5.9.3 Confounding variables in SWAP.

Unfortunately, ocular media absorption (OMA) and forward light scatter diffusely reduce the visual field in SWAP (Moss et al. 1995). Various methods to correct SWAP for the effects of lenticular absorption and light scatter have been advocated, although none appear to be clinically viable (Sample and Weinreb 1990; Sample et al. 1996; Polo et al. 1997; Teesalu et al. 1997). The age-related decline in sensitivity is greater for SWAP than for W-W perimetry, having corrected for the influence of ocular media absorption (Wild et al. 1998). The age-decline increases with increased eccentricity and is more pronounced in the superior field than in the inferior field (Sample et al. 1997b; Wild et al. 1998).

SWAP exhibits increased short-term and long-term fluctuation (Wild and Moss 1996; Wild et al. 1998) compared to W-W perimetry. The variability persists even when accounting for the differences in the measurement scales employed. The situation is further confounded by the increased between-individual normal variability of SWAP compared to W-W perimetry (Wild et al. 1998). The normal between-individual variability is greater in the absence of correction for OMA (Wild et al. 1998). The increased variability has major implications for the statistical interpretation of SWAP data, including wider confidence limits for normality.

The examination duration of the visual field with SWAP is approximately 15% longer than W-W perimetry using the equivalent HFA program (Wild et al. 1998). The increase may be due to the differences in the nature of the detection task demanded. Consequently, the routine use of the FASTPAC 24-2 Program for SWAP has been advocated to reduce the examination duration.

The confidence limits for normality with FASTPAC are similar to those of the Full Threshold algorithm (Wild et al. 1998).

The learning effect in SWAP is prolonged beyond that found in W-W perimetry. This suggests that some of the increased within- and between-test variability for SWAP could be attributable to a lack of perimetric experience (Wild and Moss 1996). The increased background luminance in SWAP compared with W-W perimetry is likely to account for a greater difference in retinal illuminance between the occluded and test eye. The difference in retinal illuminance contributes towards the Ganzfeld blankout (Cubbidge 1997), which is considerably more apparent in SWAP compared to that exhibited in W-W perimetry.

A reduction in sensitivity has been reported for all colour vision mechanisms which suggests that glaucoma may not selectively damage the short-wavelength-sensitive pathway (Greenstein et al. 1996). In part, as a consequence of the variable factors of OMA, longer test duration, fatigue, learning effects, and the wider confidence limits for normality that confound the statistical interpretation of SWAP results, alternative perimetric techniques are being developed and evaluated. Frequency doubling technology perimetry is one such recently introduced technique that could have potential in glaucoma screening and management.

5.10 Frequency Doubling Technology (FDT) Perimetry.

5.10.1 Frequency doubling perception and clinical application.

Kelly (1966) combined both spatial and temporally modulated sinusoidal waveforms and noted a frequency doubling (FD) phenomenon over a limited range of stimuli. Photopic stimuli with low spatial frequencies of less than 3 cycles per degree (cpd) whose contrast is reversed at greater than 7Hz appear to have twice their actual spatial frequency A schematic representation of the frequency-doubled perceived image is shown in Figure 5.1a. The FD illusion persists as the contrast levels of the grating are decreased. The specific choice of spatial and temporal frequencies for a given retinal eccentricity dictate the likelihood of the illusion being perceived (Kelly 1981).

Kelly suggested that the FD phenomenon might be mediated by a particular class of retinal neurons, due to a rectification process, provided by on-off cells, similar to those within the ganglion cell layer. However, he doubted whether the ganglion cells, alone, were sufficient to create the phenomenon but considered the ganglion cells to be necessary as part of a non-linear pathway (Kelly 1981).

Non-linear response to evenly spaced sine wave gratings have been observed previously (Cornsweet 1970). High frequencies evoke the impression that the light bands are widened relative to the dark bands, whilst low frequencies reverse the effect. This 'brightness' non-

linearity, would seem to be further transformed by the introduction of flicker to create the frequency doubling illusion.

Richards & Felton (1973) found that the spatial frequency varied with flicker rate and was observer dependent. They claimed, as had Kelly (1966) previously, that the doubling persisted at threshold contrast suggesting that flicker might still be identified at low levels of contrast despite the grating, itself, being unresolved. Evidence exists for a disparity-sensitive adaptation occurring in response to the 'fundamental' or actual spatial frequency, which is accompanied by a 'frequency doubling' experience (Richards and Felton 1973). The conclusion reached by Richards & Felton was that although a retinal element, such as the magnocellular ganglion cells, may be a component of the illusion, the frequency doubling percept is created at a higher level in the visual system than disparity processing. Tyler (1974) discounted this hypothesis following observations that horizontal and vertical gratings gave an equal degree of doubling irrespective of monocularly or binocular viewing. This would not be the case if disparity processing were involved. He favoured the opinion that separate channels were used for static contrast detection and flicker detection (which included spatial frequency-doubling) and proposed amacrine cells as the mediators for the spatial-frequency doubling illusion. Visibility of the illusion requires change and reversal of the illumination. Since the amacrine cells responses are transient, with a similar onset and offset response, they appear to be suitable candidates for the flicker detection.

Visibility of the FD illusion and certain pattern ERG parameters have been found to co-vary supporting a retinal origin for the illusion (Bedford and Maddess 1997; Maddess et al. 1997). However, Maddess (1992) considered that the illusion could originate in signals found in Y-like non-linear retinal ganglion cells. Within the retina there appears to be a subgroup of magnocellular cells, the Mγ cells whose receptive field summation responses are non-linear (Kaplan and Shapley 1990). Although much of the evidence for cells with non-linear responses has been provided in the cat (Victor and Shapley 1979) and in primate retina (Shapley and Perry 1986), the proportion of Mγ cells in the human retina is thought to be similar (Maddess et al. 1992; Sterling et al. 1994). At the LGN of macaque monkeys, 5-25% of the cells in the magnocellular layer have non-linear characteristics in response, which equates to 1-2% of all the cells, and this has been shown to accurately reflect the retinal ganglion cell response (Kaplan and Shapley 1986; Shapley and Perry 1986).

The number of ganglion cells that sample the retinal image is determined by the degree of their receptive field overlap and is a measure of the coverage factor. Estimates for a coverage factor of between 0.2 and 0.7 have been suggested based upon the relative proportions of the Mγ cell to the entire M-cell population and the published estimates of the M-cell coverage factor (Maddess et al. 1992). Maddess suggested that if the FD illusion was mediated through the Mγ pathway, undersampling of the retinal image, either as a consequence of the normal sparse distribution of the cells or through damage, may be revealed as early FD functional deficits

(Maddess et al. 1992). This led Maddess and associates to seek evidence for an aliasing effect associated with the FD illusion to support the hypothesis that the Mγ cells were involved in the visual processing. They found that estimates of the cell density from aliasing effects were similar to that quoted for the Mγ cell density, and that the aliasing effect was not dependent upon the grating orientation (implying that the sampling array was disordered). Proposals for alternative potential sources of non-Mγ cell responses to the FD illusion have included a weak P-cell response to rapid contrast variations in photopic luminance conditions or rod-inputs to the M- or P-cell responses at low luminance levels (Maddess et al. 1992). However these non-Mγ cell responses were considered to be negligible compared with the Mγ cell responses, provided sufficient numbers of Mγ cells were still present.

The nature of the Mγ pathway may, however, render it particularly sensitive to glaucomatous damage. Indeed, the Mγ ganglion cells are some of the largest cells with sparse representation and overlap, so that even a loss of single Mγ ganglion cell is likely to result in a distinct deficit of retinal coverage. Based upon histological evidence suggesting that the magnocellular ganglion cells are selectively damaged in glaucoma (Glovinsky et al. 1991; Quigley et al. 1995), the concept of frequency doubling perimetry has been applied to glaucoma. The Frequency Doubling Technology perimeter is now commercially available.

Initial reports have indicated that glaucomatous damage is associated with elevated threshold measurements for the FD illusion (Maddess and Henry 1992) and FDT perimetry results have similar characteristics to W-W perimetry in both normal and glaucomatous individuals (Johnson and Samuels 1997).

5.10.2 FDT Perimeter Design.

The FDT instrument is compact, lightweight and portable. The visual field screener incorporates a 40° horizontal by 40° vertical square display screen upon which stimuli are presented at random intervals. Each stimulus comprises a low spatial frequency (0.5 cpd) sinusoidal, black and white, grating which undergoes high temporal frequency counterphase flicker (25Hz). The theoretical perceived stimulus is of a grating whose spatial frequency appears to have twice the fundamental spatial frequency. Light from the FDT cathode ray tube is collimated to the eyepiece and redirected to the patient's pupil. The optical system comprises two injection moulded acrylic elements with aspheric surfaces with an overall focal length of 86mm. The system is based on the Badal optometer in which the rear focal plane of the optical system coincides with the patient's pupil. Assuming that the patient does not accommodate due to the apparent proximity of the stimuli, the retinal image size of each stimulus should stay the same despite some misalignment of the head and eye position provided that the entire CRT screen is in view (Personal communication with J Herrmann, Welch Allyn, Inc.). The stimuli are relatively large compared to that employed in the HFA, being a central five degree radius circular pattern and sixteen ten degree square targets, four per quadrant, with the exception of small cut-out

sections of the patterns adjacent to the central circular pattern for the C-20 program. An alternative program is available, the N-20, that extends the standard C-20 program by providing two additional 10 degree square targets above and below the horizontal midline between 20 and 30 degrees eccentricity into the nasal visual field. Both suprathreshold and full-threshold algorithms are available.

The luminance of the background is 100cdm^{-2} and each stimulus is presented for up to 720ms duration. The sequence in which the stimulus locations are tested is randomly determined for each test. A decibel scale is employed for threshold values such that 0dB corresponds to the stimulus contrast at the brightest level. Generally, it follows that a 0.1 log unit attenuation in the contrast level is considered to correspond to 1dB, whilst a 1 log unit attenuation is quoted as 10dB. The contrast range available can be varied from 1% to 100% in $\log_{10}$ steps. The range of possible threshold values is between 0dB maximum contrast for the highest threshold, up to 33.1dB for minimum contrast, for the lowest threshold. The formula used to calculate the contrast dB values is $\log_{10}(2048/c)*10$ where c ranges from 1 (minimum contrast) to 2048 (maximum contrast). These values were originally provided in the early software versions. The values are now automatically converted by the instrument's software to generate values that are more comparable to conventional incremental light threshold estimates. The results of each examination can be viewed on the instrument operator display screen or from the printout, immediately following the examination. Alternatively, the results can be downloaded to a separate PC for storage and future display (see Figure 5.1b).

A C-20-5 or C-20-1 suprathreshold program can be performed in less than a minute for each eye. The initial contrast luminance level is chosen to be brighter than the expected level that is seen by 95% and 99%, respectively, of the normal population for the given age of a patient. In the case of the C-20-1 program, if 'seen', the contrast sensitivity is considered normal at that location and no further stimulus presentations are made at that location. If 'not seen', on two occasions, the contrast is retested with a successively brighter luminance that 99.5% and then 100% of the normal population would be expected to see. A defect is classed as mild, moderate or severe depending on the contrast level at which the stimulus was eventually repeatedly missed. In the C-20-5 program the contrast level settings are at 95%, 98%, and 99% of the expected normal values, and the defect is classified by $p \geq 5\%$, $p<5\%$, $p<2\%$, and $p<1\%$ (stimulus not seen at the 1% probability level). The C-20-5 program is considered to have greater sensitivity, and poorer specificity than the C-20-1 program for detecting early glaucomatous visual field defects (Manual-FDT 1997).

The C-20 and N-20 full threshold programs use an adaptive, modified binary search (MOBS) computer automated staircase procedure to determine the minimum contrast necessary for the stimulus to be detected, i.e. the contrast threshold. The procedure uses information gained with each stimulus presentation to determine the next step in the staircase. The MOBS strategy overcomes errors in the standard binary search strategy arising from the variable nature of the

visual response, by rechecking the boundaries of the brackets and regressing where necessary (Tyrrell and Owens 1988). The initial stimulus contrast is set at the p=0.5% contrast level, based upon the age of the particular individual. The actual luminance depends on the calibration of the video monitor. At this level a 'seen response' is expected to the stimulus presentation in 99.5% of normal individuals. If 'seen', a lower contrast is shown in decreasing step sizes until the stimulus is 'not seen'. The contrast is then increased in similar step sizes, as determined by the MOBS algorithm. At least four reversals are required, and the upper and lower boundaries need to be within 0.3 log units of each other. The choice of the MOBS staircase procedure was based upon the reported greater accuracy and efficiency when compared to that of conventional staircases (Johnson and Chauhan 1992).

An extensive normative database is incorporated into the instrument's software. The data is apparently based upon the perception of flicker rather than upon the recognition of the actual grating or upon the number of lines seen. Additional statistical analysis is available through a PC link, and a more detailed printout can be generated for each test, although there is no facility for serial analysis at present.

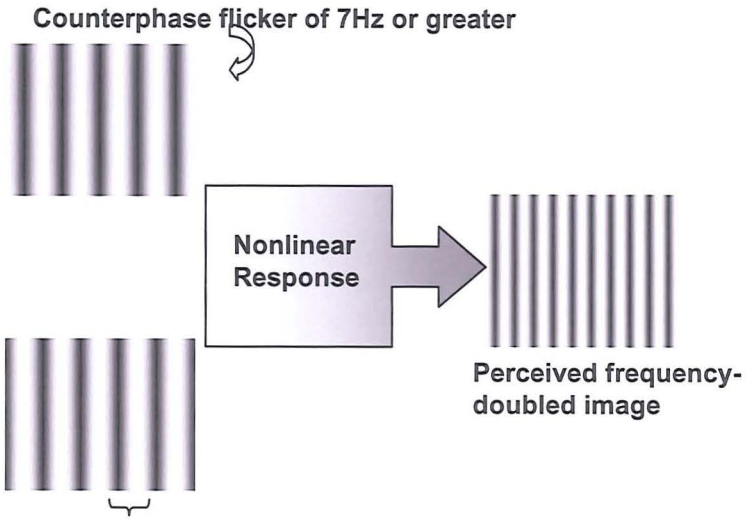

Figure 5.1a

Figure 5.1b

Figure 5.1. Schematic representation of (a) the FD illusion and (b) the FDT Instrument in use. The results of a visual field examination can be viewed on the operator display screen (1), on a paper printout (2), or downloaded to a separate PC (3).

5.11 Aims.

The aim was twofold. Firstly, to determine the within- and between-visit variability for global and pointwise measures of sensitivity for a frequency doubling stimulus using Frequency Doubling Technology (FDT) in normal subjects and in patients with ocular hypertension and in patients with glaucoma. Secondly to compare the within- and between-visit variability with that of conventional W-W perimetry and SWAP thereby evaluating non-selective perimetry (W-W) with that apparently reflecting magnocellular pathway function (FDT) and that apparently reflecting either small bi-stratified ganglion cell function and/or parvocellular pathway function (SWAP).

5.12 Sample.

The sample comprised 26 healthy, normal volunteers, 17 patients with ocular hypertension (OHT), 9 patients with high-risk ocular hypertension (OHT(H)) and 24 patients with stable primary open-angle glaucoma (POAG). The mean age of the Normal group was 56.0 (SD 17.9) years, and of the OHT group 65.9 (SD 12.0) years, and of the OHT(H) group 65.7 (SD 5.4) years and of the POAG group 68.2 (SD 10.0) years. The SWAP results for two Normal individuals were unavailable, but their FDT and W-W perimetry results were available and included in the analysis.

5.13 Methods.

Details of the inclusion criteria and the sequence of visits are provided in Chapter 3. At each of the two perimetric sessions, one randomly chosen eye of each subject was examined with W-W perimetry and SWAP using Program 24-2 and the Full Threshold strategy of the Humphrey Field Analyzer (HFA) 750 and FDT perimetry using Program C-20 of the Frequency Doubling Technology instrument. The order of perimetric examination was randomised for each subject and maintained for both visits. The examination of the three visual fields at each visit was separated by at least a ten-minute rest period. Retinal adaptation was established prior to visual field testing by asking the individuals to look into the illuminated perimeter bowl or display screen for at least three minutes prior to testing.

For the FDT test procedure, a series of stimuli of high contrast were presented randomly on the screen in the course of the set-up procedure to familiarise the subject with the nature of the stimulus. Each subject was instructed to fixate the small square black dot in the centre of the screen for the duration of the test, whilst depressing a response button each time the flickering bars were seen irrespective of whether they were very distinct or faint. The individual was encouraged to blink regularly.

Following completion of each test, the default printout was obtained directly from the instrument. The default printout included details of the program used; the time at which the test was undertaken; the duration of the test; the eye tested; the measured threshold values; the

corresponding Total Deviation probability plot; the number of, and response to, the catch trials; and the MD and PSD global indices.

Each set of results was then downloaded immediately through a PC link to an independent computer. The Viewfinder software package allowed access to more detailed analysis of the data, including, for each location, the respective numerical values of the Total and Pattern deviations and the Pattern Deviation probability analysis. A number of software versions were used in the course of the study as upgraded material became available (see Table 5.1).

Date of Conversion	July 1997	November 1997	March 1999
FDT Instrument Software Versions	7.11	1.2	2.60
FDT_PC Software Versions	2.00	6.20	FDT Viewfinder 1.0
Changes Introduced	Original software	Scaling to Humphrey HFA results	Normative Database incorporated for Pattern Deviation analysis

Table 5.1 Summary of the Software versions employed during the course of the data collection.

5.14 Analysis.

5.14.1 Global Analysis.

The visual field data for W-W perimetry and for SWAP were evaluated in terms of the visual field indices Mean Sensitivity (MS), Mean Deviation (MD), Pattern Standard Deviation (PSD), Corrected Pattern Standard Deviation (CPSD), Short-term Fluctuation (SF) and the test duration. The data for the FDT instrument was expressed in terms of MS, MD, PSD and test duration. The Short-term Fluctuation is not calculated by the FDT perimeter as no points undergo double determinations of their thresholds.

In the case of W-W perimetry and SWAP, where a double determination of sensitivity had been undertaken at a given stimulus location, the value of sensitivity was taken as the mean of the two determinations.

5.14.2 Pointwise analysis.

The difference in sensitivity for each individual at each stimulus location between each visit was calculated (i.e. the within-instrument between-visit variability). The difference in the Total Deviations at each location between each visit for each individual was expressed as a function of the Total Deviation of the measured value at that location at Visit One for that individual. The data for all individuals was combined to produce distributions of the difference in Total Deviations as a function of the baseline Total Deviation. This mode of analysis removed the

influence of differences in age between individuals across the three diagnostic groups and also the influence of stimulus eccentricity.

An identical analysis was undertaken for the difference in the Pattern Deviations at each location between each visit for each individual and the results were expressed as a function of the Pattern Deviation of the measured value at that location at Visit One for that individual.

Figure 5.2 illustrates the spatial arrangement of the stimulus locations for the HFA Full-Threshold program for W-W perimetry and SWAP and the FDT C-20 Program and the defined regions used in the study for eccentricity analysis.

The nature of the test stimuli in FDT perimetry and their pattern of presentation are markedly different to the other two forms of perimetry and consequently a direct comparison between the tests is complex. The data corresponding to the foveal and parafoveal stimulus for the FDT and the four stimuli situated at 3°, 3° in each quadrant for W-W perimetry and SWAP were excluded (see Figure 5.2). The analysis was performed on data from comparable locations for FDT and W-W perimetry and SWAP. The between-visit comparison in the Pattern Deviation probability values at each stimulus location across the individuals within each diagnostic group was presented as a 5 x 5 contingency table for each pair of visits. The tables were collapsed into 2 x 2 contingency tables to permit statistical analysis.

5.14.3 Statistical Analysis.

A separate repeated measures ANOVA was undertaken for each of the visual field indices and for examination duration. The sequence of perimetry, age and the diagnostic group were considered as separate between-subject factors. The type of perimetry and the two visits, were considered as separate within-subject factors.

The difference in the distributions of Pattern Deviation probability values for each within-perimetry between-visit comparison were analysed using separate Continuity Corrected Chi-Squared Tests on the 2 x 2 contingency tables for each pair of visits.

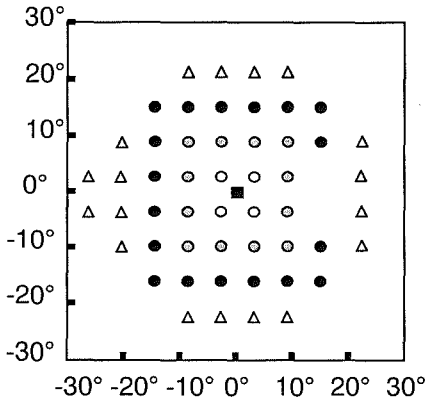

KEY

△ HFA perimetry locations that fall outside the central 20° area and not used in comparisons with FDT perimetry

● HFA locations defined as outer central region for eccentricity analysis

⊙ HFA locations defined as inner central region for eccentricity analysis

○ HFA locations not used for eccentricity and pointwise PD probability value analyses

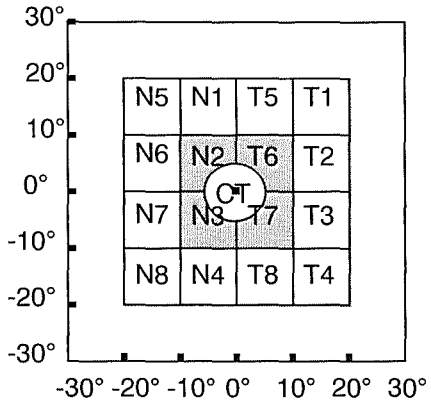

KEY

N2, N3, T6 & T7 are the FDT locations defined as inner central region and the remaining locations are defined as the outer central region for eccentricity analysis. Location CT removed from the eccentricity and pointwise PD probability value analyses .

Figure 5.2. Diagram to show the spatial arrangement of the stimulus locations for the HFA Program 24-2 Full Threshold for W-W perimetry and SWAP (upper) and the FDT Program C-20 (lower) for the right eye, and the locations used for the eccentricity and comparative analyses across each type of perimetry.

5.15 Results.

5.15.1 The within- and between-visit difference in the Global Indices for the three types of perimetry as a function of diagnostic group.

The Group Mean and one SD of the Global Indices at Visit One and at Visit Two as function of diagnosis for the three types of perimetry is given in Table 5.2. The ANOVA summary table is given in Table 5.3.

5.15.1.1 Mean Sensitivity (MS).

The Group Mean MS was surprisingly independent of age ($p=0.200$). However, the MS differed across the three diagnostic groups ($p<0.001$) and was worse for the POAG group. The MS was independent of the sequence of perimetry ($p=0.265$) and visit ($p=0.660$). The Group Mean MS was highest for FDT and lowest for SWAP ($p=0.027$).

The SD was higher i.e. the within-group variation was greater for SWAP compared to FDT (ratio 2.18) and for FDT compared to W-W perimetry (ratio 2.13) in the Normal group (Table 5.2). The corresponding ratio for SWAP to W-W perimetry was 4.61. For the POAG group, the SD was similar between FDT and W-W perimetry but both were slightly greater than for SWAP. For the OHT group, the SDs were, in general, lower than for the POAG but higher than for the Normal group.

5.15.1.2 Mean Deviation (MD).

The Group Mean MD was, as would be expected, independent of age ($p=0.231$). It differed across the three diagnostic groups ($p<0.001$) and was more negative for the POAG group. The MD was independent of the sequence of perimetry ($p=0.324$) and visit ($p=0.885$). The Group Mean MD was more positive for FDT and most negative for W-W perimetry ($p=0.008$).

The SD was higher i.e. the within-group variation was greater for SWAP compared to FDT (ratio 1.42) and for FDT compared to W-W perimetry (ratio 1.87) in the Normal group (Table 5.2). The corresponding ratio for SWAP to W-W perimetry was 2.66. For the POAG group, the SD was greatest for W-W perimetry and least for FDT. For the OHT group, the SDs were, in general, more similar and were lower than for the POAG group but similar to the Normal group.

5.15.1.3 Pattern Standard Deviation (PSD).

The Group Mean PSD was independent of age ($p=0.752$). It differed across the three diagnostic groups ($p<0.001$) and as would be expected was greatest for the POAG group. The PSD was independent of the sequence of perimetry ($p=0.224$) and visit ($p=0.304$). The Group Mean PSD was generally greatest for FDT and least for W-W perimetry ($p=0.035$) with the exception of the POAG group.

The SD was similar for the three types of perimetry: the ratio for SWAP compared to FDT was 1.41 and for FDT compared to W-W perimetry was 1.87 in the Normal group (Table 5.2). The corresponding ratio for SWAP to W-W perimetry was 1.33. For the POAG group, the SD was greatest for W-W perimetry and similar for FDT and SWAP. For the OHT group, the SDs were similar and were lower than for the POAG but generally similar to the Normal group.

5.15.1.4 Short-term fluctuation (SF).

The Group Mean SF was independent of age ($p=0.821$). It differed across the three diagnostic groups ($p<0.001$) and as would be expected was greatest for the POAG group. The SF was independent of the sequence of perimetry ($p=0.897$) and visit ($p=0.857$). The Group Mean SF was higher for SWAP than for W-W perimetry across all groups but the differences did not reach statistical significance ($p=0.950$).

5.15.1.5 Corrected Pattern Standard Deviation (PSD).

The Group Mean CPSD was independent of age ($p=0.484$). It differed across the three diagnostic groups ($p<0.001$) and was greatest for the POAG group. The CPSD was independent of the sequence of perimetry ($p=0.111$) and visit ($p=0.916$). The Group Mean CPSD for SWAP was not statistically different from W-W perimetry across the groups ($p=0.726$).

5.15.1.6 Examination Duration.

The Group Mean examination duration was independent of age ($p=0.206$). It differed across the three diagnostic groups ($p=0.05$) and was in general longer for the POAG group. The examination duration was independent of the sequence of perimetry ($p=0.873$) and visit ($p=0.741$). The Group Mean examination duration varied between the three techniques ($p<0.001$) but the variation was similar across each of the three groups ($p=0.942$). It was shortest for FDT perimetry.

(a) NORMAL (n = 26)

	FDT Perimetry		W-W Perimetry		SWAP	
	Visit 1	Visit 2	Visit 1	Visit 2	Visit 1	Visit 2
MS (dB)	30.61 (3.12)	30.86 (2.88)	27.96 (1.51)	28.09 (1.32)	20.22 (6.50)	20.65 (6.56)
MD (dB)	0.56 (2.46)	0.83 (2.15)	-0.57 (1.38)	-0.63 (1.08)	0.46 (3.26)	0.80 (3.29)
PSD (dB)	3.82 (0.84)	3.56 (0.87)	1.68 (0.34)	1.72 (0.58)	2.76 (0.66)	2.58 (0.57)
CPSD (dB)			0.88 (0.57)	0.97 (0.63)	1.88 (1.02)	1.70 (0.97)
SF (dB)			1.25 (0.37)	1.23 (0.36)	1.68 (0.47)	1.58 (0.35)
Time (min)	4.33 (0.38)	4.44 (0.40)	9.99 (1.02)	10.00 (0.86)	11.83 (1.24)	11.25 (1.07)

(b) OHT (n = 26)

	FDT Perimetry		W-W Perimetry		SWAP	
	Visit 1	Visit 2	Visit 1	Visit 2	Visit 1	Visit 2
MS (dB)	27.93 (4.34)	27.73 (4.28)	26.72 (2.71)	26.78 (2.59)	18.98 (4.07)	19.98 (4.10)
MD (dB)	-0.99 (2.68)	-1.09 (2.82)	-1.04 (2.15)	-1.05 (2.19)	-0.89 (3.52)	0.21 (3.33)
PSD (dB)	4.00 (0.78)	3.87 (1.02)	2.18 (0.89)	2.03 (0.72)	3.01 (0.95)	2.96 (0.89)
CPSD (dB)			1.33 (1.01)	1.14 (0.82)	1.96 (1.28)	2.08 (1.18)
SF (dB)			1.48 (0.67)	1.47 (0.69)	1.82 (0.65)	1.79 (0.50)
Time (min)	4.45 (0.29)	4.59 (0.38)	10.80 (1.43)	10.76 (1.23)	11.59 (1.02)	11.69 (1.58)

(c) POAG (n = 24)

	FDT Perimetry		W-W Perimetry		SWAP	
	Visit 1	Visit 2	Visit 1	Visit 2	Visit 1	Visit 2
MS (dB)	21.56 (7.01)	20.97 (7.31)	20.07 (7.02)	19.97 (7.01)	12.46 (5.44)	12.78 (5.19)
MD (dB)	-5.62 (4.74)	-5.97 (4.93)	-8.25 (7.51)	-8.32 (7.60)	-7.40 (6.20)	-7.09 (6.01)
PSD (dB)	7.38 (2.43)	7.68 (2.48)	7.51 (3.95)	7.47 (4.04)	6.57 (2.57)	6.58 (2.61)
CPSD (dB)			7.09 (4.08)	7.05 (4.08)	5.98 (2.89)	6.09 (2.94)
SF (dB)			1.97 (0.77)	2.15 (1.25)	2.12 (1.01)	2.00 (0.81)
Time (min)	4.70 (0.44)	4.75 (0.50)	11.83 (2.09)	11.52 (1.78)	11.76 (2.61)	11.85 (2.20)

Table 5.2. The (a) Normal, (b) OHT and (c) POAG Group, mean Mean Sensitivity (MS), mean Mean Deviation (MD), mean Pattern Standard Deviation (PSD), mean Corrected Pattern Standard Deviation (CPSD), mean Short-term Fluctuation (SF) and mean Examination Duration (Time) for Full Threshold FDT perimetry, Full Threshold W-W perimetry and Full Threshold SWAP. One standard deviation of the mean is given in parentheses.

	Perimetry Indices					
FACTOR	**MS**	**MD**	**PSD**	**SF**	**CPSD**	**TIME**
Age	NS	NS	NS	NS	NS	NS
Diagnosis	p<0.001	p<0.001	p<0.001	p<0.001	p<0.001	p=0.048
Order	NS	NS	NS	NS	NS	NS
Visit	NS	NS	NS	NS	NS	NS
Visit x Age	NS	NS	p=0.014	NS	NS	NS
Visit x Diagnosis	NS	NS	NS	NS	p=0.046	NS
Visit x Order	NS	NS	NS	NS	NS	NS
Test	p=0.027	p=0.008	p=0.035	NS	NS	p<0.001
Test x Age	NS	p=0.012	NS	NS	NS	NS
Test x Diagnosis	NS	NS	NS	NS	NS	NS
Test x Order	p=0.043	NS	NS	NS	NS	NS
Visit x Test	p=0.038	p=0.013	NS	NS	NS	NS
Visit x Test x Age	NS	NS	NS	NS	NS	NS
Visit x Test x Diagnosis	p=0.043	p=0.015	NS	p=0.046	NS	NS
Visit x Test x Order	NS	NS	NS	NS	NS	NS
Age x Diagnosis	NS	NS	NS	NS	NS	NS
Visit x Order x Diagnosis	NS	NS	NS	NS	NS	NS
Visit x Age x Diagnosis	NS	NS	NS	NS	NS	NS
Test x Order x Diagnosis	NS	NS	NS	NS	NS	NS
Test x Age x Diagnosis	NS	NS	NS	NS	NS	NS
Visit x Test x Order x Diagnosis	NS	NS	NS	NS	NS	NS
Visit x Test x Age x Diagnosis	NS	p=0.015	NS	NS	NS	NS

Table 5.3. Summary of the ANOVA for FDT and W-W perimetry and SWAP.

5.15.2 The between-perimetric strategy variation in Total Deviation and Pattern Deviation values at Visit One and Visit Two as a function of stimulus location in the Normal and OHT groups.

5.15.2.1 Total Deviation for FDT, W-W and SWAP.

The Group Mean Total Deviation (upper value) and one SD of the mean (lower value) at each stimulus location at each visit for the three types of perimetry for the Normal group is shown in Figure 5.3, and for the OHT group, Figure 5.4.

The Group Mean TD for FDT and SWAP at each stimulus location was almost invariably more positive at the second visit compared to the first visit, both for the Normal group and the OHT group. There was no consistent pattern between the Group Mean Total Deviation for the two visits, across each of the stimulus locations for W-W perimetry, for either diagnostic group.

5.15.2.2 Pattern Deviation for FDT, W-W and SWAP.

The Group Mean Pattern Deviation (upper value) and one SD of the mean (lower value) at each stimulus location at each visit for the three types of perimetry for the Normal group is shown in Figure 5.5, and for the OHT group, Figure 5.6. A similar trend was present to that of the Total Deviation for FDT perimetry for the Normal group, but inconsistent for the OHT group. There was no consistent pattern between the Group Mean Pattern Deviation for the two visits, across each of the stimulus locations for SWAP or W-W perimetry, for either diagnostic group,

5.15.3 The variation in Group mean Sensitivity between the upper and lower hemifields for FDT, W-W and SWAP.

The Group mean difference in Sensitivity between the upper and lower hemifield (as a proportion of the lower hemifield) for each corresponding stimulus location (upper value) and the associated one SD of the mean (lower value) at each visit for the three types of perimetry for the Normal and OHT groups is shown in Figure 5.7 and Figure 5.8.

The Group mean difference in Sensitivity between locations of corresponding eccentricity across the upper and lower hemifields, for each of the three types of perimetry was minimal and was similar for FDT and W-W perimetry across the Normal and OHT groups. The Group Mean Sensitivity for the upper hemifield was generally less than the lower hemifield, for both groups, across each form of perimetry. The asymmetry, and the within-group variation both for the Normal and the OHT group increased with increase in eccentricity.

a) FDT Perimetry (Full Threshold C-20) at Visit One

1.96	**1.24**	**1.15**	**1.67**	
4.68	5.22	4.86	4.61	
1.48	**0.69**	**0.81**	**1.61**	
3.39	4.25	4.66	4.42	
3.42	**1.13**	**1.57**	**1.62**	
3.96	3.40	3.34	4.32	
2.31	**2.42**	**1.69**	**1.22**	
3.92	3.99	3.55	5.27	Fovea
			0.81	
			3.77	

b) FDT Perimetry (Full Threshold C-20) at Visit Two

1.85	**1.92**	**1.47**	**1.73**	
4.01	4.35	3.80	5.05	
2.34	**2.01**	**1.46**	**1.86**	
3.83	3.55	3.59	3.55	
2.38	**2.98**	**2.22**	**1.51**	
3.18	5.85	3.68	3.13	
2.07	**2.73**	**1.84**	**1.78**	
3.22	3.28	3.48	3.15	Fovea
			0.42	
			4.33	

c) W-W Perimetry (Full Threshold 24-2) at Visit One

		-0.42	**-0.04**	**-0.62**	**-0.85**		
		2.76	2.44	3.10	3.08		
	-0.88	**-1.04**	**-0.62**	**-0.50**	**-0.58**	**-0.46**	
	3.22	2.01	2.08	2.79	2.14	2.85	
-0.96	**-0.23**	**-0.46**	**-1.00**	**-1.08**	**-1.08**	**-1.38**	**-0.77**
2.32	1.70	1.70	1.70	2.08	1.76	2.10	2.25
0.00	**-0.15**	**-0.54**	**-1.00**	**-1.42**	**-0.58**	**-0.85**	**-0.12**
2.73	2.24	1.73	1.98	1.63	1.94	1.85	1.68
0.00	**-0.38**	**0.00**	**-0.88**	**-0.69**	**-0.58**	**-0.96**	**-0.62**
1.77	2.26	1.85	1.82	1.78	1.96	2.05	1.65
-1.08	**-0.50**	**-0.31**	**-1.23**	**-0.58**	**0.15**	**-0.38**	**0.27**
2.70	2.27	1.64	1.99	2.06	1.85	1.86	2.03
	-0.46	**-0.96**	**-1.23**	**-0.58**	**-0.27**	**-0.08**	
	2.21	1.89	2.01	2.23	2.18	1.98	
		-0.42	**-0.50**	**0.15**	**0.50**		Fovea
		2.74	2.86	1.99	2.27		**N/A**
							N/A

d) W-W Perimetry (Full Threshold 24-2) at Visit Two

		-0.23	**0.04**	**-0.73**	**-0.62**		
		3.44	2.90	3.07	2.93		
	-0.08	**-0.62**	**-1.08**	**-0.27**	**-0.19**	**-0.77**	
	2.37	2.02	1.70	2.25	2.17	2.37	
-0.96	**-0.19**	**-0.50**	**-1.42**	**-1.50**	**-1.27**	**-0.92**	**-0.62**
2.54	1.86	1.48	1.45	2.02	2.18	2.28	1.79
-0.69	**0.00**	**-0.23**	**-1.15**	**-0.69**	**-1.19**	**-1.19**	**-0.88**
3.20	1.62	2.03	2.15	1.44	1.60	2.02	1.84
-0.85	**-0.81**	**0.04**	**-1.00**	**-0.46**	**-0.15**	**-0.73**	**0.00**
2.92	2.06	1.71	1.47	1.24	1.78	1.73	1.74
	-0.65	**-0.38**	**-0.46**	**-1.31**	**-0.77**	**-0.46**	**0.04**	**0.58**
	2.38	1.79	1.63	1.59	1.63	1.65	1.71	1.65
		-0.92	**-0.42**	**-0.54**	**-0.23**	**-0.19**	**-0.19**	
		2.00	1.68	1.30	1.66	2.08	1.92	
			-0.38	**-0.77**	**0.12**	**0.19**		Fovea
			2.59	2.21	1.75	1.63		**N/A**
								N/A

e) SWAP (Full Threshold 24-2) at Visit One

			0.75	**1.17**	**0.33**	**1.71**	
			5.29	6.53	6.98	5.40	
		0.38	**1.33**	**1.46**	**0.42**	**1.33**	**0.71**
		5.36	5.05	3.90	5.52	4.57	6.31
	-0.35	**0.75**	**0.46**	**1.33**	**1.13**	**0.50**	**1.46**	**1.71**
	5.26	3.42	4.33	4.27	4.07	4.13	4.29	4.52
-1.29	**0.25**	**0.58**	**0.75**	**0.71**	**1.00**	**1.04**		**1.46**
6.03	6.05	4.73	3.78	3.91	4.17	3.82		5.08
-1.46	**-1.04**	**0.25**	**0.17**	**0.17**	**0.63**	**0.04**		**1.33**
7.17	5.65	3.40	3.40	3.53	3.36	3.53		3.80
	-0.42	**-0.04**	**0.50**	**0.21**	**-0.75**	**-0.04**	**1.38**	**1.54**
	4.32	3.14	3.22	3.71	3.61	2.88	3.75	3.84
		0.00	**0.46**	**0.71**	**-0.29**	**0.67**	**1.83**	
		3.76	3.41	3.41	3.86	3.76	3.68	
			0.58	**0.00**	**1.17**	**1.42**		Fovea
			4.71	4.23	3.77	3.24		**N/A**
								N/A

f) SWAP (Full Threshold 24-2) at Visit Two

			2.04	**1.39**	**0.78**	**2.09**	
			5.29	6.26	5.89	5.85	
		1.61	**1.78**	**0.70**	**0.74**	**0.91**	**1.83**
		4.90	4.06	4.35	4.51	4.77	5.15
	1.09	**1.00**	**1.26**	**0.22**	**0.61**	**-0.13**	**0.91**	**1.78**
	4.25	4.32	3.51	3.79	4.03	3.55	4.20	4.89
0.00	**0.09**	**1.04**	**0.91**	**0.22**	**1.04**	**1.04**		**0.87**
5.55	4.80	3.78	3.87	3.54	3.82	4.12		4.86
-0.70	**0.43**	**1.04**	**0.13**	**-0.13**	**1.83**	**0.39**		**0.87**
5.48	4.53	3.24	3.42	3.11	4.00	3.01		4.53
	-1.87	**-0.78**	**0.61**	**0.70**	**0.87**	**0.17**	**1.35**	**1.09**
	5.23	4.07	3.12	3.34	3.85	4.01	3.96	3.59
		0.65	**0.74**	**1.17**	**0.22**	**1.17**	**1.78**	
		3.70	3.63	2.89	3.48	4.04	3.70	
			0.35	**1.43**	**1.61**	**1.13**		Fovea
			5.12	4.39	4.20	4.63		**N/A**
								N/A

Figure 5.3. The Group Mean Total Deviation (dB) for each stimulus location (upper value) and one SD of the mean (lower value) for Visit One and Visit Two for FDT perimetry ((a) & (b)), for W-W perimetry ((c) & (d)) and for SWAP ((e) & (f)) for the Normal group.

a) FDT Perimetry (Full Threshold C-20) at Visit One

-0.41	**-1.87**	**-0.96**	**-1.58**	
5.81	5.36	5.35	4.49	
-2.02	**-1.56**	**0.78**	**-0.46**	
5.75	4.17	4.08	4.00	
-0.38	**-0.42**	**0.52**	**0.53**	
4.24	4.08	5.19	4.17	
0.05	**-0.28**	**0.66**	**-0.53**	
5.17	5.23	4.87	5.27	Fovea
			-0.80	
			3.85	

b) FDT Perimetry (Full Threshold C-20) at Visit Two

-0.32	**-1.99**	**-0.99**	**-1.04**	
4.99	4.74	4.90	4.15	
-1.59	**-1.90**	**0.21**	**-0.87**	
5.43	5.86	4.43	5.44	
-0.65	**-0.52**	**-0.13**	**-0.26**	
4.36	4.17	4.95	4.59	
-0.95	**-0.37**	**-0.25**	**0.57**	
5.12	5.30	4.38	3.89	Fovea
			0.16	
			3.74	

c) W-W Perimetry (Full Threshold 24-2) at Visit One

		-1.50	**-0.96**	**-1.42**	**-1.81**		
		5.16	3.86	5.25	5.61		
	-1.27	**-1.54**	**-1.96**	**-1.23**	**-1.58**	**-0.50**	
	3.78	3.19	3.61	3.36	3.73	3.13	
-1.81	**-1.54**	**-0.69**	**-1.12**	**-1.23**	**-0.96**	**-1.77**	**-1.46**
6.10	3.28	2.20	2.36	3.13	3.89	3.59	3.01
-2.04	**-1.15**	**-0.92**	**-1.73**	**-0.62**	**-0.23**	**-1.00**	**-1.62**
4.67	3.87	2.00	2.05	2.17	1.88	2.40	2.82
-1.96	**-1.96**	**-0.65**	**-1.15**	**-0.54**	**-0.46**	**-0.54**	**-0.50**
5.72	4.42	1.72	2.29	1.88	2.23	2.40	2.61
-1.35	**-1.15**	**-0.46**	**-1.08**	**-0.58**	**-0.15**	**-0.50**	**-1.00**
4.80	2.34	1.94	2.08	2.10	2.56	2.82	3.03
	-1.69	**-1.15**	**-1.85**	**-0.69**	**-0.77**	**-0.50**	
	3.46	2.89	3.17	2.45	2.64	2.45	
		-1.85	**-1.31**	**-0.88**	**-0.46**		Fovea
		4.86	3.28	3.12	2.87		**N/A**
							N/A

d) W-W Perimetry (Full Threshold 24-2) at Visit Two

		-1.19	**-0.88**	**-1.31**	**-1.31**		
		4.15	4.85	6.89	5.65		
	-1.12	**-1.15**	**-1.69**	**-1.12**	**-1.08**	**-1.50**	
	2.98	3.35	3.54	3.57	3.57	3.81	
-1.35	**-1.38**	**-0.85**	**-1.08**	**-1.08**	**-1.50**	**-1.50**	**-0.96**
4.19	2.61	2.31	2.48	2.58	3.18	3.26	4.49
-2.35	**-1.08**	**-1.77**	**-1.50**	**-1.04**	**-0.88**	**-0.81**	**-0.54**
4.91	2.65	2.35	2.53	1.99	2.25	2.53	2.92
-1.81	**-0.62**	**-0.92**	**-0.85**	**-0.50**	**-0.50**	**-0.77**	**-0.73**
4.78	2.53	2.87	2.46	2.21	2.04	2.47	2.18
-1.12	**-1.27**	**-0.69**	**-0.69**	**-0.85**	**-0.23**	**-0.85**	**-0.92**
2.52	2.54	2.45	2.15	2.03	2.73	2.51	3.40
	-1.38	**-2.00**	**-1.27**	**-0.77**	**-0.88**	**-0.85**	
	4.05	3.87	2.88	2.23	2.18	2.74	
		-1.04	**-0.77**	**-0.81**	**-0.23**		Fovea
		8.70	8.74	9.99	10.35		**N/A**
							N/A

e) SWAP (Full Threshold 24-2) at Visit One

		-1.54	**-1.12**	**-0.38**	**0.88**		
		5.83	6.72	5.56	5.01		
	-0.85	**-0.92**	**-0.73**	**-0.12**	**0.54**	**0.00**	
	4.85	4.64	5.23	4.70	4.48	5.80	
-1.50	**-1.54**	**-0.42**	**-0.27**	**-0.19**	**0.08**	**-0.23**	**-0.38**
5.30	4.64	4.53	5.26	4.06	3.16	3.68	4.36
-3.12	**-2.27**	**-1.23**	**-1.23**	**-1.00**	**0.35**	**0.69**	**0.62**
7.30	5.62	5.31	5.60	3.43	4.27	4.02	4.32
-2.81	**-1.38**	**-1.12**	**-0.73**	**-1.50**	**-0.12**	**-0.27**	**-0.46**
7.88	5.96	4.19	4.15	4.08	3.80	3.92	5.12
-2.38	**-1.19**	**-0.65**	**-1.04**	**0.15**	**-0.23**	**0.31**	**-0.08**
5.22	3.73	2.92	3.68	4.14	3.39	4.06	4.08
	-3.23	**-2.62**	**-1.85**	**-1.38**	**-0.19**	**-0.50**	
	4.74	5.04	4.59	4.13	3.45	3.41	
		-2.42	**-2.77**	**-1.85**	**-1.27**		Fovea
		5.51	5.37	4.76	4.26		**N/A**
							N/A

f) SWAP (Full Threshold 24-2) at Visit Two

		0.31	**0.27**	**0.73**	**1.65**		
		5.64	5.43	5.19	4.79		
	0.62	**0.04**	**-0.42**	**0.42**	**1.04**	**0.23**	
	4.06	3.48	4.35	4.29	3.66	5.03	
0.00	**0.58**	**-0.15**	**0.77**	**0.15**	**0.31**	**0.62**	**-0.27**
4.44	3.47	3.74	3.19	3.70	3.64	3.74	5.27
-0.46	**-0.88**	**-0.15**	**-0.81**	**-0.08**	**1.08**	**0.58**	**0.73**
7.32	6.10	4.66	5.43	3.36	3.39	3.51	4.09
-1.23	**-0.15**	**-0.88**	**-0.42**	**-0.92**	**0.73**	**-0.15**	**0.00**
7.37	4.79	3.92	4.13	3.79	3.53	4.12	3.79
-1.19	**-0.92**	**-1.04**	**-1.00**	**0.38**	**0.38**	**0.04**	**0.58**
4.84	3.75	3.56	4.15	3.94	4.29	6.02	3.42
	-2.00	**-2.23**	**-1.12**	**-0.27**	**-0.38**	**0.08**	
	5.39	4.85	3.99	3.61	3.87	3.95	
		-1.50	**-1.62**	**-0.31**	**-0.88**		Fovea
		7.85	7.36	7.49	8.49		**N/A**
							N/A

Figure 5.4. The Group Mean Total Deviation (dB) for each stimulus location (upper value) and one SD of the mean (lower value) for Visit One and Visit Two for FDT perimetry ((a) & (b)), for W-W perimetry ((c) & (d)) and for SWAP ((e) & (f)) for the OHT group.

a) FDT Perimetry (Full Threshold C-20) at Visit One

-2.21	**-2.92**	**-3.02**	**-2.49**	
3.06	2.91	3.21	3.54	
-2.68	**-3.47**	**-3.35**	**-2.55**	
2.31	3.14	3.32	3.11	
-0.75	**-3.03**	**-2.60**	**-2.55**	
2.94	2.13	2.31	2.86	
-1.86	**-1.74**	**-2.47**	**-2.95**	
2.67	1.94	1.70	3.38	Fovea
				-3.36
				2.88

b) FDT Perimetry (Full Threshold C-20) at Visit Two

-2.13	**-2.07**	**-2.52**	**-2.25**	
3.13	3.11	2.37	3.68	
-1.64	**-1.98**	**-2.52**	**-2.13**	
2.76	1.75	1.89	1.93	
-1.61	**-1.01**	**-1.76**	**-2.47**	
2.08	4.34	2.06	2.61	
-1.91	**-1.26**	**-2.15**	**-2.20**	
2.20	1.66	2.06	2.27	Fovea
				-3.56
				2.64

c) W-W Perimetry (Full Threshold 24-2) at Visit One

			-1.46	**-1.19**	**-1.77**	**-1.85**		
			2.32	1.96	2.45	2.38		
		-2.04	**-2.12**	**-1.69**	**-1.46**	**-1.77**	**-1.50**	
		2.76	1.66	1.57	2.30	1.99	2.45	
	-2.00	**-1.58**	**-1.50**	**-2.04**	**-2.19**	**-2.00**	**-2.46**	**-1.96**
	1.88	1.42	1.45	1.25	1.92	1.50	1.48	2.05
-1.15	**-1.23**	**-1.54**	**-2.00**	**-2.58**	**-1.77**	**-1.81**		**-1.15**
2.26	1.63	1.39	1.44	1.27	1.37	1.50		1.64
-1.15	**-1.58**	**-1.23**	**-2.23**	**-1.77**	**-1.65**	**-2.12**		**-1.62**
1.54	1.58	1.11	1.07	1.42	1.50	1.97		1.68
	-2.15	**-1.69**	**-1.38**	**-2.27**	**-1.62**	**-1.42**	**-1.62**	**-0.81**
	2.33	1.74	1.42	1.19	1.65	1.68	1.77	1.63
		-1.62	**-2.19**	**-2.38**	**-1.69**	**-1.38**	**-1.23**	**-1.54**
		1.53	1.74	1.65	1.76	1.63	1.42	1.79
			-1.54	**-1.69**	**-1.00**	**-0.58**		Fovea
			1.79	2.17	1.30	1.45		**N/A**
								N/A

d) W-W Perimetry (Full Threshold 24-2) at Visit Two

			-1.50	**-1.12**	**-1.42**	**-1.54**		
			2.97	2.49	3.04	2.00		
		-1.35	**-1.77**	**-2.31**	**-1.73**	**-1.58**	**-2.04**	
		1.44	1.73	1.54	1.99	1.70	1.54	
	-2.27	**-1.58**	**-1.58**	**-2.62**	**-2.81**	**-2.35**	**-2.15**	**-1.88**
	2.32	1.30	1.21	1.10	1.65	1.90	2.20	1.66
-1.92	**-1.38**	**-1.38**	**-2.42**	**-1.92**	**-2.62**	**-2.27**		**-2.23**
2.71	1.44	1.63	1.68	1.38	1.36	1.59		1.77
-2.19	**-2.15**	**-1.54**	**-2.38**	**-1.69**	**-1.38**	**-1.96**		**-1.15**
2.45	1.69	1.30	1.42	1.19	1.63	1.46		1.43
	-1.62	**-1.85**	**-1.73**	**-2.58**	**-1.96**	**-1.88**	**-1.42**	**-0.69**
	2.26	1.32	1.46	1.14	1.61	1.45	1.63	1.26
		-2.27	**-1.85**	**-1.77**	**-1.46**	**-1.65**	**-1.54**	
		1.82	1.59	0.99	1.53	1.44	1.33	
			-1.77	**-1.92**	**-1.27**	**-1.19**		Fovea
			2.25	1.55	1.40	1.36		**N/A**
								N/A

e) SWAP (Full Threshold 24-2) at Visit One

			-2.71	**-2.33**	**-3.29**	**-1.79**		
			3.11	3.89	4.35	3.36		
		-3.17	**-2.13**	**-2.46**	**-3.17**	**-2.17**	**-2.79**	
		3.52	2.76	1.89	2.91	2.53	3.98	
	-3.88	**-2.75**	**-3.13**	**-2.13**	**-2.42**	**-3.17**	**-1.96**	**-1.83**
	4.27	2.23	3.46	1.94	2.52	2.37	2.80	2.87
-5.17	**-3.38**	**-2.63**	**-2.75**	**-2.71**	**-2.58**	**-2.54**		**-2.13**
4.92	4.31	3.16	1.87	2.54	3.06	2.06		3.23
-4.88	**-4.63**	**-3.29**	**-3.25**	**-3.29**	**-2.83**	**-3.58**		**-2.17**
5.55	3.67	2.42	2.45	2.12	2.28	2.24		2.46
	-4.00	**-3.50**	**-2.96**	**-3.38**	**-4.33**	**-3.75**	**-2.17**	**-1.96**
	2.73	2.43	2.27	2.36	2.30	2.21	3.00	2.71
		-3.58	**-3.21**	**-2.88**	**-3.83**	**-2.92**	**-1.96**	
		2.38	2.41	2.03	2.53	1.95	2.01	
			-2.88	**-3.54**	**-1.92**	**-2.17**		Fovea
			2.51	3.34	3.08	2.01		**N/A**
								N/A

f) SWAP (Full Threshold 24-2) at Visit Two

			-1.52	**-2.13**	**-2.78**	**-1.65**		
			3.22	3.91	3.84	3.50		
		-2.09	**-1.78**	**-2.83**	**-2.74**	**-2.70**	**-1.74**	
		3.37	2.07	2.82	2.40	2.74	3.70	
	-2.57	**-2.65**	**-2.57**	**-3.35**	**-3.04**	**-3.96**	**-2.74**	**-1.91**
	3.34	2.62	2.48	1.85	2.64	2.31	2.30	2.33
-3.74	**-3.57**	**-2.78**	**-2.48**	**-3.22**	**-2.74**	**-2.74**		**-2.74**
4.08	4.04	2.11	1.56	2.45	2.60	1.66		2.43
-4.39	**-3.26**	**-2.83**	**-3.35**	**-3.57**	**-1.83**	**-3.30**		**-2.52**
4.25	2.80	1.99	1.77	2.21	2.10	2.38		2.84
	-5.39	**-4.17**	**-3.13**	**-3.04**	**-2.83**	**-3.52**	**-2.35**	**-2.48**
	3.63	2.10	2.16	1.64	2.10	2.95	2.72	1.97
		-2.91	**-3.09**	**-2.48**	**-3.17**	**-2.52**	**-1.91**	
		2.39	1.53	2.19	1.80	2.06	2.25	
			-3.22	**-2.22**	**-2.00**	**-2.39**		Fovea
			3.45	2.94	2.11	2.92		**N/A**
								N/A

Figure 5.5. The Group Mean Pattern Deviation (dB) for each stimulus location (upper value) and one SD of the mean (lower value) for Visit One and Visit Two for FDT perimetry ((a) & (b)), for W-W perimetry ((c) & (d)) and for SWAP ((e) & (f)) for the Normal group.

a) FDT Perimetry (Full Threshold C-20) at Visit One

-2.75	**-4.22**	**-3.31**	**-3.92**	
3.50	3.08	3.06	3.05	
-4.36	**-3.90**	**-1.56**	**-2.80**	
3.58	2.93	2.85	1.85	
-2.72	**-2.77**	**-1.82**	**-1.81**	
2.41	2.03	2.77	2.49	
-2.29	**-2.62**	**-1.68**	**-2.87**	
3.52	2.85	2.36	2.79	Fovea
			-3.14	
			2.77	

b) FDT Perimetry (Full Threshold C-20) at Visit Two

-2.35	**-4.02**	**-3.01**	**-3.06**	
3.11	2.94	2.94	4.15	
-3.61	**-3.93**	**-1.82**	**-2.90**	
3.13	3.96	2.49	3.16	
-2.68	**-2.55**	**-2.16**	**-2.29**	
2.58	1.58	2.94	2.73	
-2.98	**-2.40**	**-2.27**	**-1.46**	
3.30	3.61	2.77	1.93	Fovea
			-1.87	
			2.50	

c) W-W Perimetry (Full Threshold 24-2) at Visit One

		-2.50	**-1.92**	**-2.42**	**-2.46**		
		4.22	2.80	3.70	4.24		
	-2.19	**-2.35**	**-2.73**	**-2.08**	**-2.58**	**-1.54**	
	2.81	2.38	2.74	2.00	2.48	1.90	
-2.85	**-2.46**	**-1.46**	**-2.12**	**-2.31**	**-2.38**	**-2.69**	**-2.23**
5.10	2.30	1.65	1.56	2.33	2.77	2.46	1.82
-2.92	**-2.19**	**-1.81**	**-2.69**	**-1.38**	**-1.46**	**-2.04**	**-2.69**
3.74	2.71	1.30	1.69	1.39	1.36	1.59	1.69
-2.96	**-3.00**	**-1.81**	**-2.08**	**-1.35**	**-1.38**	**-1.35**	**-1.31**
4.84	3.31	1.67	1.70	1.26	1.36	1.60	1.54
-2.27	**-2.12**	**-1.31**	**-1.92**	**-1.62**	**-1.19**	**-1.62**	**-1.92**
3.45	1.31	1.35	1.23	1.58	1.63	1.79	1.79
	-2.73	**-2.31**	**-2.62**	**-1.65**	**-1.69**	**-1.50**	
	2.29	2.36	2.17	1.52	1.49	1.33	
		-2.73	**-2.19**	**-1.77**	**-1.38**		Fovea
		3.54	2.40	2.03	1.60		**N/A**
							N/A

d) W-W Perimetry (Full Threshold 24-2) at Visit Two

		-1.88	**-1.92**	**-2.38**	**-2.46**		
		3.33	3.54	5.31	4.09		
	-2.19	**-2.15**	**-2.81**	**-2.12**	**-2.27**	**-2.35**	
	2.32	2.19	2.40	1.99	2.41	2.30	
-2.19	**-2.19**	**-1.96**	**-2.19**	**-1.77**	**-2.35**	**-2.73**	**-2.31**
3.71	1.36	1.71	1.39	1.84	2.54	2.16	2.74
-3.23	**-1.73**	**-2.73**	**-2.62**	**-2.19**	**-1.81**	**-2.12**	**-1.46**
3.72	1.46	1.54	1.47	1.44	2.00	1.61	2.20
-2.96	**-1.65**	**-1.88**	**-1.88**	**-1.46**	**-1.42**	**-1.88**	**-1.58**
3.54	1.52	1.61	1.68	1.14	1.39	1.75	1.55
-2.12	**-2.23**	**-1.62**	**-1.65**	**-1.62**	**-1.00**	**-1.96**	**-1.85**
1.48	1.66	1.24	1.65	1.86	1.74	1.56	1.64
	-2.54	**-2.85**	**-2.19**	**-1.54**	**-1.77**	**-2.04**	
	2.86	2.36	1.98	1.58	1.48	1.71	
		-1.88	**-1.85**	**-1.85**	**-0.92**		Fovea
		2.21	2.44	1.95	1.52		**N/A**
							N/A

e) SWAP (Full Threshold 24-2) at Visit One

		-3.96	**-3.31**	**-2.62**	**-1.81**		
		4.08	4.71	4.19	3.62		
	-3.00	**-2.77**	**-3.08**	**-2.58**	**-1.73**	**-2.38**	
	3.45	3.87	3.72	3.82	2.78	3.68	
-3.85	**-3.88**	**-3.00**	**-2.65**	**-2.46**	**-2.38**	**-2.50**	**-2.81**
3.89	3.14	2.97	3.15	2.63	2.02	2.39	2.83
-5.12	**-4.27**	**-3.77**	**-3.65**	**-3.42**	**-2.23**	**-2.04**	**-1.69**
4.97	3.33	3.37	3.49	2.00	2.93	2.27	2.49
-4.88	**-3.77**	**-3.69**	**-3.15**	**-3.69**	**-2.38**	**-2.58**	**-2.69**
5.50	3.90	3.03	2.82	2.43	2.33	2.45	3.32
-4.85	**-3.69**	**-3.35**	**-3.46**	**-2.27**	**-2.62**	**-2.04**	**-2.42**
4.12	2.28	2.38	3.24	2.38	2.25	2.73	2.40
	-5.77	**-5.19**	**-4.15**	**-3.69**	**-2.62**	**-2.88**	
	3.57	3.42	2.78	2.91	2.26	2.03	
		-4.88	**-5.04**	**-4.08**	**-3.50**		Fovea
		3.69	3.76	3.05	3.60		**N/A**
							N/A

f) SWAP (Full Threshold 24-2) at Visit Two

		-2.00	**-2.35**	**-2.35**	**-1.00**		
		4.22	4.24	4.20	4.21		
	-2.12	**-2.62**	**-3.04**	**-2.58**	**-1.62**	**-2.23**	
	2.67	2.77	3.34	3.24	2.71	3.88	
-2.96	**-2.38**	**-3.04**	**-1.77**	**-2.69**	**-2.69**	**-2.58**	**-3.00**
3.12	2.71	2.36	1.82	2.11	2.65	2.30	3.79
-3.69	**-4.15**	**-3.27**	**-3.54**	**-2.77**	**-1.62**	**-2.04**	**-2.15**
5.68	4.22	3.45	4.01	2.12	2.86	2.65	2.49
-4.38	**-3.15**	**-3.50**	**-3.15**	**-3.73**	**-2.15**	**-3.00**	**-2.73**
5.19	2.85	2.55	2.15	2.75	2.41	2.61	2.11
-4.12	**-6.08**	**-3.92**	**-3.81**	**-2.35**	**-2.73**	**-3.08**	**-2.23**
3.08	11.80	2.12	2.32	2.71	2.65	5.15	1.92
	-4.96	**-5.08**	**-3.92**	**-3.35**	**-3.50**	**-2.77**	
	3.43	2.88	2.19	1.92	2.27	1.97	
		-4.88	**-4.69**	**-3.31**	**-3.73**		Fovea
		4.44	3.51	3.08	2.15		**N/A**
							N/A

Figure 5.6. The Group Mean Pattern Deviation (dB) for each stimulus location (upper value) and one SD of the mean (lower value) for Visit One and Visit Two for FDT perimetry ((a) & (b)), for W-W perimetry ((c) & (d)) and for SWAP ((e) & (f)) for the OHT group.

a) FDT Perimetry (Full Threshold C-20) at Visit One

-0.02 0.11	**-0.02** 0.11	**-0.05** 0.12	**0.00** 0.21
-0.04 0.09	**0.01** 0.11	**-0.03** 0.11	**0.01** 0.16

Fovea

b) FDT Perimetry (Full Threshold C-20) at Visit Two

-0.01 0.12	**0.00** 0.10	**-0.04** 0.09	**-0.03** 0.14
0.01 0.10	**0.00** 0.13	**-0.06** 0.09	**0.01** 0.09

Fovea

c) W-W Perimetry (Full Threshold 24-2) at Visit One

		-0.06 0.09	**-0.06** 0.13	**-0.12** 0.11	**-0.16** 0.08		
	-0.05 0.10	**-0.05** 0.08	**-0.03** 0.09	**-0.06** 0.10	**-0.09** 0.09	**-0.10** 0.09	
-0.01 0.11	**-0.02** 0.08	**-0.03** 0.04	**-0.02** 0.06	**-0.05** 0.08	**-0.07** 0.06	**-0.06** 0.09	**-0.08** 0.07
0.00 0.10	**-0.01** 0.07	**-0.03** 0.05	**-0.01** 0.05	**-0.02** 0.04	**-0.02** 0.05	**-0.01** 0.07	**0.00** 0.07

Fovea

d) W-W Perimetry (Full Threshold 24-2) at Visit Two

		-0.06 0.13	**-0.05** 0.09	**-0.14** 0.08	**-0.14** 0.10		
	0.00 0.08	**-0.05** 0.09	**-0.07** 0.06	**-0.07** 0.09	**-0.08** 0.07	**-0.10** 0.08	
-0.03 0.11	**-0.01** 0.06	**-0.02** 0.04	**-0.03** 0.04	**-0.06** 0.08	**-0.07** 0.07	**-0.07** 0.09	**-0.08** 0.08
0.00 0.12	**0.00** 0.08	**-0.01** 0.07	**-0.01** 0.07	**-0.02** 0.04	**-0.05** 0.04	**-0.03** 0.07	**-0.04** 0.06

Fovea

e) SWAP (Full Threshold 24-2) at Visit One

		-0.23 0.20	**-0.21** 0.30	**-0.29** 0.25	**-0.28** 0.19		
	-0.15 0.22	**-0.13** 0.15	**-0.15** 0.12	**-0.15** 0.16	**-0.18** 0.13	**-0.22** 0.20	
-0.08 0.27	**-0.06** 0.12	**-0.10** 0.13	**-0.06** 0.11	**-0.03** 0.16	**-0.10** 0.12	**-0.06** 0.17	**-0.10** 0.15
0.00 0.40	**0.03** 0.21	**0.00** 0.14	**-0.01** 0.11	**0.00** 0.12	**-0.02** 0.12	**0.00** 0.13	**-0.03** 0.16

Fovea

f) SWAP (Full Threshold 24-2) at Visit Two

		-0.16 0.16	**-0.22** 0.21	**-0.31** 0.18	**-0.26** 0.18		
	-0.09 0.21	**-0.11** 0.10	**-0.19** 0.13	**-0.17** 0.12	**-0.18** 0.13	**-0.19** 0.17	
0.07 0.31	**-0.02** 0.15	**-0.07** 0.09	**-0.11** 0.08	**-0.10** 0.11	**-0.10** 0.14	**-0.07** 0.17	**-0.07** 0.13
0.01 0.31	**-0.03** 0.21	**-0.02** 0.13	**0.00** 0.08	**-0.02** 0.10	**-0.07** 0.09	**-0.01** 0.10	**-0.04** 0.15

Fovea

Figure 5.7. The Group mean difference in Sensitivity (dB) between the upper and lower hemifield (as a proportion of the lower hemifield) for each corresponding stimulus location (upper value) and one standard deviation of the mean (lower value) for Visit One and Visit Two for FDT perimetry (a & b), for W-W perimetry (c & d) and for SWAP (e & f) for the Normal group.
The locations with a higher Group mean sensitivity in the lower hemifield are shaded grey.

a) FDT Perimetry (Full Threshold C-20) at Visit One

-0.02 0.16	-0.02 0.16	-0.08 0.14	-0.07 0.13	
-0.05 0.14	-0.02 0.10	0.00 0.14	-0.03 0.10	
				Fovea

b) FDT Perimetry (Full Threshold C-20) at Visit Two

0.03 0.19	-0.01 0.21	-0.05 0.17	-0.09 0.10	
-0.02 0.14	-0.03 0.16	-0.01 0.14	-0.02 0.18	
				Fovea

c) W-W Perimetry (Full Threshold 24-2) at Visit One

			-0.06 0.17	-0.07 0.14	-0.15 0.17	-0.20 0.16		
		-0.01 0.14	-0.06 0.14	-0.07 0.10	-0.09 0.10	-0.12 0.10	-0.09 0.11	
	0.17 1.06	-0.04 0.10	-0.04 0.06	-0.03 0.07	-0.06 0.10	-0.09 0.11	-0.09 0.11	-0.06 0.09
0.07 0.50	0.02 0.12	-0.02 0.05	-0.03 0.07	-0.01 0.06	-0.01 0.05	-0.04 0.06		0.35 2.07
								Fovea

d) W-W Perimetry (Full Threshold 24-2) at Visit Two

			-0.07 0.14	-0.09 0.17	-0.15 0.22	-0.19 0.18		
		-0.02 0.12	-0.02 0.17	-0.03 0.27	-0.09 0.09	-0.10 0.11	-0.12 0.11	
	-0.04 0.16	-0.03 0.08	-0.05 0.08	-0.04 0.07	-0.05 0.08	-0.09 0.11	-0.07 0.09	-0.06 0.12
-0.02 0.18	-0.04 0.07	-0.04 0.07	-0.04 0.06	-0.04 0.08	-0.04 0.10	-0.02 0.06		-0.01 0.08
								Fovea

e) SWAP (Full Threshold 24-2) at Visit One

			-0.27 0.35	-0.27 0.34	-0.26 0.32	-0.19 0.48		
		0.04 0.48	-0.10 0.26	-0.17 0.20	-0.16 0.24	-0.19 0.17	-0.20 0.23	
	0.17 1.17	-0.13 0.19	-0.11 0.14	-0.08 0.23	-0.13 0.15	-0.11 0.10	-0.11 0.14	-0.15 0.17
0.38 1.97	-0.04 0.32	-0.06 0.18	-0.07 0.16	-0.01 0.17	-0.03 0.14	-0.01 0.08		0.10 0.51
								Fovea

f) SWAP (Full Threshold 24-2) at Visit Two

			-0.14 0.33	-0.20 0.38	-0.28 0.25	-0.21 0.27		
		0.00 0.28	-0.06 0.22	-0.17 0.20	-0.17 0.20	-0.14 0.20	-0.22 0.21	
	-0.05 0.23	-0.04 0.16	-0.07 0.14	-0.02 0.17	-0.12 0.13	-0.11 0.15	-0.08 0.20	-0.18 0.20
0.18 1.28	-0.06 0.28	0.00 0.22	-0.06 0.19	0.00 0.11	-0.03 0.09	0.00 0.13		-0.01 0.13
								Fovea

Figure 5.8. The Group mean difference in Sensitivity (dB) between the upper and lower hemifield (as a proportion of the lower hemifield) for each corresponding stimulus location (upper value) and one standard deviation of the mean (lower value) for Visit One and Visit Two for FDT perimetry (a & b), for W-W perimetry (c & d) and for SWAP (e & f) for the OHT group.
The locations with a higher Group mean sensitivity in the lower hemifield are shaded grey.

5.15.4 The variation in Group Mean Sensitivity with eccentricity for FDT, W-W and SWAP.

The locations used for the inner central and outer central regions in the analysis are defined in Figure 5.2. The Group mean difference in Sensitivity between the inner central and outer central region of the visual field (as a proportion of the outer central region) and the associated one SD of the mean at each visit for the three types of perimetry for the Normal and OHT groups is shown in Table 5.4. There is minimal difference for the mean of two concentric 10° regions in the Group Mean Sensitivity across the central 20° field for FDT or W-W perimetry. The Group Mean Sensitivity decreased with eccentricity, across the central 20° field, with SWAP both in the Normal and the OHT group.

5.15.5 The between-visit variation in Mean Deviation and in Pattern Standard Deviation.

The Group Mean difference in MD and the accompanying 95% limits of agreement for the three types of perimetry are shown in Table 5.5 and in Figures 5.9 –5.11. The Group Mean difference in MD for each of the three types of perimetry was minimal and was similar for each test across each diagnostic group.

The Group Mean difference in PSD and the accompanying 95% limits of agreement for the three types of perimetry are shown in Table 5.6 and in Figures 5.12-5.14. The Group Mean difference in PSD for each of the three types of perimetry was again minimal and was again similar for each type across each diagnostic group.

FDT

	V1		V2	
	MEAN	SD	MEAN	SD
NORMAL	0.04	0.05	0.05	0.05
OHT	0.03	0.07	0.03	0.07

W-W

	V1		V2	
	MEAN	SD	MEAN	SD
NORMAL	0.05	0.02	0.04	0.02
OHT	0.07	0.04	0.08	0.04

SWAP

	V1		V2	
	MEAN	SD	MEAN	SD
NORMAL	0.10	0.05	0.09	0.04
OHT	0.18	0.10	0.15	0.09

Table 5.4. The Group mean difference in Sensitivity (dB) between the inner and the outer central regions of the visual field (as a proportion of the outer central field) and one standard deviation of the mean for Visit One and Visit Two for FDT perimetry (top), for W-W perimetry (middle) and for SWAP (bottom) for the Normal and OHT groups.

FDT Perimetry

	Group Mean Difference		95% Limits of Agreement	
		SD	UPPER	LOWER
NORMAL	0.27	1.61	3.42	-2.87
OHT	0.14	1.07	2.24	-1.96
OHT(H)	-0.56	1.59	2.57	-3.68
ALL OHT	-0.10	1.29	2.43	-2.63
POAG	-0.35	1.16	1.92	-2.62

W-W Perimetry

	Group Mean Difference		95% Limits of Agreement	
		SD	UPPER	LOWER
NORMAL	-0.06	0.90	1.75	-1.87
OHT	0.48	0.84	2.12	-1.16
OHT(H)	-0.92	1.58	2.18	-4.02
ALL OHT	0.00	-1.31	2.56	-2.57
POAG	-0.07	1.59	3.05	-3.19

SWAP

	Group Mean Difference		95% Limits of Agreement	
		SD	UPPER	LOWER
NORMAL	0.43	1.24	2.87	-2.01
OHT	0.85	1.04	2.89	-1.19
OHT(H)	0.38	1.78	3.86	-3.11
ALL OHT	0.69	1.33	3.29	-1.91
POAG	0.31	1.26	2.78	-2.15

Table 5.5. The Group Mean difference in MD and one SD for the Normal, OHT, OHT(H), ALL OHT and POAG groups, between two visits for FDT perimetry (upper), for W-W perimetry (middle) and for SWAP (lower). The upper and lower 95% limits of agreement are provided. (The values are quoted in decibels).

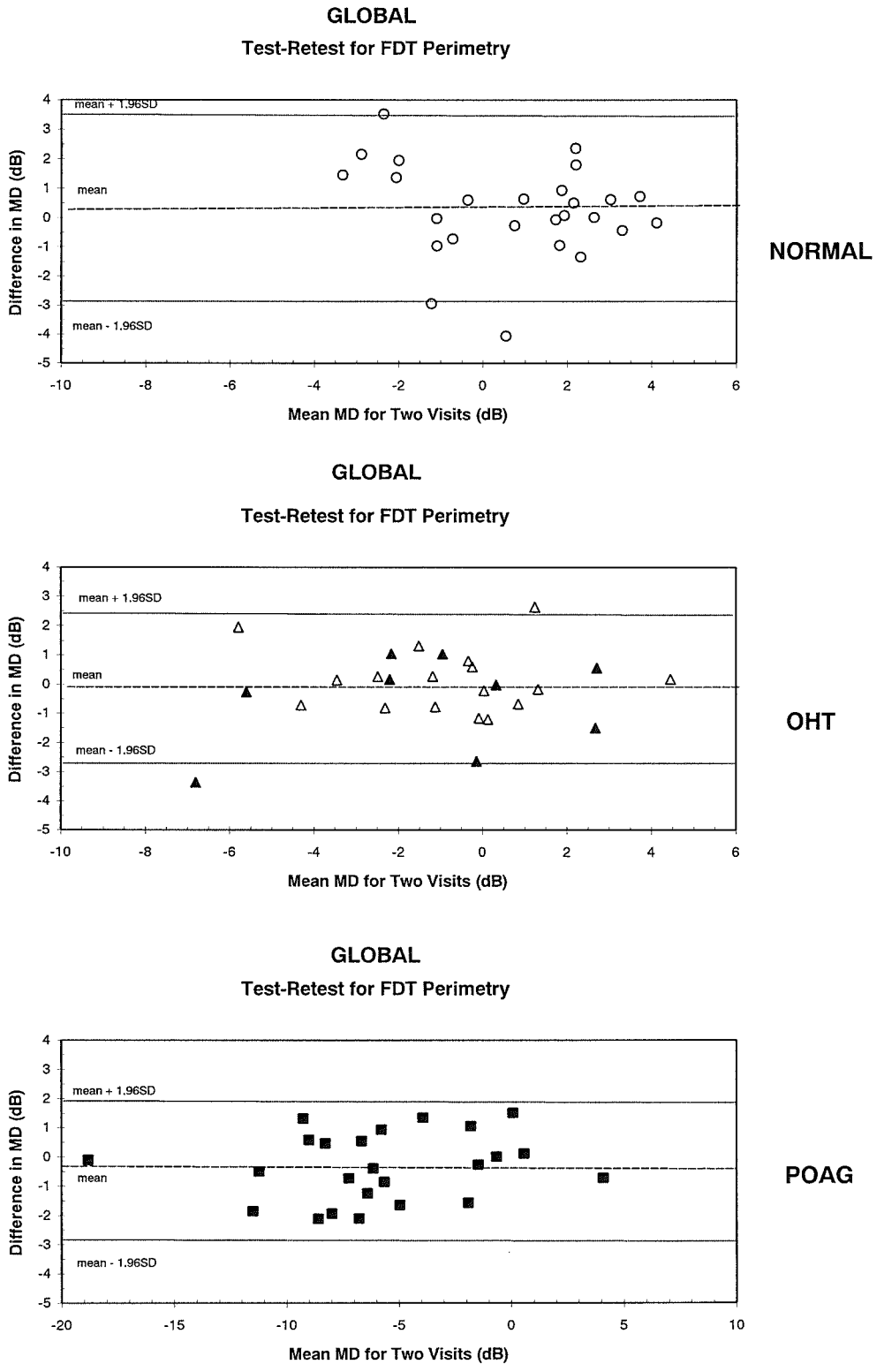

Figure 5.9. The difference in MD as a function of the mean MD of the two visits for the Normal group (top), for the OHT group (middle; open triangles), OHT(H) group (middle; closed triangles) and for the POAG group (bottom) with FDT perimetry. Note the different scale in the abscissa.

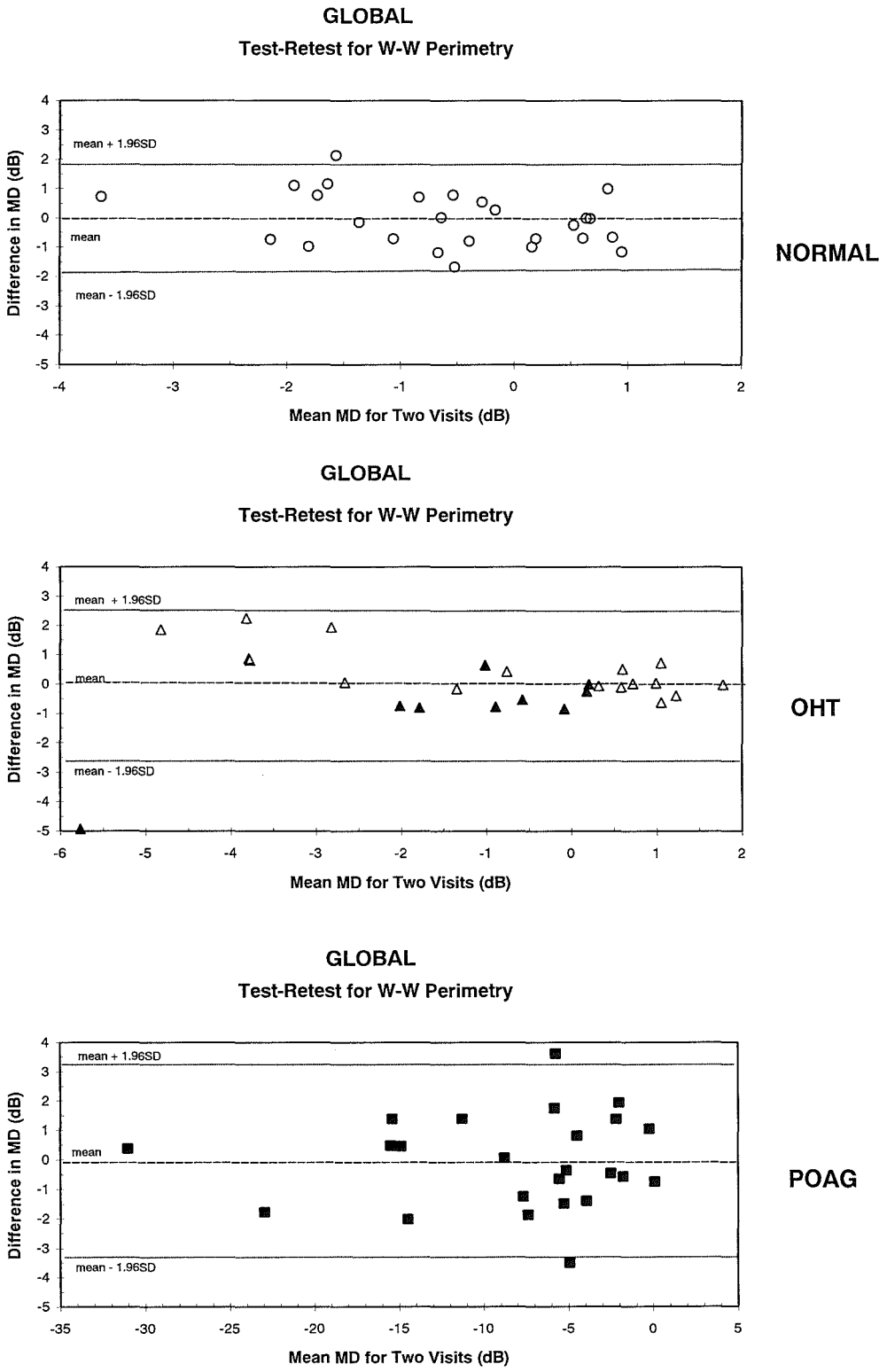

Figure 5.10. The difference in MD as a function of the mean MD of the two visits for the Normal group (top), for the OHT group (middle; open triangles), OHT(H) group (middle; closed triangles) and for the POAG group (bottom) with W-W perimetry. Note the different scale in the abscissa.

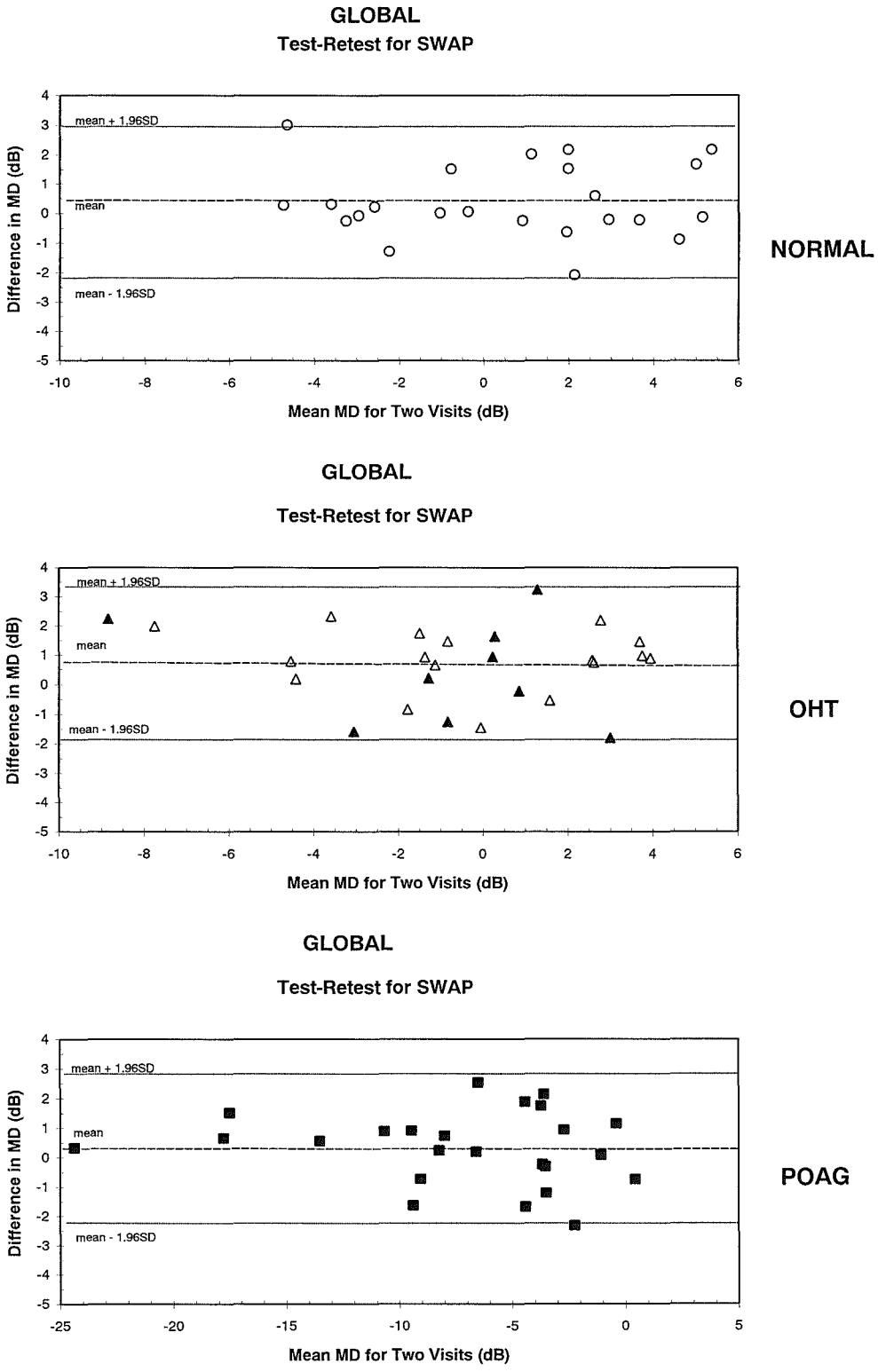

Figure 5.11. The difference in MD as a function of the mean MD of the two visits for the Normal group (top), for the OHT group (middle; open triangles), OHT(H) group (middle; closed triangles) and for the POAG group (bottom) with SWAP. Note the different scale in the abscissa.

FDT Perimetry

	Group Mean Difference		95% Limits of Agreement	
		SD	UPPER	LOWER
NORMAL	-0.26	1.07	1.83	-2.35
OHT	-0.38	0.85	1.29	-2.04
OHT(H)	0.33	0.96	2.22	-1.56
ALL OHT	-0.13	0.94	1.70	-1.97
POAG	0.28	0.95	2.17	-1.57

W-W Perimetry

	Group Mean Difference		95% Limits of Agreement	
		SD	UPPER	LOWER
NORMAL	0.04	0.41	0.85	-0.64
OHT	-0.13	0.56	0.97	-1.24
OHT(H)	-0.17	0.64	1.08	-1.43
ALL OHT	-0.15	0.58	0.99	-1.28
POAG	-0.04	1.58	3.06	-3.14

SWAP

	Group Mean Difference		95% Limits of Agreement	
		SD	UPPER	LOWER
NORMAL	-0.21	0.59	0.95	-1.38
OHT	0.01	0.60	1.2	-1.21
OHT(H)	-0.13	0.69	1.23	-1.49
ALL OHT	-0.05	0.63	1.19	-1.28
POAG	0.01	0.78	1.54	-1.52

Table 5.6. The Group Mean difference in PSD and one SD for the Normal, OHT, OHT(H), ALL OHT and POAG groups, between two visits for FDT perimetry (upper), for W-W perimetry (middle) and for SWAP (lower). The upper and lower 95% limits of agreement are provided. (The values are quoted in decibels).

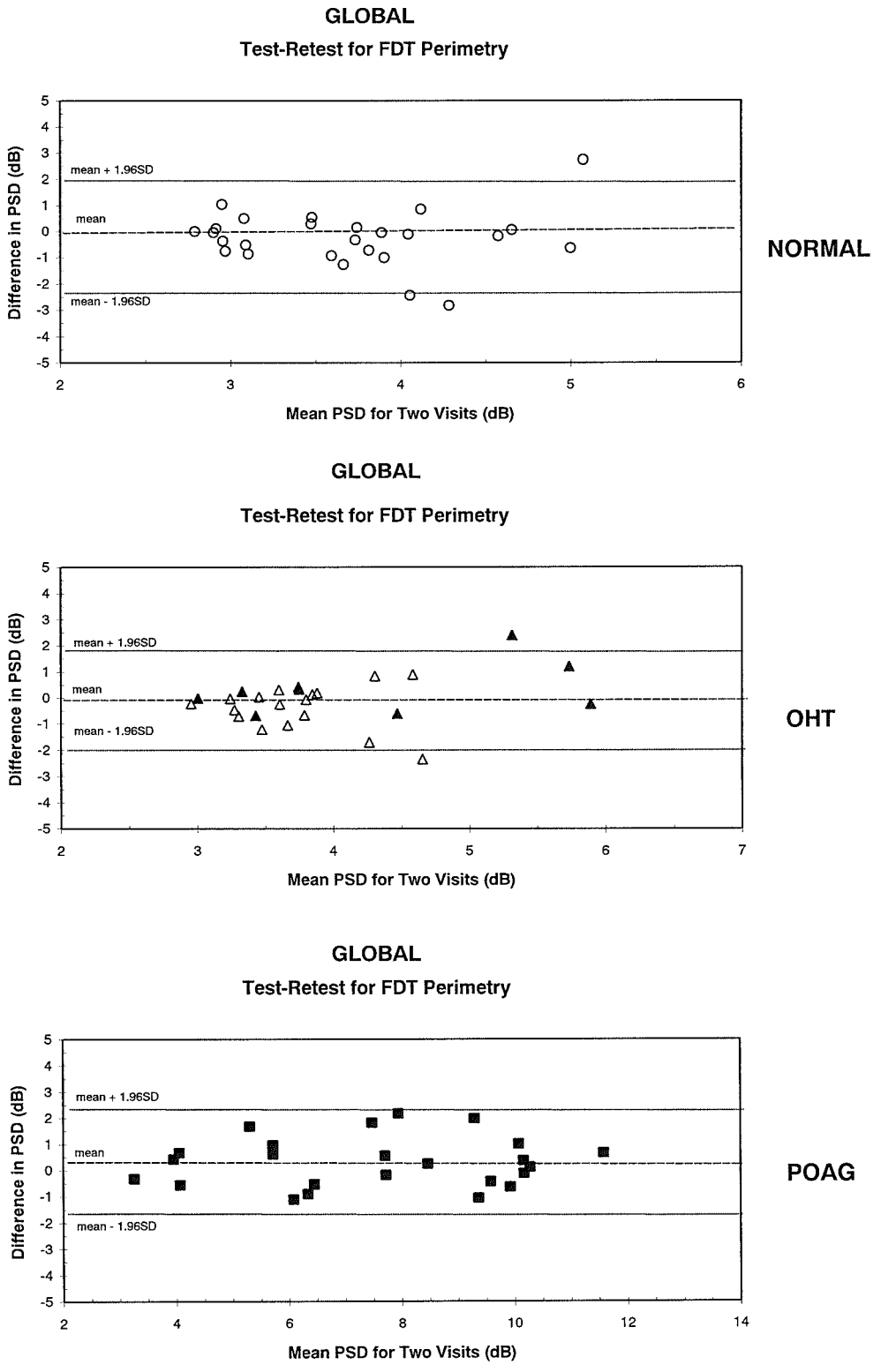

Figure 5.12. The difference in PSD as a function of the mean PSD of the two visits for the Normal group (top), for the OHT group (middle; open triangles), OHT(H) group (middle; closed triangles) and for the POAG group (bottom) with FDT perimetry. Note the different scale in the abscissa.

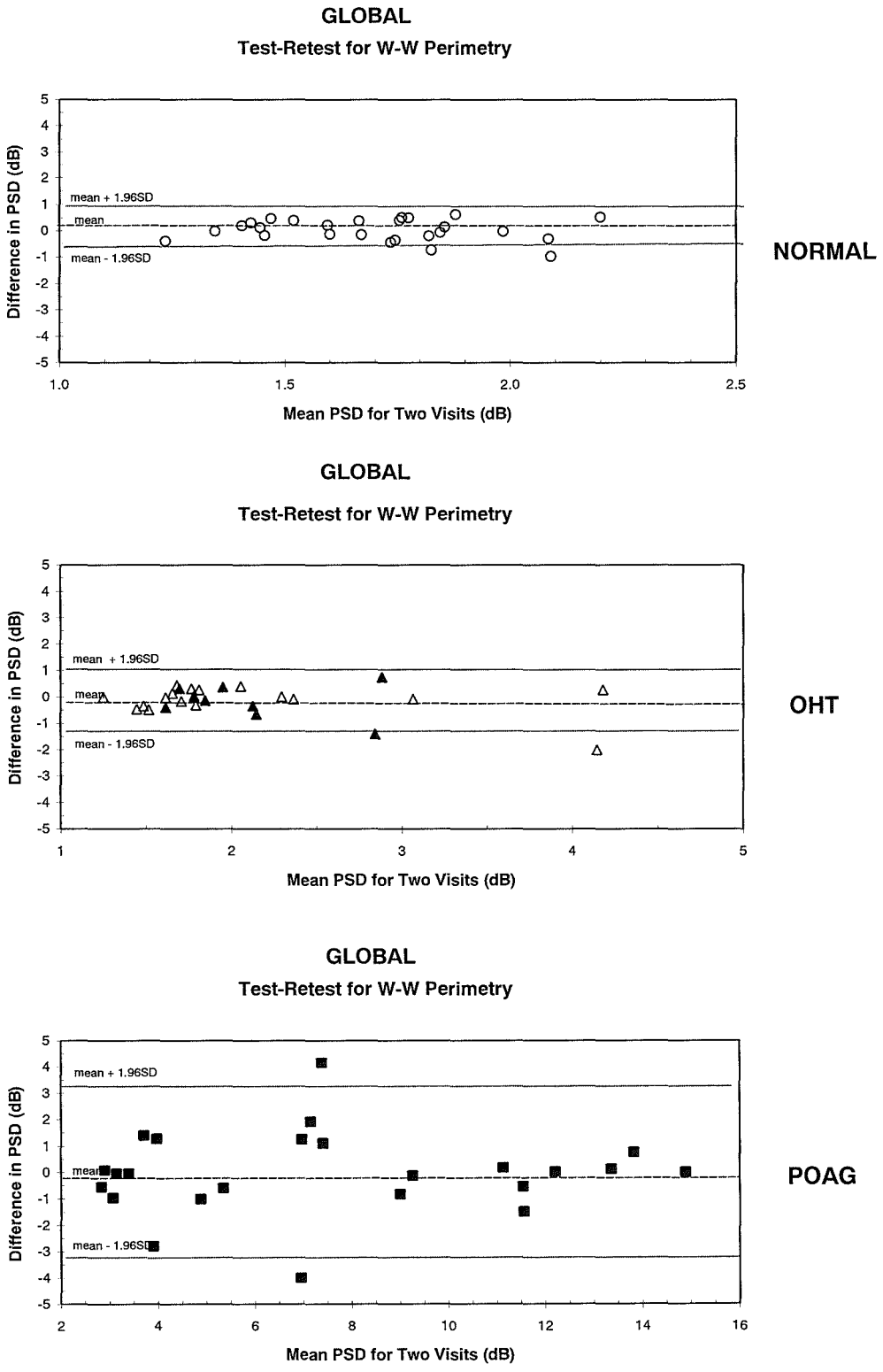

Figure 5.13. The difference in PSD as a function of the mean PSD of the two visits for the Normal group (top), for the OHT group (middle; open triangles), OHT(H) group (middle; closed triangles) and for the POAG group (bottom) with W-W perimetry. Note the different scale in the abscissa.

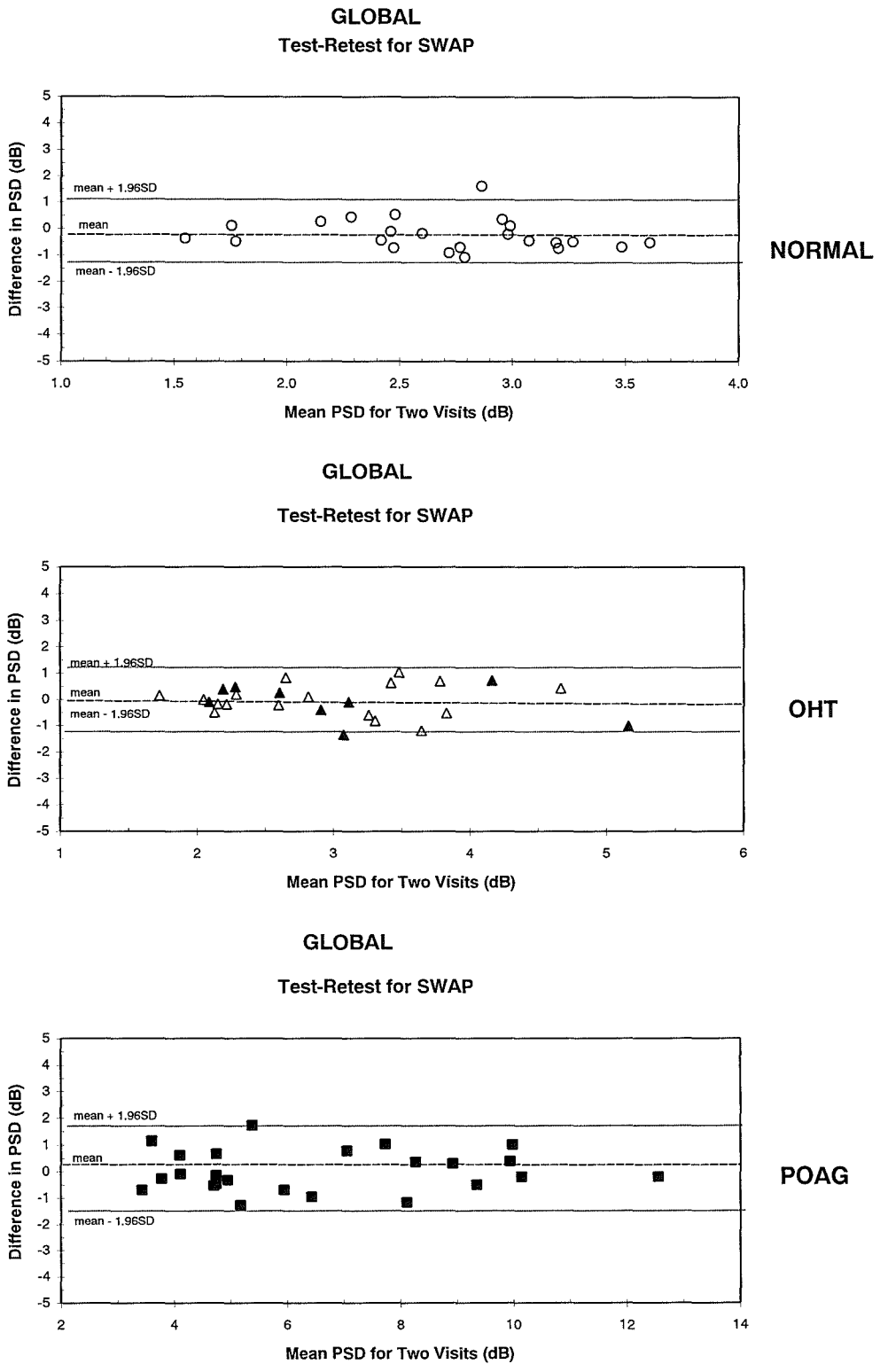

Figure 5.14. The difference in PSD as a function of the mean PSD of the two visits for the Normal group (top), for the OHT group (middle; open triangles), OHT(H) group (middle; closed triangles) and for the POAG group (bottom) with SWAP. Note the different scale in the abscissa.

5.15.6 The between-visit variation in Total Deviation between the three types of perimetry.

The 95th, 50th and 5th percentiles of the difference in Total Deviation at each stimulus location between Visit One and Visit Two as a function of the Total Deviation at the given stimulus location at Visit One, for each of the three types of perimetry across the three diagnostic groups, are given in Figures 5.15-5.17.

The distribution of the between-visit variability is similar for the Normal and OHT groups, and slightly wider for the POAG group across each of the three types of perimetry. The width of the distribution was narrow for the more positive TD values. The distribution broadened for the mid-range TD values and tended to become less broad for the extreme low TD values associated with absolute defects. The variation in the distribution was greatest for the POAG group with each of the three perimetric techniques.

The Figure 5.15-5.17 illustrates that as the TD of a location decreases and becomes more negative, the between-test variability increased for the OHT and the POAG group, with all three perimeters. The increase in between-test variability is greater for the POAG group than for the OHT group and is greatest for W-W perimetry. The between-test variability in TD is similar for increasingly negative values of TD within the Normal group across each perimetric strategy.

5.15.7 The between-visit variability in Pattern Deviation between the three types of perimetry.

The 95th, 50th and 5th percentiles of the difference in Pattern Deviation at each stimulus location between Visit One and Visit Two as a function of the Pattern Deviation at the given stimulus location at Visit One for each of the three types of perimetry across the three diagnostic groups are given in Figures 5.18-5.20.

The variation in the distribution for the Pattern Deviations for each of perimetric strategy used, across each of the diagnostic groups, was similar to those for the Total Deviations.

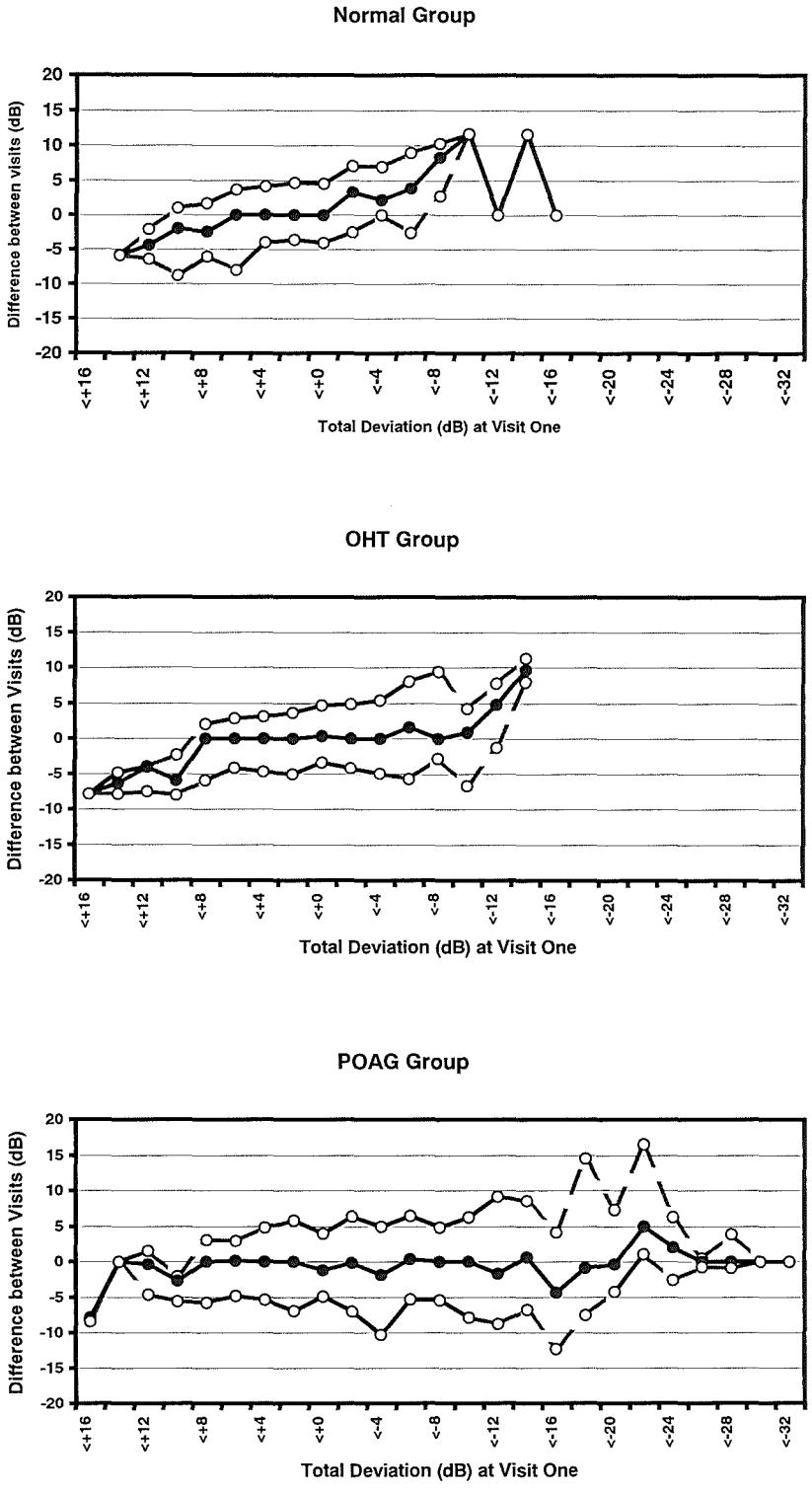

Figure 5.15. The 95th, 50th and 5th percentiles for the distribution of the differences in Total Deviation at each stimulus location between Visit One and Visit Two as a function of the Total Deviation at the given stimulus location at Visit One in the Normal group (top), for the entire OHT group (middle), and for the POAG group (bottom) with FDT perimetry.

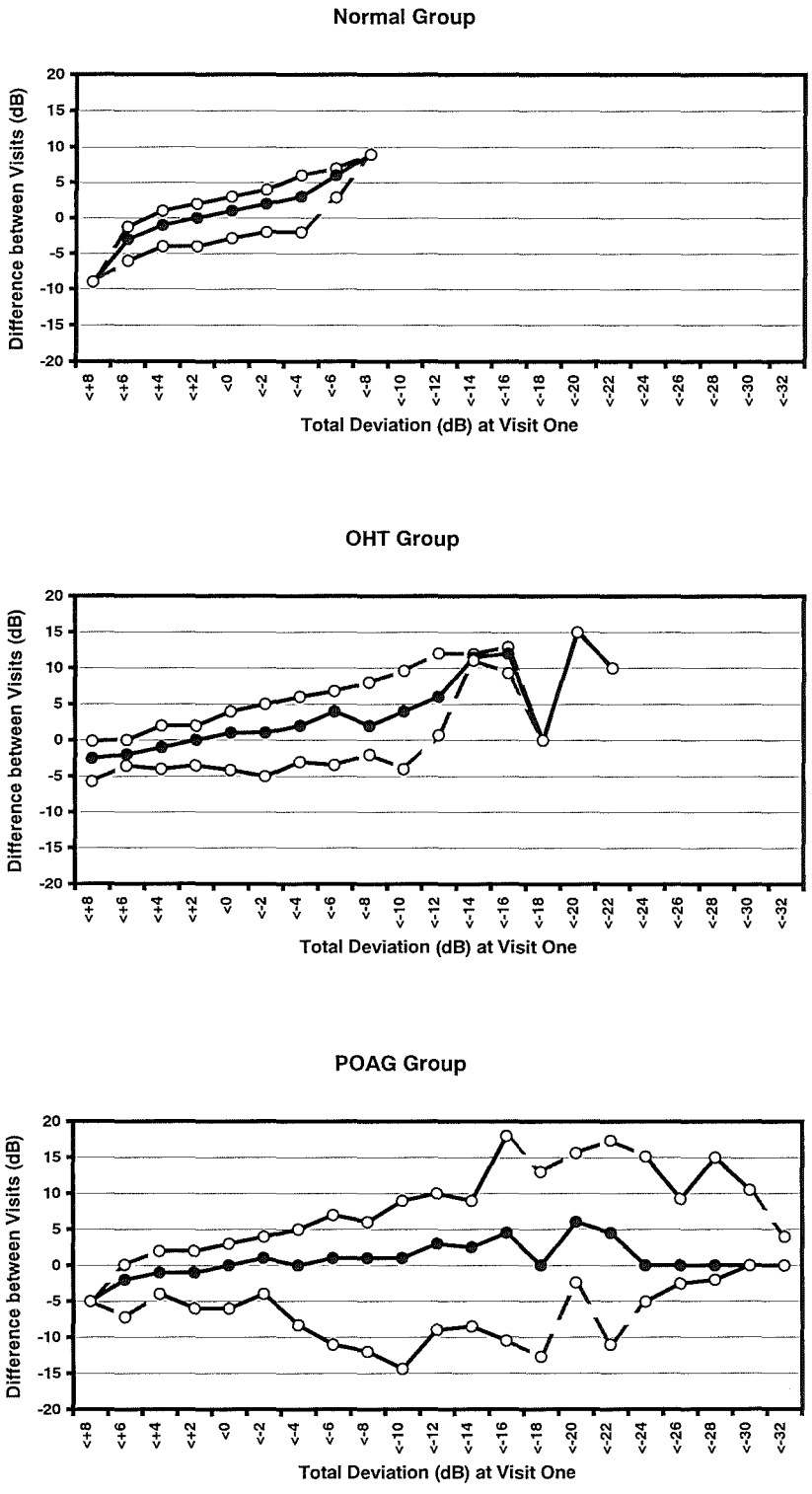

Figure 5.16. The 95th, 50th and 5th percentiles for the distribution of the differences in Total Deviation at each stimulus location between Visit One and Visit Two as a function of the Total Deviation at the given stimulus location at Visit One in the Normal group (top), for the entire OHT group (middle), and for the POAG group (bottom) with W-W perimetry.

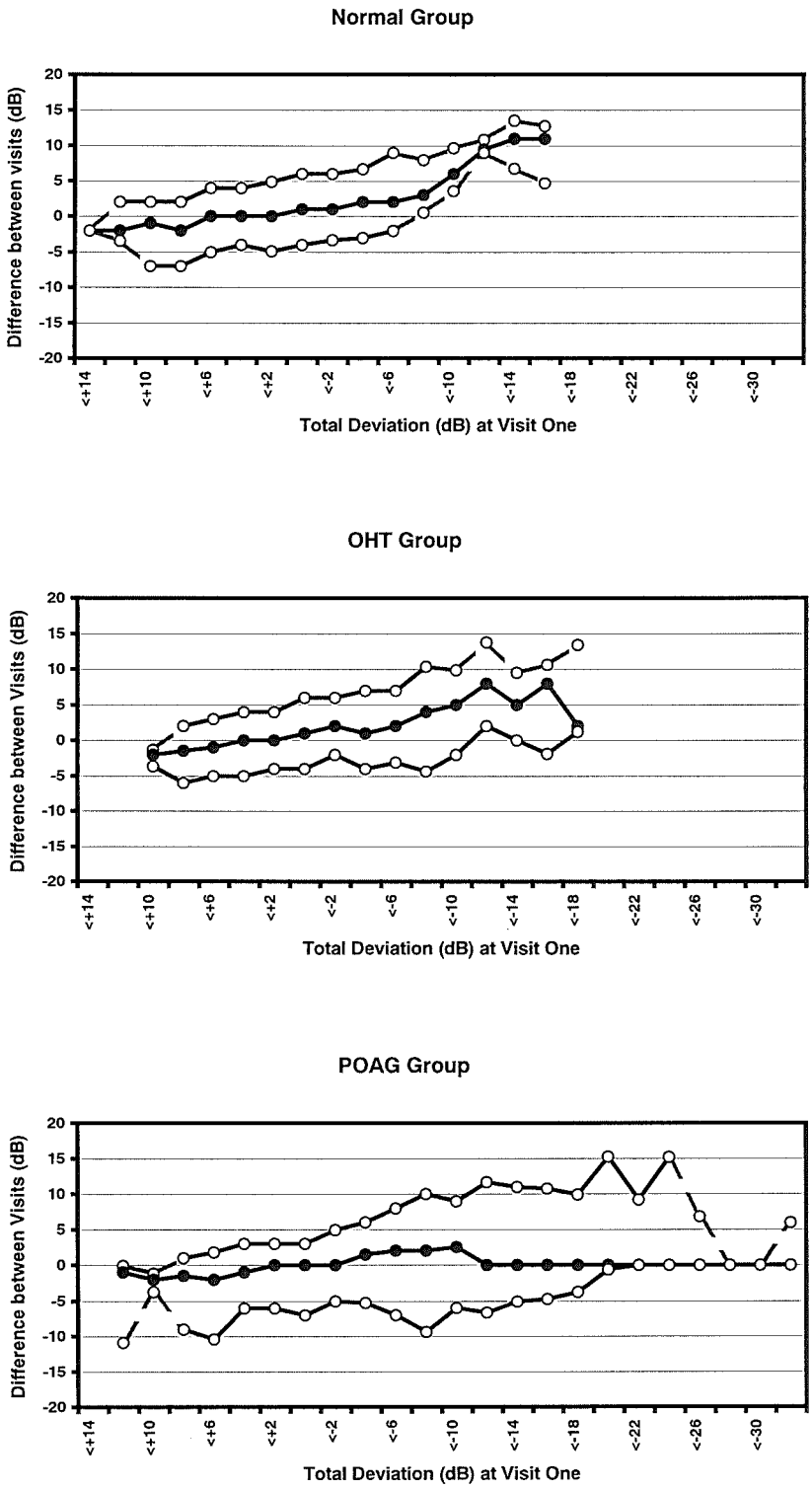

Figure 5.17. The 95th, 50th and 5th percentiles for the distribution of the differences in Total Deviation at each stimulus location between Visit One and Visit Two as a function of the Total Deviation at the given stimulus location at Visit One in the Normal group (top), for the entire OHT group (middle), and for the POAG group (bottom) with SWAP.

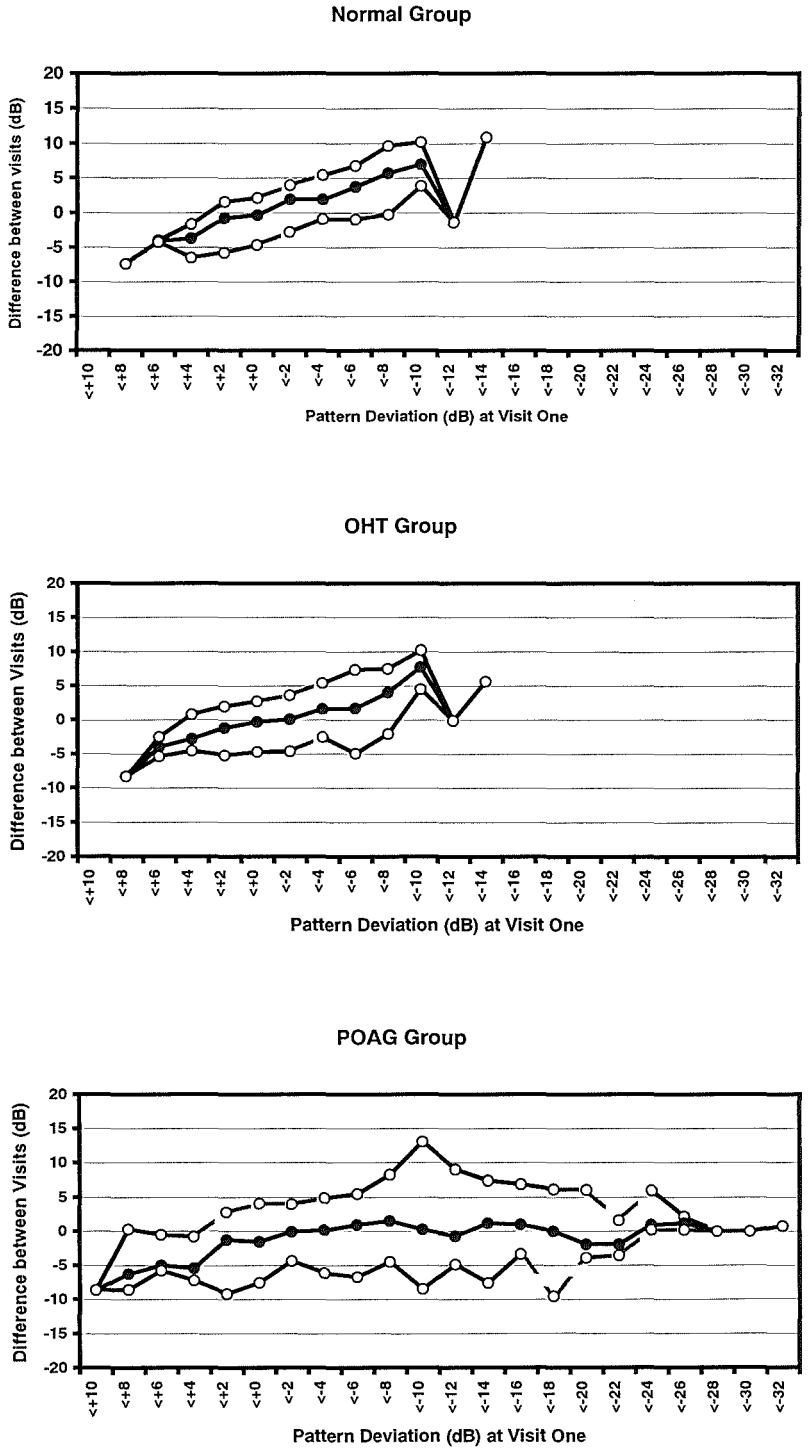

Figure 5.18. The 95th, 50th and 5th percentiles for the distribution of the difference in Pattern Deviation at each stimulus location between Visit One and Visit Two as a function of the Pattern Deviation at the given stimulus location at Visit One in the Normal group (top), for the entire OHT group (middle), and for the POAG group (bottom) with FDT perimetry.

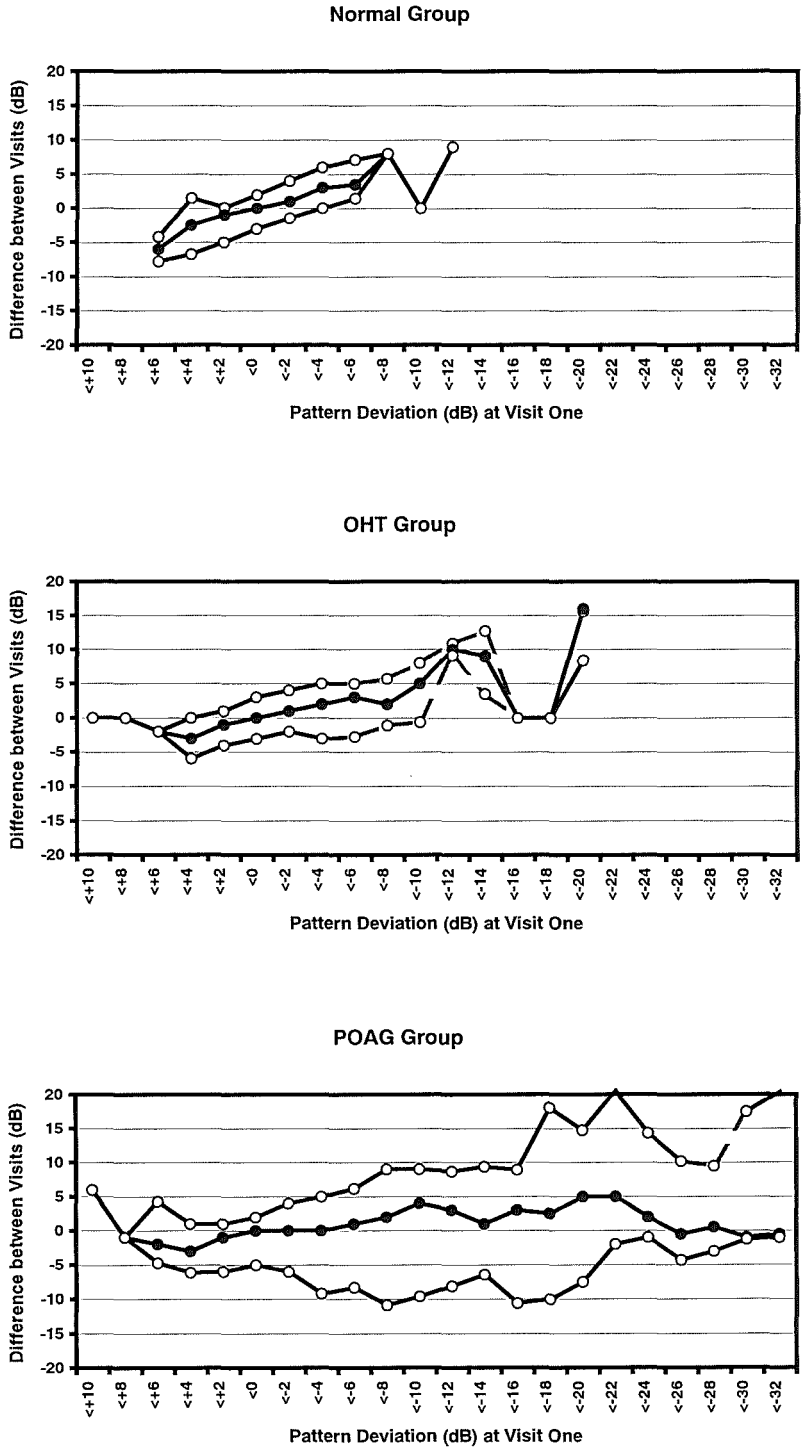

Figure 5.19. The 95th, 50th and 5th percentiles for the distribution of the difference in Pattern Deviation at each stimulus location between Visit One and Visit Two as a function of the Pattern Deviation at the given stimulus location at Visit One in the Normal group (top), for the entire OHT group (middle), and for the POAG group (bottom) with W-W perimetry.

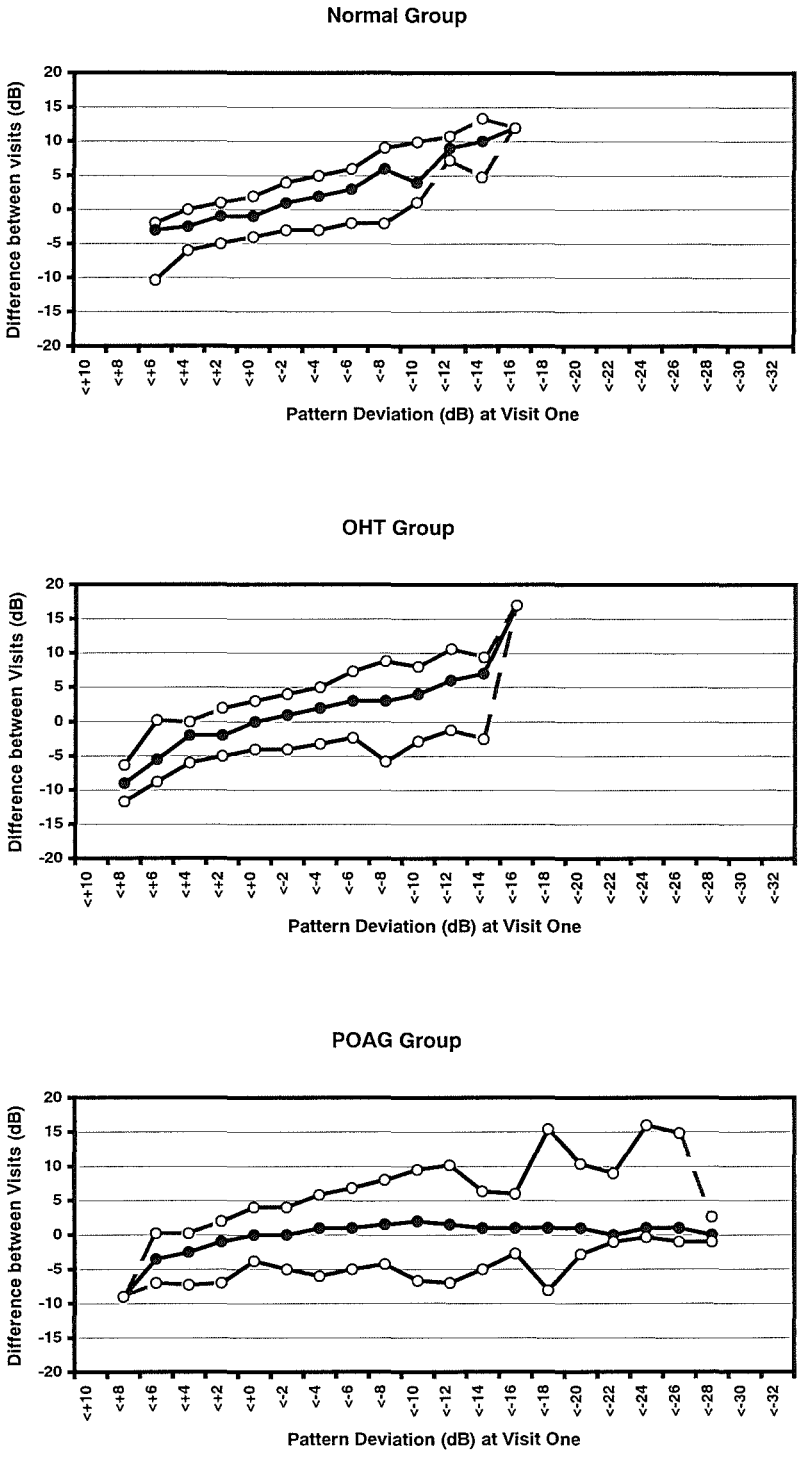

Figure 5.20. The 95th, 50th and 5th percentiles for the distribution of the difference in Pattern Deviation at each stimulus location between Visit One and Visit Two as a function of the Pattern Deviation at the given stimulus location at Visit One in the Normal group (top), for the entire OHT group (middle), and for the POAG group (bottom) with SWAP.

5.15.8 The pointwise differences in Pattern Deviation probability values.

The Figures 5.21-5.23 show the contingency tables for each type of perimetry for each diagnostic group. The difference in the distribution of the non-significant to significant 'p' values between the two visits were generally not statistically significant for the type of perimetry across the three groups. FDT perimetry for the Normal group exhibited a reduction in the number of PD values showing statistical significance at the second visit ($p = 0.04$). SWAP for the OHT group exhibited a similar result ($p = 0.000$) (see Table 5.7).

Where an association was found between visit and probability values, inspection of the contingency tables suggest that some locations which exhibited a significant deviation from normal at Visit One, were shown to be non-significant at Visit Two. A learning effect could account for the difference.

To correct for the difference in the number of stimulus locations examined, the data were analysed in proportionate terms for all the comparable locations (Figure 5.24). The FDT instrument showed more statistically significant defects both at Visit One and Visit Two than either W-W perimetry or SWAP. In consequence the proportion of locations which exhibited identical probability over the two tests were significantly lower for FDT perimetry than either W-W perimetry or SWAP. The results suggest that the between-visits results for statistically significant defects are more variable for FDT perimetry than HFA Full Threshold algorithms.

When the analysis was performed only for those locations that appeared outside the 95% confidence limits for normality at both visits, there were more statistically significant defects at Visit One for the Normal group than for Visit Two, across the three types of perimetry. The proportion of stimulus locations whose level of significance remained identical between the two visits was greatest for the POAG group who by definition, have established evidence of a visual field defect (Figure 5.24).

	Perimetry		
Diagnostic Group	**FDT**	**W-W**	**SWAP**
NORMAL	4.308 (p=0.0379)	0.527 (p=0.4680)	2.591 (p=0.1074)
OHT	1.212 (p=0.2710)	0.074 (p=0.7851)	12.067 (p=0.0005)
OHT(H)	0.261 (p=0.6092)	1.556 (p=0.2122)	0.882 (p=0.3476)
POAG	0.006 (p=0.9407)	1.349 (p=0.2455)	3.418 (p=0.0645)

Table 5.7. The Continuity Correction Chi-Squared Values, and in parentheses the Continuity Correction 'p' values, for the comparison of the frequency of non-significant to significant stimulus locations, for each type of perimetry, across the three diagnostic groups, at each of the two visits. Derived by collapsing each of the 5 x 5 contingency tables into 2 x 2 contingency tables.

a) NORMAL GROUP

FDT VISIT 1 \ FDT VISIT 2	NS	<5%	<2%	<1%	<0.5%
NS	368	11	1	0	0
<5%	19	4	0	2	0
<2%	4	1	0	0	0
<1%	4	1	0	0	0
<0.5%	1	0	0	0	0

b) OHT GROUP

FDT VISIT 1 \ FDT VISIT 2	NS	<5%	<2%	<1%	<0.5%
NS	233	11	1	1	0
<5%	14	3	0	1	0
<2%	5	0	0	1	0
<1%	2	0	0	0	0
<0.5%	0	0	0	0	0

c) OHT(H) GROUP

FDT VISIT 1 \ FDT VISIT 2	NS	<5%	<2%	<1%	<0.5%
NS	113	9	1	1	2
<5%	7	1	1	2	0
<2%	1	1	1	0	0
<1%	1	2	0	1	0
<0.5%	0	0	0	0	0

d) POAG GROUP

FDT VISIT 1 \ FDT VISIT 2	NS	<5%	<2%	<1%	<0.5%
NS	204	19	3	10	4
<5%	21	16	3	3	1
<2%	2	6	2	2	4
<1%	6	3	2	8	7
<0.5%	5	0	3	2	48

Figure 5.21. The set of contingency tables for the within-individual within-instrument between-visit difference in the number of Pattern Deviation probability values at each stimulus location. The data is collected across all individuals for comparable locations for the (a) Normal group (b) the OHT group, (c) the OHT(H) group and (d) for the POAG group, using FDT perimetry.

a) NORMAL GROUP

W-W VISIT 1 \ W-W VISIT 2	NS	<5%	<2%	<1%	<0.5%
NS	751	8	3	0	0
<5%	13	0	1	0	0
<2%	1	0	0	0	0
<1%	1	0	1	0	0
<0.5%	1	0	0	0	0

b) OHT GROUP

W-W VISIT 1 \ W-W VISIT 2	NS	<5%	<2%	<1%	<0.5%
NS	463	10	6	1	0
<5%	15	2	2	0	1
<2%	4	1	0	1	0
<1%	0	0	1	1	0
<0.5%	1	1	0	0	0

c) OHT(H) GROUP

W-W VISIT 1 \ W-W VISIT 2	NS	<5%	<2%	<1%	<0.5%
NS	247	4	0	1	1
<5%	12	1	0	0	0
<2%	1	0	0	0	0
<1%	1	1	0	0	0
<0.5%	0	0	1	0	0

d) POAG GROUP

W-W VISIT 1 \ W-W VISIT 2	NS	<5%	<2%	<1%	<0.5%
NS	411	29	15	6	19
<5%	14	12	11	2	2
<2%	6	3	1	1	5
<1%	10	3	4	2	8
<0.5%	17	2	3	12	122

Figure 5.22. The set of contingency tables for the within-individual within-instrument between-visit difference in the number of Pattern Deviation probability values at each stimulus location. The data is collected across all individuals for comparable locations for the (a) Normal group (b) the OHT group, (c) the OHT(H) group and (d) for the POAG group, using W-W perimetry.

a) NORMAL GROUP

SWAP VISIT 1 \ SWAP VISIT 2	NS	<5%	<2%	<1%	<0.5%
NS	662	7	0	0	0
<5%	11	0	0	0	0
<2%	3	2	0	0	2
<1%	1	0	0	0	0
<0.5%	2	0	0	0	0

b) OHT GROUP

SWAP VISIT 1 \ SWAP VISIT 2	NS	<5%	<2%	<1%	<0.5%
NS	474	13	4	0	1
<5%	5	1	1	0	3
<2%	1	1	1	0	2
<1%	0	0	0	0	0
<0.5%	2	0	0	0	1

c) OHT(H) GROUP

SWAP VISIT 1 \ SWAP VISIT 2	NS	<5%	<2%	<1%	<0.5%
NS	246	4	1	1	0
<5%	8	0	0	0	1
<2%	1	0	1	0	0
<1%	0	0	1	0	0
<0.5%	3	1	0	0	2

d) POAG GROUP

SWAP VISIT 1 \ SWAP VISIT 2	NS	<5%	<2%	<1%	<0.5%
NS	457	21	6	2	5
<5%	38	14	6	3	6
<2%	10	6	12	1	4
<1%	8	1	5	9	4
<0.5%	11	6	6	9	70

Figure 5.23. The set of contingency tables for the within-individual within-instrument between-visit difference in the number of Pattern Deviation probability values at each stimulus location. The data is collected across all individuals for comparable locations for the (a) Normal group (b) the OHT group, (c) the OHT(H) group and (d) for the POAG group, using SWAP.

a) NORMAL GROUP

INCLUDING REPEATED NS LOCATIONS	FDT	W-W	SWAP
More statistically significant defect at visit 1 (%)	7.2	2.2	2.8
Identical significance at visits 1 & 2 (%)	89.4	96.3	95.9
More statistically significant defect at visit 2 (%)	3.4	1.5	1.3

NOT INCLUDING REPEATED NS LOCATIONS	FDT	W-W	SWAP
More statistically significant defect at visit 1 (%)	62.5	58.6	67.9
Identical significance at visits 1 & 2 (%)	8.3	0.0	0.0
More statistically significant defect at visit 2 (%)	29.2	41.4	32.1

b) OHT GROUP

INCLUDING REPEATED NS LOCATIONS	FDT	W-W	SWAP
More statistically significant defect at visit 1 (%)	7.7	4.5	1.8
Identical significance at visits 1 & 2 (%)	86.8	91.4	93.5
More statistically significant defect at visit 2 (%)	5.5	4.1	4.7

NOT INCLUDING REPEATED NS LOCATIONS	FDT	W-W	SWAP
More statistically significant defect at visit 1 (%)	53.8	48.9	25.0
Identical significance at visits 1 & 2 (%)	7.7	6.4	8.3
More statistically significant defect at visit 2 (%)	38.5	44.7	66.7

c) OHT(H) GROUP

INCLUDING REPEATED NS LOCATIONS	FDT	W-W	SWAP
More statistically significant defect at visit 1 (%)	8.3	5.9	5.2
Identical significance at visits 1 & 2 (%)	80.6	91.9	92.2
More statistically significant defect at visit 2 (%)	11.1	2.2	2.6

NOT INCLUDING REPEATED NS LOCATIONS	FDT	W-W	SWAP
More statistically significant defect at visit 1 (%)	38.7	69.6	58.3
Identical significance at visits 1 & 2 (%)	9.7	4.3	12.5
More statistically significant defect at visit 2 (%)	51.6	26.1	29.2

d) POAG GROUP

INCLUDING REPEATED NS LOCATIONS	FDT	W-W	SWAP
More statistically significant defect at visit 1 (%)	13.0	10.3	13.9
Identical significance at visits 1 & 2 (%)	72.4	76.1	78.1
More statistically significant defect at visit 2 (%)	14.6	13.6	8

NOT INCLUDING REPEATED NS LOCATIONS	FDT	W-W	SWAP
More statistically significant defect at visit 1 (%)	27.8	23.9	38.0
Identical significance at visits 1 & 2 (%)	41.1	44.4	39.9
More statistically significant defect at visit 2 (%)	31.1	31.7	22.1

Figure 5.24. The within-individual within-instrument between-visit difference in the number of Pattern Deviation probability values at each stimulus location across all individuals for comparable locations for each diagnostic group tested using FDT perimetry, W-W perimetry and SWAP. The first row of tables are for the normal group, the second row of tables show the OHT group, the third row of tables show the OHT(H) group, and the fourth row of tables show the POAG group. The data is expressed as a pecentage including locations that were non-significant at the 95% level at both visits (left) and excluding locations that were non-significant at the 95% level at both visits (right).

5.16 Discussion.

The results of the ANOVA for MS indicate a lack of an age-related decline in the normal MS. This is contrary to the 0.6dB per decade reduction in MS for FDT perimetry (Adams et al. 1999) and for W-W perimetry and SWAP (Brenton and Phelps 1986; Jaffe et al. 1986; Johnson et al. 1988a). The absence of an age-related decline in sensitivity is likely to be due to the truncated age distribution of the study population: the majority of the individuals were older than 50 years of age.

The results show that FDT Full Threshold perimetry can be completed in less than half the time required to perform either W-W Full Threshold perimetry or SWAP with the Full Threshold Algorithm across each of the three groups. This can be attributed, in part, to the smaller number of stimulus locations and the MOBS staircase procedure used for FDT perimetry. The reduction in examination duration of more than 50% for FDT perimetry using the Full Threshold C-20 program compared to Full Threshold W-W perimetry with Program 24-2 is similar to previous reports (Kondo et al. 1998; Sponsel et al. 1998; Chauhan and Johnson 1999; Johnson et al. 1999). The shorter examination duration for W-W perimetry compared to that of SWAP using the equivalent program and thresholding algorithm is in accord with Wild et al (1998). As expected, but not previously published, FDT Full Threshold perimetry is also considerably quicker than Full threshold SWAP.

The study showed that the within-visit variability for FDT was similar to W-W perimetry. The variation in the Group mean TD across the visual field was greater for SWAP, particularly in the OHT group. An increased variability with increase in eccentricity concerning SWAP is already known (Wild et al. 1995; Sample et al. 1997b).

The results indicate a bias towards a higher Group Mean Sensitivity in the lower hemifield compared to the upper hemifield, although the asymmetry is minimal with FDT or W-W perimetry for the Normal and OHT groups. The findings are in agreement with Johnson et al (1999) for similar diagnostic groups. The asymmetry between each hemifield is greater, and increased with eccentricity for SWAP in agreement with Sample et al (1997b). The variation in Group mean Sensitivity is minimal across the central 20^{o} field for FDT in Normals and OHTs, which agrees with Chauhan et al (1999), and is similar to that for W-W perimetry. A slight decrease in sensitivity (not quantified) with increase in visual field eccentricity was found with FDT perimetry, however, using 54 stimuli locations in a 24-2 spatial arrangement (Johnson et al. 1999). The decline in sensitivity was probably identified by increasing the resolution of the stimuli locations. Group Mean Sensitivity decreased with eccentricity for SWAP, as found by Sample et al (1997b).

A perimetric strategy with high reproducibility is likely to be a better indicator of change and progression than one with large between-visit variability. The results show minimal variation between-visit for MD and PSD for each type of perimetry across the three diagnostic groups.

In the study, the pointwise TD results for FDT perimetry showed the best test-retest reproducibility for the POAG group, for the moderate to severely depressed locations (-16dB to –32dB). The pointwise TD (Figures 5.15 –5.17) and PD (Figures 5.18 – 5.20) test-retest values with W-W perimetry were more reproducible than either FDT perimetry or SWAP for the Normal group.

The between-visit variability for the Total Deviation and Pattern Deviation increased with increasing deviation for the OHT group and with increasing defect depth for the POAG group with each of the three perimetric tests. The variation with increasing TD and PD was minimal in the Normal group. The results agree with Chauhan et al (1999) for W-W and FDT perimetry. The results for the Normal group agree with the pointwise 1.0-1.5dB between-visit variability in sensitivity reported for FDT perimetry using a 54 location, 24-2 stimulus pattern (Johnson et al. 1999).

Since the repeated visual field examinations were performed within a one month period, fluctuations that occurred in the stable POAG group represent between-test variability and not actual change. An increase in defect depth attributable to progressive glaucomatous damage must be in excess of the expected between-visit variation. The results indicate that the pointwise between-visit variation is less for FDT perimetry than W-W perimetry for the moderately to severely depressed locations.

Efforts to compare the performance of the individuals within the groups across the three different perimetric modes in terms of accuracy prove difficult. The distribution in SWAP between-visit variability was truncated at approximately -18dB due to the limitations with the dynamic range of the instrument arising from the high background luminance levels required to ensure adequate isolation of the SWS pathway and an inadequate stimulus brightness. Therefore, comparisons between FDT or W-W perimetry and SWAP are not wholly appropriate in view of the SWAP design constraints.

The positive shift in the between-visit variability with increase in defect depth as defined by the TD and PD for the Normal group with each of the three perimeters suggested a small learning effect. The effect was also apparent in the OHT and POAG groups for W-W perimetry and SWAP but was absent with FDT perimetry. Learning effects for FDT perimetry are reportedly small (lester et al. 1999c) or negligible (Johnson et al. 1999). Similarly for W-W perimetry (Wild et al. 1989; Heijl and Bengtsson 1996; Anderson and Patella 1999) the learning effects are small for normals and at those locations in patients with glaucoma where the visual field loss is

minimal or severe. None of the global indices were dependent upon the sequence of perimetric tests undertaken , across the diagnostic groups.

The results showed that each of the Global indices were able to differentiate between the three diagnostic groups, irrespective of visit, with each of the three perimetric strategies. There was an overlap between the three groups for each of the global indices, within each type of perimetry. The findings agree with the overlap found with FDT and W-W perimetry between normals and those with glaucoma (Chauhan and Johnson 1999), and between individuals with OHT and those with POAG (Iester et al. 2000b).

A high level both of sensitivity and specificity is desirable for discriminating between those individuals with and without glaucomatous visual field damage. A high specificity is of considerable importance in those populations where the particular disease is relatively rare, as is the case with glaucoma. The HFA 24-2 or 30-2 program for W-W perimetry is almost invariably used as the 'gold standard' against which FDT perimetry is compared. A number of studies have reported favourable levels both of sensitivity and specificity. The magnitude of sensitivity and specificity increased with increasing severity of the glaucomatous damage. An initial study reported 93% sensitivity with 100% specificity using a Full threshold algorithm (Johnson and Samuels 1997). An 85% sensitivity and 90% specificity was achieved using the FDT Full threshold C-20 program for a group of individuals with glaucoma who exhibited a MD no worse than –6db for the HFA 30-2 W-W perimetry. This improved to 100% sensitivity and specificity for those with a MD with W-W perimetry of between –12db and –22dB (Cello et al. 2000). Selecting those individuals with moderate to severe glaucomatous visual field loss from a non-stratified group improved the sensitivity and specificity from 80% and 93% to 95% and 93% respectively (Patel et al. 2000). A population-based study against a gold standard of HFA 24-2 FASTPAC program, reported 92% sensitivity and 93% specificity (Yamada et al. 1999), whilst a clinic-based study which also used FDT perimetry in the screening mode but compared the results against a significant GHT result or CPSD probability score achieved levels of 91% sensitivity with 94% specificity (Quigley 1998).

Increasing the number of stimuli locations and reducing the size of the stimuli can provide better separation between the results for the normal and glaucomatous eye (Johnson and Samuels 1997; Johnson et al. 1999). It is unclear what effect the considerably fewer stimulus locations available with the C-20 program for FDT perimetry compared to the 24-2 programs with W-W perimetry and SWAP could have upon the subsequent follow-up of glaucomatous visual field loss.

5.17 Conclusions.

FDT perimetry is capable of discriminating between normals and those individuals with POAG in a similar manner to W-W perimetry and SWAP. The results for those individuals with ocular hypertension can lie between normals and those with POAG in FDT perimetry as already found with W-W perimetry and SWAP. However, the magnitude of the results for FDT perimetry should not be compared directly to W-W perimetry or SWAP.

The within-visit Global indices are more positive with FDT than either SWAP or W-W perimetry. Whether this is a consequence of the HFA-equivalent scale employed for FDT perimetry or an actual increased sensitivity to the stimulus employed in FDT perimetry remains to be clarified. The considerably shorter examination duration for FDT perimetry compared to W-W perimetry and SWAP, and the minimal variation in the Global indices between visits, across all diagnostic groups, suggests that fatigue and learning effects are negligible, but could be evident for individual stimulus locations. The between-visit variability in the global indices, MD and PSD is similar between each type of perimetry. The between-visit variability in TD and PD at individual stimulus locations is generally least for W-W perimetry, but increases more with increasing defect depth compared to either FDT perimetry or SWAP.

CHAPTER 6. RETINAL NERVE FIBRE ANALYSIS USING OPTICAL COHERENCE TOMOGRAPHY.

6.1 Normal variation of the Retinal Nerve Fibre Layer (RNFL).

6.1.1 Histological Composition of the RNFL.

The histology of the retinal architecture has been reviewed by Hogan (1971), Pollock (1986) and Jonas (1996). The ganglion cell axons within the retina are surrounded by a network of glial cells consisting of fibrous astrocytes, Müller cells, and microglia and by blood vessels. These structures form the retinal nerve fibre layer (RNFL). Within the RNFL, the astrocytes separate the unmyelinated receptive surfaces of the retinal neurons and their axons from adjacent nerve fibres. This separation prevents unwanted signals being generated in neighbouring neurons, and additionally provides the structural support with the Müller cell processes for the vessels and neurons. The astrocytes are large cells with many long processes and are predominantly located in the ganglion cell and inner plexiform layer, but are also present in the RNFL. The retinal arterioles and capillaries, situated within the RNFL, provide nourishment for the inner retina and for the Müller cell processes. The Müller cell processes provide structural support for the neural tissue and, in transverse section, are arranged in vertical, linear tunnels to partition groups of axons into bundles. The processes widen beneath the internal limiting membrane and their basement membranes form an undulating 0.5μm thick glial canopy. The basement membranes of the Müller and glial cells and the collagenous vitreous fibrils comprise the 1-2μm thick inner limiting membrane.

At the ONH, the glial support in the nasal and temporal regions is thicker and more regular than at the vertical poles (Quigley and Addicks 1982; Pollock and Miller 1986). The Müller cell processes, and to a lesser extent the astrocytes, constitute approximately 20-30% of a nerve fibre bundle (Hogan et al. 1971; Ogden 1983a). The amount of glial tissue varies across the retina, and is unrelated to the RNFL thickness (Ogden 1983b). The astrocytes are scattered throughout the RNFL. The density of the astrocyte nuclei is greatest in the arcuate regions and adjacent to the ONH (Ogden 1978).

The protective 'microglia', a specialised type of macrophage, are activated in response to injury to phagocytose tissue cells, bacteria and foreign debris (Forrester et al. 1996).

6.1.2 Horizontal Arrangement of the Retinal Nerve Fibres.

The distribution and course of the nerve fibres towards the ONH varies between individuals (Radius 1979). The ganglion cell axons are broadly organised spatially, both vertically and horizontally, within the RNFL. (Shields 1998). The nerve fibre organisation in the primate optic nerve, chiasm and optic tracts was demonstrated by Hoyt and Luis (1962) and in the primate retina and the ONH by Radius (1979) and Ogden (1983a).

Figure 6.1. Schematic diagram to show the horizontal and vertical distribution of the retinal nerve fibre bundles. The inset depicts the cross-sectional arrangement of the axons (from Shields 1998).

Fibres that originate within 0.5mm of the fovea are called papillomacular (Ogden 1984). It is accepted that the fibres from the nasal side of the macula follow a straight course towards the ONH, forming the papillomacular bundle (Hoyt and Tudor 1963). Those fibres arising temporal to the macula, arch around the papillomacular bundle and are directed to the superior, superior temporal, inferior and inferior temporal margins and neuroretinal rim of the ONH. A horizontal temporal raphe, anatomically forms the boundary between the superior and inferior halves of the retina and extends from the fovea to the peripheral temporal retina (Vrabec 1966; Pollock and Miller 1986) (Figure 6.1).

6.1.3 Vertical Arrangement of the Retinal Nerve Fibres.

Traquair (1949) reported minimal vertical spatial arrangement of the fibres. However, despite the suggestion that the peripheral axons rest upon the axons arising from ganglion cells closer to the optic disc (Polyak 1957; Ogden 1983a), it is now generally accepted that the peripheral axons lie deeper in the nerve fibre layer compared to the fibres arising from the peripapillary ganglion cells (Wolff and Penman 1950; Radius 1979; Minckler 1980; Airaksinen et al. 1981). The deeper fibres remain close to the outer borders of the optic nerve when entering the ONH (Figure 6.1). Nerve fibres exhibit no segregation or organisation within the bundles (Ogden 1984).

6.1.4 Diameter of the Retinal Nerve Fibres.

The axon thickness of midget cells range from 0.2μm to 2.5μm with a mean size of 1.0 ± 0.04μm, whilst parasol cell axon diameters range from 0.8μm to 4.2μm with a mean diameter of 1.6 ± 0.03μm (Weber et al. 1998). The axon diameter varies across the different regions of the primate retina (Ogden 1984). Relatively more small diameter fibres are present in the papillomacular bundle, whilst the nasal bundle includes a greater number of large diameter fibres. The relative proportions of large and small fibres are similar for the nasal bundles as they approach the ONH. The arcuate bundles acquire a greater proportion of smaller diameter fibres as they approach the ONH, and the papillomacular bundle a greater proportion of larger diameter fibres. Larger diameter fibres are associated with large ganglion cell bodies. The small, midget ganglion cells are highly concentrated within the foveal region and in the arcuate regions close to the ONH, whilst the larger parasol ganglion cells are scattered throughout the remainder of the ganglion cell layer (Silveira and Perry 1991; Dacey 1993b). The variation in the diameter of the fibres within each bundle can be attributed to the distribution of the ganglion cell sizes and their respective axons, and accounts for some of the regional variation in RNFL thickness. The number of nerve fibres within each bundle varies with region and between individuals. (Ogden 1984).

6.1.5 RNFL Thickness.

The RNFL thickness decreases with increasing distance from the ONH in monkey (Radius 1980; Ogden 1983b) and in human (Varma et al. 1996). It is thickest in the inferior and superior arcuate regions and thinnest in the temporal region in monkey (Radius 1980; Quigley and Addicks 1982) and in human (Varma et al. 1996; Dichtl et al. 1999). Histological measurements of the RNFL thickness in monkey range from 228-320μm within 100μm of the superior polar peripapillary region, 194-320μm in the inferior polar region, and is approximately 33μm thick in the temporal region and 37 μm thick in the nasal region. In the superior and inferior foveal margin region the RNFL is approximately 40μm thick, and the layer reduces in thickness to 5-9μm in the periphery (Radius 1980) (Appendix A.2).

The RNFL thickness in human measured at the optic disc border is 266 ± 64μm in the inferior quadrant, 240 ± 57μmin the superior quadrant, 220 ± 70μm in the nasal quadrant; and 170 ± 58μm. in the temporal quadrant (Dichtl et al. 1999). RNFL thickness reduces with increasing age (Varma et al. 1996). This can be explained by the constituent fibres declining in number with age (Balazsi et al. 1984; Mikelberg et al. 1989; Mikelberg et al. 1991). No association is present between disc area and RNFL thickness (Varma et al. 1996) (Appendix A.2).

6.1.6 Optical properties of the normal RNFL.

The RNFL has been studied with regard to the spectral (Knighton et al. 1989; Knighton and Huang 1999a), directional (Knighton et al. 1992; Knighton and Zhou 1995) and birefringent (Dreher et al. 1992) properties. However, the optical properties of the RNFL, and the mechanism by which it reflects light, are only partially understood. Practical evidence, and theoretical analysis (Zhou and Knighton 1997) suggests that, optically, the RNFL behaves as a series of approximately parallel cylinders. In the toad, (Knighton and Zhou 1995), whose RNFL contains a higher proportion of small unmyelinated axons compared to humans, the reflectance of the RNFL is proportional to the thickness and declines linearly with distance from the ONH. The relationship between reflectance and thickness depends upon the regular parallel arrangement of the fibres and the incident angle of the illuminating light. Clinically, the reflections from the nerve fibre bundles as viewed by ophthalmoscopy, brighten as they approach the ONH (Pollock and Miller 1986). The RNFL in human and in macaque exhibits linear birefringence parallel to the direction of nerve fibre bundles. The retardation of polarised light incident on the birefringent RNFL is proportional to the histological measurement of the RNFL thickness (Weinreb et al. 1990; Morgan et al. 1998). Animal studies have shown that the RNFL has both a directional and a spectral variation in the reflectance properties (Knighton and Huang 1999a). The highly directional nature of the reflectance at all wavelengths indicates that the reflectance arises from light scattering by cylindrical structures (Knighton and Huang 1999a). The directionality is a significant potential source of variation in measurements derived from reflectance data. The nature of the reflectance is dependent upon both the diameter of the cylinders and the wavelength of light used (Knighton and Huang 1999a). Evidence suggests

that the RNFL reflectance arises from a bi-modal distribution of cylinder diameters (Knighton and Huang 1999a). The reflectance from thin cylinders (of the order 0.02μm) is believed to dominate the reflectance pattern at short wavelengths, whilst the reflectance primarily arising from cylinder diameters of 0.35-0.90μm predominates for wavelengths longer than approximately 680nm (Knighton and Huang 1999a). Examples of small diameter cylindrical elements include the intra-axonal mitochondria or the extra-axonal glial processes, whilst the large diameters may include single axons, or bundles of microtubules (Zhou and Knighton 1997). It can be argued that different structures may be assessed by RNFL photography employing a blue (495nm) or green (540nm) exciter filter compared to confocal scanning laser ophthalmoscopy (670nm), or compared to scanning laser polarimetry (780nm) or compared to optical coherence tomography (830-850nm).

It would seem possible that RNFL regions with different distributions of nerve fibre size, due to either physiological or pathological causes, might be recognised by comparing the reflectance properties of the given RNFL as a function of wavelength. Interestingly, a temporal variation in RNFL appearance has been documented in rat, suggesting a dynamic change in the size of, or spacing between, the scattering cylinders (Knighton and Huang 1999b). The optimum choice of wavelength and polarisation for the illuminating beam may, in future, need to be based upon the normal and abnormal optical state of the tissue under investigation.

The retinal pigment epithelium and choroid demonstrate a high level of background reflectance. These layers are not regularly arranged spatially and their contribution to the reflectance distribution from the deeper penetrating, longer wavelengths can be a significant source of measurement variation (Knighton and Huang 1999b).

6.1.7 Clinical assessment of the normal RNFL.

Resolution of an individual axon, with a diameter less than 20μm, is not yet clinically feasible. However, as the axons converge on the ONH, the faintly opaque nerve fibre bundles may be recognised ophthalmoscopically, as fine 'brush-strokes' or striations contrasted against the underlying pigmented tissue. Radius (1979) showed histologically that the striations represented individual axon bundles within the nerve fibre layer. The dark bands correspond to the glial supportive tissue and the bright bands to the axon bundles. The nerve fibre bundle visibility is normally greatest in the inferior temporal arcuate retinal regions, fading towards the periphery and ceases in regions of atrophy, and can be attributed to the variations in the thickness of the RNFL (Jonas and Dichtl 1996). A minimum thickness of 20μm for the RNFL is necessary for the observation of the striations (Quigley and Addicks 1982). Several other factors, including fundal pigmentation (van Norren 1986; Delori 1989) and appropriate illumination (Airaksinen et al. 1985a; Peli et al. 1987) determine the nerve fibre bundle visibility. A lightly pigmented retinal epithelium poorly outlines the RNFL and, in general, the darker the background, the greater the contrast and visibility of the RNFL. The use of red-free ophthalmoscopy was originally proposed

by Vogt in 1913 (Vogt 1913), but it was during the 1970's that Hoyt expounded the virtue of red-free illumination, and this was later combined with photography (Hoyt et al. 1972; Hoyt and Frisen 1973). The best results have been obtained with black-and white, high resolution, fine-grain film and a narrow-band interference filter of 495nm or 560nm wavelength. However, optimum choice depends upon the fundal pigmentation and clarity of the ocular media. A blue filter provides better contrast for those with lightly pigmented fundi whilst a green filter minimises the light scatter encountered in cataractous patients (Frisen 1980; Sommer et al. 1983; Airaksinen et al. 1985a; Peli et al. 1987).

Several instruments purport to provide a measure of the RNFL thickness. The Rodenstock Optic Nerve Head Analyzer and the Heidelberg Retinal Tomograph derive the RNFL thickness based upon a height value determined relative to the surrounding area. These techniques rely upon the determination of a reference plane. The validity of the technique therefore depends upon the choice and stability of the reference plane. The GDX Nerve Fibre Analyzer measures the retardation of polarised light double-passed through the RNFL. The retardation is assumed to be proportional to the tissue thickness. The theory assumes a regular arrangement of the NFL tubule structure, scan penetration at least through the RNFL, and stable and predictable polarising characteristics of the normal and abnormal RNFL.

6.2 Variation in RNFL composition and thickness with glaucoma.

Knowledge of the changes in tissue arrangement and composition, with glaucoma, is essential prior to the development of any technology for clinically quantifying the RNFL thickness.

6.2.1 Histological findings associated with RNFL damage in glaucoma.

The histological evidence for the pattern of RNFL degeneration in glaucoma has been acquired from experimental damage induced in monkey and from post-mortem human tissue (Wolter 1955; Radius and Anderson 1979; Dichtl et al. 1999). Focal retinal damage induced by photocoagulation in monkey (Radius and Anderson 1979) causes marked cystic degeneration of the RNFL within one week and leads to a disruption of the regular arrangement of the microtubules. The loss of axons over the ensuing four-week period was evident clinically by the rapid decline in the visibility of the retinal striations. Müller cell processes remained in the attenuated RNFL and the degenerative axons were absorbed (Radius and Anderson 1979). In one human retina a dense network of large proliferative astrocytes replaced the axons following the rapid development of advanced glaucoma (Wolter 1955). Histomorphometric analysis (Dichtl et al. 1999) of 21 patients with end stage glaucoma, showed that 40±18μm of mean overall RNFL tissue remained for the peripapillary regions despite presumed total axonal loss.

6.2.2 Clinical Assessment of RNFL damage in glaucoma.

It is difficult to visualise the striated pattern of the faintly opaque nerve fibre bundle by ophthalmoscopy or with standard fundus photography. However, Hoyt and colleagues (1972; 1972) described narrow slit-like nerve fibre layer defects by direct ophthalmoscopy and red-free light in glaucoma. Using gradings of RNFL photographs, Quigley et al (1980) found a sensitivity of 84% and specificity of 97% for glaucomatous defects. Other localised changes which include large wedge-shaped defects, and diffuse defects in the RNFL have also been identified (Sommer et al. 1984; Quigley 1993). Airaksinen et al (1984) evaluating RNFL photographs, identified both diffuse and localised defects in glaucoma patients and a high proportion of purely localised defects in ocular hypertensive patients.

The pattern of the earliest glaucomatous changes to the optic disc is equivocal and has been reported as a generalised enlargement of the cup (Pederson and Anderson 1980; Jonas et al. 1988c; Tuulonen and Airaksinen 1991), or a primarily focal notching of the NRR (Odberg and Riise 1985). Focal or generalised thinning of the NRR is related to the number and distribution of the nerve fibre bundles within the ONH which, in turn, is related to the number of ganglion cell axons and the consequent RNFL thickness. The initial damage to the RNFL can either be a focal, wedge-shaped defect (Sommer et al. 1977), diffuse thinning (Tuulonen and Airaksinen 1991) or a combination of each. Generally, diffuse RNFL thinning is associated with diffuse ONH damage whilst wedge-shaped RNFL defects occur with focal notching. Tuulonen et al (1991) found focal and diffuse changes at similar stages in the course of RNFL damage. Some studies have suggested that the pattern of RNFL and ONH damage is dependent on the level of the IOP (Iwata 1979; Shiose et al. 1987; Sogano et al. 1993) whilst others have disputed this suggestion (Pederson and Anderson 1980; Tuulonen and Airaksinen 1991).

Currently, there is no satisfactory clinical 'gold standard' for the absolute measurement of the parapapillary RNFL thickness. Confocal scanning laser ophthalmoscopy with the HRT, (Mikelberg 1993; Weinreb et al. 1993; Rohrschneider et al. 1994; Chauhan and Macdonald 1995; Mikelberg 1995; Asawaphureekorn et al. 1996; Malinovsky 1996; Orgül et al. 1996; Uchida et al. 1996; Zangwill et al. 1996; Iester and Mikelberg 1997; Bathija et al. 1998; Chauhan and Johnson 1999) provides relative values for these regions.

It had been hypothesised that the HRT parameter, HVC might identify focal damage to the RNFL. However, the HVC has poor ability to discriminate between normals and glaucomatous patients (Hatch et al. 1997). In addition, the HVC has shown poor reproducibility being grossly affected by individual pixel measurements (Mikelberg 1993; Chauhan and LeBlanc 1994). The, HRT parameter, Mean Height Contour (the average of all the height measurements of the contour line), the forerunner of the mean RNFL thickness, can discriminate between normals and glaucomatous patients (Tsai et al. 1995b; Hatch et al. 1997).

The regular arrangement of the axons within the RNFL, causes linear polarisation of illuminating light (Weinreb et al. 1990; Tuulonen and Airaksinen 1996). The Nerve Fibre Analyzer (NFA) utilises the birefringent properties of the RNFL to provide an assessment of RNFL thickness. The instrument combines a confocal scanning diode laser ophthalmoscope of 780nm wavelength with an integrated polarimeter to provide a controllable source of polarised light (Weinreb et al. 1990; Dreher et al. 1992). The near infrared polarised beam undergoes a double pass through the RNFL and reflection occurs at a deeper layer within the retina, presumably the retinal pigment epithelium. The resultant state of polarisation (retardation) of the reflected light is assumed to be linearly related to the relative thickness of the RNFL (Weinreb et al. 1990). The measurements, although not absolute, are considered to be free of magnification errors and are independent of a reference plane. Early within-operator reproducibility showed the CoV to range from between 3.6% and 4.5%, to 10.20% (Chi et al. 1995; Weinreb et al. 1995b). The mean difference (±SD) between operator is quoted as 17.4 ± 6.4μm (Swanson and Lynn 1995). An early study attributed the wide between-operator variability to poor patient alignment, quality and distribution of illumination and focussing (Swanson and Lynn 1995). An improved design, the NFA II rectified some between-operator variability and a corneal compensator is incorporated to reduce corneal- and lens-induced polarisation artefacts (Junghardt et al. 1996; Hoh et al. 1998). An additional optical detector is included to measure the total intensity of the reflected light and used to scale the detected polarised light to minimise the variation in illumination intensity settings (Hoh et al. 1998). The variation in parapapillary RNFL thickness surrounding the ONH determined by the NFA is characterized by a double-hump pattern. The peaks correspond to the superior and inferior arcuate nerve fibre bundles (Dreher et al. 1992; Weinreb et al. 1995b; Tjon-Fo-Sang et al. 1996). A modest relationship exists between the magnitude of the retardation and histopathological measurement of monkey RNFL (Weinreb et al. 1990; Weinreb et al. 1995b), particularly inferiorly (Morgan et al. 1998). The relationship between the amount of retardation and age is equivocal (Chi et al. 1995; Tjon-Fo-Sang et al. 1996; Poinoosawmy et al. 1997; Choplin et al. 1998; Funaki et al. 1998). The retardation reduces with increase in distance from the disc margin, as expected with thinning of the RNFL (Chi et al. 1995; Weinreb et al. 1995b; Poinoosawmy et al. 1997). Retardation values are also lower at the crossing of major blood vessels (Weinreb et al. 1995b), where the vessels are known to lie amongst the axonal bundles. The distribution of the magnitude of the retardation values corresponds to known distribution of the thickness of the RNFL in normal, ocular hypertensive and glaucomatous eyes and to the polarizing properties of the RNFL. Funaki et al (1998) reported that the size of the optic disc was related to the retardation of the peripapillary RNFL. The retardation within a normal population is reduced in Blacks compared to age- and gender-matched Whites (Poinoosawmy et al. 1997; Tjon-Fo-Sang and Lemij 1998). The latest version of the Nerve Fibre Analyzer, the GDx Glaucoma Scanning System, has accounted for the racial difference by incorporating a correction for racial origin.

The mean retardation values are higher in normals compared to ocular hypertensives (Tjon-Fo-Sang et al. 1996) and, as would be expected, in glaucomatous eyes (Weinreb et al. 1995b;

Choplin et al. 1998). However, there is considerable overlap in the distribution of the values between all three groups. The relationship between NFL retardation and the extent of visual field damage expressed in terms of the visual field indices is equivocal. Weinreb et al (1995a) reported that the retardation ratio decreased with a worsening of the MD index, measured both globally and regionally. Marraffa et al (1997) found a reasonable correlation between the MD for the superior region and the retardation values from the inferior retina. Chen et al (1998) also reported a moderate correlation between the MD and the nerve fibre layer retardation. In normal-tension glaucoma patients exhibiting hemifield loss, the retardation was significantly lower in the region corresponding to the field defect (Reyes et al. 1998). However, there was also evidence of retardation in the unaffected regions. Other reports, have shown poor correlation (Tjon-Fo-Sang and Lemij 1997). Niessen et al (1996) found little correlation between the results from red-free photography and from polarimetry.

6.3 Optical Coherence Tomography (OCT).

Applications of the single-beam, B-scan OCT system, include both anterior and posterior imaging, of the normal and abnormal eye (Huang et al. 1991; Hee et al. 1995b; Hee et al. 1995a; Hee et al. 1995c; Hee et al. 1995d; Hee et al. 1995e; Puliafito et al. 1995; Schuman et al. 1995a; Baumann et al. 1998; Hee et al. 1998).

6.3.1 Optical Principles of OCT.

The technical details of OCT have been fully described (Huang et al. 1991; Swanson et al. 1993; Hee et al. 1995b; Schuman et al. 1995b; Puliafito et al. 1996), and are summarised below. Analogies are generally drawn between the OCT optical system and the acoustic equivalent A- and B-scan ultrasonography. Echo-delay with ultrasound can be directly measured as the velocity of sound is far slower than light; however, the depth resolution is limited by the wavelength of sound, in ocular tissue, to about 150 μm. Whilst high-frequency ultrasound can improve the resolution to about 20μm, the limited penetration restricts the use to anterior segment applications. OCT imaging, unlike ultrasound imaging, requires no physical contact with the eye. The imaging procedure of OCT is based upon the optical principle of echo-delay using a superluminescent, near infra-red wavelength, diode laser (830-850nm). The velocity of light is very high, so that echo-delay cannot be directly measured electronically. Instead, low coherence interferometry is employed.

Interferometry is based upon the use of interference patterns. When the waveforms from two coherent sources of light are brought together, the combined effect can be predicted by the principle of superposition, in which the particle displacements at a point due to each individual coherent light source can be algebraically summed. Coherent light sources are those which have exactly the same frequency and amplitude of particle vibration and whose vibrations are always in phase with each other. However, if one of the wavefronts is delayed, as a result of passing through a denser medium, travels a longer distance, or undergoes reflection at a

denser medium, the phases can become mismatched. The degree of mismatch indicates the optical path difference. Provided that the path difference between the two original sources is a whole wavelength, the interference remains constructive. If the waveforms are 180° out of phase the resultant effect is zero as the displacements at any instant are equal and opposite to each other. This is known as destructive interference.

In the case of light sources, coherence is difficult to achieve between independent sources; therefore, the use of a single source with a double or multiple narrow slit aperture is employed to create two or more light beams. Alternatively, a biprism or beamsplitter can be used to separate the beam.

By comparing the time delay created between two optical beams of identical origin, one travelling a known reflected distance, and the other an unknown reflected path distance, tissue separation can be assessed. The measurement of time-of-flight delays for light signals reflected from surfaces or interfaces, otherwise known as optical time domain interferometry or reflectometry is normally limited to a few centimetres. The use of optical low coherence domain interferometry to localise reflective interfaces within the eye and retina by delays in time-of-flight for a known light beam significantly improves the resolution to a micron-scale (Youngquist et al. 1987). The coherence length limits the length of the optical path delay for which interference patterns can be demonstrated. The low coherence attribute of the incident beam ensures that the strength of the signal declines markedly with poor matching from the phase delay of the returning signal. This permits the longitudinal location of reflecting structures to be identified with a greater resolution than for completely coherent sources. The interferometric signals are only detected when the reference and sample beams closely match when recombined. A resolution of 10μm and an optical dynamic range of 100dB or more can be achieved.

The basic principle involves a partially reflecting mirror within an interferometer, which splits the light output from a low-coherent source. A probe beam travels a distance L_s, and is reflected back from the tissue and returns to the mirror. Simultaneously, a reference beam travels a distance L_r, is reflected from a reference mirror and returns to the beam splitter. The two beams are recombined at the beamsplitter, and their interference effects ($L_r + L_s$) are collected by a photodetector (Figure 6.2a) (Puliafito et al. 1996). A confocal optical system isolates the primarily backscattered light from the unwanted reflections by illuminating a small retinal region and capturing the returning light almost exclusively from the same point, through a series of apertures that excludes non-conjugate sources (Figure 6.2b).

An interference signal occurs when the distance travelled by both beams is within the source coherence length. The intensity of the interference pattern measured by the detector oscillates with the path length difference between the reference and sample paths. When the path length is a whole optical wavelength, constructive interference occurs and the signal has maximum intensity. If the difference is half a wavelength, the interference is destructive and the intensity

detected is minimal. The coherence length of the source determines the longitudinal resolution that equates to approximately 10μm in the retina, or 14μm in air, assuming a constant refractive index of 1.36 within the retina.

Huang et al (1991) proposed the creation of two-dimensional, cross-sectional images from three-dimensional structures (tomography) using low coherence interferometry. This involved the in vitro acquisition of a series of sequential, uniaxial reflectivity profiles across the human retina which were subsequently aligned to form a B-scan image.

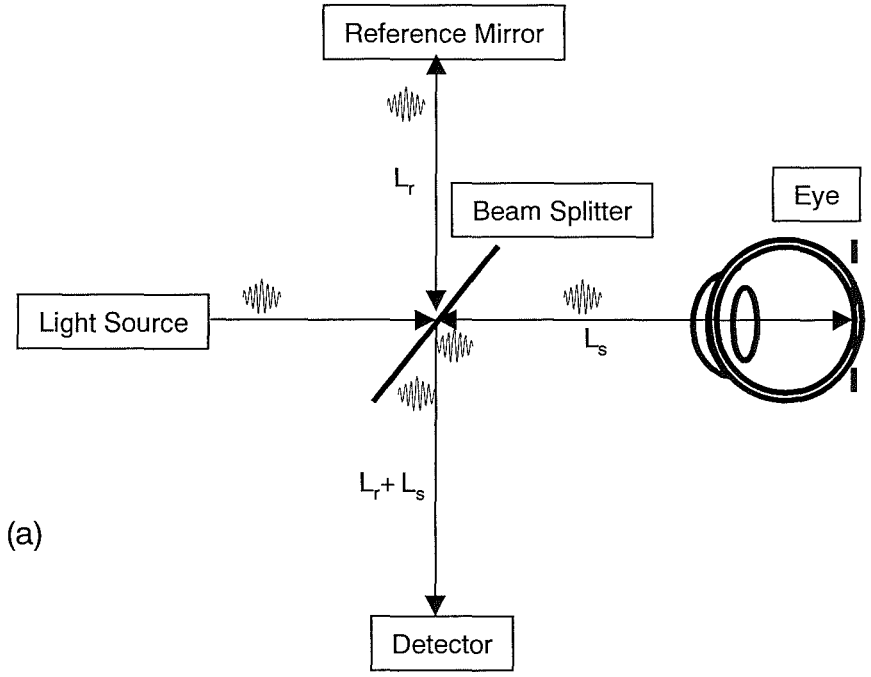

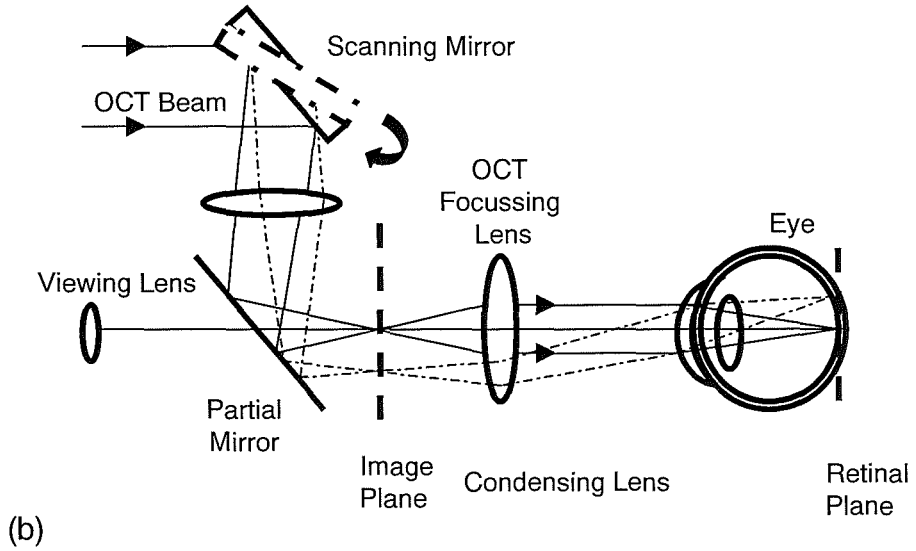

Figure 6.2. Schematic diagrams to show (a) the use of low-coherence interferometry to measure small distances, in vivo, within the human eye, and (b) the OCT optical system used for transverse scanning of the retina (after Puliafito et al. 1996).

(a) An OCT circular scan performed around the Optic Nerve Head

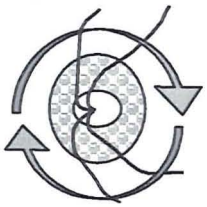

(b) Example of a single A-scan. The boundary locations of the upper RNFL surface (1) and the RPE/choriocapillaris layer (2). The 'noise' intensity level (3) and the 'threshold' intensity level determined by the software algorithm (4). The lower boundary of the RNFL layer determined by the algorithm (5). The RNFL thickness is equivalent to the distance (1) to (5).

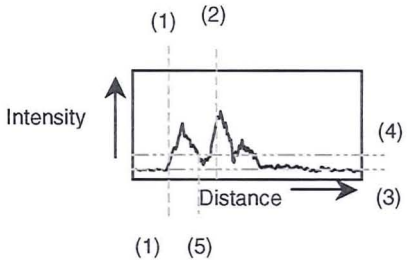

(c) OCT colour-coded reflectivity image with image interpretation of stratified appearance (after Toth et al 1998).

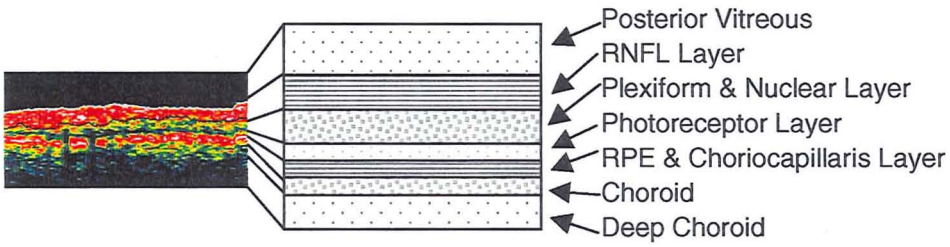

(d) OCT RNFL thickness for a circular 1.5 R scan centred on the ONH derived from 100 'A-scans' as a function of region presented in graphical form (Nasal, Superior, Temporal, Inferior, Nasal) and as sector data.

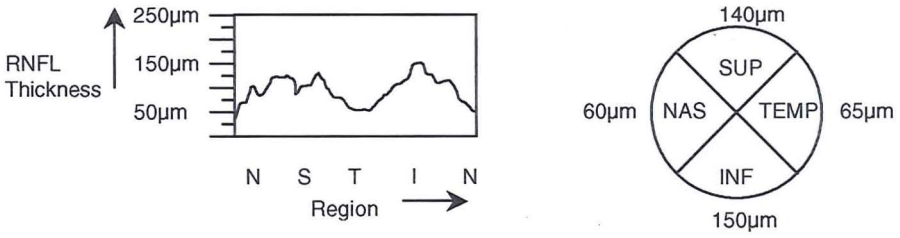

Figure 6.3. A series of schematic diagrams to show the processes involved in generating the OCT derived RNFL thickness data.

6.3.2 Construction of a Tomographic Image.

An A-scan profile is constructed of reflectivity against penetration of the incident beam into the neurosensory retina to a depth of approximately 250-300μm. The profile is derived by rapidly varying the length of the reference optical delay path and measuring the interference signal. For the commercially available OCT system (Manual-OCT 1996), a series of 100 A-scans, in a circular path, are obtained across the retina, centred on the ONH, and are combined to form a two-dimensional B-scan image (Figure 6.3a & 6.3b) The reflectivity images are digitised, aligned and false colour-coded for presentation and ease of interpretation. The colour indicates the relative logarithmic level of reflectance (Figure 6.3c).

The series of A-scans can be delivered in a linear or circumlinear arrangement. The linear option can be used singly; repeated; radially orientated; as a cross-hair; as a series of 6 raster lines or as a continuous rectangular scan. The length of each linear scan can be varied from 1.17mm to 7.27mm. The circumlinear option can be used as a single or repeated circular scan; as a composite circle created by 4 arc scans; with a fixed or variable radius; or as 1.5 or 2.0 times an operator-selected radius (an option suitable for peripapillary evaluations). The radius of each circular scan can be varied from 0.48mm to 5.80mm.

6.3.3 Interpretation of a Tomographic Image.

The processed images from a scan show two relatively highly reflectance (RHR) bands, in 'warm' colours, separated by a thin relatively low reflectance (RLR) band in 'cooler' shades. OCT uses the time delay of the backscattered light to determine the depth of the retinal layer interfaces. The reference planes are provided by the edge detection of the highly reflective vitreoretinal and pigment epithelium/choriocapillaris interfaces (Figure 6.3c). Algorithms in the computer software use thresholds to identify the changes in reflectance to delineate the retinal and nerve fibre layer boundaries. In the case of the RNFL measurements, the upper limit of the first reflective band is delineated in the commercial software by a thin white line. The lower limit is determined by the algorithm within the software and is designated by a thin blue line. The distance between the white and blue lines is considered to represent the RNFL thickness. The software provides a profile of the variation in RNFL thickness in the scanned region and summarised values for the average global RNFL thickness and also for each of four sectors (Figure 6.3d).

Interpretation of the images involves the identification of differences in the relative reflectivity of different tissue layers arising from morphological changes in the tissue. The apparent reflectivity measured by the OCT is a combination of the actual reflectivity and the scattering and absorption characteristics of overlying tissue. The apparent reflectivity of the outer retinal layers, retinal pigment epithelium and choriocapillaris are affected by the optical transparency of the cornea, anterior chamber, crystalline lens, vitreous chamber and the inner retinal layers (Puliafito et al. 1996) (Figure 6.3c).

Scarred or hazy cornea; dense cataract and in particular posterior subcapsular cataracts; and poor instrument alignment cause a diffuse hypo-reflectivity for all retinal layers and for the choroid. Small pupils and vitreous opacities cause full thickness local losses of all the layers, but the region affected can dynamically change as the alignment of the scanning beam is altered. Focal areas of hypo-reflectivity can be created beneath discrete areas of hyper-reflectivity. Blood or hard exudates have high scattering coefficients which are seen as enhanced regions of reflectivity, with marked attenuation of the incident light creating a 'shadow' and obscuring any detail beneath. Serous fluid is optically transparent and is often recognised by an area devoid of backscatter but surrounded by a reflective border (Puliafito et al. 1996). The morphology and organisation of the reflective layers potentially provides a pictorial representation of the pathogenesis of retinal disease.

6.3.4 Assumptions concerning the derivation of a Tomograhic Image.

A number of assumptions are associated with the image acquisition and subsequent analysis. The angle of the incident light is considered to be normal to the tissue surface, and the signal to undergo linear attenuation as it crosses a presumed homogenous nerve fibre layer (Puliafito et al. 1996). The characteristics of the signal at each retinal interface are assumed to be predictable and that only purely back-scattered reflected light is detected. The polarising effect of the nerve fibre bundles is assumed to be uniform across the entire scanned surface and the effect on the interference patterns to be predictable.

6.3.5 Axial resolution of the Tomographic Image.

The axial resolution of the OCT scan is related to the properties of the diode light source, in particular the coherence length of the light generated (Puliafito et al. 1996). The transverse resolution is dependent upon the width of the optical beam focussed on the retina and upon the spacing between adjacent scans and subsequent pixels in the resultant tomogram. For a 3.4mm diameter, 360° circular scan, with a circumference of 10.7mm, the transverse resolution using a total of 100 'A'-scans is approximately 87μm and the axial resolution approximately 10μm. The 'arc' angle between each pixel is about 3.6°.

6.3.6 Optimisation of a Tomographic Image.

Huang et al (1991) recommended careful angular alignment to achieve near normal incidence when assessing specular surfaces such as retinal tissue boundaries, as the reflected signal is angular dependent. This effect is particularly evident at the optic nerve head margins where the nerve fibres turn away from the scanning beam to enter the scleral canal. The use of infrared or near infrared illumination can improve the imaging of subretinal features as they permit increased penetration of the tissue for deeper layer analysis. Such a technique increases the reflectance and yet minimises the amount of light exposure thereby ensuring ocular safety.

Merely increasing the light levels does not, necessarily, provide better visibility of the structures since sufficient relative contrast between the different tissue types is required to allow the designated features to be discerned within the image.

The fibre-optics used in the commercial model of the OCT does not emit, or collect, light with a well-defined state of polarisation (Personal communication with A Kirschbaum, Humphrey Systems Inc.). An adjustment facility is available on the operators' console to allow for alteration of the signal strength and polarisation state in order to optimise the returning signal.

The optical basis of the OCT system potentially allows the polarisation and wavelength-dependent optical properties of the retina to be independently explored (Huang et al. 1991; deBoer et al. 1997; Lexer et al. 1997). Polarisation of the incident light arising from the birefringent properties of the retina is used to enhance the distinction between layers but could theoretically be used as an indicator of structural change, should the degree of polarisation significantly alter.

Position of the scans, optimisation of the reflectance patterns and exclusion of poor quality images is highly operator dependent. However, the subsequent RNFL boundary recognition and RNFL thickness measurements are determined by the OCT software and are therefore independent of the operator.

6.3.7 Accuracy and Reproducibility of OCT measurements.

Measurements of retinal thickness and RNFL thickness derived by a prototype OCT using five repeated parapapillary circular scans and also internal fixation, exhibit a reproducibility of approximately 5-9μm for overall retinal thickness and 10-20μm for overall RNFL thickness (Schuman et al. 1996). The within-subject variation can be minimised by using at least three scans (Schuman et al. 1996). A Coefficient of Variation of 11.9%, for measurement of the RNFL thickness in areas associated with field loss can be achieved by increasing the sampling density four-fold (Gurses-Ozden et al. 1999). The magnitude of the Coefficient of Variation is thought to be dependent upon the thickness of the measured tissue (Gurses-Ozden et al. 1999). The magnitude of the between-individual variation may still limit the detection of early glaucoma (Schuman et al. 1995b). The within- and between-individual and the within- and between-visit variation using the commercial model of the OCT has not been fully investigated.

6.3.8 Validity of the OCT Image.

Evidence for good correlation of OCT results and retinal histological studies permit the clinical application of RNFL evaluation. Huang et al (1991) used a single human cadaver eye acquired through an eye bank, whose cornea and lens had been removed prior to the scans. The quantitative and qualitative data for the RNFL and underlying retinal tissue were comparable between histological and OCT findings.

Visual inspection of the false-colour coded displays for cross-sectional OCT images and corresponding histological sections in monkey (Toth et al. 1997) and chicken (Huang et al. 1998) eye have suggested a close relationship between the reflectivity patterns and the retinal layers. Toth et al (1997), in a comparison of retinal morphology using OCT and light microscopy for primate eyes, found a relatively high level of reflectivity arising at the presumed RNFL. The depth of the apparent RNFL corresponded to the NFL thickness as determined by microscopy, and reduced in thickness with increase in eccentricity from the optic disc margins. The differences between the relatively high reflective regions (RHR) and the relatively low reflecting regions (RLR) has been attributed to the orientation of microtubules within the tissue, the size of the elements and the structure of the various components within the layer.

OCT scanning and imaging is based upon the reflectivity and backscatter properties of retinal tissue, which differs from the optical properties encountered in histological sections. The stratified appearance of the OCT scan cannot provide the same degree of resolution for structural analysis that light microscopy can offer. However the advantage of OCT lies in the non-invasive nature of the technique.

OCT yields the expected characteristic variation in the topography of the RNFL (Schuman et al. 1995b; Gramer and Dirmeyer 1998), and the decline in thickness with age (Schuman et al. 1995b; Gramer and Dirmeyer 1998). The technique can detect focal glaucomatous damage (Pieroth et al. 1999).

6.4 Aims.

The aim of the study was twofold. Firstly, to determine the within- and the between-visit variability for OCT of the RNFL thickness as determined by the Humphrey Systems Optical Coherence Tomography Scanner (OCT), for both global and sector evaluation, as a function of the type and number of circular scans. Secondly, to determine the relationship between the RNFL thickness, derived by global and sector evaluation, and age, diagnosis and the functional and structural integrity of the eye thereby providing information on the validity of the technique of optical coherence tomography.

6.5 Sample.

The sample comprised 26 normal volunteers, 27 patients with ocular hypertension (OHT) and 23 patients with stable primary open-angle glaucoma (POAG). The mean age of the Normal group was 56.0 (SD 17.9) years of the OHT group 65.2 (SD 10.4) years and of the POAG group 67.9 (SD 10.1) years.

6.6 Methods.

The OCT scans were acquired using the commercially available Humphrey Optical Coherence Tomography scanner, OCT 2000 incorporating software version A4.1. For each subject, the age, axial length (obtained using A-scan ultrasound) and best sphere refractive correction was input into the instruments database prior to scanning.

A series of 3 different circular scans were chosen from those available in the instrument menu: the ONH 1.5R scan and the ONH 2.0R scan, where R represents the given radius of the optic nerve head, and a fixed radius of 1.73mm.

The subjects were positioned comfortably with their head resting within the instrument's headrest. The optical axis of the scanning unit was aligned with the subject fixating the internal fixation target. The internal fixation light was a 36 x 16 green LED matrix which reportedly offers superior reproducibility compared to an external fixation target provided the fixating eye has an acuity of 6/9 or better (Hee et al. 1995b). The scanning unit was positioned approximately 9mm from the corneal surface. The real-time video image of the fundus was focused on the viewing monitor and the ONH was centred on the screen. The landmark locator was positioned on a suitable vessel bifurcation on the nerve head.

The given scan was aligned concentrically with the ONH margin and the scan radius adjusted to the maximum radius of the given ONH. The software then automatically increased the scan radius to the required retinal location. The landmark location and position of the scan were then fixed relative to each other. The scanning process was then instigated. The z-offset was adjusted to centre the cross-sectional scanned image on the display. The polarisation state of the illuminating beam was adjusted to maximise the reflectance values. A series of continuous scans were generated until an uninterrupted scanned image was obtained. Tear film irregularities which interfered with the quality of the scan, and which were attributable to excessive scattering of the signal at the corneal and pre-corneal tear interfaces, were minimised by asking the patient to blink as necessary. The image was then digitally frozen and the quality assessed for artifacts caused by overlapping of successive scans, vignetting from overlying structures, lid artifacts or overall low reflectance values for the two high reflectance bands. A good quality image was saved to the hard drive. The duration of a given scan was 2 seconds and the time to save the image to the hard drive was 20 seconds. Seven good quality images were acquired within each session. Each subject was briefly rested between each scan. The subjects were encouraged to remain in the same head position. Correct alignment of the landmark position was monitored throughout the session. The seven scans required at least four minutes for acquisition under optimum conditions. A signal-to-noise level of at least 45dB was necessary for each scan in order to ensure reliable recognition of the relevant boundaries by the software.

To assist in obtaining reproducible results from consecutive and repeat scans with independent visits, a number of systems are employed. Using a x, y co-ordinate system the scan beam position is stored relative to the patients' fixation co-ordinates. A landmark illuminated spot is projected onto the examinees fundus and positioned by the operator, whilst viewing the live fundus image on a monitor, onto a clearly recognisable anatomical feature, a vessel bifurcation is commonly chosen.

The relative location of the landmark position and the OCT circular scan line are recorded and stored by the instrument software for each individual scan, at an initial visit, and can be retrieved and re-implemented at subsequent visits.

To reactivate the same initial scan settings a previous scan is selected from the list of existing scans and the 'repeat scan' option is selected. The initial landmark and OCT scan beam parameters are automatically provided. Both can then be moved simultaneously by operating the trackball on the instrument console panel, to ensure that the landmark remains aligned to a pre-chosen retinal feature. A blood vessel bifurcation within the ONH was chosen for the identifying feature at the first visit, and maintained throughout.

Choosing the repeat scan option should ensure that the landmark position is relocated consistent with a previous landmark position employed at a previous visit, and was recommended for longitudinal studies.

For the study, on the first scan for the first visit, the operator defined the landmark and scan positions. Sequential images were obtained without redefining the scan parameters, and the landmark position. Minor lapses in fixation of the subjects eye, which inevitably occurred throughout the scanning process, required appropriate corrective movement of the landmark position which was achieved by manipulation of the trackball.

At the second visit, the 'repeat scan' option was chosen to provide the same location of the landmark that had been defined on the first image of the initial visit. Once again, the landmark position was maintained on the same retinal feature for the series of sequential scans.

Early imaging attempts had suggested that the 'repeat scan' option gave marginally improved between-visit results, than a totally independent landmark position, although not proven statistically. Therefore, the repeat scan option was employed whenever possible for the repeated visits. In 15 individuals the software generated, for at least one set of second visit scans, a landmark-scan position that was slightly offset, such that the scan was not exactly concentric to the ONH. Undoubtedly the parapapillary retinal location scanned would then differ from the original choice, and would lead to an erroneous measure of between-visit variability in RNFL thickness measurements. In those cases the landmark position and scan were repositioned, locked relative to each other and then used for the series of seven images.

The images were analysed by the OCT software and the RNFL thickness was derived by the proprietary algorithms within the software. For the circular scans, a global measure of RNFL thickness is obtained, a mean RNFL thickness for each of 12 clock hour segments, and a mean for each of four 90° quadrants arranged in a St. Andrews cross orientation. The global and quadrant RNFL thickness for each scanned image for each individual were manually transferred to an Excel spreadsheet.

The mean of the seven Global and Sector RNFL thickness estimates was calculated for each individual, for each of the three scan radii for each of the two visits.

6.7 Analysis.

6.7.1 Global Analysis.

The within-visit between-individual variation was expressed in terms of the Coefficient of Variation (CoV) for each individual for each scan radius and in terms of the cumulative distribution of the within-individual SDs.

The within-group between-visit agreement was determined using the method described by Bland and Altman (1986) for each of the scan radii, for each of the diagnostic groups. The mean of the differences between visits represents the bias present between the two sets of measurements acquired at separate visits, and the 95% limits of agreement, representing the measurement error, are constructed as the mean of the differences ±1.96 x the SD of the differences (Zadnik et al. 1994).

The RNFL thickness data were then analysed using repeated measures Analyses of Variance (ANOVA) with age, disc area and diagnosis as between-subjects main effects and age x diagnosis and disc area x diagnosis as between-subjects interactions. The measure of disc area was obtained from the HRT.

Five separate analyses were performed. Initially, a separate analysis was carried out for the RNFL thickness derived by each of the three scan radii (1.5R, 2.0R and 1.73mm). The effect of visit (two levels) and of number of consecutive scans within a visit (seven levels), were considered as within-subjects factors as were the interactions of these effects with the between-subjects effects. The remaining two analyses were then undertaken for the RNFL thickness using only the thickness derived by the first and seventh scans. One analysis considered the RNFL thickness for the three scan radii and the other analysis, the RNFL thickness for the 1.5R and 2.0R radii only. The within-subjects effects were scan radii (three and two levels in the two analyses, respectively), visit (two levels) and number of scans within visit (two levels). The tests for main effects were performed controlling for all other main effects; tests for interactions were also controlled for all main effects.

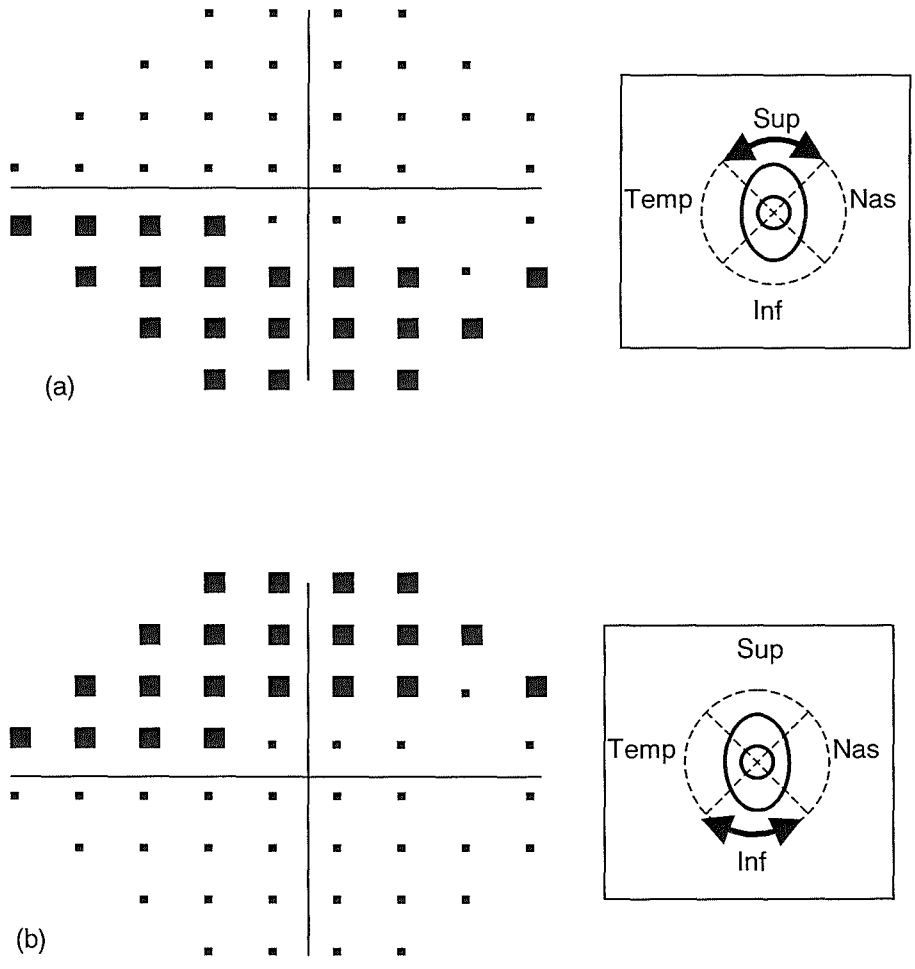

Figure 6.4 Schematic diagram to show the W-W perimetric locations and the corresponding OCT sector RNFL scan locations chosen for evaluating the relationship between (a) the Superior sector OCT RNFL thickness and the Inferior hemifield PD probability scores and (b) the Inferior sector OCT RNFL thickness and the Superior hemifield PD probability scores.

The Greenhouse-Geisser correction was applied where appropriate within each ANOVA.

The results from the ANOVA evaluated the within- and the between-visit variability of the retinal nerve fibre layer thickness as a function of age, diagnosis and the type and number of circular scan. The results also permitted an assessment of the validity of the OCT to discriminate the effects of age, diagnostic group and eccentricity on the measure of RNFL.

The validity of the measure of RNFL thickness was also considered in terms of mean RNFL thickness as derived by HRT, with structural outcome of the ONH defined in terms of the variables generated by HRT and with functional outcome, namely the visual field global indices, MD and PSD, derived by HFA W-W and FDT perimetry.

6.7.2 Sector Analysis.

Five ANOVAs were similarly undertaken for the RNFL thickness from each of the four sectors. The validity of each sector RNFL thickness was considered in a similar manner to the Global evaluation using the corresponding functional and structural variables.

To determine the relationship between the sector RNFL thickness and the visual field, only the superior and the inferior sectors were considered. The sector RNFL thickness was compared to the summed results of several stimuli locations within the corresponding W-W and FDT perimetry hemifield. The PD probability at each selected location was scored according to the following table:

PD PROBABILITY	SCORE
$P \geq 5\%$	0
$P < 5\%$	2
$P < 2\%$	5
$P < 1\%$	9
$P < 0.5\%$	14

The probability scores for each location within a hemifield, excluding those locations adjacent to the blind spot and the fovea, were then summed and the logarithmic value calculated (Figure 6.4). The choice of equivalent perimetry locations to the RNF bundle distribution are based upon the GHT partitions of the visual field (Åsman and Heijl 1992b). The resultant summed value was presented as a function of the corresponding sector RNFL thickness for each scan radius, for the OHT, OHT(H) and the POAG groups only. The PD probability values were chosen since they are age- and eccentricity-corrected and representative measures of focal damage.

6.8 Results.

6.8.1 Within-visit variability of the Global RNFL thickness.

The CoVs for each of the normal individuals, each of the patients with ocular hypertension and each of the patients with POAG at Visit One are given in Table 6.1. The within-visit variation in Global RNFL thickness as defined by one SD is shown as a function of the Global mean RNFL thickness in Figure 6.5. The cumulative frequency distribution of the within-visit variation for Visit One and Two, for each of the three scan radii across the diagnostic groups is presented in Figures 6.6 and 6.7 The variation was greatest for the 1.5R scan radius. For all three scan radii, the SD tended to increase proportionately to the decrease in the Global RNFL thickness. For those RNFL thickness greater than approximately 40μm, the SD was in the region 5-10 μm. Similar trends were evident for the 2.0R and 1.73 scan radii. The variation was least for the Normal group, across all three scan radii.

1.5R	GLOBAL			
	VISIT 1		VISIT 2	
	MEAN	SD	MEAN	SD
NORMAL	5.77	4.01	5.07	2.72
OHT	11.69	7.86	11.01	7.17
POAG	19.94	16.23	15.53	10.47

2.0R	GLOBAL			
	VISIT 1		VISIT 2	
	MEAN	SD	MEAN	SD
NORMAL	6.88	4.06	5.98	3.83
OHT	9.68	6.25	10.67	6.13
POAG	18.10	14.18	15.59	7.01

1.73mm	GLOBAL			
	VISIT 1		VISIT 2	
	MEAN	SD	MEAN	SD
NORMAL	5.79	3.12	5.47	2.68
OHT	10.19	6.61	10.97	5.42
POAG	18.37	17.35	15.62	9.53

Table 6.1. The Coefficients of Variation (%) for the Global RNFL thickness (μm), for the Normal group, the OHT group, and the POAG group, for each of the three scan radii, for each of the two visits.

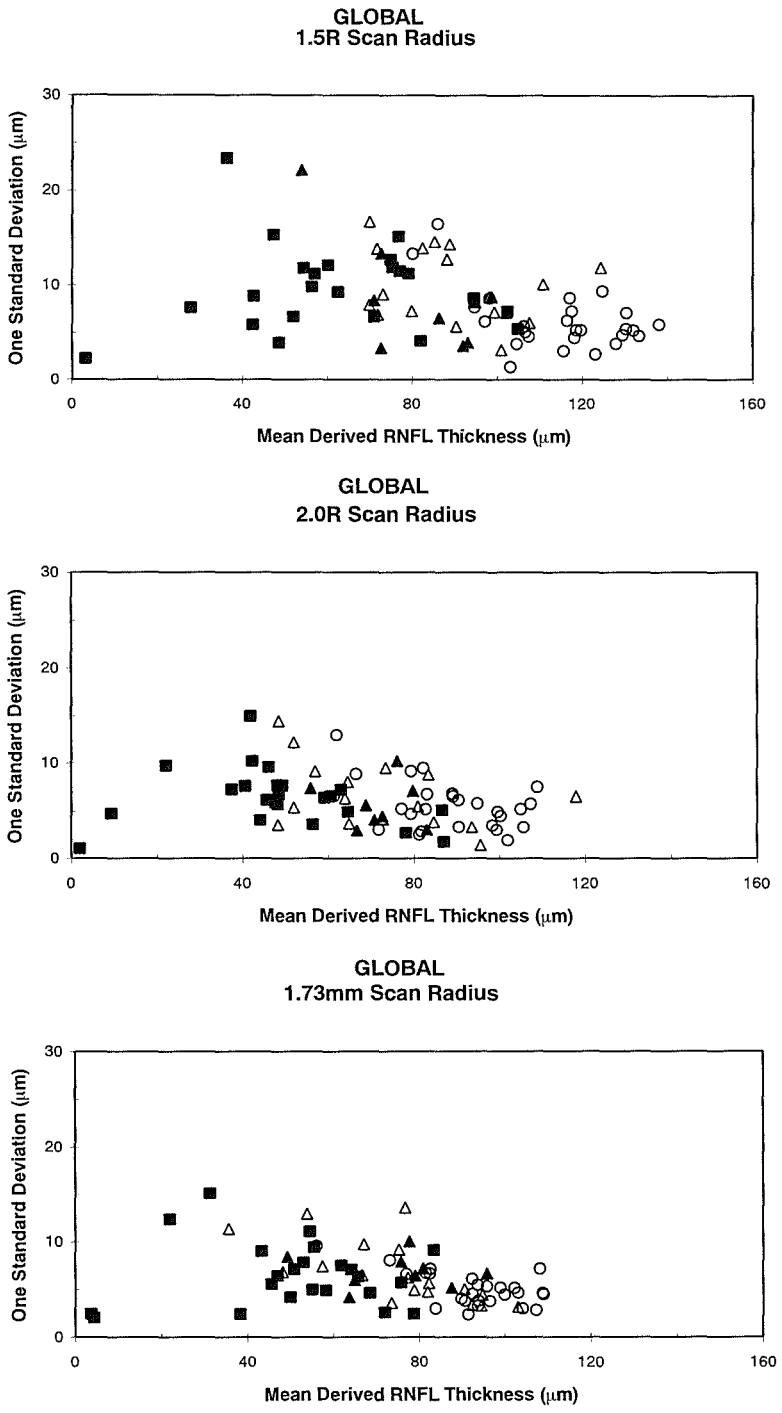

Figure 6.5. The within-visit variation as defined by one SD in Global RNFL thickness, at Visit One, for the 1.5R scan radius (top), for the 2.0R scan radius (middle) and for the 1.73mm scan radius (bottom), for the Normal group (open circles), for the OHT group (open triangles), for the OHT(H) group (closed triangles) and for the POAG group (closed squares). Each data point represents a single individual.

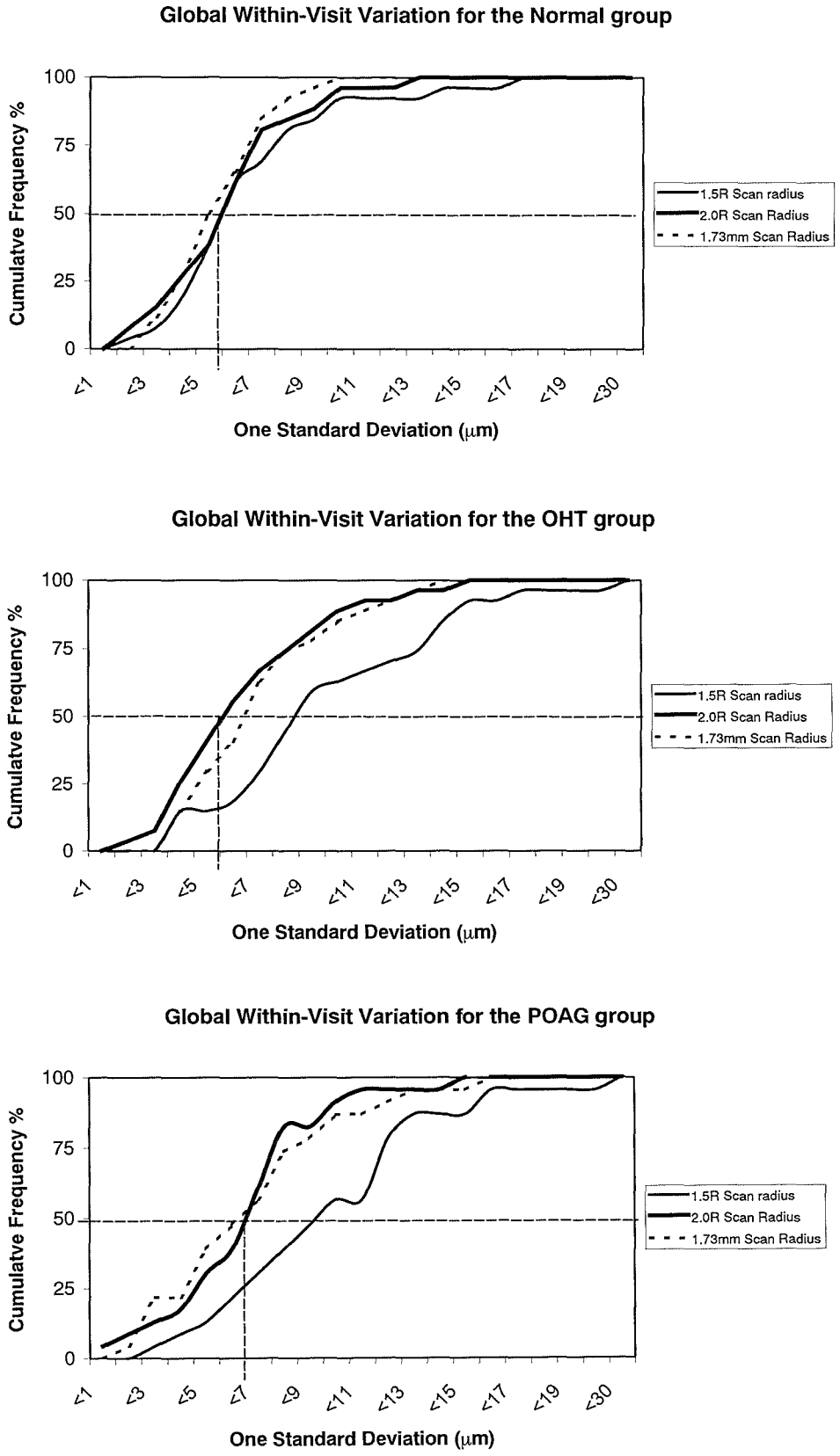

Figure 6.6. The cumulative frequency (%) distribution of the within-visit variation for the Normal group (top), OHT group (middle) and the POAG group (bottom) for each of the three scan radii, at Visit One.

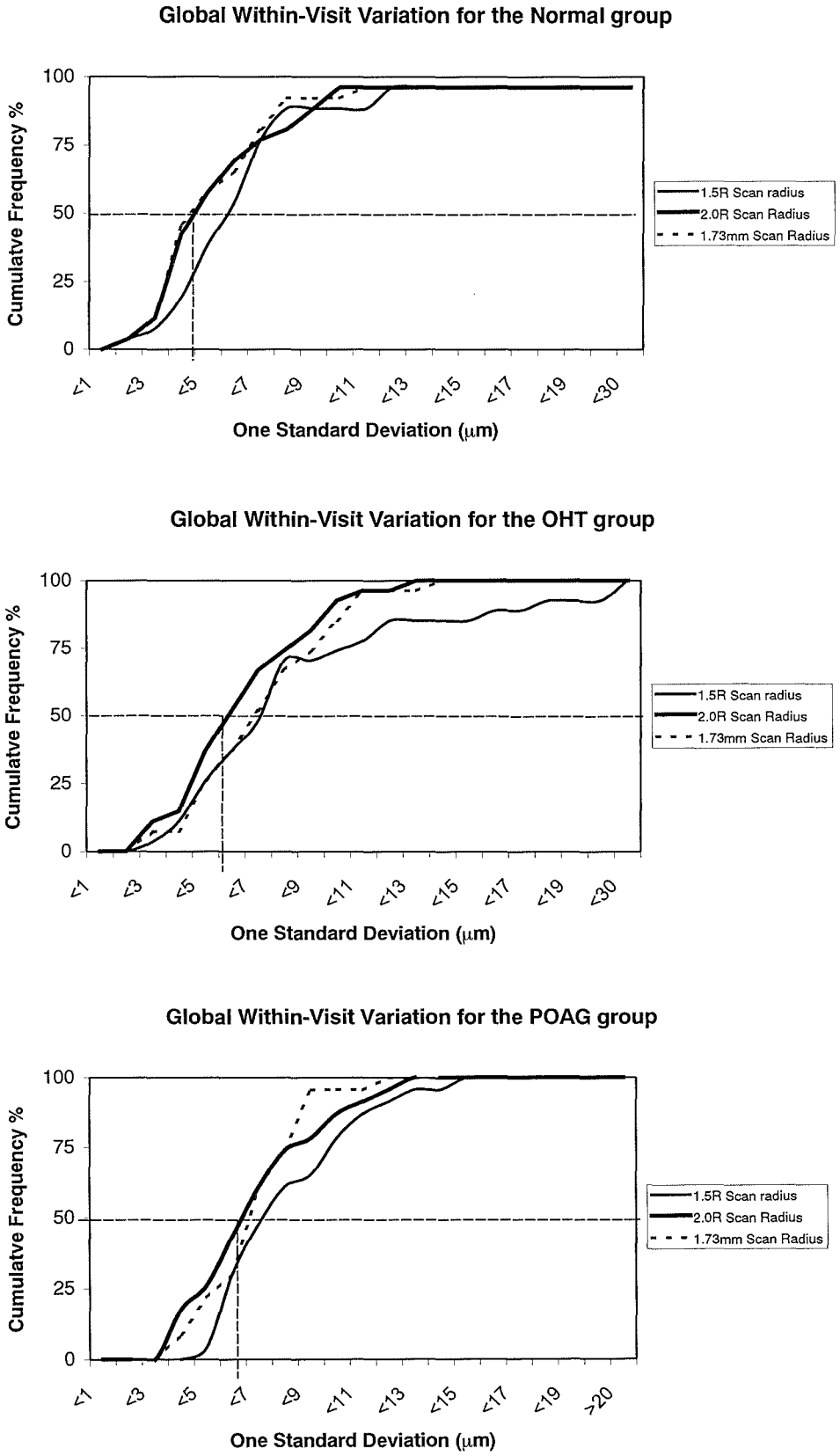

Figure 6.7. The cumulative frequency (%) distribution of the within-visit variation for the Normal group (top), OHT group (middle) and the POAG group (bottom) for each of the three scan radii, at Visit Two.

6.8.2 Between-visit variability of the Global RNFL thickness.

The Group Mean and one SD of the Global RNFL thickness at Visit One and at Visit Two as a function of the type of circular scan and of diagnosis is given in Table 6.2. The ANOVA summary table is given in Table 6.3. The limits of agreement for the RNFL thickness between the first and second visit are given in Table 6.4.

6.8.2.1 1.5R Scan radius.

The RNFL thickness did not vary between the first and second visits (p=0.245). The difference in the RNFL thickness between the two visits is presented as a function of the mean of the two visits in Figure 6.8. The RNFL thickness did not vary with the number of scans (p=0.735), or with DA (p=0.111). However, the thickness became greater at the second visit as the disc area increased (p=0.018). The increased thickness at the second visit with increase in DA was independent of diagnostic group (p=0.709) but a trend was evident for the OHT group (Figure 6.9). The increased thickness at the second visit with increase in DA became less pronounced with increase in the number of scans (p=0.01).

6.8.2.2 2.0R Scan radius.

The RNFL thickness across all three diagnostic groups was greater at the first visit compared to the second visit (p=0.023). The limits of agreement for the RNFL thickness between the first and second visit are graphically presented in Figure 6.10. The RNFL thickness was again independent of the number of scans (p=0.735) and with disc area (p=0.206). The difference between visits again became greater as the disc area increased (p=0.002) (Table 6.3 and Figure 6.11). The increased thickness at the second visit with increase in disc area was independent of diagnostic group (p=0.427) but a trend was again evident for the OHT group. The thickness was independent of the number of scans (p=0.735).

6.8.2.3 1.73 mm Scan radius.

The RNFL thickness was independent of visit (p=0.222), of disc area (p=0.491), and of the number of scans (p=0.881) (Table 6.3). The variation between the two visits as a function of the mean of the two visits is shown in Figure 6.12, and as a function of DA, in Figure 6.13.

(a) 1.5R Scan Radius

	GLOBAL			
	VISIT 1		VISIT 2	
	MEAN	SD	MEAN	SD
NORMAL	114.71	15.54	113.61	14.86
OHT	87.05	15.73	85.44	21.47
POAG	62.14	24.07	63.55	22.52

(b) 2.0R Scan Radius

	GLOBAL			
	VISIT 1		VISIT 2	
	MEAN	SD	MEAN	SD
NORMAL	87.34	15.17	87.25	14.97
OHT	70.11	16.91	66.89	20.36
POAG	49.07	20.56	47.60	16.21

(c) 1.73mm Scan Radius

	GLOBAL			
	VISIT 1		VISIT 2	
	MEAN	SD	MEAN	SD
NORMAL	92.24	12.83	93.24	10.78
OHT	75.04	16.28	71.29	19.77
POAG	51.50	21.01	52.35	18.21

Table 6.2. The Group Mean and SD of the Global RNFL thickness (μm), at Visit One and Visit Two for (a) the 1.5R scan radius, for (b) the 2.0R scan radius and (c) for the 1.73mm scan radius for the Normal, OHT, and POAG groups.

Global

	Scan Radius		
FACTOR	**1.5R**	**2.0R**	**1.73mm**
Age	p=0.0151	p=0.020	p=0.003
Diagnosis	p<0.001	p<0.001	p<0.001
Disc Area	NS	NS	NS
Visit	NS	p=0.023	NS
Visit x Age	NS	NS	NS
Visit x Diagnosis	NS	NS	NS
Visit x Disc Area	p=0.018	p=0.002	NS
Number of Scans	NS	NS	NS
Number of Scans x Age	NS	NS	NS
Number of Scans x Diagnosis	NS	NS	NS
Number of Scans x Disc Area	NS	NS	NS
Visit x Number of Scans	NS	NS	NS
Visit x Number of Scans x Age	NS	NS	NS
Visit x Number of Scans x Diagnosis	NS	NS	NS
Visit x Number of Scans x Disc Area	p =0.01	NS	NS
Area x Diagnosis	NS	NS	NS
Age x Diagnosis	NS	NS	NS
Visit x Disc Area x Diagnosis	NS	NS	NS
Visit x Age x Diagnosis	NS	NS	NS
Number of Scans x Disc Area x Diagnosis	NS	NS	NS
Number of Scans x Age x Diagnosis	NS	NS	NS
Visit x Number of Scans x Disc Area x Diagnosis	NS	NS	NS
Visit x Number of Scans x Age x Diagnosis	NS	p = 0.044	NS

Table 6.3. Summary of the ANOVA for the Global RNFL thickness determined by each of the three scan radii.

(a) 1.5R Scan Radius

	Group Mean Difference (μm)		95% Limits of Agreement	
		SD	UPPER	LOWER
NORMAL	-0.40	6.97	13.26	-14.06
OHT	-1.60	17.73	33.14	-36.35
POAG	1.41	11.13	23.23	-20.42

(b) 2.0R Scan Radius

	Group Mean Difference (μm)		95% Limits of Agreement	
		SD	UPPER	LOWER
NORMAL	0.43	7.54	15.21	-14.34
OHT	-3.22	12.97	22.19	-28.63
POAG	-1.47	11.72	21.51	-24.45

(c) 1.73mm Scan Radius

	Group Mean Difference (μm)		95% Limits of Agreement	
		SD	UPPER	LOWER
NORMAL	1.65	7.15	15.67	-12.37
OHT	-3.75	13.28	22.28	-29.78
POAG	0.85	8.00	16.53	-14.83

Table 6.4. The Group Mean difference and SD of the Global RNFL thickness (μm), between the two visits for (a) the 1.5R scan radius, for (b) the 2.0R scan radius and for (c) the 1.73mm scan radius, for the Normal, OHT, and POAG groups. The upper and lower limits of agreement for 95% confidence are provided.

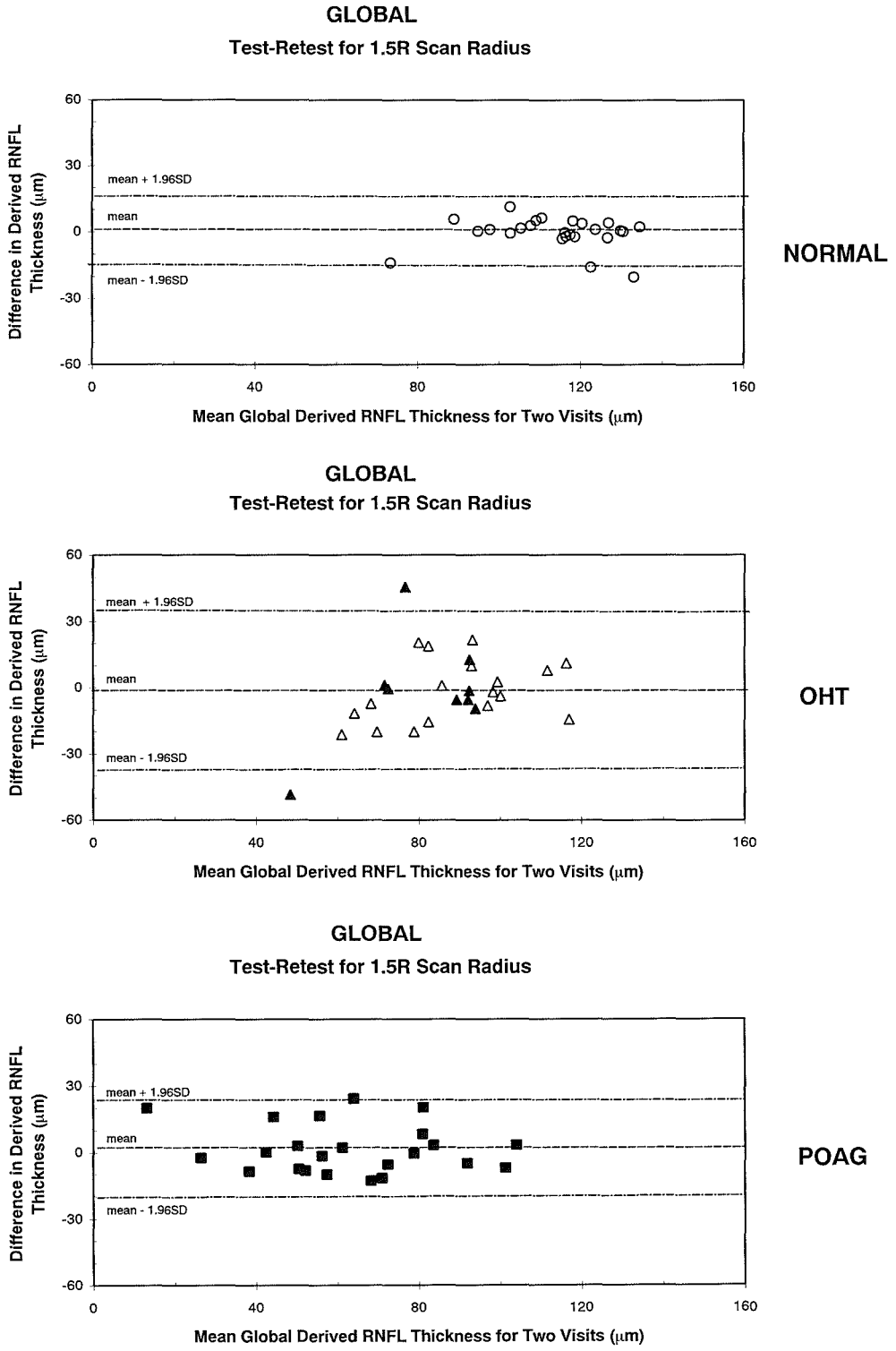

Figure 6.8. The difference in mean Global RNFL thickness as a function of the mean Global RNFL thickness for the two visits, for the Normal group (top), for the OHT group (open triangles) and OHT(H) group (closed triangles) (middle) and for the POAG group (bottom) with the 1.5R scan radius. The mean and the 95% confidence limits are shown.

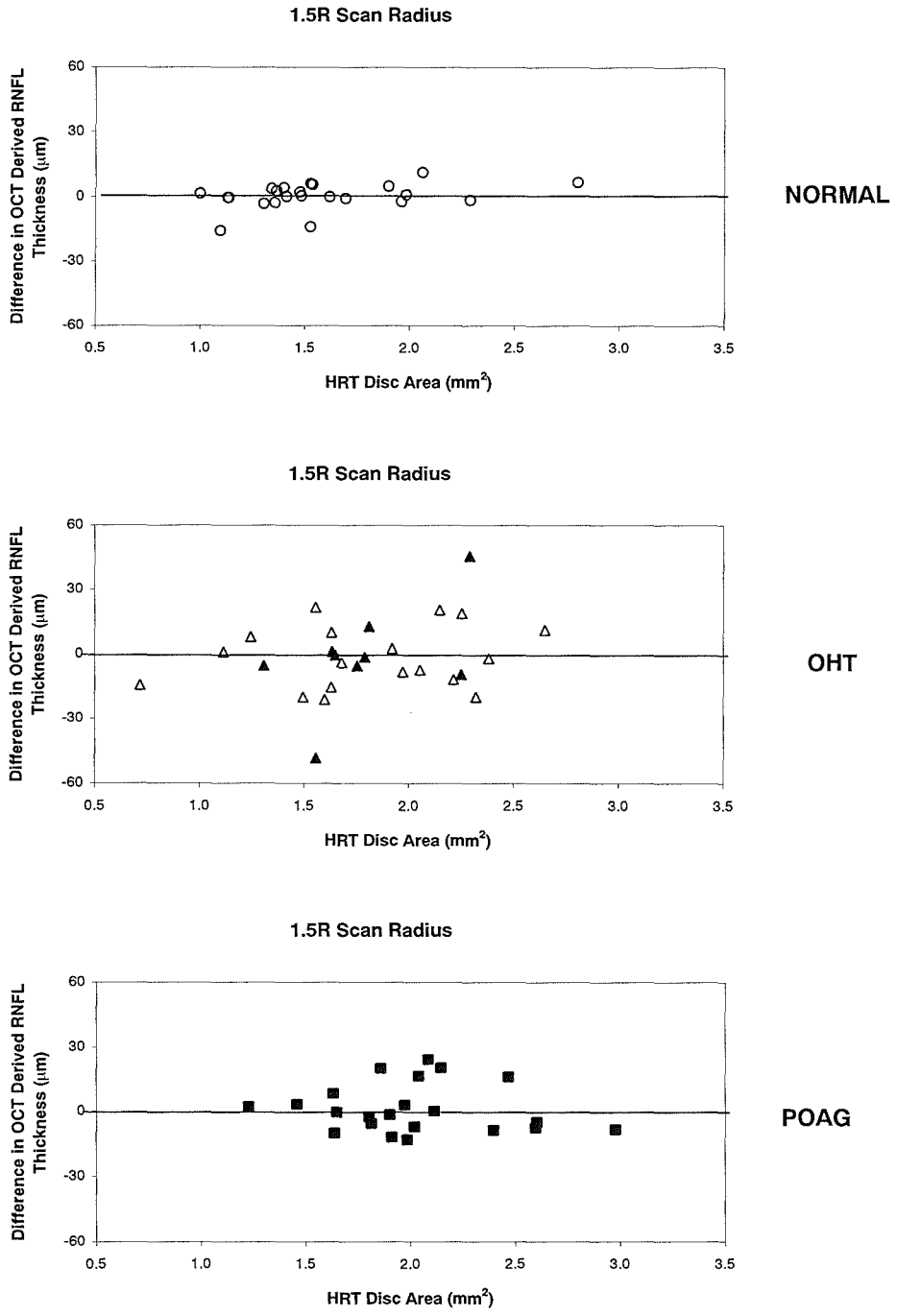

Figure 6.9. The difference in the Global RNFL thickness between the first and second visits referred to the second visit as a function of the HRT derived Disc Area, for the 1.5R scan radius, for the Normal group (top), for the OHT and OHT(H) group (middle) and for the POAG group (bottom). Each data point represents the mean of 7 scans for each individual. The line indicates zero difference.

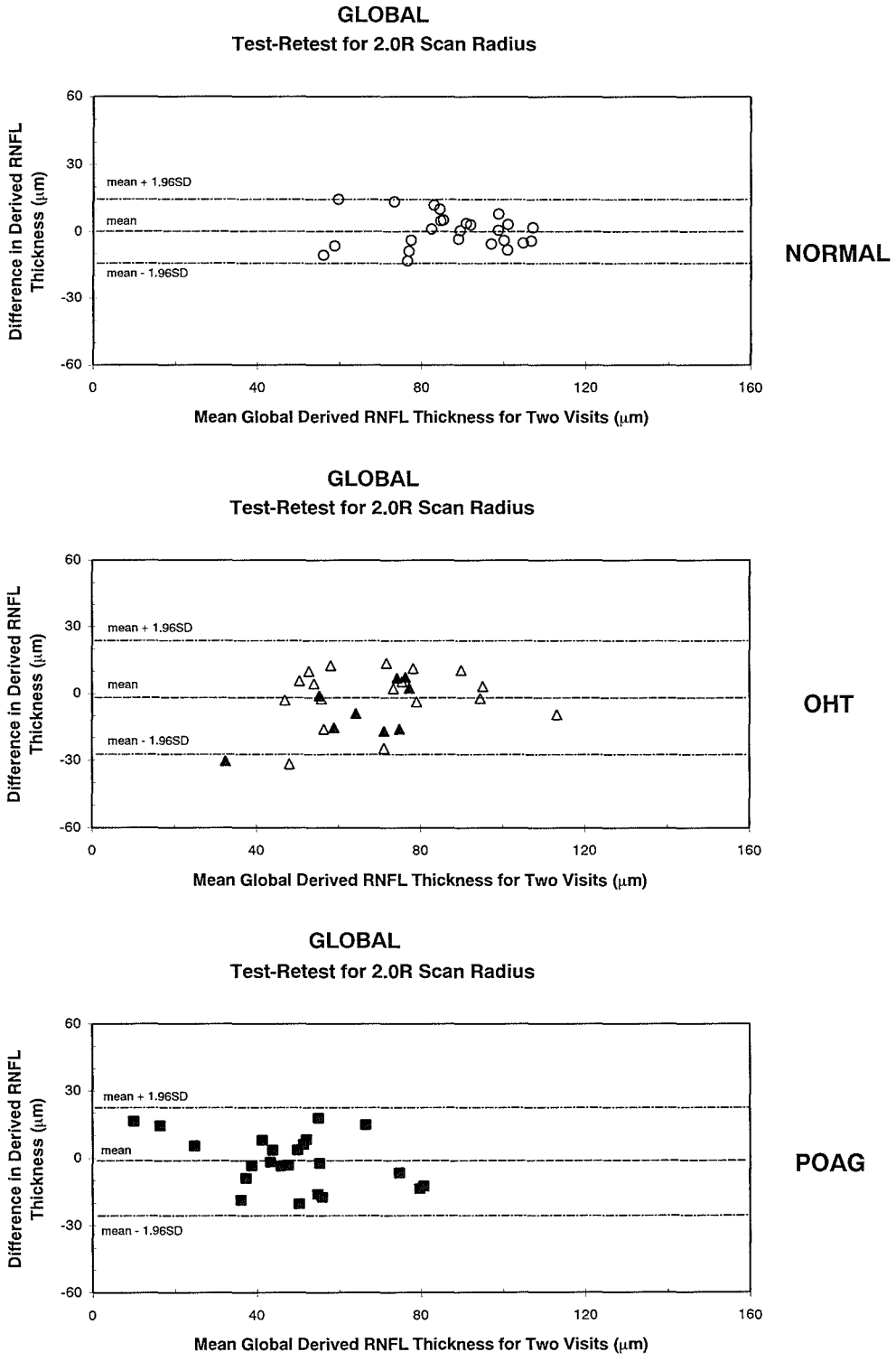

Figure 6.10. The difference in Global RNFL thickness as a function of the mean Global RNFL thickness for the two visits, for the Normal group (top), for the OHT group (open triangles) and OHT(H) group (closed triangles) (middle) and for the POAG group (bottom) with the 2.0R scan radius. The mean and the 95% confidence limits are shown.

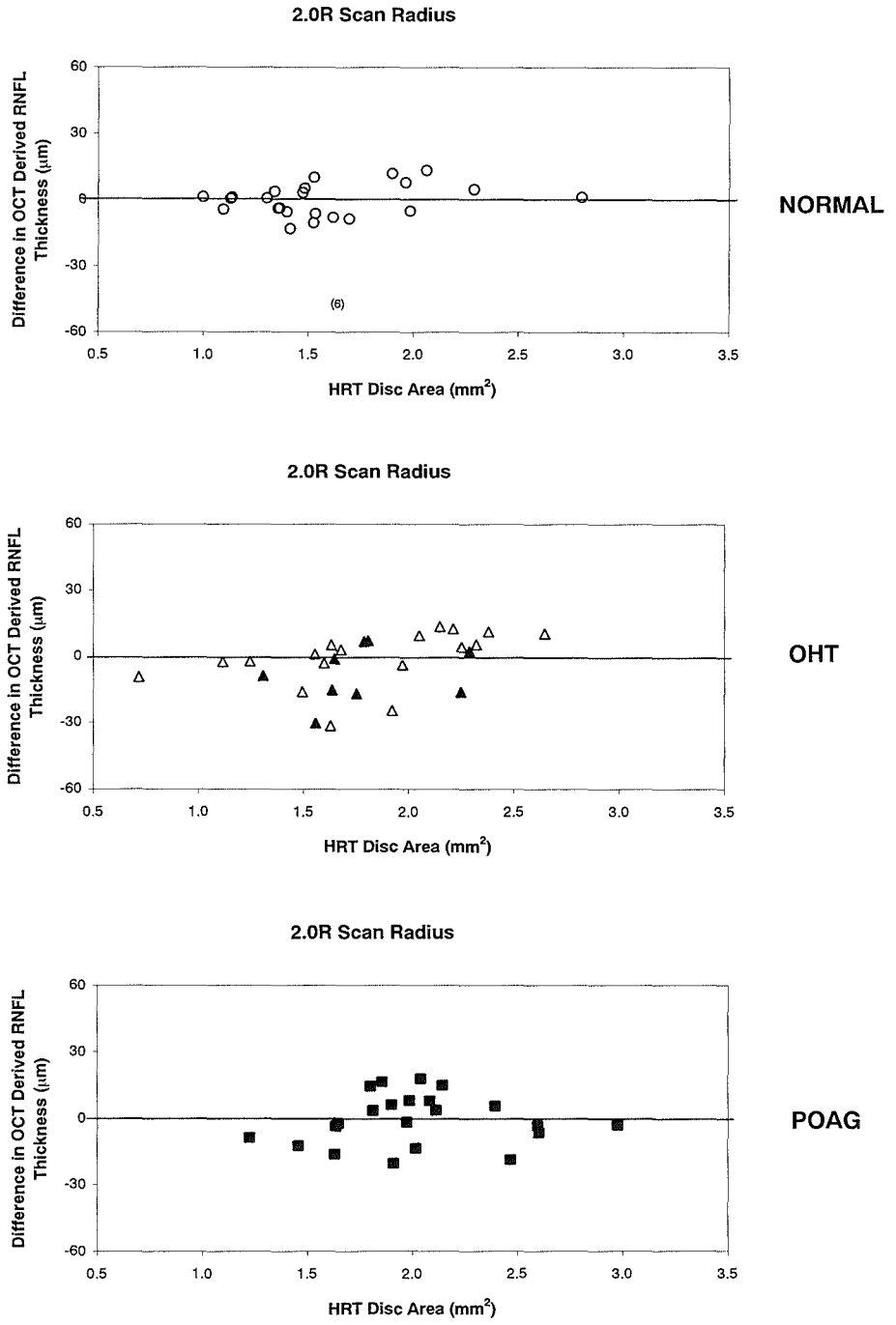

Figure 6.11. The difference in the Global RNFL thickness between the first and second visits referred to the second visit as a function of the HRT derived Disc Area, for the 2.0R scan radius, for the Normal group (top), for the OHT and OHT(H) group (middle) and for the POAG group (bottom). Each data point represents the mean of 7 scans for each individual. The line indicates zero difference.

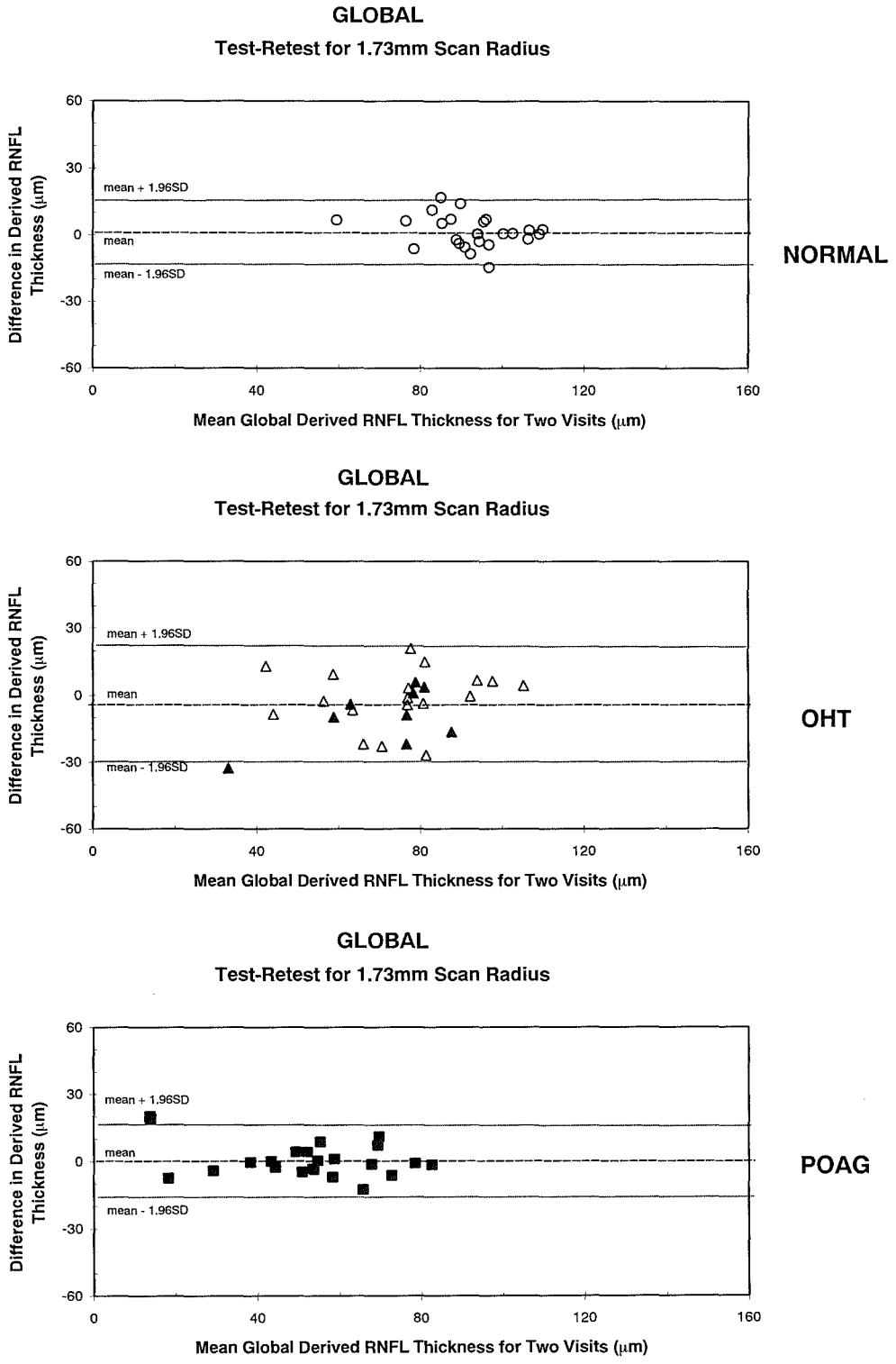

Figure 6.12. The difference in Global RNFL thickness as a function of the mean Global RNFL thickness for the two visits, for the Normal group (top), for the OHT group (open triangles) and OHT(H) group (closed triangles) (middle) and for the POAG group (bottom) with the 1.73mm scan radius. The mean and the 95% confidence limits are shown.

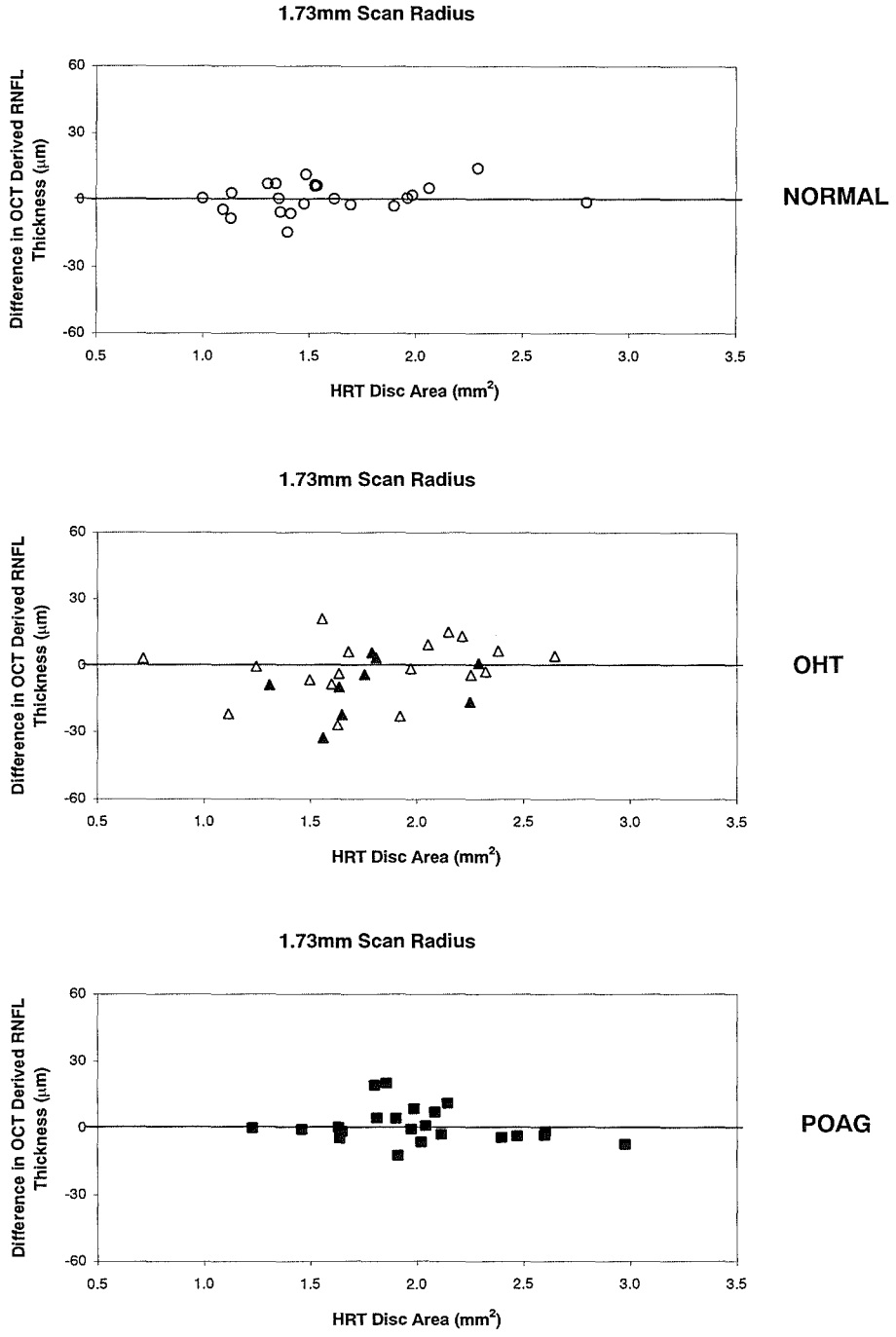

Figure 6.13. The difference in the Global RNFL thickness between the first and second visits referred to the second visit as a function of the HRT derived Disc Area, for the 1.73mm scan radius, for the Normal group (top), for the OHT and OHT(H) group (middle) and for the POAG group (bottom). Each data point represents the mean of 7 scans for each individual. The line indicates zero difference.

6.8.3 Relationship between Global RNFL thickness and age, diagnostic group HRT derived RNFL thickness and related HRT topographical parameters, and visual function (i.e. Validity).

6.8.3.1 1.5R Scan radius.

6.8.3.1.1 Age.

The RNFL thickness declined with increase in age ($p=0.015$, $R^2=0.18$) (Figure 6.14). The decline in RNFL thickness for the Normal group was 3.6μm per decade (Table 6.5).

6.8.3.1.2 Diagnostic category.

As would be expected, the thickness varied across the three diagnostic groups ($p<0.001$) (Table 6.3). The Group mean RNFL at Visit One was approximately 24% thinner for the OHT group than for the Normal group and 45% thinner for the POAG group compared to the Normal group (Table 6.6). Similar findings were present at Visit Two.

6.8.3.1.3 RNFL thickness derived by HRT.

The relationship between the OCT Global RNFL thickness and the Global RNFL thickness derived by the HRT for each of the diagnostic groups and for all groups combined is given in Figure 6.15. The coefficient of determination for the Normal group was 0.05, for the OHT group 0.18, for the OHT(H) group 0.06, for the POAG group 0.04 and for the Combined group 0.25 (Table 6.7).

6.8.3.1.4 RDAR derived by the HRT.

The relationship between the Global RNFL thickness and the neuroretinal rim area derived by the HRT, and corrected for DA for each of the diagnostic groups and for all groups combined, is given in Figure 6.16. The RDAR increased with an increase in the RNFL thickness ($R^2=0.43$) (Table 6.7).

6.8.3.1.5 CSM derived by the HRT.

The relationship between the Global RNFL thickness and the HRT derived CSM for each of the diagnostic groups and for all groups combined is given in Figure 6.17. The CSM became more positive as the RNFL thickness decreased ($R^2=0.42$).

6.8.3.1.6 Additional HRT variables.

The relationship between the Global RNFL thickness and the remaining HRT variables that were evaluated are given for each diagnostic group and for all groups combined in Table 6.7. The mean Global RNFL thickness derived by OCT for all groups combined was weakly associated with the RV ($R^2=0.12$), the RA ($R^2=0.11$), the HVC ($R^2=0.01$), and the RNFL cross-sectional area ($R^2=0.18$). A decline in the RNFL thickness was associated with an increase in the CA ($R^2=0.34$), and the CDAR ($R^2=0.38$).

6.8.3.1.7 Visual field.

The relationship between the Global RNFL thickness and the visual field, as provided by the global indices, Mean Deviation (MD) and Pattern Standard Deviation (PSD) for W-W perimetry, are given in Figure 6.18 and Figure 6.19 respectively. The relationship between the MD for W-W perimetry and the Global RNFL thickness appeared to be non-linear. The W-W MD was relatively constant provided the Global RNFL thickness remained greater than 80μm, for the 1.5R scan radius, but become increasingly more negative once the RNFL thickness had fallen below this value. Similarly, a marked but very variable increase in the W-W PSD was present between individuals with a RNFL thickness of less than 80μm. The two outliers with POAG in Figure 6.19 exhibiting a RNFL of approximately 100μm each exhibited dense arcuate defects confined to a single hemifield.

The relationship between Global RNFL thickness and the equivalent global indices for FDT perimetry are shown in Figure 6.20 and Figure 6.21 respectively. The MD for FDT declined, and became progressively more negative with a decrease in the RNFL thickness. The relationship tended to be more linear, compared to that for W-W perimetry. A marked but very variable increase in the PSD for FDT was similarly present with a RNFL thickness of less than 80μm.

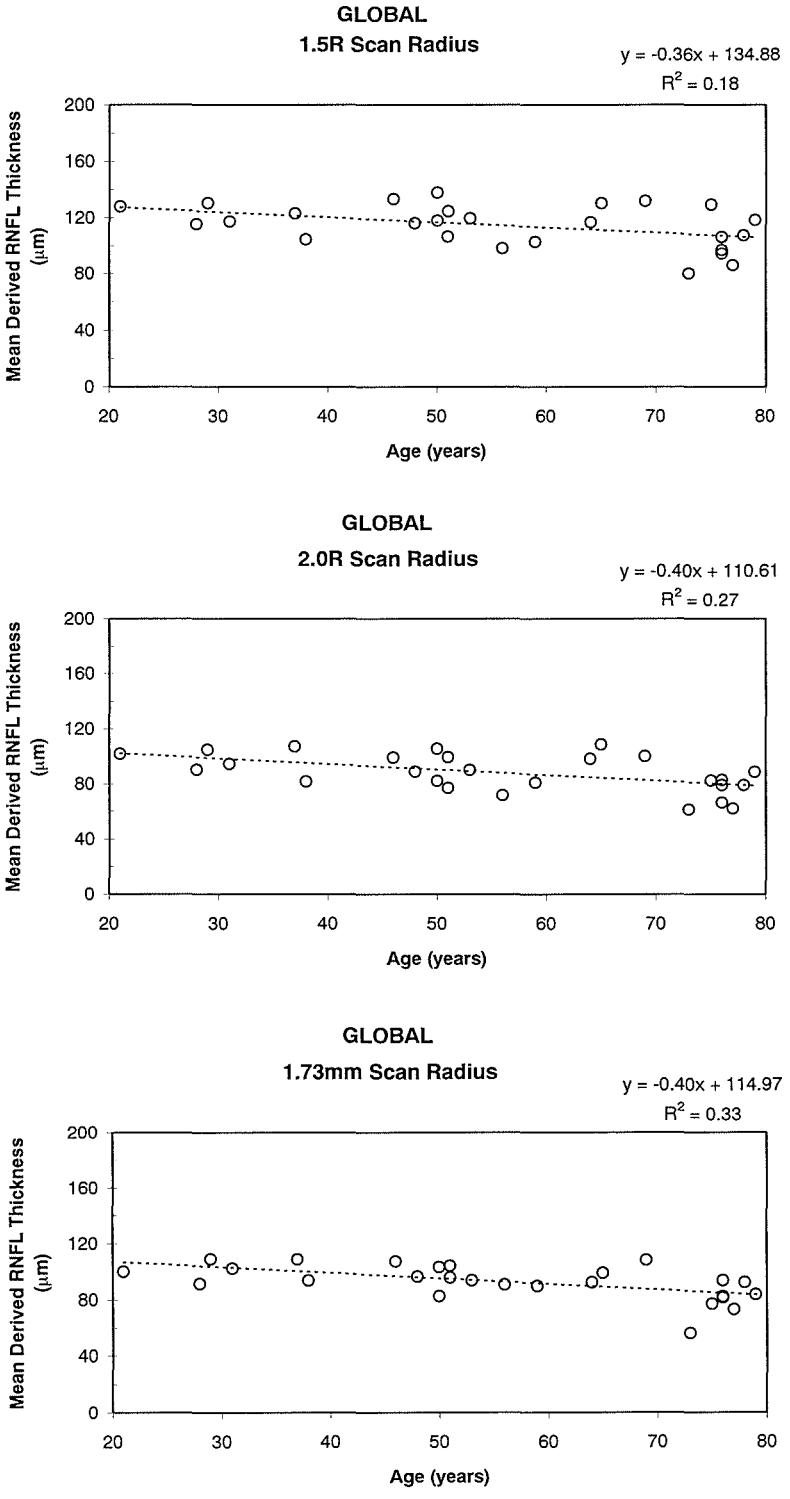

Figure 6.14. The mean Global RNFL thickness for the Normal group, as a function of age for the 1.5R scan radius (top), for the 2.0R scan radius (middle) and for the 1.73mm scan radius (bottom). Each data point represents a single individual.

Reduction in Group Mean Global RNFL thickness (μm) with increasing age in the Normal Group

	Rate per Year	R^2
1.5R	-0.36	0.18
2.0R	-0.40	0.27
1.73mm	-0.40	0.33

Table 6.5. Reduction in the Group Mean Global RNFL thickness for each of the three scan radii, with increasing age, for the Normal group.

(a) Percentage Reduction in Group Mean RNFL thickness for the OHT group compared to that of the Normal Group

	VISIT ONE (%)	VISIT TWO (%)
1.5R	24.1	24.8
2.0R	19.7	23.3
1.73mm	18.6	23.5

(b) Percentage Reduction in Group Mean RNFL thickness for the POAG group compared to that of the Normal Group

	VISIT ONE (%)	VISIT TWO (%)
1.5R	45.8	44.1
2.0R	43.8	45.4
1.73mm	44.2	43.8

Table 6.6. The percentage reduction in the Group Mean Global RNFL thickness, for (a) the OHT group and for (b) the POAG group compared to that of the Normal group, for each of the three scan radii.

GLOBAL
1.5R Scan Radius

	NORMAL	OHT	OHT(H)	All OHT	POAG	ALL
RNFLT	0.05	0.18	0.06	0.17	0.04	0.25
RDAR	0.07	0.01	0.06	0.01	0.28	0.43
RV	0.05	0.02	0.10	0.01	0.06	0.14
CSM	0.20	0.20	0.05	0.09	0.22	0.42
HVC	0.00	0.00	0.24	0.02	0.08	0.01
RNFLX	0.02	0.03	0.01	0.04	0.00	0.11
CDAR	0.07	0.01	0.06	0.01	0.28	0.43
RA	0.00	0.04	0.17	0.03	0.12	0.12
CA	0.06	0.03	0.05	0.02	0.19	0.38
DA	0.04	0.08	0.03	0.06	0.10	0.17

GLOBAL
2.0R Scan Radius

	NORMAL	OHT	OHT(H)	All OHT	POAG	ALL
RNFLT	0.04	0.16	0.45	0.19	0.13	0.29
RDAR	0.04	0.01	0.00	0.01	0.32	0.38
RV	0.00	0.06	0.18	0.02	0.17	0.12
CSM	0.17	0.29	0.04	0.16	0.22	0.42
HVC	0.00	0.01	0.39	0.01	0.04	0.01
RNFLX	0.01	0.00	0.50	0.03	0.07	0.14
CDAR	0.04	0.01	0.00	0.01	0.32	0.38
RA	0.02	0.11	0.11	0.04	0.28	0.11
CA	0.07	0.06	0.11	0.02	0.16	0.34
DA	0.08	0.19	0.34	0.08	0.03	0.16

GLOBAL
1.73mm Scan Radius

	NORMAL	OHT	OHT(H)	All OHT	POAG	ALL
RNFLT	0.06	0.04	0.11	0.05	0.10	0.26
RDAR	0.00	0.03	0.00	0.02	0.17	0.34
RV	0.00	0.00	0.03	0.01	0.10	0.16
CSM	0.04	0.05	0.00	0.02	0.16	0.32
HVC	0.01	0.00	0.53	0.04	0.06	0.03
RNFLX	0.04	0.02	0.16	0.04	0.09	0.18
CDAR	0.00	0.03	0.00	0.02	0.17	0.34
RA	0.01	0.01	0.06	0.01	0.25	0.19
CA	0.00	0.02	0.05	0.00	0.04	0.24
DA	0.00	0.00	0.18	0.00	0.00	0.05

Table 6.7. Summary table of the R^2 values, for the assumed linear relationship between the Global RNFL thickness and the HRT derived stereometric parameters, including the mean RNFL thickness, for each of the three scan radii.

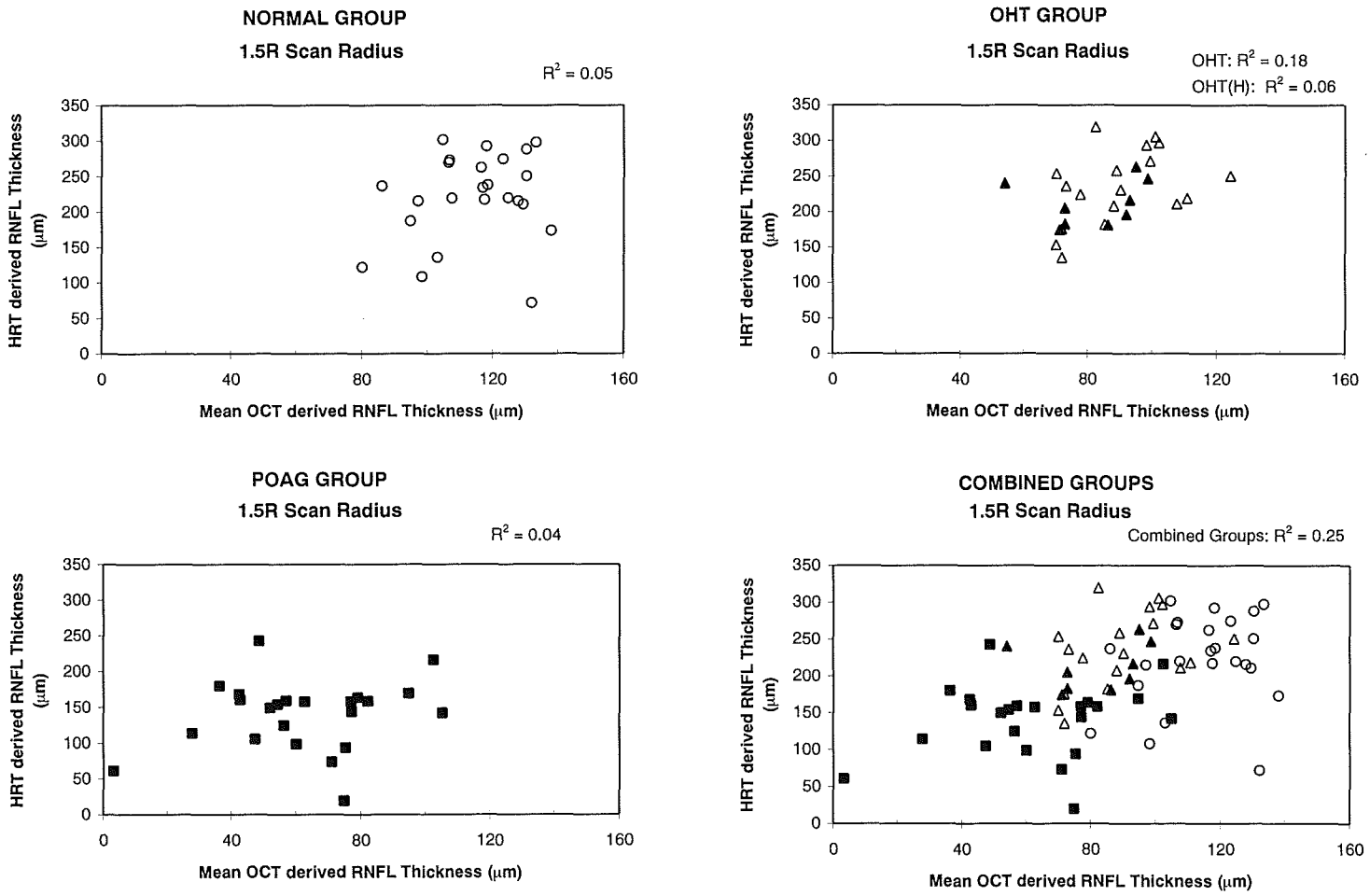

Figure 6.15. The relationship between the mean Global OCT derived RNFL thickness and the mean Global HRT derived RNFL thickness, at Visit One, for the 1.5R scan radius, for the Normal group (open circles) (upper left), for the OHT group (open triangles) and OHT(H) (closed triangles) (upper right), for the POAG group (closed squares) (lower left) and for all the groups (lower right). Each data point represents a single individual.

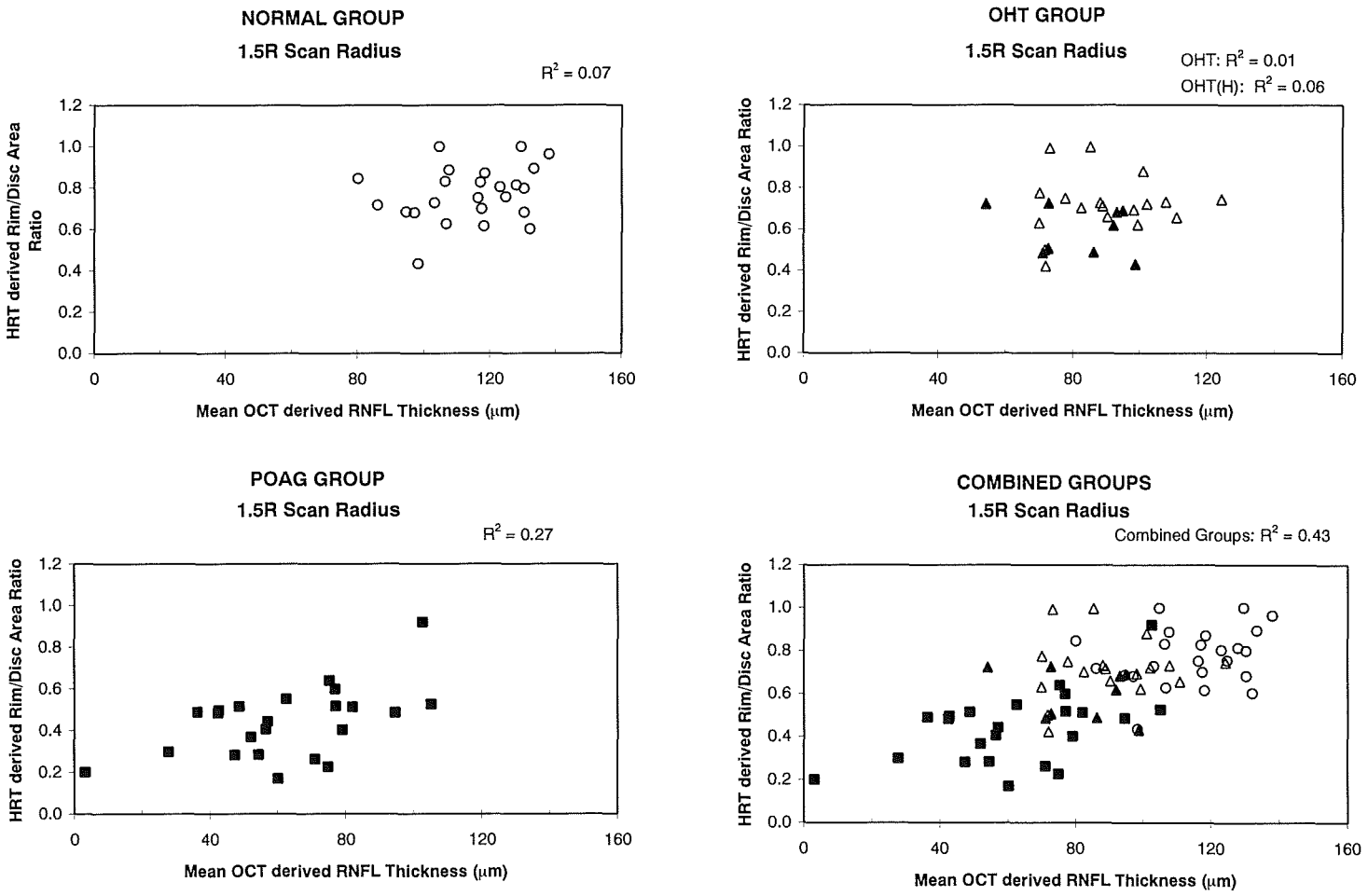

Figure 6.16. The relationship between the mean Global OCT derived RNFL thickness and the mean Global HRT derived Rim Area corrected for Disc Area, at Visit One, for the 1.5R scan radius, for the Normal group (open circles) (upper left), for the OHT group (open triangles) and OHT(H) (closed triangles) (upper right), for the POAG group (closed squares) (lower left) and for all the groups (lower right). Each data point represents a single individual.

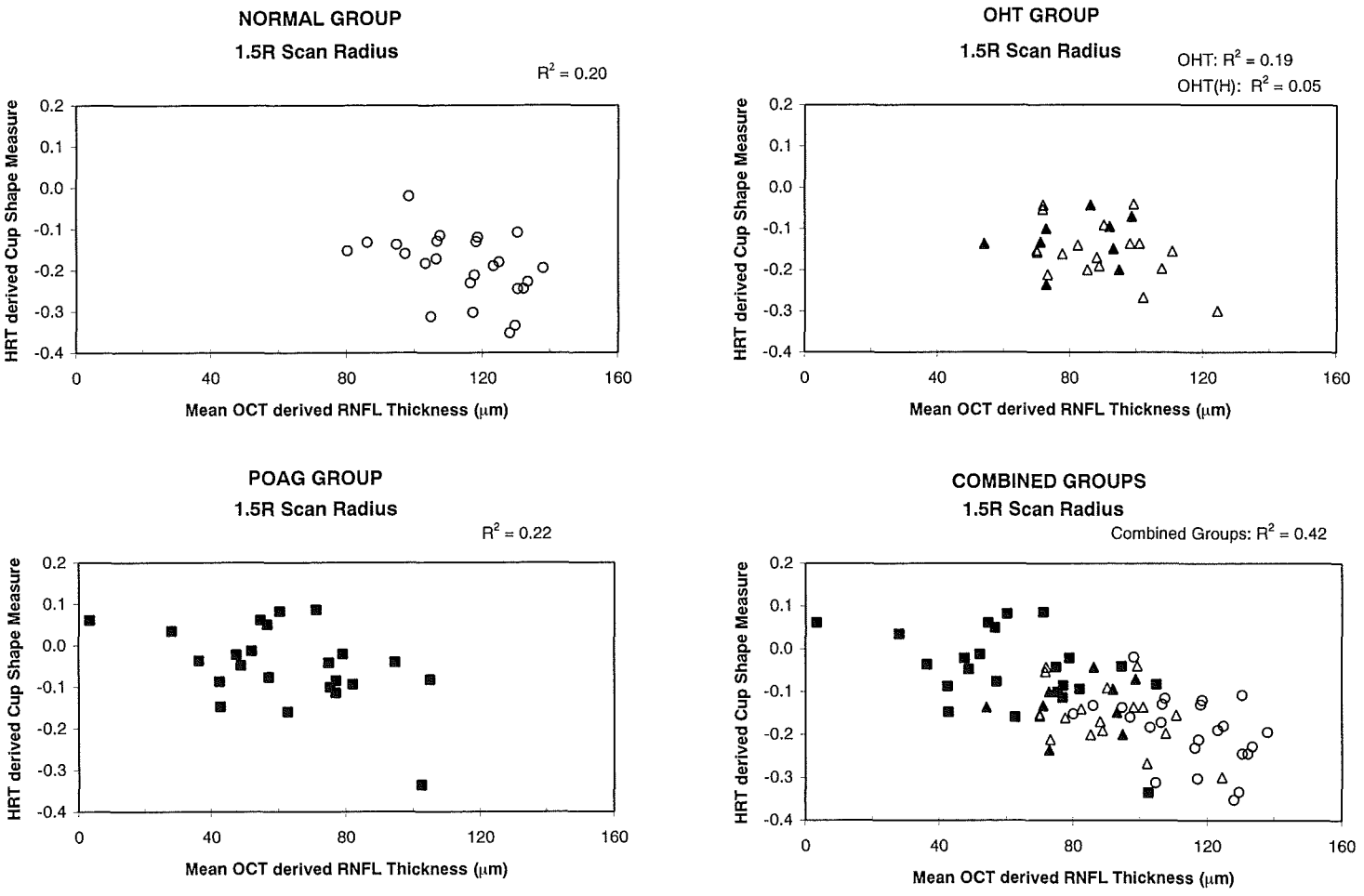

Figure 6.17. The relationship between the mean Global OCT derived RNFL thickness and the mean Global HRT derived Cup Shape Measure at Visit One, for the 1.5R scan radius, for the Normal group (open circles) (upper left), for the OHT group (open triangles) and OHT(H) (closed triangles) (upper right), for the POAG group (closed squares) (lower left) and for all the groups (lower right). Each data point represents a single individual.

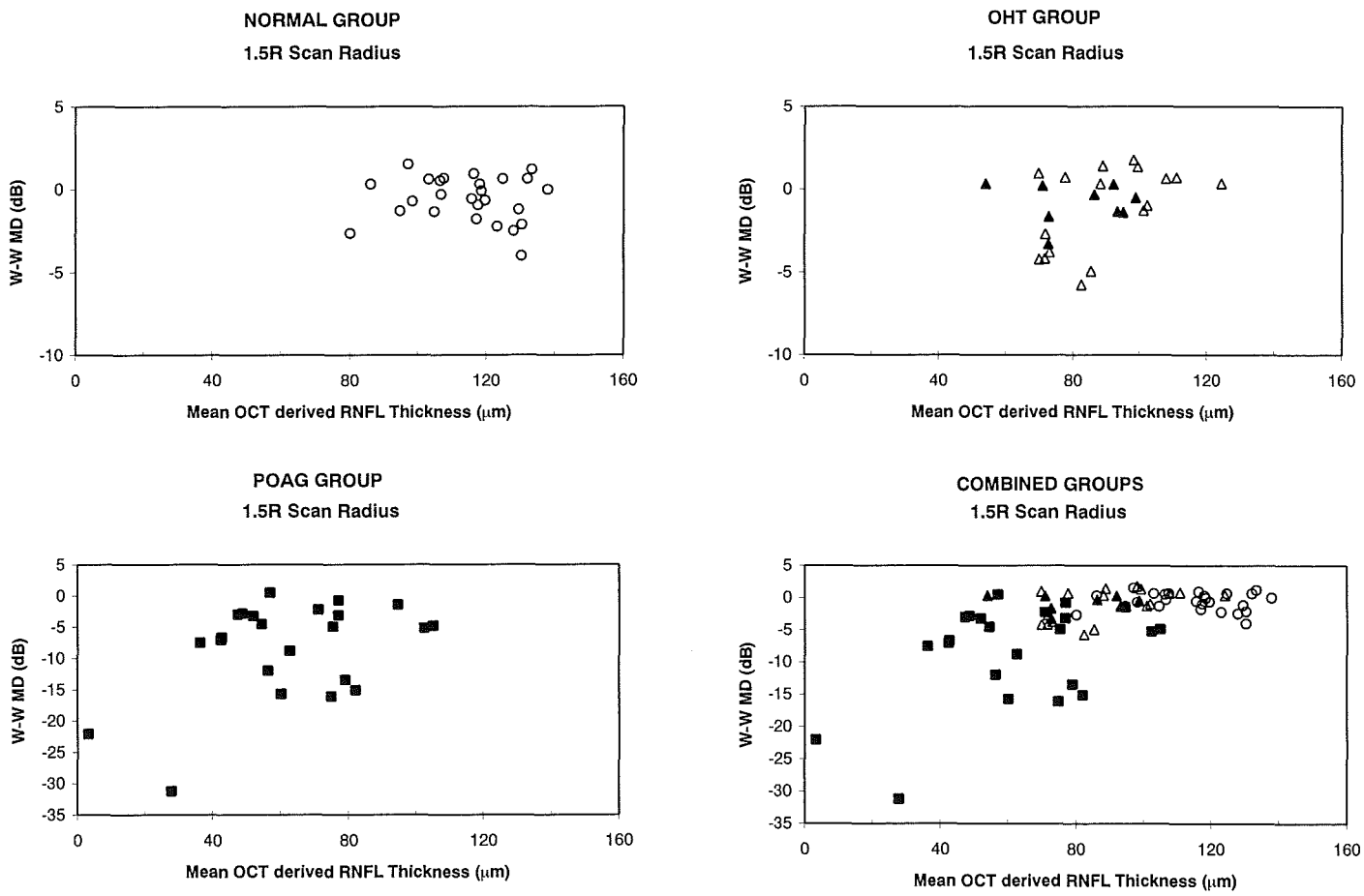

Figure 6.18. The relationship between the mean Global RNFL thickness and the W-W Mean Deviation (MD), at Visit One, for the 1.5R scan radius, for the Normal group (open circles) (upper left), for the OHT group (open triangles) and OHT(H) (closed triangles) (upper right), for the POAG group (closed squares) (lower left) and for all the groups (lower right). Each data point represents a single individual. Note the different y-axis scale used for the Normal and OHT group plots compared to the POAG and Combined group plots.

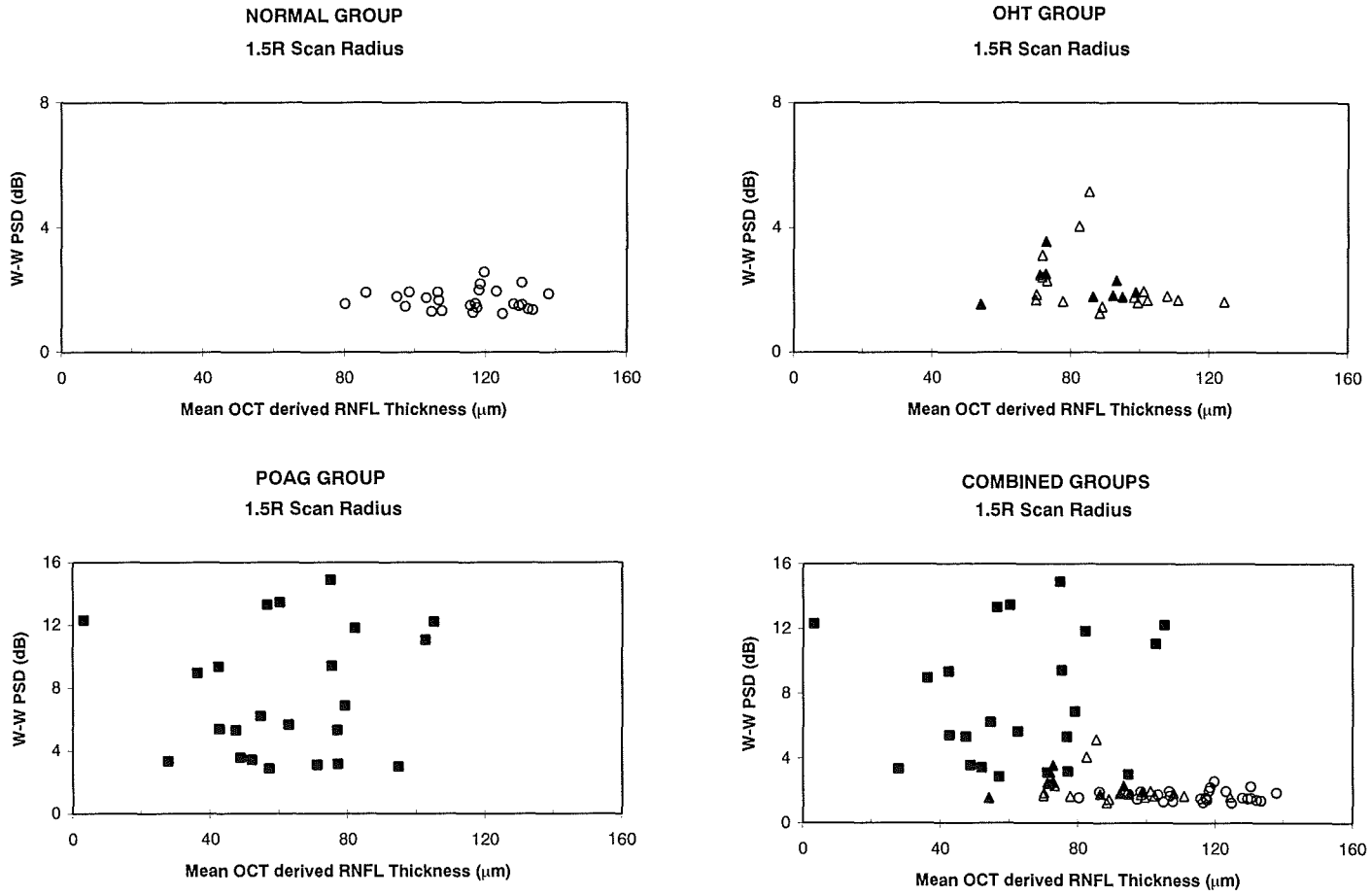

Figure 6.19. The relationship between the mean Global RNFL thickness and the W-W Pattern Standard Deviation (PSD), at Visit One, for the 1.5R scan radius, for the Normal group (open circles) (upper left), for the OHT group (open triangles) and OHT(H) (closed triangles) (upper right), for the POAG group (closed squares) (lower left) and for all the groups (lower right). Each data point represents a single individual. Note the different y-axis scale used for the Normal and OHT group plots compared to the POAG and Combined group plots.

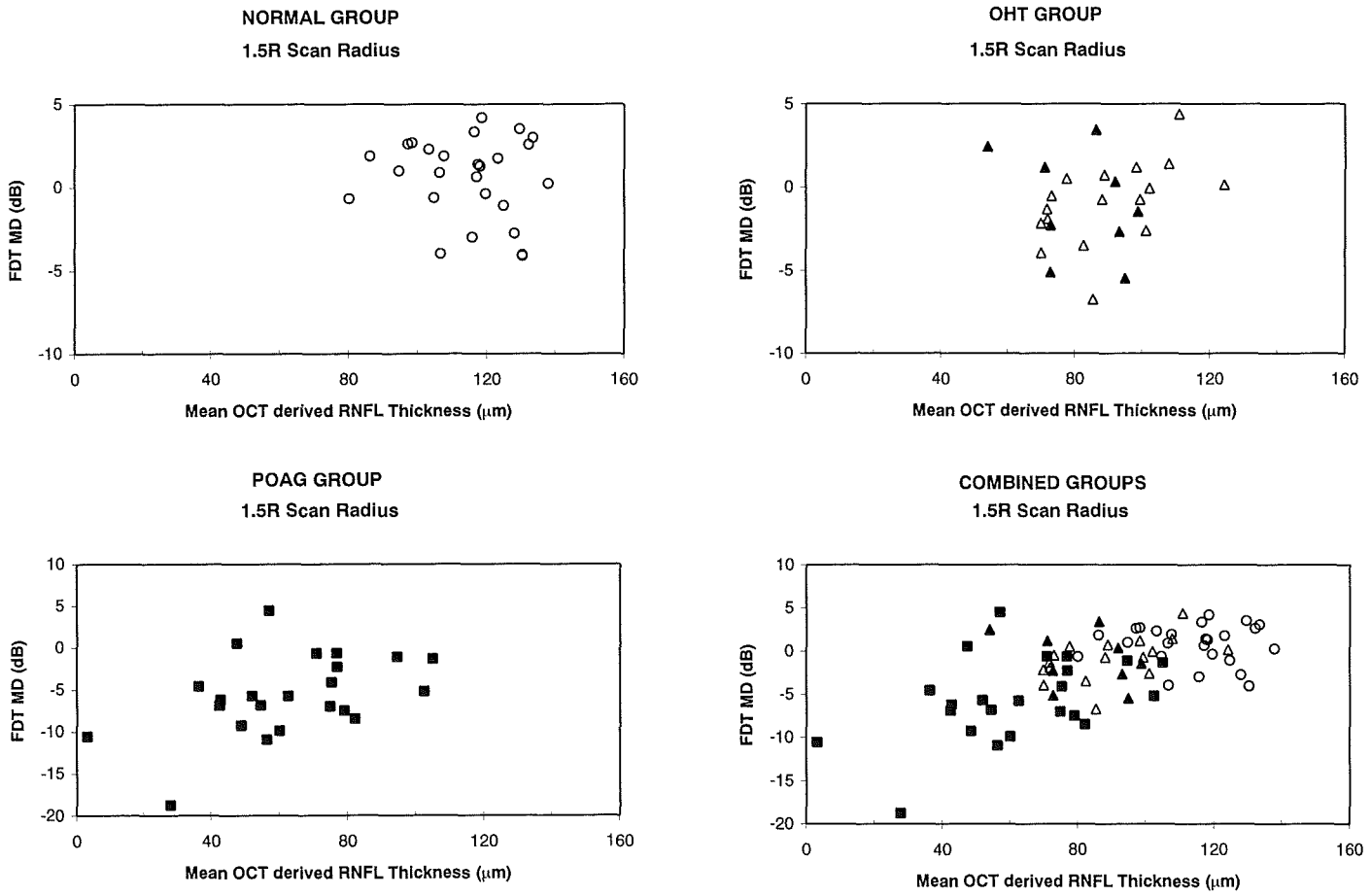

Figure 6.20. The relationship between the mean Global RNFL thickness and the FDT Mean Deviation (MD), at Visit One, for the 1.5R scan radius, for the Normal group (open circles) (upper left), for the OHT group (open triangles) and OHT(H) (closed triangles) (upper right), for the POAG group (closed squares) (lower left) and for all the groups (lower right). Each data point represents a single individual. Note the different y-axis scale used for the Normal and OHT group plots compared to the POAG and Combined group plots.

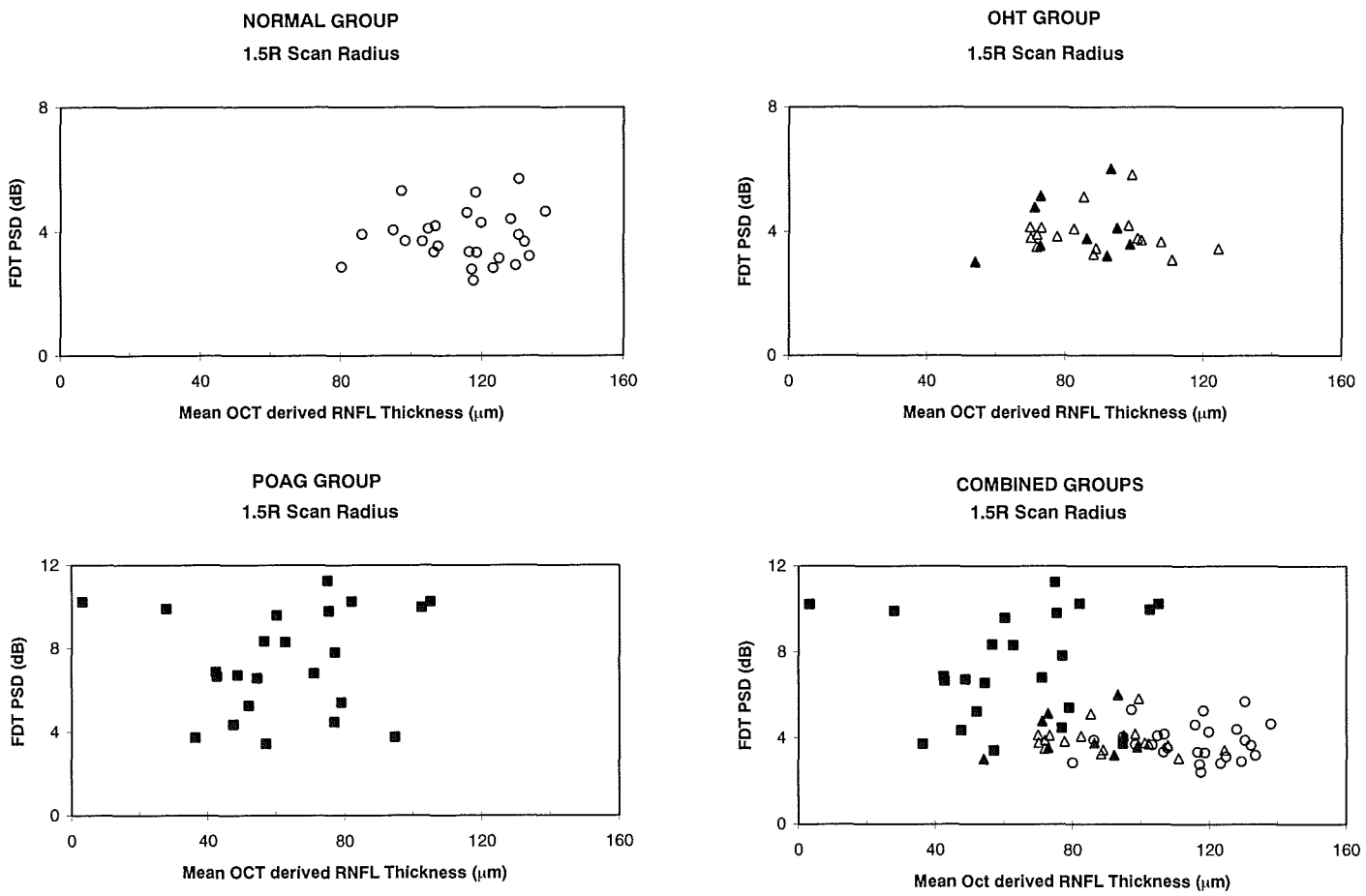

Figure 6.21. The relationship between the mean Global RNFL thickness and the FDT Pattern Standard Deviation (PSD), at Visit One, for the 1.5R scan radius, for the Normal group (open circles) (upper left), for the OHT group (open triangles) and OHT(H) (closed triangles) (upper right), for the POAG group (closed squares) (lower left) and for all the groups (lower right). Each data point represents a single individual. Note the different y-axis scale used for the Normal and OHT group plots compared to the POAG and Combined group plots.

6.8.3.2 2.0R Scan radius.

6.8.3.2.1 Age.

The RNFL thickness declined with increase in age ($p=0.020$, $R^2=0.27$) (Figure 6.14). The decline in RNFL thickness for the Normal group was 4.0μm per decade.

6.8.3.2.2 Diagnostic category.

The thickness also varied across the three diagnostic groups ($p<0.001$) (Table 6.3). The Group mean RNFL at the baseline visit was 19.7% thinner in the OHT group than in the Normal group and 43.8% thinner in the POAG group compared to the Normal group (Table 6.6).

6.8.3.2.3 RNFL thickness derived by HRT.

The Global RNFL thickness for the combined groups increased as the RNFL thickness derived by HRT increased. ($R^2 = 0.29$; Table 6.7).

6.8.3.2.4 RDAR derived by the HRT.

The Global RNFL thickness for the combined groups decreased as the RDAR decreased ($R^2=0.34$).

6.8.3.2.5 CSM derived by the HRT.

The CSM for the combined groups became more positive as the RNFL thickness declined similar to the result found for the 1.5R scan radius ($R^2=0.41$).

6.8.3.2.6 Additional HRT variables.

As found with the 1.5R scan radius, the mean Global derived RNFL thickness was weakly associated with the RV ($R^2=0.12$), the RA ($R^2=0.11$), the HVC ($R^2=0.01$). A decline in the RNFL thickness was associated with an increase in the CA ($R^2=0.34$), and the CDAR ($R^2=0.38$) and a decrease in the RNFL cross-sectional area ($R^2=0.38$).

6.8.3.2.7 Visual field.

The W-W MD remained relatively constant for a Global RNFL thickness greater than approximately 70μm, however, the MD become increasingly more negative as the RNFL thickness fell below 70μm. The W-W PSD increased in a variable manner between individuals as the RNFL thickness became thinner than 70μm.

The MD for FDT similarly declined, and became progressively more negative with a decrease in the RNFL thickness. The PSD again exhibited a marked and variable increase for RNFL thickness of less than approximately 70μm.

6.8.3.3 1.73 mm Scan radius.

6.8.3.3.1 Age.

The RNFL thickness again declined with increase in age (p=0.002, R^2=0.33) (Figure 6.14). The decline in RNFL thickness for the Normal group was 4.0μm per decade.

6.8.3.3.2 Diagnostic category.

The thickness also varied across the three diagnostic groups (p<0.001) (Table 6.3). The Group Mean RNFL at the baseline visit was 18.6% thinner for the OHT group than for the Normal group and 44.2% thinner for the POAG group compared to the Normal group (Table 6.6).

6.8.3.3.3 RNFL thickness derived by HRT.

The Global RNFL thickness increased with increase in HRT derived RNFL thickness (R^2=0.26 Combined group) (Table 6.7).

6.8.3.3.4 RDAR derived by the HRT.

The global RNFL thickness decreased as the RDAR decreased (R^2=0.26) (Table 6.7).

6.8.3.3.5 CSM derived by the HRT.

The CSM became more positive as the Global RNFL thickness declined similar to the result found for the 1.5R scan radius (R^2=0.32) (Table 6.7).

6.8.3.3.6 Additional HRT variables.

The mean Global derived RNFL thickness was again weakly associated with the RV (R^2=0.16), the RA (R^2=0.19), the HVC (R^2=0.03) and the RNFL cross-sectional area (R^2=0.18). A decline in the RNFL thickness was associated with an increase in the CA (R^2=0.24) and the CDAR (R^2=0.34) (Table 6.7).

6.8.3.3.7 Visual field.

The MD became more negative and the PSD more positive and more variable between individuals as the Global RNFL thickness decreased, once the thickness had declined below approximately 80μm.

6.8.4 ANOVA for the Global RNFL thickness as a function of scan radius, diagnostic group and visit.

The RNFL thickness declined with increase in age ($p=0.016$) (Table 6.8). The RNFL thickness was independent of disc area ($p=0.146$). The thickness varied across the three diagnostic groups; it was thickest in the Normal group, thinner in the OHT group and was thinnest in the POAG group ($p<0.001$). (Table 6.8). The RNFL thickness decreased with increase in scan radius ($p<0.001$) and this reduction in thickness varied between groups ($p=0.011$) and was more marked for the Normal group (Table 6.9 and Figure 6.22). The RNFL thickness for both radii tended to be greater at the second visit as disc area increased ($p<0.001$). For 3 outliers, the RNFL thickness with the 1.5R scan was thinner compared to that for the 2.0R scan. The cause is unknown, but is likely to be an artefact.

Global	Scan Radii
FACTOR	**1.5R and 2.0R**
Age	p=0.016
Diagnosis	p<0.001
Disc Area	NS
Scan Radius	p<0.001
Scan Radius x Age	NS
Scan Radius x Diagnosis	p=0.011
Scan Radius x Disc Area	NS
Visit	NS
Visit x Age	NS
Visit x Diagnosis	NS
Visit x Disc Area	p<0.001
Number of Scans	NS
Number of Scans x Age	NS
Number of Scans x Diagnosis	NS
Number of Scans x Disc Area	NS
Number of Scans x Disc Area x Diagnosis	NS
Number of Scans x Age x Diagnosis	NS
Scan Radius x Visit	NS
Scan Radius x Visit x Age	NS
Scan Radius x Visit x Diagnosis	NS
Scan Radius x Visit x Disc Area	NS
Scan Radius x Number of Scans	NS
Scan Radius x Number of Scans x Age	NS
Scan Radius x Number of Scans x Diagnosis	NS
Scan Radius x Number of Scans x Disc Area	NS
Scan Radius x Number of Scans x Disc Area x Diagnosis	NS
Scan Radius x Number of Scans x Age x Diagnosis	NS
Scan Radius x Number of Scans x Disc Area x Age	NS
Visit x Number of Scans	p =0.030
Visit x Number of Scans x Age	NS
Visit x Number of Scans x Diagnosis	NS
Visit x Number of Scans x Disc Area	p =0.003
Visit x Number of Scans x Disc Area x Diagnosis	NS
Visit x Number of Scans x Age x Diagnosis	NS
Visit x Disc Area x Diagnosis	NS
Visit x Age x Diagnosis	NS
Scan Radius x Visit x Number of Scans	NS
Scan Radius x Visit x Number of Scans x Age	NS
Scan Radius x Visit x Number of Scans x Diagnosis	NS
Scan Radius x Visit x Number of Scans x Disc Area	NS
Scan Radius x Visit x Number of Scans x Disc Area x Diagnosis	NS
Scan Radius x Visit x Number of Scans x Disc Area x Age	NS
Scan Radius x Visit x Age x Diagnosis	NS
Scan Radius x Disc Area x Diagnosis	NS
Scan Radius x Age x Diagnosis	NS
Area x Diagnosis	NS
Age x Diagnosis	NS

Table 6.8. Summary of the ANOVA for Global RNFL thickness determined using only the thickness derived by the first and seventh scans for the 1.5R and 2.0R scan radii .

	GLOBAL			
	VISIT 1		VISIT 2	
	MEAN	SD	MEAN	SD
NORMAL	26.48	6.94	25.99	9.28
OHT	16.88	11.35	18.56	12.02
POAG	13.07	9.85	15.95	13.47

Table 6.9. The Group Mean and SD of the difference in Global RNFL thickness (μm) between the 1.5R scan radius and the 2.0R scan radius, for the each of the three diagnostic groups.

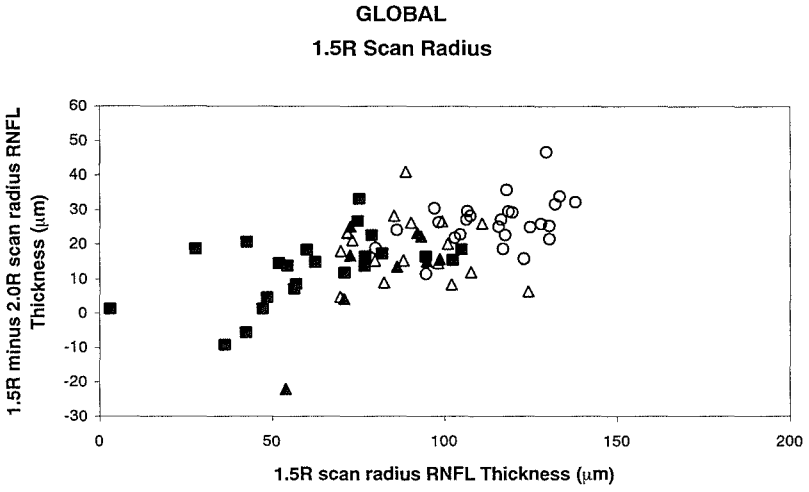

Figure 6.22. The difference in Global RNFL thickness between the 1.5R scan radius and the 2.0R scan radius, as a function of the Global RNFL thickness for the 1.5R scan radius, for the Normal group (open circles) for the OHT group (open triangles), for the OHT(H) group (closed triangles) and for the POAG group (open squares). Each data point represents a single individual.

6.8.5 Within-visit variability of the Sector RNFL thickness.

The Group mean COV for the Sector RNFL thickness at Visit One and at Visit Two as function of the type of circular scan and of diagnosis is given in Table 6.10, for the Superior, Inferior, Temporal and Nasal sectors. The within-visit variation is shown as one SD as a function of the Mean RNFL thickness for the Superior sector for each of the three scan radii is shown in Figure 6.23.

The Group mean COV was lowest for the Normal group across each of the sectors and across each scan radius. It was greatest for the POAG group across each of the sectors and across each scan radius. The COV was greatest for the Temporal and Nasal sectors irrespective of diagnostic group.

1.5R Scan Radius.

	SUPERIOR				INFERIOR				TEMPORAL				NASAL			
	Visit 1		Visit 2		Visit 1		Visit 2		Visit 1		Visit 2		Visit 1		Visit 2	
	MEAN	SD	MEAN	SD	MEAN	SD	MEAN	SD	MEAN	SD	MEAN	SD	MEAN	SD	MEAN	SD
NORMAL	7.74	5.72	7.40	3.66	8.33	4.67	6.83	3.21	10.27	7.80	11.33	8.36	12.91	7.43	12.72	10.06
OHT	14.22	8.21	13.37	7.14	13.43	11.18	14.07	9.03	21.55	14.31	26.83	24.22	27.53	14.85	29.43	26.14
POAG	17.31	13.74	19.34	15.26	24.98	14.91	20.11	11.90	34.28	28.98	47.36	53.50	36.07	24.92	39.88	31.46

2.0R Scan Radius.

	SUPERIOR				INFERIOR				TEMPORAL				NASAL			
	Visit 1		Visit 2		Visit 1		Visit 2		Visit 1		Visit 2		Visit 1		Visit 2	
	MEAN	SD	MEAN	SD	MEAN	SD	MEAN	SD	MEAN	SD	MEAN	SD	MEAN	SD	MEAN	SD
NORMAL	8.62	5.34	8.86	5.39	8.41	4.05	7.94	4.81	12.40	7.68	12.25	11.97	18.04	10.40	17.42	9.86
OHT	11.75	7.15	13.53	8.70	11.68	7.73	13.67	8.61	16.75	9.61	22.33	12.00	34.39	23.18	47.59	48.26
POAG	21.14	20.48	19.29	13.40	24.27	17.36	26.29	18.81	32.38	30.24	27.42	20.72	49.53	30.38	46.89	23.25

1.73mm Scan Radius.

	SUPERIOR				INFERIOR				TEMPORAL				NASAL			
	Visit 1		Visit 2		Visit 1		Visit 2		Visit 1		Visit 2		Visit 1		Visit 2	
	MEAN	SD	MEAN	SD	MEAN	SD	MEAN	SD	MEAN	SD	MEAN	SD	MEAN	SD	MEAN	SD
NORMAL	7.86	4.56	7.86	3.44	7.38	3.15	8.22	4.71	9.73	5.83	11.00	4.99	17.14	10.42	14.56	5.20
OHT	12.00	6.78	13.93	11.26	12.71	8.60	13.64	9.08	18.86	18.90	20.16	12.22	32.94	18.84	31.34	20.31
POAG	21.58	19.24	19.94	14.35	23.16	18.66	25.62	28.61	43.41	56.09	34.93	53.21	44.38	33.75	40.61	20.39

Table 6.10. The Group Mean Coefficients of Variation (%) for the Superior, Inferior, Temporal and Nasal Sector RNFL thickness (μm), for the Normal group, the OHT group, and the POAG group, for each of the three scan radii, for each of the two visits.

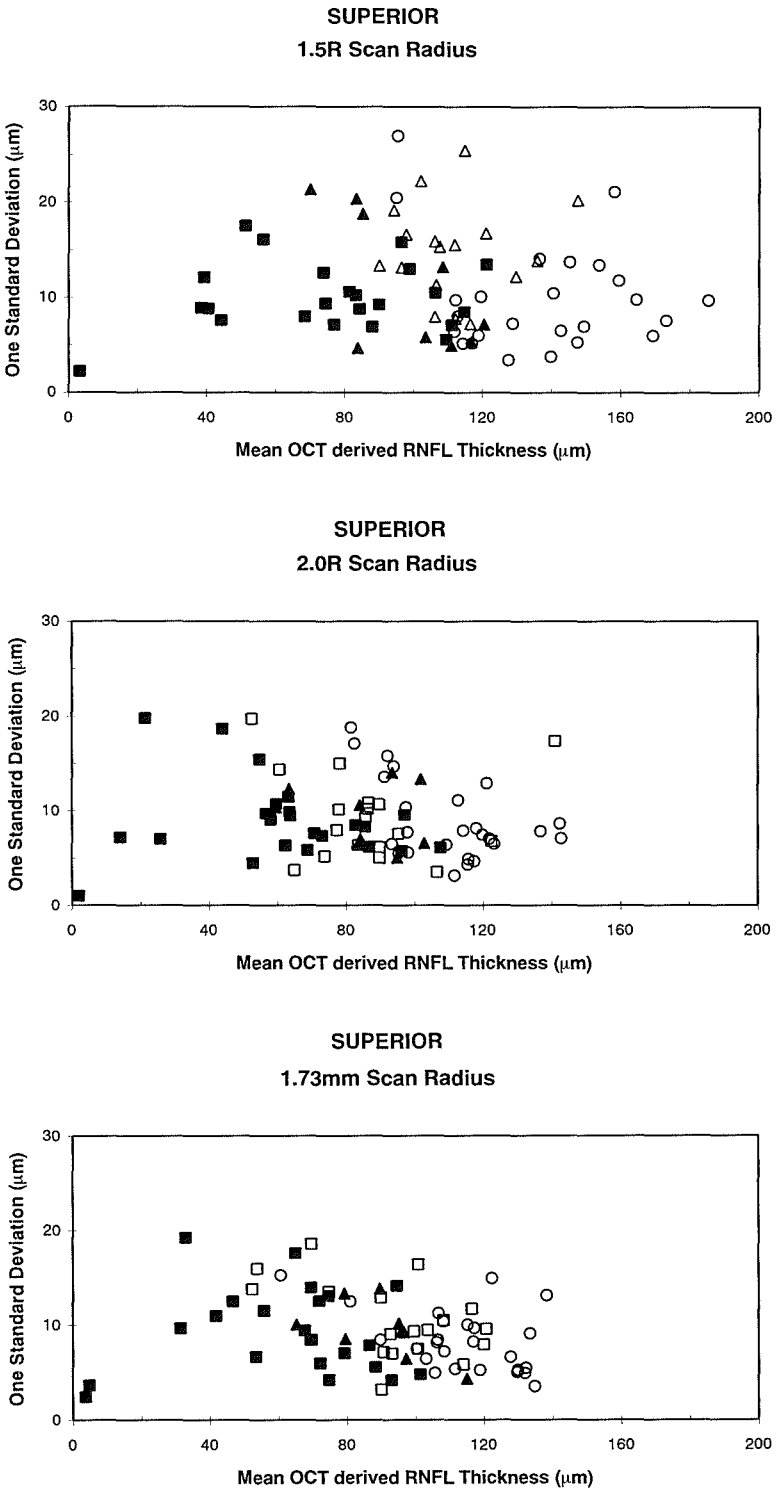

Figure 6.23. The within-visit variation as defined by one SD of the mean Superior Sector RNFL thickness, at Visit One, for the 1.5R scan radius (top), for the 2.0R scan radius (middle) and for the 1.73mm scan radius (bottom), for the Normal group (open circles), for the OHT(H) group (open triangles), for theOHT(H) group (closed triangles) and for the POAG group (closed squares). Each data point represents a single individual.

6.8.6 Between-visit variability of the Superior Sector RNFL thickness.

The Group mean and one SD of the Sector RNFL thickness at Visit One and at Visit Two as a function of scan radius and of diagnosis is given in Table 6.11 for the each of the sectors. The ANOVA summary table for each of the sectors is given in Table 6.12.

6.8.6.1 1.5R Scan radius.

The RNFL thickness did not vary between the first and second visits (p=0.503) for the Superior sector. The limits of agreement for the RNFL thickness of this sector between the first and second visits are given in Table 6.13. The difference in the RNFL thickness between the two visits is presented as a function of the mean of the two visits in Figure 6.24. For the sake of brevity, graphical presentation of the data is only provided for the superior 1.5R scan radii. The results for the remaining sectors and scan radii are given in tabulated form. The RNFL thickness was independent of the number of scans (p=0.256). The RNFL thickness increased with increase in disc area (p=0.013) (Figure 6.25).

6.8.6.2 2.0R Scan radius.

The limits of agreement for the RNFL thickness between the first and second visit are shown in Table 6.13. The RNFL thickness did not vary between visits (p=0.508) and was independent of the number of scans (p=0.941). The RNFL thickness increased with increase in disc area (p=0.026).

6.8.6.3 1.73 mm Scan radius.

The RNFL thickness was independent of visit (p=0.395) and of the number of scans (p=0.609) (Table 6.12). The limits of agreement for the RNFL thickness between the first and second visit are given in Table 6.13. The RNFL thickness was independent of disc area (p=0.694).

1.5R Scan Radius.

	SUPERIOR				INFERIOR				TEMPORAL				NASAL			
	Visit 1		Visit 2		Visit 1		Visit 2		Visit 1		Visit 2		Visit 1		Visit 2	
	MEAN	SD	MEAN	SD	MEAN	SD	MEAN	SD	MEAN	SD	MEAN	SD	MEAN	SD	MEAN	SD
NORMAL	136.40	23.93	136.50	22.20	139.82	15.33	137.08	15.86	84.90	18.67	83.82	18.31	96.34	21.88	95.98	17.44
OHT	106.37	17.04	99.33	26.27	108.54	20.01	107.93	24.01	60.70	19.65	61.42	20.95	70.74	21.43	69.83	26.53
POAG	76.21	29.90	80.31	28.11	72.81	27.67	73.54	23.24	44.02	28.25	46.16	24.53	53.23	27.00	53.19	27.57

2.0R Scan Radius.

	SUPERIOR				INFERIOR				TEMPORAL				NASAL			
	Visit 1		Visit 2		Visit 1		Visit 2		Visit 1		Visit 2		Visit 1		Visit 2	
	MEAN	SD	MEAN	SD	MEAN	SD	MEAN	SD	MEAN	SD	MEAN	SD	MEAN	SD	MEAN	SD
NORMAL	108.97	19.05	108.92	19.67	107.97	16.23	108.29	15.74	68.02	16.28	69.19	17.30	61.47	20.98	62.01	17.66
OHT	85.92	19.25	82.80	22.82	85.96	20.81	88.35	26.05	53.62	21.03	50.60	21.41	49.16	18.74	44.11	23.45
POAG	61.35	26.73	61.48	23.43	57.17	25.06	53.76	21.92	42.71	20.70	41.43	17.55	33.82	22.65	31.21	19.05

1.73mm Scan Radius.

	SUPERIOR				INFERIOR				TEMPORAL				NASAL			
	Visit 1		Visit 2		Visit 1		Visit 2		Visit 1		Visit 2		Visit 1		Visit 2	
	MEAN	SD	MEAN	SD	MEAN	SD	MEAN	SD	MEAN	SD	MEAN	SD	MEAN	SD	MEAN	SD
NORMAL	112.85	17.65	114.07	13.60	117.70	12.71	114.36	11.53	73.45	15.44	73.97	15.90	68.12	16.57	68.91	13.44
OHT	92.78	18.38	87.25	22.61	95.98	21.94	91.07	24.54	56.02	15.18	55.09	18.87	54.00	20.91	50.36	26.04
POAG	62.99	26.20	66.51	23.03	62.00	27.69	64.14	25.42	43.34	22.66	43.22	19.84	37.28	22.19	37.46	20.45

Table 6.11. The Group Mean and SD of the Sector RNFL thickness (μm), at Visit One and Visit Two for the 1.5R scan radius (top), for the 2.0R scan radius (middle) and for the 1.73mm scan radius (bottom) for the Normal, OHT, and POAG groups.

	Superior			Inferior			Temporal			Nasal		
FACTOR	**1.5R**	**2.0R**	**1.73mm**	**1.5R**	**2.0R**	**1.73mm**	**1.5R**	**2.0R**	**1.73mm**	**1.5R**	**2.0R**	**1.73mm**
Age	p=0.002	p=0.014	p=0.003	NS	NS	NS	p<0.001	p=0.002	p<0.001	NS	NS	NS
Diagnosis	p<0.001	p<0.001	p<0.001	p<0.001	p<0.001	p<0.001	p<0.001	p<0.001	p<0.001	p<0.001	p<0.001	p<0.001
Disc Area	p=0.016	p=0.026	NS	NS	NS	NS	p=0.013	p=0.007	NS	NS	NS	p=0.035
Visit	NS	NS	NS	NS	p=0.014	NS	NS	NS	NS	NS	NS	NS
Visit x Age	NS	NS	NS	NS	NS	NS	NS	NS	NS	NS	NS	NS
Visit x Diagnosis	NS	NS	NS	NS	p=0.022	NS	NS	NS	NS	NS	NS	NS
Visit x Disc Area	NS	NS	NS	NS	p<0.001	NS	p=0.004	p=0.018	NS	NS	NS	NS
Number of Scans	NS	NS	NS	NS	NS	NS	NS	NS	NS	NS	NS	NS
Number of Scans x Age	NS	NS	NS	NS	NS	NS	NS	NS	NS	NS	p=0.039	NS
Number of Scans x Diagnosis	NS	NS	NS	NS	NS	p = 0.030	NS	NS	NS	NS	NS	NS
Number of Scans x Disc Area	NS	NS	NS	NS	NS	p = 0.041	NS	NS	NS	NS	NS	NS
Visit x Number of Scans	p=0.04	NS	NS	NS	NS	NS	NS	NS	p=0.040	NS	NS	NS
Visit x Number of Scans x Age	NS	NS	NS	NS	NS	NS	NS	NS	NS	NS	NS	NS
Visit x Number of Scans x Diagnosis	NS	NS	NS	NS	NS	p = 0.052	NS	NS	NS	NS	NS	NS
Visit x Number of Scans x Disc Area	NS	NS	NS	NS	NS	NS	p=0.007	NS	NS	p<0.001	NS	NS
Area x Diagnosis	NS	NS	NS	NS	NS	NS	NS	NS	NS	NS	NS	NS
Age x Diagnosis	NS	NS	NS	NS	NS	NS	NS	NS	NS	NS	NS	NS
Visit x Disc Area x Diagnosis	NS	NS	NS	NS	NS	NS	NS	NS	NS	NS	NS	NS
Visit x Age x Diagnosis	NS	NS	NS	NS	NS	NS	NS	NS	NS	NS	NS	NS
No.of Scans x Disc Area x Diagnosis	NS	NS	NS	NS	NS	NS	NS	NS	NS	NS	NS	NS
No.of Scans x Age x Diagnosis	NS	NS	NS	NS	NS	NS	NS	NS	NS	NS	NS	NS
Visit x Number of Scans x Disc Area x Diagnosis	NS	NS	NS	NS	NS	NS	p=0.050	NS	NS	NS	NS	NS
Visit x Number of Scans x Age x Diagnosis	NS	NS	NS	NS	NS	NS	NS	NS	NS	NS	NS	NS

Table 6.12. Summary of the ANOVA for the Superior, Inferior, Temporal and Nasal Sector RNFL thickness determined by each of the three scan radii.

1.5R Scan Radius.

	SUPERIOR				INFERIOR				TEMPORAL				NASAL			
			95% L.O.A				95% L.O.A				95% L.O.A				95% L.O.A	
	G.M.D	SD	Upper	Lower	G.M.D	SD	Upper	Lower	G.M.D	SD	Upper	Lower	G.M.D	SD	Upper	Lower
NORMAL	0.28	9.28	18.47	-17.91	-1.73	9.83	17.52	-20.99	-1.13	9.68	18.98	-20.11	1.22	11.50	23.76	-21.31
OHT	-7.04	22.31	36.68	-50.75	-0.61	20.64	39.84	-41.06	0.72	16.38	32.83	-31.38	-0.90	20.92	40.10	-41.91
POAG	4.10	11.86	27.34	-19.15	0.73	14.74	29.62	-28.16	2.15	13.21	28.03	-23.74	-0.05	15.12	29.60	-29.69

2.0R Scan Radius.

	SUPERIOR				INFERIOR				TEMPORAL				NASAL			
			95% L.O.A				95% L.O.A				95% L.O.A				95% L.O.A	
	G.M.D	SD	Upper	Lower	G.M.D	SD	Upper	Lower	G.M.D	SD	Upper	Lower	G.M.D	SD	Upper	Lower
NORMAL	0.30	9.42	18.76	-18.17	0.81	8.10	16.66	-15.05	0.93	12.71	25.86	-23.99	2.05	9.82	21.29	-17.20
OHT	-3.50	16.65	29.14	-36.14	-1.64	18.06	33.76	-37.04	-3.00	12.97	22.43	-28.42	-5.14	16.82	27.84	-38.12
POAG	0.14	10.49	20.70	-20.43	-3.41	15.22	26.42	-33.24	-1.28	14.87	27.88	-30.43	-2.61	12.99	22.86	-28.08

1.73mm Scan Radius.

	SUPERIOR				INFERIOR				TEMPORAL				NASAL			
			95% L.O.A				95% L.O.A				95% L.O.A				95% L.O.A	
	G.M.D	SD	Upper	Lower	G.M.D	SD	Upper	Lower	G.M.D	SD	Upper	Lower	G.M.D	SD	Upper	Lower
NORMAL	1.61	10.47	22.13	-18.91	0.65	8.14	16.60	-15.31	0.33	10.44	20.80	-20.13	2.10	10.36	22.38	-18.24
OHT	-5.54	14.71	23.30	-34.38	-4.91	15.39	25.25	-35.07	-0.93	15.47	29.40	-31.26	-3.64	18.73	33.08	-40.35
POAG	3.52	10.44	23.98	-16.95	2.14	16.51	34.50	-30.21	-0.12	12.09	23.57	-23.82	0.18	8.38	16.61	-16.25

Table 6.13. The Group mean difference and SD of the Superior, Inferior, Temporal and Nasal sector RNFL thickness (mm), between the two visits, for the 1.5R scan radius (top), for the 2.0R scan radius (middle) and for the 1.73mm scan radius (bottom) for the Normal, OHT and POAG groups. The upper and lower limits of agreement for the 95% confidence interval are provided. (G.M.D = Group Mean Difference; L.O.A = Limits of Agreement).

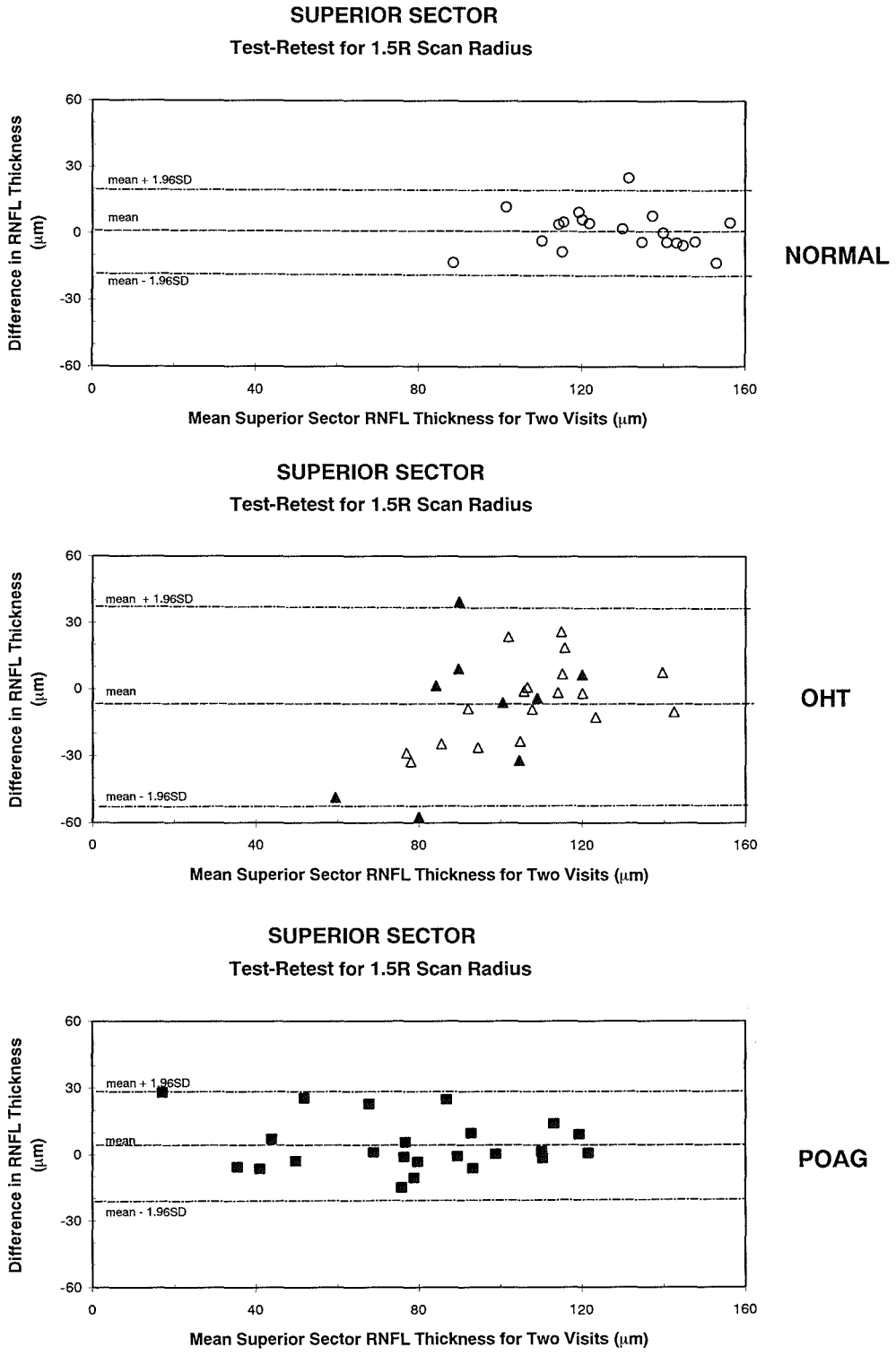

Figure 6.24. The difference in the Superior Sector RNFL thickness as a function of the mean Superior sector RNFL thickness for the two visits, for the Normal group (top), for the OHT group (open triangles) and OHT(H) group (closed triangles) (middle) and for the POAG group (bottom) with the 1.5R scan radius. The mean and the 95% confidence limits are shown.

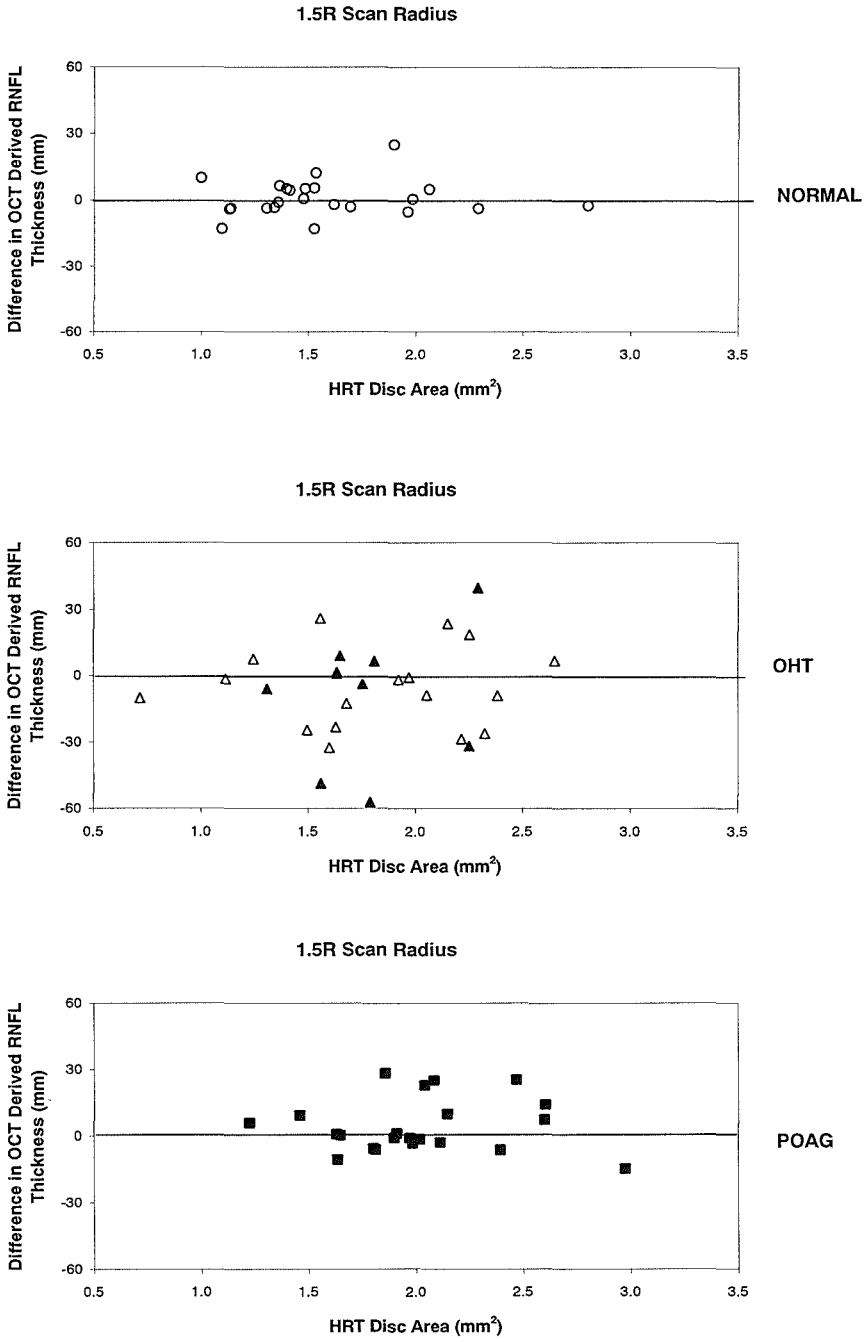

Figure 6.25. The difference in the Superior Sector RNFL thickness between the first and second visits referred to the second visit as a function of the HRT derived Disc Area, for the 1.5R scan radius, for the Normal group (top), for the OHT and OHT(H) group (middle) and for the POAG group (bottom). Each data point represents the mean of 7 scans for each individual.The line indicates zero difference.

6.8.7 Relationship between the Superior sector RNFL thickness and age, diagnostic group, HRT derived RNFL thickness, related HRT topographical parameters, and visual function (i.e. Validity).

6.8.7.1 1.5R Scan radius.

6.8.7.1.1 Age.

The RNFL thickness declined with increase in age ($p=0.002$, $R^2=0.22$) (Figure 6.26, Table 6.12). The decline in RNFL thickness for the Normal group was 6.3μm, per decade (Table 6.14).

6.8.7.1.2 Diagnostic category.

As would be expected, the thickness varied across the three diagnostic groups ($p<0.001$) (Table 6.12). The Group mean RNFL for the baseline visit was approximately 22% thinner for the OHT group than for the Normal group and 44% thinner for the POAG group compared to the Normal group (Table 6.15).

6.8.7.1.3 RNFL thickness derived by HRT.

The OCT superior sector RNFL thickness was weakly associated with the HRT derived superior RNFL thickness ($R^2=0.15$) (Table 6.16, Figure 6.27)).

6.8.7.1.4 RDAR derived by the HRT.

The superior sector RNFL thickness decreased as the superior RDAR decreased ($R^2=0.43$) (Table 6.16, Figure 6.27).

6.8.7.1.5 CSM derived by the HRT.

The superior sector RNFL thickness decreased as the CSM became more positive ($R^2=0.44$) (Table 6.16, Figure 6.27).

6.8.7.1.6 Additional HRT variables.

The superior sector RNFL thickness decreased as the CA ($R^2=0.41$) and CDAR ($R^2=0.43$) increased, was weakly associated with RNFL cross-sectional area ($R^2=0.10$) and RA ($R^2=0.13$) and was independent of the HVC ($R^2=0.00$) (Table 6.16).

6.8.7.1.7 Visual field.

The relationship between the Superior sector RNFL thickness and the visual field, as provided by the log summed PD probability scores for the corresponding region for W-W perimetry, are given in Figure 6.28. The relationship between the log summed PD probability scores for W-W perimetry and the Superior sector RNFL thickness appeared to be non-linear. The W-W log summed PD probability scores are generally greater than 1.5 (AU) once the RNFL thickness has fallen below 80μm. There is a wide variation in the W-W log summed PD probability scores for a RNFL thickness between 80 and 120μm. W-W log summed PD probability scores of less than 1.00 but greater than zero can arise from single isolated defective locations and generally

can be considered as 'noise'. The outlier with POAG in Figure 6.28 exhibiting a RNFL thickness of approximately 40μm with a low PD probability score, exhibited an extensive diffuse visual field defect.

The relationship between Superior sector RNFL thickness and the equivalent log summed PD probability scores for the corresponding region for FDT perimetry are shown in Figure 6.29. The log summed PD probability scores for FDT increased, and became markedly more variable with a decrease in the RNFL thickness. The relationship was weaker and more variable, compared to that for W-W perimetry. The outlier with POAG in Figure 6.29 exhibiting a RNFL of approximately 4μm with a PD probability score of zero, exhibited an extensive diffuse visual field defect.

6.8.7.2. 2.0R Scan radius.

6.8.7.2.1 Age.

The RNFL thickness declined with increase in age ($p=0.014$, $R^2=0.18$) (Table 6.12). The reduction in RNFL thickness for the Normal group was 4.0μm, per decade (Table 6.14).

6.8.7.2.2 Diagnostic category.

The thickness varied across the three diagnostic groups; it was again thinner in the OHT group than in the Normal group and was again thinnest in the glaucoma group ($p<0.001$). (Table 6.11). The Group mean RNFL for the baseline visit was approximately 21% thinner for the OHT group than for the Normal group and 44% thinner for the POAG group compared to the Normal group (Table 6.15).

6.8.7.2.3 RNFL thickness derived by HRT.

The OCT superior sector RNFL thickness was largely independent of the HRT derived superior RNFL thickness ($R^2=0.12$) (Table 6.12).

6.8.7.2.4 RDAR derived by the HRT.

The superior sector RNFL thickness decreased as the RDAR decreased ($R^2=0.41$) (Table 6.16).

6.8.7.2.5 CSM derived by the HRT.

The CSM became more positive as the RNFL thickness decreased ($R^2=0.43$).

6.8.7.2.6 Additional HRT variables.

The superior sector RNFL thickness for the 2.0R scan radius decreased as the CA ($R^2=0.39$) and the CDAR ($R^2=0.41$) increased and the RNFL cross-sectional area ($R^2=0.41$) decreased, but was independent of the HVC ($R^2=0.00$), and RA ($R^2=0.12$).

6.8.7.2.7 Visual field.

The relationship between the log summed PD probability scores for Inferior hemifield W-W perimetry and the Superior sector RNFL thickness for the 2.0R scan radius appeared to be non-linear (Figure 6.28). The W-W log summed PD probability scores are generally greater than 1.0 (AU) once the RNFL thickness has fallen below approximately 70μm. The W-W log summed PD probability scores are variable for an RNFL thickness between 70 and 110μm.

The log summed PD probability scores for FDT increased, and became markedly more variable with a decrease in the RNFL thickness as shown in Figure 6.29.

6.8.7.3 1.73mm Scan radius.

6.8.7.3.1 Age.

The superior sector RNFL thickness declined with increase in age ($p=0.003$; $R^2=0.26$) (Table 6.12), with a 5.1μm per decade reduction in RNFL thickness for the Normal group (Table 6.14).

6.8.7.3.2 Diagnostic category.

The superior sector RNFL thickness varied across the three diagnostic groups; it was thinner in the OHT group than in the Normal group and was thinnest in the POAG group ($p<0.001$). (Tables 6.11). The Group mean RNFL for the baseline visit was approximately 18% thinner for the OHT group than for the Normal group and 44% thinner for the POAG group compared to the Normal group (Table 6.15).

6.8.7.3.3 RNFL thickness derived by HRT.

The superior sector RNFL thickness was largely independent of the HRT derived superior RNFL thickness ($R^2=0.17$) (Table 6.16).

6.8.7.3.4 RDAR derived by the HRT.

The superior sector RNFL thickness decreased as the RDAR decreased ($R^2=0.38$) (Table 6.16).

6.8.7.3.5 CSM derived by the HRT.

The CSM became more positive as the RNFL thickness decreased ($R^2=0.38$) (Table 6.16).

6.8.7.3.6 Additional HRT variables.

The Superior sector RNFL thickness decreased as the CA ($R^2=0.31$) and CDAR ($R^2=0.38$) increased but was weakly associated with RA ($R^2=0.23$) largely independent of the RNFL cross-sectional area ($R^2=0.16$) and independent of ($R^2=0.00$), and HVC (Table 6.16).

6.8.7.3.7 Visual field.

The relationship between the log summed PD probability scores for the Inferior hemifield W-W perimetry and the Superior sector RNFL thickness for the 1.73mm scan radius appeared to be

weak (Figure 6.28). The W-W log summed PD probability scores are generally greater than 1.0 (AU) once the RNFL thickness has fallen below approximately 75μm. The W-W log summed PD probability scores are variable for an RNFL thickness between 75 and 120μm.

The log summed PD probability scores for FDT increased, and are more variable with a decrease in the RNFL thickness as shown in Figure 6.29.

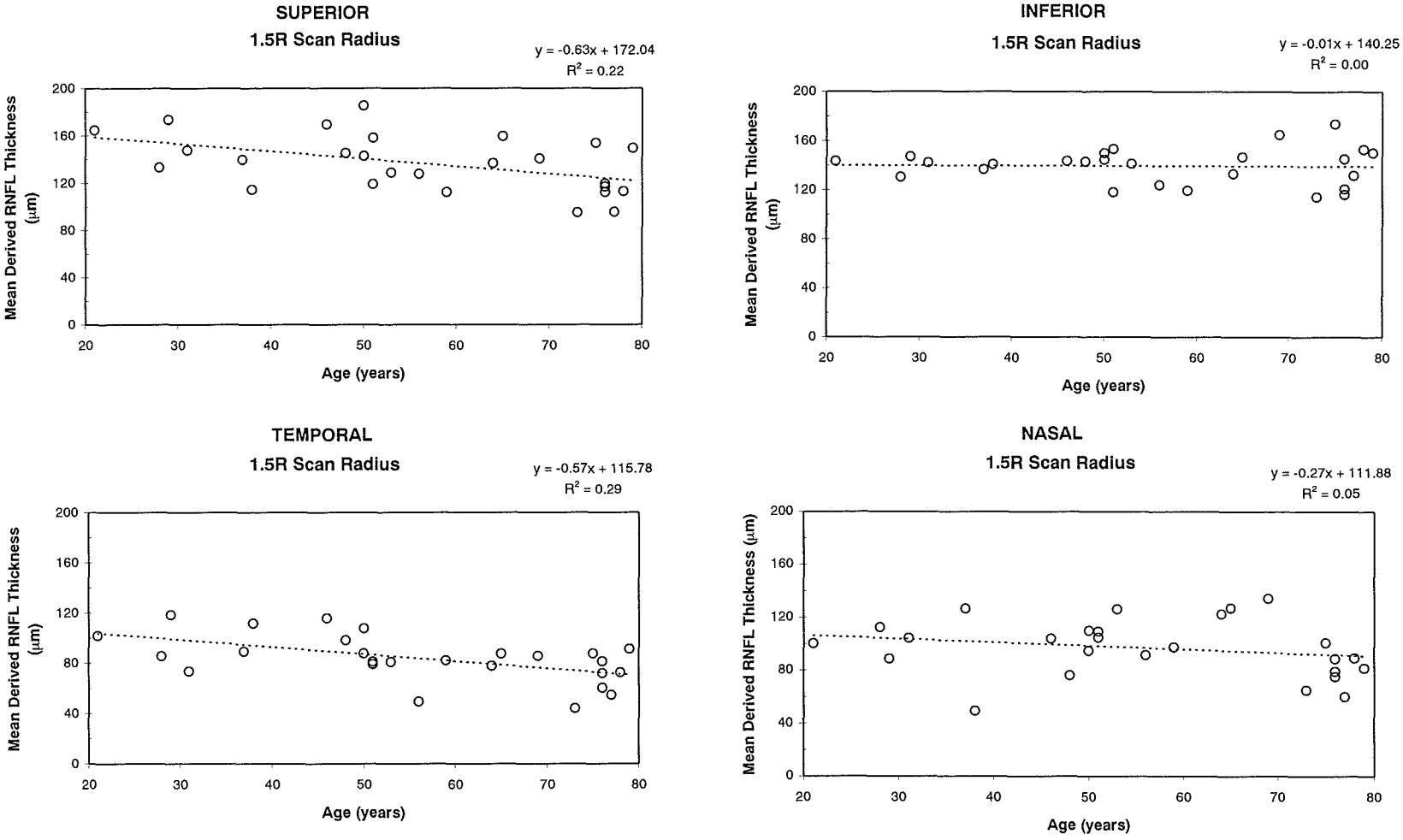

Figure 6.26. The mean RNFL thickness for the Normal group as a function of age, with the 1.5R scan radius, for the Superior (upper left), for the Inferior (upper right), for the Temporal (lower left) and for the Nasal (lower right) sectors. Each data point represents a single individual.

Reduction in Group Mean Superior Sector RNFL thickness (μm) with increasing age in the Normal Group

	Rate per Year	R^2
1.5R	-0.63	0.20
2.0R	-0.40	0.18
1.73mm	-0.51	0.26

Reduction in Group Mean Inferior Sector RNFL thickness (μm) with increasing age in the Normal Group

	Rate per Year	R^2
1.5R	-0.01	0.00
2.0R	-0.35	0.18
1.73mm	-0.21	0.10

Reduction in Group Mean Temporal Sector RNFL thickness (μm) with increasing age in the Normal Group

	Rate per Year	R^2
1.5R	-0.57	0.29
2.0R	-0.49	0.34
1.73mm	-0.5	0.41

Reduction in Group Mean Nasal Sector RNFL thickness (μm) with increasing age in the Normal Group

	Rate per Year	R^2
1.5R	-0.27	0.05
2.0R	-0.31	0.08
1.73mm	-0.24	0.07

Table 6.14. The reduction in Group Mean RNFL thickness for each of the three scan radii, for the Superior, Inferior, Temporal and Nasal sectors, with increasing age, for the Normal group.

1.5R Scan Radius.

	SUPERIOR		INFERIOR		TEMPORAL		NASAL	
	Visit One	Visit Two	Visit One	Visit Two	Visit One	Visit Two	Visit One	Visit Two
	(%)	(%)	(%)	(%)	(%)	(%)	(%)	(%)
OHT	22.0	27.2	22.4	21.3	28.5	26.7	26.6	27.2
POAG	44.1	41.2	47.9	46.4	48.2	44.9	44.7	44.6

2.0R Scan Radius.

	SUPERIOR		INFERIOR		TEMPORAL		NASAL	
	Visit One	Visit Two	Visit One	Visit Two	Visit One	Visit Two	Visit One	Visit Two
	(%)	(%)	(%)	(%)	(%)	(%)	(%)	(%)
OHT	21.2	24.0	16.7	18.4	21.2	26.7	20.0	28.9
POAG	43.7	43.6	47.1	50.4	37.2	40.1	45.0	49.7

1.73mm Scan Radius.

	SUPERIOR		INFERIOR		TEMPORAL		NASAL	
	Visit One	Visit Two	Visit One	Visit Two	Visit One	Visit Two	Visit One	Visit Two
	(%)	(%)	(%)	(%)	(%)	(%)	(%)	(%)
OHT	17.8	23.5	16.3	20.4	23.7	25.5	20.7	26.9
POAG	44.2	41.7	45.9	43.9	41.0	41.6	45.3	45.6

Table 6.15. The percentage reduction in the Group Mean Superior, Inferior, Temporal and Nasal sector RNFL thickness for the OHT and POAG groups compared to that of the Normal group, for each of the three scan radii.

SUPERIOR
1.5R Scan Radius

	NORMAL	OHT	OHT(H)	All OHT	POAG	ALL
RNFLT	0.03	0.13	0.03	0.15	0.09	0.15
RDAR	0.03	0.06	0.00	0.09	0.24	0.43
RV	0.03	0.01	0.01	0.00	0.14	0.16
CSM	0.29	0.29	0.03	0.14	0.20	0.44
HVC	0.00	0.00	0.21	0.04	0.06	0.00
RNFLX	0.02	0.00	0.01	0.01	0.02	0.10
CDAR	0.03	0.06	0.00	0.09	0.24	0.43
RA	0.01	0.07	0.01	0.00	0.08	0.13
CA	0.03	0.13	0.01	0.11	0.23	0.41
DA	0.05	0.20	0.00	0.08	0.17	0.23

SUPERIOR
2.0R Scan Radius

	NORMAL	OHT	OHT(H)	All OHT	POAG	ALL
RNFLT	0.00	0.10	0.63	0.17	0.09	0.12
RDAR	0.04	0.09	0.02	0.04	0.26	0.41
RV	0.00	0.00	0.27	0.00	0.23	0.13
CSM	0.36	0.24	0.06	0.11	0.20	0.43
HVC	0.04	0.01	0.28	0.03	0.04	0.00
RNFLX	0.01	0.01	0.53	0.01	0.03	0.08
CDAR	0.04	0.09	0.02	0.04	0.26	0.41
RA	0.03	0.06	0.07	0.02	0.18	0.12
CA	0.06	0.20	0.18	0.07	0.19	0.39
DA	0.10	0.25	0.28	0.10	0.08	0.22

SUPERIOR
1.73mm Scan Radius

	NORMAL	OHT	OHT(H)	All OHT	POAG	ALL
RNFLT	0.03	0.08	0.21	0.11	0.11	0.17
RDAR	0.01	0.20	0.03	0.11	0.20	0.38
RV	0.00	0.10	0.02	0.09	0.22	0.21
CSM	0.20	0.09	0.01	0.08	0.15	0.38
HVC	0.00	0.03	0.03	0.03	0.07	0.00
RNFLX	0.01	0.04	0.26	0.08	0.09	0.16
CDAR	0.01	0.20	0.03	0.11	0.20	0.38
RA	0.05	0.06	0.05	0.06	0.23	0.23
CA	0.00	0.10	0.21	0.04	0.08	0.31
DA	0.01	0.00	0.27	0.01	0.00	0.08

Table 6.16. Summary table of the R^2 values, for the assumed linear relationship between the Superior Sector RNFL thickness and the HRT derived stereometric parameters, including the mean RNFL thickness, for each of the three scan radii.

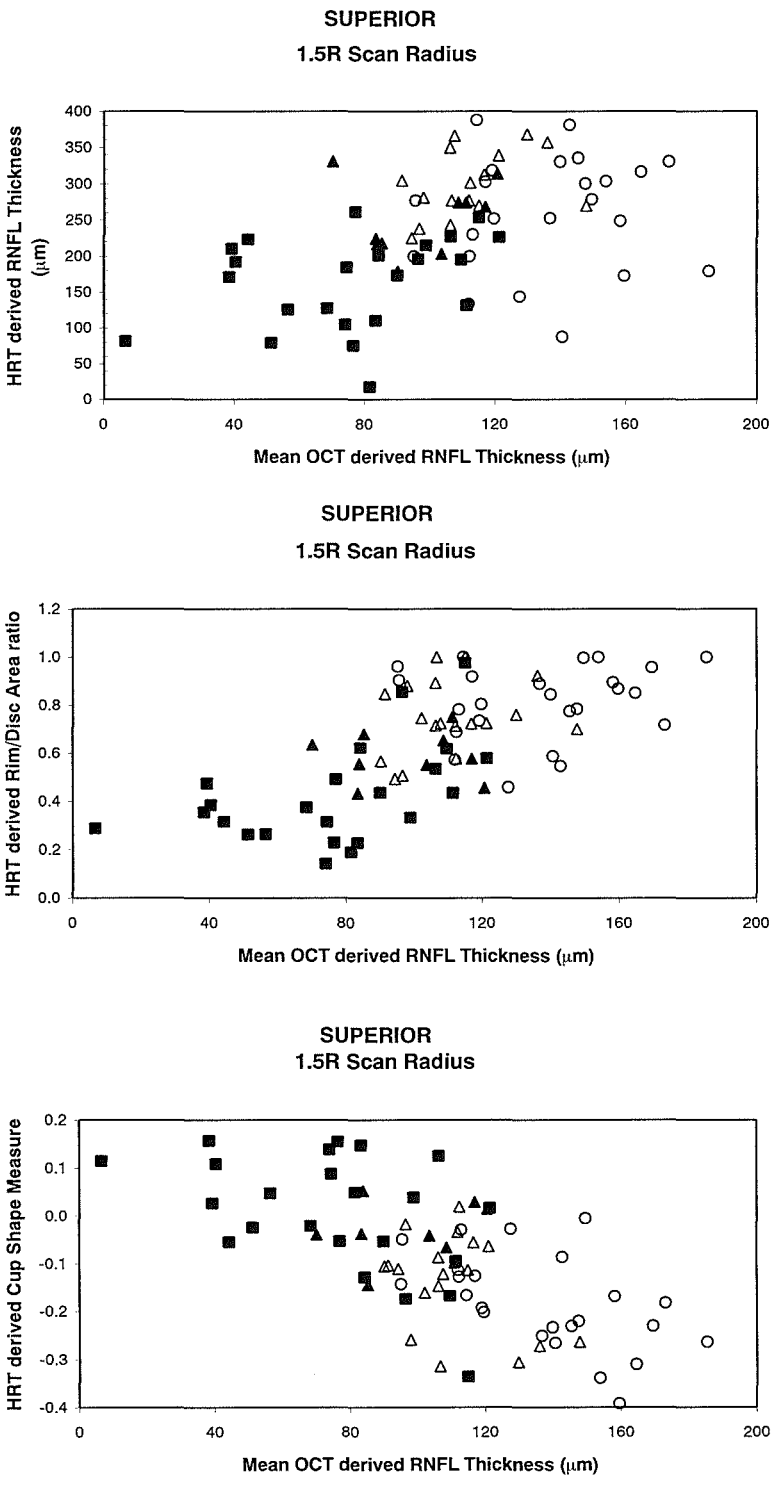

Figure 6.27. The relationship between the Superior sector RNFL thickness and the Superior sector HRT derived RNFL thickness (top), for the Rim/Disc Area Ratio (middle) and for the Cup Shape measure (bottom) at Visit One, for the 1.5R scan radius, for the Normal group (open circles), for the OHT group (open triangles), for the OHT(H) group (closed triangles) and for the POAG group (closed squares). Each data point represents a single individual.

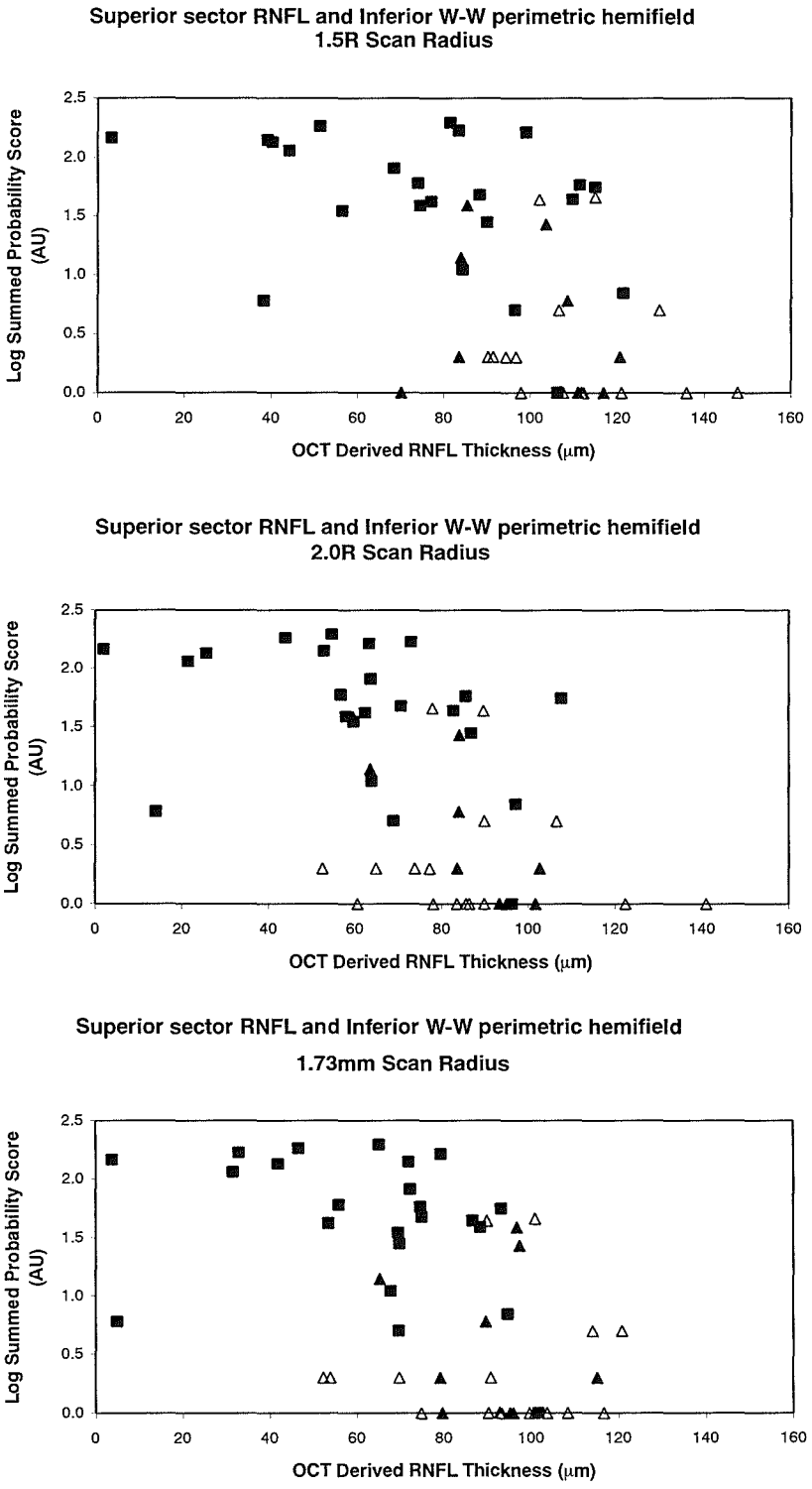

Figure 6.28. The relationship between the Superior Sector RNFL thickness and the W-W Inferior hemifield log summed PD probability scores, at Visit One, for the 1.5R scan radius (top), for the 2.0R scan radius (middle) and for the 1.73mm scan radius (bottom), for the OHT group (open triangles), for the OHT (H) group (closed triangles) and for the POAG group (closed squares). Each data point represents a single individual.

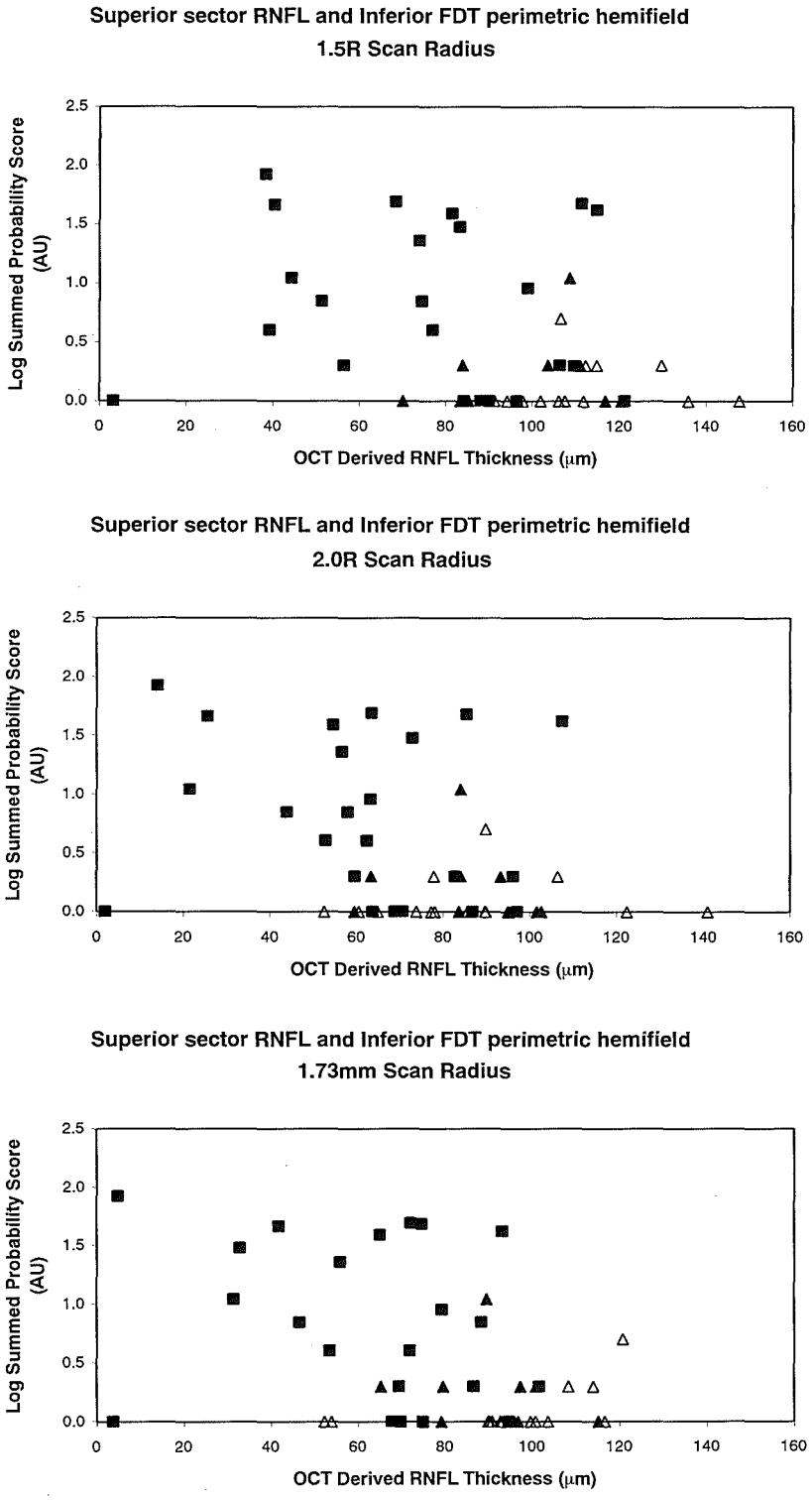

Figure 6.29. The relationship between the Superior Sector RNFL thickness and the FDT Inferior hemifield log summed PD probability scores, at Visit One, for the 1.5R scan radius (top), for the 2.0R scan radius (middle) and for the 1.73mm scan radius (bottom), for the OHT group (open triangles), for the OHT (H) group (closed triangles) and for the POAG group (closed squares). Each data point represents a single individual.

6.8.8 ANOVA for the Superior Sector RNFL thickness as a function of scan radius, diagnostic group and visit.

The RNFL thickness declined with increase in age (p=0.006) (Table 6.17). The RNFL thickness was thicker with decrease in disc area (p=0.026). The thickness varied across the three diagnostic groups; it was thickest in the Normal group, thinner in the OHT group and was thinnest in the POAG group (p<0.001) (Table 6.11). The RNFL thickness decreased with increase in scan radius (p<0.001) (Table 6.18 and Figure 6.30). For 3 outliers, the RNFL thickness with the 1.5R scan was thinner compared to that for the 2.0R scan in the superior, inferior, and nasal sectors.

Superior	Scan Radii
FACTOR	1.5R and 2.0R
Age	p=0.006
Diagnosis	p<0.001
Disc Area	p=0.026
Scan Radius	p<0.001
Scan Radius x Age	NS
Scan Radius x Diagnosis	NS
Scan Radius x Disc Area	NS
Visit	NS
Visit x Age	NS
Visit x Diagnosis	NS
Visit x Disc Area	NS
Number of Scans	NS
Number of Scans x Age	NS
Number of Scans x Diagnosis	NS
Number of Scans x Disc Area	NS
Number of Scans x Disc Area x Diagnosis	NS
Number of Scans x Age x Diagnosis	NS
Scan Radius x Visit	NS
Scan Radius x Visit x Age	NS
Scan Radius x Visit x Diagnosis	NS
Scan Radius x Visit x Disc Area	NS
Scan Radius x Number of Scans	NS
Scan Radius x Number of Scans x Age	NS
Scan Radius x Number of Scans x Diagnosis	NS
Scan Radius x Number of Scans x Disc Area	NS
Scan Radius x Number of Scans x Disc Area x Diagnosis	NS
Scan Radius x Number of Scans x Age x Diagnosis	p =0.046
Scan Radius x Number of Scans x Disc Area x Age	NS
Visit x Number of Scans	p =0.027
Visit x Number of Scans x Age	NS
Visit x Number of Scans x Diagnosis	NS
Visit x Number of Scans x Disc Area	p =0.021
Visit x Number of Scans x Disc Area x Diagnosis	NS
Visit x Number of Scans x Age x Diagnosis	NS
Visit x Disc Area x Diagnosis	NS
Visit x Age x Diagnosis	NS
Scan Radius x Visit x Number of Scans	NS
Scan Radius x Visit x Number of Scans x Age	NS
Scan Radius x Visit x Number of Scans x Diagnosis	NS
Scan Radius x Visit x Number of Scans x Disc Area	NS
Scan Radius x Visit x Number of Scans x Disc Area x Diagnosis	NS
Scan Radius x Visit x Number of Scans x Disc Area x Age	NS
Scan Radius x Visit x Age x Diagnosis	NS
Scan Radius x Disc Area x Diagnosis	NS
Scan Radius x Age x Diagnosis	NS
Area x Diagnosis	NS
Age x Diagnosis	NS

Table 6.17. Summary of the ANOVA for the Superior Sector RNFL thickness determined using only the thickness derived by the first and seventh scans for the 1.5R and 2.0R scan radii .

	SUPERIOR			
	VISIT 1		VISIT 2	
	MEAN	SD	MEAN	SD
NORMAL	26.79	12.21	27.55	11.24
OHT	20.07	14.10	16.53	16.55
POAG	14.87	11.67	18.83	11.53

	INFERIOR			
	VISIT 1		VISIT 2	
	MEAN	SD	MEAN	SD
NORMAL	30.85	14.01	28.13	16.12
OHT	18.55	14.76	19.58	17.09
POAG	15.64	15.64	19.78	15.29

	TEMPORAL			
	VISIT 1		VISIT 2	
	MEAN	SD	MEAN	SD
NORMAL	14.93	9.45	15.00	7.61
OHT	7.10	14.27	10.82	17.25
POAG	1.30	14.79	4.73	16.35

	NASAL			
	VISIT 1		VISIT 2	
	MEAN	SD	MEAN	SD
NORMAL	34.27	9.56	32.78	11.78
OHT	21.49	18.04	25.72	17.03
POAG	19.41	15.08	21.98	17.55

Table 6.18. The Group Mean and SD of the difference in (a) Superior Sector; (b) Inferior Sector; (c) Temporal Sector; and (d) Nasal Sector RNFL thickness (μm) between the 1.5R scan radius and the 2.0R scan radius, for each of the diagnostic groups.

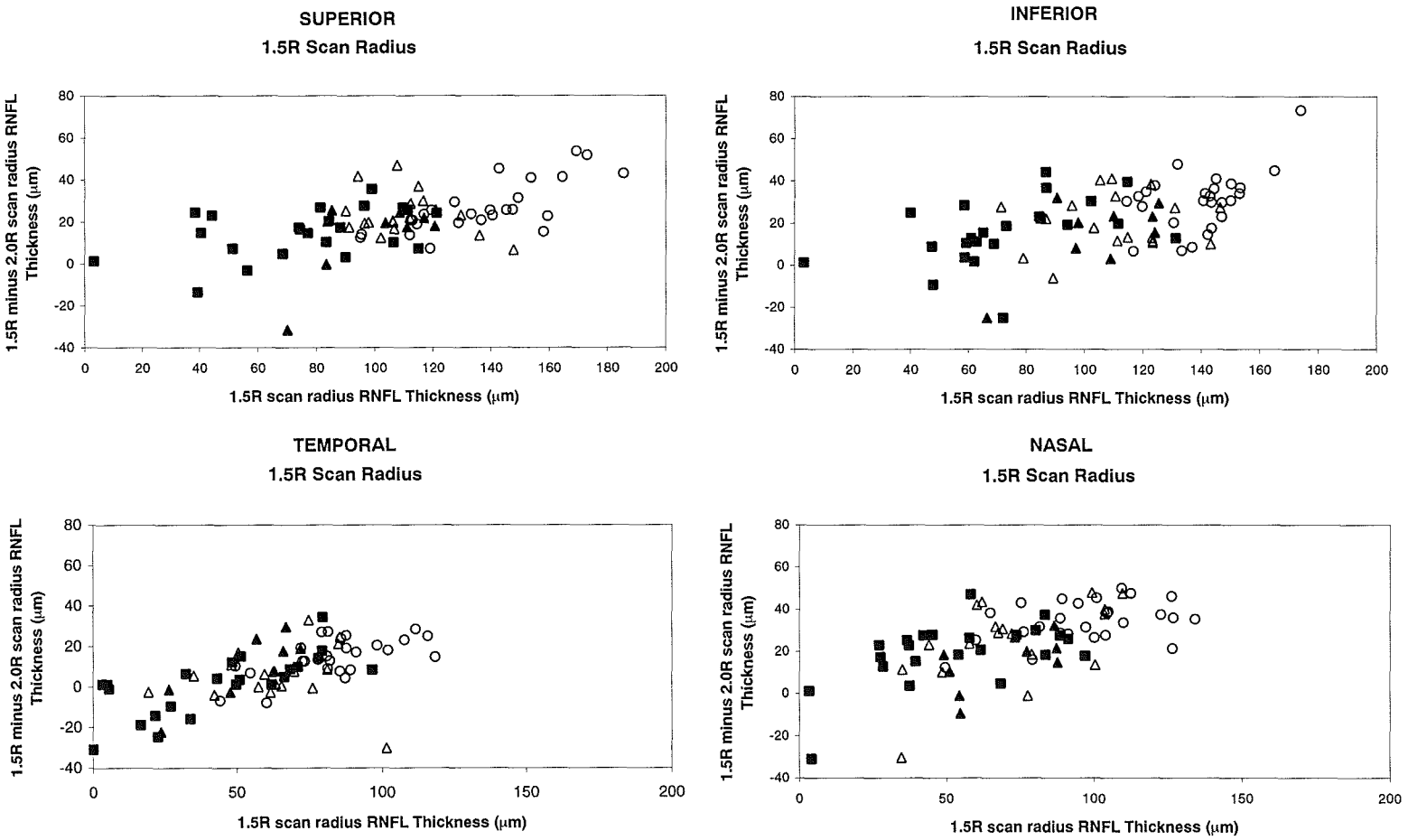

Figure 6.30. The difference in the (a) Superior sector; (b) Inferior sector; (c) Temporal sector; and (d) Nasal sector RNFL thickness between the 1.5R scan radius and the 2.0R scan radius, as a function of the corresponding sector RNFL thickness for the 1.5R scan, for the Normal group (open circles) for the OHT group (open triangles), for the OHT(H) group (closed triangles) and for the POAG group (open squares). Each data point represents a single individual.

6.8.9 Between-visit variability of the Inferior Sector RNFL thickness.

6.8.9.1 1.5R Scan radius.

The RNFL thickness did not vary between the first and second visits (p=0.252). The RNFL thickness did not vary with the number of scans (p=0.945), and was independent of the disc area (p=0.697) (R^2=0.12) (Table 6.12). The limits of agreement for the RNFL thickness between the first and second visit are given in Table 6.13. However, the RNFL thickness was greater at the second visit as the disc area increased (p=0.022).

6.8.9.2 2.0R Scan radius.

The RNFL thickness was greater at the second visit (p=0.014). The thickness was independent of the number of scans (p=0.703). The RNFL thickness was independent of disc area (p=0.732) (R^2=0.12).

6.8.9.3 1.73 mm Scan radius.

The RNFL thickness was independent of visit (p=0.598), of the number of scans (p=0.446), and of the disc area (p=0.180) (R^2=0.02).

6.8.10 Relationship between the Inferior sector RNFL thickness and age, diagnostic group, HRT derived RNFL thickness, related HRT topographical parameters, and visual function (i.e. Validity).

6.8.10.1 1.5R Scan radius.

6.8.10.1.1 Age.

The RNFL thickness was independent of age (p=0.290, (R^2=0.00) (Tables 6.12 and 6.14; Figure 6.26).

6.8.10.1.2 Diagnostic category.

As would be expected, the thickness varied across the three diagnostic groups (p<0.001) (Table 6.12). The Group mean RNFL for the baseline visit was approximately 22% thinner for the OHT group than for the Normal group and 48% thinner for the POAG group compared to the Normal group (Table 6.15). The RNFL thickness was greater at the second visit for the OHT group (p<0.001).

6.8.10.1.3 RNFL thickness derived by HRT.

The inferior sector RNFL thickness was largely independent of the HRT derived inferior RNFL thickness (R^2=0.11)(Table 6.19).

6.8.10.1.4 RDAR derived by the HRT.

The inferior sector RNFL thickness decreased as the RDAR decreased (R^2=0.48) (Table 6.19).

6.8.10.1.5 CSM derived by the HRT.

The inferior sector CSM became more positive as the RNFL thickness decreased (R^2=0.30) (Table 6.19).

6.8.10.1.6 Additional HRT variables.

The inferior sector RNFL thickness decreased as the CA (R^2=0.41) and CDAR (R^2=0.48) increased, but was largely independent of RA (R^2=0.16) and independent of the HVC (R^2=0.02), and the RNFL cross-sectional area (R^2=0.07) (Table 6.19).

6.8.10.1.7 Visual field.

The relationship between the Inferior sector RNFL thickness and the visual field, as provided by the log summed PD probability scores for the corresponding superior hemifield for W-W perimetry, are given in Figure 6.31. The relationship between the log summed PD probability scores for W-W perimetry and the Inferior sector RNFL thickness appeared to be non-linear. There is a wide variation in the W-W log summed PD probability scores for a given RNFL thickness.

The relationship between Inferior sector RNFL thickness and the equivalent log summed PD probability scores for the corresponding region for FDT perimetry are shown in Figure 6.32. The log summed PD probability scores for FDT are more variable with a decrease in the RNFL thickness and are lower compared to that for W-W perimetry.

6.8.10.2 2.0R Scan radius.

6.8.10.2.1 Age.

The inferior RNFL thickness was independent of age (p=0.201, R^2=0.18) (Table 6.12).

6.8.10.2.2 Diagnostic category.

The thickness varied across the three diagnostic groups; it was thinner in the OHT group than in the Normal group and was thinnest in the glaucoma group (p<0.001) (Table 6.11 and 6.12). The Group mean RNFL for the baseline visit was approximately 17% thinner for the OHT group than for the Normal group and 47% thinner for the POAG group compared to the Normal group (Table 6.15).

6.8.10.2.3 RNFL thickness derived by HRT.

The inferior sector RNFL thickness was largely independent of the HRT derived inferior RNFL thickness (R^2=0.17) (Table 6.19).

6.8.10.2.4 RDAR derived by the HRT.

The RNFL thickness increased as the RDAR increased (R^2=0.47) (Table 6.19).

6.8.10.2.5 CSM derived by the HRT.

The RNFL thickness decreased as the CSM increased (R^2=0.26) (Table 6.19).

6.8.10.2.6 Additional HRT variables.

The inferior sector RNFL thickness decreased with increase in the CA (R^2=0.40) and CDAR (R^2=0.47) and decreased as RNFL cross-sectional area decreased (R^2=0.47). It was largely independent of RA (R^2=0.15) and independent of the HVC (R^2=0.01), (Table 6.19).

6.8.10.2.7 Visual field.

The relationship between the Superior hemifield log summed PD probability scores for W-W perimetry and the Inferior sector RNFL thickness for the 2.0R scan radius appeared to be weak (Figure 6.31). The W-W log summed PD probability scores generally increase, and become markedly more variable as the RNFL thickness decreased below approximately 90μm.

The log summed PD probability scores for FDT increased, and became markedly more variable with a decrease in the RNFL thickness as shown in Figure 6.32.

6.8.10.3 1.73mm Scan radius.

6.8.10.3.1 Age.

The inferior RNFL thickness was independent of age (p =0.076; R^2=0.10)(Table 6.12).

6.8.10.3.2 Diagnostic category.

The thickness varied across the three diagnostic groups; it was thinner in the OHT group than in the normal group and was thinnest in the glaucoma group (p<0.001). (Tables 6.11 and 6.12). The Group mean RNFL for the baseline visit was approximately 16% thinner for the OHT group than for the Normal group and 46% thinner for the POAG group compared to the Normal group (Table 6.15).

6.8.10.3.3 RNFL thickness derived by HRT.

The inferior sector RNFL thickness was largely independent of the HRT derived inferior RNFL thickness (R^2=0.15) (Table 6.19).

6.8.10.3.4 RDAR derived by the HRT.

The RNFL thickness increased with an increased RDAR (R^2=0.41) (Table 6.19).

6.8.10.3.5 CSM derived by the HRT.

The RNFL thickness decreased with an increase in the CSM (R^2=0.23) (Table 6.19).

6.8.10.3.6 Additional HRT variables.

The Inferior sector RNFL thickness decreased with an increase in the CDAR (R^2=0.41) and the CA (R^2=0.28) and decrease in RA (R^2=0.24) (Table 6.19). It was largely independent of the RNFL cross-sectional area (R^2=0.15) and independent of HVC (R^2=0.05) (Table 6.19).

6.8.10.3.7 Visual field.

The relationship between the log summed PD probability scores for W-W perimetry and the Inferior sector RNFL thickness for the 1.73mm scan radius is weak (Figure 6.31). The W-W log summed PD probability scores generally increase, and become markedly more variable as the RNFL thickness decreased below approximately 80μm.

The log summed PD probability scores for FDT increased, and became markedly more variable with a decrease in the RNFL thickness as shown in Figure 6.32.

INFERIOR
1.5R Scan Radius

	NORMAL	OHT	OHT(H)	All OHT	POAG	ALL
RNFLT	0.05	0.26	0.00	0.19	0.00	0.11
RDAR	0.24	0.23	0.25	0.07	0.29	0.48
RV	0.21	0.04	0.30	0.01	0.10	0.14
CSM	0.08	0.08	0.03	0.05	0.18	0.30
HVC	0.05	0.00	0.20	0.01	0.00	0.02
RNFLX	0.02	0.18	0.00	0.12	0.00	0.07
CDAR	0.24	0.23	0.24	0.07	0.28	0.48
RA	0.04	0.08	0.29	0.01	0.19	0.16
CA	0.22	0.10	0.23	0.02	0.11	0.41
DA	0.09	0.00	0.02	0.00	0.00	0.12

INFERIOR
2.0R Scan Radius

	NORMAL	OHT	OHT(H)	All OHT	POAG	ALL
RNFLT	0.04	0.14	0.22	0.13	0.15	0.17
RDAR	0.28	0.09	0.00	0.05	0.32	0.47
RV	0.07	0.01	0.01	0.01	0.26	0.10
CSM	0.17	0.02	0.02	0.02	0.11	0.26
HVC	0.01	0.00	0.03	0.00	0.01	0.01
RNFLX	0.03	0.04	0.24	0.05	0.13	0.13
CDAR	0.28	0.09	0.00	0.05	0.32	0.47
RA	0.04	0.00	0.02	0.00	0.31	0.15
CA	0.32	0.08	0.05	0.02	0.11	0.40
DA	0.14	0.05	0.13	0.02	0.00	0.12

INFERIOR
1.73mm Scan Radius

	NORMAL	OHT	OHT(H)	All OHT	POAG	ALL
RNFLT	0.01	0.10	0.46	0.12	0.13	0.15
RDAR	0.02	0.15	0.00	0.07	0.25	0.41
RV	0.00	0.05	0.06	0.05	0.28	0.16
CSM	0.05	0.01	0.01	0.00	0.13	0.23
HVC	0.05	0.02	0.09	0.03	0.00	0.05
RNFLX	0.00	0.07	0.52	0.11	0.15	0.15
CDAR	0.02	0.15	0.00	0.07	0.25	0.41
RA	0.03	0.07	0.07	0.06	0.41	0.24
CA	0.02	0.06	0.08	0.01	0.02	0.28
DA	0.00	0.01	0.28	0.03	0.09	0.02

Table 6.19. Summary table of the R^2 values, for the assumed linear relationship between the Inferior Sector RNFL thickness and the HRT derived stereometric parameters, including the mean RNFL thickness, for each of the three scan radii.

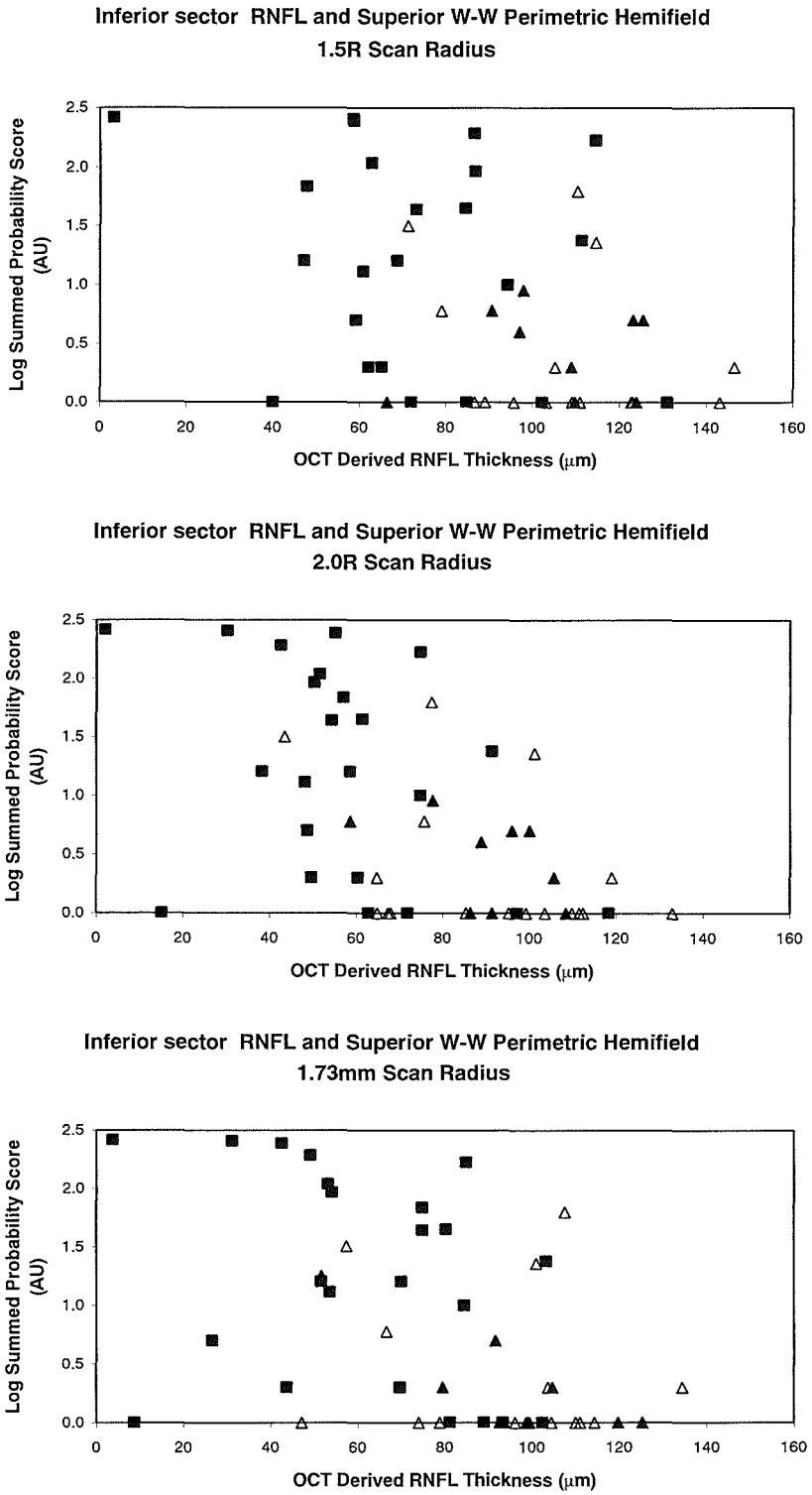

Figure 6.31. The relationship between the Inferior Sector RNFL thickness and the W-W Superior hemifield log summed PD probability scores, at Visit One, for the 1.5R scan radius (top), for the 2.0R scan radius (middle) and for the 1.73mm scan radius (bottom), for the OHT group (open triangles), for the OHT (H) group (closed triangles) and for the POAG group (closed squares). Each data point represents a single individual.

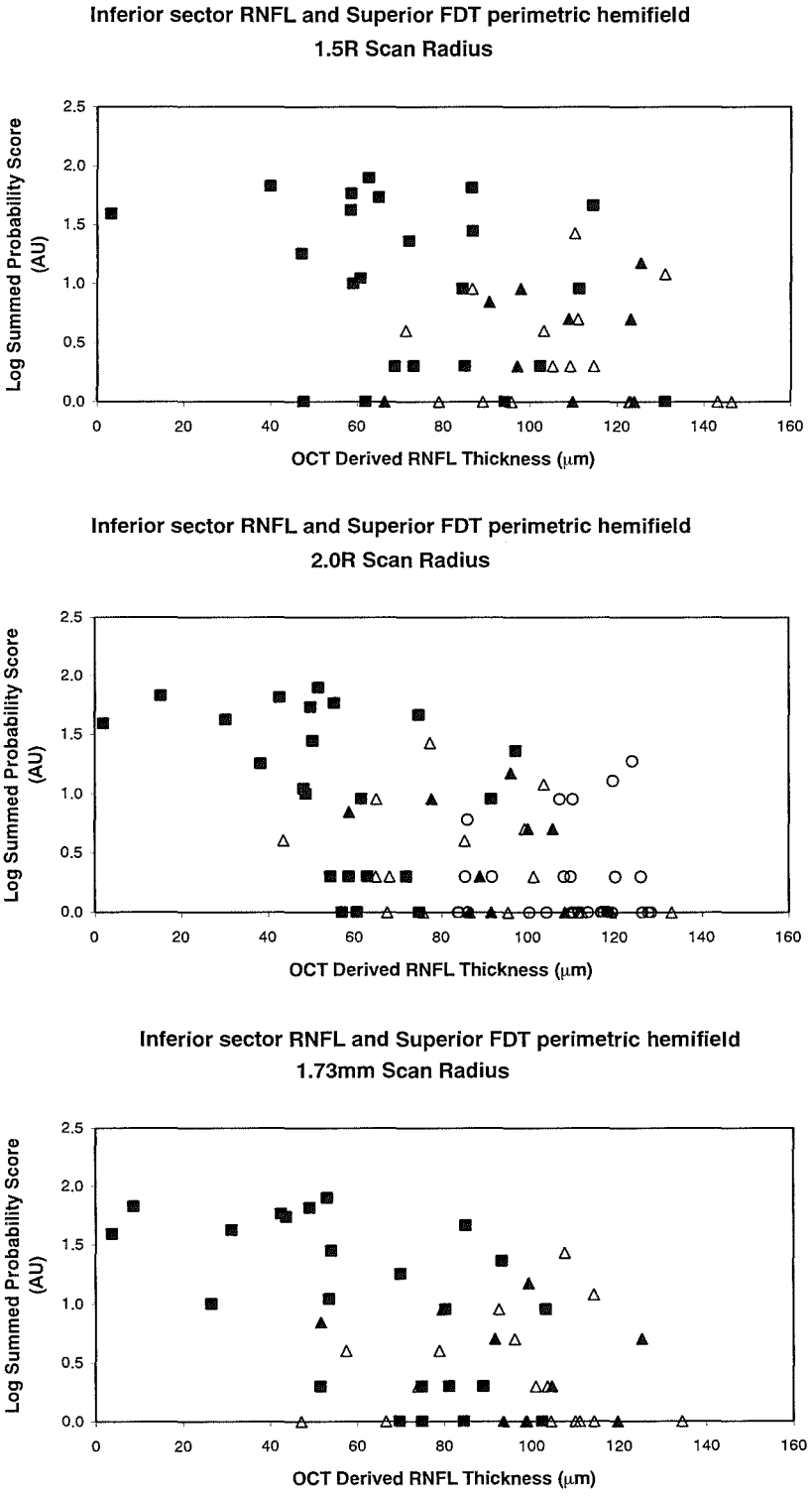

Figure 6.32. The relationship between the Inferior Sector RNFL thickness and the FDT Superior hemifield log summed PD probability scores, at Visit One, for the 1.5R scan radius (top), for the 2.0R scan radius (middle) and for the 1.73mm scan radius (bottom), for the OHT group (open triangles), for the OHT (H) group (closed triangles) and for the POAG group (closed squares). Each data point represents a single individual.

6.8.11 ANOVA for Inferior Sector RNFL thickness as a function of scan radius, diagnostic group and visit.

The RNFL thickness was independent of age ($p=0.189$) (Table 6.20). The RNFL thickness was independent of disc area ($p=0.894$). The thickness varied across the three diagnostic groups; it was thickest in the Normal group, thinner in the OHT group and was thinnest in the POAG group ($p<0.001$). (Table 6.20). The RNFL thickness decreased with increase in scan radius ($p=0.037$). The RNFL thickness for both radii tended to be greater at the second visit as disc area increased ($p<0.001$).

Inferior	Scan Radii
FACTOR	**1.5R and 2.0R**
Age	NS
Diagnosis	p<0.001
Disc Area	NS
Scan Radius	p =0.037
Scan Radius x Age	NS
Scan Radius x Diagnosis	p =0.041
Scan Radius x Disc Area	NS
Visit	NS
Visit x Age	NS
Visit x Diagnosis	NS
Visit x Disc Area	p<0.001
Number of Scans	NS
Number of Scans x Age	NS
Number of Scans x Diagnosis	NS
Number of Scans x Disc Area	NS
Number of Scans x Disc Area x Diagnosis	NS
Number of Scans x Age x Diagnosis	NS
Scan Radius x Visit	NS
Scan Radius x Visit x Age	NS
Scan Radius x Visit x Diagnosis	NS
Scan Radius x Visit x Disc Area	NS
Scan Radius x Number of Scans	NS
Scan Radius x Number of Scans x Age	NS
Scan Radius x Number of Scans x Diagnosis	NS
Scan Radius x Number of Scans x Disc Area	NS
Scan Radius x Number of Scans x Disc Area x Diagnosis	NS
Scan Radius x Number of Scans x Age x Diagnosis	NS
Scan Radius x Number of Scans x Disc Area x Age	NS
Visit x Number of Scans	NS
Visit x Number of Scans x Age	NS
Visit x Number of Scans x Diagnosis	NS
Visit x Number of Scans x Disc Area	NS
Visit x Number of Scans x Disc Area x Diagnosis	NS
Visit x Number of Scans x Age x Diagnosis	NS
Visit x Disc Area x Diagnosis	NS
Visit x Age x Diagnosis	p =0.013
Scan Radius x Visit x Number of Scans	NS
Scan Radius x Visit x Number of Scans x Age	NS
Scan Radius x Visit x Number of Scans x Diagnosis	NS
Scan Radius x Visit x Number of Scans x Disc Area	NS
Scan Radius x Visit x Number of Scans x Disc Area x Diagnosis	NS
Scan Radius x Visit x Number of Scans x Disc Area x Age	NS
Scan Radius x Visit x Age x Diagnosis	NS
Scan Radius x Disc Area x Diagnosis	NS
Scan Radius x Age x Diagnosis	NS
Area x Diagnosis	NS
Age x Diagnosis	NS

Table 6.20. Summary of the ANOVA for the Inferior Sector RNFL thickness determined using only the thickness derived by the first and seventh scans for the 1.5R and 2.0R scan radii .

6.8.12 Between-visit variability of the Temporal Sector RNFL thickness.

The limits of agreement for the RNFL thickness between the first and second visit are given in Table 6.13.

6.8.12.1 1.5R Scan radius.

The RNFL thickness did not vary between the first and second visits (p=0.176), or with the number of scans (p=0.817) (Table 6.12). The RNFL thickness increased with increase in disc area (p=0.013) (R^2=0.31). The thickness tended to be greater at the second visit with increase in disc area (p=0.004).

6.8.12.2 2.0R Scan radius.

The RNFL thickness did not vary between the first and second visits (p=0.729), or with the number of scans (p=0.690). The RNFL thickness increased with increase in disc area (p=0.007). The RNFL thickness tended to be greater at the second visit with increase in disc area (p=0.018).

6.8.12.3 1.73 mm Scan radius.

The RNFL thickness was independent of visit (p=0.826), of the number of scans (p=0.625) and of disc area (p=0.138).

6.8.13 Relationship between the Temporal sector RNFL thickness and age, diagnostic group, HRT derived RNFL thickness, related HRT topographical parameters, and visual function (i.e Validity).

6.8.13.1 1.5R Scan radius.

6.8.13.1.1 Age.

The RNFL thickness declined with increase in age (p<0.001, R^2=0.29) (Table 6.12). The decline in RNFL thickness for the Normal group was 5.7µm per decade (Table 6.14 and Figure 6.26).

6.8.13.1.2 Diagnostic category.

The thickness again discriminated between the three diagnostic groups (p<0.001) (Table 6.12). The Group mean RNFL for the baseline visit was approximately 29% thinner for the OHT group than for the Normal group and 48% thinner for the POAG group compared to the Normal group (Table 6.15).

6.8.13.1.3 RNFL thickness derived by HRT.

The temporal sector RNFL thickness increased with an increase in the HRT derived temporal RNFL thickness (R^2=0.31) (Table 6.21).

6.8.13.1.4 RDAR derived by the HRT.

The RNFL thickness increased with an increase in the RDAR (R^2=0.31) (Table 6.21).

6.8.13.1.5 CSM derived by the HRT.

The RNFL thickness decreased as the CSM increased (R^2=0.31) (Table 6.21).

6.8.13.1.6 Additional HRT variables.

The Temporal sector RNFL thickness increased as the CDAR (R^2=0.24) and CA (R^2=0.32) decreased and was independent of the HVC (R^2=0.05), RNFL cross-sectional area (R^2=0.00) and RA (R^2=0.09).

TEMPORAL
1.5R Scan Radius

	NORMAL	OHT	OHT(H)	All OHT	POAG	ALL
RNFLT	0.12	0.03	0.80	0.01	0.00	0.03
RDAR	0.11	0.02	0.13	0.00	0.34	0.24
RV	0.02	0.06	0.00	0.02	0.23	0.09
CSM	0.13	0.13	0.28	0.09	0.29	0.30
HVC	0.22	0.03	0.34	0.00	0.08	0.05
RNFLX	0.08	0.00	0.68	0.08	0.04	0.00
CDAR	0.11	0.02	0.13	0.00	0.34	0.24
RA	0.00	0.06	0.02	0.01	0.24	0.09
CA	0.16	0.00	0.23	0.03	0.33	0.32
DA	0.17	0.09	0.21	0.10	0.18	0.19

TEMPORAL
2.0R Scan Radius

	NORMAL	OHT	OHT(H)	All OHT	POAG	ALL
RNFLT	0.05	0.05	0.19	0.01	0.11	0.05
RDAR	0.03	0.01	0.00	0.00	0.46	0.18
RV	0.00	0.07	0.02	0.02	0.38	0.04
CSM	0.03	0.04	0.02	0.04	0.41	0.23
HVC	0.09	0.00	0.09	0.01	0.01	0.03
RNFLX	0.03	0.00	0.04	0.02	0.03	0.02
CDAR	0.03	0.01	0.00	0.00	0.46	0.18
RA	0.04	0.06	0.00	0.02	0.42	0.06
CA	0.13	0.05	0.03	0.05	0.32	0.27
DA	0.23	0.25	0.07	0.14	0.10	0.20

TEMPORAL
1.73mm Scan Radius

	NORMAL	OHT	OHT(H)	All OHT	POAG	ALL
RNFLT	0.03	0.06	0.30	0.01	0.09	0.05
RDAR	0.01	0.00	0.05	0.01	0.28	0.21
RV	0.02	0.00	0.00	0.00	0.24	0.07
CSM	0.06	0.01	0.15	0.04	0.33	0.27
HVC	0.14	0.02	0.01	0.00	0.02	0.06
RNFLX	0.01	0.00	0.28	0.01	0.04	0.03
CDAR	0.01	0.00	0.05	0.01	0.28	0.21
RA	0.06	0.00	0.00	0.00	0.28	0.10
CA	0.05	0.07	0.08	0.08	0.14	0.24
DA	0.14	0.11	0.11	0.11	0.02	0.12

Table 6.21. Summary table of the R^2 values, for the assumed linear relationship between the Temporal Sector RNFL thickness and the HRT derived stereometric parameters, including the mean RNFL thickness, for each of the three scan radii.

6.8.13.2 2.0R Scan radius.

6.8.13.2.1 Age.

The RNFL thickness declined with increase in age ($p<0.001$, $R^2=0.34$) (Table 6.12). The decline in RNFL thickness for the Normal group was 4.9µm per decade (Table 6.14).

6.8.13.2.2 Diagnostic category.

The thickness varied across the three diagnostic groups; it was thinner in the OHT group than in the normal group and was thinnest in the glaucoma group ($p<0.001$). (Table 6.11 and 6.12). The Group mean RNFL for the baseline visit was approximately 21% thinner for the OHT group than for the Normal group and 37% thinner for the POAG group compared to the Normal group (Table 6.15).

6.8.13.2.3 RNFL thickness derived by HRT.

The temporal sector RNFL thickness was independent of the HRT derived temporal RNFL thickness ($R^2=0.05$) (Table 6.21).

6.8.13.2.4 RDAR derived by the HRT.

The RNFL thickness was independent of the RDAR ($R^2=0.18$).

6.8.13.2.5 CSM derived by the HRT.

The RNFL thickness was independent of the CSM ($R^2=0.23$).

6.8.13.2.6 Additional HRT variables.

The Temporal sector RNFL thickness increased as the CA ($R^2=0.27$) decreased. It was independent of the CDAR ($R^2=0.18$), the RA ($R^2=0.06$), the HVC ($R^2=0.03$) and the RNFL cross-sectional area ($R^2=0.02$).

6.8.13.3. 1.73mm Scan radius.

6.8.13.3.1 Age.

The RNFL thickness declined with increase in age ($p<0.001$, $R^2=0.41$) (Table 6.12). The decline in RNFL thickness for the Normal group was 5.0µm per decade (Table 6.14).

6.8.13.3.2 Diagnostic category.

The thickness varied across the three diagnostic groups; it was thinner in the OHT group than in the Normal group and was thinnest in the glaucoma group ($p<0.001$). (Tables 6.11 and 6.12). The Group mean RNFL for the baseline visit was approximately 24% thinner for the OHT group than for the Normal group and 41% thinner for the POAG group compared to the Normal group (Table 6.15).

6.8.13.3.3 RNFL thickness derived by HRT.

The Temporal sector RNFL thickness for the 1.73mm scan radius was independent of the HRT derived temporal RNFL thickness (R^2=0.05) (Table 6.21).

6.8.13.3.4 RDAR derived by the HRT.

The RNFL thickness increased as the RDAR increased (R^2=0.21).

6.8.13.3.5 CSM derived by the HRT.

The RNFL thickness decreased as the CSM increased (R^2=0.27).

6.8.13.3.6 Additional HRT variables.

The Temporal sector RNFL thickness increased as the CA (R^2=0.24) and CDAR (R^2=0.21) decreased and was independent of the HVC (R^2=0.06), RNFL cross-sectional area (R^2=0.03) and RA (R^2=0.10).

6.8.14 ANOVA for the Temporal Sector RNFL thickness as a function of scan radius, diagnostic group and visit.

The RNFL thickness declined with increase in age ($p<0.001$) (Table 6.22). The RNFL thickness increased with decrease in disc area ($p=0.007$). The thickness varied across the three diagnostic groups; it was thickest in the Normal group, thinner in the OHT group and was thinnest in the POAG group ($p<0.001$). (Table 6.11). The RNFL thickness decreased with increase in scan radius ($p=0.005$) and this reduction in thickness was greater with increase in age ($p=0.019$).

Temporal	Scan Radii
FACTOR	1.5R and 2.0R
Age	p<0.001
Diagnosis	p<0.001
Disc Area	p=0.007
Scan Radius	p=0.005
Scan Radius x Age	p=0.019
Scan Radius x Diagnosis	NS
Scan Radius x Disc Area	NS
Visit	NS
Visit x Age	p=0.012
Visit x Diagnosis	NS
Visit x Disc Area	p<0.001
Number of Scans	NS
Number of Scans x Age	NS
Number of Scans x Diagnosis	NS
Number of Scans x Disc Area	NS
Number of Scans x Disc Area x Diagnosis	NS
Number of Scans x Age x Diagnosis	NS
Scan Radius x Visit	NS
Scan Radius x Visit x Age	NS
Scan Radius x Visit x Diagnosis	NS
Scan Radius x Visit x Disc Area	NS
Scan Radius x Number of Scans	NS
Scan Radius x Number of Scans x Age	NS
Scan Radius x Number of Scans x Diagnosis	NS
Scan Radius x Number of Scans x Disc Area	NS
Scan Radius x Number of Scans x Disc Area x Diagnosis	NS
Scan Radius x Number of Scans x Age x Diagnosis	NS
Scan Radius x Number of Scans x Disc Area x Age	NS
Visit x Number of Scans	NS
Visit x Number of Scans x Age	NS
Visit x Number of Scans x Diagnosis	NS
Visit x Number of Scans x Disc Area	p =0.006
Visit x Number of Scans x Disc Area x Diagnosis	NS
Visit x Number of Scans x Age x Diagnosis	NS
Visit x Disc Area x Diagnosis	NS
Visit x Age x Diagnosis	NS
Scan Radius x Visit x Number of Scans	NS
Scan Radius x Visit x Number of Scans x Age	NS
Scan Radius x Visit x Number of Scans x Diagnosis	NS
Scan Radius x Visit x Number of Scans x Disc Area	NS
Scan Radius x Visit x Number of Scans x Disc Area x Diagnosis	NS
Scan Radius x Visit x Number of Scans x Disc Area x Age	NS
Scan Radius x Visit x Age x Diagnosis	NS
Scan Radius x Disc Area x Diagnosis	NS
Scan Radius x Age x Diagnosis	NS
Area x Diagnosis	NS
Age x Diagnosis	NS

Table 6.22. Summary of the ANOVA for the Temporal Sector RNFL thickness determined using only the thickness derived by the first and seventh scans for the 1.5R and 2.0R scan radii .

6.8.15 Between-visit variability of the Nasal Sector RNFL thickness.

6.8.15.1 1.5R Scan radius.

The RNFL thickness did not vary between the first and second visits (p=0.903), or with the number of scans (p=0.740) (Table 6.12). The limits of agreement for the RNFL thickness between the first and second visit are given in Table 6.13. The RNFL thickness was independent of disc area (p=0.694).

6.8.15.2 2.0R Scan radius.

The RNFL thickness did not vary between the first and second visits (p=0.267), or with the number of scans (p=0.243) (Table 6.12). The RNFL thickness was independent of disc area (p=0.856).

6.8.15.3 1.73 mm Scan radius.

The RNFL thickness did not vary between the first and second visits (p=0.155), or with the number of scans (p=0.698) (Table 6.12). The RNFL thickness was essentially independent of disc area (p=0.035).

6.8.16 Relationship between the Nasal sector RNFL thickness and age, diagnostic group, HRT derived RNFL thickness, related HRT topographical parameters, and visual function.(ie Validity).

6.8.16.1 1.5R Scan radius.

6.8.16.1.1 Age.

The nasal sector RNFL thickness was independent of age (p=0.829) (R^2=0.05) (Table 6.12 and 6.14; Figure 6.26).

6.8.16.1.2 Diagnostic category.

The RNFL thickness discriminated across the three diagnostic groups (p<0.001) (Table 6.12). The Group mean RNFL for the baseline visit was approximately 27% thinner for the OHT group than for the Normal group and 45% thinner for the POAG group compared to the Normal group (Table 6.15).

6.8.16.1.3 RNFL thickness derived by HRT.

The nasal sector RNFL thickness was independent of the HRT derived nasal RNFL thickness (R^2=0.01) (Table 6.23).

6.8.16.1.4 Neuroretinal Rim Area derived by the HRT.

The RNFL thickness was independent of the RDAR (R^2=0.12).

6.8.16.1.5 Cup Shape Measure (CSM) derived by the HRT.

The nasal RNFL thickness was independent of the CSM (R^2=0.04).

6.8.16.1.6 Additional HRT variables.

The nasal sector RNFL thickness was independent of the CDAR (R^2=0.12), the CA (R^2=0.10), the HVC (R^2=0.04), the RNFL cross-sectional area (R^2=0.05) and the RA (R^2=0.06) (Table 6.23).

NASAL
1.5R Scan Radius

	NORMAL	OHT	OHT(H)	All OHT	POAG	ALL
RNFLT	0.19	0.17	0.18	0.17	0.00	0.01
RDAR	0.05	0.00	0.02	0.00	0.05	0.12
RV	0.04	0.00	0.01	0.01	0.01	0.03
CSM	0.03	0.03	0.00	0.00	0.15	0.04
HVC	0.01	0.16	0.33	0.01	0.17	0.04
RNFLX	0.11	0.17	0.18	0.17	0.00	0.05
CDAR	0.05	0.00	0.02	0.00	0.05	0.12
RA	0.02	0.06	0.01	0.02	0.00	0.01
CA	0.02	0.00	0.00	0.00	0.05	0.10
DA	0.05	0.03	0.01	0.02	0.08	0.06

NASAL
2.0R Scan Radius

	NORMAL	OHT	OHT(H)	All OHT	POAG	ALL
RNFLT	0.06	0.28	0.14	0.17	0.00	0.03
RDAR	0.03	0.00	0.16	0.00	0.02	0.08
RV	0.06	0.00	0.21	0.00	0.00	0.02
CSM	0.02	0.05	0.07	0.04	0.02	0.03
HVC	0.09	0.52	0.41	0.12	0.14	0.09
RNFLX	0.04	0.28	0.14	0.17	0.00	0.06
CDAR	0.03	0.00	0.16	0.00	0.02	0.08
RA	0.00	0.02	0.44	0.00	0.00	0.02
CA	0.02	0.00	0.03	0.00	0.01	0.06
DA	0.01	0.02	0.50	0.00	0.01	0.02

NASAL
1.73mm Scan Radius

	NORMAL	OHT	OHT(H)	All OHT	POAG	ALL
RNFLT	0.03	0.05	0.02	0.00	0.01	0.01
RDAR	0.12	0.12	0.28	0.01	0.00	0.04
RV	0.03	0.00	0.01	0.00	0.04	0.02
CSM	0.13	0.08	0.03	0.04	0.00	0.00
HVC	0.03	0.22	0.06	0.05	0.07	0.04
RNFLX	0.02	0.05	0.02	0.00	0.01	0.03
CDAR	0.12	0.13	0.28	0.01	0.00	0.04
RA	0.00	0.00	0.21	0.01	0.00	0.02
CA	0.10	0.18	0.17	0.06	0.00	0.02
DA	0.07	0.04	0.09	0.05	0.00	0.00

Table 6.23. Summary table of the R^2 values, for the assumed linear relationship between the Nasal Sector RNFL thickness and the HRT derived stereometric parameters, including the mean RNFL thickness, for each of the three scan radii.

6.8.16.2 2.0R Scan radius.

6.8.16.2.1 Age.

The RNFL thickness was independent of age (p=0.168) (R^2=0.08) (Table 6.12 and 6.14).

6.8.16.2.2 Diagnostic category.

The thickness varied across the three diagnostic groups; it was again thinner in the OHT group than in the normal group and was thinnest in the glaucoma group (p<0.001). (Table 6.11 and 6.12). The Group mean RNFL for the baseline visit was approximately 20% thinner for the OHT group than for the Normal group and 45% thinner for the POAG group compared to the Normal group (Table 6.15).

6.8.16.2.3 RNFL thickness derived by HRT.

The Nasal sector RNFL thickness was independent of the HRT derived Nasal RNFL thickness (R^2=0.03) (Table 6.23).

6.8.16.2.4 RDAR derived by the HRT.

The RNFL thickness was independent of the RDAR (R^2=0.08) (Table 6.23).

6.8.16.2.5 CSM derived by the HRT.

The RNFL thickness was independent of the CSM (R^2=0.03).

6.8.16.2.6 Additional HRT variables.

The nasal sector RNFL thickness was independent of the CDAR (R^2=0.08), the CA (R^2=0.06), the HVC (R^2=0.09), the RNFL cross-sectional area (R^2=0.06) and the RA (R^2=0.02).

6.8.16.3 1.73mm Scan radius.

6.8.16.3.1 Age.

The RNFL thickness was independent of age (p=0.077) (R^2=0.07) (Table 6.12 and 6.14).

6.8.16.3.2 Diagnostic category.

The thickness varied across the three diagnostic groups; it was thinner in the OHT group than in the Normal group and was thinnest in the glaucoma group (p<0.001). (Tables 6.11 and 6.12). The Group mean RNFL for the baseline visit was approximately 21% thinner for the OHT group than for the Normal group and 45% thinner for the POAG group compared to the Normal group (Table 6.15).

6.8.16.3.3 RNFL thickness derived by HRT.

The Nasal sector RNFL thickness was independent of the HRT derived Nasal RNFL thickness (R^2=0.01) (Table 6.23).

6.8.16.3.4 RDAR derived by the HRT.

The RNFL thickness was independent of the RDAR (R^2=0.04) (Table 6.23).

6.8.16.3.5 CSM derived by the HRT.

The RNFL thickness was independent of the CSM (R^2=0.00).

6.8.16.3.6 Additional HRT variables.

The nasal sector RNFL thickness for the 1.73mm scan radius was independent of the, CDAR (R^2=0.04), the CA (R^2=0.02), the HVC (R^2=0.04), the RNFL cross-sectional area (R^2=0.03) and the RA (R^2=0.02).

6.8.17 ANOVA for the Nasal Sector RNFL thickness as a function of scan radius, diagnostic group and visit.

The RNFL thickness was independent of age (p=0.427) (Table 6.24) and of disc area (p=0.967). The thickness varied across the three diagnostic groups; it was thickest in the Normal group, thinner in the OHT group and was thinnest in the POAG group (p<0.001). (Table 6.11 and 6.24). The RNFL thickness decreased with increase in scan radius (p=0.007) and this reduction in thickness varied between groups (p=0.009) and was more marked for the Normal group.

Nasal	Scan Radii
FACTOR	1.5R and 2.0R
Age	NS
Diagnosis	p<0.001
Disc Area	NS
Scan Radius	p=0.007
Scan Radius x Age	NS
Scan Radius x Diagnosis	p=0.009
Scan Radius x Disc Area	NS
Visit	NS
Visit x Age	NS
Visit x Diagnosis	NS
Visit x Disc Area	NS
Number of Scans	NS
Number of Scans x Age	NS
Number of Scans x Diagnosis	NS
Number of Scans x Disc Area	NS
Number of Scans x Disc Area x Diagnosis	NS
Number of Scans x Age x Diagnosis	NS
Scan Radius x Visit	NS
Scan Radius x Visit x Age	NS
Scan Radius x Visit x Diagnosis	NS
Scan Radius x Visit x Disc Area	NS
Scan Radius x Number of Scans	NS
Scan Radius x Number of Scans x Age	NS
Scan Radius x Number of Scans x Diagnosis	NS
Scan Radius x Number of Scans x Disc Area	NS
Scan Radius x Number of Scans x Disc Area x Diagnosis	NS
Scan Radius x Number of Scans x Age x Diagnosis	NS
Scan Radius x Number of Scans x Disc Area x Age	NS
Visit x Number of Scans	p =0.017
Visit x Number of Scans x Age	NS
Visit x Number of Scans x Diagnosis	NS
Visit x Number of Scans x Disc Area	p =0.003
Visit x Number of Scans x Disc Area x Diagnosis	NS
Visit x Number of Scans x Age x Diagnosis	NS
Visit x Disc Area x Diagnosis	NS
Visit x Age x Diagnosis	NS
Scan Radius x Visit x Number of Scans	NS
Scan Radius x Visit x Number of Scans x Age	NS
Scan Radius x Visit x Number of Scans x Diagnosis	NS
Scan Radius x Visit x Number of Scans x Disc Area	NS
Scan Radius x Visit x Number of Scans x Disc Area x Diagnosis	NS
Scan Radius x Visit x Number of Scans x Disc Area x Age	NS
Scan Radius x Visit x Age x Diagnosis	NS
Scan Radius x Disc Area x Diagnosis	NS
Scan Radius x Age x Diagnosis	NS
Area x Diagnosis	NS
Age x Diagnosis	NS

Table 6.24. Summary of the ANOVA for the Nasal Sector RNFL thickness determined using only the thickness derived by the first and seventh scans for the 1.5R and 2.0R scan radii .

6.9 Discussion.

The within-visit between-individual variation (i.e. one standard deviation) across each of the three diagnostic groups using the methodology described here was approximately 6-7μm for both the Global (range 1μm – 16μm) and Sector (mean range 1μm – 21μm) RNFL thickness for each of the three Scan radii. This value is clinically similar to the average SD of approximately 6μm, reported by Bowd et al (2000) for the Global RNFL thickness across a similar group of normals, OHTs and POAGs.

The upper and lower 95% limits of agreement for the Global RNFL thickness measured at each of the two visits were approximately ±14μm for the Normal group for all three scan diameters. The corresponding values for the OHT group were approximately ±27μm and for the POAG group ±20μm. The limits of agreement were larger with the 1.5R Scan radius for the OHT group. These values have implications for the measurement of RNFL thickness at follow-up visits. A reduction in thickness of at least 14μm will be required in the normal RNFL thickness before progressive damage can be identified. For individuals with 'average' damage to the RNFL thickness a difference of at least 20-27μm will be necessary before further thinning can be considered significant.

The global and sector within-visit variability is clearly smaller than the between-visit variability. Similar results have been reported with the prototype instrument (Schuman et al. 1996). Schuman and colleagues also found greater variability with scans used close to the disc margins and advocated the 1.73mm scan as the optimum radius.

The within-visit variability increased with a decrease in the RNFL thickness across all the diagnostic groups, but was particularly apparent once the RNFL thickness approached 50μm. The increased variability therefore limits the application of the technique to the monitoring of early and moderate stages of RNFL atrophy. The between-visit variability was slightly wider for the OHT group. The reasons for the wider limit are unclear, although it is possible that an operator learning effect might have been present.

The within-visit between-individual variability as expressed in terms of the group mean Coefficients of Variation for the individual sectors was approximately twice as great in the OHT group when compared to the Normal group, and approximately three times as large for the POAG group than the Normal group in each sector across the three scan radii. The within-visit variability was least for the superior and inferior RNFL thickness measurements across all groups. The temporal and nasal RNFL sectors exhibited greater within-visit variability with glaucomatous optic nerve head atrophy.

The increased variability with areas of glaucomatous damage may be related to inequalities in the RNFL, but whether this variation is attributable to the thinning tissue, the surface irregularity

or both has not been ascertained. It is not known whether the variation differs for a given RNFL thickness with or without an associated functional loss.

Baumann et al (1998) reported that the automated method for assessing the retinal thickness was less reliable in regions close to fixation, and attributed this to a decline in the quality of the internal limiting membrane (ILM) reflectivity. It was suggested that the computer software might need refinement for regional assessment. Peripapillary areas that have undergone RNFL thinning as a result of physiological or pathological degeneration might also be associated with a decline in the quality of the ILM reflectivity.

The RNFL thickness was thickest in the superior and inferior sectors for all groups across all three scan radii. The within-group variability was greatest for the POAG group for all sectors. Similar findings have been found with the prototype OCT (Schuman et al. 1996).

Several factors could influence the precision of the estimated RNFL thickness within- and between-visits. Fluctuations in the polarisation state of the scanning beam with temperature changes and the angle of incidence of the scanning beam made with respect to the RNFL boundaries are known to affect global and, in particular, regional measurements of the RNFL thickness (Knighton and Qian 2000). The magnitude of the reflected light tends to vary slightly throughout the scanning procedure. Minor alterations to the polarisation state and the angle of incidence of the scanning beam and the maintenance of a good tear film can optimise the magnitude of the reflected signal. An edge-detection process in the OCT software algorithm is used to identify the boundaries of the vitreoretinal. and retino-choroidal interface. Having identified these two boundaries, the algorithm establishes a threshold reflectance level to determine the location of the RNFL. An incorrect choice of threshold level used in the process to identify of the lower boundary of the RNFL can also introduce an error in the RNFL thickness measurement.

Poor fixation, head rotation and/or tilt between scan acquisitions, vertical and anterior-posterior head movement associated with muscle tension and mouth-breathing, excessive or inadequate blinking and lid artefacts due to congenital upper lid ptosis or fatigue can each impede the measurement of RNFL thickness by OCT.

Measurements made through the centre of the pupil will result in an optimum incident and reflected beam (Knighton and Qian 2000), however, if the scan beam is directed through an off-axis region, the reflectance pattern of the returning light will be altered depending on whether the incident light has been displaced nasally or temporally on each successive and subsequent scan.

The change in the pattern of reflectance, will also be confounded by the between-individual variation in the distribution, course and orientation of the nerve fibre bundles, and the potential

progressive changes that are likely to accompany physiological and pathological decline in the fibre numbers, and their microstructural composition. The contribution to the reflectance pattern from the surrounding glial tissue and from heterogenous tissue boundary interfaces, particularly when associated with damage, is still unclear. Any inconsistency between the region associated with the RHR and RLR and the underlying anatomy is likely to arise from attenuation of the incident signal by overlying structures or absorption of the signal by intracellular or extracellular fluid. A relatively constant level of backscatter originates throughout the RNFL and the inner plexiform layer tissue provided the layers are substantially thicker than the depth resolution of the instrument (Huang et al. 1998). However, the component of the 'A'-scan waveform originating primarily at the level of the RNFL changes shape as a function of the RNFL thickness. The approximately square waveform becomes narrower as the thickness reduces, although the amplitude remains constant provided the thickness is greater than the theoretical resolution of the instrument.

Chauhan et al (1999) questioned the validity of attributing the highly reflective inner band to the RNFL alone. They demonstrated that a surface-related signal contributed to the thickness of the band and that this could persist despite the complete removal of the RNFL. In addition, they found that the location of the outer highly reflective band corresponded to the position of melanin within the retinal pigment epithelium and that the band thickness was not a true representation of the RPE layer thickness. The ability to obtain precise OCT measurements of specific retinal layers was doubted and the lack of standardised polarisation effects was considered to be a further confounding factor.

The slow progressive damage that accompanies glaucomatous optic neuropathy is concurrent with the physiological age-related change in the optic nerve composition. The slope for the RNFL thickness with increase in age as measured with the 1.73mm scan radius (4.0μm per decade) was identical to that found using the prototype OCT instrument (Pakter et al. 1995).

An age-related reduction in RNFL thickness has also been demonstrated using polarimetry (Chi et al. 1995; Lemij et al. 1995; Weinreb et al. 1995b; Poinoosawmy et al. 1997). A thinned RNFL with increasing age can also be recognised ophthalmoscopically by a diffuse loss in clarity of the RNFL striations (Jonas et al. 1989b; Jonas and Schiro 1993). The age change to the RNFL thickness in human corresponds with the loss of ganglion cell axons with increase in age (Dolman et al. 1980; Johnson et al. 1987; Mikelberg et al. 1989; Repka and Quigley 1989; Jonas et al. 1990b; Mikelberg et al. 1991; Jonas et al. 1992c). An age-related decline of the equatorial rods, cones and cells in the ganglion cell layer and pigment epithelial cells also occurs (Gao and Hollyfield 1992); the rate of cell loss varies between each cell type and declines over the age of forty. The photoreceptor loss is less pronounced in the fovea than in the peripheral retina. Rod photoreceptors and ganglion cell layer cells are lost, with increasing age, at a greater rate than the cones (Gao and Hollyfield 1992; Panda-Jonas et al. 1995).

The reduction in RNFL thickness with age exhibited a regional variation. The superior and temporal parapapillary RNFL thickness, measured using the 1.5R scan radius, showed a marked decline of approximately 0.63μm per year and 0.57μm per year respectively. The corresponding proportionate reduction in RNFL thickness was 23.7% superiorly and 32.8% temporally. The rate of inferior RNFL thinning with increase in age was 0.27μm. The nasal RNFL thickness did not vary with age. Similar rates of decline have been recently found by Bowd and colleagues (Bowd et al. 2000). Schumann and coworkers (1995b), however, using the prototype OCT, found the RNFL thickness to decrease with increasing age in all sectors, but particularly in the nasal and inferior sectors; although, the majority of their data were derived from glaucomatous individuals.

The age-related decline in RNFL thickness is also supported by histological studies. RNFL thickness is inversely related to age, particularly in the superionasal and inferotemporal regions within 500μm of the disc margin (Varma et al. 1996). A regional variation in the age-related decline of the RNFL thickness has also been found by polarimetry. Weinreb et al (1995b) reported that the retardation decreased with increasing age in the superior and inferior parapapillary regions, but not in the temporal or nasal regions. However, Chi et al (1995) found the nasal and inferior regions of the parapapillary RNFL thickness to decline at a greater rate than the superior and temporal NFL thickness with increasing age.

The relatively larger age-related decline documented for the temporal region with the OCT in the study is most surprising. The temporal region includes the papillomacula bundle of fibres and the majority of the ganglion fibres in this region tend be thin (Ogden 1984), and to arise from the concentration of cones at the fovea. The rate of decline in foveal cone photoreceptor density is slow compared to the peripheral photoreceptor loss, and visual acuity is generally maintained despite advancing age. It would seem unlikely that the integrity of the retinogeniculate pathway could be sustained with a significant loss of RNFL tissue in the papillomacula region over a lifetime. No geographic difference in mean axon density has been reported in histological studies for the superior, inferior, nasal or temporal regions, or between the central and peripheral portions of the intracranial optic nerve that might suggest an age-related regional selective loss of axons (Johnson et al. 1987). However, the retinotopic reorganisation of fibres along the retinogeniculate pathway may obscure such a feature.

Global RNFL thickness, almost invariably, decreased with an increase in scan radius, with the greatest effect evident in the Normal group. These findings agree with the results from the prototyope OCT (Schuman et al. 1996), and the histological evidence of decrease in RNFL thickness with increasing distance from the disc margin (Radius 1980; Quigley and Addicks 1982; Varma et al. 1996).

Similarly, the RNFL thickness for each of the sectors decreased with an increase in scan radius, particularly for the Normal group. The Inferior and Nasal regions exhibited the greatest

decrease in RNFL thickness across each of the diagnostic groups. These findings are consistent with those from the prototype OCT (Schuman et al. 1996) and with histological estimates of RNFL thickness (Varma et al. 1996; Dichtl et al. 1999). For a number of individuals the RNFL was thinner for the 2.0R scan radius compared to the 1.5R scan radius suggesting that the RNFL reduced in thickness close to the ONH. The tendency was particularly evident in the Temporal sector. It is unclear whether this is due to the limited resolution of the OCT instrument or a true phenomenon.

			Regional Thickness; mean ± standard deviation (μm)or range				
Author	OCT	Scan Radius (mm)	Global	Superior	Temporal	Inferior	Nasal
(Schuman et al. 1996)	P	1.70	153 ± 12	179 ± 15	126 ± 15	175 ± 19	131 ± 21
(Schuman et al. 1996)	P	1.45	169 ± 12				
(Schuman et al. 1996)	P	1.70	153 ± 13				
(Schuman et al. 1996)	P	2.25	125 ± 12				
(Mistlberger et al. 1999)	C	1.70	90.86 ± 14.17				
(Hoh et al. 2000)	C	1.70	90.86 ± 14.17				
(Bowd et al. 2000)	C	1.70	85.8 (80.2-91.7)	105.7 (98.0-112.6)	66.2 (61.3-71.2)	107.6 (99.3-115.9)	61.8 (53.0-65.6)

P = Prototype model; C = Commercial model.

Table 6.25. Non-Invasive estimates of Normal Human Retinal Nerve Fibre Layer Thickness using the OCT with circular scans around the ONH.

OCT scans centred upon the ONH with a fixed radius are likely to sample regions closer to the disc margin in those individuals with large discs than those with small discs. Large discs are believed to be associated with a greater number of fibres. Assuming that the rate of change in the RNFL thickness with eccentricity is similar for all disc sizes, one would expect the RNFL thickness at any given linear distance from the disc margin to be greater for those individuals with large discs. However, the study showed that the RNFL thickness was independent of disc area for each of the three scan radii. These findings are in agreement with Mistlberger and colleagues (1999) and Bowd and colleagues (2000) (see Table 6.25). The lack of a relationship

may be explained by a wide variation in both the thickness and number of nerve fibres irrespective of disc area.

The results exhibited some overlap of the global RNFL thickness values between the diagnostic groups. However, the mean RNFL thickness was markedly thinner in the OHT group compared to the Normal group, and also markedly thinner in the POAG group when compared to either the Normal or the OHT groups for the global values and for each of the sectors using each of the scans. The findings are consistent with those of both Mistleberger et al (1999) and Bowd and colleagues (2000). The results suggest that a proportion of the OHT group could have early glaucomatous damage. Longitudinal follow-up of these particular individuals could provide confirmatory evidence.

Despite the difference in techniques between the two instruments, the global RNFL thickness measured with OCT was reasonably correlated with the RNFL thickness derived by the HRT. The lack of a stronger correlation between the data could be explained by a number of outliers. The degree of correlation is similar to that reported by Mistlberger et al (1999). The HRT derived RNFL thickness was approximately 90μm greater than that measured by the OCT. The difference in magnitude can be largely attributed to the difference in the distance from the optic disc margins at which the measurements are made.

The HRT parameter is a surrogate for the actual RNFL thickness as it is based upon a reference plane that is dependent upon the definition of a contour line drawn by the instrument operator and upon the height values of a very small region within the contour line. Whilst this region is considered to be the most stable compared to other regions in glaucoma, errors in the determination of the reference height of the reference plane can give rise to artefactual low or high measures of the HRT derived RNFL thickness.

Radius and Pederson (Radius and Pederson 1984) reported a positive correlation between the rim tissue area and the number of axons in glaucomatous monkey eyes and it has also been argued that the disc rim area is indicative of the number of nerve fibres in an eye (Airaksinen et al. 1985c). Assuming that the neural rim area is a surrogate measure of axonal tissue, the number of remaining axons can be estimated. Detection of early glaucomatous damage either using optic disc photographs combined with planimetry (Jonas et al. 1988d) or with the HRT is more difficult with smaller optic disc sizes than for the larger disc sizes, particularly in those with an area less than 2.00 mm^2 (lester and Mikelberg 1997; Emdadi et al. 1998). To correct for the effect of the variation in individual optic disc size on the rim area when identifying patterns of early glaucomatous disc damage, additional HRT parameters, namely, the rim to total disc area ratio (RDAR) and sector rim to disc area ratio have been evaluated (Emdadi et al. 1998). In the study, the rim area was corrected for disc area. There was a strong tendency for the ratio to be small in those individuals with a thin RNFL, suggesting that glaucomatous thinning of the RNFL is associated with a decrease in the corrected rim area.

The superior and inferior sector RNFL thickness were strongly related to the respective, sector RDARs whilst the temporal sector RNFL thickness was modestly related to the RDAR. There was no relationship between the nasal sector RNFL thickness and the nasal sector RDAR. The findings support the hypothesis that regional thinning of the RNFL is associated with regional thinning of the neuroretinal rim, particularly at the superior and inferior poles of the ONH.

The results show a high degree of association between the CSM and the OCT derived RNFL thickness for the POAG group and for all three groups combined. The relationship can be attributed to the loss of rim tissue that is accompanied by excavation of the cup and of RNFL thinning. The agreement between RNFL thickness and CSM is particularly evident in the superior region, and is slightly less for the inferior and temporal regions. No obvious relationship was evident between the nasal region. The temporal involvement may explained by the inferotemporal and superotemporal contributions to the mean temporal sector values. Further evaluation of these particular regions is possible with the HRT software; however, the OCT scan resolution employed in the study precluded detailed investigation of the inferotemporal and superotemporal regions.

The relationship between the RNFL thickness and the global indices for both W-W and FDT perimetry were non-linear. The lack of variation in the indices until the Global RNFL thickness had declined below 80μm and the Superior and Inferior Sector RNFL thickness had declined below 100μm suggest that a considerable number of nerve fibres can be lost before a visual deficit is detectable. These findings agree with the early reports that RNFL assessment is a more sensitive indicator of glaucomatous damage to the ganglion cell population and nerve fibre bundles than perimetry (Quigley et al. 1982a; Harwerth et al. 1999).

6.10 Conclusions.

The results of the present study have shown that the commercial OCT instrument can provide RNFL thickness measurements with a maximum resolution of approximately 6-7μm. The limits of agreement between successive visits over several weeks were approximately 27μm. The clinical implication of these findings is that the commercial OCT instrument may well be useful in monitoring longitudinal changes in the RNFL thickness in the absence of a direct measurement of the RNFL.

CHAPTER 7. OCULAR HAEMODYNAMICS IN GLAUCOMA.

7.1 Introduction.

The mechanical and vascular theories proposed for the pathogenesis of glaucoma have generated much discussion over the years. Von Graefe (1857) proposed that mechanical forces applied to the lamina cribrosa from a raised intraocular pressure (IOP) created the cupped appearance at the optic disc. Jaeger (1858), postulated that an impaired ocular blood flow with subsequent ischaemia, particularly within the short posterior ciliary arteries (SPCAs), was the cause of the glaucomatous optic neuropathy. The lamina cribrosa is generally accepted as the site for the initial damage, and the ciliary blood supply to this region has attracted close attention (Hayreh 1996a).

A number of fundamental assumptions are generally made concerning the possible vascular pathogenesis of glaucoma (Cioffi 1998). Firstly, it is assumed that ischaemia of the ONH causes, or increases, the susceptibility of the optic nerve to glaucomatous damage. Secondly, the deficient vascular beds that are involved in the neuropathy might be more easily identified once the vascular anatomy and physiology specific to the anterior ONH are understood. Unfortunately, the anterior ONH has a complex three-dimensional network of blood vessels, with a dual blood supply, which may not be independent, and shows wide between-individual variation (Hayreh 1995). The number and distribution of the posterior ciliary vessels, the distribution of the choroidal watershed zones and the degree of completion of the Zinn-Haller circle may potentially adversely affect the vascular condition of the ONH, and yet these features are extremely difficult to document clinically (Ohno-Matsui et al. 1998; Ruskell 1998). Various metabolic, myogenic and neurogenic mechanisms that are currently being investigated are also likely to show between-individual variation in the normal eye (Flammer and Orgül 1998). The investigation of a single aspect of the ocular circulation for all those at risk of developing, or with confirmed, glaucoma is, therefore, unlikely to provide a complete understanding of the vascular status. Finally, the existing investigative instruments and techniques are assumed to be capable of providing valid measurements of the ONH circulation.

Studies of ocular haemodynamics have paid particular attention to the normal response in healthy volunteers to controlled changes in IOP (Riva et al. 1997) and blood gas pertubation (Roff et al. 1999). Several techniques have been employed, individually, and in combination, to assess autoregulation within the ocular circulation (Harris et al. 1998a). It is clear from these studies that knowledge of the anatomical vascular arrangement, and isolated recordings of tissue perfusion, offer too simplistic an approach to the ONH vascular system.

Despite the existence of the between-individual variation associated with ocular haemodynamics, documentation of the blood flow parameters within- and between-individuals who have some evidence of ONH damage with or without demonstrable visual field damage

may provide an insight into the nature of POAG. The findings, however, are unlikely to explain the pathogenesis for all individuals with primary open angle glaucoma whilst there is still debate as to whether the presence of a vascular deficit is a primary or secondary event in the glaucomatous process.

7.2 Anatomical Arrangement of the Optic Nerve Head and Peripapillary Regional Vasculature.

The anatomical arrangement of the ONH vasculature has been described in detail (Hayreh 1974a; Onda 1995)(see Figure 7.1a). Briefly, the retina, ONH and choroid receive their blood supply through the central retinal artery (CRA) and the posterior ciliary arteries (PCAs), vessels that arise from the ophthalmic artery (OA), a branch of the internal carotid artery (ICA) (Hayreh 1995).

The OA may give rise to between one and five PCAs. Generally there are two PCAs, a medial and a lateral PCA, and rarely, a much smaller, superior PCA (Hayreh 1995). The vessels generally arise from the OA at a similar site to the CRA (Hayreh 1970) approximately 10-15mm behind the globe (Harris et al. 1998b). The PCAs each divide into approximately 10-20 branches. Two of these vessels, referred to as long posterior ciliary arteries (LPCAs), run further anteriorly, before piercing the sclera to provide a vascular supply to the ciliary body and the iris (Hayreh 1990). Those PCA branches that enter the sclera near the optic nerve, on the medial and lateral sides of the optic nerve, are known as the short posterior ciliary arteries (SPCAs). The SPCAs serve the choroid and the ONH. The photoreceptors and bipolar cells rely upon the extensive capillary network in the inner choroid, or choriocapillaris, and the large vessels of the outer choroid for their blood supply (Hayreh 1990).

The ONH can be subdivided into four regions, namely, the superficial nerve fibre layer, the prelamina, the lamina and the retrolamina region (Hayreh 1995; Harris et al. 1998b). Capillaries from the CRA and its branches serve the superficial nerve fibre layer (NFL), at the surface of the ONH beneath the inner limiting membrane, in addition to the inner two-thirds of the retina which includes the ganglion cell layer and the inner plexiform layer, as far as the external border of the inner nuclear layer (Hayreh 1995) (see Figure 7.1b). The prelamina region which lies between the superficial NFL and the lamina cribrosa is supplied from the peripapillary choroid (Hayreh 1995), but no direct supply from the peripapillary choriocapillaris has been found (Harris et al. 1998b). The lamina region is supplied entirely by branches directly from the short PCAs or indirectly via centripetally directed capillaries from the arterial circle of Zinn-Haller. The circle is formed by a number of the SPCAs at the level of the sclera (Hayreh 1995). Some vessels arising from the circle pass forward into the peripapillary choroid, and others turn posteriorly to anastomose with pial vessels in the retrolamina region (Hayreh 1995). A major part of the ocular blood flow circulates through the choroidal vessels, with a small proportion flowing through the retinal vessels (Hayreh 1990).

7.2.1 Choroidal Blood Supply and Watershed Zones.

The choriocapillaris were considered to form a continuous meshwork of vessels, based upon post-mortem injection cast models, with extensive anastamoses between the choroidal arteries and between the veins (Hayreh 1974b). However, clinical experience of choroidal pathology, and in-vivo studies in monkey and man have shown the choroidal vascular bed to behave as an end-artery system (Hayreh 1995). Between the distribution area of each end-artery 'watershed zones' are created. These watershed zones have relatively poor vascular coverage and are more vulnerable to ischaemia in the event of a fall in perfusion pressure. The between-individual variation in the number and distribution of the PCAs and SPCAs leads to a very variable distribution of watershed zones and perfused sections within the choroid. Some of the watershed zones can pass directly across the optic disc region and may account for the between-individual differences in response to an impaired blood supply and the subsequent diverse pattern of glaucomatous damage.

7.2.2 The Lamina and Prelamina Region of the ONH.

Evidence suggests the existence of a sectoral blood supply to the lamina and prelamina region of the ONH (Hayreh 1995). Incomplete occlusion of one of the PCAs supplying the optic nerve could, therefore, lead to a sectoral lesion and a corresponding glaucomatous nerve fibre defect (Hayreh 1970). The presence of an associated arcuate visual field defect in glaucoma, in the absence of a retinal lesion, suggests sectoral damage in the optic nerve. Evidence for a vascular involvement in their origin emanates from studies which demonstrate a sectoral blood supply to the ONH and choroid in primates (Hayreh 1970). Observation of in-vivo patterns of the choroidal vascular bed and adjacent regions of the ONH prior to the fluorescein filling of the retinal vessels has indicated a segmental distribution of the PCAs that supply these areas.

The ciliary circulation to the ONH is susceptible to damage from raised IOP and there is evidence to suggest a regional vulnerability arising from the segmental distribution of the blood supply (Hayreh 1974a). Hayreh has demonstrated the importance of the level of the IOP and of the arterial blood pressure in the choroidal and posterior ciliary vessels, in monkey (Hayreh et al. 1970). However, the extent to which the choroid and ciliary circulation contribute to the lamina region of the ONH is controversial (Hayreh 1985; Onda 1995; Orgül and Meyer 1995).

Figure 7.1 Schematic diagram of the anatomical arrangement of (a) the arterial supply of the ONH (Hayreh 1963), and (b) the distribution of the retinal capillaries within the inner layers of the retina (Hogan 1971).

7.2.3 The Superficial Retinal Nerve Fibre Layer of the ONH and the Retinal Peripapillary Region.

Arterioles arising from the CRA generally provide the blood supply for the NFL at the ONH surface, the RNFL and the inner retina. In the peripapillary retina, the capillary network in the inner retina is supplemented by an additional capillary bed whose vessels course alongside the nerve fibre bundles in the RNFL layer (Henkind 1967). Occasionally a small cilioretinal vessel, presumed to arise from the SPCA circulation, is present to nourish a sector of the temporal neuroretinal rim and adjacent parapapillary retina (Hayreh 1995). The presence of a cilioretinal vessel can contribute to the preservation of central vision following retinal vascular occlusion (Hayreh 1963) and may influence the blood supply to both the retina and the ONH. Both adverse (Shihab et al. 1985) and beneficial (Lee and Schwartz 1992) effects of their presence on the visual outcome in glaucoma have been documented.

7.3 Blood Flow Measurement.

The use of animals permits the direct measurement of the ONH blood flow, but the invasive nature of the procedures employed is unacceptable in human investigations (Hayreh 1997a). Direct visualisation of the ONH blood supply in humans, is extremely difficult, due to the three-dimensional arrangement of the vessels. In addition, the retinal and choroidal vascular systems lie in close proximity to each other and their contributions to ocular blood flow are grossly disproportionate (Hill 1976). The retinal circulation accounts for 2-10%, whilst the choroid provides about 90%. Although there is no accepted technique that is considered a gold standard for ONH blood flow determination, several complimentary systems capable of good resolution in selected vascular regions are generally employed to clinically document blood flow (Hayreh 1997a). These include colour Doppler imaging (CDI), blue-field entoptic simulation, pulsatile ocular blood flow (POBF) evaluation, laser Doppler velocimetry (LDV), laser Doppler flowmetry (LDF), and scanning laser Doppler flowmetry (SLDF).

7.3.1 Colour Doppler Imaging.

To assess the retrobulbar haemodynamics, ultrasonography in the form of CDI is used to acquire information from the OA, SPCAs and CRA (Williamson and Harris 1996; Harris et al. 1998b). The technique combines a B-scan grey-scale image of the ocular structure with a colour representation of the blood flow based upon Doppler-shifted frequencies.

The blood flow velocities are measured from the waveform of velocity generated by detected Doppler frequency shifts arising from a pulsed-Doppler signal (Williamson and Harris 1996). A number of terms are commonly quoted which summarise the characteristics of the waveform. The peak systolic velocity (PSV) and the end diastolic velocity (EDV) describe the maximum velocities during the systolic and diastolic stages of the respiratory cycle, respectively, whilst the Resistive Index (RI) and the Pulsatile Index (PI) provide a measure of the resistance to the flow.

An increase in the PSV and EDV can indicate either an increase in blood flow or the occurrence of vessel narrowing. A decrease in RI implies a decrease in vascular resistance at an unspecified site beyond the vessel under investigation (Harris et al. 1996c). Interpretation of the haemodynamic significance of signals detected by CDI is speculative as a lack of knowledge with regard to vessel diameters confounds attempts to convert the blood velocity measurements to a flow value (Williamson and Harris 1996).

Generally, high velocity values tend to provide better reproducibility than the low values (Williamson and Harris 1996). However, this technique is unsuitable for estimating the blood flow at the ONH due to the limited resolution, unreliable identification of the vessel under investigation and the need to derive a measure of the flow from a velocity and vascular resistance measurement (Hayreh 1997a).

7.3.2 Blue-Field Entoptic Simulation.

Investigations into the choroidal circulation have used blue-field entoptic simulation (Robinson et al. 1985). Quantification of the mean velocity of leucocytes is assumed to represent the mean velocity of whole blood, and is achieved by a simulation technique, in which an observer adjusts the velocity of computer simulated leucocytes displayed on a monitor to match that of their own entoptically perceived leucocytes. The technique evaluates the leukocyte circulation within the fovea, and provides no information about the ONH circulation (Hayreh 1997a).

7.3.3 Pulsatile Ocular Blood Flow.

A rhythmic fluctuation in the IOP is associated with a variation in the ocular blood flow as a bolus of blood enters the eye during each cardiac systole (Langham et al. 1989). POBF studies have provided a measure of the ocular pulse and chorioretinal contribution to the ocular circulation. The technique estimates the pulsatile component of the chorioretinal circulation (Silver et al. 1989; Silver and Farrell 1994; Butt and O'Brien 1995). A pneumatic-suspended probe is applied to the anaesthetised cornea. The air suspension allows the piston within the probe to move freely backwards and forwards in response to the ocular pulse. By analysing the waveform and amplitude, the pulse volume can be determined. Combining the pulse volume and heart rate during a continuous series of pneumatonometric readings provides a measure of the POBF. In determining the POBF, several assumptions are made to allow mathematical arguments to be developed to support the theory that pulsatile ocular blood flow can be estimated from the IOP variation; the eye behaves as an elastic-walled chamber with a pulsatile, incompressible fluid inflow; the IOP amplitude changes in the ocular pulse are related to changes in the volume of blood; blood flow is only considered to travel forwards, with a constant non-pulsatile outflow and the non-pulsatile, diastolic component is not measured. (Krakau 1992; Silver and Farrell 1994).

The technique provides equivalent and comparable IOP measurements to Goldmann tonometry (Silver et al. 1989). Yang and co-workers (1997) obtained a reliability coefficient of 0.92 for a wide range of OBF values (290-2196 $\mu l/min^{-1}$). A reduction in ocular rigidity causes a reduction in the calculated POBF (Silver and Farrell 1994), whilst axial length (James et al. 1991), myopia (Ravalico et al. 1997), IOP (Price et al. 1999) and eye volume (proportional to the axial length of the eye) (Massey et al. 1999) are all negatively related to the POBF. The POBF is significantly reduced for some individuals with low tension glaucoma compared to normals (Fontana et al. 1998), however, the between-individual variation is considerable (Yang et al. 1997), and is likely to limit the use of the technique as a single diagnostic tool. The pressure pulse mainly represents the blood flow in the choroid as the ONH blood flow forms only a small part of the ocular blood flow, therefore, the value of POBF measurements for investigating optic neuropathies is still unclear.

7.3.4 Laser Doppler Velocimetry and Laser Doppler Flowmetry

LDV and LDF permits retinal haemodynamic evaluation (Petrig and Riva 1996; Hayreh 1997a). LDV measures blood velocity in the retinal arteries and veins, by exploiting the Doppler effect (Bebie 1996). Basically, when laser light is reflected off the moving red blood cells (RBCs) in a blood vessel, the frequency of the laser light undergoes a change. The frequency shift is proportional to the velocity of the RBCs. In contrast to the acoustic Doppler shifts that occur to the pitch (frequency) of sound heard by an observer as a car passes by an observer, the frequency shifts are extremely small and cannot be measured directly. Instead, the coherent property of the laser source is exploited by creating interference waves between the frequency-shifted light reflected from the moving blood cells and the non-frequency shifted light reflected from the vessel walls (assumed to be stationary). The resultant waveform has a 'beat' frequency equal to the difference between the individual frequencies, whose intensity varies with time. The velocity of the RBCs is proportional to the beat frequency. Volumetric flow data can be calculated by combining the velocity measurements with photographic data on the calibre of the vessels. The ability to determine continuous blood flow with the technique provides the opportunity to monitor the response to a flickering light, changes in perfusion pressure and adjustments made to the inspired gases. Blood cell velocities and calculated blood flow tend to be higher in the large diameter vessels than in the small vessels (Riva et al. 1985). The average total retinal volumetric flow rate is approximately 34μl/min., whilst the maximum velocity is approximately 2.5cm/sec. The technique cannot be used for the capillary beds where the flow direction is random (Bohdanecka et al. 1998).

LDF is based upon multiple scattering angles encountered in a capillary bed and is dependent upon a constant probability of interaction between the laser beam and RBCs. The technique was developed to provide measurements of the blood flow at the ONH and within the retinal capillary bed (Riva et al. 1992; Petrig and Riva 1996). The mean CoVs for blood velocity, volume and flow at the ONH in normals is approximately 16%, 16% and 18% respectively (Grunwald et al. 1998). The technique predominantly measures the blood flow in the superficial

layers of the ONH, although the exact depth is unknown. The instrument is less sensitive in measuring the flow in the prelamina and deeper ONH regions (Petrig et al. 1999). The ONH circulatory parameters obtained with the LDF are negatively correlated with CDR and visual field damage (Grunwald et al. 1998).

7.3.5 Scanning Laser Doppler Flowmetry.

Michelson (1995) combined the technique of LDV that Riva and co-workers (1992) had introduced for large vessel analysis, with a scanning laser ophthalmoscope, a reduced illumination area and a capacity to measure smaller capillary flow to create a scanning laser Doppler flowmeter (SLDF). SLDF provides a measure of the moving RBCs velocity within the retinal and anterior ONH vessels and ensures that the influence of Doppler shifts arising from interactions outside the focal plane is limited (Michelson et al. 1996b). This was commercially marketed as the Heidelberg Retina Flowmeter (HRF) attached to the Heidelberg Retina Tomograph (HRT). The measurements are acquired within seconds, without undue patient discomfort.

The probe laser source employed by the HRF has a wavelength of 780nm at a fixed intensity level. The default image field size employed is 10 degrees by 2.5 degrees which is equivalent to a 2.7mm by 0.7mm retinal size. The wavelength of the laser light source and the confocal arrangement of its optical system limit the sampling depth for the HRF. Light of wavelength 780nm is absorbed by the retinal pigment epithelium preventing the evaluation of the choroidal blood flow, whilst the theoretical longitudinal optical resolution of the system is limited to 300-400μm. The sampling density is 256 by 64 pixels permitting a 10μm by 10μm horizontal resolution. Each of the 64 lines, composed of 256 separate points, that create the image are scanned 128 times before the next line is scanned, at a rate of 4000Hz. The repeated scan of each point provides a measure of the temporal variation in the reflected light. A sampling rate of 4000Hz is used, as valid estimates of the fluctuating frequency signal require the scanning rate to be at least twice the maximum expected Doppler-shifted signal frequency, which in the case of capillary beds is 2000Hz. The maximum theoretically detectable velocity is 0.78mm/s for the HRF with a laser source wavelength of 780nm, derived from the equation:

$$V = \Delta f \lambda/2$$

where V = velocity, Δf = frequency shift, and λ is the wavelength of the illuminating light.

The line acquisition time is 0.032 seconds and the entire image is acquired in 2.048 seconds. Upon completion, a series of 64 scanned line images are displayed on a computer screen. A fast Fourier transformation algorithm performed on the image yields a map of the blood perfusion of a retinal region of interest (Michelson and Schmauss 1995).

The theoretical principles of LDF can be applied to capillary beds assuming that random scattering events occur to the light reflected from the moving RBCs and the surrounding stationary tissue (Bonner and Nossal 1990). The resultant Doppler signal, arising from the capillary beds, is composed of numerous, low amplitude, multiple velocity-shifted frequencies, due to the irregular arrangement of the vascular system, and the random scattering of reflected light at the RBCs. The range of frequencies in this combined output is proportional to the range of RBC velocities, and generates a distribution or 'spectrum'. The entire spectrum is proportional to the blood flow and Fourier analysis of this spectrum provides information about the range of velocities from which the mean velocity value can be estimated (Michelson and Schmauss 1995; Michelson et al. 1996b).

For each pixel location, the Doppler frequency shifts attributed to moving RBCs are detected during the scanning process. The temporal intensity variation of the reflected light is dependent upon the beat frequencies generated by interference between the shifted and non-shifted frequencies (Figure 7.2a). A fast Fourier transformation allows the individual waveforms of the reflected light beat frequencies to be identified, and the distribution, or 'spectrum' of frequencies, forms a Power spectrum (Figure 7.2b). The power value indicates the number of cells exhibiting a particular frequency shift, the frequency value is an indicator of the blood cells velocity and the integrated function is a measure of the blood volume at a given location in relative units. The product of each power value and its respective frequency, when integrated is a measure of the flow (Michelson et al. 1996b). Given by the equation:

$$\varpi = \sum_{125Hz}^{2000Hz} \frac{fP(f)df}{P_{(f=0Hz)}} - C$$

where f is the frequency, P(f).df is the power of the photodetector current associated with a frequency range of df about f (given in Hz), and C is the 'noise' component of the system, which is derived from the power values for the frequencies in the range 1500Hz to 2000Hz for the HRF system. The term, $P_{(f=0Hz)}$ given in the equation is a measure of the 'zero' offset, which refers to the direct current (DC) signal output measured at the photodiode detector in the HRF, that is obtained for an actual flow value of zero.

The offset is attributed to the random variation in the intensity of the backscattered light that has not arisen from Doppler shifted encounters. The offset could prove to be a significant factor in comparisons of blood flow measurement acquired through tissue in which the scattering, transmission and absorption properties differs significantly between individuals and with the course of a disease (Chauhan and Smith 1997). The relationship between the true blood flow and the HRF flow value tends to be linear within the recommended working range of 125 to 2000Hz (Michelson and Schmauss 1995) for the Doppler-shifted frequencies with the HRF as it is applied to capillary blood flow (Chauhan and Smith 1997).

The average velocity of the RBCs is derived from the equation:

$$\text{Velocity} = \frac{\text{Flow}}{\text{Volume}}$$

The HRF provides non-invasive quantification, in relative units, of the blood perfusion in the retinal capillary bed and the superficial vascular tissue of the ONH (Michelson and Schmauss 1995; Michelson et al. 1996b; Nicolela et al. 1996b). The HRF can permit reproducible and valid measurements of retinal and ONH blood flow (Michelson et al. 1996a; Michelson et al. 1996b). However, there is considerable potential for within- and between-individual variation in the retinal and ONH ocular haemodynamics. The variation can be reflected in the HRF measures of reproducibility. Blood flow determined by the HRF can be influenced by incidence angle of the scanning beam (Kagemann et al. 1998), retinal illuminance (given by the DC value) (Embleton et al. 1999; Tsang et al. 1999) and retinal location (Bohdanecka et al. 1998). In addition, the default 10 x 10 pixel sampling box can exhibit a high between-visit variability (CoV approximately 30%) compared to the within-visit variability (CoV of 6% to 10%) (Kagemann et al. 1998). The range of the linear relationship between HRF-measured flow and actual flow and the normal values for the HRF arbitrary units remains to be fully defined (Tsang et al. 1999).

The HRF values for the variation of retinal blood flow, volume and velocity are generally derived from single perfusion maps. The cardiac cycle is known to produce a variation in the blood flow. Pulse synchronisation has been advocated as a means to correct for this potential source of error in the haemodynamic measurements (Sullivan et al. 1999). However, until the intensity fluctuation of the detected Doppler signal associated with the pulse rate can be controlled, the use of repeated measures to derive mean haemodynamic values is a viable alternative.

Measures of ocular blood flow as determined by the various instruments are not readily comparable. Each instrument evaluates a specific aspect of the ocular haemodynamics and access to vessels in a particular ocular region, for each measurement, is limited by the technique employed. Despite the lack of direct access to ONH blood flow measurements, indirect measurements of the more accessible, retinal and superficial RNFL of the ONH capillary beds may provide information on the ocular blood flow changes in glaucoma. Although the between-individual variation in the anatomical and physiological arrangement of the vascular beds confounds the generalisation of the findings, the general trends in ocular haemodynamics associated with physiological, pharmacological and pathological factors can be useful in the understanding of the ocular circulation in health and in disease.

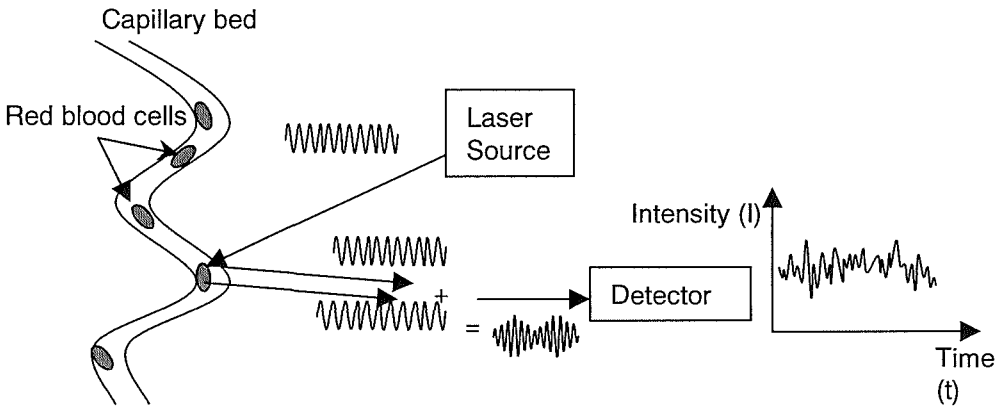

a). The intensity fluctuation of the detected signal is dependent upon the Doppler frequency shifts and is plotted as a function of time, the Intensity Distribution.

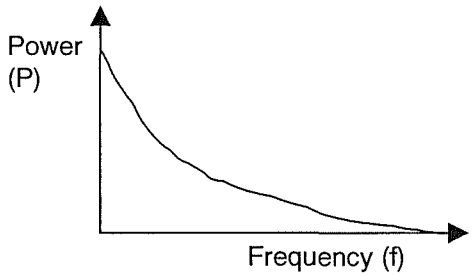

b) A Fourier transformation converts the intensity waveform into the Power Spectrum The power (P) is proportional to the number of moving red blood cells (RBC) for a given frequency; whilst the frequency is proportional to the velocity of a given RBC. Integration of the area enclosed by the power spectrum provides the total number of moving RBC's at a given measured location ('Volume'). Integration of all the power values against their respective frequency provides provides a measure of the 'Flow'.The ratio of the 'Flow' to the 'Volume' is equal to the average 'Velocity' of the RBC's.

Figure 7.2. Schematic diagrams to illustrate the stages involved in the determination of the relative haemodynamic parameters; Volume, Flow and Velocity from the detected intensity of the reflected light.

7.4 Regulation of the Blood Flow.

An adequate exchange of metabolites within the tissue is necessary to maintain function. Blood flow is related to the rate of metabolism. The photoreceptors are considered to have an extremely high level of metabolic activity particularly in darkness, requiring supplies of oxygen, glucose and amino acids, and removal of carbon dioxide and other waste products. As tissue activity increases, the glucose consumption increases and a higher blood flow rate is demanded (Riva et al. 1983). Axoplasmic transport also uses energy and periods of ischaemia that prevent the adequate provision of nutrients and waste disposal are likely to interfere with the axonal transport system (Hayreh et al. 1979).

Blood flow in any tissue is dependent upon the resistance to blood flow and the perfusion pressure (Hayreh 1995). The resistance to flow is related to the blood viscosity and the diameter and muscle tone of the blood vessels supplying the tissue. The perfusion pressure in a vascular bed is equal to the mean systemic arterial pressure minus the venous pressure. In the ONH vessels the IOP approximates to the central retinal venous pressure. The mean ocular perfusion pressure (PP) can therefore be estimated from the equations:

$$PP = 2/3\ BP_m - IOP$$

$$\text{assuming that: } BP_m = BP_d + 1/3\ (BP_s - BP_d)$$

where IOP is the intraocular pressure and BP_s and BP_d are the brachial artery systolic and diastolic blood pressure respectively For a given arterial pressure, there is an inverse relationship between the IOP and the perfusion pressure in the ONH. The blood flow would fluctuate as the perfusion pressure varied in the absence of autoregulation and a compensatory change to the tone of the blood vessels.

Blood flow autoregulation is defined as the ability of a tissue to maintain relatively constant flow rates, despite moderate alterations in perfusion pressure, caused by systemic blood pressure or IOP changes (Hayreh 1995). The retinal and ONH blood flow both show evidence of autoregulation (Hayreh 1997b; Flammer and Orgül 1998; Harris et al. 1998a). The autoregulatory mechanism appears to have the capacity to respond to both myogenic and metabolic variation (Hayreh 1997b). The choroidal circulation however, has shown minimal control in response to changed perfusion pressure (Bill and Sperber 1990; Hayreh 1997b; Flammer and Orgül 1998). Autoregulation, however, only operates over a limited range of perfusion pressures as constriction and dilation of terminal arterioles is limited. The level of perfusion pressure below which autoregulation in the ONH breaks down is quoted as approximately 30mmHg, but the value is likely to vary between individuals (Hayreh 1997b). Systemic diseases such as diabetes mellitus, and arterial hyper- or hypotension can interfere with the autoregulatory mechanisms ability to respond to normal physiological variations in perfusion pressure and can lead to tissue damage (Hayreh 1995).

Vascular insufficiency can also be the result of vasospasm, basically described as an abnormal vascular response to such stimuli as cold, stress or nicotine (O'Brien 1998; Flammer et al. 1999). The process leads to inadequate blood vessel dilation and to inappropriate vasoconstriction.

7.5 Factors Affecting Ocular Blood Flow.

7.5.1 Physiological Factors.

7.5.1.1 Age.

Age is a risk factor for glaucomatous optic neuropathy; however this may simply reflect systemic and vascular changes associated with the ageing process (Hayreh 1994). Evidence for an age-related variation in blood flow is equivocal. Fontana and colleagues (1998) demonstrated a reduction of POBF with increasing age, whilst Yang et al (1997) found the POBF to be independent of age. Similarly, within the rim area of the ONH, increasing age only exerts a minimal effect upon the blood flow parameters derived by the HRF (Groh et al. 1996). In contrast, LDF derived ONH capillary blood velocity exhibits a 4.7% per decade reduction (Rizzo et al. 1991). A reduction of approximately 8% per decade in retinal blood flow has also been found using the HRF (Groh et al. 1996). Similarly using CDI, investigations of the OA have shown a reduction in the PSV and EDV and an increase in RI in the CRA with increasing age (Baxter and Williamson 1995; Williamson et al. 1995).

7.5.1.2 Gender.

POBF tends to be higher in women than in men (Yang et al. 1997), however, the POBF is dependent upon heart rate, and a proportion of the gender difference may be attributable to the greater heart rate found in females. The gender difference in POBF varies with age. There is a consistent age-dependency in males of 0.65 microlitres per sec reduction in POBF per decade, which also applies in females over the age of 50 years. However, between 20-50 years the POBF is age independent in females (Massey et al. 1999). No gender difference is found for blood flow velocity in the OA and CRAs (Williamson et al. 1995). It is unclear what effect gender has upon the ONH or retinal circulation.

7.5.1.3 Refractive error-related variations.

Retinal blood flow, as determined by HRF (Hollo et al. 1997a), and POBF (Ravalico et al. 1997) is reduced in myopes and decreases with increase in myopic refractive error (James et al. 1991; Fontana et al. 1998). It is unclear what effect, if any, refractive error has upon the ONH or retinal circulation.

7.5.1.4 IOP-related variations.

An acute reduction in mean retinal perfusion pressure that accompanies a rapid rise in IOP is offset by a marked increase in RBC velocity in retinal veins as an autoregulatory response to normalise the blood flow in normal eyes (Riva et al. 1986). In glaucoma, however, an elevation of IOP produces a decrease in mean velocity and an increase in RI in both the CRA and PCAs (Trible and Anderson 1998). Poor autoregulation in some glaucomatous individuals, if accompanied by exaggerated diurnal IOP variations could be a contributory factor to the glaucomatous process (Pillunat et al. 1998).

7.5.1.5 Cardiac cycle.

Arterial pulsations produce rhythmic oscillations in blood flow. The maximum RBC velocity in the retinal arteries varies markedly during each cardiac cycle (Feke and Riva 1978), and the pulsatile flow velocity is in phase with the cycle (Riva et al. 1985). Similarly, the retinal capillary blood flow as measured by HRF using a 10 x 10 pixel frame, fluctuates by as much as 50% throughout the duration of the cardiac cycle (Sullivan et al. 1999). POBF also increases with increasing pulse rate (Yang et al. 1997). It is therefore apparent that heart rate, and the status of the cardiac cycle have a significant effect upon the ocular haemodynamics.

7.5.1.6 Posture-related variations.

When changing from the upright to the supine posture, normal individuals and those with POAG show a significant change in heart rate and BP_d, without demonstrating a change in BP_s (James and Smith 1991; Trew and Smith 1991a). Healthy individuals and patients with POAG exhibit an increase of EDV and RI in the OA. In addition, normal individuals show a decrease in the RI of the CRA; however patients with POAG do not show a change in the RI, which is suggestive of faulty autoregulation (Evans et al. 1999). Generally, the IOP rises by 0.3mmHg to 4.7mmHg, when changing from a sitting to a supine position (Kothe 1994). In contrast, to the IOP which increases in the supine position compared to the seated position, the POBF decreases in healthy eyes, in eyes with OHT, and also in NTG (Trew and Smith 1991a; Kothe 1994). The decrease is also present in POAG, to a greater degree (Trew and Smith 1991b). The process involved in the variation of IOP with posture position are unclear; however autoregulation is likely to be involved, and a consistent posture for the patient should be employed when acquiring IOP and blood flow measurements.

7.5.1.7 Smoking-related variations.

The systemically absorbed products of tobacco smoke cause an acute increase in cerebral vessel (Wennmalm 1982), OA (Rojanapongpun and Drance 1993) and ONH (Tamaki et al. 1999) blood flow. An increase in the macula leucocyte velocity (Robinson et al. 1985) and a small or negligible increase in IOP (Tamaki et al. 1999) are also found. One component of the between-individual variation in the magnitude of blood flow is attributed to variations in nicotine absorption and tissue response (Armitage et al. 1976). The increased choroidal blood flow

velocity is probably a response to the effects of systemically absorbed carbon monoxide and nicotine upon tissue oxygenation and the need to maintain adequate oxygen levels for retinal metabolism (Robinson et al. 1985). However, the PSV and RI in the OA are lower in habitual smokers compared to non-smokers (Williamson et al. 1995), despite an expected increase in RI since nicotine is a vasoconstrictor. The reduction in the retinal and ONH capillary blood flow in response to hyperoxia is less in smokers compared with non-smokers which suggests that the regulatory capacity is impaired in smokers (Langhans et al. 1997). An increase in IOP and oxygen consumption through nicotine absorption could contribute to the damage caused by an existing disease, for example glaucoma, associated with a compromised vascular autoregulatory system. However, Klein and colleagues (1993) found no difference between smokers and non-smokers with regard to the frequency of glaucoma. The wide between-individual variation in circulatory response to nicotine exposure confounds attempts to account for the effects of smoking in blood flow studies.

7.5.1.8 Caffeine consumption-related variations.

Caffeine acts as a central nervous system stimulant. Caffeine, in addition to the effects upon blood velocity in the cerebral circulation (Mathew and Wilson 1985), produces a reduction in macula leucocyte velocity and presumably blood flow (Lorfi and Grunwald 1991). The change in ocular blood flow velocity is attributed to retinal vasoconstriction resulting from the inhibitory effect of caffeine upon the potent vasodilator, adenosine. In addition, a small increase in IOP with caffeine intake is found for patients with glaucoma (Higginbotham et al. 1989).

Unfortunately, caffeine is present in a wide range of food and drink and merely accounting for coffee consumption might not avoid the influence of caffeine upon blood flow measurements.

7.5.1.9 Isocapnic Hyperoxia and Isoxic Hypercapnia.

Isocapnic hyperoxia (breathing 100% oxygen) causes a reduction, and isoxic hypercapnia (breathing increased levels of carbon dioxide) an increase, in ONH capillary blood flow similar to that demonstrated in the brain and retina, a feature typical of metabolic autoregulation (Harris et al. 1996a). Hypercapnia increases peripapillary retinal and SPCA blood flow parameters as determined by HRF and CDI (Roff et al. 1999). In addition, using the HRF, the inferior temporal quadrant of the peripapillary retina demonstrates a lesser degree of responsiveness to vasodilation, induced by hypercapnia, and a greater response to vasoconstriction, induced by hyperoxia, than found in the superior temporal quadrant (Chung et al. 1999a).

7.5.1.10 Regional variation ocular haemodynamics.

LDF demonstrated a regional variation in ONH and retinal blood flow. The velocity in the arterial temporal vessels is approximately 15% greater than in the nasal vessels, whilst there is no difference between the superior and inferior vessels of the ONH (Rizzo et al. 1991). The volumetric flow rate is greater in the temporal parapapillary retinal vessels compared to the

nasal vessels, whilst no difference is present between the superior and inferior vessels in the normal eye (Riva et al. 1985). The velocity in the retinal vessels increases with the diameter of the vessel, although the average velocities for the retinal arteries and veins are similar between the temporal and nasal and between the superior and inferior regions using LDF (Riva et al. 1985). Similarly, the temporal peripapillary flow is significantly higher than the nasal peripapillary flow (Hollo et al. 1997a), and is greater in the inferior temporal quadrant compared to the superior temporal quadrant for normals, determined with the HRF (Chung et al. 1999a). No significant differences in retrobulbar ocular haemodynamics are found between right and left eyes for the OAs and CRAs (Williamson et al. 1995).

7.5.2 Pharmacological Factors.

7.5.2.1 Systemic Medication.

Acetazolamide and carbon dioxide enhance the cerebral perfusion by dilating the cerebral vessels leading to an increase in blood flow velocity and a reduction in the RI, in addition to lowering the IOP. However, these systemic agents do not change the PSV or EDV in the OA or in the CRA, although when combined they tend to lower the RI in the CRA (Harris et al. 1996c). In contrast, there is evidence from LDV that acetazolamide increases retinal and macular capillary perfusion (Grunwald and Zinn 1992; Rassam et al. 1993).

Calcium-channel blockers, for example, Nifedipine, can have a beneficial effect upon visual function in glaucoma, particularly in NTG (Kanellopoulos et al. 1996). The effect is attributed to a possible improvement in ocular perfusion and, as such, would most likely benefit those individuals with ocular vasospasm. However, studies into ocular haemodynamic response to Nimodipine (Piltz et al. 1998) and to Nifedepine are inconclusive (Harris et al. 1997).

7.5.2.2 Topical Medication.

A single dose of a topical β-blocker causes an increase in the retinal circulation in the normal (Grunwald 1986) and OHT eye (Grunwald 1990). Untreated individuals with POAG are known to have a lower EDV in the CRA and SPCA and a higher RI in the CRA and SPCA than in normals, and the introduction of the non-selective β-blocker, TimopticXE, returns the levels to values that approach, but are below, the normal (Evans et al. 1998). However, whilst retinal blood flow increases as a long-term effect of a topical selective β-adrenergic blocking agent, Betaxolol, the retinal flow decreases with a dose of the non-selective β-blocker, Timolol, in normals (Yoshida et al. 1998). Betaxolol also tends to increase EDV and RI in the OA, PCAs and the CRA in NTG, whilst Timolol, despite lowering IOP, has no apparent effect on retrobulbar haemodynamics.

The topical carbonic anhydrase inhibitor, Dorzolamide, used as an ocular hypotensive agent, increases blood velocity in the retinal and superficial ONH circulation without any effect upon retrobulbar haemodynamics in healthy eyes (Harris et al. 1996b).

7.5.3 Ocular Disease.

7.5.3.1 Associated with glaucomatous optic neuropathy.

Direct support for a vasogenic mechanism in glaucoma is proving to be rather elusive, since acute ischaemia of the optic nerve tends to produce a different ONH appearance to that of glaucoma. Acute anterior ischaemic optic neuropathy is accompanied by a sudden significant drop in visual acuity, a relative afferent pupil defect and disc pallor with minimal optic disc excavation (Quigley 1977). The effects of chronic ischaemia or prolonged periods of insufficient blood flow, do not appear to be well-documented. Glaucoma is associated with reduced blood flow but it is not clear whether this is a primary or secondary event.

The risk of developing glaucoma is related to the level of IOP (David et al. 1977). Many individuals, despite high IOPs, seem to sustain no functional damage, whilst some other individuals maintain IOP levels that are considered well within a statistically normal range and yet show evidence of progressive axonal and functional loss (Levene 1980; Sommer 1989).

IOP tends to be the same in men and women, and yet the prevalence of NTG in females is significantly higher than in males (Levene 1980). Although measurements of IOP in both Blacks and Whites have shown similar levels of IOP, there is a greater prevalence of glaucoma in Blacks (Sommer 1991). The IOP decreases with increase in age in the Japanese and yet the risk of glaucomatous damage increases with increase in age (Shiose 1990). In addition, reducing the levels of IOP in POAG, through medical and/or surgical intervention does not ensure the prevention of further visual loss (Bergea et al. 1999). The indirect evidence, therefore, suggests that glaucomatous optic neuropathy is in part, attributable to, or associated with, impaired micro-vascular blood flow.

There is evidence to suggest that defective autoregulation of the blood flow in the ONH (Robert et al. 1989; Hayreh 1997b) and the retina (Grunwald et al. 1984) is present in glaucomatous optic neuropathy. Systemic arterial hyper- and hypo-tension (Hayreh 1996b), nocturnal arterial hypotension (Hayreh et al. 1998), atherosclerosis (Flammer et al. 1999) and vasospasm (O'Brien 1998) have all been linked with glaucomatous visual field loss thereby suggesting a defective autoregulatory component in POAG.

ONH blood velocity (Hamard et al. 1994) and flow (Grunwald et al. 1998) is reduced in POAG. Glaucoma patients without systemic hypertension, have a lower ONH blood flow than those with systemic hypertension (Grunwald et al. 1999). A decrease in blood pressure can be accompanied by a decrease in ONH perfusion, which is likely to have serious implications for those individuals with an impaired autoregulatory mechanism. The pulsatile component of the total ocular blood flow is reduced in POAGs compared with OHTs (Trew and Smith 1991a) and also in NTG's compared with normal individuals particularly in the eye that shows greatest field

loss (Fontana et al. 1998). In contrast, choroidal blood flow estimated from LDF recordings taken at the fovea is similar in glaucomatous and normal eyes (Grunwald et al. 1998). Blood flow deficits exist in the ONH and peripapillary retina in POAGs, independent of IOP levels (Michelson et al. 1996a). The blood flow, volume and velocity are reduced in the superior retina and in the lamina region in POAGs, when compared to normals, whilst no difference was found at the neuroretinal rim or in the inferior temporal regions (Nicolela et al. 1996b). Full-field analysis with the HRF has revealed that NTG is associated with a reduced peripapillary retinal blood flow although no difference had been apparent using the default 10 x 10 pixel measurement frame (Chung et al. 1999b). Hollo and associates (1997a) suggested that a thinning of the RNFL might expose the choroidal vessels to the HRF sampling laser beam leading to artefactually high blood flow values; however, this has not been demonstrated to date (Chung et al. 1999b).

Despite evidence that reduced blood flow is associated with glaucoma and that the impaired flow is possibly a contributory factor in the development of the disease, there is no direct proof that vascular insufficiency causes glaucoma.

7.5.3.2 Associations between Ocular Haemodynamics and structural and perimetric parameters.

Despite the peripapillary retinal blood flow and the papillary blood flow being reduced in POAG, Michelson and colleagues (1996a) found no relationship between these blood flow parameters and the CDR or the W-W perimetry MD. However, Kerr et al (1998), found that the maximum blood volume in the lamina region was positively correlated to the W-W MD in POAG. A low peripapillary capillary blood flow has been shown to be associated with increase in CA, mean cup depth and CDAR in normals and with increase in CDAR and CV in POAG (Fan et al. 2000).

Little is known about the variation in ocular haemodynamics in ocular hypertension, and the relationship between the retinal blood flow and the degree of RNFL thinning associated with glaucomatous damage.

7.6 Aims.

The aim was twofold. Firstly, to determine the within-individual, within-visit, and between-visit variation in parapapillary retinal and neural rim capillary blood flow, volume and velocity in normal subjects and in patients with ocular hypertension and in patients with glaucoma using the Heidelberg Retina Flowmeter (HRF; Heidelberg Engineering, Heidelberg, Germany). Secondly, to determine the relationship between the regional blood flow, volume and velocity and the structural and functional integrity across the three diagnostic groups.

7.7 Sample.

The sample comprised 10 normal individuals, 23 OHTs and 22 POAGs. From the initial cohort of subjects described in Chapter 3, 15 normal individuals and 2 POAG individuals had been excluded as the HRF instrument was unavailable during part, or all, of the period in which the series of ONH, RNFL and blood flow images and visual field examinations were performed. Of those individuals who completed all the sessions, 5 OHTs, 2 OHT(H) and 3 POAGs had also been excluded as a result of incomplete data arising from minor eye movements corrupting the 10 by 10 pixel frame (100μm x 100μm) on one or more images.

The mean (±SD) age of the 10 individuals in the normal group was 54.8 (± 23.4) years, of the 23 individuals in the OHT group was 65.5 (± 10.3) years and of the 22 individuals in the POAG group was 67.6 (± 10.2) years.

No attempt was made to control the sample for the type of systemic anti-hypertensive treatment or, with the exception of those patients receiving pilocarpine, for the type of ocular therapy. No attempt was made to match between groups for nicotine or caffeine consumption or to control for consumption immediately prior to the blood flow measurement.

Brachial artery systolic and diastolic blood pressure (BP_s and BP_d respectively and pulse rate were obtained using sphygmomanometry by nursing staff immediately after measurement of blood flow. The mean brachial artery pressure (BP_m) was calculated from the equation:

$$BP_m = BP_d + 1/3\ (BP_s - BP_d)$$

Perfusion pressure (PP) for the study eye was estimated according to the equation:

$$PP = 2/3\ BP_m - IOP$$

	NORMAL	OHT	POAG
Group size (N)	10	23	22
Males (N)	6	9	12
Age (mean ± SD) (yrs)	54.6 ± 23.4	65.5 ± 10.3	67.6 ± 10.2
Smokers (N)	1	3	0
History of Systemic Hypertension (N)	3	9	4
IOP (mean ± SD) (mmHg)	13.1 ± 3.0	24.0 ± 3.9	19.0 ± 3.4
Systolic BP (mean ± SD) (mmHg)	139.2 ± 20.5	141.6 ± 22.0	138.6 ± 16.4
Diastolic BP (mean ± SD) (mmHg)	80.0 ± 15.3	80.8 ± 11.5	82.8 ± 10.6
Mean Arterial BP (mean ± SD) (mmHg)	92.8 ± 13.7	94.4 ± 14.7	92.4 ± 10.9
Pulse rate (mean ± SD) (min.)	67.5 ± 9.3	68.7 ± 8.7	74.9 ± 10.5
Current Ocular Medication			
None (N)	10	9	4
β-Blockers, e.g. Timolol or Betaxolol (N)	0	12	10
Carbonic Anhydrase Inhibitors (CAI), e.g. Dorzolamide (N)	0	0	4
CAI & β-Blockers (N)	0	1	2
α_2 Agonists, e.g. Brimonidine (N)	0	1	0
Prostaglandin F_2 analogues & β-Blockers e.g. Latanaprost & Timolol(N)	0	0	2

Table 7.1. Demographics of the diagnostic groups analysed in the study on ocular haemodynamics.

7.8 Methods.

All subjects were imaged through pupils dilated with Tropicamide 1% instilled at least thirty minutes prior to the imaging session. One eye from each individual was selected for the study as described in Chapter 3 (Methodology). Fixation was directed towards a stationary target 2m in front of the subject.

Perfusion maps were obtained for three zones; three repeated images were acquired at an upper zone centred on the superior pole of the ONH that overlapped onto the surrounding superior temporal and superior nasal parapapillary retina; six images were acquired for the middle zone which crossed the centre of the ONH and extended either side to include the temporal and nasal parapapillary retina; three images were acquired for the lower zone centred

on the inferior region of the ONH which extended beyond the disc margin to include the inferior nasal and inferior temporal parapapillary retina (Figure 7.3). The locations were kept constant across each set of images for a given individual, both within- and between-visits.

The images were focussed on the superficial peripapillary retina. The focus setting from the initial scan was maintained within- and between-visits, with the sensitivity settings chosen to provide a light yellow shade for the brightest pixels, avoiding any bleached white pixels within the given zone. Identical focus and illumination settings were used for the optic nerve head and for the surrounding retina.

A quality control inspection was undertaken for each acquired series of images displayed on the computer monitor. Those images failing outside the desired standard were immediately discarded and further scans were obtained. The quality control inspection included a subjective assessment of the overall saturation level of the image series to ensure that excessive under- or over-exposure had been avoided; and an assessment to ensure that horizontally shifted or interrupted vertical bands within a single image, indicative of excessive eye movements during the scan process, had been avoided. In a series of images, the complete absence of a detectable shift of the vertical bands in all 64 images was extremely rare. Generally three or four corrupted images were observed, and these were considered acceptable for permanent storage and further analysis.

Once accepted, a Fourier transformation was performed by the software on each series of images and a perfusion map was generated. Selection of the desired sample locations within the perfusion maps was then undertaken following all image acquisition.

For each individual, an acetate sheet was aligned to the computer screen and the outline of the ONH margin and the position of the major vessels was transferred manually onto the sheet. The 10 x 10 pixel square has previously been employed in both clinical and reproducibility studies (Groh et al. 1996; Michelson et al. 1996a; Michelson et al. 1996b; Nicolela et al. 1996b; Kerr et al. 1998). A reference 10 by 10 pixel box, placed adjacent to both the disc margin and a large vessel, was added to the cover sheet. Identification of the location for sample boxes on subsequent images for that individual was based upon the initial alignment of the disc margin, the major vessels and the reference box. This procedure was used to ensure sampling at identical regions and to avoid bias in measurements. A 10 by 10 pixel measurement box was then placed in the desired region, on an area devoid of a major blood vessel or corrupted by an eye movement. The sample sites were chosen to provide average reflectivity, DC values of between 30 and 190 (arbitrary units) as advocated recently (Embleton et al. 1999). An x,y, co-ordinate system permitted control of the position of the measurement box. The pixel distance from the reference box was noted and used in all repeated images for that region. On the few occasions in which the sample area was corrupted by an eye movement, data was used from the nearest uncorrupted area.

The mean values within the sample box, for blood volume, flow and velocity, at each selected location, for the repeated images at each of the two visits for each individual were transferred to a spreadsheet for further statistical analysis.

7.9 Analysis.

The within-visit variation was expressed as the Group mean and SD of each HRF parameter and the Coefficient of Variation (CoV).

Three separate repeated measures Analysis of Variance (ANOVA) were used to evaluate ocular blood volume, flow, and velocity, respectively, within each of the three zones. Age and diagnostic category were considered as separate between-subjects factors and visit and number of scans as within-subjects factors.

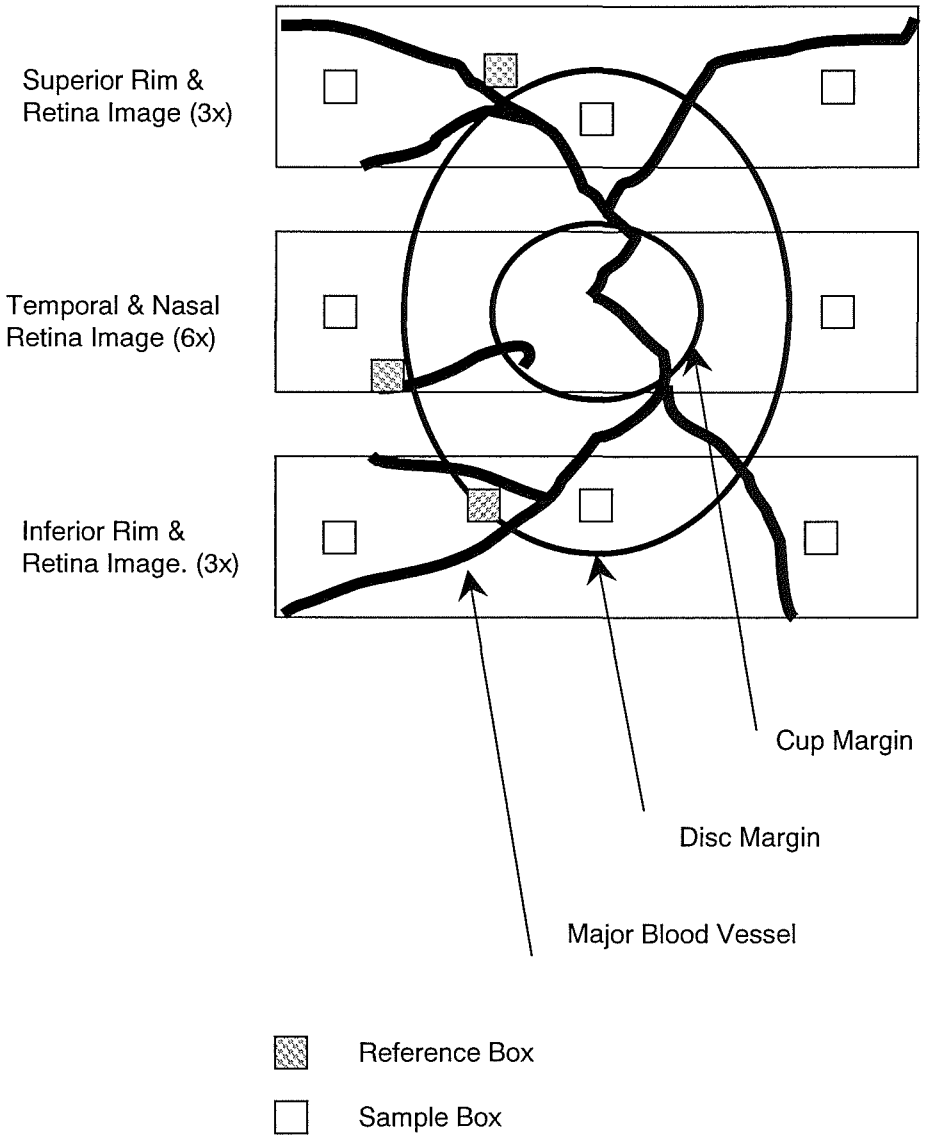

Figure 7.3. Schematic diagram to show the reference outlines noted on each acetate sheet for identification of sample location on repeated images for each person.

7.10 Results.

7.10.1 Within-visit variability of the regional retinal capillary blood volume, flow, and velocity.

The Group mean Coefficient of Variation (CoV) for the three or six image acquisitions for volume, flow and velocity for each of three diagnostic groups at Visit One are given in Table 7.2. The within-visit variation in regional parapapillary retinal haemodynamics as defined by one SD is shown as a function of the blood volume, flow and velocity for the respective regions in Figure 7.4(a) & (b), 7.4(cont)(c) & (d) and Figure 7.5(a) & (b).

7.10.1.1 Volume.

The Group mean CoV for the measurement of volume in the Normal group was least in the inferior temporal retina (CoV=10.75%) and was greatest in the temporal retina (CoV=18.57%). The CoVs were similar across the regions for both the OHT and POAG groups; however the CoVs were larger for the OHT group than for the POAG group and generally least for the Normal group for each of the regions.

7.10.1.2 Flow.

The Group mean CoV for the measurement of flow was lowest for the Normal group in most of the regions, particularly in the inferior temporal region (CoV=17.99%), than for either the OHT or the POAG groups. It was generally greatest for the OHT group, particularly in the temporal retina (CoV=28.56%).

7.10.1.3 Velocity.

The Group mean CoV for the measurement of velocity was generally lowest for the Normal group in most of the regions compared to that for either the OHT or the POAG groups. The CoV was lowest for the Normal group in the inferior temporal region (CoV=17.31%). The CoV tended to be similar in the OHT and POAG groups.

	Normal	Ocular Hypertension	Glaucoma
	Average ± SD CoV(%)	Average ± SD CoV(%)	Average ± SD CoV(%)
Superior Temporal Retina			
Volume (AU).	15.75 ± 12.19	17.71 ± 9.95	16.45 ± 9.30
Flow (AU).	18.88 ± 12.91	23.48 ± 12.80	20.67 ± 12.51
Velocity (AU)	17.71 ± 12.19	22.64 ± 12.31	19.93 ± 12.38
Superior Nasal Retina			
Volume (AU).	16.37 ± 8.40	17.86 ± 11.43	17.20 ± 9.22
Flow (AU).	19.96 ± 13.55	27.08 ± 19.61	25.45 ± 14.14
Velocity (AU)	18.96 ± 12.80	24.28 ± 15.14	24.74 ± 13.46
Inferior Temporal Retina			
Volume (AU).	10.75 ± 6.42	18.03 ± 10.23	15.72 ± 10.42
Flow (AU).	17.99 ± 8.50	23.53 ± 13.24	22.01 ± 11.28
Velocity (AU)	17.31 ± 7.19	22.60 ± 12.60	21.14 ± 10.80
Inferior Nasal Retina			
Volume (AU).	16.66 ± 10.31	17.99 ± 9.95	15.64 ± 10.04
Flow (AU).	23.28 ± 14.97	21.19 ± 10.97	21.44 ± 13.58
Velocity (AU)	22.81 ± 14.33	20.03 ± 10.25	20.30 ± 12.41
Temporal Retina			
Volume (AU).	18.57 ± 8.25	21.99 ± 11.07	16.61 ± 8.01
Flow (AU).	22.19 ± 9.43	28.56 ± 13.41	21.37 ± 11.34
Velocity (AU)	21.29 ± 9.44	26.95 ± 12.11	20.60 ± 10.87
Nasal Retina			
Volume (AU).	18.11 ± 4.22	18.65 ± 9.26	18.05 ± 10.16
Flow (AU).	21.57 ± 5.26	24.81 ± 14.75	22.99 ± 11.22
Velocity (AU)	21.38 ± 4.67	23.55 ± 13.16	21.71 ± 9.40

Table 7.2. Within-session Group Mean ± SD of the Coefficient of Variation (CoV%) of repeated measures for the ocular haemodynamic parameters for Visit One.

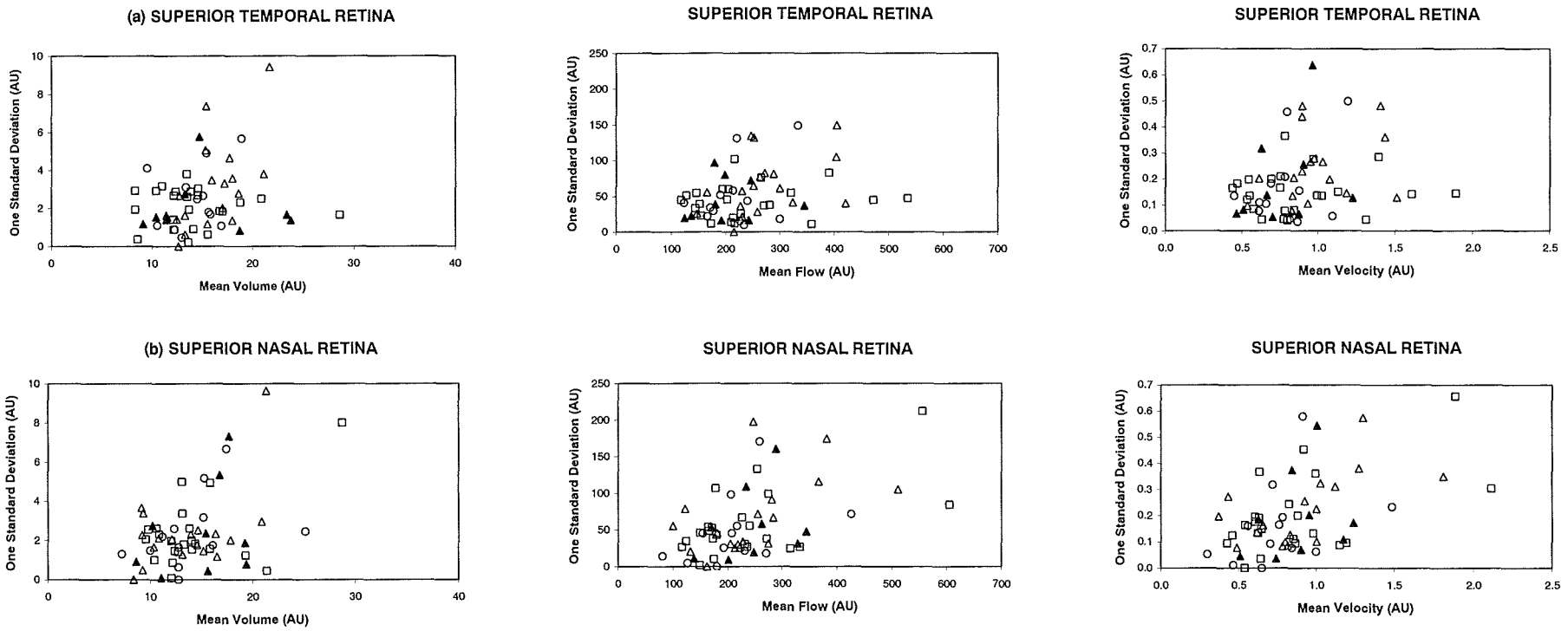

Figure 7.4. The within-visit variability in HRF derived mean blood volume, flow and velocity at Visit One in the (a) Superior Temporal and (b) Superior Nasal retina for the Normal group (open circles), for the OHT group (open triangles), for the OHT(H) group (closed triangles) and for the POAG group (open squares). Each data point represents a single individual.

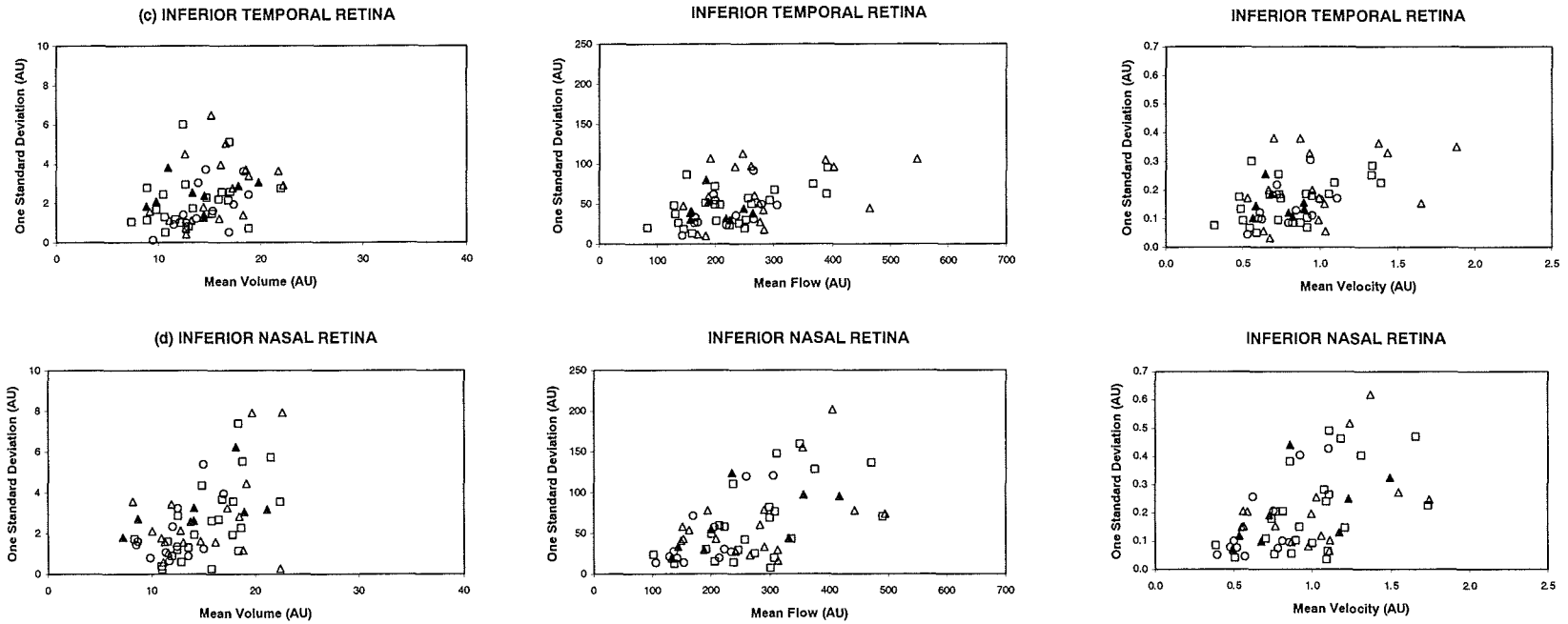

Figure 7.4(cont). The within-visit variability in HRF derived mean blood volume, flow and velocity at Visit One in the (c) Inferior Temporal and (d) Inferior Nasal retina for the Normal group (open circles), for the OHT group (open triangles), for the OHT(H) group (closed triangles) and for the POAG group (open squares). Each data point represents a single individual.

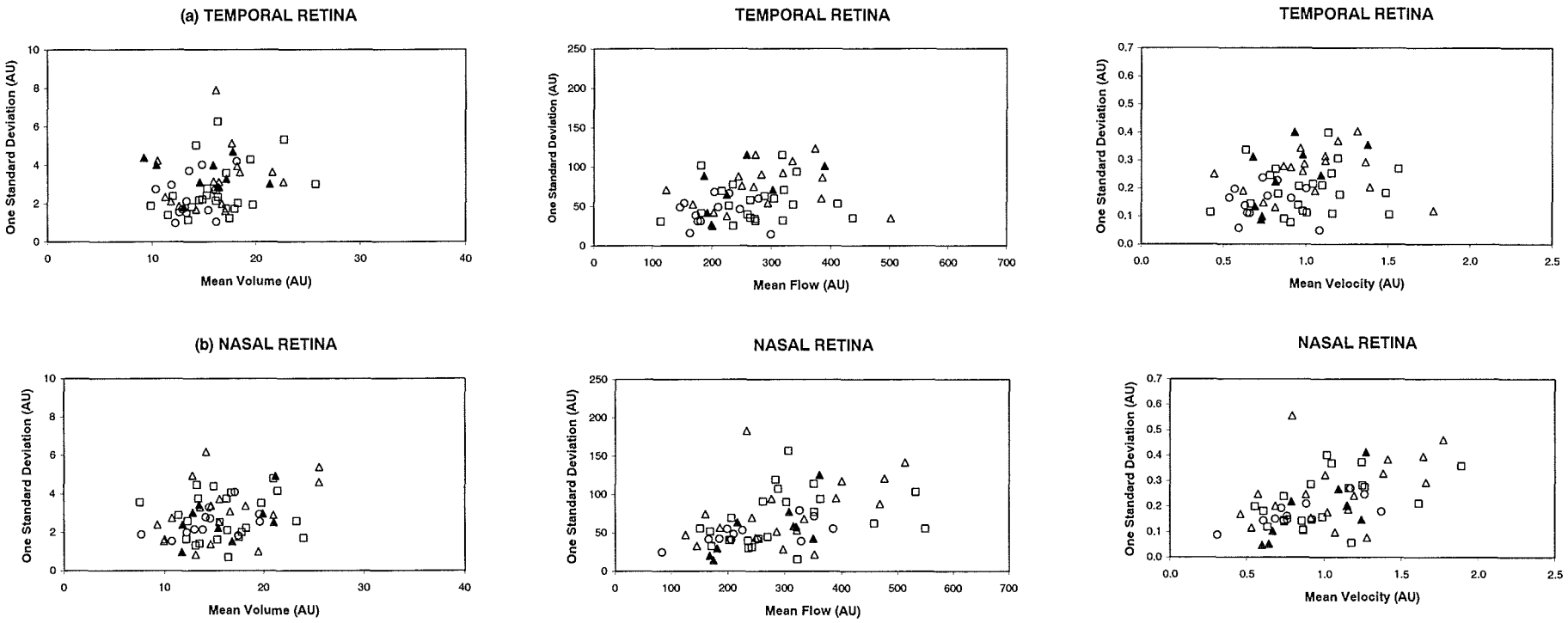

Figure 7.5. The within-visit variability in HRF derived mean blood volume, flow and velocity at Visit One in the (a) Temporal and (b) Nasal retina for the Normal group (open circles), for the OHT group (open triangles), for the OHT(H) group (closed triangles) and for the POAG group (open squares). Each data point represents a single individual.

7.10.2 Between-visit variability of the regional retinal capillary blood volume, flow, and velocity.

The Group mean and one SD of the retinal capillary blood volume, flow, and velocity at Visit One and at Visit Two as a function of the region and of the diagnosis is given in Table 7.3 and Table 7.4.

7.10.2.1 Volume.

The limits of agreement for the blood volume between the first and second visits are given in Table 7.5. The limits of agreement for the superior temporal parapapillary retina are presented for illustrative purposes in Figure 7.6. The blood volume tended to be greater at the second visit for each of the three diagnostic groups for all regions with the exception of the nasal parapapillary retina, although the differences did not reach statistical significance. The limits of agreement were generally wider for the OHT group than either the Normal or the POAG groups.

7.10.2.2 Flow.

The limits of agreement for the blood flow between the first and second visits are given in Table 7.5.The difference in the flow between the two visits is presented as a function of the mean of the two visits for the superior temporal parapapillary retina in Figure 7.7. The blood flow tended to be greater at the second visit for the OHT and POAG groups for all the regions except for the nasal parapapillary retina, although the difference did not reach statistical significance. The limits of agreement were generally wider for the OHT group than either the Normal or the POAG groups.

7.10.2.3 Velocity.

The blood velocity did not vary between the first and second visits. The limits of agreement for the blood velocity between the first and second visits are given in Table 7.5. The difference in the velocity between the two visits is presented as a function of the mean of the two visits for the superior temporal parapapillary retina in Figure 7.8. The variation in the group mean between-visit difference was considerably greater in the nasal parapapillary retina than for the other retinal regions across each of the diagnostic groups. The limits of agreement were generally wider for the OHT group than for either the Normal or the POAG groups.

	Normal	Ocular Hypertension	Glaucoma
	Mean (SD)	Mean (SD)	Mean (SD)
Superior Temporal Retina			
Volume (AU).	14.21 ± 2.68	15.33 ± 3.41	14.18 ± 2.34
Flow (AU).	216.64 ± 56.20	253.84 ± 69.07	246.66 ± 49.69
Velocity (AU)	0.79 ± 0.23	0.91 ± 0.27	0.84 ± 0.17
Superior Nasal Retina			
Volume (AU).	13.96 ± 2.58	14.16 ± 3.09	14.16 ± 2.94
Flow (AU).	209.76 ± 50.60	250.34 ± 80.74	244.20 ± 74.95
Velocity (AU)	0.76 ± 0.17	0.91 ± 0.25	0.88 ± 0.25
Inferior Temporal Retina			
Volume (AU).	14.69 ± 1.97	14.85 ± 3.03	13.40 ± 2.46
Flow (AU).	224.76 ± 45.92	256.07 ± 65.49	225.49 ± 52.18
Velocity (AU)	0.81 ± 0.16	0.92 ± 0.22	0.82 ± 0.18
Inferior Nasal Retina			
Volume (AU).	12.05 ± 2.54	15.29 ± 3.43	15.41 ± 3.16
Flow (AU).	184.04 ± 61.08	272.48 ± 73.33	278.61 ± 77.55
Velocity (AU)	0.67 ± 0.21	0.97 ± 0.24	1.00 ± 0.26
Temporal Retina			
Volume (AU).	13.56 ± 2.75	16.39 ± 4.70	16.35 ± 3.01
Flow (AU).	205.48 ± 47.0	290.97 ± 103.77	286.73 ± 62.50
Velocity (AU)	0.75 ± 0.16	1.02 ± 0.30	1.03 ± 0.21
Nasal Retina			
Volume (AU).	14.26 ± 2.64	15.98 ± 3.28	15.93 ± 3.28
Flow (AU).	243.38 ± 51.39	301.14 ± 83.44	287.46 ± 70.06
Velocity (AU)	0.86 ± 0.18	1.07 ± 0.28	1.02 ± 0.23

Table 7.3. Within-session Group Mean ± SD for the ocular haemodynamic parameters for Visit One.

	Normal	Ocular Hypertension	Glaucoma
	Mean (SD)	Mean (SD)	Mean (SD)
Superior Temporal Retina			
Volume (AU).	16.26 ± 4.16	16.32 ± 4.22	15.63 ± 2.27
Flow (AU).	258.63 ± 64.20	277.46 ± 90.63	275.90 ± 61.00
Velocity (AU)	0.92 ± 0.21	0.99 ± 0.30	0.99 ± 0.21
Superior Nasal Retina			
Volume (AU).	13.87 ± 2.48	14.07 ± 2.90	14.79 ± 3.65
Flow (AU).	201.97 ± 53.88	250.32 ± 55.71	264.03 ± 103.50
Velocity (AU)	0.73 ± 0.19	0.90 ± 0.19	0.94 ± 0.32
Inferior Temporal Retina			
Volume (AU).	15.38 ± 3.02	15.34 ± 3.39	13.71 ± 2.96
Flow (AU).	232.17 ± 59.25	260.74 ± 65.02	235.26 ± 65.52
Velocity (AU)	0.83 ± 0.20	0.92 ± 0.22	0.85 ± 0.23
Inferior Nasal Retina			
Volume (AU).	12.22 ± 1.78	15.24 ± 2.33	16.25 ± 3.08
Flow (AU).	179.72 ± 33.30	274.83 ± 49.11	289.26 ± 81.88
Velocity (AU)	0.66 ± 0.12	0.98 ± 0.17	1.04 ± 0.28
Temporal Retina			
Volume (AU).	15.41 ± 3.39	17.20 ± 3.52	16.01 ± 3.30
Flow (AU).	243.59 ± 83.71	298.68 ± 72.69	287.50 ± 72.80
Velocity (AU)	0.87 ± 0.26	1.06 ± 0.24	1.03 ± 0.24
Nasal Retina			
Volume (AU).	13.82 ± 3.81	15.82 ± 3.92	15.83 ± 2.66
Flow (AU).	220.08 ± 66.73	291.06 ± 82.87	282.80 ± 70.23
Velocity (AU)	0.80 ± 0.24	1.04 ± 0.27	1.02 ± 0.24

Table 7.4. Within-session Group Mean ± SD for the ocular haemodynamic parameters for Visit Two.

SUPERIO-TEMPORAL RETINA

	VOLUME				FLOW				VELOCITY			
			95% L.O.A				95% L.O.A				95% L.O.A	
	GMD	SD	UPPER	LOWER	GMD	SD	UPPER	LOWER	GMD	SD	UPPER	LOWER
NORMAL	2.05	4.99	11.84	-7.73	41.99	66.61	172.54	-88.57	0.14	0.22	0.56	-0.29
ALL OHT	0.99	4.05	8.92	-6.94	23.62	91.86	203.67	-156.43	0.08	0.31	0.68	-0.53
POAG	1.34	3.01	7.25	-4.57	27.01	76.78	177.48	-123.47	0.09	0.26	0.60	-0.41

SUPERIO-NASAL RETINA

	VOLUME				FLOW				VELOCITY			
			95% L.O.A				95% L.O.A				95% L.O.A	
	GMD	SD	UPPER	LOWER	GMD	SD	UPPER	LOWER	GMD	SD	UPPER	LOWER
NORMAL	-0.09	3.75	7.25	-7.44	-7.79	60.39	110.57	-126.15	-0.02	0.20	0.37	-0.42
ALL OHT	-0.09	2.30	4.42	-4.60	-0.02	54.20	106.21	-106.25	0.00	0.17	0.32	-0.33
POAG	0.58	3.47	7.38	-6.23	20.17	84.25	185.31	-144.97	0.06	0.26	0.57	-0.46

INFERIO-TEMPORAL RETINA

	VOLUME				FLOW				VELOCITY			
			95% L.O.A				95% L.O.A				95% L.O.A	
	GMD	SD	UPPER	LOWER	GMD	SD	UPPER	LOWER	GMD	SD	UPPER	LOWER
NORMAL	0.70	2.45	5.49	-4.10	7.41	36.32	78.60	-63.77	0.02	0.12	0.25	-0.21
ALL OHT	0.50	6.15	12.55	-11.56	4.68	145.08	289.03	-279.67	0.01	0.47	0.92	-0.91
POAG	0.46	3.56	7.44	-6.52	14.79	80.01	171.62	-142.03	0.05	0.27	0.58	-0.49

INFERIOR-NASAL RETINA

	VOLUME				FLOW				VELOCITY			
			95% L.O.A				95% L.O.A				95% L.O.A	
	GMD	SD	UPPER	LOWER	GMD	SD	UPPER	LOWER	GMD	SD	UPPER	LOWER
NORMAL	0.17	1.74	3.58	-3.24	-4.33	45.03	83.93	-92.58	-0.01	0.16	0.30	-0.33
ALL OHT	-0.05	4.07	7.92	-8.03	2.34	90.95	180.60	-175.91	0.01	0.31	0.62	-0.59
POAG	0.94	3.10	7.02	-5.14	13.92	70.97	153.02	-125.19	0.05	0.24	0.52	-0.43

TEMPORAL RETINA

	VOLUME				FLOW				VELOCITY			
			95% L.O.A				95% L.O.A				95% L.O.A	
	GMD	SD	UPPER	LOWER	GMD	SD	UPPER	LOWER	GMD	SD	UPPER	LOWER
NORMAL	1.09	3.25	7.46	-5.28	13.65	66.11	143.23	-115.92	0.04	0.21	0.46	-0.38
ALL OHT	-0.45	5.41	10.16	-11.06	-13.17	97.17	177.27	-203.62	-0.05	0.34	0.61	-0.72
POAG	0.45	3.83	7.95	-7.05	10.56	74.23	156.04	-134.92	-0.01	0.27	0.52	-0.55

NASAL RETINA

	VOLUME				FLOW				VELOCITY			
			95% L.O.A				95% L.O.A				95% L.O.A	
	GMD	SD	UPPER	LOWER	GMD	SD	UPPER	LOWER	GMD	SD	UPPER	LOWER
NORMAL	0.96	4.05	8.90	-6.97	9.00	66.78	139.89	-121.88	0.03	0.24	0.49	-0.43
ALL OHT	-0.62	3.21	5.67	-6.92	-9.39	67.85	123.58	-142.37	-0.04	0.24	0.43	-0.50
POAG	-0.03	2.39	4.65	-4.70	1.06	56.16	111.13	-109.02	0.01	0.20	0.39	-0.38

TABLE 7.5. The Group mean difference and SD for each peripapillary retinal region, for the blood volume, flow and velocity, in arbitrary units, across each of the diagnostic groups. The upper and lower limits of agreement are provided. (G.M.D = Group Mean Difference; L.O.A = Limits of Agreement).

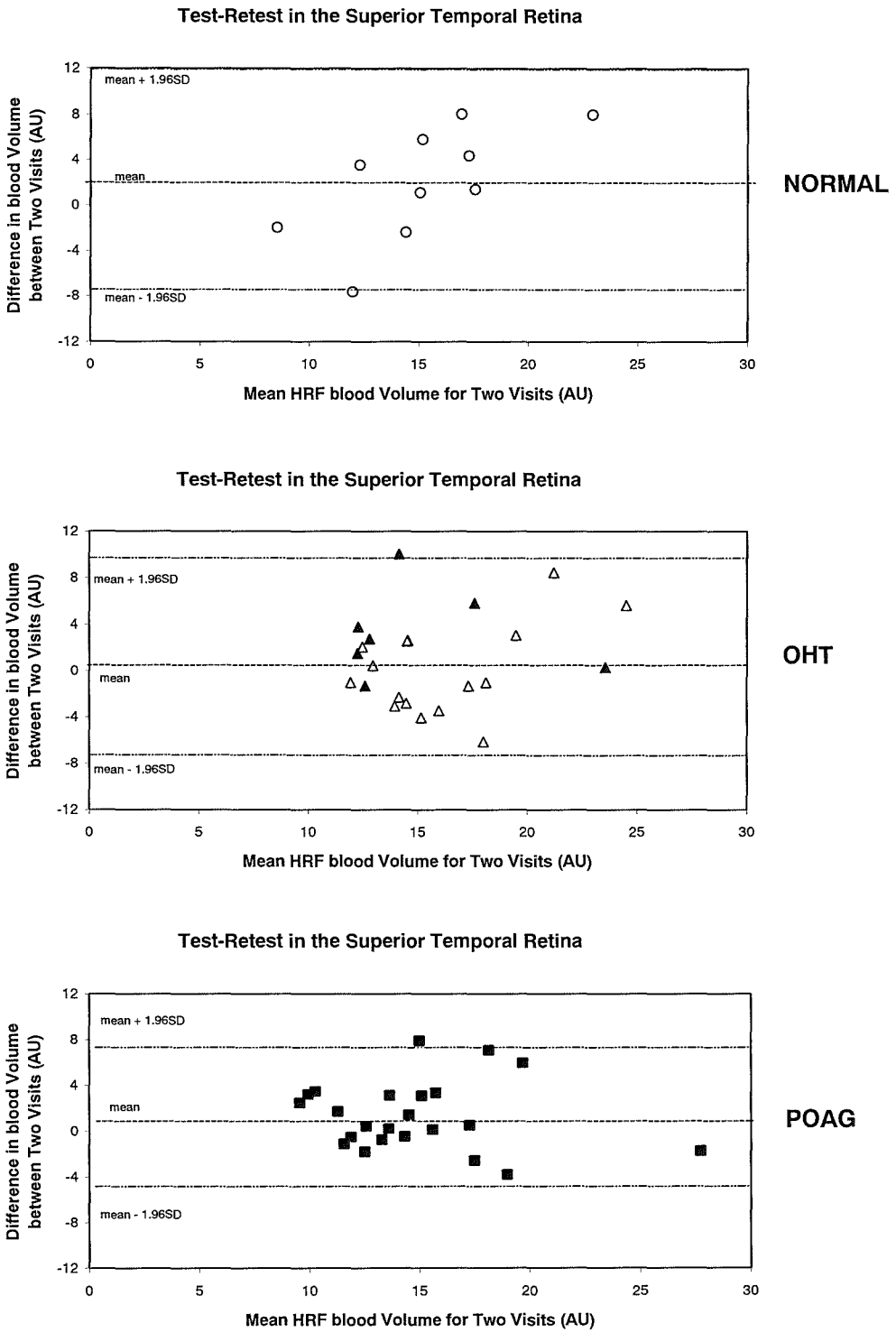

Figure 7.6. The difference in mean Superior Temporal retinal blood Volume as a function of the mean Superior Temporal retinal blood Volume for the two visits, for the Normal group (top), for the OHT group (open triangles) and OHT(H) group (closed triangles) (middle) and for the POAG group (bottom). The mean and the 95% confidence limits are shown.

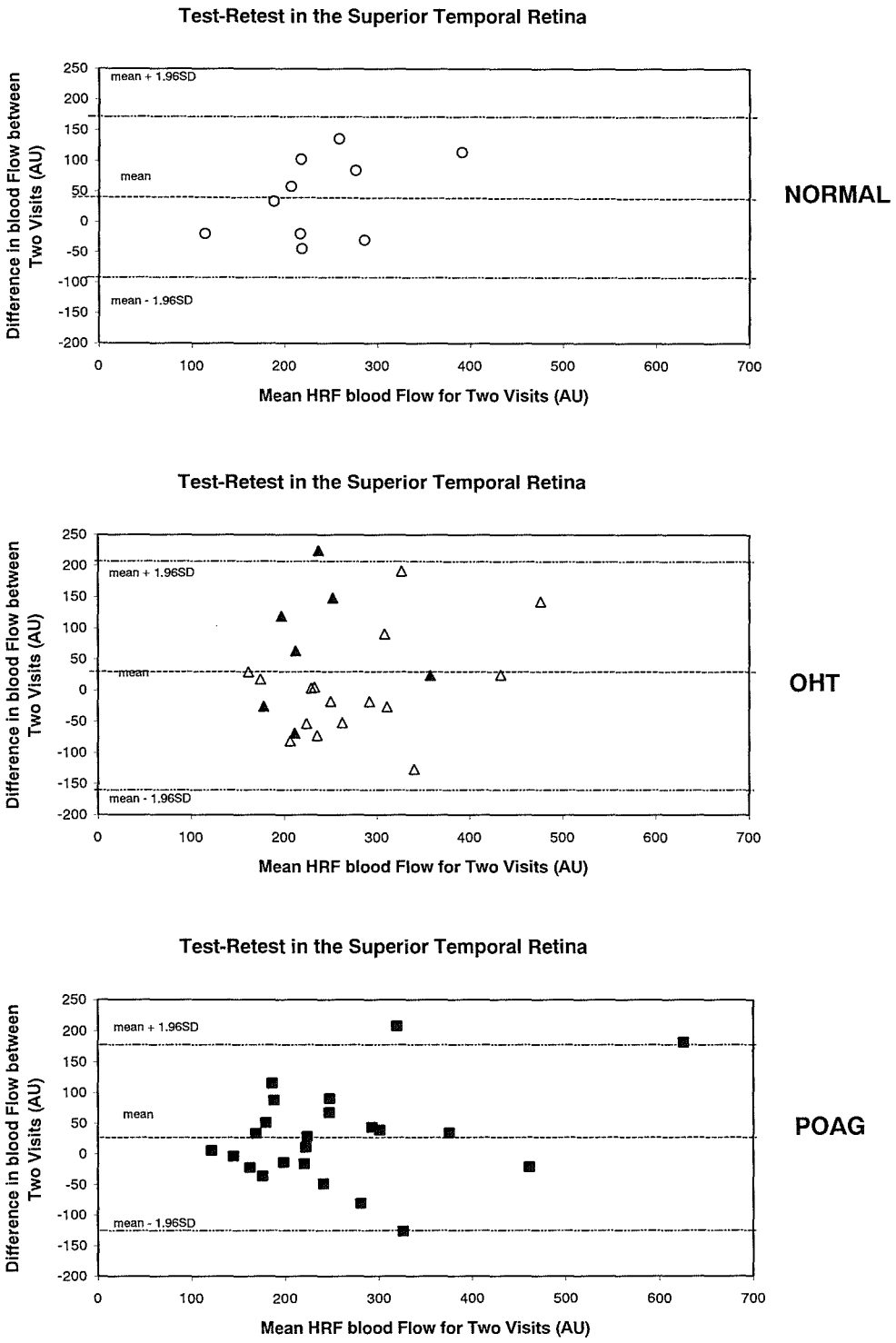

Figure 7.7. The difference in mean Superior Temporal retinal blood Flow as a function of the mean Superior Temporal retinal blood Flow for the two visits, for the Normal group (top), for the OHT group (open triangles) and OHT(H) group (closed triangles) (middle) and for the POAG group (bottom). The mean and the 95% confidence limits are shown.

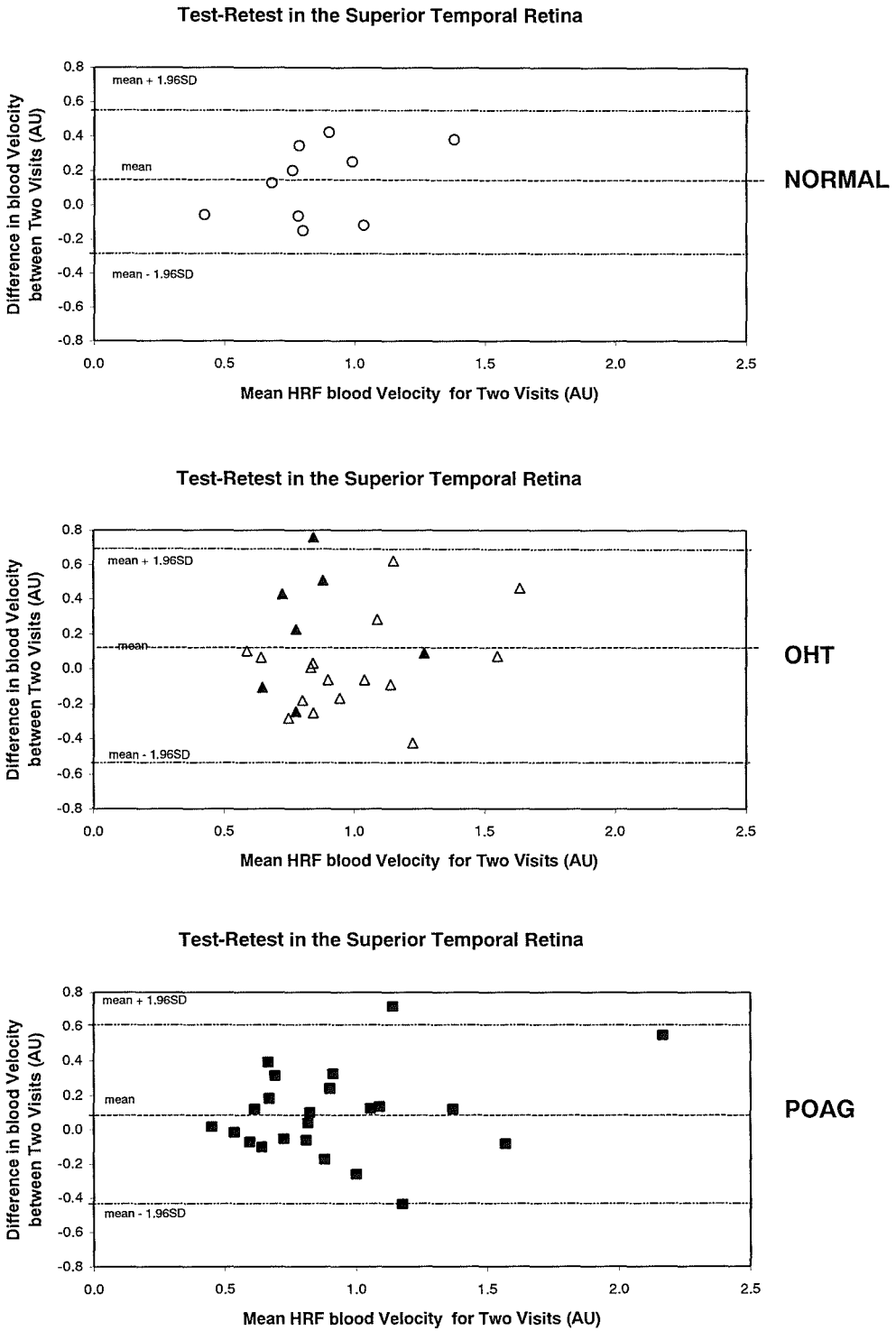

Figure 7.8. The difference in mean Superior Temporal retinal blood Velocity as a function of the mean Superior Temporal retinal blood Velocity for the two visits, for the Normal group (top), for the OHT group (open triangles) and OHT(H) group (closed triangles) (middle) and for the POAG group (bottom). The mean and the 95% confidence limits are shown.

7.10.3 Variability of the regional retinal capillary blood volume, flow, and velocity, as a function of age, diagnosis, the number of scans, and between the two visits.

None of the between-subject factors influencing blood volume, flow, or velocity reached statistical significance at any one of the regions. As would be expected, none of the between- or within-subject interactions reached statistical significance.

7.10.3.1 Volume.

The blood volume did not vary with age, for the superior temporal retina (STR) (p=0.172); for the superior nasal region (SNR) (p=0.801); for the inferior temporal retina (ITR) (p=0.112); for the inferior nasal retina (INR) (p=0.833); for the temporal retina (TR) (p=0.093); or for the nasal retina (NR) (p=0.951) or with diagnosis (STR, p=0.687; SNR, p=0.957; ITR, p=0.082; INR, p=0.114; TR, p=0.156; NR, p=0.587). Blood volume was also independent of the number of scans (STR, p=0.687; SNR, p=0.975; ITR, p=0.679; INR, p=0.529; TR, p=0.576; NR, p=0.167), and did not vary between the two visits (STR, p=0.243; SNR, p=0.195; ITR, p=0.576; INR, p=0.849; TR, p=0.954; NR, p=0.847).

7.10.3.2 Flow.

The blood flow did not vary with age (STR, p=0.452; SNR, p=0.182; ITR, p=0.933; INR, p=0.389; TR, p=0.951; NR, p=0.281), and was independent of diagnosis (STR, p=0.926; SNR, p=0.904; ITR, p=0.284; INR, p=0.113; TR, p=0.176; NR, p=0.543). Blood flow was also independent of the number of scans (STR, p=0.225; SNR, p=0.174; ITR, p=0.455; INR, p=0.919; TR, p=0.862; NR, p=0.912), and did not vary between the two visits (STR, p=0.619; SNR, p=0.998; ITR, p=0.702; INR, p=0.701; TR, p=0.425; NR, p=0.084).

7.10.3.3 Velocity.

The blood velocity was independent of the age (STR, p= p=0.422; SNR, p=0.145; ITR, p=0.995; INR, p=0.281; TR, p=0.925; NR, p=0.315) and of diagnosis (STR, p=0.918; SNR, p=0.903; ITR, p=0.347; INR, p=0.099; TR, p=0.184; NR, p=0.568). Blood velocity was also independent of the number of scans (STR, p=0.687; SNR, p=0.975; ITR, p=0.679; INR, p=0.529; TR, p=0.576; NR, p=0.167), and did not vary between the two visits (STR, p=0.267; SNR, p=0.184; ITR, p=0.480; INR, p=0.923; TR, p=0.646; NR, p=0.757).

7.10.4 Relationship between the Temporal and Nasal HRF derived parapapillary retinal haemodynamic parameters and Temporal and Nasal Sector OCT derived RNFL thickness, three selected Temporal and Nasal Sector HRT derived topographical parameters, and two Global Indices for W-W perimetry.

7.10.4.1 RNFL thickness derived by OCT.

The temporal and nasal sector OCT derived RNFL thickness was independent of the respective regional HRF derived temporal and nasal blood volume (Temporal R^2=0.00; Nasal R^2=0.12), blood flow (Temporal R^2=0.03; Nasal R^2=0.12), and blood velocity (Temporal R^2=0.09; Nasal R^2=0.08) (Figure 7.9 & Figure 7.10).

7.10.4.2 RNFL thickness derived by HRT.

The temporal and nasal sector HRT derived mean RNFL thickness was independent of the respective regional HRF derived mean temporal and nasal blood volume (Temporal R^2=0.01; Nasal R^2=0.00), blood flow (Temporal R^2=0.00; Nasal R^2=0.03), and blood velocity (Temporal R^2=0.00; Nasal R^2=0.02) (Figure 7.11 & Figure 7.12).

7.10.4.3 RDAR derived by HRT.

The temporal and nasal sector HRT derived mean RDAR was independent of the respective regional HRF derived mean temporal and nasal blood volume (Temporal R^2=0.00; Nasal R^2=0.03), blood flow (Temporal R^2=0.00; Nasal R^2=0.01), and blood velocity (Temporal R^2=0.00; Nasal R^2=0.01) (Figure 7.13 & Figure 7.14).

7.10.4.4 CSM derived by HRT.

The temporal and nasal sector HRT derived mean CSM was independent of the respective regional HRF derived mean temporal and nasal blood volume (Temporal R^2=0.01; Nasal R^2=0.00), blood flow (Temporal R^2=0.00; Nasal R^2=0.01), and blood velocity (Temporal R^2=0.00; Nasal R^2=0.01) (Figure 7.15 & Figure 7.16).

7.10.4.5 Visual Field.

The Global index MD with W-W perimetry was independent of the regional HRF derived mean temporal and nasal blood volume (Temporal R^2=0.00; Nasal R^2=0.06), blood flow (Temporal R^2=0.00; Nasal R^2=0.08), and blood velocity (Temporal R^2=0.02; Nasal R^2=0.07) (Figure 7.17 & Figure 7.18). Similarly, the Global index PSD with W-W perimetry was independent of the regional HRF derived mean temporal and nasal blood volume (Temporal R^2=0.00; Nasal R^2=0.01), blood flow (Temporal R^2=0.00; Nasal R^2=0.00), and blood velocity (Temporal R^2=0.00; Nasal R^2=0.00) (Figure 7.19 & Figure 7.20).

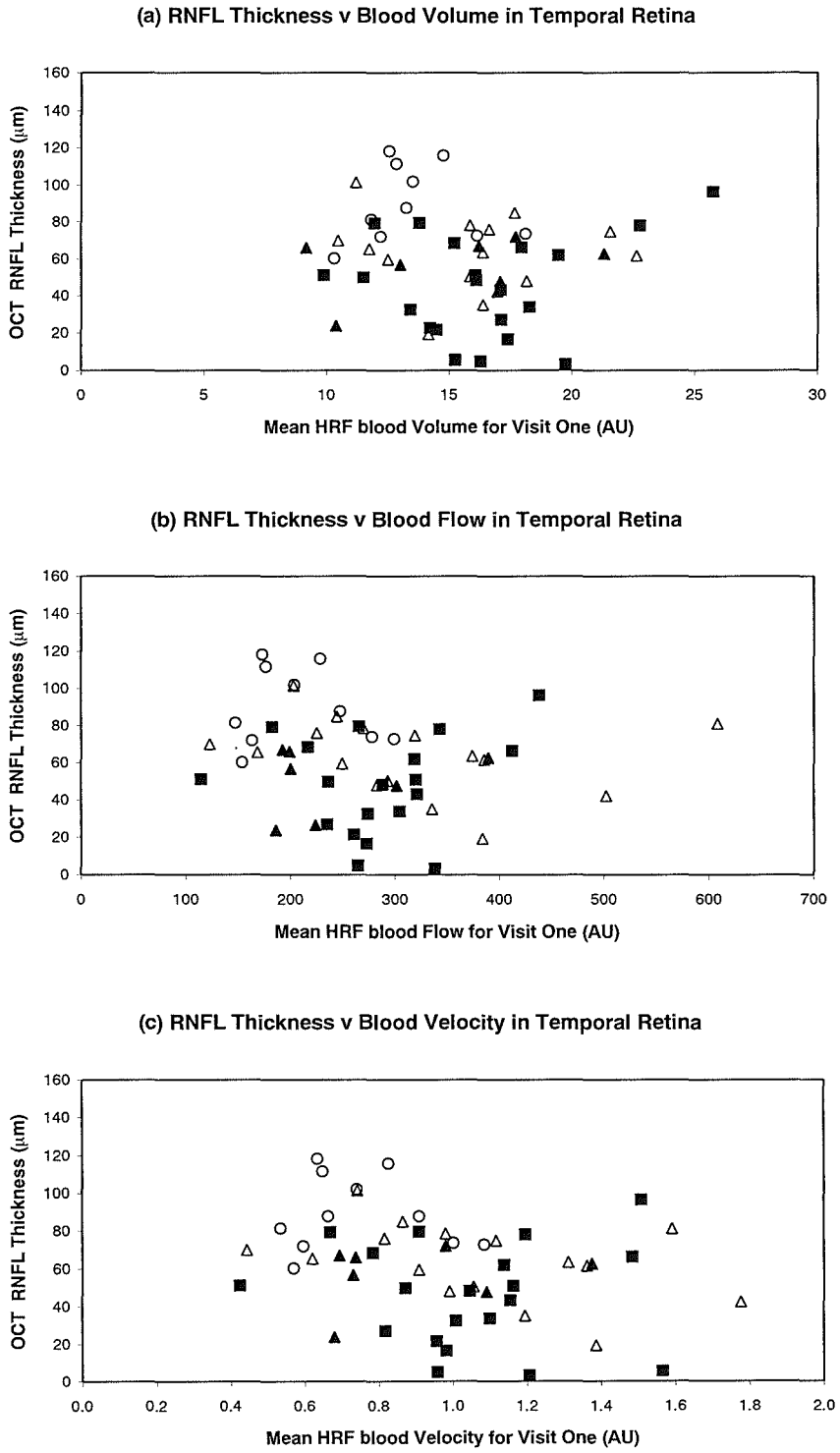

Figure 7.9. The mean Temporal retinal blood (a) volume, (b) flow and (c) velocity as a function of the mean Temporal OCT derived RNFL Thickness at Visit One, for the Normal group (open circles), for the OHT group (open triangles) and OHT(H) group (closed triangles) and for the POAG group (closed squares).

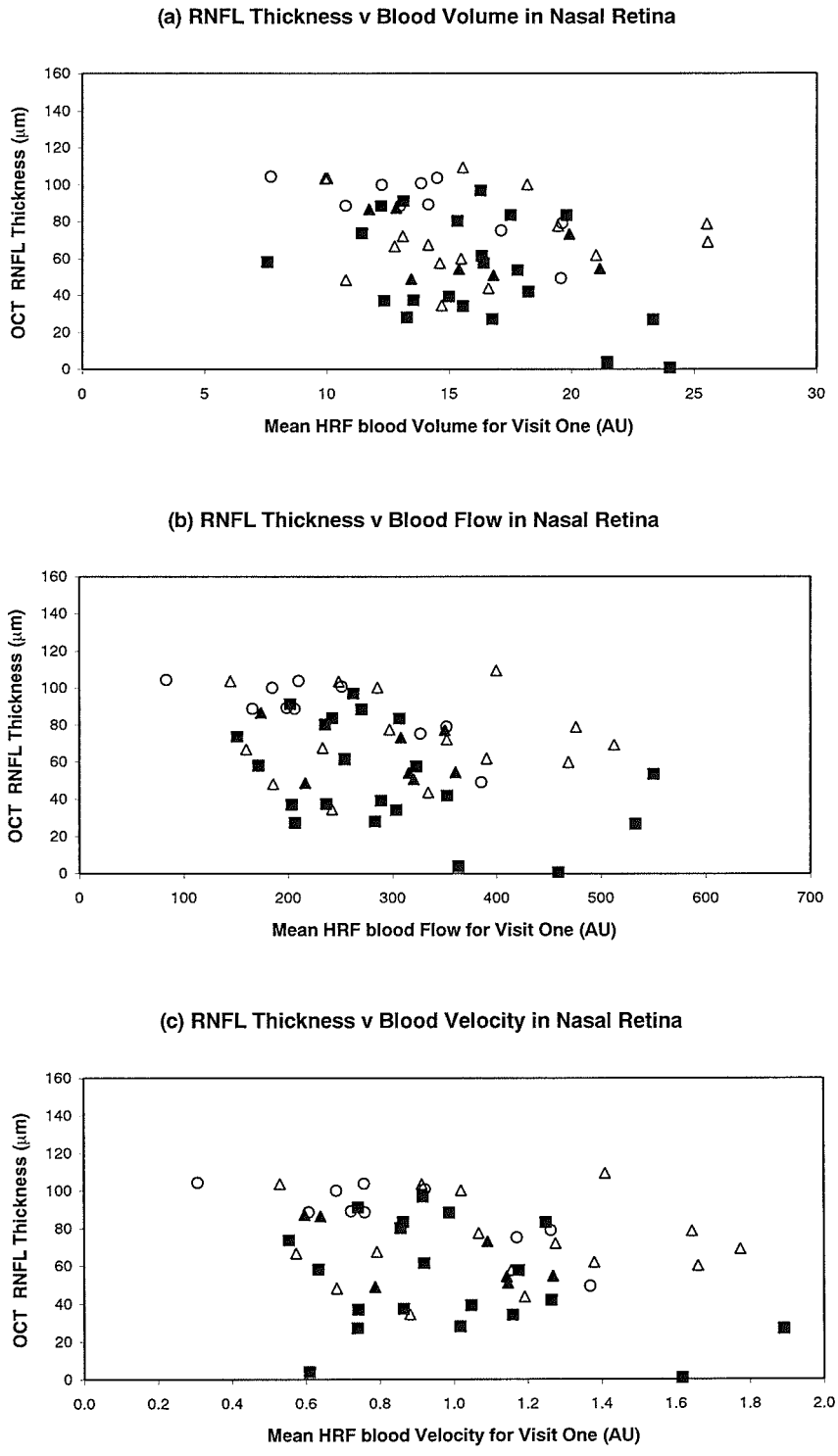

Figure 7.10. The mean Nasal retinal blood (a) volume, (b) flow and (c) velocity as a unction of the mean Nasal OCT derived RNFL Thickness at Visit One, for the Normal group (open circles), for the OHT group (open triangles) and OHT(H) group (closed triangles) and for the POAG group (closed squares).

(a) HRT mean RNFL Thickness v Blood Volume in Temporal Retina

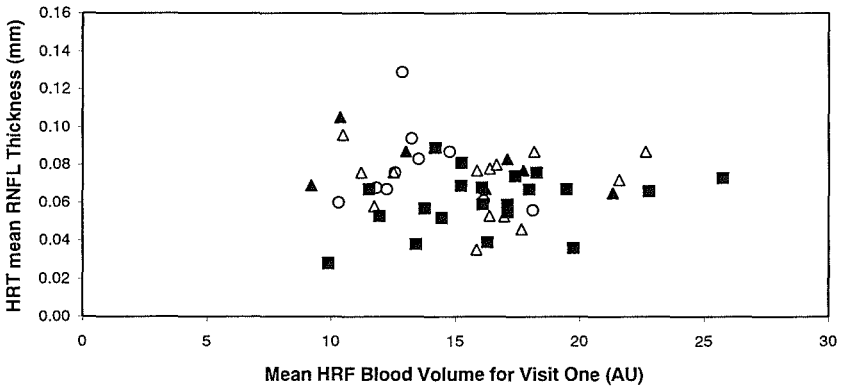

(b) HRT mean RNFL Thickness v Blood Flow in Temporal Retina

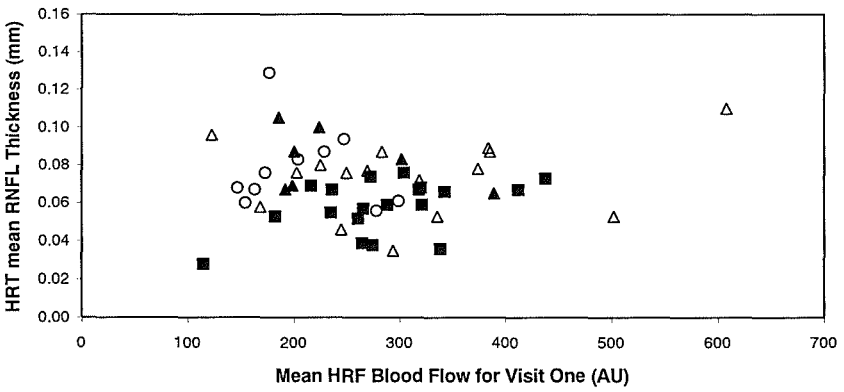

(c) HRT mean RNFL Thickness v Blood Velocity in Temporal Retina

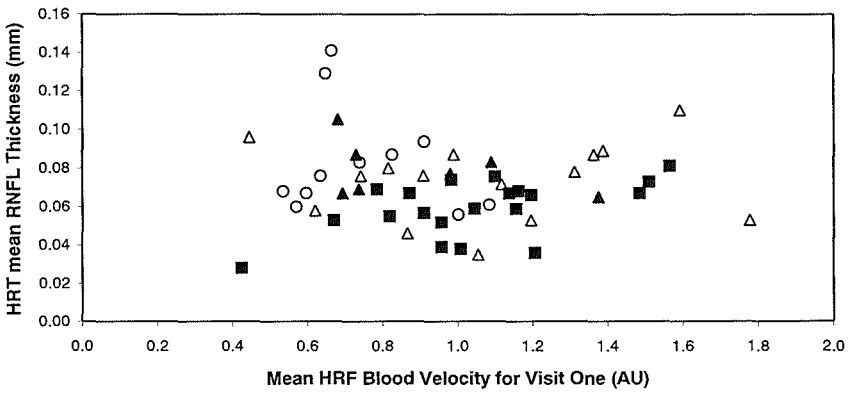

Figure 7.11. The mean Temporal retinal blood (a) volume, (b) flow and (c) velocity as a function of the Temporal HRT mean RNFL Thickness at Visit One, for the Normal group (open circles), for the OHT group (open triangles) and OHT(H) group (closed triangles) and for the POAG group (closed squares).

(a) HRT mean RNFL Thickness v Blood Volume in Nasal Retina

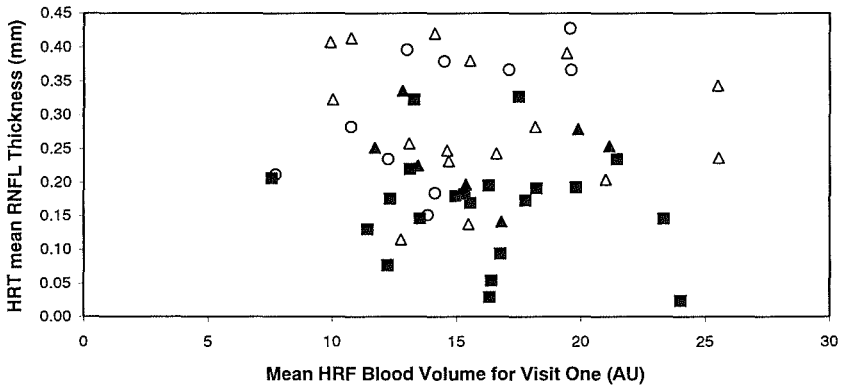

(b) HRT mean RNFL Thickness v Blood Flow in Nasal Retina

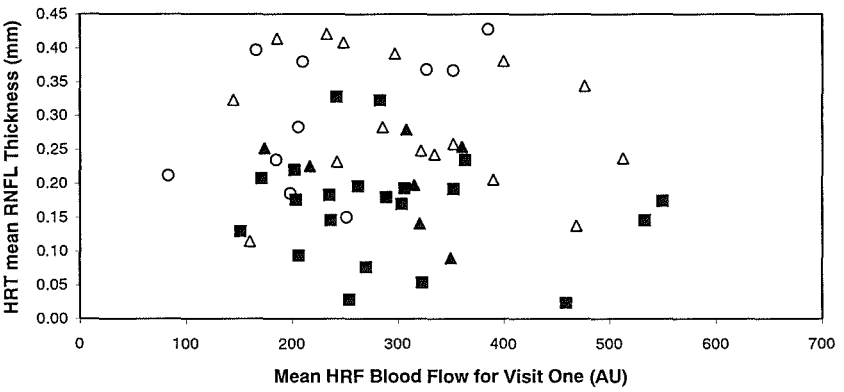

(c) HRT mean RNFL Thickness v Blood Velocity in Nasal Retina

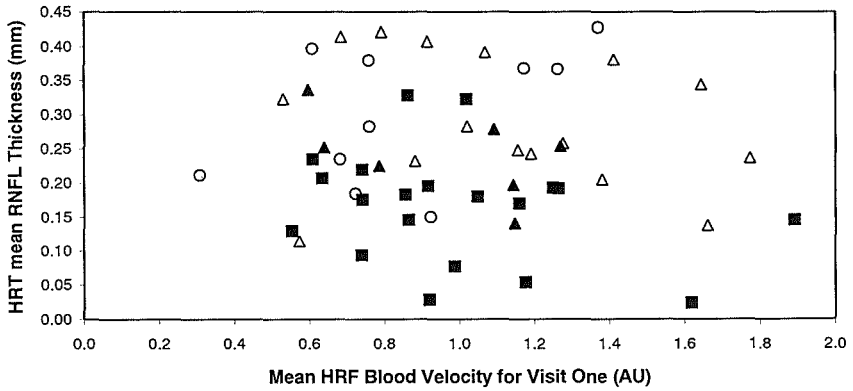

Figure 7.12. The mean Nasal retinal blood (a) volume, (b) flow and (c) velocity as a function of the Nasal HRT mean RNFL Thickness at Visit One, for the Normal group (open circles), for the OHT group (open triangles) and OHT(H) group (closed triangles) and for the POAG group (closed squares).

(a) HRT Rim-Disc Area Ratio v Blood Volume in Temporal Retina

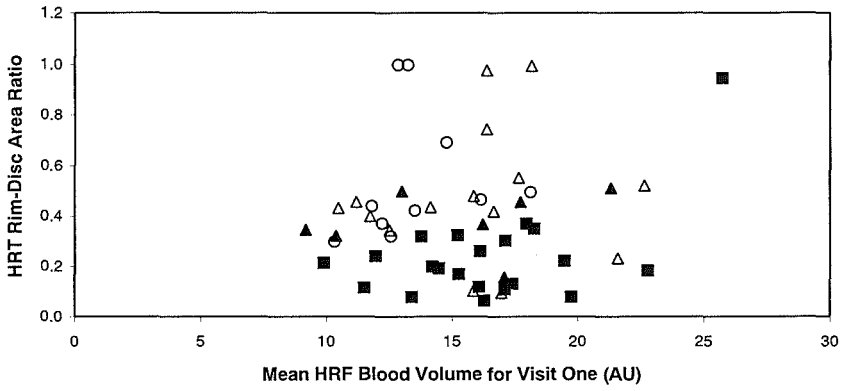

(b) HRT Rim-Disc Area Ratio v Blood Flow in Temporal Retina

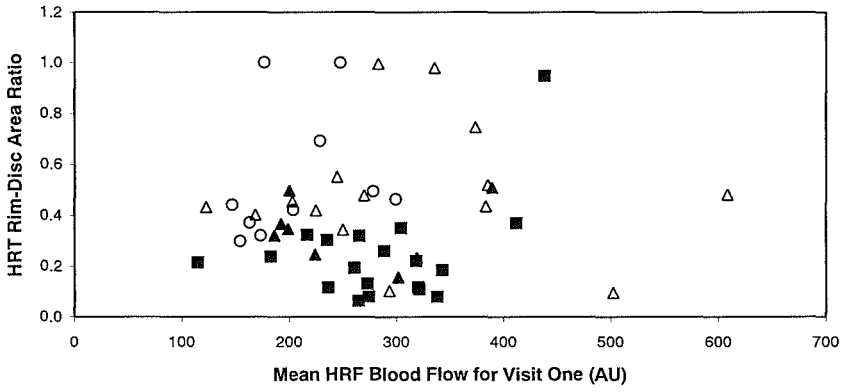

(c) HRT Rim-Disc Area Ratio v Blood Velocity in Temporal Retina

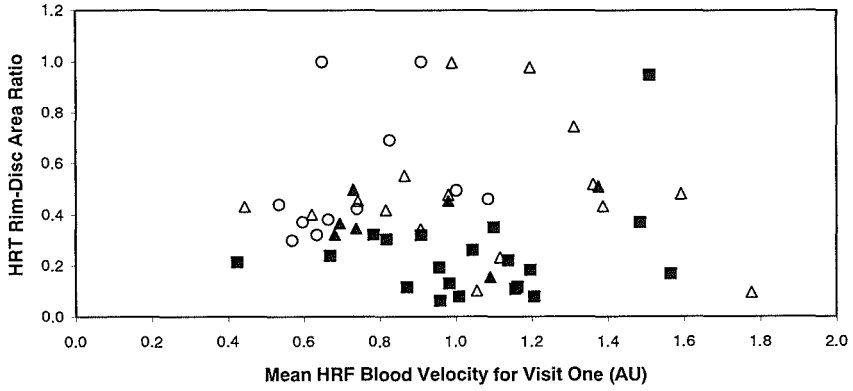

Figure 7.13. The mean Temporal retinal blood (a) volume, (b) flow and (c) velocity as a function of the Temporal HRT derived Rim-Disc Area Ratio at Visit One, for the Normal group (open circles), for the OHT group (open triangles) and OHT(H) group (closed triangles) and for the POAG group (closed squares).

(a) HRT Rim-Disc Area Ratio v Blood Volume in Nasal Retina

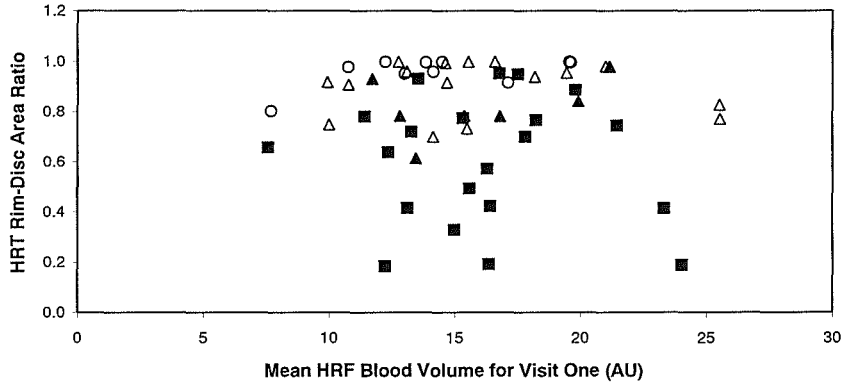

(b) HRT Rim-Disc Area Ratio v Blood Flow in Nasal Retina

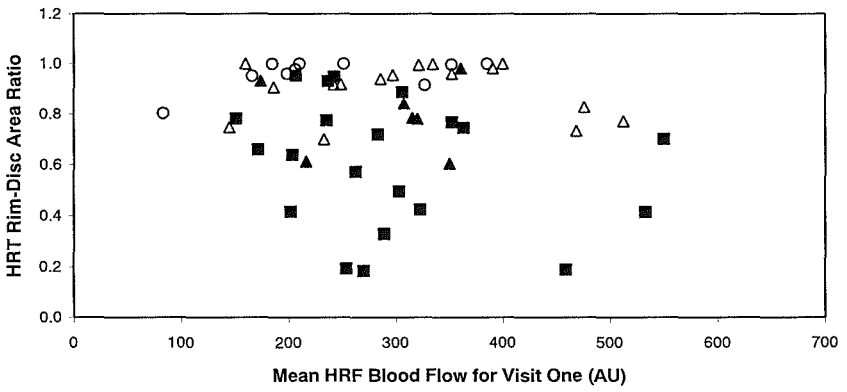

(c) HRT Rim-Disc Area Ratio v Blood Velocity in Nasal Retina

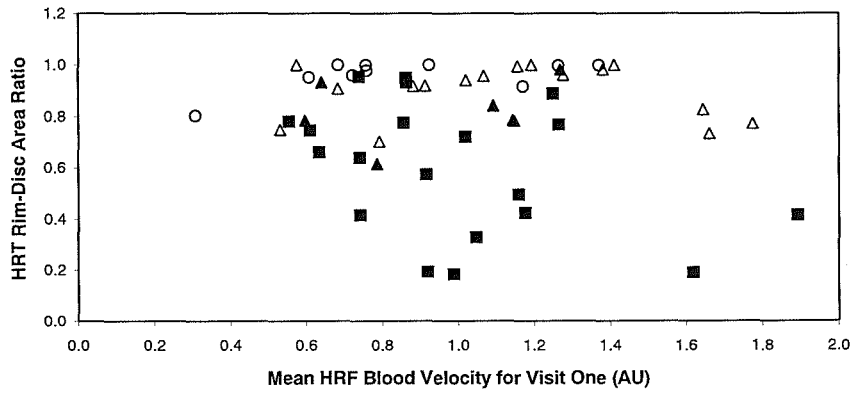

Figure 7.14. The mean Nasal retinal blood (a) volume, (b) flow and (c) velocity as a function of the Nasal HRT derived Rim-Disc Area Ratio at Visit One, for the Normal group (open circles), for the OHT group (open triangles) and OHT(H) group (closed triangles) and for the POAG group (closed squares).

(a) HRT Cup Shape Measure v Blood Volume in Temporal Retina

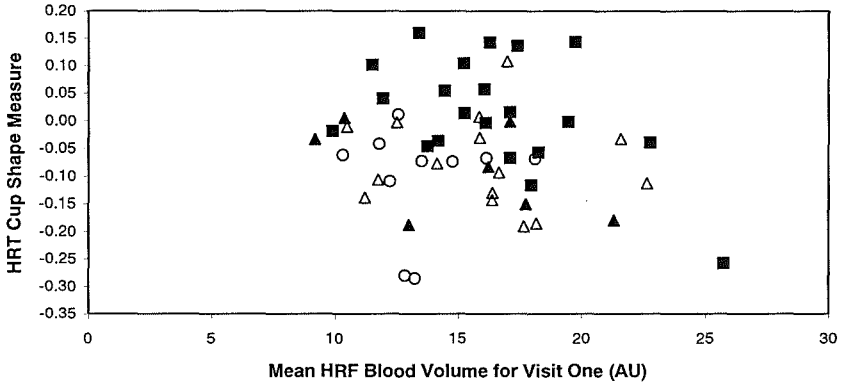

(b) HRT Cup Shape Measure v Blood Flow in Temporal Retina

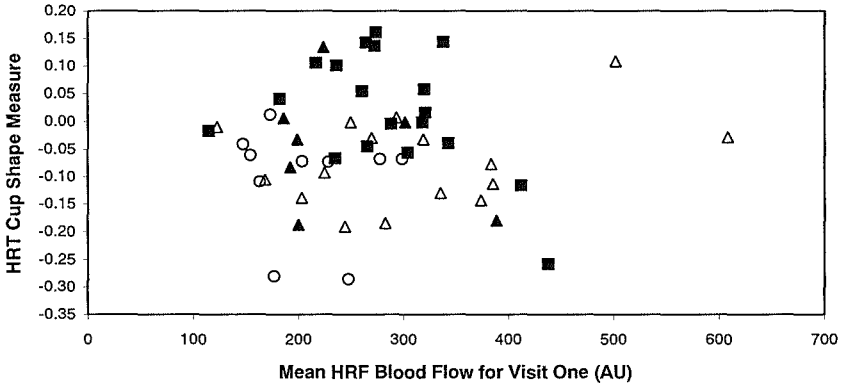

(c) HRT Cup Shape Measure v Blood Velocity in Temporal Retina

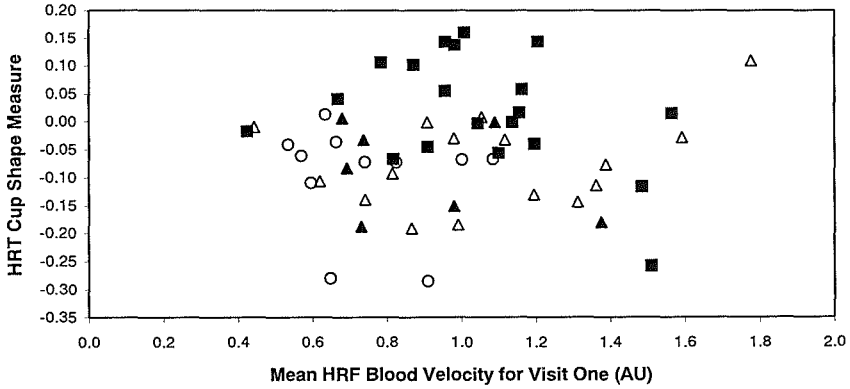

Figure 7.15. The mean Temporal retinal blood (a) volume, (b) flow and (c) velocity as a function of the Temporal HRT Cup Shape Measure at Visit One, for the Normal group (open circles), for the OHT group (open triangles) and OHT(H) group (closed triangles) and for the POAG group (closed squares).

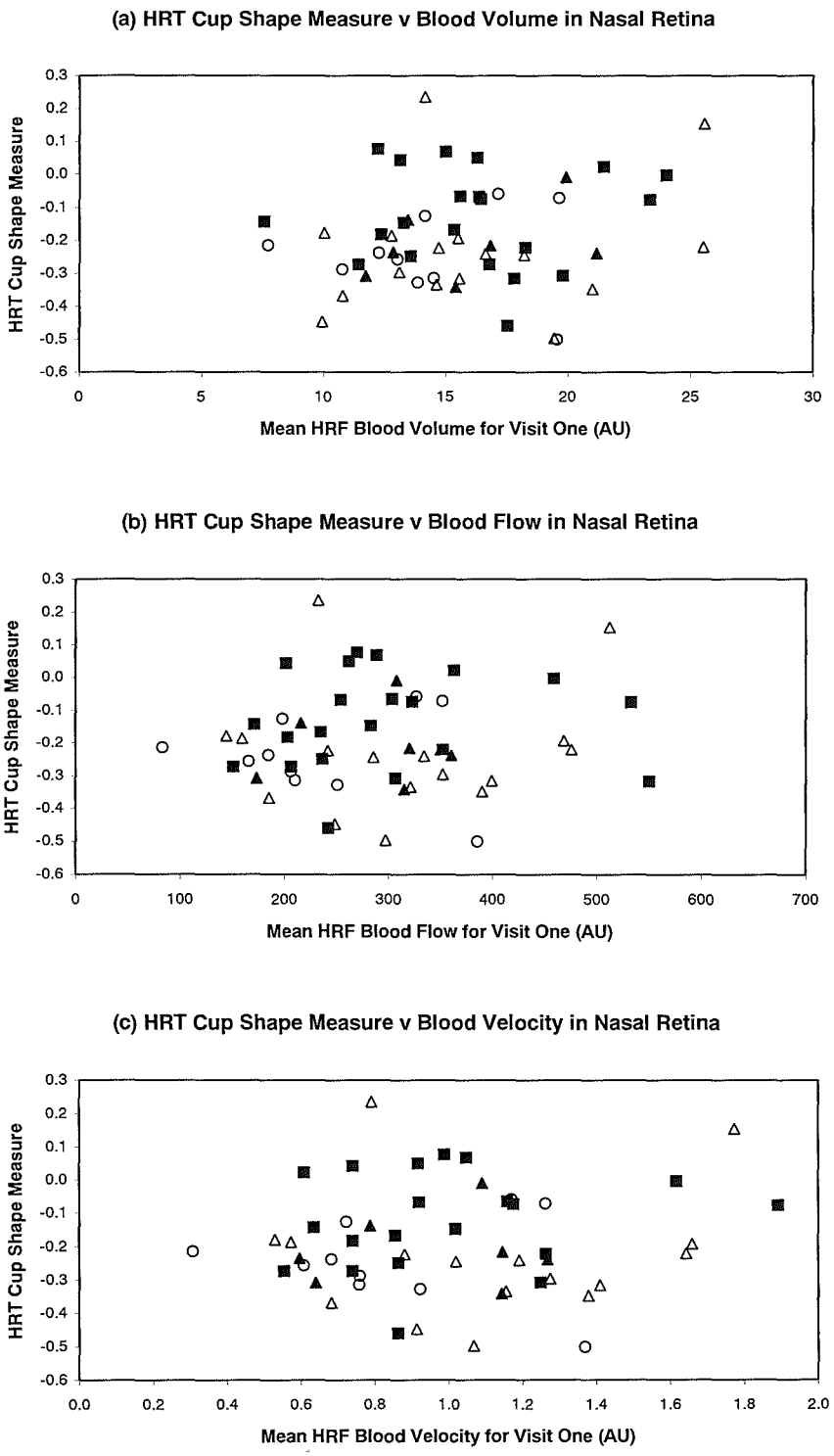

Figure 7.16. The mean Nasal retinal blood (a) volume, (b) flow and (c) velocity as a function of the Nasal HRT Cup Shape Measure at Visit One, for the Normal group (open circles), for the OHT group (open triangles) and OHT(H) group (closed triangles) and for the POAG group (closed squares).

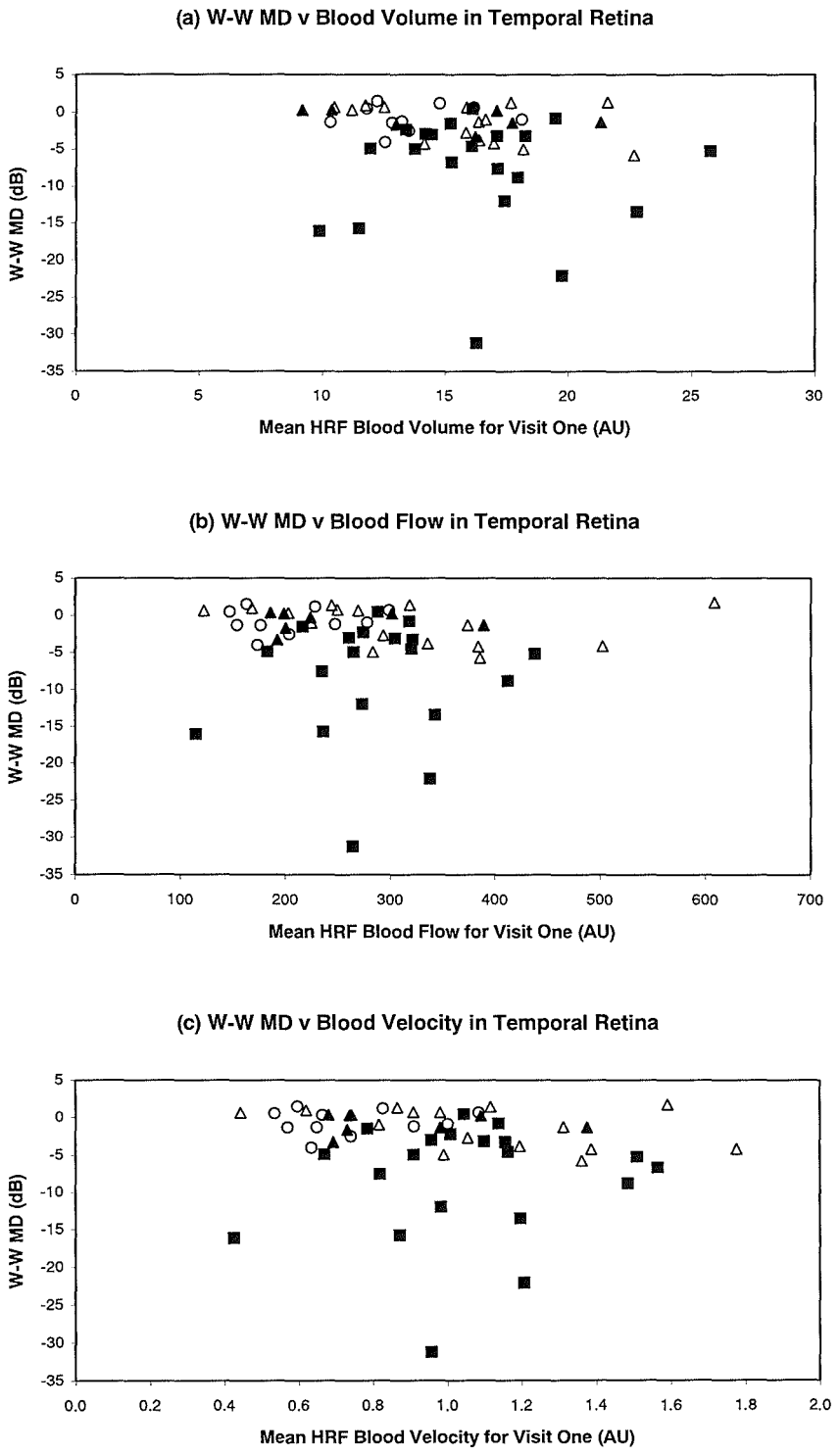

Figure 7.17. The mean Temporal retinal blood (a) volume, (b) flow and (c) velocity as a function of the W-W MD (dB) at Visit One, for the Normal group (open circles), for the OHT group (open triangles) and OHT(H) group (closed triangles) and for the POAG group (closed squares).

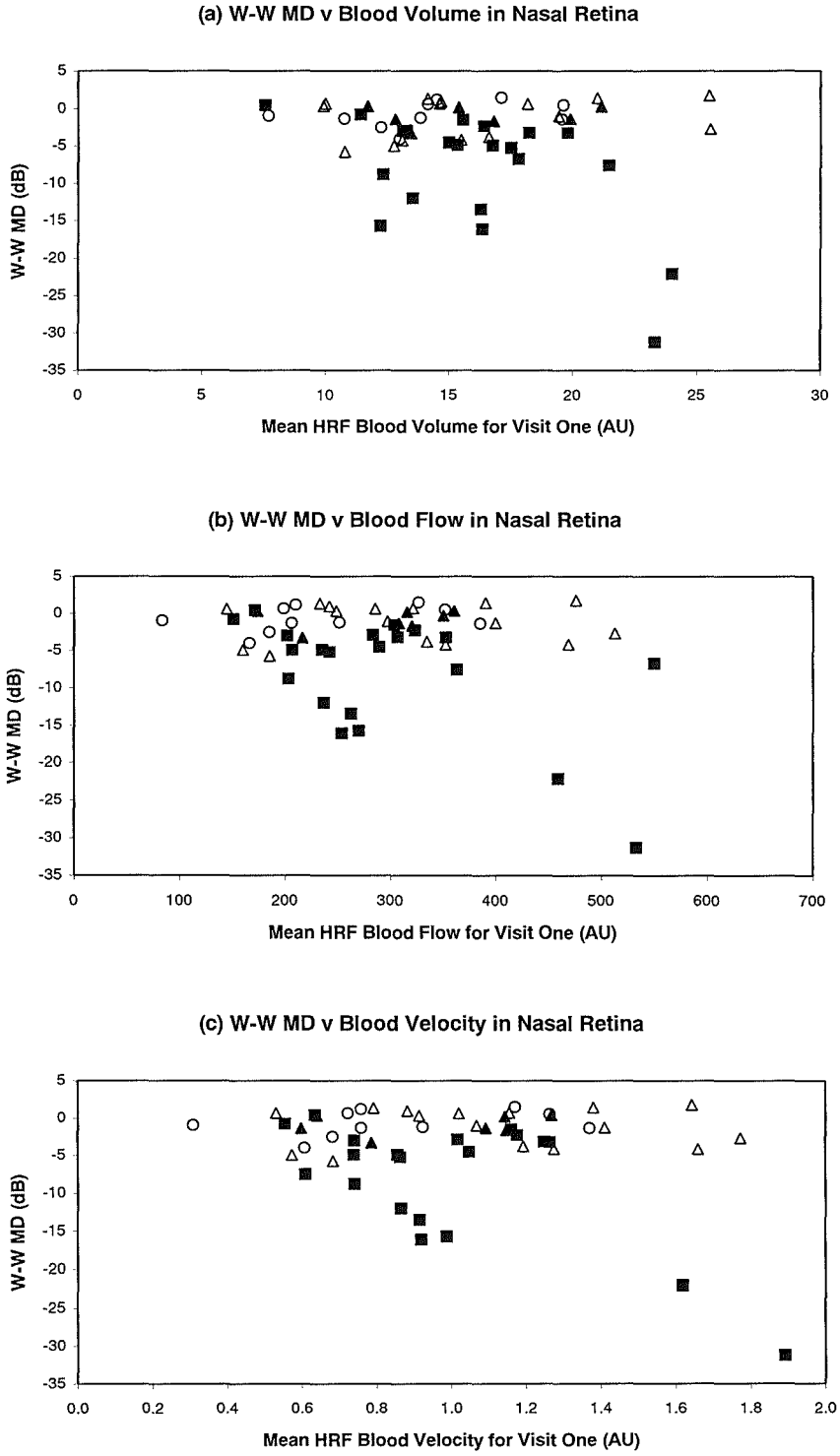

Figure 7.18. The mean Nasal retinal blood (a) volume, (b) flow and (c) velocity as a function of the W-W MD (dB) at Visit One, for the Normal group (open circles), for the OHT group (open triangles) and OHT(H) group (closed triangles) and for the POAG group (closed squares).

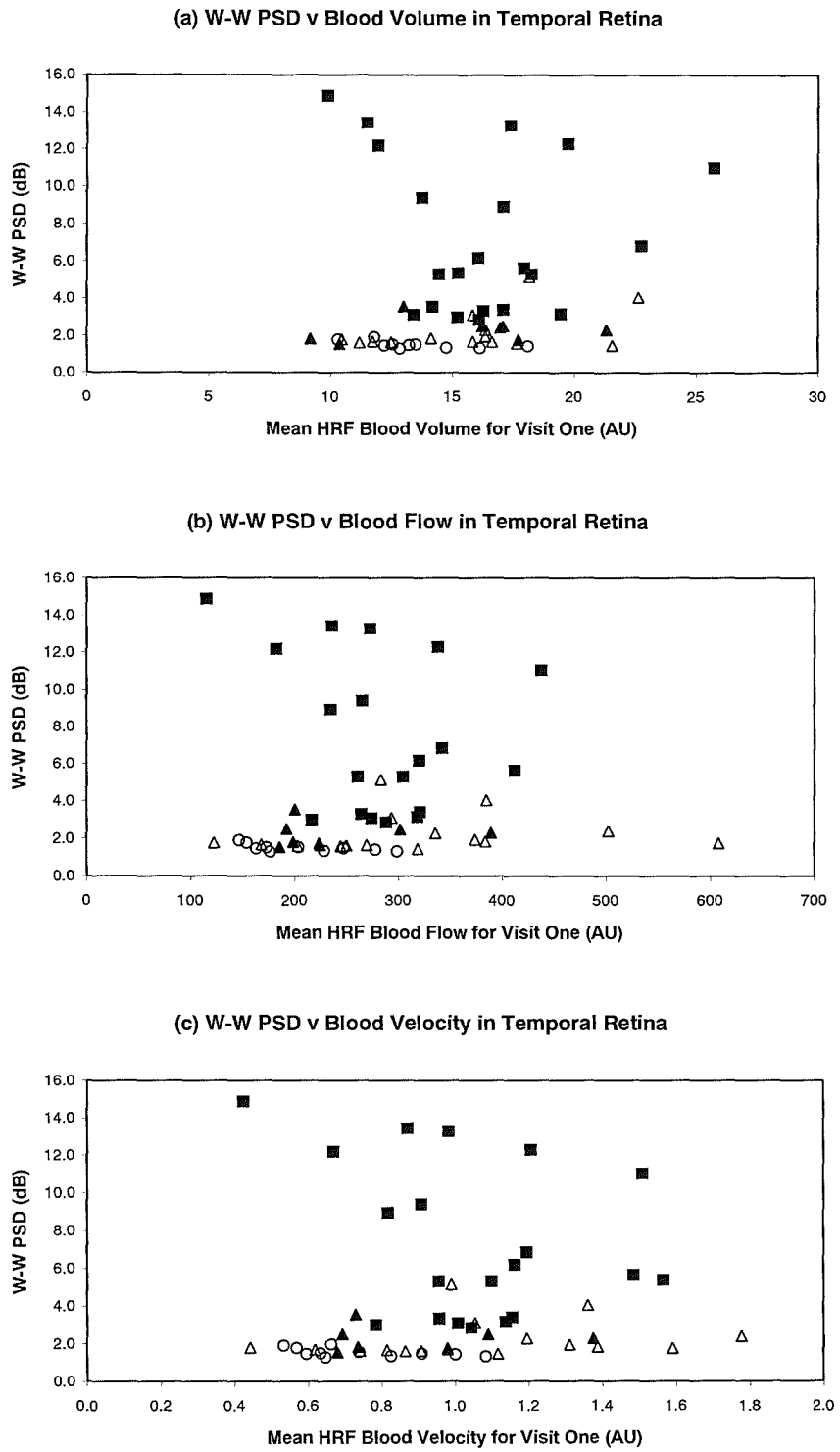

Figure 7.19. The mean Temporal retinal blood (a) volume, (b) flow and (c) velocity as a function of the W-W PSD (dB) at Visit One, for the Normal group (open circles), for the OHT group (open triangles) and OHT(H) group (closed triangles) and for the POAG group (closed squares).

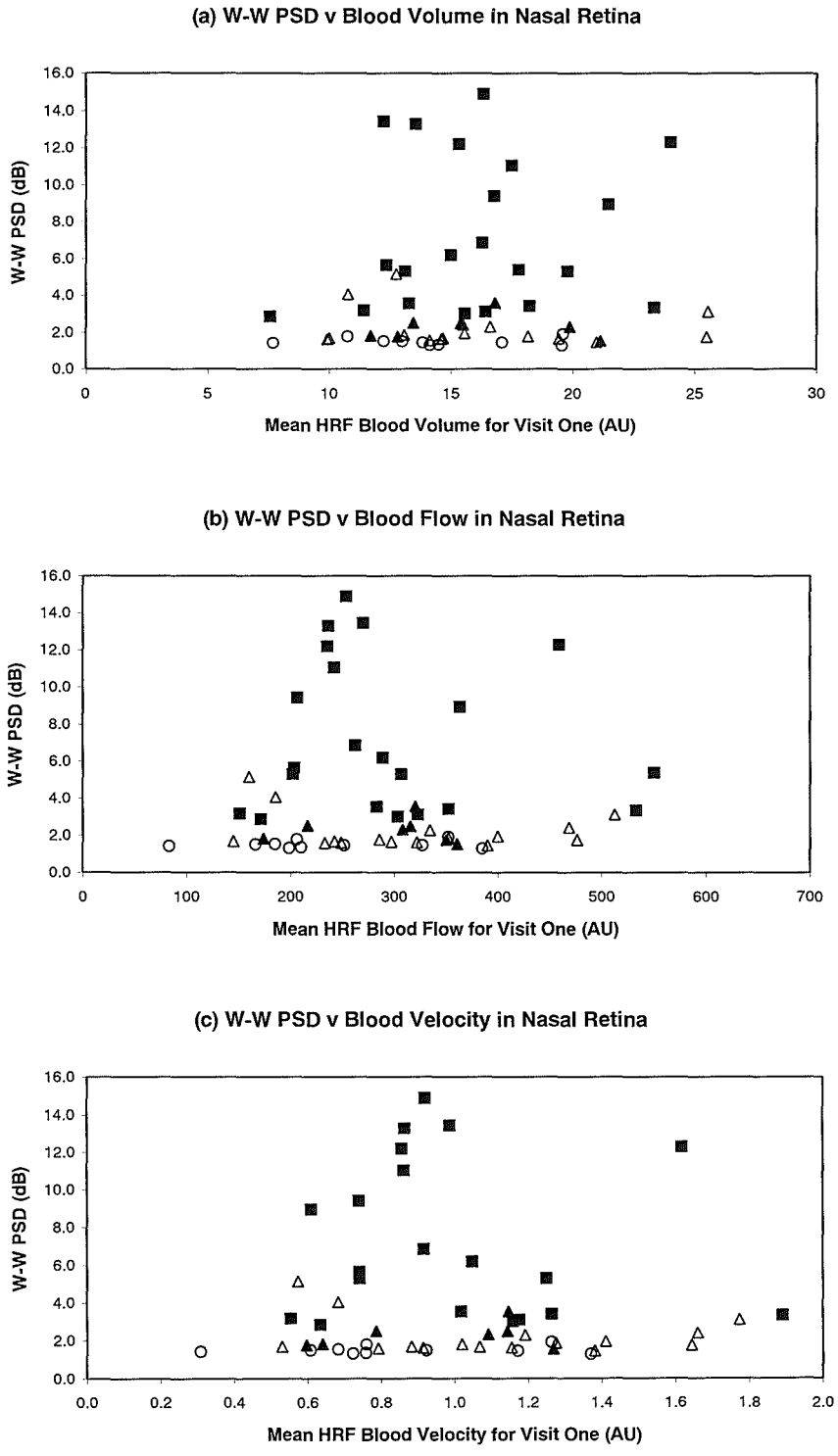

Figure 7.20. The mean Nasal retinal blood (a) volume, (b) flow and (c) velocity as a function of the W-W PSD (dB) at Visit One, for the Normal group (open circles), for the OHT group (open triangles) and OHT(H) group (closed triangles) and for the POAG group (closed squares).

7.11 Discussion.

The group mean CoV for each region was similar for flow, volume and velocity. The findings are in agreement with Michelson and Schmauss (1995) who reported the within-visit reliability coefficient values using the HRF in normal individuals to be similar for each of the parameters. The measure of CoV for each parameter, in each region, for the study is approximately 2-3 times greater than those reported by Kageman and associates (1998). The differences in magnitudes between the two studies may be attributable to the younger age of the sample employed by Kageman et al (1998) with the inherent better subject fixation characteristics.

The measurements of blood flow, velocity and volume were least variable for the Normal group followed by the POAG group, and most variable for the OHT group. The within-visit variability for the three parameters varied between regions for the Normal group, and was least in the inferior temporal retina. The variability for the OHT and POAG groups was similar between regions (Volume, CoV 16%-22%; Flow, CoV 21%-29%; Velocity, CoV 20%-27%). Hollo et al (1997b) found the variability for the temporal and nasal retina to be lower for POAGs (Temporal, CoV=12%; Nasal, CoV=12%) than for normals (Temporal, CoV=19%; Nasal, CoV=26%).

Capillary blood flow is pulsatile. Assuming the average pulse rate to be 75 beats per minute and that the acquisition of an HRF image takes approximately 2 seconds, HRF measurements will vary according to the point in the cardiac cycle at which they were acquired. Depending upon the phase of the cardiac cycle during which sequential HRF images are acquired, the retinal perfusion measurements can vary by as much as 50% (Sullivan et al. 1999). The retinal blood flow is proportional to the perfusion pressure which, in turn, is dependent upon a number of factors that include, IOP, mean arterial blood pressure, and pulse rate. These factors are in turn affected by topical and systemic medication. The OHT group had a higher group mean IOP than either the Normal or the POAG groups, and approximately 65% of the OHT group were on topical anti-glaucoma medication. None of the Normal group and more than 80% of the POAG group were on topical medication. The capillary blood flow may have been more erratic for the OHT group, as a whole, than for either of the other groups because of the within- and between-group differences in medication.

The retinal illuminance during the acquisition process is dependent upon differences in scan brightness. A measure of the retinal illuminance is provided by the output received at the photodiode detector and is expressed as the DC value for each pixel in the perfusion maps. Early recommendations for the use of the HRF advocated that over-exposure and the presence of 'white' bleached out pixels should be avoided to ensure that the reflected light received by the photodetector was analysed appropriately. The advice was adhered to for the study. The level of illumination can influence the values obtained for the blood flow (Embleton et al. 1999; Kagemann et al. 1999; Tsang et al. 1999) and related measurements. Variations in the retinal illuminance can lead to errors in the measured parameters. The intensity distribution of the pixel

brightness across an image is used to determine the estimated noise within a scanned area (Michelson et al. 1996b). An index of 'noise' is derived from a regression equation for the estimated noise as a function of the intensity of brightness at each pixel. The noise index changes for each image, and the power spectrum prior to the generation of the perfusion maps is corrected for image brightness by subtracting the noise index. Bright images are assumed to have more noise and the entire image is corrected for the overall brightness. The flow and volume are weighted according to the intensity of the images, which leads to higher flow readings for dark areas and lower values for bright areas. In addition, variations in the local and global brightness give rise to variations in the 'offset' of the y-axis for the relationship between the HRF measured velocities and the true values (Tsang et al. 1999). A change in the offset contributes to errors in HRF measurements between pixels both within- and between-images for a single individual and for within- and between-images, between-individuals. The areas of interest in repeated images in the study were aligned and both the control panel sensitivity settings, and retinal illuminance were monitored to minimise errors due to the variation in change of image content and illumination. However, variations in retinal illuminance between-individuals due to different levels of retinal pigmentation could not be avoided.

The neuroretinal rim haemodynamic data collected was not evaluated in the study as the rim areas exhibited markedly lower levels of brightness compared to the retina. The HRF parameters for the retinal and rim regions when corrected for image brightness were unlikely, therefore, to be directly comparable. Indeed, an increased variation has been found for the temporal neuroretinal rim (Bohdanecka et al. 1998) along with higher blood flow rates at the optic nerve head than in the surrounding retina (Groh et al. 1996).

The magnitude of the measurements for each region and parameter were independent of the number of images obtained. Most reports fail to indicate the number of images scanned unless they are specifically evaluating the reproducibility coefficient (Bohdanecka et al. 1998). It is assumed, therefore, that only single images have generally been used, and the variability in the measurements quoted in other studies is merely that for adjacent pixel or window measurements.

The range of the between-visit variation for each parameter, in each region was similar to the range of the within-visit variation. The variation differed between each blood flow parameter. The between- and within-visit variation was greatest for the parameter flow The increased between-visit variation compared to the within-visit variation has also been reported by Kageman et al (1998). They found an average, within-visit CoV for volume, velocity, and flow of 9.6%, 6.5% and 6.6% respectively, whilst the between-visit CoV for flow measurements of the peripapillary retinal tissue increased to approximately 30%.

The results also suggested that the between-visit variation was greatest for the OHT group and was generally lowest for the Normal group. Nicolela et al (1997), however, found the perfusion measurements to be more reproducible for those with glaucoma than for normal individuals.

Pixel-by-pixel analysis of the entire image results in reduced between-visit variability (Kagemann et al. 1998). Full-field analysis can exclude pixel data influenced by neighbouring large vessels, saccades, poorly exposed pixels, and can be corrected for cardiac pulsation. It also results in improved between-observer variability (Michelson et al. 1998b). Analysis of full-field data also reveals regional retinal differences in the vascular response to hyperoxia and hypercapnia (Chung et al. 1999a). The use of full-field analysis has been strongly advocated (Kagemann et al. 1998; Michelson et al. 1998b) although the software to undertake this type of analysis is not included in the current software version.

The blood flow, velocity and volume were each independent of age for each of the peripapillary retinal areas studied. The findings are in contrast to the reduction in flow and velocity with increasing age found for the ONH (Rizzo et al. 1991; Cranstoun et al. 1994), and for the peripapillary retina (Groh et al. 1996). The lack of an age-dependency in the study can be attributed to the wide between-individual variation across all three groups. The age-related variation may be too small compared to the measurement error present in the study.

The group mean blood volume, velocity and flow tended to be lowest for the Normal group, followed by the POAG group and highest for the OHT group across each of the peripapillary retinal regions, although the difference was not statistically significant. Considerable overlap was present in the measures of blood flow, velocity and volume, between each of the retinal regions, across the three diagnostic groups.

A reduction in retinal blood flow in the POAG group had been expected since Quigley et al (1984) have reported that the number of retinal capillaries decreases with increasing loss of neuronal tissue. Previous studies of peripapillary retinal and optic disc flow in glaucoma have found conflicting results, with some authors finding reduced flow in POAG (Michelson et al. 1996a; Nicolela et al. 1996b), whilst others have found similar levels of perfusion between POAG and NTG patients and normal individuals (Hollo 1997; Hollo et al. 1997a; Hollo et al. 1997b).

Michelson et al (1996a), found significantly decreased capillary blood flow for the temporal and nasal retina and temporal neural rim in glaucomatous individuals compared to normals. In contrast, Nicolela and colleagues (1996b) found no statistically significant difference in the blood volume, velocity and flow for the superior, inferior, inferior temporal retina or the temporal neural rim between normal and patients with POAG. They did find reduced parameters for the superior temporal retina and at the lamina cribrosa in POAG compared to normals. Similarly, Kerr et al (1998), found no statistically significant difference in blood volume, velocity, or flow

between untreated primary open-angle glaucoma patients compared to a group of ocular hypertensives for the nasal retina. They did, however, find an increased velocity in the temporal retina and a reduced neuroretinal rim circulation for the POAG group. Similarly, (Chung et al. 1999b) found no difference in the temporal and nasal peripapillary retinal blood flow between normal individuals and patients with normal–tension glaucoma (NTG) using the 10 x 10 pixel box. However, reduced capillary perfusion of the peripapillary retina was detected in the NTG group by employing full-field analysis evaluation. This suggests that the use of a 'default' 10 x 10 pixel box is not necessarily the most appropriate method to measure the blood flow data. The conflicting results reported may arise in part from the variability associated with the 10 x 10 pixel box.

The depth in the retinal tissue at which the Doppler shifts are being measured is unclear. It is assumed that a high absorption by the retinal pigment epithelium prevents the choroidal vasculature from being measured (Michelson and Schmauss 1995). In areas of retinal thinning, for example in the peripapillary regions of myopes with parapapillary atrophy and in glaucoma patients, the measuring laser beam can theoretically penetrate through to the choroid allowing the deep vascular beds to contribute to the Doppler signal (Hollo et al. 1997a). The resultant blood volume, velocity and flow measurements could therefore be erroneously high. The normal or relatively high readings obtained for blood flow in patients with POAG may represent not only the retinal capillary perfusion but may also include contributions from the choroidal circulation.

Ocular blood flow can alter in response to IOP (Schwartz and Kern 1980; Michelson and Schmauss 1995) and age change (Williamson et al. 1995; Groh et al. 1996), and this might account for small, but non-significant differences noted between the normal and OHT groups in the study. Most of the OHT and POAG patients were using topical anti-glaucoma medication, some of which were likely to have had effects upon the ocular circulation. The topical medication for IOP control in the OHT and POAG group was not altered during the course of the study. However, no washout period for any drug in any patient was proposed, or sought through ethical approval, and the lack of homogeneity in the types of medication used confounds the analysis.

The lack of a statistically significant difference in any of the blood flow parameters between the groups could be attributable to the heterogeneity of the groups. Comparisons of blood flow between low-risk and high-risk ocular hypertensives and between low-tension- and high-tension glaucoma individuals could not be undertaken as the sample sizes were too small. Data collection was unexpectedly postponed and a decision was subsequently taken to abandon further recruitment following an investigation into the safety of the particular HRF instrument employed for the study. The sample size of the Normal group was particularly affected by this decision.

The haemodynamic parameters measured with the HRF are known to vary with retinal location, particularly in those regions adjacent to major blood vessels (Nicolela et al. 1997) Kerr (1998), and these areas were specifically avoided in the study.

7.12 Conclusions.

The results of the present study have shown that the within-visit variability for the commercial HRF instrument for each of the haemodynamic parameters is least for the Normal group (mean CoV approximately 11%-24% for Volume, 18%-29% for Flow, and 17%-26% for Velocity), across each of the retinal regions, but particularly the inferior temporal region.

The haemodynamic parameters did not vary statistically between visits for the regions, across each of the diagnostic groups. However, the limits of agreement between the visits for each of the haemodynamic parameters varied between the regions across the groups. They were generally widest for the OHT group.

The technique used in the study to acquire and analyse HRF derived measurements of retinal haemodynamics did not discriminate for the parapapillary retina between Normal individuals and those with ocular hypertension or with primary open-angle glaucoma. The clinical implication of these findings is that the commercial HRF instrument using the 10 x 10 pixel sample box for perfusion map analysis of the parapapillary retina is unable to demonstrate a difference in retinal haemodynamics between the normal and the glaucomatous eye.

PAGE

NUMBERING

AS ORIGINAL

CHAPTER 8. SUMMARY OF RESULTS, CONCLUSIONS AND PROPOSALS FOR FUTURE WORK.

8.1 Summary of Results and Conclusions.

8.1.1 Determination of the within- and between-test variability for tomographical descriptors of the optic nerve head as derived by the Heidelberg Retina Tomograph (HRT) for both global and sector analysis, with particular emphasis on those measures that reflect the retinal nerve fibre layer integrity, correcting for age and disc area across three diagnostic groups.

The within-and between-visit variability both for global and sector stereometric data was similar, or slightly better, with the HRT software version 2.01 compared to earlier versions, using the imported contour line from a mean topography image, provided that the published recommended quality control procedures were adhered to during the acquisition of the images.

The magnitude of each of the stereometric parameters was independent of age; however, most were dependent upon disc area. It is recommended, therefore, that disc area should always be taken into consideration when assessing the variation, between individuals, of parameters that describe the ONH configuration.

8.1.2 Determination of the within- and between-visit variability for pointwise and global measures of sensitivity for a frequency doubling stimulus using Frequency Doubling Technology (FDT), across three diagnostic groups, and their comparison with the corresponding variability in conventional white-on-white perimetry (W-W) and short-wavelength automated perimetry (SWAP).

The ideal stimuli for automated perimetry provide reliable, reproducible measures of visual function with the least examination time, minimal learning effect, and the provision of high levels of sensitivity and specificity for detecting deficits.

The considerably shorter examination duration for FDT perimetry compared to W-W perimetry and SWAP, and the minimal variation in the Global indices between visits, across all diagnostic groups, suggests that fatigue and learning effects are likely to be less. The between-visit variability in the global indices, MD and PSD was similar between each type of perimetry.

The within-visit variability for TD and PD across the visual field was least for W-W perimetry, and lower in the Normal group than in the OHT group. The within-visit variation in Group mean

TD and PD across the visual field was similar between FDT and W-W perimetry. As expected, the within-visit variation across the visual field was greatest for SWAP.

The between-visit variability in TD and PD at the individual stimulus locations was generally least for W-W perimetry, but increased more with increasing defect depth for W-W perimetry compared to either FDT perimetry or SWAP.

The within-visit Global indices were more positive with FDT than either SWAP or W-W perimetry. Whether this is a consequence of the HFA-equivalent scale employed for FDT perimetry remains to be clarified. The use of a decibel scale, by definition, implies that the relationship is relative and caution should be exercised when interpreting these results.

8.1.3 Determination of the within- and between-visit variability for optical coherence tomography of the retinal nerve fibre layer thickness as determined by the Humphrey Systems Optical Coherence Tomography Scanner (OCT), for both global and sector analysis, as a function of the type and number of circular scans.

In order to recognise progressive loss of axonal tissue, imaging techniques for the measurement of the RNFL thickness require a level of reproducibility that is better than the anticipated degree of change that is attributable to tissue loss. For axonal loss to be attributed to glaucoma or other pathological process, the axonal thinning has to exceed the within- and between-subject variability associated with the measurement procedure.

RNFL thickness measurements with a maximum resolution of approximately 6-7μm were achieved using the commercially available OCT instrument. A reduction in thickness of at least 14μm will be required in the normal RNFL thickness and a difference of at least 20-27μm in RNFL thickness for those with known early damage before progressive damage can be identified. The increased variability associated with a decrease in RNFL thickness limits the application of the technique to the monitoring of early and moderate stages of RNFL atrophy. The reduction in RNFL thickness with age exhibited a regional variation, being more apparent in the temporal and superior parapapillary regions. Global RNFL thickness decreased with an increase in distance from the disc margin. Despite some overlap of the global RNFL thickness values between the diagnostic groups, the mean RNFL thickness was markedly thinner in the OHT and POAG groups. The magnitude of the RNFL thickness measurements was independent of the number of scans.

The commercial OCT instrument may well be useful in monitoring longitudinal changes in the RNFL thickness in the absence of a direct measurement of the RNFL.

The relationship between the RNFL thickness and the global indices for both W-W and FDT perimetry was non-linear. Visual field defects became manifest only when the RNFL thickness had reduced below a certain value, which due to a normal between–individual variation in RNFL thickness could be difficult to predict. The RNFL thickness was found to be associated with the variations in five Global HRT sterometric parameters: RNFL thickness, CSM, CA, RDAR, CDAR. The relationship between the Sector Oct and HRT RNFL thickness was weaker than for the Global measure. For the remaining stereometric parameters, the association was strongest for the superior and inferior sectors and negligible for the nasal sector. Sector RNFL thickness validation using the current imaging techniques could be limited.

8.1.4 Determination of the within- and between-visit, and the within- and between-individual variability in parapapillary retinal haemodynamics determined by scanning laser doppler flowmetry using the Heidelberg Retina Flowmeter (HRF).

The Group mean within- and between-visit variability for the three HRF parameters velocity, flow and volume was similar across the six parapapillary regions, and was least for the Normal group. The haemodynamic parameters were independent of visit, age, number of scans, region or diagnostic group.

No relationship was present between the haemodynamic parameters and either the functional integrity derived by the various visual field techniques, or the structural integrity of the ONH and RNFL integrity derived either by the HRT or the OCT.

8.2 Proposals for Future work.

8.2.1 The determination of HRT parameters associated with congenital ocular anomalies.

The optic disc size should be taken into account when evaluating optic disc topography, particularly in glaucoma. The measurement of ONH topography using HRT in cases of abnormally large, small or tilted discs, and the consequent effect upon the reference plane height determination has not been investigated. Whilst it may not be easy to recruit a large sample size of suitable individuals that exhibit such conditions, documenting the topography could provide further information concerning the morphological nature. In addition, the height of the retinal surface within each pixel is determined by the location of maximum reflectance for each scan profile. This is generally assumed to be at the ILM, however retinal abnormalities, such as myelinated nerve fibres may give rise to a high reflectance signal and might introduce an error in the surface height location. Investigation of the reflectance pattern in areas of enhanced myelination and the subsequent determination of reference plane height would be of interest.

8.2.2 The within- and between-visit variability of regional RNFL thickness using OCT with increased sampling density and resolution.

The sector analysis used for the OCT consisted of four regions with a spatial sampling density of 25 A-scans per sector. The existing data can be further analysed in terms of 12 'clock-hour' segments to provide information about regional variation of the RNFL thickness, however, the sampling density is reduced to approximately 9 'A-scans' per segment. The latest OCT software allows arc scans to be performed that have an increased sampling density of 100 A-scans per 90°. However, whilst an increase in sampling density could theoretically increase the transverse resolution it is likely to be at the expense of scan time and errors arising from eye movement. The within-and between-visit variability for the different sampling densities requires evaluation.

8.2.3 The longitudinal evaluation of regional RNFL thickness using OCT in healthy eyes, in ocular hypertensives and in glaucomatous eyes.

Cross-sectional data indicates an age-related decline in the RNFL thickness both globally and with a regional variation. The between-individual variation in RNFL thickness can influence the estimate of the decrease in RNFL thickness with increase in age, and glaucoma further confounds the estimation. Follow-up studies on the existing individuals over a 5, 10 and 15 year period could provide information on the age-related decline in RNFL thickness, the development of RNFL thinning in those currently diagnosed with ocular hypertension who subsequently develop glaucoma, and any progressive RNFL thinning in those with glaucoma.

8.2.4 The evaluation of RNFL thickness variation associated with congenital ocular anomalies using OCT.

The RNFL thickness can be qualitatively documented by OCT. Variations in the number, distribution and characteristics of axons within the optic nerve head and in the peripapillary retina, can be associated with non-progressive, congenital abnormalities that exhibit visual field loss. Examples of these are colobomata, megalopapilla, hypoplastic discs, tilted discs and retinal myelinated nerve fibres. Further work evaluating these stable anomalies may help to extend the understanding of the relationship between the RNFL reflectance, the OCT derived RNFL thickness and visual function.

8.2.5 The longitudinal variation in FDT perimetry in Glaucoma.

Change analysis and Glaucoma change probability analysis is available for W-W perimetry. The within- and between-visit Total Deviations at each location demonstrated by FDT perimetry were similar to W-W perimetry. Therefore it is feasible to consider developing an equivalent form both of change and GCP analysis for FDT perimetry. By creating a serial analysis database for a group of stable POAG individuals, the probability of no change for each location could be determined and subsequently used for the clinical evaluation of glaucomatous progression.

8.2.6 The HRF full-field analysis of blood flow and the relationship to parapapillary RNFL thickness.

Current developments in the HRF Full-field analysis software may provide more reliable measurements of the retinal capillary blood flow. The inclusion of large areas of perfused tissue, with careful avoidance of the major blood vessels and artefacts due to eye motion, has also allowed improved discrimination between glaucomatous and non-glaucomatous individuals. The use of this type of data analysis combined with regional OCT derived RNFL thickness data may assist in identifying which parapapillary retinal areas have impaired perfusion prior to, or following, axonal loss.

REFERENCES.

Adams, C. W., Bullimore, M. A., Wall, M., Fingeret, M. and Johnson, C. A. (1999). Normal aging effects for frequency doubling technology perimetry. *Optometry and Vision Science* 76: 582-587.

Airaksinen, P. J. and Alanko, H. I. (1983). Effect of retinal nerve fibre loss on the optic nerve head configuration in early glaucoma. *Graefe's Archive for Clinical and Experimental Ophthalmology* 220: 193-196.

Airaksinen, P. J. and Drance, S. M. (1984). Diffuse and localized nerve fibre loss in glaucoma. *American Journal of Ophthalmology* 98: 566-571.

Airaksinen, P. J., Drance, S. M. and Douglas, G. R. (1985a). Visual field and retinal nerve fibre layer comparisons in glaucoma. *Archives of Ophthalmology* 103: 205-207.

Airaksinen, P. J., Drance, S. M., Douglas, G. R. and Schulzer, M. (1985b). Neuroretinal rim areas and visual field indices in glaucoma. *American Journal of Ophthalmology* 99: 107-110.

Airaksinen, P. J., Drance, S. M. and Schulzer, M. (1985c). Neuroretinal rim area in early glaucoma. *American Journal of Ophthalmology* 99: 1-4.

Airaksinen, P. J. and Heijl, A. (1983). Visual field and retinal nerve fibre layer in early glaucoma after optic disc haemorrhage. *Acta Ophthalmologica* 61: 186-194.

Airaksinen, P. J., Mustonen, E. and Alanko, H. I. (1981). Optic disc haemorrhages precede retinal nerve fibre layer defects in ocular hypertension. *Acta Ophthalmologica* 59: 627-641.

Airaksinen, P. J. and Nieminen, H. (1985). Retinal nerve fibre layer photography in glaucoma. *Ophthalmology* 92: 877-879.

Airaksinen, P. J., Tuulonen, A. and Alanko, H. I. (1992). Rate and pattern of neuroretinal rim area decrease in ocular hypertension and glaucoma. *Archives of Ophthalmology* 110: 206-210.

Airaksinen, P. J., Tuulonen, A. and Werner, E. B. (1996). *Clinical evaluation of the optic disc and retinal nerve fibre layer*. The Glaucomas: Basic Sciences. R. Ritch, B. Shields and T. Krupin. St Louis, MO, Mosby Year Book: 617-657.

Anderson, D. R. (1989). Glaucoma: The damage caused by pressure. XLVI Edward Jackson memorial Lecture. *American Journal of Ophthalmology* 108: 485-495.

Anderson, D. R. and Hendrickson, A. (1974). Effect of intraocular pressure on rapid axoplasmic transport in monkey optic nerve. *Investigative Ophthalmology and Visual Science* 13: 771-783.

Anderson, D. R. and Patella, V. M. (1999). *Automated Static Perimetry*. St Louis, Mosby, Inc.

Anderson, R. S. and O'Brien, C. (1997). Psychophysical evidence for a selective loss of M ganglion cells in glaucoma. *Vision Research* 37: 1079-1083.

ANSI (1993). American National Standard for Safe Use of Lasers, ANSI Z136.1. Orlando, Laser Institute of America.

Armaly, M. F. (1965). On the distribution of applanation pressure. I. Statistical features and the effect of age, sex and family history of glaucoma. *Archives of Ophthalmology* 73: 11-18.

Armitage, A. K., Dollery, C. T., George, C. F., Houseman, T. H., Lewis, P. J. and Turner, D. M. (1976). Absorption and metabolism of nicotine from cigarettes. *British Medical Journal* 4: 313-316.

Asawaphureekorn, S., Zangwill, L. and Weinreb, R. N. (1996). Ranked-segment distribution curve for interpretation of optic nerve topography. *Journal of Glaucoma* 5: 79-90.

Åsman, P. (1992). Computer-Assisted Interpretation of Visual-Fields in Glaucoma. *Acta Ophthalmologica* 70: 9-47.

Åsman, P. and Heijl, A. (1992a). Evaluation of methods for automated hemifield analysis in perimetry. *Archives of Ophthalmology* 110: 820-826.

Åsman, P. and Heijl, A. (1992b). Glaucoma Hemifield Test - Automated visual field evaluation. *Archives of Ophthalmology* 110: 812-819.

Åsman, P. and Heijl, A. (1992c). Weighting According to Location in Computer-Assisted Glaucoma Visual Field Analysis. *Acta Ophthalmologica* 70: 671-678.

Åsman, P. and Heijl, A. (1994). Diffuse visual field loss and glaucoma. *Acta Ophthalmologica* 72: 303-308.

Åsman, P., Heijl, A., Olsson, J. and Rootzén, H. (1992). Spatial analyses of glaucomatous visual fields; a comparison with traditional visual field indices. *Acta Ophthalmologica* 70: 679-686.

Åsman, P. and Olsson, J. (1995). Physiology of cumulative defect curves: Consequences in glaucoma perimetry. *Acta Ophthalmologica Scandinavica* 73: 197-201.

Atchison, D. A. (1987). Effect of defocus on visual field measurement. *Ophthalmic and Physiological Optics* 7: 259-265.

Balazsi, A. G., Rootman, J., Drance, S. M. and Schulzer, M. (1984). The effect of age on the nerve fibre population of the optic nerve. *American Journal of Ophthalmology* 97: 760-766.

Bartz-Schmidt, K. U., Sengersdorf, A., Esser, P., Walter, P., Hilgers, R. D. and Krieglstein, G. K. (1996). The cumulative normalised rim/disc area ratio curve. *Graefe's Archives for Clinical & Experimental Ophthalmology* 234: 227-231.

Bathija, R., Zangwill, L., Berry, C. C., Sample, P. A. and Weinreb, R. N. (1998). Detection of early glaucomatous structural damage with confocal scanning laser tomography. *Journal of Glaucoma* 7: 121-127.

Baumann, M., Gentile, R. C., Liebmann, J. M. and Ritch, R. (1998). Reproducibility of retinal thickness measurements in normal eyes using optical coherence tomography. *Ophthalmic Surgery and Lasers* 29: 280-285.

Baxter, G. M. and Williamson, T. H. (1995). Color Doppler Imaging of the Eye: Normal ranges, reproducibility and observer variation. *Journal of Ultrasound in Medecine* 14: 91-96.

Bebie, H. (1996). *Introduction to the Doppler Effect*. Ocular Blood Flow. Glaucoma-Meeting. H. J. Kaiser, J. Flammer and P. Hendrickson. Basel, Karger: 93-99.

Bebie, H. and Fankhauser, F. (1976a). Static Perimetry: Accuracy and Fluctuations. *Acta Ophthalmologica* 54: 339-348.

Bebie, H. and Fankhauser, F. (1976b). Static Perimetry: Strategies. *Acta Ophthalmologica* 54: 325-338.

Bebie, H., Flammer, J. and Bebie, T. (1989). The Cumulative Defect Curve - Separation of local and diffuse components of visual field damage. *Graefe's Archive for Clinical and Experimental Ophthalmology* 227: 9-12.

Becker, B. (1971). Diabetes mellitus and primary open-angle glaucoma. The XXVII Edward Jackson Memorial Lecture. *American Journal of Ophthalmology* 71: 1-16.

Bedford, S. and Maddess, T. (1997). Observability of the spatial frequency doubled illusion correlation with a multi-region PERG. *Investigative Ophthalmology and Visual Science* 38: s 363.

Bengtsson, B. (1976). The variation and covariation of cup and disc diameters. *Acta Ophthalmologica* 54: 804-818.

Bengtsson, B. (1981). The prevalence of glaucoma. *British Journal of Ophthalmology* 65: 46-49.

Bengtsson, B. and Heijl, A. (1998a). Evaluation of a new perimetric threshold strategy, SITA, in patients with manifest and suspect glaucoma. *Acta Ophthalmologica Scandinavica* 76: 268-272.

Bengtsson, B. and Heijl, A. (1998b). SITA Fast, a new rapid perimetric threshold test. Description of methods and evaluation in patients with manifest and suspect glaucoma. *Acta Ophthalmologica Scandinavica* 76: 431-437.

Bengtsson, B. and Heijl, A. (1999). Inter-subject variability and normal limits of the SITA standard, SITA fast, and the Humphrey full threshold computerized perimetry strategies, SITA STATPAC. *Acta Ophthalmologica Scandinavica* 77: 125-129.

Bengtsson, B. and Heijl, A. (2000). False-negative responses in glaucoma perimetry: Indicators of patient performance or test reliability. *Investigative Ophthalmology and Visual Science* 41: 2201-2204.

Bengtsson, B., Heijl, A. and Olsson, J. (1998). Evaluation of a new threshold visual field strategy, SITA, in normal subjects. *Acta Ophthalmologica Scandinavica* 76: 165-169.

Bengtsson, B., Holmin, C. and Krakau, C. E. T. (1981). Disc haemorrhages and glaucoma. *Acta Ophthalmologica* 59: 1-14.

Bengtsson, B., Lindgren, A., Heijl, A., Lindgren, G., Asman, P. and Patella, M. (1997a). Perimetric probability maps to separate change caused by glaucoma from that caused by cataract. *Acta Ophthalmologica Scandinavica* 75: 184-188.

Bengtsson, B., Olsson, J., Heijl, A. and Rootzen, H. (1997b). A new generation of algorithms for computerized threshold perimetry, SITA. *Acta Ophthalmologica Scandinavica* 75: 368-375.

Bergea, B., Bodin, L. and Svedburgh, B. (1999). Impact of intraocular pressure regulation on visual fields in open-angle glaucoma. *Ophthalmology* 106: 997-1005.

Bill, A. and Sperber, G. O. (1990). Control of retinal and choroidal blood flow. *Eye* 4: 319-325.

Birch, M. K., Wishart, O. K. and O'Donnell, N. P. (1995). Determining progressive visual field loss in serial Humphrey visual fields. *Ophthalmology* 102: 1227-1235.

Bland, J. M. and Altman, D. G. (1986). Statistical methods for assessing agreement between two methods of clinical measurement. *Lancet* 1: 307-310.

Bohdanecka, Z., Orgül, S., Prünte, C. and Flammer, J. (1998). Influence of acquisition parameters on hemodynamic measurements with the Heidelberg Retina Flowmeter at the optic disc. *Journal of Glaucoma* 7: 151-157.

Bonner, R. F. and Nossal, R. (1990). *Principles of laser Doppler flowmetry.* Laser Doppler Blood Flowmetry. A. P. Shepherd and P. A. Odberg. Boston, Kluwer Academic: 17-45.

Bowd, C., Weinreb, R. N., Williams, J. M. and Zangwill, L. (2000). The retinal nerve fiber layer thickness in ocular hypertensive, normal, and glaucomatous eyes with optical coherence tomography. *Investigative Ophthalmology & Visual Science* 118: 22-26.

Boycott, B. and Wassell, H. (1999). Parallel processing in the mammalian retina. The Proctor Lecture. *Investigative Ophthalmology and Visual Science* 40: 1313-1327.

Brenton, R. S. and Phelps, C. D. (1986). The normal visual field on the Humphrey Field Analyzer. *Ophthalmologica* 193: 56-74.

Brigatti, L. and Caprioli, J. (1995). Correlation of visual-field with scanning confocal laser optic disc measurements in glaucoma. *Archives Of Ophthalmology* 113: 1191-1194.

Brigatti, L., Weitzman, M. and Caprioli, J. (1995). Regional test-retest variability of confocal scanning laser tomography. *American Journal of Ophthalmology* 120: 433-440.

Britton, R. J., Drance, S. M., Schulzer, M. and Douglas, G. R. (1987). The area of the neuroretinal rim of the optic nerve in normal eyes. *American Journal of Ophthalmology* 103: 497-504.

Broadway, D. C. and Drance, S. M. (1998). Glaucoma and vasospasm. *British Journal of Ophthalmology* 82: 862-870.

Broadway, D. C., Drance, S. M., Parfitt, C. M. and Mikelberg, F. S. (1998). The ability of scanning laser ophthalmoscopy to identify various glaucomatous optic disc appearances. *American Journal of Ophthalmology* 125: 593-604.

Burk, R. and Rohrschneider, K. (1992). Are large optic nerve heads susceptible to glaucomatous damage at normal intra-ocular pressures? *Graefe's Archive for Clinical and Experimental Ophthalmology* 230: 552-560.

Burk, R. and Rohrschneider, K. (1993). Laser scanning tomography and stereophotogrammetry. *Graefe's Archive for Clinical and Experimental Ophthalmology* 231: 193-198.

Burk, R., Rohrschneider, K., Volcker, H. and Gerhard, Z. (1990). *Analysis of three dimensional optic disc topography by laser scanning tomography*. Scanning laser ophthalmoscopy and tomography. J. Nasemann and R. Burk. Munich, Quintessenz: 161-176.

Burk, R. O. W., Airaksinen, P. J., Tuulonen, A., Rohrschneider, K., Volcker, H. E. and Konig, J. (1995). Reference plane for three dimensional topographic optic disc analysis with the Heidelberg Retina Tomograph. *Investigative Ophthalmology and Visual Science* 36: s627.

Burk, R. O. W., Tuulonen, A. and Airaksinen, P. J. (1998). Laser scanning tomography of localised nerve fibre layer defects. *British Journal of Ophthalmology* 82: 1112-1117.

Burk, R. O. W., Vihanninjoki, K., Bartke, T., Tuulonen, A., Airaksinen, P. J., Volcker, H. E. and Konig, J. M. (2000). Development of the standard reference plane for the Heidelberg retina tomograph. *Graefe's Archive for Clinical and Experimental Ophthalmology* 238: 375-384.

Butt, Z. and O'Brien, C. (1995). Reproducibility of pulsatile ocular blood flow measurements. *Journal of Glaucoma* 4: 214-218.

Calkins, D. J., Tsukamoto, Y. and Sterling, P. (1998). Microcircuitry and mosaic of a blue-yellow ganglion cell in the primate retina. *The Journal of Neuroscience* 18: 3373-3385.

Caprioli, J. (1992). Discrimination between normal and glaucomatous eyes. *Investigative Ophthalmology and Visual Science* 33: 153-159.

Caprioli, J., Klingbeil, U., Sears, M. and Pope, B. (1986). Reproducibility of Optic Disk Measurements With Computerized Analysis of Stereoscopic Video Images. *Archives of Ophthalmology* 104: 1035-1039.

Caprioli, J. and Miller, J. M. (1987). Optic disc rim area is related to disc size in normal subjects. *Archives of Ophthalmology* 105: 1683-1685.

Caprioli, J., Miller, J. M. and Sears, M. (1987a). Quantitative evaluation of the optic nerve head in patients with unilateral visual field loss from primary open-angle glaucoma. *Ophthalmology* 94: 1484-1487.

Caprioli, J., Park, H. J., Uguru, S. and Hoffman, D. (1998). Slope of the peripapillary nerve fibre layer surface in glaucoma. *Investigative Ophthalmology and Visual Science* 39: 2321-2328.

Caprioli, J., Prum, B. and Zeyen, T. (1996). Comparison of methods to evaluate the optic nerve head and nerve fiber layer for glaucomatous change. *American Journal of Ophthalmology* 121: 659-667.

Caprioli, J., Sears, M. and Miller, J. M. (1987b). Patterns of early visual field loss in open-angle glaucoma. *American Journal of Ophthalmology* 103: 512-517.

Caprioli, J. and Spaeth, G. (1985). Comparison of the optic nerve head in high- and low-tension glaucoma. *Archives of Ophthalmology* 103: 1145-1149.

Caprioli, J. and Spaeth, G. L. (1984). Comparison of visual field defects in the low tension glaucomas with those in the high tension glaucomas. *American Journal of Ophthalmology* 97: 730-737.

Casagrande, V. A. (1994). A third parallel visual pathway to primate area V1. *Trends in Neuroscience* 17: 305-310.

Casson, E. J., Johnson, C. A. and Shapiro, L. R. (1993). Longitudinal comparison of temporal-modulation perimetry with white-on-white and blue-on-yellow perimetry in ocular hypertension and early glaucoma. *Journal of the Optometric Society of America (A)* 10: 1792-1806.

Cello, K. E., Nelson-Quigg, J. M. and Johnson, C. A. (2000). Frequency doubling technology perimetry for detection of glaucomatous visual field loss. *American Journal of Ophthalmology* 129: 314-322.

Chaturvedi, N., Hedley-Whyte, E. I. and Dreher, E. B. (1993). Lateral geniculate nucleus in glaucoma. *American Journal of Ophthalmology* 116: 182-188.

Chauhan, B. and LeBlanc, R. (1994). Test-retest variability of topographic measurements with confocal scanning laser topography. *American Journal of Ophthalmology* 118: 9-15.

Chauhan, B. C. (1989). A cluster analysis for threshold perimetry. *Graefe's Archive for Clinical and Experimental Ophthalmology* 227: 216-220.

Chauhan, B. C. (1996). Confocal scanning laser tomography. *Canadian Journal of Ophthalmology* 31: 152-156.

Chauhan, B. C., Drance, S. M., Douglas, G. R. and Johnson, C. A. (1989). Visual field damage in normal-tension and high-tension glaucoma. *American Journal of Ophthalmolgy* 108: 636-642.

Chauhan, B. C. and Johnson, C. A. (1999). Test-retest variability of frequency-doubling perimetry and conventional perimetry in glaucoma patients and normal subjects. *Investigative Ophthalmology and Visual Science* 40: 648-656.

Chauhan, B. C., LeBlanc, R. P., Shaw, A. M., Chan, A. B. and McCormick, T. A. (1997). Repeatable diffuse visual field loss in open-angle glaucoma. *Ophthalmology* 104: 532-538.

Chauhan, B. C. and Macdonald, C. A. (1995). Influence of time separation on variability estimates of topographic measurements with confocal scanning laser ophthalmoscopy. *Journal of Glaucoma* 4: 189-193.

Chauhan, B. C. and McCormick, T. A. (1995). Effect of the cardiac cycle on topographic measurements using confocal scanning laser tomography. *Graefe's Archive for Clinical and Experimental Ophthalmology* 233: 568-572.

Chauhan, B. C. and Smith, F. M. (1997). Confocal scanning laser doppler flowmetry: Experiments in a model flow system. *Journal of Glaucoma* 6: 237-245.

Chauhan, B. C. and Tomkins, J. D. (1993). Characteristics of frequency-of-seeing curves in normal subjects, patients with suspected glaucoma, and patients with glaucoma. *Investigative Ophthalmology and Visual Science* 34: 3534-3540.

Chauhan, D. S. and Marshall, J. (1999). The interpretation of Optical Coherence Tomography images of the retina. *Investigative Ophthalmology and Visual Science* 40: 2332-2342.

Chen, Y.-Y., Chen, P. P., Xu, L., Ernst, P. K., Wang, L. and Mills, R. P. (1998). Correlation of peripapillary nerve fibre layer thickness by scanning laser polarimetry with visual field defects in patients with glaucoma. *Journal of Glaucoma* 7: 312-316.

Chi, Q.-M., Tomita, G., Inazumi, k., Hayakama, T., Ido, T. and Kitazawa, Y. (1995). Evaluation of the effect of aging on the retinal nerve fibre layer thickness using scanning laser polarimetry. *Journal of Glaucoma* 4: 406-413.

Chi, T., Ritch, R., Stockler, D. and al, e. (1989). Racial differences in optic nerve head parameters. *Archives of Ophthalmology* 107: 836-839.

Choplin, N. T., Lundy, D. C. and Dremer, A. W. (1998). Differentiating patients with glaucoma from glaucoma suspects and normal subjects by nerve fibre layer assessment with scanning laser polarimetry. *Ophthalmology* 105: 2068-2076.

Choplin, N. T., Sherwood, M. B. and Spaeth, G. L. (1990). The effect of stimulus size on the measured threshold values in automated perimetry. *Ophthalmology* 97: 371-374.

Chung, H. S., Harris, A., Halter, P. J., Kageman, L. J., Roff, E. J., Garzozi, H. J., Hosking, S. L. and Martin, B. (1999a). Regional differences in retinal vascular reactivity. *Investigative Ophthalmology and Visual Science* 40: 2448-2453.

Chung, H. S., Harris, A., Kageman, L. and Martin, B. (1999b). Peripapillary retinal blood flow in normal tension glaucoma. *British Journal of Ophthalmology* 83: 466-469.

Chylack, L. T., Wolfe, J. K. and Friend, F. (1993). Quantitating cataract and nuclear brunescence. *Optometry and Vision Science* 70: 886-895.

Cioffi, G. A. (1998). Three assumptions: Ocular blood flow and glaucoma. *Journal of Glaucoma* 7: 299-300.

Cioffi, G. A., Robin, A. L., Eastman, R. D., Perell, H. F., Safarazi, F. A. and Kelman, S. E. (1993). Confocal laser scanning ophthalmoscope - Reproducibility of optic nerve head topographic measurements with the confocal laser scanning ophthalmoscope. *Ophthalmology* 100: 57-62.

Coffey, M., Reidy, A., Wormald, R., Xian, W. X., Wright, L. and Courtney, P. (1993). Prevalence of glaucoma in the West of Ireland. *British Journal of Ophthalmology* 77: 17-21.

Cornsweet, T. (1970). *Visual Perception.* New York, Academic Press.

Cranstoun, S. D., Petrig, B. L., Riva, C. E. and Baine, J. (1994). Optic nerve head blood flow in the human eye by laser Doppler flowmetry (LDF) (abstract). *Investigative Ophthalmology and Visual Science* 35 (suppl): 1658.

Crichton, A., Drance, S. M., Douglas, G. R. and Schulzer, M. (1989). Unequal intraocular pressure and its relation to asymmetric visual field defects in low-tension glaucoma. *Ophthalmology* 96: 1312-1314.

Cubbidge, R. P. (1997). Examination variability in short-wavelength automated perimetry (PhD Thesis). Vision Sciences. Birmingham, University of Aston: 1-312.

Curcio, C. A. and Allen, K. A. (1990). Topography of ganglion cells in human retina. *The Journal of Comparative Neurology* 300: 5-25.

Dacey, D. M. (1993a). Morphology of a small-field bistratified ganglion cell type in the macaque and human retina. *Visual Neuroscience* 10: 1081-1098.

Dacey, D. M. (1993b). The mosaic of midget ganglion cells in human retina. *Journal of Neuroscience* 13: 5334-5355.

Dacey, D. M. (1994). Physiology, Morphology and Spatial Densities of Identified Ganglion- Cell Types in Primate Retina. *Ciba Foundation Symposia* 184: 12-28.

Dacey, D. M. and Lee, B. B. (1994). The blue-on opponent pathway in primate retina originates from a distinct bistratified ganglion-cell type. *Nature* 367: 731-735.

Damms, T. and Dannheim, F. (1993). Sensitivity and specificity of optic disc parameters in chronic glaucoma. *Investigative Ophthalmology and Visual Science* 34: 2246-2250.

Dandona, L., Hendrickson, A. and Quigley, H. A. (1991). Selective effects of experimental glaucoma on axonal transport by retinal ganglion cells to the dorsal lateral geniculate nucleus. *Investigative Ophthalmology & Visual Science* 32: 1593-1599.

David, R., Livingston, D. G. and Luntz, M. H. (1977). Ocular hypertension - a long-term follow-up of treated and untreated patients. *British Journal of Ophthalmology* 61: 668-674.

de Jong, L. A. M. S., Snepvangers, C. E. J., van den Berg, T. J. T. P. and Langerhorst, C. T. (1990). Blue-yellow perimetry in the detection of early glaucomatous damage. *Documenta Ophthalmologica* 75: 303-314.

deBoer, J. F., Milner, T. E. and van Gemeri, M. J. C. (1997). Two-dimensional birefringence imaging in biological tissue by polarization-sensitive optical coherence tomography. *Applied Optics* 22: 934-936.

Demirel, S. and Johnson, C. A. (2000). Isolation of short-wavelength sensitive mechanisms in normal and glaucomatous visual field regions. *Journal of Glaucoma* 9: 63-73.

DeValois, R. L. and DeValois, K. K. (1993). A multi-stage colour model. *Vision Research* 33: 1053-1065.

Dichtl, A., Jonas, J. B. and Mardin, C. Y. (1996). Comparison between tomographic scanning evaluation and photographic measurement of the neuroretinal rim. *American Journal of Ophthalmology* 121: 494-501.

Dichtl, A., Jonas, J. B. and Naumann, G. O. H. (1999). Retinal nerve fibre layer thickness in human eyes. *Graefe's Archive for Clinical and Experimental Ophthalmology* 237: 474-479.

Dolman, C. L., McCormick, A. Q. and Drance, S. M. (1980). Aging and the Optic Nerve. *Archives of Ophthalmology* 98: 2053-2058.

Drance, S., Schulzer, M., Douglas, G. R. and Sweeney, V. P. (1978). Use of discriminate analysis. II. Identification of persons with glaucomatous visual field defects. *Archives of Ophthalmology* 96: 1571-1573.

Drance, S. M. (1969). The early visual field defects in glaucoma. *Investigative Ophthalmology and Visual Science* 8: 84-91.

Drance, S. M. (1989). The early structural and functional disturbance of chronic open-angle glaucoma. *Ophthalmology* 92: 853-857.

Drance, S. M. (1991). Diffuse visual field loss in open-angle glaucoma. *Ophthalmology* 98: 1533-1538.

Drance, S. M. (1992). Bowman Lecture: Glaucoma-Changing Concepts. *Eye* 6: 337-345.

Drance, S. M. (1997). Glaucoma; A look beyond IOP (Editorial). *American Journal of Ophthalmology* 123: 817-819.

Drance, S. M., Douglas, G. R., Airaksinen, P. J., Schulzer, M. and Hitchings, R. A. (1987). Diffuse visual field loss in chronic open-angle and low-tension glaucoma. *American Journal of Ophthalmology* 104: 577-580.

Drance, S. M., Schulzer, M., Thomas, B. and Douglas, G. R. (1981). Multivariate Analysis in Glaucoma: Use of discriminate analysis in predicting glaucomatous visual field damage. *Archives of Ophthalmology* 99: 1019-1022.

Dreher, A., Reiter, K. and Weinreb, R. (1992). Spatially resolved birefringence of the retinal nerve fibre layer. *Applied Optics* 31: 3730-3735.

Dreher, A. W., Tso, P. C. and Weinreb, R. N. (1991). Reproducibility of topographic measurements of the normal and glaucomatous optic-nerve head with the Laser Tomographic Scanner. *American Journal of Ophthalmology* 111: 221-229.

Dreher, A. W. and Weinreb, R. N. (1991). Accuracy of topographic measurements in a model eye with the Laser Tomographic Scanner. *Investigative Ophthalmology and Visual Science* 32: 2992-2996.

Elschnig, A. (1900). Das Colobom am Sehnerveneintritte und der Conus nach unten. *Archives of Ophthalmology* 51: 391-430.

Embleton, S. J., Hosking, S. L., Pettinger, C., Kagemann, L., Chabra, A., Chung, H. S. and Harris, A. (1999). Blood flow measurements of optic nerve head rim tissue as a function of illumination with scanning laser doppler flowmetry. *Investigative Ophthalmology and Visual Science* 40: S276.

Emdadi, A., Kono, Y., Sample, P. A., Maskaleris, G. and Weinreb, R. N. (1999). Parapapillary atrophy in patients with focal visual field loss. *American Journal of Ophthalmology* 128: 595-600.

Emdadi, A., Zangwill, L., Sample, P. A., Kono, Y., Anton, A. and Weinreb, R. N. (1998). Patterns of optic disc damage in patients with early focal visual field loss. *American Journal of Ophthalmology* 126: 763-771.

Emery, J. M., Landis, D., Paton, D. and Boniuk, M. (1978). The lamina cribrosa in normal and glaucomatous human eyes. *Transactions of the American Academy of Ophthalmology and Otolaryngology* 78: 290-297.

Evans, D. W., Harris, A., Chung, H. S., Cantor, L. B. and Garzorzi, H. J. (1998). Effects of long-term hypotensive therapy with non-selective Beta-Blockers on ocular hemodynamics in primary open- angle glaucoma. *Journal of Glaucoma* 8: 12-17.

Evans, D. W., Harris, A., Garrett, M., Chung, H. K. and Kagemann, L. (1999). Glaucoma patients demonstrate faulty autoregulation of ocular blood flow during posture change. *British Journal of Ophthalmology* 83: 809-813.

Fan, A. X., Chung, H. S., McCranor, L., Zarfati, D., Kagemann, L. and Hirst, D. (2000). The relationship between optic disc morphology and retinal hemodynamics in glaucoma as measured by HRT and HRF. *Investigative Ophthalmology and Visual Science* 41: S557.

Fankhauser, F. (1979). Problems related to the design of automatic perimeters. *Documenta Ophthalmologica* 47: 89-138.

Fankhauser, F. and Bebie, H. (1979). Threshold fluctuations, interpolations and spatial resolution in perimetry. *Documenta Ophthalmologica Proceedings Series* 19: 295-309.

Fankhauser, F. and Haeberlin, H. (1980). Dynamic range and stray light. An estimate of the falsifying effects of stray light in perimetry. *Documenta Ophthalmologica* 50: 143-167.

Fantes, F. E. and Anderson, D. R. (1989). Clinical histologic correlation of human peripapillary anatomy. *Ophthalmology* 96: 20-25.

Fechtner, R. D. and Weinreb, R. N. (1994). Mechanisms of optic nerve damage in primary open angle glaucoma. *Survey of Ophthalmology* 39: 23-42.

Feke, G. T. and Riva, C. E. (1978). Laser doppler measurements of blood velocity in human retinal vessels. *Journal of the Optical Society of America* 68: 526-531.

Fitzke, F. W., Hitchings, R. A., Poinoosawmy, D., McNaught, A. I. and Crabb, D. P. (1996). Analysis of visual field progression in glaucoma. *British Journal of Ophthalmology* 80: 40-48.

Fitzke, F. W. and McNaught, A. I. (1994). The diagnosis of visual field progression in glaucoma. *Current Opinion in Ophthalmology* 5: 110-115.

Flammer, J. (1986). The concept of visual-field indices. *Graefe's Archive for Clinical and Experimental Ophthalmology* 224: 389-392.

Flammer, J., Drance, S. M., Fankhauser, F. and Augustiny, L. (1984a). Differential light threshold in automated static perimetry: factors influencing short-term fluctuation. *Archives of Ophthalmology* 102: 876-879.

Flammer, J., Drance, S. M. and Zulauf, M. (1984b). Differential light threshold: short- and long-term fluctuation in patients with glaucoma, normal controls and patients with suspected glaucoma. *Archives of Ophthalmology* 102: 704-706.

Flammer, J., Haefliger, I. O., Orgül, S. and Resink, T. (1999). Vascular dysregulation: A principal risk factor for glaucomatous damage? *Journal of Glaucoma* 8: 212-219.

Flammer, J. and Orgül, S. (1998). Optic nerve blood-flow abnormalities in glaucoma. *Progress in Retinal and Eye Research* 17: 267-289.

Flanagan, J., Moss, I. D., Wild, J., Hudson, C., Prokopich, L., Whitaker, D. and O'Neill, E. C. (1993a). Evaluation of FASTPAC - a new strategy for threshold estimation with the Humphrey Field Analyzer. *Graefe's Archive for Clinical and Experimental Ophthalmology* 231: 465-469.

Flanagan, J., Wild, J. and Trope, G. (1993b). Evaluation of FASTPAC - a new strategy for threshold estimation with the Humphrey Field Analyzer in a glaucomatous population. *Ophthalmology* 100: 949-954.

Fontana, L., Poinoosawmy, D., Bunce, C. V. and O' Brien, C. (1998). Pulsatile ocular blood flow investigation in asymetric normal tension glaucoma and normal subjects. *British Journal of Ophthalmology* 82: 731-736.

Forrester, J., Dick, A. D., McMenamin, P. and Lee, W. R. (1996). *The Eye: Basic Science in Practice.* London, W.B.Saunders Company Ltd.

Fraser, S., Bunce, C. V. and Wormald, R. (1999). Risk factors for late presentation in chronic glaucoma. *Investigative Ophthalmology and Visual Science* 40: 2251-2257.

Frisen, L. (1980). Photography of the retinal nerve fibre layer : an optimized procedure. *British Journal of Ophthalmology* 64: 641-650.

Funaki, S., Shirakashi, M. and Abe, H. (1998). Relation between size of optic disc and thickness of retinal nerve fibre layer in normal subjects. *British Journal of Ophthalmology* 82: 1242-1245.

Gaasterland, O., Tanishima, T. and Kuwabara, T. (1978). Axoplasmic flow during chronic experimental glaucoma: I. Light and electron microscopic studies of the monkey optic nerve head during development of glaucomatous cupping. *Investigative Ophthalmology and Visual Science* 17: 838-846.

Gao, H. and Hollyfield, J. G. (1992). Aging of the human retina. *Investigative Ophthalmology and Visual Science* 33: 1-17.

Garway-Heath, D. F. and Hitchings, R. A. (1998). Quantitative evaluation of the optic nerve head in early glaucoma. *British Journal of Ophthalmology* 82: 352-361.

Garway-Heath, D. F., Poinoosawmy, D., Wollstein, G., Viswanathan, A., Kamal, D., Fontana, L. and Hitchings, R. A. (1999). Inter- and Intra- observer variation in the analysis of optic disc images: comparison of the Heidelberg retina tomograph and computer assisted planimetry. *British Journal of Ophthalmology* 83: 664-669.

Garway-Heath, D. F., Ruben, S. T., Viswanathan, A. and Hitchings, R. A. (1998). Vertical cup / disc ratio in relation to optic disc size : its value in the assessment of the glaucoma suspect. *British Journal of Ophthalmology* 82: 1118-1124.

Garway-Heath, D. F., Wollstein, G. and Hitchings, R. A. (1997). Aging changes of the optic nerve head in relation to open angle glaucoma. *British Journal of Ophthalmology* 81: 840-845.

Ghafour, I. M., Allan, D. and Foulds, W. (1983). Common causes of blindness and visual handicap in the West of Scotland. *British Journal of Ophthalmology* 67: 209-213.

Glovinsky, Y., Quigley, H. A. and Dunkelberger, G. R. (1991). Retinal ganglion cell loss is size dependent in experimental glaucoma. *Investigative Ophthalmology and Visual Science* 32: 484-491.

Gramer, E. and Dirmeyer, M. (1998). Optical Coherence Tomography (OCT) to measure nerve fibre layer thickness in normal eyes. *Investigative Ophthalmology and Visual Science* 39: S933.

Greenidge, K. C., Spaeth, G. L. and Traverso, C. E. (1985). Change in appearance of the optic disc associated with lowering of intraocular pressure. *Ophthalmology* 92: 897-903.

Greenstein, V. C., Halevy, D., Zaldi, Q. and Koenig, K. L. (1996). Chromatic and luminance system deficits in glaucoma. *Vision Research* 36: 621-629.

Greve, E. L. (1973). Single and multiple stimulus static perimetry in glaucoma; the two phases of perimetry. *Documenta Ophthalmologica* 36: 1-355.

Groh, M. J. M., Michelson, G., Langhans, M. J. and Harazy, J. (1996). Influence of age on retinal and optic nerve head blood circulation. *Ophthalmology* 103: 529-534.

Grunwald, J. E. (1986). Effect of topical timolol on human retinal circulation. *Investigative Ophthalmology and Visual Science* 27: 1713-1719.

Grunwald, J. E. (1990). Effect of topical timolol maleate on the retinal circulation of human eyes with ocular hypertension. *Investigative Ophthalmology and Visual Science* 31: 521-526.

Grunwald, J. E., Piltz, J., Hariprasad, S. M. and Dupont, J. (1998). Optic nerve and choroidal circulation in glaucoma. *Investigative Ophthalmology and Visual Science* 30: 2329-2336.

Grunwald, J. E., Piltz, J., Hariprasad, S. M., Dupont, J. and Maguire, M. G. (1999). Optic nerve blood flow in glaucoma: Effect of systemic hypertension. *American Journal of Ophthalmology* 127: 516-522.

Grunwald, J. E., Riva, C. E., Stone, R. A. and Keates, E. U. (1984). Retinal autoregulation in open angle glaucoma. *Ophthalmology* 91: 1690-1694.

Grunwald, J. E. and Zinn, H. (1992). The acute effect of acetazolamide on macular blood flow. *Investigative Ophthalmology and Visual Science* 33: 504-407.

Gundersen, K. G. and Åsman, P. (2000). Comparison of ranked segment analysis (RSA) and cup to disc ratio in computer-assisted optic disc evaluation. *Acta Ophthalmologica Scandinavica* 78: 137-141.

Gundersen, K. G., Heijl, A. and Bengtsson, B. (1998). Age, gender, IOP, refraction and optic disc topography in normal eyes. A cross-sectional study using raster and scanning laser tomography. *Acta Ophthalmologica Scandinavica* 76: 170-175.

Gundersen, K. G., Heijl, A. and Bengtsson, B. (2000). Comparability of three-dimensional optic disc imaging with different techniques - A study with confocal scanning laser tomography and raster tomography. *Acta Ophthalmologica Scandinavica* 78: 9-13.

Gurses-Ozden, R., Ishikawa, H., Hoh, S.-T., Liebmann, J. M., Mistlberger, A., Greenfield, D. S., Dou, H. L. and Ritch, R. (1999). Increasing sampling density improves reproducibility of optical coherence tomography measurements. *Journal of Glaucoma* 8: 238-241.

Haas, A., Flammer, J. and Schneider, U. (1986). Influence of age on the visual fields of normal subjects. *American Journal of Ophthalmology* 101: 199-203.

Hamard, P., Hamard, H. and Dufaux, J. (1994). Blood flow rate in the microvasculature of the optic nerve head in primary open angle glaucoma. A new approach. *Survey of Ophthalmology* 38 (Suppl. may): s87-s94.

Harper, R. A. and Reeves, B. C. (1999). Glaucoma screening. The importance of combining test data. *Optometry and Vision Science* 76: 537-543.

Harris, A., Anderson, D. R., Pillunat, L., Joos, K., Knighton, R. W., Kagemann, L. and Martin, B. J. (1996a). Laser doppler flowmetry measurement of changes in human optic nerve head blood flow in response to blood gas pertubations. *Journal of Glaucoma* 5: 258-265.

Harris, A., Arend, O., Arend, S. and Martin, B. J. (1996b). Effects of topical dorzolamide on retinal and retrobulbar hemodynamics. *Acta Ophthalmologica Scandinavica* 74: 4896-4899.

Harris, A., Ciuilla, T. A., Chung, H. S. and Martin, B. (1998a). Regulation of retinal and optic nerve blood flow. *Archives of Ophthalmology* 116: 1491-1495.

Harris, A., Evans, D. W., Cantor, L. B. and Martin, B. (1997). Hemodynamics and visual function effects of oral Nifedipine in patients with normal-tension glaucoma. *American Journal of Ophthalmology* 124: 296-302.

Harris, A., Kagemann, L. and Cioffi, G. (1998b). Assessment of human ocular hemodynamics. *Survey of Ophthalmology* 42: 509-533.

Harris, A., Tippke, S., Sievers, C., Picht, G., Lieb, W. and Martin, B. J. (1996c). Acetazolamide and CO_2: Acute effects on cerebral and retrobulbar haemodynamics. *Journal of Glaucoma* 5: 39-45.

Hart, W. M. (1987). Acquired Dyschromatopsia. *Survey of Ophthalmology* 32: 10-31.

Hart, W. M. and Becker, B. (1982). The onset and evolution of glaucomatous visual field defects. *Ophthalmology* 89: 268-279.

Hart, W. M. and Burde, R. M. (1985). Color contrast perimetry. The spatial distribution of color defects in optic nerve and retinal diseases. *Ophthalmology* 92: 768-776.

Hart, W. M., Silverman, S. E., Trick, G. L., Nesher, R. and Gordon, M. O. (1990). Glaucomatous visual field damage. Luminance and color-contrast sensitivities. *Investigative Ophthalmology and Visual Science* 31: 359-367.

Harwerth, R. S., Carter-Dawson, L., Shen, F., Smith, E. L. and Crawfor, M. L. T. (1999). Ganglion cell losses underlying visual field defects from experimental glaucoma. *Investigative Ophthalmology and Visual Science* 40: 2242-2250.

Hatch, W. V., Flanagan, J. G., Etchells, E. E. and Williams-Lyn, D. E. (1997). Laser scanning tomography of the optic nerve head in ocular hypertension and glaucoma. *British Journal of Ophthalmology* 81: 871-876.

Hatch, W. V., Flanagan, J. G., Williams-Lyn, D., Buys, Y. M., Farra, T. and Trope, G. (1999). Interobserver agreement of Heidelberg Retina Tomograph parameters. *Journal of Glaucoma* 8: 232-237.

Hayreh, S. S. (1963). The cilio-retinal arteries. *British Journal of Ophthalmology* 47: 71-89.

Hayreh, S. S. (1970). Pathogenesis of visual field defects. Role of the ciliary circulation. *British Journal of Ophthalmology* 54: 289-311.

Hayreh, S. S. (1974a). Anatomy and physiology of the optic nerve head. *Transactions of the American Academy of Ophthalmology and Otolaryngology* 78: 240-247.

Hayreh, S. S. (1974b). The chorio capillaris. *Graefe's Archive for Clinical and Experimental Ophthalmology* 192: 165-179.

Hayreh, S. S. (1985). Inter-individual variation in blood supply of the optic nerve head: Its importance in various ischaemic disorders of the optic nerve head, glaucoma, low tension glaucoma and allied disorders. *Documenta Ophthalmologica* 59: 217-246.

Hayreh, S. S. (1990). In vivo, choroidal circulation and it's watershed zones. *Eye* 4: 243-248.

Hayreh, S. S. (1994). Progress in the understanding of the vascular etiology of Glaucoma. *Current Opinion in Ophthalmology* 5: 26-35.

Hayreh, S. S. (1995). The optic nerve head circulation in health and disease. *Experimental Eye Research* 61: 259-272.

Hayreh, S. S. (1996a). Blood supply of the optic nerve head. *Ophthalmologica* 210: 285-295.

Hayreh, S. S. (1996b). Duke-Elder lecture. Systemic arterial blood pressure and the eye. *Eye* 10: 5-28.

Hayreh, S. S. (1997a). Evaluation of optic nerve head circulation: Review of the methods used. *Journal of Glaucoma* 6: 319-330.

Hayreh, S. S. (1997b). Factors influencing blood flow in the optic nerve head. *Journal of Glaucoma* 6: 412-425.

Hayreh, S. S., March, W. and Anderson, D. R. (1979). Pathogenesis of block of rapid orthograde axonal transport by elevated intraocular pressure. *Experimental Eye Research* 28: 515-523.

Hayreh, S. S., Podhajsky, P. and Zimmerman, M. B. (1998). Role of nocturnal arterial hypotension in optic nerve head ischaemic disorders. *Ophthalmologica* 213: 76-96.

Hayreh, S. S., Revie, J. H. S. and Edwalis, J. (1970). Vasogenic origin of visual field defects and optic nerve changes in glaucoma. *British Journal of Ophthalmology* 54: 461-472.

Hecht, S., Shlaer, S. and Pirenne, M. H. (1942). Energy, Quanta and Vision. *Journal of General Physiology* 25: 819-840.

Hee, M. R., Izatt, J. A., Swanson, E. A., Huang, D., Schuman, J. S., Lin, C. P., Puliafito, C. A. and Fujimoto, J. G. (1995a). Optical Coherence Tomography for ophthalmic imaging - New technique delivers micron-scale resolution. *IEEE Engineering in Medicine and Biology Magazine* 14: 67-76.

Hee, M. R., Izatt, J. A., Swanson, E. A., Huang, D., Schuman, J. S., Lin, C. P., Puliafito, C. A. and Fujimoto, J. G. (1995b). Optical Coherence Tomography of the human retina. *Archives of Ophthalmology* 113: 325-332.

Hee, M. R., Puliafito, C. A., Duker, J. S., Reichel, E., Coker, J., Wilkins, J., Schuman, J. S., Swanson, E. A. and Fujimoto, J. G. (1998). Topography of diabetic macular edema with Optical Coherence Tomography. *Ophthalmology* 105: 360-370.

Hee, M. R., Puliafito, C. A., Wong, C., Duker, J. S., Reichel, E., Rutledge, B., Schuman, J. S., Swanson, E. A. and Fujimoto, J. G. (1995c). Quantitative assessment of macular edema with Optical Coherence Tomography. *Archives of Ophthalmology* 113: 1019-1029.

Hee, M. R., Puliafito, C. A., Wong, C., Duker, J. S., Reichel, E., Schuman, J. S., Swanson, E. A. and Fujimoto, J. G. (1995d). Optical Coherence Tomography of macular holes. *Ophthalmology* 102: 748-756.

Hee, M. R., Puliafito, C. A., Wong, C., Reichel, E., Duker, J. S., Schuman, J. S., Swanson, E. A. and Fujimoto, J. G. (1995e). Optical coherence tomography of central serous chorioretinopathy. *American Journal of Ophthalmology* 120: 65-74.

Heijl, A. (1984). Computerised perimetry. *Transactions of the Ophthalmological Society (UK).* 104: 76-87.

Heijl, A. (1985). *The Humphrey Field Analyzer, construction and concepts*. Documenta Ophthalmologica Proceedings Series. A. Heijl and E. Greve. Dordrecht, Dr . W. Junk: 77-84.

Heijl, A. (1989a). A clinical study of perimetric probability maps. *Archives of Ophthalmology* 107: 199-203.

Heijl, A. (1989b). Lack of diffuse loss of differential light sensitivity in early glaucoma. *Acta Ophthalmologica* 67: 353-360.

Heijl, A. (1993). Perimetric point density and detection of glaucomatous visual field loss. *Acta Ophthalmologica* 71: 445-450.

Heijl, A. and Bengtsson, B. (1996). The effect of perimetric experience in patients with glaucoma. *Archives of Ophthalmology* 114: 19-22.

Heijl, A., Lindgren, A. and Lindgren, G. (1989a). Test-retest variability in glaucomatous visual field. *American Journal of Ophthalmology* 108: 130-135.

Heijl, A., Lindgren, G. and Lindgren, A. (1990/1991). *Extended empirical statistical package for evaluation of single and multiple field in glaucoma: Statpac 2.* Perimetry Update. R. P. Mills and A. Heijl. Amsterdam, Kugler & Ghedini: 303-315.

Heijl, A., Lindgren, G. and Olsson, J. (1987). A package for the statistical analysis of visual fields. *Documenta Ophthalmologica Proceedings Series* 49: 153-168.

Heijl, A., Lindgren, G., Olsson, J. and Asman, P. (1989b). Visual field interpretation with empiric probability maps. *Archives of Ophthalmology* 107: 204-208.

Heijl, A. and Lundqvist, L. (1984). The frequency-distribution of earliest glaucomatous visual-field defects documented by automatic perimetry. *Acta Ophthalmologica* 62: 658-664.

Henkind, P. (1967). Radial peripapillary capillaries of the retina. Anatomy: Human and comparative. *British Journal of Ophthalmology* 51: 115-123.

Henson, D. B., Artes, P. H. and Chauhan, B. C. (1999). Diffuse loss of sensitivity in early glaucoma. *Investigative Ophthalmology and Visual Science* 40: 3147-3151.

Hernandez, M. R., Andrzejewska, W. and Neufeld, A. H. (1990). Changes in the extracellular matrix of the human optic nerve head in primary open-angle glaucoma. *American Journal of Ophthalmology* 109: 180-188.

Hernandez, M. R., Luo, X. X., Andrzejewska, W. and Neufeld, A. H. (1989). Age-related changes in the extracellular matrix of the human optic nerve head. *American Journal of Ophthalmology* 107: 476-484.

Heron, G., Adams, A. J. and Husted, R. (1988). Central visual fields for short-wavelength sensitive pathways in glaucoma and ocular hypertension. *Investigative Ophthalmology and Visual Science* 29: 64-72.

Higginbotham, E. J., Kilimanjaro, H. A., Wilensky, J. T., Batenhorst, R. L. and Herman, D. (1989). The effect of caffeine on the IOP in glaucoma patients. *Ophthalmology* 5: 624-626.

Hill, D. W. (1976). Measurement of retinal blood flow. *Transactions of the Ophthalmological Society (UK)* 96: 199-201.

Hitchings, R., Varma, R. and Poinoosawmy, D. (1993). *Optic disc photographs*. The optic nerve in glaucoma. R. Varma and G. L. Spaeth. Philadelphia, J.B.Lippincott Company: 159-168.

Hodapp, E., Parrish, R. K. and Anderson, D. R. (1993). *Clinical decisions in glaucoma*. St Louis, Mosby.

Hogan, M. J., Alvarado, J. A. and Weddell, J. E. (1971). *Histology of the Human Eye. An atlas and textbook*. Philadelphia, London,Toronto, Mexico City, Sydney, Tokyo, Rio de Janeiro, W.B.Saunders Company.

Hoh, S. T., Greenfield, D. S., Mistlberger, A., Liebmann, J. M., Ishikawa, H. and Ritch, R. (2000). Optical coherence tomography and scanning laser polarimetry in normal, ocular hypertensive, and glaucomatous eyes. *American Journal of Ophthalmology* 129: 129-135.

Hoh, S. T., Ishikawa, H. and Greenfield, D. S. (1998). Peripapillary nerve fibre layer thickness measurement reproducibility using scanning laser polarimetry. *Journal of Glaucoma* 7: 12-15.

Hollo, G. (1997). Scanning laser Doppler flowmeter study of retinal and optic disk blood flow in glaucomatous patients (Correspondence). *American Journal of Ophthalmology* 123: 859-860.

Hollo, G., Greve, E. L. and Van den Berg, T. J. T. P. (1997a). Evaluation of the peripapillary circulation in healthy and glaucomatous eyes with scanning laser doppler flowmetry. *International Ophthalmology* 20: 71-77.

Hollo, G., van den Berg, T. J. T. P. and Greve, E. L. (1997b). Scanning laser Doppler flowmetry in glaucoma. *International Ophthalmology* 20: 63-70.

Hollows, F. C. and Graham, P. A. (1966). Intra-ocular pressure, glaucoma, and glaucoma suspects in a defined population. *British Journal of Ophthalmology* 50: 570-586.

Hosking, S. L. and Flanagan, J. G. (1996). Prospective study design for the Heidelberg Retina Tomograph: the effect of change in focus setting. *Graefe's Archive for Clinical and Experimental Ophthalmology* 234: 306-310.

Hoyt, W. F. and Frisen, L. (1973). Fundoscopy of nerve fibre layer defects in glaucoma. *Investigative Ophthalmology and Visual Science* 12: 814-829.

Hoyt, W. F. and Luis, O. (1962). Visual fiber anatomy in the infrageniculate pathway of the primate. *Archives of Ophthalmology* 68: 94-106.

Hoyt, W. F. and Newman, N. M. (1972). The earliest observable defect in glaucoma? *The Lancet*: 692-693.

Hoyt, W. F., Schlicke, B. and Eckelhoff, R. J. (1972). Fundoscopic appearance of a nerve fibre bundle defect. *British Journal of Ophthalmology* 56: 577-583.

Hoyt, W. F. and Tudor, R. C. (1963). The course of peripapillary temporal retinal axons through the anterior optic nerve. *Archives of Ophthalmology* 69: 503-507.

Huang, D., Swanson, E. A., Lin, C. P., Schuman, J. S., Stinson, W. G., Chang, W., Hee, M. R., Flotte, T., Gregory, K., Puliafito, C. A. and Fujimoto, J. G. (1991). Optical coherence tomography. *Science* 254: 1178-1181.

Huang, Y., Cideciyan, A. V., Papastergiou, G. I., Banin, E., Semple-Rowland, S. L., Milam, A. H. and Jacobson, S. G. (1998). Relation of Optical Coherence Tomography to microanatomy in normal and rd chickens. *Investigative Ophthalmology and Visual Science* 39: 2405-2416.

Hudson, C., Wild, J. and O'Neill, E. (1994). Fatigue effects during a single session of automated static perimetry. *Investigative Ophthalmology & Visual Science* 35: 268-280.

Hudson, C. and Wild, J. M. (1992). The assessment of physiological statokinetic dissociation by automated perimetry. *Investigative Ophthalmology and Visual Science* 33: 3162-3168.

Hudson, C., Wild, J. M. and Archer-Hall, J. (1993). Maximizing the dynamic range of the Humphrey Field Analyzer for blue-on-yellow perimetry. *Ophthalmic and Physiological Optics* 31: 405-408.

Hurvich, L. M. and Jameson, D. (1957). An opponent-process theory of colour vision. *Psychological Review* 64: 384-404.

Hutchings, N., Wild, J. M. and Hussey, M. K. (1993). The homogenous and heterogenous components of the long term fluctuation in glaucomatous field loss. *Investigative Ophthalmology and Visual Science* 34: 1263.

Iester, M., Broadway, D. C., Mikelberg, F. S. and Drance, S. M. (1997a). A comparison of healthy, ocular hypertensive, and glaucomatous optic disc topographic parameters. *Journal of Glaucoma* 6: 363-370.

Iester, M., Courtright, P. and Mikelberg, F. S. (1998). Retinal nerve fibre layer height in high-tension glaucoma and healthy eyes. *Journal of Glaucoma* 7: 1-7.

Iester, M., Courtright, P. and Mikelberg, F. S. (1999a). The confocal laser scanning discriminant analysis formula and measures of visual field. *Acta Ophthalmologica Scandinavica* 77: 64-66.

Iester, M., de Ferrari, R. and Zanini, M. (1999b). Topographic analysis to discriminate glaucomatous from Normal Optic Nerve Heads with a Confocal Scanning Laser: New Optic Disk analysis without any observer input. *Survey of Ophthalmology (Suppl)* 44: S33-S40.

Iester, M., Jonas, J. B., Mardin, C. Y. and Budde, W. M. (2000a). Discriminant analysis models for early detection of glaucomatous optic disc changes. *British Journal of Ophthalmology* 84: 464-468.

Iester, M., Mermoud, A. and Schnyder, C. (2000b). Frequency doubling technique in patients with ocular hypertension and glaucoma - Correlation with Octopus perimeter indices. *Ophthalmology* 107: 288-294.

Iester, M. and Mikelberg, F. (1997). The effect of optic disc size on diagnostic precision with the Heidelberg Retinal Tomogaph. *Ophthalmology* 104: 545-549.

Iester, M., Mikelberg, F. S., Swindale, N. V. and Drance, S. M. (1997b). ROC Analysis of Heidelberg Retina Tomograph optic disc shape measures in glaucoma. *Canadian Journal of Ophthalmology* 32: 382-388.

Iester, M. and Mikelberg, S. (1999). Optic nerve head morphologic characteristics in high-tension and normal-tension glaucoma. *Archives of Ophthalmology* 117: 1010-1013.

Iester, M., Pandolfo, A., Traverso, C. E., Zingirian, M. and Capris, P. (1999c). Frequency doubling technique. Learning effect, short and long term fluctuation. *Acta Ophthalmologica Scandinavica* 77: 15-16.

Iester, M., Swindale, M. V. and Mikelberg, F. S. (1997c). Sector-based analysis of optic nerve head shape parameters and visual field indices in healthy and glaucomatous eyes. *Journal of Glaucoma* 6: 371-376.

Irak, I., Zangwill, L., Garden, V., Shakiba, S. and Weinreb, R. N. (1996). Change in optic disk topography after trabeculectomy. *American Journal of Ophthalmology* 122: 690-695.

Iwata, K. (1979). Topographical analysis on the genesis of glaucomatous cupping. *Glaucoma* 1: 16.

Jaeger, E. (1858). Ueber Glaucom und Seine Hielung Durch Iridectomie. *Zeitschr Ges der Aerzte zu Wien* 14: 465-474, 484-491.

Jaffe, J., Alvarado, J. and Juster, R. (1986). Age-related changes of the normal visual field. *Archives of Ophthalmology* 104: 1021-1025.

James, C. B. and Smith, S. E. (1991). Pulsatile ocular blood flow in patients with low-tension glaucoma. *British Journal of Ophthalmology* 75: 466-470.

James, C. B., Trew, D. R. and Clark, K. (1991). Factors influencing the ocular pulse. Axial length. *Graefe's Archive for Clinical and Experimental Ophthalmology* 229: 341-344.

Janknecht, P. and Funk, J. (1994). Optic-Nerve Head Analyzer and Heidelberg Retina Tomograph: Accuracy and reproducibility of topographic measurements in a model eye and in volunteers. *British Journal of Ophthalmology* 78: 760-768.

Janknecht, P. and Funk, J. (1995). Optic-Nerve Head Analyzer and Heidelberg Retina Tomograph: Relative error and reproducibility of topographic measurements in a model eye with simulated cataracts. *Graefe's Archive for Clinical and Experimental Ophthalmology* 233: 523-529.

Jay, J. L. and Murdoch, J. R. (1993). The rate of visual field loss in untreated primary open angle glaucoma. *British Journal of Ophthalmology* 77: 176-178.

Johnson, B. M., Miao, M. and Sadun, A. A. (1987). Age-related decline of human optic nerve axon populations. *Age* 10: 5-9.

Johnson, C. A. (1994). Selective versus nonselective losses in glaucoma. *Jounal of Glaucoma* 3: s32-s44.

Johnson, C. A., Adams, A. J., Casson, E. J. and Brandt, J. D. (1993a). Blue-on-yellow perimetry can predict the development of glaucomatous visual field loss. *Archives of Ophthalmology* 111: 645-650.

Johnson, C. A., Adams, A. J., Casson, E. J. and Brandt, J. D. (1993b). Progression of early glaucomatous visual field loss as detected by blue-on-yellow and standard white-on-white automated perimetry. *Archives of Ophthalmology* 111: 651-656.

Johnson, C. A., Adams, A. J., Casson, E. J. and Nelson-Quigg, J. M. (1991). *Can short wavelength sensitivity losses predict the development of glaucomatous visual field defects?* Noninvasive assessment of the visual system. Washington, D.C. 1: 2216-2219.

Johnson, C. A., Adams, A. J., Twelker, J. D. and Quigg, J. M. (1988a). Age-related changes in the central visual field for short-wavelength-sensitive pathways. *Journal of the Optometric Society of America (A)* 5: 2131-2139.

Johnson, C. A., Adams, C. W. and Lewis, R. A. (1988b). Fatigue Effects in Automated Perimetry. *Applied Optics* 27: 1030-1037.

Johnson, C. A., Brandt, J. B., Khong, A. M. and Adams, A. J. (1995). Short-wavelength automated perimtery in low-, medium-, and high-risk ocular hypertensive eyes. *Archives of Ophthalmology* 113: 70-76.

Johnson, C. A. and Chauhan, B. C. (1992). Properties of staircase procedures for estimating thresholds in automated perimetry. *Investigative Ophthalmology and Visual Science* 33: 2966-2974.

Johnson, C. A., Cioffi, G. and Van Buskirk, E. M. (1999). Frequency doubling technology perimetry using a 24-2 stimulus presentation pattern. *Optometry and Vision Science* 76: 571-581.

Johnson, C. A. and Nelson-Quigg, J. M. (1993). A prospective three-year study of response properties of normal subjects and patients during automated perimetry. *Ophthalmology* 100: 269-274.

Johnson, C. A. and Samuels, S. J. (1997). Screening for glaucomatous visual field loss with frequency-doubling perimetry. *Investigative Ophthalmology and Visual Science* 38: 413-425.

Johnson, M. A. and Choy, D. (1987). On the definition of age-related norms for visual function testing. *Applied Optics* 26: 1449-1454.

Jonas, J., Konigsreuther, K. A. and Naumann, G. O. H. (1992a). Optic disc histomorphometry in normal eyes and eyes with secondary angle-closure glaucoma : I Intrapapillary region. *Graefe's Archive for Clinical and Experimental Ophthalmology* 230: 129-133.

Jonas, J. and Papastathopoulos, K. (1996). Optic disk shape in glaucoma. *Graefe's Archive for Clinical and Experimental Ophthalmology* 234 (Suppl 1): S167-173.

Jonas, J. B. and Dichtl, A. (1996). Evaluation of the retinal nerve fiber layer. *Survey of Ophthalmology* 40: 369-378.

Jonas, J. B. and Dichtl, A. (1997). Optic disc morphology in myopic primary open -angle glaucoma. *Graefe's Archive for Clinical and Experimental Ophthalmology* 235: 627-633.

Jonas, J. B., Fernandez, M. and Naumann, G. O. H. (1992b). Glaucomatous parapapillary atrophy: occurrence and correlations. *Archives of Ophthalmology* 110: 214-222.

Jonas, J. B., Fernandez, M. C. and Naumann, G. O. H. (1990a). Glaucomatous optic nerve atrophy in small discs with low cup-to-disk ratios. *Ophthalmology* 97: 1211-1215.

Jonas, J. B., Fernandez, M. C. and Sturmer, J. (1993). Pattern of glaucomatous neuroretinal rim loss. *Ophthalmology* 100: 63-68.

Jonas, J. B. and Grundler, A. E. (1997). Correlation between mean visual field loss and morphometric optic disk variables in the open-angle glaucomas. *American Journal of Ophthalmology* 124: 488-497.

Jonas, J. B., Gusek, G. C., Guggenmoos-Holzmann, I. and Naumann, G. O. H. (1988a). Optic disk, cup and neuroretinal rim size, configuration, and correlations in normal eyes. *Investigative Ophthalmology and Visual Science* 29: 1151-1158.

Jonas, J. B., Gusek, G. C., Guggenmoos-Holzmann, I. and Naumann, G. O. H. (1988b). Size of the optic nerve scleral canal and comparison with intravital determination of optic disk dimensions. *Graefe's Archive for Clinical and Experimental Ophthalmology* 226: 213-215.

Jonas, J. B., Gusek, G. C. and Hernandez, M. C. (1991a). Correlation of the blind spot size to the area of the optic disk and parapapillary atrophy. *American Journal of Ophthalmology* 111: 559-565.

Jonas, J. B., Gusek, G. C. and Hernandez, M. C. (1991b). Correlation of the optic disc size to glaucoma susceptibility. *Ophthalmology* 98: 675-680.

Jonas, J. B., Gusek, G. C. and Naumann, G. O. H. (1988c). Optic disk morphometry in chronic primary open-angle glaucoma: I. Morphometric intrapapillary characteristics. *Graefe's Archive for Clinical and Experimental Ophthalmology* 226: 522-530.

Jonas, J. B., Gusek, G. C. and Naumann, G. O. H. (1988d). Optic disk morphometry in chronic primary open-angle glaucoma: II. Correlation of the intrapapilllary parameters to visual field indices. *Graefe's Archive for Clinical and Experimental Ophthalmology* 226: 531-538.

Jonas, J. B., Gusek, G. C. and Naumann, G. O. H. (1988e). Optic disk morphometry in high myopia. *Graefe's Archive for Clinical and Experimental Ophthalmology* 226: 587-590.

Jonas, J. B., Muller-Bergh, J. A., Schlortzer-Schrehardt, U. M. and Naumann, G. O. H. (1990b). Histomorphometry of the human optic nerve. *Investigative Ophthalmology and Visual Science* 31: 736-744.

Jonas, J. B. and Naumann, G. O. H. (1989a). Parapapillary chorioretinal atrophy in normal and glaucoma eyes: II. Correlations. *Investigative Ophthalmology & Visual Science* 30: 919-926.

Jonas, J. B. and Naumann, G. O. H. (1989b). Parapapillary retinal vessel diameter in normal and glaucoma eyes: I. Morphometric data. *Investigative Ophthalmology and Visual Science* 30: 1599-1603.

Jonas, J. B., Nguyen, N. X., Guseh, G. C. and Naumann, G. O. H. (1989a). Parapapillary chorioretinal atrophy in normal and glaucoma eyes: I. Morphometric data. *Investigative Ophthalmology & Visual Science* 30: 908-918.

Jonas, J. B., Nguyen, N. X. and Naumann, G. O. H. (1989b). The retinal nerve fiber layer in normal eyes. *Ophthalmology* 96: 627-632.

Jonas, J. B. and Schiro, D. (1993). Visibility of the normal retinal nerve fibre layer correlated with rim width and vessel caliber. *Graefe's Archive for Clinical and Experimental Ophthalmology* 231: 207-211.

Jonas, J. B. and Schiro, D. (1994). Localized wedge shaped defects of the retinal nerve fibre layer in glaucoma. *British Journal of Ophthalmology* 78: 285-290.

Jonas, J. B., Schmidt, A. M., Muller-Bergh, J. A., Scholtzer-Schrehardt, U. M. and Naumann, G. O. H. (1992c). Human optic nerve count and optic disc size. *Investigative Ophthalmology and Visual Science* 33: 2012-2008.

Jonas, J. B. and Xu, I. (1993). Parapapillary chorioretinal atrophy in normal-pressure glaucoma. *American Journal of Ophthalmology* 115: 501-505.

Jonas, J. B. and Xu, I. (1994). Optic disk hemorrhages in glaucoma. *American Journal of Ophthalmology* 118: 1-8.

Jonas, J. B., Zach, F.-M., Gusek, G. C. and Naumann, G. O. H. (1989c). Pseudoglaucomatous physiologic large cups. *American Journal of Ophthalmology* 107: 137-144.

Jonescu-Cuypers, C. P., Thumann, G., Hilgers, R.-D., Bartz-Schmidt, K. U., Krott, R. and Kriegelstein, G. K. (1998). Long-term fluctuations of the normalised rim/disc area ratio quotient in normal eyes. *Graefe's Archive for Clinical and Experimental Ophthalmology* 237: 181-186.

Joos, K. M., Pillunat, L. E., Knighton, R. W., Anderson, D. R. and Feuer, W. (1997). Reproducibility of Laser Doppler Flowmetry in the Human Optic Nerve Head. *Journal of Glaucoma* 6: 212-216.

Junghardt, A., Schmid, M. K., Schipper, I., Wildberger, H. and Seifert, B. (1996). Reproducibility of the data determined by Scanning Laser Polarimetry. *Graefe's Archive for Clinical and Experimental Ophthalmology* 234: 628-632.

Kagemann, L., Harris, A., Chung, H. S., Evans, D. and Buck, S. (1998). Heidelberg retinal flowmetry: factors affecting blood flow measurement. *British Journal of Ophthalmology* 82: 131-136.

Kagemann, L., Harris, A., Chung, H. S., Martin, B. J., Kiesling, K. and Elvambuena, R. (1999). Pointwise analysis reveals that Heidelberg Retinal Flowmeter measurements of human retinal blood flow are influenced by illumination level. *Investigative Ophthalmology and Visual Science* 40: S508.

Kanellopoulos, J., Erickson, K. and Netland, P. (1996). Systemic calcium channel blockers and glaucoma. *Journal of Glaucoma* 5: 357-362.

Kaplan, E. and Shapley, R. M. (1986). X and Y cells in the lateral geniculate nucleus of macaque monkeys. *Journal of Physiology* 330: 125-143.

Kaplan, E. and Shapley, R. M. (1990). New views of primate retinal function. *Progress in Retinal Research* 9: 273-336.

Katz, J. and Sommer, A. (1988). Reliability indexes of automated perimetric tests. *Archives of Ophthalmology* 106: 1252-1254.

Kelly, D. (1966). Frequency doubling in visual responses. *Journal of the Optometric Society of America* 56: 1628-1633.

Kelly, D. H. (1981). Non-linear visual responses to flickering sinusoidal gratings. *Journal of the Optometric Society of America* 71: 1051-1055.

Kerr, J., Nelson, P. and O'Brien, C. (1998). A comparison of ocular blood flow in untreated primary open-angle glaucoma and ocular hypertension. *American Journal of Ophthalmology* 126: 42-51.

King, A. J. W., Bolton, N., Aspinall, P. and O'Brien, C. (2000). Measurement of peripapillary retinal nerve fibre layer volume in glaucoma. *American Journal of Ophthalmology* 129: 599-607.

Klein, B. E. K., Klein, R. and Ritter, L. L. (1993). Relationship of drinking alcohol and smoking to prevalence of open-angle glaucoma. *Ophthalmology* 100: 1609-1613.

Klein, B. E. K., Klein, R., Sponsel, W. E., Franke, T., Cantor, L. B., Martone, J. and Menage, M. J. (1992). Prevalence of Glaucoma: The Beaver Dam Study. *Ophthalmology* 99: 1499-1504.

Knighton, R. W., Bavarez, C. and Bharracharya, A. (1992). The directional reflectance of the nerve fibre layer of the toad. *Investigative Ophthalmology and Visual Science* 33: 2603-2611.

Knighton, R. W. and Huang, K.-R. (1999a). Directional and spectral reflectance of the rat retinal nerve fibre layer. *Investigative Ophthalmology and Visual Science* 40: 639-647.

Knighton, R. W. and Huang, K.-R. (1999b). Visible and near infra-red imaging of the nerve fibre layer of the isolated rat retina. *Journal of Glaucoma* 8: 31-37.

Knighton, R. W., Jacobson, S. G. and Kemp, C. M. (1989). The spectral reflectance of the nerve fibre layer of the macaque retina. *Investigative Ophthalmology and Visual Science* 30: 2393-2402.

Knighton, R. W. and Qian, C. (2000). An optical model of the human retinal nerve fiber layer: Implications of directional reflectance for variability of clinical measurements. *Journal of Glaucoma* 9: 56-62.

Knighton, R. W. and Zhou, Q. (1995). The relation between the reflectance and thickness of the retinal nerve fibre layer. *Journal of Glaucoma* 4: 117-123.

Kondo, Y., Yamamoto, T. and Sato, Y. (1998). A frequency-doubling perimetric study in normal-tension glaucoma with hemi-field defect. *Journal of Glaucoma* 7: 261-265.

Kono, Y., Zangwill, L., Sample, P., Jonas, J. B., Emdadi, A., Gupta, N. and Weinreb, R. N. (1999). Relationship between parapapillary atrophy and visual field abnormality in primary open-angle glaucoma. *Archives of Ophthalmology* 127: 674-680.

Kothe, A. C. (1994). The effect of posture on intraocular pressure and pulsatile ocular blood flow in normal and glaucomatous eyes. *Survey of Ophthalmology* 38: S191-S197.

Krakau, C. E. T. (1992). Calculation of the pulsatile ocular blood flow. *Investigative Ophthalmology and Visual Science* 33: 2754-2756.

Kruse, F. E., Burk, R. O. W., Volcker, H. E., Zinser, G. and Harbarth, U. (1989). Reproducibility of topographic measurements of the optic-nerve head with laser tomographic scanning. *Ophthalmology* 96: 1320-1324.

Kubota, T., Jonas, J. B. and Naumann, G. O. H. (1993). Direct Clinico-Histological Correlation of Parapapillary Chorioretinal Atrophy. *British Journal of Ophthalmology* 77: 103-106.

Lachenmayr, B. J., Drance, S. M., Chauhan, B. C., House, P. H. and Lalani, S. (1991). Diffuse and localized glaucomatous field loss in light-sense, flicker and resolution perimetry. *Graefes Archive For Clinical and Experimental Ophthalmology* 229: 267-273.

Langham, M. E., Farrell, R. A., O'Brien, V., Silver, D. M. and Schilder, P. (1989). Blood flow in the human eye. *Acta Ophthalmologica (supplementum)* 67: 9-13.

Langhans, M., Michelson, G. and Grom, M. (1997). Effect of breathing 100% oxygen on retinal and optic nerve head capillary blood flow in smokers and non-smokers. *British Journal of Ophthalmology* 81: 365-369.

Lee, B. B. (1996). Receptive field structure in the primate retina. *Vision Research* 36: 631-644.

Lee, S. S. and Schwartz, B. (1992). Role of the temporal cilioretinal artery in retaining central visual field in open -angle glaucoma. *Ophthalmology* 99: 696-699.

Lemij, H. G., de Vries, J. and Tjon-Fo-Sang, M. J. (1995). Retinal nerve fibre layer thickness in humans as determined with the Nerve Fibre Analzer. *Investigative Ophthalmology and Visual Science* 36: S973.

Lennie, P. (1980). Parallel visual pathways: A Review. *Vision Research* 20: 561-594.

Leske, M. C. (1983). The epidemiology of open-angle glaucoma. *American Journal of Epidemiology* 118: 166-191.

Levene, R. Z. (1980). Low-Tension Glaucoma: A Critical Review and New Material. *Survey of Ophthalmology* 24: 621-664.

Lexer, F., Hitzenberger, C. K., Fercher, A. F. and Kulhavy, M. (1997). Wavelength-tuning interferometry of intraocular distances. *Applied Optics* 36: 6548-6553.

Lichter, P. R. (1976). Variability of expert observers in evaluating the optic disc. *Transactions of the Ophthalmological Society (UK)* 74: 532-572.

Lim, C. S., O'Brien, C. and Bolton, N. M. (1996). A simple clinical method to measure the optic disc size in glaucoma. *Journal of Glaucoma* 5: 241-245.

Lindenmuth, K. A., Skuta, G. L., Rabbani, R. and Musch, D. C. (1989). Effects of pupillary constriction on automated perimetry in normal eyes. *Ophthalmology* 96: 1298-1301.

Lindenmuth, K. A., Skuta, G. L., Rabbani, R., Musch, D. C. and Bergstrom, T. J. (1990). Effects of pupillary dilation on automated perimetry in normal patients. *Ophthalmology* 97: 367-370.

Littmann, H. and Williams, T. G. (1992). Determination of the true size of an object on the fundus of the living eye. *Optometry and Vision Science* 69: 717-720.

Livingstone, M. S. and Hubel, D. H. (1987). Psychophysical evidence for separate channels for the perception of form, colour, movement and depth. *Journal of Neuroscience* 7: 3416-3468.

Lorfi, K. and Grunwald, J. E. (1991). The effect of caffeine on the human macula circulation. *Investigative Ophthalmology and Visual Science* 32: 3028-3032.

Lusky, M., Bosem, M. and Weinreb, R. N. (1993). Reproducibility of optic nerve head topography measurements in eyes with undilated pupils. *Journal of Glaucoma* 2: 104-109.

Lynn, J. R. (1969). Examination of the field in glaucoma. *Investigative Ophthalmology and Visual Science* 8: 76-86.

Maddess, T., Bedford, S., James, A. C. and Rose, K. A. (1997). A multiple frequency PERG investigation of the frequency doubled illusion. *Investigative Ophthalmology and Visual Science*: s.363.

Maddess, T., Hemmi, J. M. and James, A. C. (1992). Evidence for spatial aliasing effects in the Y-like cells of the magnocellular visual pathway. *Vision Research* 38: 1843-1859.

Maddess, T. and Henry, G. H. (1992). Performance of nonlinear visual units in ocular hypertension and glaucoma. *Clinical Vision Science* 7: 371-383.

Mainster, M. (1982). Scanning Laser Ophthalmoscope. *Ophthalmology* 89: 852-857.

Malinovsky, V. E. (1996). An overview of the Heidelberg Retina Tomograph. *Journal of the American Optometric Association* 67: 457-467.

Manual-FDT (1997). Frequency Doubling Technology User's Guide. Skaneateles Falls, New York, Welch Allyn Inc. Medical Products.

Manual-HRT (1997). Heidelberg Retina Tomograph Operation Manual Version 2.01-0. Heidelberg, Germany, Heidelberg Engineering GmbH.

Manual-OCT (1996). Optical Coherence Tomography Users Manual: A4 Software Guide. San Leandro, California, USA, Humphrey Instruments.

Manual-OCTOPUS (1990). Octopus 1-2-3 operating instructions. Revision 1. Switzerland, Interzeag AG, Schlieren.

Mardin, C. and Horn, F. K. (1998). Influence of optic disc size on the sensitivity of the Heidelberg retina tomograph. *Graefe's Archive for Clinical and Experimental Ophthalmology* 236: 641-645.

Mardin, C., Horn, F. K., Jonas, J. B. and Budd, W. M. (1999). Preperimetric glaucoma diagnosis by confocal scanning laser tomography of the optic disc. *British Journal of Ophthalmology* 83: 299-304.

Marraffa, M., Mansoldo, C., Morbio, R., DeNatale, R., Tomazzoli, L. and Bonomi, L. (1997). Does nerve fiber layer thickness correlate with visual field defects in glaucoma? A study with the nerve fiber analyzer. *Ophthalmologica* 211: 338-340.

Massey, A., Geyer, O. and Silver, D. M. (1999). The effect of eye volume and age on pulsatile ocular blood flow. *Investigative Ophthalmology and Visual Science* 40: s490.

Mathew, R. J. and Wilson, W. H. (1985). Caffeine induced changes in cerebral circulation. *Stroke* 5: 814-817.

Meyer, J. H., Guhlmann, M. and Funk, J. (1997). Blind spot size depends on the optic disc topography: A study using SLO controlled scotometry and the Heidelberg retina tomograph. *British Journal of Ophthalmology* 81: 355-359.

Michelson, G., Langhans, M. J. and Groh, M. J. M. (1996a). Perfusion of the juxtapapillary retina and the neuroretinal rim area in primary open-angle glaucoma. *Journal of Glaucoma* 5: 91-98.

Michelson, G., Langhans, M. J., Harazny, J. and Dichtl, A. (1998a). Visual field defect and perfusion of the juxtapapillary retina and the neuroretinal rim area in primary open angle glaucoma. *Graefe's Archive for Clinical and Experimental Ophthalmology* 236: 80-85.

Michelson, G. and Schmauss, B. (1995). Two-dimensional mapping of the perfusion of the retina and optic nerve head. *British Journal of Ophthalmology* 79: 1126-1132.

Michelson, G., Schmauss, B., Langhans, M. J., Harazny, J. and Groh, M. J. M. (1996b). Principle, validity, and reliability of scanning laser-doppler flowmetry. *Journal of Glaucoma* 5: 99-105.

Michelson, G., Welzenbach, J., Pal, I. and Harazny, J. (1998b). Automatic full-field analyses of perfusion images gained by scanning laser doppler flowmetry. *British Journal of Ophthalmology* 82: 1294-1300.

Mikelberg, F. S. (1993). Reproducibility of topographic parameters obtained with the Heidelberg Retinal Tomograph. *Journal of Glaucoma* 2: 101-103.

Mikelberg, F. S. (1995). Ability of the Heidelberg Retinal Tomograph to detect early glaucomatous visual field loss. *Journal of Glaucoma* 4: 242-247.

Mikelberg, F. S., Douglas, G. R., Schulzer, M., Airaksinen, P. J., Wijsman, K. and Mawson, D. (1986a). The correlation between cup-disk ratio, neuroretinal rim area, and optic disk area measured by the video-ophthalmograph (Rodenstock Analyzer) and clinical measurement. *American Journal of Ophthalmology* 101: 7-12.

Mikelberg, F. S., Drance, S. M., Schulzer, M., Yidegiligne, H. M. and Weis, M. M. (1989). The normal human optic nerve. Axon count and axon diameter distribution. *Ophthalmology* 96: 1325-1328.

Mikelberg, F. S., Schulzer, M., Drance, S. M. and Lau, W. (1986b). The rate of progression of scotomas in glaucoma. *American Journal of Ophthalmology* 101: 1-6.

Mikelberg, F. S., Yidegiligne, H. M., White, V. A. and Schulzer, M. (1991). Relation between optic nerve axon number and axon diameter to scleral canal area. *Ophthalmology* 98: 60-63.

Miller, J. M. and Caprioli, J. (1992). An optimal reference plane to detect glaucomatous nerve fibre layer abnormalities with computerized image analysis. *Graefe's Archive for Clinical and Experimental Ophthalmology* 230: 124-128.

Miller, K. M. and Quigley, H. A. (1988). The clinical appearance of the lamina cribrosa as a function of the extent of glaucomatous optic nerve damage. *Ophthalmology* 95: 135-138.

Mills, R. P., Barnabey, H. S., Migliazzo, C. V. and Li, Y. (1993). Does saving time using FASTPAC or suprathreshold testing reduce quality of visual fields. *Ophthalmology* 101: 1596-1603.

Minckler, D. (1980). The organization of nerve fibre bundles in the primate optic nerve head. *Archives of Ophthalmology* 98: 1630-1636.

Minckler, D. S. and Spaeth, G. L. (1981). Optic nerve damage in glaucoma. *Survey of Ophthalmology* 26: 128-148.

Mistlberger, A., Liebmann, Greenfield, D. S., Pons, M. E., Hoh, S.-H., Ishikawa, H. and Ritch, R. (1999). Heidelberg retina tomography and Optical Coherence Tomography in normal, ocular hypertensive, and glaucomatous eyes. *Ophthalmology* 106: 2027-2032.

Morgan, J. E. (1994). Selective cell death in glaucoma: does it really occur? *British Journal of Ophthalmology* 78: 875-880.

Morgan, J. E., Uchida, H. and Caprioli, J. (2000). Retinal ganglion cell death in experimental glaucoma. *British Journal of Ophthalmology* 84: 303-310.

Morgan, J. E., Waldock, A., Jeffery, G. and Cowey, A. (1998). Retinal nerve fibre layer polarimetry: histological and clinical comparison. *British Journal of Ophthalmology* 82: 684-490.

Morgan, R. K., Feuer, W. J. and Anderson, D. R. (1991). Statpac 2 glaucoma change probability. *Archives of Ophthalmology* 109: 1690-1692.

Moss, I. D., Wild, J. M. and Whitaker, D. J. (1995). The influence of age-related cataract on blue-on-yellow perimetry. *Investigative Ophthalmology and Visual Science* 36: 764-773.

Nasemann, J. E. and Burk, R. O. W., Eds. (1990). *Scanning laser ophthalmoscopy and tomography*. Munchen, Quintessenz.

Nevarez, J., Rockwood, E. J. and Anderson, D. R. (1988). The configuration of peripapillary tissue in unilateral glaucoma. *Archives of Ophthalmology* 106: 901-903.

Nickells, R. W. (1996). Retinal ganglion cell death in glaucoma: The How, the Why, and the Maybe. *Journal of Glaucoma* 5: 345-356.

Nicolela, M. T., Drance, S. M., Rankin, S. J., Buckley, A. R. and Walman, B. E. (1996a). Color Doppler imaging in patients with asymmetric glaucoma and unilateral visual field loss. *American Journal of Ophthalmology* 121: 502-510.

Nicolela, M. T., Hnik, P. and Drance, S. M. (1996b). Scanning Laser-Doppler Flowmeter study of retinal and optic disk blood-flow in glaucomatous patients. *American Journal of Ophthalmology* 122: 775-783.

Nicolela, M. T., Hnik, P., Schulzer, M. and Drance, S. M. (1997). Reproducibility of retinal and optic nerve head blood flow measurements with scanning laser Doppler flowmetry. *Journal of Glaucoma* 6: 157-164.

Niessen, A. G. J. E., Vandenberg, T. J. T. P., Langerhorst, C. T. and Greve, E. L. (1996). Retinal nerve fiber layer assessment by Scanning Laser Polarimetry and standardized photography. *American Journal of Ophthalmology* 121: 484-493.

O'Brien, C. (1998). Vasospasm and glaucoma. *British Journal of Ophthalmology* 82: 855-857.

O'Connor, D. J., Zeyen, T. and Caprioli, J. (1993). Comparisons of methods to detect glaucomatous optic-nerve damage. *Ophthalmology* 100: 1498-1503.

Odberg, T. and Riise, D. (1985). Early diagnosis of glaucoma. The value of successive stereophotography of the optic disc. *Acta Ophthalmologica* 63: 257.

Ogden, T. E. (1978). Nerve fibre layer astrocytes of the primate retina: morphology, distribution and density. *Investigative Ophthalmology and Visual Science* 17: 499-510.

Ogden, T. E. (1983a). Nerve fibre layer of the macaque retina: retinotopic organization. *Investigative Ophthalmology and Visual Science* 24: 85-98.

Ogden, T. E. (1983b). Nerve fibre layer of the primate retina: Thickness and glial content. *Vision Research* 23: 581-587.

Ogden, T. E. (1984). Nerve fibre layer of the primate retina: morphological analysis. *Investigative Ophthalmology and Visual Science* 25: 19-29.

Ohno-Matsui, K., Futagami, S., Yamashita, S. and Tokoro, T. (1998). Zinn-Haller arterial ring observed by ICG angiography in high myopia. *British Journal of Ophthalmology* 82: 1357-1362.

Onda, E. (1995). Microvasculative of the human optic nerve. *American Journal of Ophthalmology* 120: 92-102.

Orgül, S., Cioffi, G. A. and Bacon, D. R. (1996). Sources of variability of topometric data with a scanning laser opthalmoscope. *Archives of Ophthalmology* 114: 161-164.

Orgül, S., Cioffi, G. A. and Van Buskirk, E. M. (1997). Variability of contour line alignment on sequential images with the Heidelberg Retina Tomograph. *Graefe's Archive for Clinical and Experimental Ophthalmology* 235: 82-86.

Orgül, S. and Meyer, P. (1995). Physiology of blood flow regulation and mechanisms involved in optic neuropathy. *Journal of Glaucoma* 4: 427-443.

Osborne, N. N., Wood, J. P. M., Chidlow, G., Bae, J.-H., Melena, J. and Nash, M. S. (1999). Ganglion cell death in glaucoma: what do we really know? *British Journal of Ophthalmology* 83: 980-986.

Pacey, I. E. P. (1998). Variability of the Perimetric Response in Normals and in Glaucoma (PhD Thesis). Vision Sciences,. Birmingham, University of Aston: 1-287.

Padgham, C. A. and Saunders, J. E. (1975). *The perception of light and colour.* London, G. Bell & Sons Ltd.

Pakter, H. M., Schuman, J. S., Hertzmark, E., Pieris, I. D., Pedut-Kloizman, T., Hee, M. R., Pieroth, L., Szwartz, J. C., Puliafito, C. A., Fujimoto, J. G. and Swanson, E. A. (1995). Normative database of nerve fiber layer thickness by age as measured by Optical Coherence Tomography (ARVO Abstract). *Investigative Ophthalmology and Visual Science* 39: S932.

Panda-Jonas, S., Jonas, J. B. and Jakobcyk-Zmija, M. (1995). Retinal photoreceptor density decreases with age. *Ophthalmology* 102: 1853-1859.

Parrish, R. K., Schiffman, J. and Anderson, D. R. (1984). Static and kinetic visual field testing. Reproducibility in normal volunteers. *Archives of Ophthalmology* 102: 1497-1502.

Patel, S. C., Friedman, D. S., Varadkar, P. and Robin, A. L. (2000). Algorithm for interpreting the results of frequency doubling perimetry. *American Journal of Ophthalmology* 129: 323-327.

Pederson, J. E. and Anderson, D. R. (1980). The mode of progressive disc cupping in ocular hypertension and glaucoma. *Archives of Ophthalmology* 98: 490-495.

Peli, E., Hedges, T. R., McInnes, T., Hamlin, J. and Schwartz, B. (1987). Nerve fibre layer photography: A comparative study. *Acta Ophthalmologica* 65: 71-80.

Perkins, E. S. and Phelps, C. S. (1982). Open-angle glaucoma, ocular hypertension, low tension glaucoma and refraction. *Archives of Ophthalmology* 100: 1462-1467.

Petrig, B. L. and Riva, C. E. (1996). *Optic nerve head laser doppler flowmetry: Principles and computer analysis.* Ocular Blood Flow. Glaucoma-Meeting. H. J. Kaiser, J. Flammer and P. Hendrickson. Basel, Karger: 120-127.

Petrig, B. L., Riva, C. E. and Hayreh, S. S. (1999). Laser doppler flowmetry and optic nerve head blood flow. *American Journal of Ophthalmology* 127: 413-425.

Phelps, C. D. and Corbett, J. J. (1985). Migraine and low tension glaucoma. *Investigative Ophthalmology and Visual Science* 26: 1105-1108.

Pieroth, L., Schuman, J. S., Hertzmark, E., Hee, M. R., Wilkins, J. R., Coker, J., Mattox, C., Pedut-Kloizman, T., Puliafito, C., Fujimoto, J. G. and Swanson, E. (1999). Evaluation of focal defects of the nerve fibre layer using optical coherence tomography. *Ophthalmology* 106: 570-579.

Pillunat, I. E., Kansow, U., Bohm, A. G., Hammard, P. and Richard, G. (1998). Diurnal ocular haemodynamics in primary open angle glaucoma. *Investigative Ophthalmology and Visual Science* 39: S896.

Piltz, J. R., Bose, S. and Lanchoney, D. (1998). The effect of Nimodipine, a centrally active calcium antagonist, on visual function and macular blood flow in patients with normal-tension glaucoma and control subjects. *Journal of Glaucoma* 7: 336-342.

Poinoosawmy, D., Fontana, L., Wu, J. X., Fitzke, F. W. and Hitchings, R. A. (1997). Variation of nerve fibre layer thickness measurements with age and ethnicity by scanning laser polarimetry. *British Journal of Ophthalmology* 81: 350-354.

Pollock, S. C. and Miller, N. R. (1986). The retinal nerve fibre layer. *International Opthalmology Clinic* 26: 201-221.

Polo, V., Abecia, E. and Pablo, L. E. (1998). Short wavelength automated perimetry and retinal nerve fibre layer evaluation in suspected cases of glaucoma. *Archives of Ophthalmology* 116: 1295-1298.

Polo, V., Pinilla, I., Abecia, E., Larrosa, J. M., Pablo, L. and Honrubia, F. M. (1997). Assessment of the ocular media absorption index. *International Ophthalmology* 20: 7-9.

Polyak, S. L. (1957). *The Vertebrate Visual System*. Chicago, University of Chicago Press.

Price, E. L., Gray, L. S. and Button, N. F. (1999). Sources of variation in the measurement of pulsatile ocular blood flow in normal subjects. *Investigative Ophthalmology and Visual Science* 40: s490.

Puliafito, C. A., Hee, M. R., Lin, C. P., Reichel, E., Schuman, J. S., Duker, J. S., Izatt, J. A., Swanson, E. A. and Fujimoto, J. G. (1995). Imaging of macular diseases with Optical Coherence Tomography. *Ophthalmology* 102: 217-229.

Puliafito, C. A., Hee, M. R., Schuman, J. S. and Fujimoto, J. G. (1996). *Optical Coherence Tomography of Ocular Diseases*. Thorofare, NJ, Slack Incorporated.

Quigley, H., Coleman, A. L. and Dorman-Pease, M. E. (1991). Large optic nerve heads have more nerve fibres in normal monkey eyes. *Archives of Ophthalmology* 109: 1441-1443.

Quigley, H., Dunkelberger, G. and Green, R. (1988). Chronic human glaucoma, causing selectively greater loss of large optic nerve fibres. *Ophthalmology* 95: 357-363.

Quigley, H., Enger, C., Katz, J. and Sommer, A. (1994). Risk factors for the development of glaucomatous visual field loss in ocular hypertension. *Archives of Ophthalmology* 112: 644-649.

Quigley, H., Hohman, R. M. and Addicks, E. (1983). Morphological changes in the lamina cribrosa correlated with neural loss in open-angle glaucoma. *American Journal of Ophthalmology* 95: 673-691.

Quigley, H. A. (1977). Cupping of the optic disc in ischaemic optic neuropathy. Symposium: Optic Nerve. *Transactions of the Ophthalmological Society (UK)* 83: 755-762.

Quigley, H. A. (1979). The histology of human glaucoma cupping and optic nerve damage: Clinicopathologic correlation in 21 eyes. *Ophthalmology* 86: 1803-1830.

Quigley, H. A. (1986). Chronic experimental glaucoma causes selectively greater loss of large optic nerve fibres. *Investigative Ophthalmology and Visual Science* 27: 42 (supp).

Quigley, H. A. (1993). Quantitative grading of nerve fibre layer photographs. *Ophthalmology* 100: 1800-1807.

Quigley, H. A. (1998). Identification of glaucoma-related visual field abnormality with the screening protocol of frequency doubling technology. *American Journal of Ophthalmology* 125: 819-829.

Quigley, H. A. and Addicks, E. M. (1980). Chronic experimental glaucoma in primates. II. Effect of extended intraocular pressure elevation on optic nerve head and axonal transport. *Investigative Ophthalmology and Visual Science* 19: 137-152.

Quigley, H. A. and Addicks, E. M. (1981). Regional differences in the structure of the lamina cribrosa and their relation to glaucomatous optic nerve damage. *Archives of Ophthalmology* 99: 137-143.

Quigley, H. A. and Addicks, E. M. (1982). Quantitative studies of retinal nerve fiber layer defects. *Archives of Ophthalmology* 100: 807-814.

Quigley, H. A., Addicks, E. M. and Green, R. (1981). Optic nerve damage in human glaucoma. II. The site of injury and susceptibility to damage. *Archives of Ophthalmology* 99: 635-649.

Quigley, H. A., Addicks, E. M. and Green, R. (1982a). Optic nerve damage in human glaucoma. I. Quantitative correlation with nerve fibre layer and visual field defect. Glaucoma, ischaemic neuropathy, papilloedema and toxic neuropathy. *Archives of Ophthalmology* 100: 135-146.

Quigley, H. A. and Anderson, D. R. (1976). The dynamics and location of axonal transport blockade by acute intraocular pressure elevation in primate optic nerve. *Investigative Ophthalmology and Visual Science* 15: 606-616.

Quigley, H. A. and Anderson, D. R. (1977). The histological basis of optic disk pallor in experimental optic atrophy. *American Journal of Ophthalmology*: 709-717.

Quigley, H. A., Brown, A. E., Morrison, J. D. and Drance, S. M. (1990). The size and shape of the optic disc in normal human eyes. *Archives of Ophthalmology* 108: 51-57.

Quigley, H. A., Dunkelberger, B. S. and Green, W. R. (1989). Retinal ganglion cell atrophy correlated with automated perimetry in human eyes with glaucoma. *American Journal of Ophthalmology* 107: 453-464.

Quigley, H. A., Hohman, R. and Addicks, E. M. (1982b). Quantitative study of optic nerve head capillaries in experimental optic disc pallor. *American Journal of Ophthalmology* 93: 689-699.

Quigley, H. A., Hohman, R. M., Addicks, E. M. and Green, R. (1984). Blood vesels of the glaucomatous optic disc in experimental primate and human eyes. *Investigative Ophthalmology and Visual Science* 25: 918-931.

Quigley, H. A., Miller, N. R. and George, T. (1980). Clinical evaluation of nerve fibre layer atrophy as an indicator of glaucomatous optic nerve damage. *Archives of Ophthalmology* 98: 1564-1571.

Quigley, H. A., Nickells, R. W., Kerrigan, L. A., Pease, M. E., Thibault, D. J. and Zack, D. J. (1995). Retinal ganglion-cell death in experimental glaucoma and after axotomy occurs by apoptosis. *Investigative Ophthalmology & Visual Science* 36: 774-786.

Quigley, H. A. and Sanchez, R. M. (1987). Chronic glaucoma selectively damages large optic nerve fibres. *Investigative Ophthalmology and Visual Science* 28: 913-920.

Quigley, H. A., Tielsch, J. M., Katz, J. and Sommer, A. (1996). Rate of progression in open-angle glaucoma estimated from cross- sectional prevalence of visual field damage. *American Journal of Ophthalmology* 122: 355-363.

Quigley, H. A., Varma, R., Tielsch, J. M., Kataz, J., Sommer, A. and Gilbert, D. L. (1999). The relationship between optic disc area and open-angle glaucoma: The Baltimore Eye Survey. *Journal of Glaucoma* 8: 347-352.

Radius, L. R. (1979). The course of axons through the retina and optic nerve head. *Archives of Ophthalmology* 97: 1154-1158.

Radius, L. R. (1980). Thickness of the retinal nerve fibre layer in primate eyes. *Archives of Ophthalmology* 98: 1625-1629.

Radius, L. R. and Anderson, D. R. (1979). The histology of retinal nerve fibre layer bundles and bundle defects. *Archives of Ophthalmology* 97: 948-950.

Radius, R. (1987). Anatomy of the optic nerve head and glaucomatous optic neuropathy. *Survey of Ophthalmology* 32: 35-44.

Radius, R. L. and Pederson, J. C. (1984). Laser-induced primate glaucoma. II. Histopathology. *Archives of Ophthalmology* 102: 1693-1698.

Ramrattan, R. S., Wolfs, R. C. W., Jonas, J. B., Hofman, A. and de Jong, P. T. V. M. (1999). Determinants of optic disc characteristics in a general population. The Rotterdam study. *Ophthalmology* 106: 1588-1596.

Rassam, S. M., Patel, V. and Kohner, E. M. (1993). The effect of acetazolamide on the retinal circulation. *Eye* 7: 697-702.

Ravalico, G., Pastorio, G., Croce, M. and Toffoli, G. (1997). Pulsatile ocular blood flow variations with axial length and refractive error. *Ophthalmologica* 211: 271-273.

Read, R. M. and Spaeth, G. L. (1974). The practical clinical appraisal of the optic disc in glaucoma, the natural history of cup progression and some specific disc-field correlations. *Transactions of the American Academy of Ophthalmology and Otolaryngology* 78: 255-274.

Rebolleda, G., Munoz, F. J., Fernandez Victorio, J. M., Pellicer, T. and Castillo, J. M. (1992). Effects of pupillary dilation on automated perimetry in glaucoma patients receiving pilocarpine. *Ophthalmology* 99: 418-423.

Repka, M. X. and Quigley, H. A. (1989). The effect of age on normal human optic nerve fibre number and diameter. *Ophthalmology* 96: 26-32.

Reyes, R. D. C., Tomita, G. and Kitazawa, Y. (1998). Retinal nerve fibre layer thickness within the area of apparently normal visual field in normal-tension glaucoma with hemifield defect. *Journal of Glaucoma* 7: 329-335.

Richards, W. and Felton, T. B. (1973). Spatial frequency doubling: Retinal or Central? *Vision Research* 13: 2129-2137.

Riva, C., Titze, P., Hero, M. and Petrig, B. L. (1997). Effect of acute decreases of perfusion pressure on choroidal blood flow in humans. *Investigative Ophthalmology and Visual Science* 38: 1752-1760.

Riva, C. E., Grunwald, J. E. and Perig, B. L. (1986). Autoregulation of human retinal blood flow an investigation with laser doppler velocimetry. *Investigative Ophthalmology and Visual Science* 27: 1706-1712.

Riva, C. E., Grunwald, J. E. and Petrig, B. L. (1983). Reactivity of the human retinal circulation to darkness: A laser doppler velocimetry study. *Investigative Ophthalmology and Visual Science* 24: 737-740.

Riva, C. E., Grunwald, J. E., Sinclair, S. H. and O'Keefe, K. (1981). Fundus camera based retinal LDV. *Applied Optics* 20: 117-120.

Riva, C. E., Grunwald, J. E., Sinclair, S. H. and Petrig, B. L. (1985). Blood velocity and volumetric flow rate in human retinal vessels. *Investigative Ophthalmology and Visual Science* 26: 1124-1132.

Riva, C. E., Harino, S., Petrig, B. L. and Shonat, R. D. (1992). Laser doppler flowmetry in the optic nerve. *Experimental Eye Research* 55: 499-506.

Rizzo, J. F. I., Feke, G. T., Goger, D. G., Ogasawara, H. and Weiter, J. J. (1991). Optic nerve head blood speed as a function of age in normal human subjects. *Investigative Ophthalmology and Visual Science* 32: 3263-3272.

Robert, Y., Steiner, D. and Hendrickson, P. (1989). Papillary circulation dynamics in glaucoma. *Graefe's Archive for Clinical and Experimental Ophthalmology* 227: 436-439.

Robinson, F., Petrig, B. L. and Riva, C. E. (1985). The acute effect of cigarette smoking on macular capillary blood flow in humans. *Investigative Ophthalmology and Visual Science* 26: 609-613.

Rodieck, R. W. (1991). *Which cells code for color?* From pigments to perception: Advances in understanding visual processes. A. Valberg and B. B. Lee. New York, Plenum Press: 83-93.

Roff, E. J., Harris, A., Chung, H. S., Hosking, S. L., Morrison, A. M., Halter, P. J. and Kageman, L. (1999). Comprehensive assessment of retinal, choroidal and retrobulbar haemodynamics during blood gas pertubation. *Graefe's Archive for Clinical and Experimental Ophthalmology* 237: 984-990.

Rohrschneider, K., Burk, R. O. W., Kruse, F. E. and Volcker, H. E. (1994). Reproducibility of the optic-nerve head topography with a new Laser Tomographic Scanning device. *Ophthalmology* 101: 1044-1049.

Rohrschneider, K., Burk, R. O. W. and Volker, H. C. (1993). Reproducibility of topometric data acquisition in normal and glaucomatous optic nerve heads with the laser tomographic scanner. *Graefe's Archive for Clinical and Experimental Ophthalmology* 23: 45-56.

Rojanapongpun, P. and Drance, S. M. (1993). The effects of nicotine on the blood flow of the ophthalmic artery and the finger circulation. *Graefe's Archive for Clinical and Experimental Ophthalmology* 231: 371-374.

Ruben, S. T., Hitchings, R. A., Fitzke, F. and Arden, G. B. (1994). Electrophysiology and psychophysics in ocular hypertension and glaucoma: Evidence for different pathomechanisms in early glaucoma. *Eye* 8: 516-520.

Rudnicka, A. R., Burk, R. O. W., Edgar, D. F. and Fitzke, F. W. (1998). Magnification characteristics of fundus imaging systems. *Ophthalmology* 105: 2186-2192.

Ruskell, G. (1998). Blood flow in the Zinn-Haller circle. *British Journal of Ophthalmology* 82: 1351-1353.

Sample, P., Weinreb, R. N. and Boynton, R. M. (1986a). Acquired dyschromatopsia in glaucoma. *Survey of Ophthalmology* 31: 54-64.

Sample, P. A., Bosworth, C. F. and Weinreb, R. N. (1997a). Short-wavelength automated perimetry and motion automated perimetry in patients with glaucoma. *Archives of Ophthalmology* 115: 1129-1133.

Sample, P. A., Boynton, R. M. and Weinreb, R. N. (1988). Isolating the color vision loss in primary open-angle glaucoma. *American Journal of Ophthalmology* 106: 686-691.

Sample, P. A., Irak, I., Martinez, G. A. and Yamagishi, N. (1997b). Asymmetries in the normal short-wavelength visual field: Implications for short-wavelength automated perimetry. *American Journal of Ophthalmology* 124: 46-52.

Sample, P. A., Johnson, C. A., Haegerstrom-Portnoy, G. and Adams, A. J. (1996). Optimum parameters for short-wavelength automated perimetry. *Journal of Glaucoma* 5: 375-383.

Sample, P. A., Martinez, G. A. and Weinreb, R. N. (1994). Short-wavelength automated perimetry without lens density testing. *American Journal of Ophthalmology* 118: 632-641.

Sample, P. A., Taylor, J. D., Martinez, G. A., Lusky, M. and Weinreb, R. N. (1993). Short-wavelength color visual fields in glaucoma suspects at risk. *American Journal of Ophthalmology* 115: 225-233.

Sample, P. A. and Weinreb, R. N. (1990). Color perimetry for assessment of primary open-angle glaucoma. *Investigative Ophthalmology and Visual Science* 31: 1869-1875.

Sample, P. A. and Weinreb, R. N. (1992). Progressive color visual field loss in glaucoma. *Investigative Ophthalmology and Visual Science* 33: 2068-2071.

Sample, P. A., Weinreb, R. N. and Boynton, R. M. (1986b). Blue-on-yellow color perimetry. *Investigative Ophthalmology and Visual Science (Suppl)* 27: 159.

Samuelson, T. W. and Spaeth, G. L. (1993). Focal and diffuse visual field defects: Their relationship to intraocular pressure. *Ophthalmic Surgery* 24: 519-525.

Sanabria, O., Feuer, W. J. and Anderson, D. R. (1991). Pseudo-loss of fixation in automated perimetry. *Ophthalmology* 98: 76-78.

Sanchez, R. M., Dunkelberger, G. R. and Quigley, H. A. (1986). The Number and Diameter Distribution of Axons in the Monkey Optic- Nerve. *Investigative Ophthalmology & Visual Science* 27: 1342-1350.

Saruhan, A., Orgül, S., Kocak, I., Prünte, C. and Flammer, J. (1998). Descriptive information of topographic parameters computed at the opic disc nerve head with the Heidelberg Retina Tomograph. *Journal of Glaucoma* 7: 420-429.

Schuman, J. S., Hee, M. R., Arya, A. V., Pedut-Kloizman, T., Puliafito, C. A., Fujimoto, J. G. and Swanson, E. A. (1995a). Optical Coherence Tomography: A new tool for glaucoma diagnosis. *Current Opinion in Ophthalmology* 6: 89-95.

Schuman, J. S., Hee, M. R., Puliafito, C. A., Wong, C., Pedut-Kloizman, T., Lin, C. P., Hertzmark, E., Izatt, J. A., Swanson, E. A. and Fujimoto, J. G. (1995b). Quantification of nerve-fiber layer thickness in normal and glaucomatous eyes using Optical Coherence Tomography - a pilot-study. *Archives of Ophthalmology* 113: 586-596.

Schuman, J. S., Pedut-Kloizman, T., Hertzmark, E., Hee, M. R., Wilkins, J. R., Coker, J. G., Puliafito, C. A., Fujimoto, J. G. and Swanson, E. A. (1996). Reproducibility of nerve fiber layer thickness measurements using Optical Coherence Tomography. *Ophthalmology* 103: 1889-1898.

Schwartz, B. and Kern, J. (1980). Age, increased ocular and blood pressures and retinal and disk fluorescein angiogram. *Archives of Ophthalmology* 98: 1980-1986.

Shapley, R. (1993). *Retinal ganglion cell function*. The optic nerve in glaucoma. R. Varma and G. L. Spaeth. Philadelphia, J.B.Lippincott Company.

Shapley, R. and Perry, V. H. (1986). Cat and monkey retinal ganglion cells and their visual functional roles. *Trends in Neuroscience* 9: 229-235.

Sharp, P. F. and Manivannan, A. (1997). The scanning laser ophthalmoscope. *Physics in Medecine and Biology* 42: 951-966.

Shields, M. B. (1998). *Chapter 5. Optic nerve head and peripapillary retina*. Textbook of Glaucoma. Baltimore, Maryland, Williams & Wilkins: 72-107.

Shihab, Z. M., Beebe, W. E. and Wentlanat, T. (1985). Possible significance of cilioretinal arteries in open-angle glaucoma. *Ophthalmology* 92: 880-883.

Shiose, Y. (1990). Intraocular pressure. New perspectives. *Survey of Ophthalmology* 34: 413-435.

Shiose, Y., Ito, T., Amano, M. and Kawase, Y. (1987). Relationship between mode of disc cupping and clinical features in primary open-angle glaucoma. *Glaucoma* 9: 150-158.

Shirakashi, M., Funaki, S., Funaki, H., Yaoedo, K. and Abe, H. (1999). Measurement of retinal nerve fibre layer by scanning laser polarimetry and high pass resolution perimetry in normal tension glaucoma with relatively high or low intraocular pressure. *British Journal of Ophthalmology* 83: 353-357.

Silveira, L. C. L. and Perry, V. H. (1991). The topography of magnocellular projecting ganglion cells (M-ganglion cells) in the primate retina. *Neuroscience* 40: 217-237.

Silver, D. and Farrell, R. (1994). Validity of pulsatile ocular blood flow measurements. *Survey of Ophthalmology* 38: s72-s80.

Silver, D. M., Farrell, R. A., Langham, M. E., O'Brien, V. and Schilder, P. (1989). Estimation of pulsatile ocular blood flow from intraocular pressure. *Acta Ophthalmologica (supplementum)* 67: 25-29.

Silverman, S. E., Trick, G. L. and Hart, W. M. (1990). Motion perception is abnormal in primary open angle glaucoma and ocular hypertension. *Investigative Ophthalmology and Visual Science* 31: 722-729.

Sogano, S., Tomita, G. and Kitazawa, Y. (1993). Changes in retinal nerve fiber layer thickness after reduction of intraocular pressure in chronic open-angle glaucoma. *Ophthalmology* 100: 1253-1258.

Sommer, A. (1989). Intraocular Pressure and Glaucoma. *American Journal of Ophthalmology* 107: 186-188.

Sommer, A. (1991). Relationship between intraocular pressures and primary open angle glaucoma among white and black americans. The Baltimore eye study. *Archives of Ophthalmology* 109: 1090-1095.

Sommer, A., D'Anna, S. and Kues, H. (1983). High resolution photography of the retinal nerve fibre layer. *Am J Ophthalmol* 96: 535-539.

Sommer, A., Katz, J., Quigley, H., Miller, N., Robin, A. and Richter, R. (1991). Clinically detectable nerve fibre atrophy precedes the onset of glaucomatous visual field loss. *Archives of Ophthalmology* 109: 77-83.

Sommer, A., Miller, N., Pollack, I., Maumenee, A. E. and George, T. (1977). The nerve fibre layer in the diagnosis of glaucoma. *Archives of Ophthalmology* 95: 2149-2156.

Sommer, A., Quigley, H. A., Robin, A. L., Miller, N. R., Katz, J. and Arkell, S. (1984). Evaluation of Nerve Fiber Layer Assessment. *Archives of Ophthalmology* 102: 1766-1771.

Sonnsjo, B. and Krakau, C. E. T. (1993). Arguments for a vascular glaucoma etiology. *Acta Ophthalmologica* 71: 433-444.

Spaeth, G. L. (1994). Reversible changes in the optic disc and visual field in glaucoma. *Current Opinion in Ophthalmology* 5: 36-45.

Sponsel, W. E., Arano, S., Trigo, Y. and Mensah, J. (1998). Clinical classification of glaucomatous visual field loss by Frequency Doubling Perimetry. *American Journal of Ophthalmology* 125: 830-836.

Sterling, P., Calkins, D. J., Kulg, K. G., Schein, S. J. and Matsumoto, Y. (1994). Parallel pathways from primate fovea. *Investigative Ophthalmology and Visual Science* 35: 2001.

Stewart, W. C. and Chauhan, B. C. (1995). Newer visual function tests in the evaluation of glaucoma. *Survey of Ophthalmology* 40: 119-135.

Stewart, W. C. and Hunt, H. H. (1993). Threshold variation in automated perimetry. *Survey of Ophthalmology* 37: 353-361.

Stone, J. (1983). *Parallel Processing in the Visual System: The Classification of Retinal Ganglion Cells and its Impact on the Neurobiology of vision.* New York, Plenum Press.

Sugiyama, K., Tomita, G., Kawase, K., Onda, E., Hisashi, S., Hayakawa, T. and Kitazawa, Y. (1999). Disc hemorrhage and peripapillary atrophy in apparently healthy subjects. *Acta Ophthalmologica Scandinavica* 77: 139-142.

Sujimoto, K., Schotzau, A., Bergamin, O. and Zulauf, M. (1998). Optimizing distribution and number of test locations in perimetry. *Graefe's Archive for Clinical and Experimental Ophthalmology* 236: 103-108.

Sullivan, P., Cioffi, G. A., Wang, L., Johnson, C. A., Van Buskirk, E. M., Sherman, K. R. and Bacon, D. R. (1999). The influence of ocular pulsatility on scanning laser Doppler flowmetry. *American Journal of Ophthalmology* 128: 81-87.

Susanna, R. and Drance, S. M. (1978). Use of discriminant analysis. I. Prediction of visual field defects from features of the glaucoma disc. *Archives of Ophthalmology* 96: 1568-1570.

Swanson, E. A., Izatt, J. A. and Hee, M. R. (1993). In vivo retina imaging by optical coherence tomography. *Optics Letters* 18: 1864-1866.

Swanson, W. H. and Lynn, J. R. (1995). Interoperator variability in images obtained by laser polarimetry of the nerve fibre layer. *Journal of Glaucoma* 4: 414-418.

Takamoto, T. and Schwartz, B. (1989). Photogrammetric Measurement of Nerve Fibre Layer Thickness. *Ophthalmology* 96: 1315-1319.

Takamoto, T. and Schwartz, B. (1993). *Stereophotogrammetry*. The optic nerve in glaucoma. R. Varma and G. L. Spaeth. Philadelphia, J.B.Lippincott Company: 193-207.

Tamaki, Y., Araie, M., Nagahara, M. and Tomita, K. (1999). Acute effects of cigarette smoking on tissue circulation in human optic nerve head and choroid retina. *Ophthalmology* 6: 564-569.

Teesalu, P., Airaksinen, P. J., Tuulonen, A., Nieminen, H. and Alanko, H. (1997). Fluorometry of the crystalline lens for correcting blue-on-yellow perimetry results. *Investigative Ophthalmology and Visual Science* 38: 697-703.

Teesalu, P., Vihanninjoki, K., Airaksinen, P. J. and Tuulonen, A. (1998). Hemifield association between blue-on-yellow visual field and optic nerve head topographic measurements. *Graefe's Archive for Clinical and Experimental Ophthalmology* 236: 339-345.

Tezel, G., Kass, M. A., Kolker, A. E. and Wax, M. B. (1996). Comparative optic disc analysis in normal pressure glaucoma, primary open angle glaucoma and ocular hypertension. *Ophthalmology* 103: 2105-2113.

Tezel, G., Kolker, A. E., Kass, M. A., Wax, M. B., Gordon, M. and Siegmund, K. D. (1997). Parapapillary chorioretinal atrophy in patients with ocular hypertension. I. An evaluation as a predictive factor for the development of glaucomatous damage. *Archives of Ophthalmology* 115: 1503-1508.

Tielsch, J. M., Katz, J., Quigley, H. A., Miller, N. R. and Sommer, A. (1988). Intraobserver and interobserver agreement in measurement of optic disc characteristics. *Ophthalmology* 95: 350-356.

Tielsch, J. M., Katz, J., Singh, K., Quigley, H. A., Gottsch, J. D. and Javitt, J. C. (1991a). A population-based evaluation of glaucoma screening: The Baltimore eye survey. *American Journal of Epidemiology* 134: 1102-1110.

Tielsch, J. M., Katz, J., Sommer, A., Quigley, H. A. and Javitt, J. C. (1994). Family history and risk of primary open angle glaucoma: the Baltimore Eye Survey. *Archives of Ophthalmology* 112: 69-73.

Tielsch, J. M., Sommer, A., Katz, J., Royall, R. M., Quigley, H. A. and Javitt, J. C. (1991b). Racial variations in the prevalence of primary open-angle glaucoma. The Baltimore eye survey. *JAMA* 266: 369-374.

Tjon-Fo-Sang, M. J., de Vries, J. and Lemij, H. G. (1996). Measurement by nerve fiber analyzer of retinal nerve fiber layer thickness in normal subjects and patients with ocular hypertension. *American Journal of Ophthalmology* 122: 220-227.

Tjon-Fo-Sang, M. J. and Lemij, H. G. (1997). The sensitivity and specificity of nerve fiber layer measurements in glaucoma as determined with scanning laser polarimetry. *American Journal of Ophthalmology* 123: 62-69.

Tjon-Fo-Sang, M. J. and Lemij, H. G. (1998). Retinal nerve fibre layer measurements in normal black subjects as determined with scanning laser polarimetry. *Ophthalmology* 105: 78-81.

Tomita, G. and Honbe, K. (1994). Reproducibility of measurements by Scanning Laser Tomography in eyes before and after pilocarpine treatment. *Graefe's Archive for Clinical and Experimental Ophthalmology* 232: 406-408.

Topouzis, F., Peng, F., Kotas-Neumann, R., Garcia, R., Sanguinet, J., Yu, F. and Colemen, A. L. (1999). Longitudinal changes in optic disc topography of adult patients after trabeculectomy. *Ophthalmology* 106: 1147-1151.

Toth, C. A., Narayan, D. G., Boppart, S. A., Hee, M., Fujimoto, J. G., Birngruber, R., Cain, C. P., DiCarlo, C. D. and Roach, P. (1997). A comparison of retinal morphology and viewed by Optical Coherence Tomography and by light microscopy. *Archives of Ophthalmology* 115: 1425-1428.

Traquair, H. M. (1949). *An introduction to Clinical Perimetry*. London, Henry Klimpton Publishers.

Trew, D. R. and Smith, S. E. (1991a). Postural studies in pulsatile ocular blood flow: I. Ocular hypertension and normotension. *British Journal of Ophthalmology* 75: 66-70.

Trew, D. R. and Smith, S. E. (1991b). Postural studies in pulsatile ocular blood flow: II. Chronic open-angle glaucoma. *British Journal of Ophthalmology* 75: 71-75.

Trible, J. R. and Anderson, D. R. (1998). Factors associated with retrobulbar hemodynamic measurement at variable intraocular pressure. *Journal of Glaucoma* 7: 33-38.

Trope, G. E. and Britton, R. (1987). A comparison of Goldmann and Humphrey automated perimetry in patients with glaucoma. *British Journal of Ophthalmology* 71: 489-493.

Tsai, C. S., Ritch, R., Shin, D. H., Wan, J. Y. and Chi, T. (1992). Age-related decline of disc rim area in visually normal subjects. *Ohthalmology* 99: 29-35.

Tsai, C. S., Zangwill, L., Gonzalez, C., Irak, I., Garden, V., Hoffman, R. and Weinreb, R. (1995a). Ethnic differences in optic nerve head topography. *Journal of Glaucoma* 4: 248-257.

Tsai, C. S., Zangwill, L. and Sample, P. (1995b). Correlation of peripapillary retinal height and visual field in glaucoma and normal subjects. *Journal of Glaucoma* 4: 110-116.

Tsang, A. C., Harris, A., Kagemann, L. and Chung, H. S. (1999). Brightness alters Heidelberg retinal Flowmeter measurements in an in-vitro model. *Investigative Ophthalmology and Visual Science* 40: 795-799.

Tuck, M. W. and Crick, P. W. (1998). The age distribution of primary open angle glaucoma. *Ophthalmic Epidemiology* 5: 173-183.

Tuulonen, A. (1993). The morphological pattern of early glaucomatous damage. *Current Opinion in Ophthalmology* 4: 29-34.

Tuulonen, A. and Airaksinen, P. J. (1991). Initial glaucomatous optic disk and retinal nerve fiber layer abnormalities and their progression. *American Journal of Ophthalmology* 111: 485-490.

Tuulonen, A. and Airaksinen, P. J. (1996). Polarimetry of the retinal nerve fibre layer. *Current Opinion in Ophthalmology* 7: 34-38.

Tuulonen, A., Airaksinen, P. J., Schwartz, B. and al, e. (1992). Neuroretinal rim area measurement by configuration and by pallor in ocular hypertension and glaucoma. *Ophthalmology* 99: 1111-1116.

Tuulonen, A., Takamoto, T. and Da-Ching (1997). Optic disk cupping and pallor measurements of patients with a disk haemorrhage. *American Journal of Ophthalmolgy* 103: 505-511.

Tyler, C. (1974). Observations on spatial-frequency doubling. *Perception* 3: 81-86.

Tyrrell, R. A. and Owens, D. A. (1988). A rapid technique to assess the resting states of the eyes and other threshold phenomena: The Modified Binary Search (MOBS). *Behaviour Research Methods, Instruments and Computers* 20: 137-141.

Uchida, H., Brigatti, L. and Caprioli, J. (1996). Detection of structural damage from glaucoma with confocal laser image analysis. *Investigative Ophthalmology and Visual Science* 37: 2393-2401.

Uchida, H., Yamamoto, T., Tomita, G. and Kitazawa, Y. (1999). Peripapillary atrophy in primary angle-closure glaucoma: A comparative study with primary open-angle glaucoma. *American Journal of Ophthalmology* 127: 121-128.

Van Buskirk, E. M. and Cioffi, G. A. (1992). Glaucomatous optic neuropathy. *American Journal of Ophthalmology* 113: 447-452.

Varma, R., Skaf, M. and Barron, E. (1996). Retinal nerve fiber layer thickness in normal human eyes. *Ophthalmology* 103: 2114-2119.

Varma, R., Spaeth, G. L. and Parker, K. W. (1993). *The optic nerve in glaucoma*. Philadelphia, J.B.Lippincott Company.

Varma, R., Steinmann, W. C. and Scott, I. U. (1992). Expert agreement in evaluating the optic disc for glaucoma. *Ophthalmology* 99: 215-221.

Varma, R., Tielsch, J. M., Quigley, H. A., Hilton, S. C., Katz, J., Spaeth, G. L. and Sommer, A. (1994). Race-, age-, gender-, and refractive error-related differences in the normal optic disc. *Archives of Ophthalmology* 112: 1068-1076.

Victor, J. D. and Shapley, R. M. (1979). The non-linear pathway of Y ganglion cells in the cat retina. *Journal of General Physiology* 74: 671-689.

Vihanninjoki, K., Tuulonen, A., Burk, R. O. W. and Airaksinen, P. J. (1997). Comparison of optic disc measurements by Heidelberg Retina Tomograph and manual planimetry techniques. *Acta Ophthalmologica Scandinavica* 75: 512-515.

Viswanathan, A. C., Fitzke, F. W. and Hitchings, R. A. (1997). Early detection of visual field progression in glaucoma: a comparison of PROGRESSOR and STATPAC 2. *British Journal of Ophthalmology* 81: 1037-1042.

Vogt, A. (1913). Herstellung eines gelbblauen Lichtfiltrats, in welchem die Macola Centrales in vivo in gelber Farbung erscheint, die Nervenfasern der Netzhaut und andere feine Einzelheiten derselben sichtbar werden,und der Grad der gelbfarbung der Linsen ophthalmoskopisch nachweisbar ist. *Graefe's Archive for Clinical and Experimental Ophthalmology* 84: 293.

Vogt, A. (1917). Die nervenfaserstreifung der menschlichen Netzhaut mit besonderer Berücksichtigung der Differentialdiagnose gegenüber pathologischen streifenförmigen Reflexen (präretinalen Fältelungen). *Klin Monatsbl Augenheilkd* 58: 399-411.

Vogt, U., Morland, A., Migdal, C. and Ruddock, K. (1998). Spatial and temporal visual filtering in patients with glaucoma and ocular hypertension. *Eye* 12: 691-696.

von Graefe, A. (1857). Ueber die Iridctomie bei Glaucom und uber den glaucomatosen Prozess. *Graefes Arch Ophthalmol* 3: 456-560.

Vrabec, F. (1966). The temporal raphe of the human retina. *American Journal of Ophthalmology* 62: 926-938.

Webb, R. H., Hughes, G. W. and Delori, F. C. (1987). Confocal Scanning Laser Ophthalmoscope. *Applied Optics* 26: 1492-1499.

Weber, A. J., Chen, H., Hubbard, W. C. and Kaufman, P. L. (2000). Experimental glaucoma and cell size, density and number in the primate lateral geniculate nucleus. *Investigative Ophthalmology and Visual Science* 41: 1370-1379.

Weber, A. J., Kaufman, P. L. and Hubbard, W. C. (1998). Morphology of single ganglion cells in the glaucomatous retina. *Investigative Ophthalmology and Visual Science* 39: 2304-2320.

Weber, J. and Rau, S. (1992). The properties of perimetric thresholds in normal and glaucomatous eyes. *German Journal of Ophthalmology* 1: 79-85.

Weber, J., Schultze, T. and Ulrich, H. (1989). The visual field in advanced glaucoma. *International Ophthalmology* 13: 47-50.

Webster, A. R., Luff, A. J., Canning, C. R. and Elkington, A. R. (1993). The effect of pilocarpine on the glaucomatous visual field. *British Journal of Ophthalmology* 77: 721-725.

Weinreb, R. N., Dreher, A. W., Coleman, A., Quigley, H., Shaw, B. and Reiter, K. (1990). Histopathologic validation of Fourier-ellipsometry measurements of retinal nerve fiber layer thickness. *Archives of Ophthalmology* 108: 557-560.

Weinreb, R. N., Lusky, M., Bartsch, D. U. and Morsman, D. (1993). Effect of repetitive imaging on topographic measurements of the optic nerve head. *Archives of Ophthalmology* 111: 636-638.

Weinreb, R. N. and Sample, P. A. (1991). *Short-wavelength visual field testing in eyes with primary open-angle glaucoma.* Glaucoma Update IV. G.K.Krieglstein. Berlin, Heidelberg, Springer-Verlag: 146-155.

Weinreb, R. N., Shakiba, S., Sample, P. A., Shahrokni, S., van Horn, S., Garden, V. S., Asawaphureekorn, S. and Zangwill, L. (1995a). Association between quantitative nerve fiber layer measurement and visual field loss in glaucoma. *American Journal of Ophthalmology* 120: 732-738.

Weinreb, R. N., Shakiba, S. and Zangwill, L. (1995b). Scanning laser polarimetry to measure the nerve fiber layer of normal and glaucomatous eyes. *American Journal of Ophthalmology* 119: 627-636.

Wennmalm, A. (1982). Effect of cigarette smoking on basal and carbon dioxide stimulated cerebral blood flow in man. *Clinical Physiology* 2: 529.

Wild, J., Dengler-Harles, M., Searle, A., O'Neill, E. and Crews, S. (1989). The influence of the learning effect on automated perimetry in patients with suspected glaucoma. *Acta Ophthalmologica* 67: 537-545.

Wild, J., Searle, A., Dengler-Harles, M., O'Neill, E. and Crews, S. (1991). Long-term follow-up of baseline learning and fatigue effects in the automated perimetry of glaucoma and ocular hypertensive patients. *Acta Ophthalmologica* 69: 210-216.

Wild, J. M., Cubbidge, R. P., Pacey, I. E. and Robinson, R. (1998). Statistical aspects of the normal visual field in short-wavelength automated perimetry. *Investigative Ophthalmology & Visual Science* 39: 54-63.

Wild, J. M. and Hudson, C. (1995). The attenuation of blue-on-yellow perimetry by the macular pigment. *Ophthalmology* 102: 911-917.

Wild, J. M., Hussey, M., Flanagan, J. G. and Trope, G. E. (1993). Pointwise topographical and longitudinal modeling of the visual field in glaucoma. *Investigative Ophthalmology and Visual Science* 34: 1907-1916.

Wild, J. M. and Moss, I. D. (1996). Baseline alterations in blue-on-yellow normal perimetric sensitivity. *Graefe's Archive for Clinical and Experimental Ophthalmology* 234: 141-149.

Wild, J. M., Moss, I. D., Whitaker, D. and O'Neill, E. C. (1995). The statistical interpretation of blue-on-yellow visual field loss. *Investigative Ophthalmology and Visual Science* 36: 1398-1410.

Wild, J. M., Pacey, I. E., Hancock, S. A. and Cunliffe, I. A. (1999a). Between-algorithm, between-individual differences in normal perimetric sensitivity: Full threshold, FASTPAC, and SITA. *Investigative Ophthalmology & Visual Science* 40: 1152-1161.

Wild, J. M., Pacey, I. E., O'Neill, E. C. and Cunliffe, I. A. (1999b). The SITA perimetric threshold algorithms in glaucoma. *Investigative Ophthalmology and Visual Science* 40: 1998-2009.

Wilensky, J. T. (1991). Diurnal variations in intraocular pressure. *Transactions of the American Ophthalmological Society* 89: 758-790.

Wilensky, J. T., Gandhi, M. D. and Pan, T. (1978). Racial influences in open-angle glaucoma. *Annals of Ophthalmology* 10: 1398-1402.

Williamson, T. H. (1994). What is the use of ocular blood flow measurement? *British Journal of Ophthalmology (Editorial)* 78: 326.

Williamson, T. H. and Harris, A. (1996). Color Doppler Ultrasound Imaging of the Eye and Orbit. *Survey of Ophthalmology* 40: 255-267.

Williamson, T. H., Lowe, G. D. O. and Baxter, G. M. (1995). Influence of age, systemic blood pressure, smoking and blood velocity on orbital blood velocities. *British Journal of Ophthalmology* 79: 17-22.

Wilson, M. R. (1990). Epidemiological features of glaucoma. *International Ophthalmology Clinics* 30: 153-159.

Wilson, R. M., Hertzman, E., Walker, A. M., Childshaw, K. and Epstein, D. L. (1987). A case-control study of risk factors in open-angle glaucoma. *Archives of Ophthalmology* 105: 1066-1071.

Wolff, E. and Penman, G. G. (1950). The position occupied by the peripheral retinal fibres in the nerve-fibre layer and at the nerve head. *Concilium Ophthalmologicum 16th, Britannia*: 625-635.

Wollstein, G., Garway-Heath, D. F. and Hitchings, R. A. (1998). Identification of early glaucoma cases with the scanning laser ophthalmoscope. *Ophthalmology* 105: 1557-1563.

Wolter, I. R. (1955). The astroglia of the human retina. *American Journal of Ophthalmology* 40: 88-99.

Yamada, N., Chen, P. P., Mills, R. P., Leen, M. M., Lieberman, M. F., Stamper, R. L. and Stanford, D. C. (1999). Screening for Glaucoma with Frequency-Doubling Technology and Damato Campimetry. *Archives of Ophthalmology* 117: 1479-1484.

Yamagishi, N., Anton, A., Sample, P. A., Zangwill, L., Lopez, A. and Weinreb, R. N. (1997). Mapping structural damage of the optic disk to visual field defect in glaucoma. *American Journal of Ophthalmology* 123: 667-676.

Yang, Y. C., Hulbert, M. F. G., Batterbury, M. and Clearkin, L. G. (1997). Pulsatile ocular blood flow measurements in healthy eyes: Reproducibility and reference values. *Journal of Glaucoma* 6: 175-179.

Yoshida, A., Ogasacuara, H., Fujio, N. and al, E. (1998). Comparison of short-and long-term effects of betaxolol and timold on human retinal circulation. *Eye* 12: 848-853.

Youngquist, R. C., Carr, S. and Davies, D. E. N. (1987). Optical coherence-domain reflectometry : a new optical evaluation technique. *Optical Letters* 12: 158-160.

Yucel, Y. H., Zhang, Q., Gupta, N., Kaufman, P. and Weinreb, R. N. (2000). Loss of neurons in magnocellular and parvocellular layers of the lateral geniculate nucleus in glaucoma. *Archives of Ophthalmology* 118: 378-384.

Zadnik, K., Mutti, D. O. and Bullimore, M. (1994). Use of statistics for comparing two measurement methods. *Optometry and Vision Science* 71: 539-540.

Zalta, A. H. (1991). Use of a central 10-degree field and size-V stimulus to evaluate and monitor small central island of vision in endstage glaucoma. *British Journal of Ophthalmology* 75: 151-154.

Zalta, A. H. (2000). Limitations of the Glaucoma Hemifield Test in identifying early glaucomatous field loss. *Annals of Ophthalmology* 32: 33-45.

Zangwill, L., Irak, I., Berry, C. and Garden, V. (1997). Effect of cataract and pupil size on image quality with confocal scanning laser ophthalmoscopy. *Archives of Ophthalmology* 115: 983-990.

Zangwill, L., Van Horn, S., Lima, M. D. S. and Sample, P. A. (1996). Optic nerve head topography in ocular hypertensive eyes using confocal scanning laser ophthalmoscopy. *American Journal of Ophthalmology* 122: 520-525.

Zeyen, T. G. and Caprioli, J. (1993). Progression of disc and field damage in early glaucoma. *Archives of Ophthalmology* 111: 62-65.

Zhou, Q. and Knighton, R. (1997). Light scattering and form birefringence of parallel and cylindrical arrays. *Applied Optics* 36: 2273-2285.

Zulauf, M. and Caprioli, J. (1991). Fluctuation of the visual field in glaucoma. *Ophthalmology clinics of North America (Contemporary Issues in Glaucoma in Ophthalmology)* 4: 671-697.

APPENDIX: A.1. DEFINITIONS OF THE HEIDELBERG RETINA TOMOGRAPHY STEREOMETRIC PARAMETERS.

Disc Area (mm^2)	The total area within the contour line, ie the disc area.
Cup Area (mm^2)	Area below the reference plane.
C/D Area Ratio	Ratio of cup area to disc area.
Rim Area (mm^2)	Area above the reference plane.
Height Variation in Contour (mm)	Difference in height between the most elevated and depressed points of the contour line.
Cup Volume (mm^3)	Volume below the reference plane.
Rim Volume (mm^3)	Volume above the reference plane.
Mean Cup Depth (mm)	Mean depth inside the contour line (relative to the curved surface).
Maximum Cup Depth (mm)	Maximum depth inside the contour (relative to the curved surface).
Cup Shape Measure	An index of the overall optic nerve head shape, also known as the third central moment or 'skewness'. The value is derived from the frequency distribution of the depth values both within the contour line and below the curved surface. Negative values of the parameter are associated with normal eyes possessing a flat cup with a high proportion of small depth values, whilst positive values indicate glaucomatous cupping, with a deep cup and steep sloping sides associated with many high depth values.
Mean RNFL thickness (mm)	Mean distance between the retinal surface along the contour line and the standard reference plane.
RNFL Cross-sectional area (mm^2)	Mean distance between the retinal surface and the standard reference plane along the contour line multiplied by the length of the contour line.
CLASS	A new parameter which classifies an optic nerve head according to a multivariate discriminant analysis (Mikelberg 1995).

APPENDIX A.2 HISTOLOGICAL ESTIMATES OF MONKEY AND HUMAN RETINAL NERVE FIBRE LAYER THICKNESS.

			Regional Thickness; mean ± standard deviation (μm)							
Author	**Monkey or Human**	**Distance from the ONH (μm)**	**Superior**	**Superior-Temporal**	**Temporal**	**Inferior-Temporal**	**Inferior**	**Inferior-Nasal**	**Nasal**	**Superior-Nasal**
(Radius 1980)	Squirrel Monkey	100	38 ± 6	73 ± 5	22 ± 5	77 ± 7	42 ± 7	58 ± 6	61 ± 9	59 ± 9
(Radius 1980)	Owl Monkey	100	39 ± 5	50 ± 6	20 ± 3	44 ± 5	44 ± 5	23 ± 3	19 ± 1	35 ± 3
(Radius 1980)	Owl Monkey	400-600	9 ± 1	9 ± 1	11 ± 1	7 ± 1	8 ± 1	10 ± 1	8 ± 1	8 ± 1
(Radius 1980)	Rhesus Monkey	100	228 ± 9	143 ± 30	33 ± 5	100 ± 21	194 ± 9	62 ± 12	37 ± 5	44 ± 6
(Radius 1980)	Rhesus Monkey	400-600	49 ± 6	75 ± 18	20 ± 9	62 ± 12	31 ± 6	9 ± 3	23 ± 2	20 ± 2
(Quigley and Addicks 1982)	Cynomolgus Monkey	At the ONH Rim	320				320			
(Quigley and Addicks 1982)	Cynomolgus Monkey	Midway ONH to Fovea	82	65	33	68	74	40	36	4
(Varma et al. 1996)	Human	At disc margin	405 ± 28	324	316 ± 24	367	376 ± 40	358	372 ± 43	367
(Varma et al. 1996)	Human	50	349	289	246	337	343	325	316	347
(Varma et al. 1996)	Human	100	307	269	226	302	318	303	290	331
(Dichtl et al. 1999)	Human	At disc margin	240 ± 57		170 ± 58		266 ± 64		220 ± 70	
(Dichtl et al. 1999)	Human	At disc margin	313 ± 38	167 ± 64	131 ± 15	276 ± 44	397 ± 58	215 ± 53	165 ± 19	218 ± 22

APPENDIX: A.3. KEY TO THE ABBREVIATIONS USED IN THE TEXT.

ANOVA	Analysis of Variance
BP_d	Diastolic Blood Pressure
BP_S	Systolic Blood Pressure
C(1.0)	Cortical Cataract (Grade 1.0)
CA	Cup Area
CDAR	Cup/Disc Area Ratio
CDI	Colour Doppler Imaging
CDR	Cup/Disc Ratio
CoV	Coefficient of Variation
CPSD	Corrected Pattern Standard Deviation
CRA	Central Retinal Artery
CS	Curved Surface
CSM	Cup Shape Measure
CV	Cup Volume
DA	Disc Area
EDV	End Diastolic Velocity
FDT	Frequency Doubling Technology
FL	Fixation Losses
FN	False Negatives
FP	False Positives
GCP	Glaucoma Change Probability
GH	General Height
GHT	Glaucoma Hemifield Test
HFA	Humphrey Field Analyzer
HRF	Heidelberg Retina Flowmeter
HRT	Heidelberg Retina Tomograph
HVC	Height Variation in Contour
ICA	Internal Carotid Artery
ILM	Inner Limiting Membrane
INR	Inferior Nasal Retina
IOP	Intraocular pressure
ITR	Inferior Temporal Retina
LC	Lamina Cribrosa
LDF	Laser Doppler Flowmetry (-er)
LDV	Laser Doppler Velocimetry
LGN	Lateral Geniculate Nucleus
LOCS	Lens Opacities Classification System
LPCA	Long Posterior Ciliary Artery
LTS	Laser Tomographic Scanner
LWS	Long-Wavelength-Sensitive
MD	Mean Deviation
MHC	Mean Height in Contour
MOBS	Modified Binary Search
MS	Mean Sensitivity
MTI	Mean Topographic Image

MWS	Medium-Wavelength-Sensitive
NC(3.0)	Nuclear Colour (Grade 3.0)
NO(3.0)	Nuclear Opalescence (Grade 3.0)
NR	Nasal Retina
NRR	Neuroretinal Rim
OA	Ophthalmic Artery
OCT	Optical Coherence Tomograph (-y)
OHT	Ocular hypertension
OHT(H)	High Risk Ocular hypertension
OMA	Ocular Media Absorption
ONH	Optic Nerve Head
P(1.0)	Posterior Subcapsular Cataract (Grade 1.0)
PCA	Posterior Ciliary Artery
PD	Pattern Deviation
PI	Pulsatile Index
POAG	Primary Open Angle Glaucoma
POBF	Pulsatile Ocular Blood Flow
PSD	Pattern Standard Deviation
PSV	Peak Systolic Velocity
RA	Rim Area
RBC	Red Blood Cell
RDAR	Rim/Disc Area Ratio
RHR	Relative High Reflectance
RI	Resistive Index
RLR	Relative Low Reflectance
RNFL	Retinal Nerve Fibre Layer
RNFLT	Retinal Nerve Fibre Layer Thickness
RSD	Ranked Segment Distribution
RV	Rim Volume
SD	Standard Deviation
SF	Short-Term Fluctuation
SITA	Swedish Interactive Thresholding Algorithm
SLDF	Scanning Laser Doppler Flowmetry
SLO	Scanning Laser Ophthalmoscope
SNR	Superior Nasal retina
SPCA	Short Posterior Ciliary Artery
STR	Superior Temporal Retina
SWAP	Short-Wavelength Automated Perimetry
SWS	Short-Wavelength-Sensitive
TD	Total Deviation
TMC	Third Moment in Contour
TOP	Tendency Orientated Perimetry
TR	Temporal Retina
W-W	White-on-White